TESIS DE LA UNIVERSIDAD DE ZARAGOZA

2023 211

Carlos Javier Ortún Terrazas

In silico approach towards neuro-occlusal rehabilitation for the early correction of dental malocclusions in children

Director/es
Cegoñino Banzo, José

ISSN 2254-7606

Prensas de la Universidad
Universidad Zaragoza

ISSN 2254-7606

Universidad Zaragoza
1542

Tesis Doctoral

IN SILICO APPROACH TOWARDS NEURO-OCCLUSAL REHABILITATION FOR THE EARLY CORRECTION OF DENTAL MALOCCLUSIONS IN CHILDREN

Autor

Carlos Javier Ortún Terrazas

Director/es

Cegoñino Banzo, José

UNIVERSIDAD DE ZARAGOZA
Escuela de Doctorado

2021

In silico Approach towards
Neuro-Occlusal Rehabilitation
for the Early Correction of Dental Malocclusions in Children

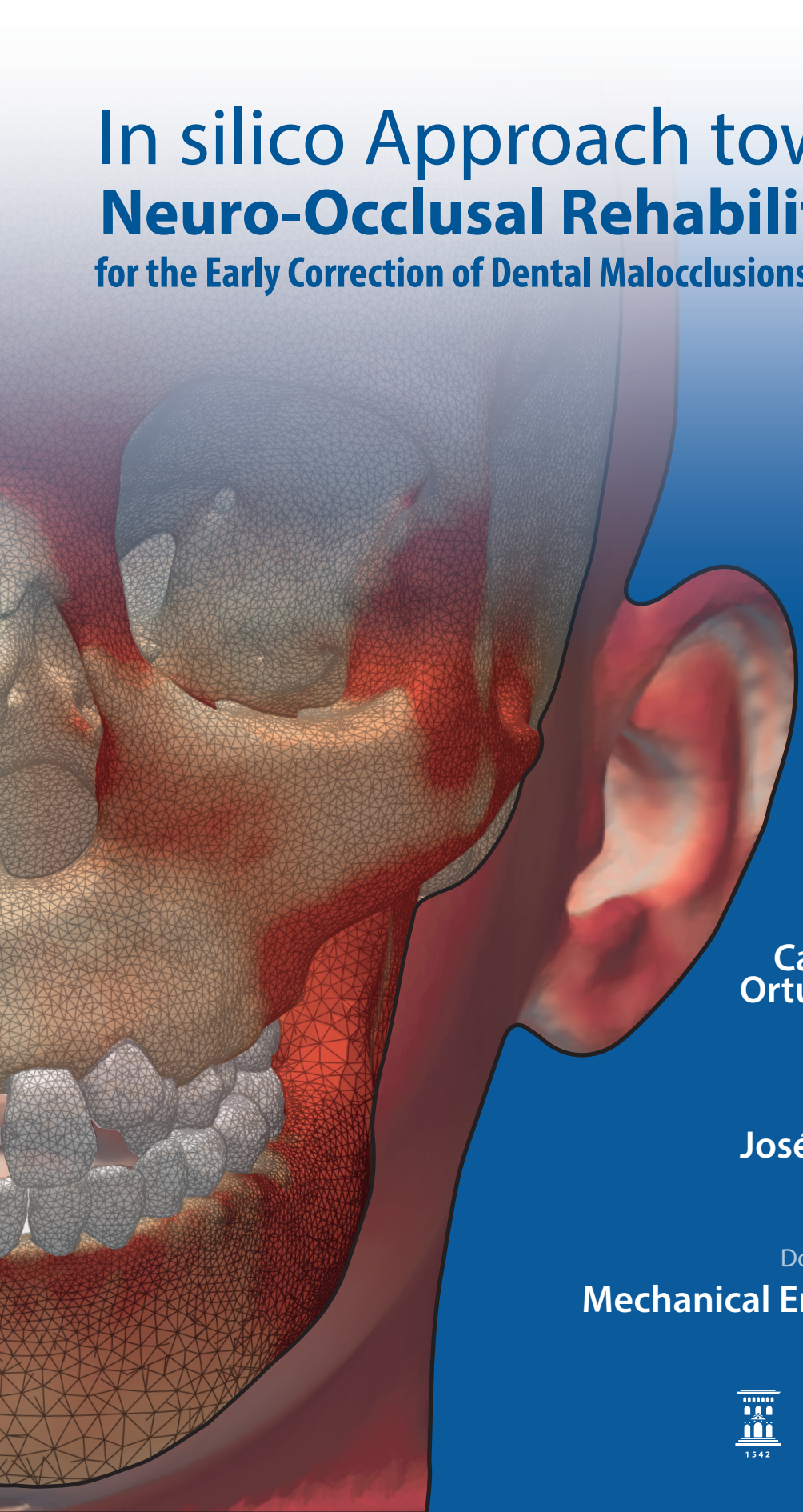

PhD thesis by

Carlos Javier Ortún Terrazas

Doctoral advisor

José Cegoñino

Doctoral Degree in

Mechanical Engineering

Universidad Zaragoza

1542

In silico Approach towards Neuro-Occlusal Rehabilitation for the Early Correction of Dental Malocclusions in Children

PhD thesis by

Carlos Javier Ortún Terrazas

Doctoral advisor

José Cegoñino

Doctoral Degree in
Mechanical Engineering

School of Engineering and Architecture
University of Zaragoza
September, 2021

Servicio de Publicaciones
ISSN 2254-7606

In silico Approach towards Neuro-Occlusal Rehabilitation for the Early Correction of Dental Malocclusions in Children

PhD thesis by

Carlos Javier Ortún Terrazas

Doctoral advisor

Dr José Cegoñino Banzo

Doctoral Degree in Mechanical Engineering

School of Engineering and Architecture

University of Zaragoza

September, 2021

D. **José Cegoñino Banzo**, Profesor Titular del Departamento de Ingeniería Mecánica de la Escuela de Ingeniería y Arquitectura de la Universidad de Zaragoza, y director de la Tesis Doctoral titulada: "*In silico* Approach towards Neuro-Occlusal Rehabilitation for the Early Correction of Dental Malocclusions in Children", realizada por el aspirante a título de doctor, D. Carlos Javier Ortún Terrazas,

DISPONE,

Que la memoria de Tesis Doctoral ha sido realizada bajo su dirección en el programa de Doctorado en Ingeniería Mecánica, en la Universidad de Zaragoza, y que se corresponde con el proyecto de Tesis aprobado por la Comisión Académica de Doctorado del Programa el 6 de octubre de 2016.

Que la memoria de Tesis Doctoral cumple con los requisitos para su presentación en modalidad de Tesis por compendio de publicaciones, establecidos por el art. 20 del Reglamento sobre Tesis Doctorales de la Universidad de Zaragoza, aprobado por acuerdo de 25 de junio de 2020, del Consejo de Gobierno de la Universidad.

Que el proyecto de Tesis reúne requisitos para optar a la mención de "Doctor Internacional" establecidos por el art. 18 del Reglamento sobre Tesis Doctorales y el art. 15 del Real Decreto 99/2011, de 28 de enero, por el que se regulan las enseñanzas oficiales de doctorado, y que ha sido modificado por el Real Decreto 195/2016 de 13 de mayo, por el que se establecen los requisitos para la expedición del Suplemento Europeo al Título Universitario de Doctor.

Por lo anterior, se APRUEBA su presentación en la modalidad de Tesis por compendio de publicaciones y con mención de "Doctor Internacional". y para que así conste, firma en Zaragoza a 16 de junio de 2021.

Fdo.: D. José Cegoñino Banzo

De acuerdo con el art.15 de Real Decreto 99/2011, modificado por la disposición final tercera del Real Decreto 195/2016, esta Tesis Doctoral reúne los requisitos para incluir la mención internacional en el título de doctor, ya que la memoria cumple con los apartados b-d del art. 15 del Real Decreto 99/2011, y el doctorando ha realizado una estancia de investigación de tres meses en una institución de enseñanza superior fuera de España (art.15.1a), concretamente en la "School of Engineering and Computer Science" de la Universidad de Hull en Reino Unido del 30 de agosto de 2018 al 1 de diciembre de 2018, bajo la supervisión del Profesor Michael J. Fagan.

Asimismo, en virtud del art.15 del Real Decreto 99/2011, modificado por el Real Decreto 195/2016, la presente memoria ha sido revisada por dos expertos Doctores pertenecientes a instituciones de Educación Superior o institutos de investigación no españoles. Concretamente, esta memoria de tesis ha sido revisada favorablemente por D. Renato Manuel Natal Jorge, Catedrático del Departamento de Ingeniería Mecánica de la Universidad de Oporto y por D. Eiji Tanaka, Catedrático en el Departamento de Ortodoncia y Ortopedia Dentofacial en la Facultad de Ciencias Biomédicas de la Universidad de Tokushima.

Adicionalmente, de acuerdo con el art. 20 del Reglamento sobre Tesis Doctorales de la Universidad de Zaragoza, esta Tesis Doctoral reúne los requisitos para ser presentada bajo la modalidad de tesis por compendio de publicaciones, al cumplir los requisitos establecidos por la Comisión Académica del programa de Doctorado (art.20.2), y tener un mínimo de cuatro artículos con unidad temática (art.20.1), de los que al menos tres están publicados en revistas del "Journal of Citation Reports", como se detalla a continuación:

- **Manuscrito 1:** Towards an early 3D-diagnosis of craniofacial asymmetry by computing the accurate midplane. A PCA-based method
  Autores: Javier Ortún-Terrazas, Michael J. Fagan, José Cegonino, Edson Illipronti-Filho, Amaya Pérez del Palomar
  Estado: Publicado, 2020. Computer Methods and Programs in Biomedicine 191, 105397. doi: 10.1016/j.cmpb.2020.105397
  Nombre de la revista: Computer Methods and Programs in Biomedicine
  Índice de impacto JCR (2019): 3.632
  Categorías de Web of Science: Computer Science, Interdisciplinary Applications; Computer Science, Theory & Methods; Engineering, Biomedical; Medical Informatics

- **Manuscrito 2:** In silico study of cuspid' periodontal ligament damage under parafunctional and traumatic conditions of whole-mouth occlusions. A patient-specific evaluation
  Autores: Javier Ortún-Terrazas, José Cegonino, Amaya Pérez del Palomar
  Estado: Publicado, 2020. Computer Methods and Programs in Biomedicine, 184, 105107. doi: 10.1016/j.cmpb.2019.105107
  Nombre de la revista: Computer Methods and Programs in Biomedicine
  Índice de impacto JCR (2019): 3.632
  Categorías de Web of Science: Computer Science, Interdisciplinary Applications; Computer Science, Theory & Methods; Engineering, Biomedical; Medical Informatics

- **Manuscrito 3:** Computational characterization of the porous-fibrous behavior of the soft tissues in the temporomandibular joint
  Autores: Javier Ortún-Terrazas, José Cegonino, Amaya Pérez del Palomar
  Estado: Publicado, 2020. Journal of Biomedical Materials Research Part B: Applied Biomaterials, 108(5), 2204-2217. doi: 10.1002/jbm.b.34558
  Nombre de la revista: Journal of Biomedical Materials Research Part B: Applied Biomaterials
  Índice de impacto JCR (2019): 2.831
  Categorías de Web of Science: Engineering, Biomedical; Materials Science, Biomaterials

- **Manuscrito 4:** Biomechanical impact of the porous-fibrous tissue behaviour in the temporomandibular joint movements. An in silico approach
  Autores: Javier Ortún-Terrazas, José Cegonino, Amaya Pérez del Palomar
  Estado: Publicado, 2021. Journal of the Mechanical Behavior of Biomedical Materials, 104542. doi: 10.1016/j.jmbbm.2021.104542
  Nombre de la revista: Journal of the Mechanical Behavior of Biomedical Materials
  Índice de impacto JCR (2019): 3.372
  Categorías de Web of Science: Engineering, Biomedical; Materials Science, Biomaterials

Además de los 4 artículos anteriores, en el capítulo 2 de esta memoria de tesis se incluyen 3 manuscritos también publicados en revistas indexadas en el "Journal of Citation Reports" y 2 manuscritos que se encuentran en fase de revisión.

"*Es más fácil caminar colina abajo que hacia arriba,*
pero las mejores vistas se ven desde lo alto"
"*It is easier to go down a hill than up,*
but the view is from the top"

Arnold Bennett

Agradecimientos

Al igual que en este proyecto de investigación, la esencia de mi etapa predoctoral la resumo no sólo por sus objetivos, sino por el camino que me ha llevado a conseguirlos. Quiero agradecer así, a todos aquellos que, como un viaje en tren, me han acompañado a lo largo de este trayecto.

En primer lugar, a mi director de tesis, el Dr. José Cegoñino, que me iniciado en este viaje y me han acompañado a lo largo de esta etapa. Su supervisión es para mí un ejemplo, que sin duda me servirá en mi futuro. También a la Dra. Amaya Pérez del Palomar cuyos trabajos previos han sido una fuente de inspiración para mis investigaciones. Quisiera agradecer también al Dr. Ángel Sampietro su generosa supervisión y consejos, tanto profesionales como personales y a los Dres. Edson Illipronti-Filho y Urbano Santana Penín por su colaboración en el arranque de esta investigación. Así como al resto de profesores del Área de Mecánica de Medios Continuos y Teoría de Estructuras, cuyas investigaciones me animan a seguir trabajando.

A mi compañero de asiento, Alberto, por acompañarme en jornadas de trabajo interminables y confiarme su amistad en los descansos de mitad de la tarde. A nuestras compañeras de mesa, Bea y Silvia, por su incansable escucha y sus risas cómplices a los chistes malos. A Javi, Julio y Gabriele por seguir hasta el final, y a Andrea, Isma, Jorge, Mar, Borau, Mena, Ana y demás dinosaurios del laboratorio que abandonaron antes el tren. También al resto de compañeros maños, catalanes, gallegos, portugueses, colombianos, mexicanos, italianos, franceses, y a los grandes amigos que dejé en Hull, tanto en el 26 de Raglan Street como en la Universidad. En especial, al Prof. Michael Fagan que hizo que mi estancia en la Universidad de Hull fuese aún más agradable. Fuera ya del mundo investigador, quiero agradecer a la familia cerbuna, a la cuadrilla y en especial a Mario y Lucia, por enseñarme a valorar el viaje y a disfrutar de los pequeños momentos. Quiero extender mi agradecimiento a mi familia y amigos de mi pueblo, Casalarreina, y en especial al "bar service" del café-vagón Plata, que me ha sofocado el calor de los meses de verano.

A mi familia. Mis padres, Jesús y Elisa, y a mi hermano, Alberto, que, como buenos conductores, me han guiado y conducido siempre para ser mejor. Este mérito es también vuestro. Por último, a mis abuelos cuya luz iluminará siempre mi camino.

Acknowledgments

As in this research, I summarize the heart of my predoctoral years not only by their goals but also by the way in which I have achieved them. Therefore, I would like to thank everyone who, like in a train journey, has been with me throughout this journey.

Firstly, to the supervisor of my dissertation, Dr José Cegoñino, who introduced and followed me throughout this journey. Their supervision has been an example, which will undoubtedly assist me in my professional future. In addition, to Dr Amaya Pérez del Palomar whose previous investigations have been a source of inspiration for my current research. I would also like to thank Dr Ángel Sampietro his generous assistance and advice, both professional and personal ones, and to Drs Edson Illipronti-Filho and Urbano Santana Penín for their collaboration in starting this research. Likewise, to the rest of the teachers in the area of Mechanics of Continuous Media and Theory of Structures, whose investigations encourage me to continue working.

To my seatmate, Alberto, for staying with me on long working days and trusting me his friendship at the mid-afternoon breaks. To our table colleagues, Bea and Silvia, for their tireless listening and their complicit humour at bad jokes. To Javi, Julio and Gabriele for following me until the journey's end, and to Andrea, Ismael, Jorge, Mar, Carlos, Andrés, Ana and the other dinosaurs in the lab who disembarked earlier. Also, to the rest of my lab colleagues from Catalonia, Galicia, Portugal, Colombia, Mexico, Italy, France, and the great mates I met in Hull, both in the 26th of Raglan Street and in the University. In particular, to Prof Michael Fagan who turned my stay at the University of Hull even more comfortable. Out of the research community, I would also like to thank the Cerbuna' family, the “cuadrilla” and in particular, to Mario and Lucia, for teaching me the value of the journey and the importance of the small things. I would also like to extend thanks to the family and friends of my village, Casalarreina, and particularly to the Plata’s bar service, which suffocated me during the heat of the summer months.

To my family. To my parents, Jesus and Elisa, and to my brother, Alberto, who, as good drivers, have always guided and encouraged me to be better. This merit is also yours. Finally, to my grandparents, whose light will always illuminate my way.

Resumen

El trabajo aquí presentado tiene por objetivo evaluar computacionalmente el efecto de los tratamientos tempranos, y en particular de la Rehabilitación Neuro-oclusal (RNO), en la corrección de maloclusiones dentales en la infancia, comprobando su impacto en el desarrollo y funcionamiento del complejo craneofacial. Esta investigación, pretende ser además una guía en la modelización computacional del complejo craneofacial, para que futuros investigadores, ingenieros, odontólogos y médicos puedan incorporar modelos biomecánicos en sus estudios.

De entre las maloclusiones, se estudió la mordida cruzada unilateral (MCU, en inglés, UXB) ya que es una causa frecuente del desarrollo asimétrico del complejo craneofacial y afecta alrededor del 11.7 % de los niños en dentición temporal. Según la RNO, algunos tratamientos tempranos, como el tallado selectivo, podrían corregir el desequilibrio oclusal y potenciar el crecimiento simétrico del complejo craneofacial en pacientes con MCU. Sin embargo, los tratamientos correctivos son a menudo retrasados hasta la edad adulta debido a la falta de evidencias científicas de la RNO, el aún desconocido desarrollo craneofacial y a la posibilidad de correcciones espontáneas durante el crecimiento, como será ampliamente introducido en esta tesis. A pesar de los esfuerzos realizados hasta la fecha, las técnicas experimentales y los modelos computacionales no han sido capaces de demostrar aún la relación que existe entre la forma y función del complejo craneofacial y justificar analíticamente así los cimientos de RNO. Un mayor conocimiento de estos aspectos podría favorecer el tratamiento temprano de las maloclusiones y mejorar la vida de los pacientes.

En esta tesis, se presenta una metodología computacional para la evaluación por el método de los elementos finitos de los resultados de la RNO y del efecto que tiene la oclusión en el desarrollo asimétrico de niños con MCU. Para ello, tal y como se describe detalladamente en esta tesis, fue fundamental la caracterización mecánica de los tejidos conectivos, el desarrollo de modelos computacionales detallados y una evaluación tridimensional precisa de la asimetría mediante algoritmos computacionales. Esta investigación constituye así el primer estudio de la RNO mediante el método de los elementos finitos, y podría considerarse como un referente en la simulación computacional de la masticación y en su relación biomecánica con el desarrollo craneofacial durante la infancia.

Palabras clave: *Biomecánica; Método de los Elementos Finitos; Rehabilitación Neuro-oclusal; Mordida cruzada unilateral; Asimetría facial; Ligamento periodontal, Articulación temporomandibular; Tejidos blandos; Hiperelasticidad.*

Summary

This dissertation aims to computationally evaluate the effect of early therapies, in particular Neuro-occlusal Rehabilitation (N.O.R), in the correction of dental malocclusions during childhood, checking their influence on the craniofacial complex's development and functionality. Moreover, this work aims to be a guide for the computational modelling of the craniofacial complex, encouraging future researchers, engineers, dentists and clinicians to include biomechanical models in their studies.

Within all the malocclusions, in this dissertation, the effect of the unilateral crossbite (UXB) was particularly analysed since it is a frequent cause of the asymmetric development of the craniofacial complex, affecting about 11.7 % of children in deciduous dentition. According to N.O.R, early treatments, such as selective grinding, could correct the occlusal imbalance and promote the symmetric development of the craniofacial complex in patients with UXB. Nevertheless, these treatments are often delayed to adulthood due to the lack of scientific evidence of N.O.R's outcomes, the uncertain development of the craniofacial complex and the possibility of spontaneous corrections during growth, as it will widely introduce in this dissertation. Despite the great efforts achieved to date, the experimental techniques and computational models have not yet demonstrated the relationship between form and function of the craniofacial complex and therefore justify analytically the N.O.R approaches. Greater knowledge of these issues could encourage the early treatment of malocclusions, improving the patients' lives.

This dissertation presents a computational methodology, using the finite element method, to evaluate the UXB's effect on asymmetric development during childhood and to prove analytically N.O.R's outcomes. To this end, as it is extensively detailed in this dissertation, the mechanical characterization of the connective tissues, the development of detailed computational models and the accurate 3D-analysis of the asymmetry were carefully conducted. This research is, therefore, the first analytical study of N.O.R treatments through the finite element method. Moreover, this dissertation could be also considered as a good reference in the computational modelling of chewing and in the biomechanical study of craniofacial development according to its shape-function relationship.

Keywords: *Biomechanics; Finite Element Method; Neuro-occlusal Rehabilitation; unilateral crossbite; facial asymmetry; periodontal ligament, temporomandibular joint; soft tissues; hyperelasticity*

Contents

List of Figures

1. Introduction

Firstly, a brief anatomic introduction of the stomatognathic system, with an emphasis on the periodontal ligament (PDL) and the temporomandibular joint (TMJ), is presented in this chapter. Then, some of the most prevalent disorders of the system's development are summarized, focusing on the mechanical effect of unilateral crossbite on its asymmetrical development. Besides, a review of the most frequent non-invasive treatments for the early correction of UXB is presented with a special focus on the N.O.R's ones.

Finally, it is supplied a wide overview of the clinical and computational studies that have studied the relationship between shape and function in the system development, highlighting their findings and limitations. At the end of this chapter, the motivation, the main goals and the outline of the thesis are also presented.

1.1 Stomatognathic system

The stomatognathic system is a morpho-functional system composed by a group of bony, muscular and neurological tissues whose growth [1] depends, among other factors, on its mechanical stimulation (Claude-Bernard principle)[2]. The main functions of the system are deglutition, phonation, breathing and chewing. The last one plays a key role in system development during the phase of deciduous dentition. When we chewed, the mandible moves by the synergic activity of the chewing muscles [3]. This movement is driven by the TMJs and occlusal planes and is limited by the mechanical stimuli sensed by the neural receptors, both in the soft tissues of the TMJs and in the PDLs, amongst others [3], [4].

1.1.1 Skeletal system

The skeletal main components of the stomatognathic system are the cranium and the inferior maxillary or mandible, but also the hyoid bone located in the neck [5], [6].

The cranium can be divided into two regions [7]: the neurocranium that protects the encephalon and the viscerocranium that composes the facial skeleton. The first one is composed of the occipital bone, sphenoid, squamous portion, mastoid portion, parietal and frontal [7]. On the other hand, the viscerocranium is formed by the lacrimal ethmoid, nasal, maxillary, zygomatic arches (shown in Figure 1a), sympathetic portion and styloid process [7]. From the biomechanical approach of this dissertation, the results will be primarily oriented to the viscerocranium regions and the mandible.

The mandible (shown in Figure 1b) is composed of a body which is horizontally and convexly curved and two lateral branches which extend from the posterior ends of the body [8]. The angle that forms the body with each branch is called the mandible angle and is a key measurement to identify mandible malformations [9]. Moreover, the mental foramina that are located in the most anterior area of the mandibular body are often used as anatomical reference points to measure mandible deviation [10]. Each mandibular branch is divided into anterior and posterior processes, coronoid and condylar processes, respectively [6]. The condylar process is moreover composed of a wide region called condylar head which is joined to the mandibular body by the condylar neck.

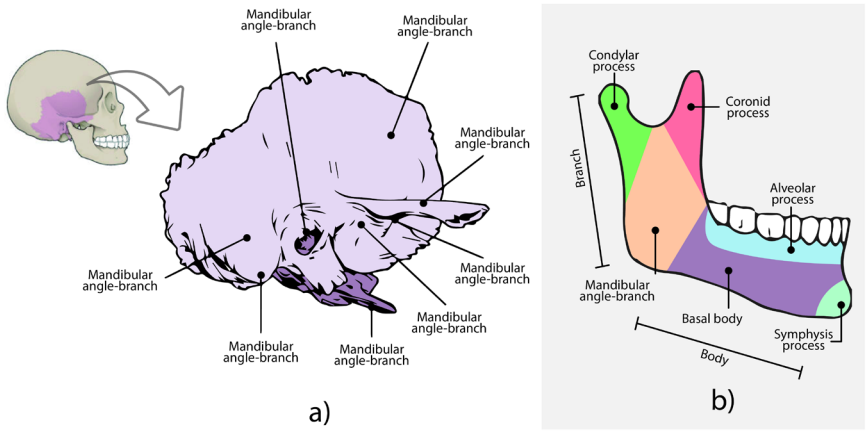

Fig. 1 a) Temporal bone (adapted from Anatomy & Physiology Anatomy [7]) and b) mandible which is divided into 6 regions based on the ossification process.

1.1.2 Muscular system

The stomatognathic system is composed of several muscles that are responsible for swallowing, facial expression, phonation, breathing and chewing [3], [4]. Nevertheless, only the muscles involved during chewing are detailed in this section because they play a key role in the biomechanical approach of this thesis.

As is well known, the chewing movement is a bilateral movement that involves three main steps [11] of opening, closing and occlusion. The mouth opening is produced through the relaxation of the elevator muscles (temporal, internal or medial pterygoid and masseter) and the simultaneous activity of the depressor muscles (external or lateral pterygoid, digastric, mylohyoid and geniohyoid) [12] (shown in Figure 2). To that end, the lower portion of the lateral pterygoid moves the condyles forward, geniohyoid and digastric pull the condyles down and back to the chin, while the mylohyoid moves the mandibular body to the hyoid bone [3].

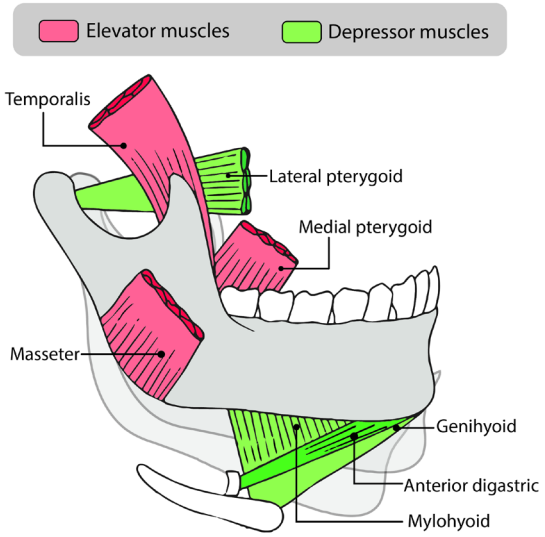

Fig. 2 Principal chewing muscles involved in the opening (muscles in green) and closing (muscles in red) movement.

On the other hand, closing motion begins with the relaxation of the depressor muscles which help to move the condyle backwards through the retrodiscal ligaments [3]. The medial pterygoid guides the mandible towards the chewing side and then the mandible is elevated by the temporal and masseter muscles. Finally, during the occlusion, the elevator muscles and the masseter, in particular, activate to grind the food bolus [13].

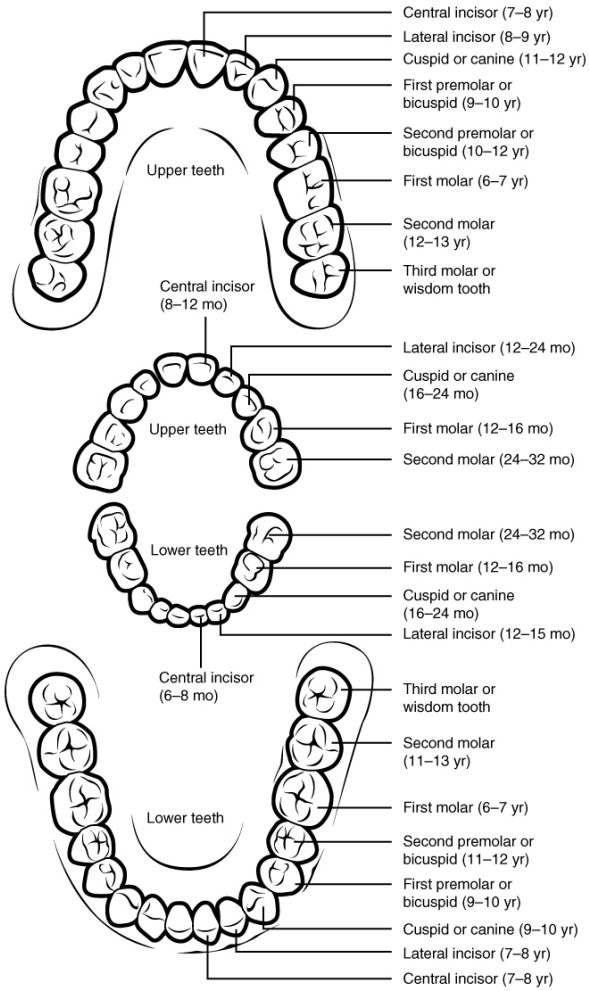

Fig. 3 Upper and lower teeth in permanent and deciduous dentitions. Figure extracted from Anatomy & Physiology Anatomy [7].

1.1.3 Dentition

Besides helping to the child feeding, teeth are essential elements in the development of dental arches [14]. Their position and their reactions in the proximal and occlusal directions allow a functional balance for an optimal occlusion, and therefore, for a balanced development of the stomatognathic system [3].

Initially, this balance is supported by the deciduous dentition (Figure 3) that is composed of 20 primary teeth, two incisors (central and lateral), a canine, and two molars for each arch [14]. The primary teeth begin to erupt at 6 months of age. Then, the permanent teeth begin to erupt [15] at around 6 years of age. This stage when deciduous teeth are being replaced by permanent teeth is referred to as mixed dentition [14]. Finally, when all deciduous teeth are replaced, the resultant permanent dentition is composed of 32 teeth, two incisors (central and lateral), a canine, two premolars, and three molars for each arch [14].

During mixed dentition, the loss of any tooth often leads an occlusion imbalance [3], [16], which may cause stomatognathic system chewing difficulties [17], TMJ dysfunctions [18] or even growth disorders [19].

1.1.4 Neural system

The neural network of the stomatognathic system involves, among others, those systems that control the motor system according to the stimulus perceived by the neural receptors. [20], [21]. The receptors of the stomatognathic system are located in the oral mucous membrane, tongue, teeth, and PDLs, TMJ and muscles [3]. According to the stimulus detected, different detectors are distinguished [22]: mechanoreceptors stimulated by the deformation of nervous terminals under a force, thermoreceptors which respond to cold and heat signals, and nociceptors capable of detecting tissue damage. From the biomechanical approach of this dissertation, mechanoreceptors are particularly noteworthy and can be divided into four types according to the specific mechanics perceived: *Ruffini endings, Pacinian corpuscles, Golgi tendon organs* and *free nerve endings*. In this section, those mechanoreceptors located in the connective tissues of the TMJ and PDL will be extensively described since their great effect on the stomatognathic system development and function.

Mechanoreceptors in the TMJ

TMJ is an articular joint that connects the mandible to the skull and enables mandible's movement. Anatomically, it is mainly composed by the articular disc, the condylar and glenoid fossa or temporal cartilage, the retrodiscal tissue, the collateral ligaments and the joint capsule [6] (Figure 4).

The TMJ disc is a biconcave, elliptical, fibrocartilaginous tissue located in the glenoid fossa of the temporal bone [23]. It distributes the loads and absorbs shocks, preventing stress concentration on the articulating surfaces of the TMJ. The TMJ's synovial fluid promotes the joint lubrication [24], as well as the hyaline cartilages [25] which cover the articular surfaces on the condyle and temporal fossa (condylar and temporal cartilages, Figure 4a and b, respectively). The cartilages of the TMJ are simultaneously subjected to compression and shear stress and therefore constitutes a complex force-field mechanism [26]. The TMJ disc is posteriorly attached by the retrodiscal tissue which serves as a volumetric compensatory mechanism for pressure equilibration [27]. Retrodiscal tissue contains collagen and elastic fibres, and numerous nerves and blood vessels [28]. Laterally, the medial and lateral collateral ligaments connect TMJ disc to the condyle, contributing to joint stabilization during TMJ movement [29].

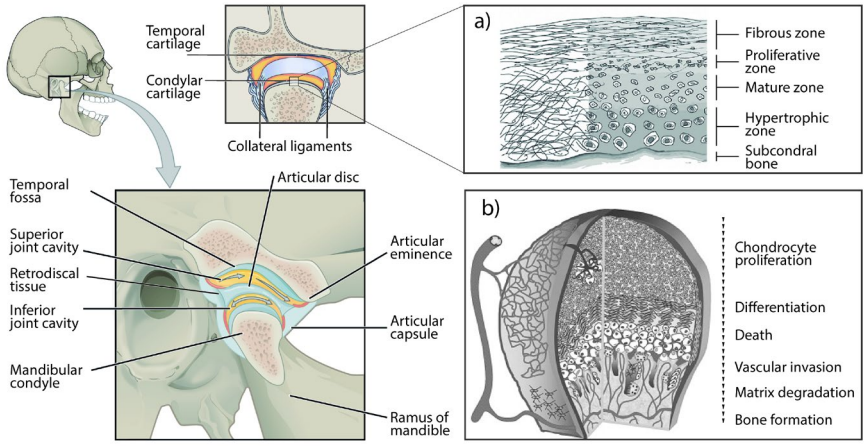

Fig. 4 Left: TMJ anatomy (adapted from Anatomy & Physiology Anatomy [7]). Regions of the condylar cartilage along with its thickness [25], b) ossification regions of the mandibular condyle (adapted from Maes and Kronenberg [30]).

TMJ's mechanoreceptors are low-threshold, extremely sensitive and specialized sensors which transmit the stimulus to the Central Nervous System (CNS). They are more highly concentrated in the lateral and posterior areas of the articular capsule, whilst the anterior part, comprising the meniscus and synovial membrane, contains few or no receptors [3]. These receptors are innervated by from the auriculotemporal and masseteric branches of the mandibular branch (V3) of the trigeminal nerve [8] (shown in Figure 5).

The characteristics of receptors in the TMJ allow us to reproduce mandibular position in space without physical references. The sensory information transmitted by the TMJ receptors codifies the position, shifting and speed of condylar movement, within a physiological shift of the mandible during the opening stage [31] of the chewing cycle [32].

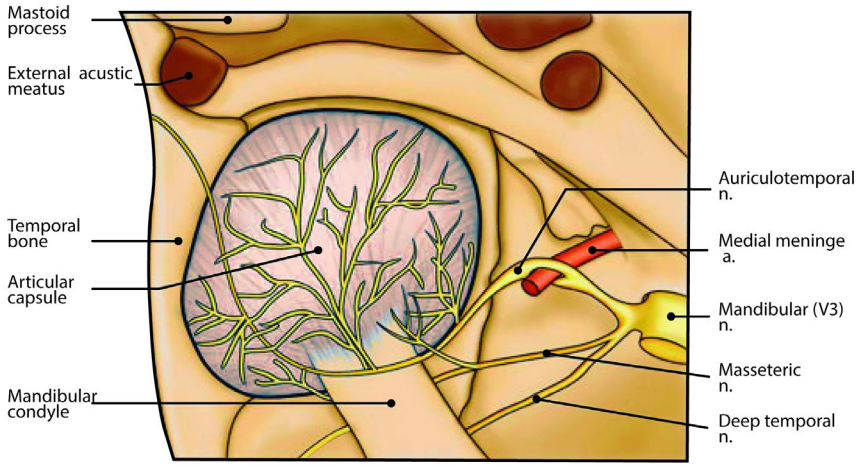

Fig. 5 Bottom view of the left TMJ. The nerves that penetrate through the articular capsule provide innervation to the TMJ. [33]

Mechanoreceptors in the PDL

In the periodontium, the mechanoreceptors of the PDL provide information about occlusal reactions [34]. The periodontium is mainly composed of the trabecular bone, cortical bone, PDL and the teeth which are mainly formed of enamel, dentin, pulp and cementum root.

Amongst them, PDL is the softest biological tissue. This behaviour confers to the PDL a key role in the load transmission, bone resorption and most common periodontal diseases [35]. Biologically, PDL can be considered as a porous vasculature solid with a highly structured collagen network [36]–[38], fibroblasts, osteoblasts and cementoblasts [39]. The ground substance has similarity to most other connective tissues with a high content of water (approximately 70% of ground weight) [40] and the matrix is mainly composed of proteins: alkaline phosphatase, hyaluronate glycosaminoglycans, proteoglycans and glycoproteins [41].

On the other hand, approximately 50-75% of the PDL volume is composed of collagen fibres,[42] primarily type I [42], III [43], and XII fibres [44]. According to the insertion of the fibres, they can classify into dentoalveolar or gingival fibrous main groups. The dentoalveolar group plays a key role to support occlusal forces and movements and consists of five different fibres bundles: alveolar crest, horizontal, oblique, apical and inter-radicular fibres [45]. Meanwhile, the fibres of the gingival group have a minor effect on the loading support, thus they will be neglected in the subsequent studies of this dissertation.

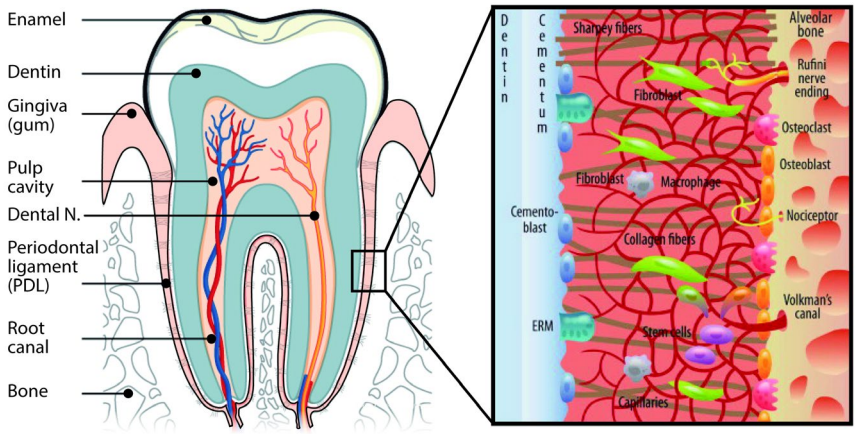

Fig. 6 Left: Scheme of the longitudinal section through a molar tooth (adapted from Anatomy & Physiology Anatomy [7]), right: detail of the PDL microstructure [46].

Among the dentoalveolar fibres, it can be found mechanoreceptors and proprioception in PDL (shown in Figure 6) which provide to CNS information about tooth loads and movements through the maxillary (V2) and mandibular (V3) (Figure 7). The most important ones seem to be Ruffini endings which are directly connected to the collagen fibres [46] (Figure 6). They respond to low forces (<1 N) and small tooth displacement (2–3 µm) [47]–[49], i.e those produced at chewing. Although in a minor way, free nerves fibres and lamellar corpuscle (similar than Pacinian corpuscles) can also be found in the PDL [3].

The maxillary nerve (Figure 7) receives the molar teeth reactions through the posterior upper alveolar nerve [50]. Meanwhile, PDLs of the premolars and anterior teeth (incisors and canines) provide the mechanical input via the middle and anterior upper alveolar nerves, which are infraorbital nerve branches [50]. On the other hand, PDLs of the inferior teeth transmit the mechanical signal to the mandibular nerve (Figure 7) through the lower dental nerves which are small branches of the lower alveolar nerve [3], [51].

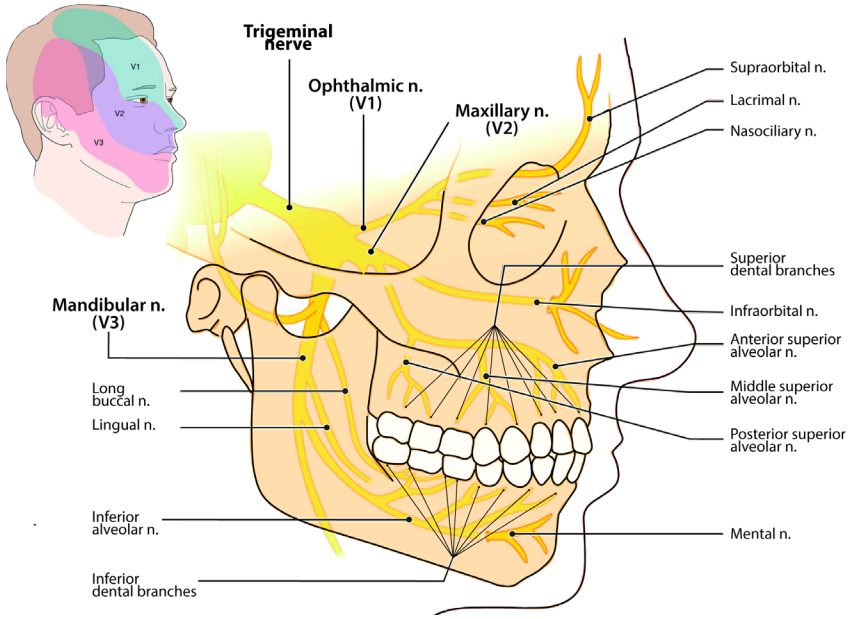

Fig. 7 The nervous network of the stomatognathic system. Adapted from *Tintinallis emergency medicine A comprehensive study guide* [52]. Top left corner: areas affected by the V1, V2 and V3 branches of the trigeminal nerve [52].

1.2 Development of the stomatognathic system

The stomatognathic system development is a complex process that is initiated during the intrauterine growth and continued throughout life. This section is focused on the second childhood period which runs from 3 years until puberty, since it is a critical stage on the system development, being more noticeably in the mandible development [53], [54].

The growth factors during this stage are commonly divided into environmental (by mechanical and functional activities) and genetic (by the genome) factors which are also subdivided into intrinsic (operating within the cell) or epigenetic (influenced by other cells or tissues) ones [55]. According to the biomechanical stimulation, environmental factors conditionate the bone ossification and bone growth by the following ossification and growth mechanisms (shown in Figure 8).

1.2.1 Ossification mechanisms

Intramembranous ossification is initiated by the formation of the mesenchymal tissue around a centre of growth with numerous capillary and specialised cells, from which the osteoblasts differentiate. Firstly, the osteoblasts synthesize the collagen and proteoglycans (organic matrix), and then the phosphorus and calcium, leading bone tissue.

Endochondral ossification is a process in which cartilage tissue is replaced by bone tissue. The process initiates through the accumulation and proliferation of mesenchymal cells that differentiate into chondroblasts. Chondroblasts secrete collagen II and produce the cartilaginous matrix that serves as a mould. Finally, the chondroblasts differentiate into osteoblasts by replacing cartilage tissue with bone tissue.

1.2.2 Growth mechanisms

Sutural growth is an ossification process of the cranial bones which begins with the proliferation of connective tissue and follows by bone apposition across the suture.

Cartilaginous growth is the dominant longitudinal growth of condyles developing through the endochondral bone formation. It is a tightly regulated process of cartilage replacement with bone.

Periosteal and endosteal growth is the mechanism of bone proliferation of the membranous cover tissue (periosteum) and the medullary cavities (endosteum) through intramembranous ossification.

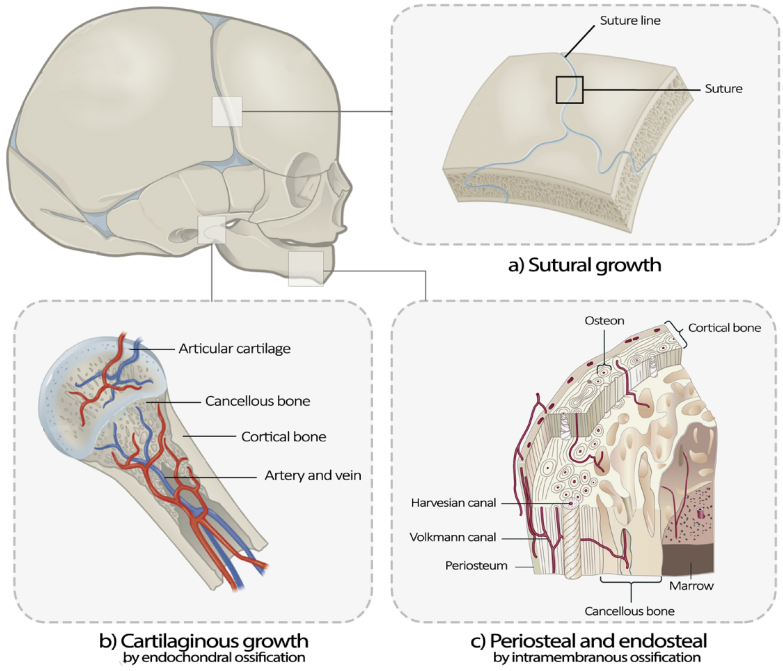

Fig. 8 The mechanisms of skeletal growth of the stomatognathic system during childhood. a) sutural growth (adapted from *Anatomy & Physiology Anatomy* [7]), b) cartilaginous growth (adapted from *Concepts of Biology* [56]) and c) periosteal and endosteal growth (adapted from *Anatomy & Physiology Anatomy* [7]).

1.2.3 Theories of craniofacial growth

From the 1930s several theories (shown in Figure 9) have described the craniofacial growth [53], [57] based on the three growth mechanisms (sutural, endochondral and intramembranous) and conditioning factors (genetic and environmental). Although none of these theories is totally valid, they help to understand the stomatognathic system growth and predict the effect of early orthodontic treatments [58]. Some of the most relevant theories are as follows:

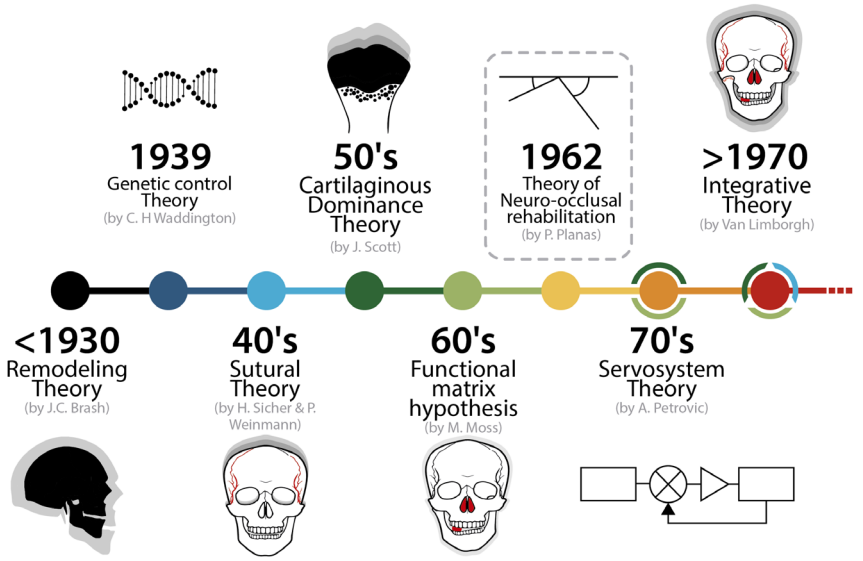

Fig. 9 Timeline of the principal theories of Craniofacial System Development.

Remodelling Theory by Brash (1924) [59] suggested that craniofacial skeletal growth occurs exclusively by the selective addition and resorption of bone at its surfaces and sutures. The cartilages and sutures of the craniofacial skeleton have little or no role in the growth of the craniofacial skeleton.

Classical or Genetic Control Theory (1939) [60], [61] defended the dominance of the genetic factors instead of functional or hormonal factors in the craniofacial growth. According to this theory, the endochondral and sutural ossification are strongly influenced by hormonal growth.

Sutural Dominance Theory by Harry Sicher and Joseph P. Weinmann (1940s) [62] suggested that sutures, cartilages and periosteum are the main responsible for bone formation, being highly influenced by intrinsic genetic control.

Cartilaginous Dominance Theory by James Scott (1953) [63] highlights the key role of cartilages as centres of the skeletal growth through endochondral ossification which is mainly controlled by intrinsic genetic factors.

Functional Matrix Hypothesis (FMH) by Melvin Moss (1962) [64], [65] considered that craniofacial growth is conditioned by environmental factors (system functions). The functional matrix of the stomatognathic system is therefore composed of the muscles, soft tissues, nerves, glands, teeth and cavities responsible for the system functions.

Servosystem Theory by Alexandre Petrovic (1970) [66] demonstrated that the growth of the mandibular condyle is highly adaptive and responsive to both extrinsic systemic factors and local biomechanical and functional factors.

Multifactorial Theory by Van Limborgh (the 1970s) [67] combines the Sutural, Cartilaginous and Functional theories to explain the facial growth. This theory assumes that postnatal growth is controlled by intrinsic genetic factors, local and general epigenetic factors, and environmental factors. Sutural growth is only a compensatory mechanism of brain growth.

These theories were followed by the later Enlow's works and his Counterpart Principle [68] which explains the growth of each part according to the development of the connected parts. Besides, the Atchley-Hall's model [69] related the FMH defined by Moss with the genetic and environmental factors to describe the mandibular morphology. They are also remarkable the animal experiments performed by Bernard G.Sarnat [70], [71] which demonstrated the supplementary role of cranium cavities in the development of the cranium bones. As well as prenatal works of Inger Kjaer [72], [73] which demonstrated the endochondral ossification of the condylar symphysis and condyle, and the intramembranous ossification followed in the mandibular body.

1.3 Malformations of the stomatognathic system

Stomatognathic system malformations can be congenital or acquired development anomalies and may involve changes in both connective and muscular tissues. Facial asymmetry, which is defined as the discordance between both sides of the face, is one of the most common malformations of the stomatognathic system development.

The scientific studies have revealed that there are several aetiological factors that, individually or combined, can affect the development of facial and dental asymmetries. These include genetic factors (facial microsomia, craniosynostosis, facial cleft), environmental factors (trauma, infections, postural disorders), functional factors (malocclusions, TMJ disorders, muscle paralysis), and those of development (skeletal and dental malformations) [74], [75]. From the biomechanical viewpoint of this dissertation, the functional factors, and especially malocclusions, may cause alterations in skeletal and dental development, as it will explain bellow.

1.3.1 Unilateral crossbite (UXB)

Although there are many examples of malocclusions that modify the chewing pattern, this dissertation is limited itself to one of the most common one, the UXB.

UXB is characterized by the lingual occlusion of the buccal cusps of the maxillary teeth with the buccal cusps of the corresponding mandibular teeth [76] in one of the two halves (shown in Figure 10). Henceforth we will refer to this side as the crossed side (XS), and to the opposite side as the non-crossed side (NXS). Within the UXB forms, the unilateral posterior crossbite (UPXB) is considered a relatively prevalent malocclusion. Its prevalence varies significantly between different populations, but it seems that UPXB affects between 4-13% of the general European population and 7.1-23.3% of the general population [77]–[80]. In the general Spanish population, the prevalence of UPXB varies between 10-24% [81] and is higher than 48% [82] in orthodontic patients.

Within the different causes of UXB, the functional UXB has a prevalence between 67-80% of the UXB cases [83]. In functional UXB cases, the mandible tends to displace laterally to achieve occlusal balance in maximum intercuspation position, leading to a functional crossbite. Although UXB or UPXB are often diagnosed via the teeth, they affect also to the rest of the stomatognathic system such as neuromuscular coordination, skeletal development and TMJ function, amongst others.

Skeletal abnormalities

Based on the FMH's basis, some authors [80], [84] have empirically related the adaptation of soft and hard tissues to the UXB and have detected some asymmetrical changes (shown in Figure 10) that are summarized as follows:

- Deviation of the midline of the inferior teeth, and consequently of the chin to the XS [85]–[87].
- Decrease of the height of the mandibular branch and of the length of the choroid and condylar processes [88]–[90] of the XS.
- Reduction of the width of the half maxillary of the XS due to buccal occlusion of the upper teeth [91].
- Greater inclination of the XS articular eminence than the NXS one [92].
- Remodelling of the glenoid fossa of the XS to a more posterior position [89], [93].
- Decrease of the thickness of the articular disc and of the clearance between the condyle and glenoid fossa of the XS. [94].
- Elevation of the ocular orbit and of the cranial base of the cross side [95], [96].
- Alterations in the response of TMJ mechanoreceptors to the unusual stretch of the tissues attached to the condyles (articular capsule and ligaments) [97].

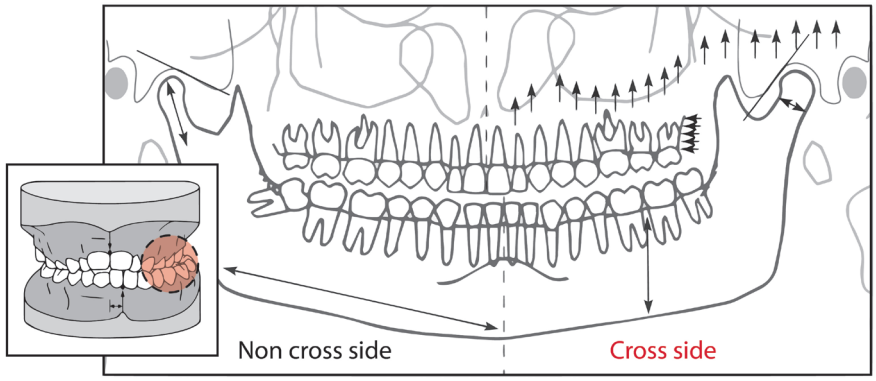

Fig. 10 Common skeletal variations in patients with UXB. Lower left corner: effect of the UXB on the occlusion.

Functional alterations

UXB causes also abnormal mandibular movements and therefore alterations in the activity of the elevator and depressor muscles [100], [101]. Several studies have identified, for instance, that the thickness of the temporal [98] is greater in the XS than in the NXS, while the thickness of the masseter is lower [99].

Besides, several electromyographic (EMG) studies [100]–[102] have noted that the activity of the posterior temporalis and masseter muscles was greater in the XS than in the NXS during rest, chewing, and maximum clenching. The differences of EMG records may be the result of the abnormal excitation of the PDL during unilateral chewing [103].

Occlusal alterations

From the occlusal level, UXB causes a higher and frequent occlusion by the XS during chewing. Consequently, the maxilla is narrowed and the superior teeth erupt incorrectly in the XS [80], [104], [105]. Meanwhile, the alveolar crest of the mandible and the lower molars move latero-posteriorly in the XS [106]. Some authors have also noted that the prevalence of parafunctional occlusion (as bruxism) in adulthood was higher for patients with untreated UXB during childhood [107].

TMJ Dysfunction

According to FMH's premises, the effect of the UXB neither can be neglected in the development of some common temporomandibular disorder (TMD) or Craniomandibular Dysfunction (CMD), since load distribution affects the development of the musculoskeletal system [108]. UXB may be the cause of 2-10% [109] of cases of CMD in the adulthood [110], [111]. Thus, some authors considered UXB as a risk factor for the anterior displacement of the articular disc, joint sounds, atrial or muscle pain [112], amongst others. However, the effect of UXB on the development of CMD is a matter of deep discussion since some authors [108], [111], [112] have not found a causal correlation between them at early ages.

1.4 Neuro-occlusal Rehabilitation (N.O.R)

In 1987, Dr Pedro Planas published his best-known publication entitled ‘‘Rehabilitación Neuro-Occlusal’’, RNO or its English acronym N.O.R (Neuro-occlusal Rehabilitation) as I am going to refer in this dissertation. Based on the 60 years of his clinical experience, in this work, Dr Planas related the craniofacial deformities with the unilateral malocclusions, mainly according to FMH’s basis [46], [56]. Although Planas’ laws were first published in 1962 [113], N.O.R constitutes the synthesis of Planas' previous works which were regularly presented at congresses and published in "*l'Orthodontie Française*" from 1949 to 1992 [113], [114], [123]–[132], [115], [133]–[136], [116]–[122]. Afterwards, Planas ex-students or N.O.R followers disseminated their reflections about N.O.R postulates. Noteworthy are the works of Kolf [137], Raymond [138]–[140], Santana Penin [141], Gaspard [142], [143] and Salvador-Planas [144], [145]. Nevertheless, despite the widespread use of N.O.R around the world (in European and especially in South American countries), some studies are seriously critical with its validity because of its empirical basis.

N.O.R [4] is the part of stomatognathic medicine which studies both the aetiology and genesis of functional and morphological disorders of the stomatognathic system. N.O.R aims to investigate the causes that produce the malocclusions, to correct, rehabilitate and revert them as soon as possible, hopefully in childhood. According to N.O.R theory, functional disorders appear in the first years of life and have a great incidence in the deciduous dentition in form of malocclusion. Thus, the main rule of this theory is to treat malocclusions early with minimum invasive treatments and prolonged them until old age.

1.4.1 Craniofacial growth from N.O.R approach

Dr Planas empirically highlighted the key role of neural receptors of PDLs and TMJs, particularly condylar cartilages in mandibular and skull growth, according to the principles of Cartilaginous Dominance Theory [63]. He also introduced the influence of phenotypes defended by the theory of genetic factors [60], [61]. Therefore, it seems that N.O.R combines the fundamental theories of growth in the same way as “*Servosystem*” [66] and “*Multifactorial*” theories [58]. Nevertheless, notwithstanding the multifactorial approach of N.O.R, its basis is predominantly established by the FMH, relating the shape and function of the stomatognathic system’s development.

According to N.O.R, the craniofacial growth could be explained by the following assumptions:

- The **cranial vault** bones grow by intramembranous and sutural ossification which are conditioned by intrinsic genetic factors.
- The **cranial base** follows an endochondral ossification with bone apposition in the cranial synchondrosis. The growth in this region is influenced by brain expansion and genetic factors.
- The **mandibular fossa** development is characterized by an increase of the articular eminence inclination and of the post glenoid region volume [146], which is influenced by the position of the temporal lobe, the tympanic ring and the outward auditory canal.
- The **maxillary** growth combines an intramembranous ossification process with the ossification of the middle palatal suture which joins both maxillary halves and adjacent sutures (frontomaxillary, zygomatic maxillary, zygomatic temporal and pterigopalatine sutures). Its growth is strongly conditioned by environmental factors produced during breathing, chewing and tooth eruption.
- The **mandibular** growth follows endochondral ossification in the symphysis and condylar region and bone apposition/resorption at the external surface. The ossification in the condylar region is induced by the exogenous stimulation produced during TMJ movements, and particularly during chewing. On the other hand, intramembranous ossification is influenced by local environmental factors including tooth eruption, periodontal stimulation and muscular forces. Based on the FMH's premises, mandible growth can be subdivided:
    - **Condylar process** follows endochondral ossification by the condylar cartilage stimulation during TMJ movements and by the influence of lateral pterygoid and the retrodiscal tissue.
    - **Coronoid process** follows intramembranous ossification by the action of the temporal muscle.
    - **Alveolar process** grows by periosteal and endosteal growth mechanisms through intramembranous ossification. Bone tissue is deposited by apposition around dental germs causing an increase of the alveolar process height [147].
    - **Symphysis process** develops through cartilaginous growth which is mainly defined by the lingual and mylohyoid muscles.

- **Mandibular angle-branch** follows intramembranous ossification mainly through the forces exerted by the masseter and medial pterygoid muscles.
- **Basal body** grows by intramembranous ossification in dorsal and ventral directions.

In summary, according to N.O.R approach [2], the stomatognathic system is mainly developed by the environmental stimulus of mechanical origin detected on the sliding surfaces of the TMJ and the PDLs, but also conditioned by genetic factors. Although the genetic stimulus is normal, pathological development can occur if the mechanical stimulus is abnormal, i.e in dental malocclusions. This exogenous or mechanical stimulation of the stomatognathic system initiates when the newborn breathes, continues with the breastfeeding and is completed with chewing stimulation that is maintained throughout adulthood.

1.4.2 Breathing - The first mechanical stimulus

As soon as the child is born, the first permanent stimulus, nasal breathing, is established. This function promotes the development of the nasal and paranasal sinuses, which are closely related to the palatal arch development [148]. Moreover, it plays a key role in mandible and tongue positioning. However, nasal breathing is sometimes substituted by mouth breathing as a result of allergic rhinitis, palatine and pharyngeal tonsil hypertrophy, nasal septal deviation, nasal polyps and turbinate hypertrophy, amongst other disorders [149]. Mouth breathing rests the tongue in a lower position [150], [151] modifying the mechanical stimulus on orofacial structures and causing then an abnormal growth such as narrowing of the maxilla, underdevelopment of the mandible, protrusion of the upper incisors, or distal position of the mandible [152].

1.4.3 Breastfeeding - The second mechanical stimulus

After the establishment of the airway, next neuro stimulating activity occurs during sucking and swallowing of breast milk [153]. Breastfeeding is beyond just nutrition; it is a key factor for the proper growth and development of the stomatognathic and orofacial musculature.

During breastfeeding, the baby breaths by the nose, keeping the physiological nasal airflow and hence transversal development of the maxilla [149]. Meanwhile, protrusive and retrusive movements excite the posterior regions of the TMJ meniscus and the upper surface of the temporal fossa [149], [154]. As a result of this movement, the mandibular branches growth in anteroposterior direction, the mandibular angle is gradually adapted and the slope of the articular eminence increases [155], [156] by the friction between articular surfaces.

Contrariwise, artificial feeding may produce an abnormal stimulation than breastfeeding. The artificial feeding is done by non-physiological lingual movements which reduce the oral stimulation in the joint cavity, potentially leading occlusal disorders. [154], [156]. Likewise, several studies [157], [158] have suggested that non-nutritive sucking (usually in the form of dummies/pacifiers or thumb-sucking) may be responsible for some forms of early malocclusion, including anterior open bite, increased overjet, and posterior crossbite.

1.4.4 Chewing - Third mechanical stimulus

Finally, with the eruption of the deciduous teeth, a new neural network with origin in the PDLs is created. This neural network is mainly stimulated during chewing movement [4], [159] whose physiology and biophysics could explain the development of the stomatognathic system [51], [160]. Opposite to above activities, chewing is not a simultaneous movement, taking place alternately on both sides of the mandible. In this dissertation, the side where the alimentary bolus is chewed will be referred to as "w*orking side*", whereas "*balancing side*" will be used for the opposite side.

The chewing pattern comprises two phases: the opening pattern (shown in Figure 11), and the closing pattern (shown in Figure 11). In conditions of physiological occlusion and healthy masticatory function, the pattern recorded at the lower interincisor point starts with the opening along the vertical axis. Then, the mandible moves laterally towards the bolus side during the last phase of opening and in the first stage of closure. Finally, it moves mediolaterally along the occlusal phase of closure until functional intercuspation is reached [3], [161], [162].

When masticatory movement is alternate, mirrored, and symmetrical, the stomatognathic structures work rhythmically and they can distribute the maximum force homogeneously, avoiding harmful overloading in some parts of the system [163]. Neural stimulation is alternatively received by the anteroposterior movements of the TMJ (caused by the pterygoid, masseter and temporal muscles) and by the PDLs through the occlusal friction [4], [164]. If chewing is physiological and bilateral, the mechanical stimulus is perceived by both mandibular halves, causing a normal and symmetrical growth of the stomatognathic system.

Nevertheless, some occlusal conditions, functional malocclusions or UXB (which were explained in section 1.3.1) may alter this symmetrical movement, creating a serious imbalance and gradually producing functional problems which can result in abnormal development of the dentoalveolar and cranial structures [3], [165], [166]. Moreover, it is also noteworthy that different diets can produce abnormal development of the mandible. In this context. Regarding this, some studies, for instance, has found greater ramus height, bone mass and condylar dimensions in subjects with a hard diet than in others with low consistency diet [167], [168].

From a clinical point of view, the bilateral efficiency of chewing is often evaluated by the closing angle (shown blue vector in Figure 11b). It represents the inclination with which the mandibular and vestibular cuspids of the lower molars and premolars approach the bolus and/or the occlusal surface of teeth on the opposing upper arch before grinding the food bolus [3], [169].

Another relevant vector for the diagnosis of abnormal chewing is the Planas' Masticatory Functional Angle (M.F.A) which measures the trajectory performed by the mandible during lateral movements, starting with a functional occlusion and sliding teeth slow and relaxed to right and left. According to the law of minimum vertical dimension, there is a physiological tendency to shift the mandible to the side of minimum vertical dimension to execute the different masticatory functions. It means that the patient will always tend to use more the side that increases less the vertical dimension during lateral movements [4], [170].

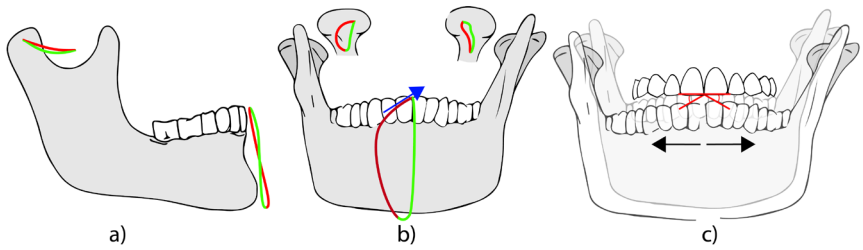

Fig. 11 Opening (green) and closing (red) tracing of the condyles and interincisor point at chewing by the left side in the a) sagittal plane and b) frontal plane (Redrawn from M.G. Piancino and S. Kyrkanides [3]. c) M.F.A.s performed by the mandible during lateral movement.

1.4.5 Early treatment

Malocclusions, such as UXB, can disrupt the anatomical function of TMJs and therefore the normal development of this joint during childhood. Because the continuous development and growth in early ages, functional disorders may lead to irreversible unusual development which is difficult to correct in later life, requiring painful, expensive and complex surgical treatments [171]. Thus, some authors [4], [107], and in particular Dr Planas, recommends early treatment of UXB to avoid future irreversible problems. Hence, N.O.R recommend treating UXBs in the deciduous dentition, referring to the therapies at this age as the "*true rehabilitation*" procedures. Nonetheless, corrective treatments are often delayed until the eruption of permanent molars because of the possibility of a spontaneous rectification [80], [172].

Early treatment starts by reducing or removing the parafunctional habit such as non-nutritive sucking, mouth breathing syndrome or unilateral chewing habits. Then, occlusal or/and skeletal treatments should be applied to correct both skeletal and occlusal abnormalities. The most appropriate treatment depends upon each patient's diagnosis and it is common to use one of the following therapies:

- **Banded expanders,** such as the Hyrax (Figure 12a) and the Haas (Figure 12b) appliances are used for maxillary expansion.
- **Quad-Helix** (Figure 12c) is an appliance with loops embedded that allow the expansion of the posterior teeth.
- **Schwarz plate** (Figure 12d) is usually used for dentoalveolar expansion.
- **Progenie plate** (Figure 12e) is mainly used in prognathism cases.

- **Planas'direct tracks (**Figure 12f) are 2 acrylic plates which are not fixed to the mouth and have no pressure or supporting forces. The teeth tend to separate from the plaques to exert lingual-buccal movements resulting in a maxillary expansion.
- **Selective grinding** or **occlusal adjustment** (Figure 12g) is a technique that modifies the occlusal surfaces to eliminate interferences. The selective grinding improves and increases the lateral excursions of the mandible and allows guiding the patient to bite alternately from both sides. This treatment should be accompanied by a gradual hardening of the diet. If the patient continues eating low consistency food, the low mechanical stimulus in the PDLs and TMJs will not stimulate the growth and development of the maxilla and mandible [173].

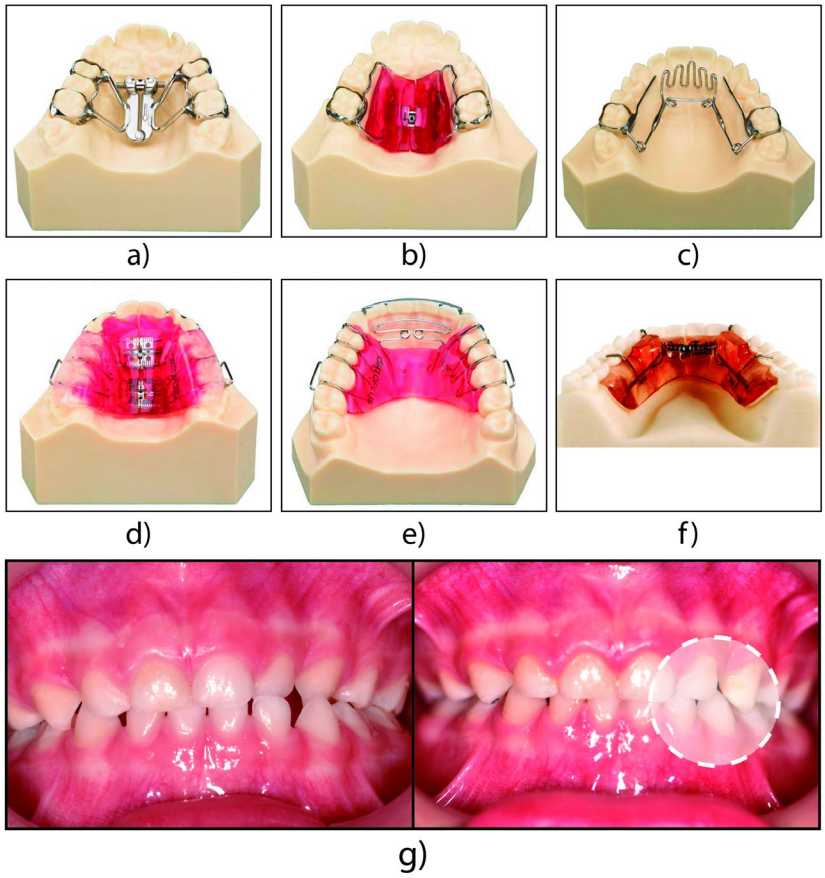

Fig. 12 Early corrective treatments. a) Hyrax, b) Haas, c) Quad-Helix, d) Schwarz plate, e) Progenie plate, f) Planas'direct tracks and g) selective grinding.

1.5 State of the art

The role of malocclusions in the abnormal development of the stomatognathic system has been widely studied from several points of view. The knowledge of how the craniofacial complex develops and grows could provide the foundation for understanding the aetiology of various dental and skeletal disorders, assist in the selection of the best treatment or know how patients might respond to treatments. However, as introduced previously, functional, sensorial and anatomical complexity of the stomatognathic system difficulties the study of its development. In this section, a short review of the clinical and computational studies conducted to date is presented, underlining the issues covered in this dissertation.

1.5.1 Clinical studies

Craniofacial malformations must be assessed by a judicious diagnosis conducted through intra and extraoral clinical examinations [174]. The intraoral examination should evaluate the malocclusion, the inclination of posterior and anterior teeth, the crossbite and the presence of functional deviation of the mandible. An important step in this the clinical examination is the determination of the closing angles [3], [169] and the M.F.As [4], [170] (explained in section 1.4.4) to determine if any premature contacts might exist and if the centric occlusion corresponds with the centric relation. Moreover, it is important to analyse the occlusal contacts by articulating paper or digital piezoelectric film sensor that quantify the occlusion intensity by the size of the mark or digital recordings, respectively. Although the articulating paper is often used in the diagnosis, the interpretation of the marks is subjective and inaccurate [175], [176]. To avoid these problems, computerized occlusal analysis systems (i.e T-Scan system) were recently developed. The T-Scan system (Tek-Scan South Boston, MA, USA) is a device composed by a piezoelectric film sensor. It records the occlusion and shows occlusal forces as columns of different colour and height according to the intensity of the force in percentage [177]. Although T-Scan is a useful device in clinical practice, it does not record the direction and magnitude of occlusal contacts, which are key features in the diagnosis of malocclusions, such as UXB.

On the other hand, extraoral evaluation involves a visual examination of soft and hard tissues and TMJ palpation, with special attention to the centre of the chin, the height of the lip commissures, and bilateral symmetry of the gonial angles and contours of the mandibular body [178]. The extraoral evaluation starts with the determination of the facial midline or sagittal midplane based on representative landmarks.

In two-dimensional (2D) imaging, commonly 2D frontal photographs, the facial midline is defined through the glabella and other landmarks such as the midpoint of the interpupillary distance, nasal base, nasal tip, philtrum, and chin midpoint [179]. In 1960, Ricketts [180] defined the facial midline through the cristal galli or the top of the nasal septum. In 1987, Grummons [181] defines it from the crista galli through the anterior nasal spine to the chin point. Although the use of 2D images is still widely used due to its low cost, its accuracy is strongly questioned due to: the high variability of the superficial landmarks in patients with facial asymmetry, the magnifying errors of the image and the unchanged position of the subject in the image.

Due to these limitations, the use of 3D cephalometric methods, such as Computed Tomography (CT), Conical Beam CT (CBCT) and Magnetic Resonance Imaging (MRI), has been expanded in the last decade for the diagnosis of facial asymmetry. However, although 3D imaging advances have increased the morphological data, it is still complicated to establish an accurate sagittal midplane [182] which compensate any asymmetrical shape. Nowadays, although they need greater development, there are three main approaches to determine the sagittal midplane [183]: the landmark-based, the voxel-based and the morphometric midplane approach [184], [185]. The landmark-based method is the easier method and is widely used in clinical practise, nevertheless it not clear which landmarks provide a more accurate result. On the other hand, voxel-based and morphometric approaches are not extended in commercial software due to its complex implementation [183]. Besides the above limitations, none of these 3 methods compensates for the asymmetric shape of the craniofacial complex, possibly leading to potential misdiagnosis and inaccurate orthodontic treatments plans. Hence, some studies criticize the validity of 3D methods and argue that they are just as accurate [186], [187] or even more inaccurate than 2D methods [188], against others that justify their validity [189]–[191].

To this uncertainty in the sagittal midplane determination, it must be also added that 3D scans are constrained just in some cases since it is more expensive and radioactive than 2D approaches. As a rule, for every adult patient with facial asymmetry symptoms, 2D photographs (extra and intraoral) and a panoramic radiograph are needed. For those who will be treated, dental casts and lateral cephalometric radiographs are used. In subjects with impacted teeth, a small field-of-view CBCT and CT image are recommended; while in those with asymmetry, a frontal cephalometric and often a large field-of-view CBCT or CT are needed. In subjects with suspected TMJ disorder or dysfunction, MRI is often indicated [192]. In children, however, CT and CBCT are usually not recommended due to the high doses of radiation involved [4], [193]. Other 3D approaches have recently appeared, such as 3D photography, which is a non-invasive, radiation-free method for quantification of longitudinal soft tissue changes during growth. Also, the intraoral scans which produce a 3D model of the teeth. Although intraoral scan eliminates the laboratory manual work and overcomes the problem of working with plaster casts [192], it is rarely used in children due to discomfort to patients.

Beside their aforementioned limitations, 2D and 3D scans cannot analyse the function of the stomatognathic system. Most of the available craniofacial development studies are empirical or statistical studies, which are continuously reviewed by metanalyses or revisions in the literature. Some revisions, for instance, questioned the relationship between the occlusal disorders and the TMDs or the outcomes of occlusal treatments to prevent further TMDs [194]. Another example could be the cause-effect relationship between UXB and facial asymmetry, some authors [17], [195] did not find significant differences between the shape of both mandibular halves, the masticatory muscles contraction or the chewing pattern in patients with UXB. From the lack of scientific evidence of all these concepts, it is not surprising that N.O.R. has been strongly criticized or rejected by some of the specialists [194]. As it was mentioned, N.O.R's basis is just described by the clinical experience ($>$ 60 years) of Dr Planas, without any scientific evidence. Until now, no study has analytically demonstrated the relationship between form and function of the stomatognathic system in UXB patients.

Despite the above-mentioned doubts, most of the professionals trust on simple selective grinding as the best choice for treating minor UXB in childhood due to the excellent cost/benefit ratio, its simplicity and its short duration [196]. Nevertheless, it seems not to be a clear consensus on the most effective, easy, convenient and stable method. Some studies [197] even doubt about the outcome of the treatment after a time-out and they even recommend to postpone it until the mixed or permanent dentition to allow a possible spontaneous correction of the UXB [198], [199]. Unfortunately, as was advised by Dr Planas, the selective grinding is an irreversible procedure and therefore, it should not conduct on permanent teeth.

In conclusion, notwithstanding recent advances in intraoral diagnosis (with digital occlusion analysis systems as T-Scan) and extraoral diagnosis (with 3D scanners, CBCT or CT), the diagnosis of malformations is still inaccurate. An analytical study, as presented here, would be capable of define properly the direction and the magnitude of the occlusal forces, analyse the effect of UXB in the system development and relate them with the craniofacial deformities. To that end, the facial malformations should be analysed using a sagittal midplane which compensates the asymmetrical features. As a result, this dissertation will analytically demonstrate the role of chewing function in the development of the craniofacial system, the effect of UXB in the development of facial asymmetries and the effectiveness of selective grinding on the malocclusion treatment, and therefore on craniofacial development. This dissertation is, therefore, a valuable scientific reference to demonstrate analytically the applicability of N.O.R in the early treatment of UXB.

1.5.2 Computational studies

One of the biggest advantages of the 3D images obtained from CT, CBCT, MRI, or intraoral scans is their combination using commercial software to simulate the stomatognathic system functions, such as chewing. In engineering, two leading computational techniques are leading the way to understand the craniofacial development according to system's function [200]: the multibody dynamic (MBD) and the finite element (FE) analyses.

MBD is an approach that calculates the connectivity between several rigid bodies with algorithms whose mathematical basis is defined according to several degrees of freedom, and mass and inertia of the rigid bodies [200]. This method is mainly used to determine the forces that act on a model knowing the relative motion of each part [200]. In studies about the craniofacial complex, in particular, it has been widely used [201]–[203] to investigate the muscular forces of chewing muscles for different mandibular movements.

On the other hand, the FE method is a numerical approximation to solve integral equations and partial differential equations which describe the physics of complex structures and joints [200]. In particular, mechanics of deformable solids use FEM to quantify stresses and displacements of a 2D or 3D structure [204]. This method was first introduced into dental biomechanical research in 1973 [205], [206] and since then it has been extensively applied to analyse dental implant effects [207], orthodontic appliances [208], periodontal response [209], teeth eruption [210] or bone remodelling [211], among other research topics. In fact, in 1985, Prof. Melvin. L. Moss, the ideologue of FMH, insisted on the role of the FE method in the study of craniofacial growth [212].

Thereafter, many computational studies [200], [202], [213], [214] have tried to explain the craniofacial growth according to the stresses and deformations of the tissues of the stomatognathic system. However, despite many years of research, the craniofacial growth process is still a controversial topic due to the several limitations for developing accurate FE models of a paediatric craniofacial complex. Some of them are, for instance, the limitation in radiation levels of 3D cephalometric scans or the mineralized state of bones during childhood, the complex discretization of the 3D domain (meshing), the unknown nature of the muscles' forces and tissues' behaviour, or the numerical problems of solving the numerous contacts

involved, amongst other limitations. These computational limitations of the FE models in modelling, meshing, during the characterization of the tissues' behaviour, or at the definition of the boundary conditions [200] will be widely explained below.

Geometry

Early FE analyses were carried out using 2D planar models defined through lateral cephalometric or frontal radiographs [215], [216]. Now, with the introduction of 3D scans (CT, CBCT and MRI), 2D models have been replaced by 3D models which reproduce more accurately the different anatomical features [169], [217], [218]. Nevertheless, the radiological limitations introduced in the previous section for paediatric patients limit their use in children. Regarding this, it is important to note the retrospective nature of the data used in this dissertation, which were obtained from previous research [219], not requiring new scans or injuries to children. In addition to radiological limitations, the reconstruction and the full validation of these 3D models is also difficult because of ethical reasons and physical constraints that make impossible to obtain in vivo data. When craniofacial growth is examined during childhood, there are even greater limitations associated with these issues than during adulthood, thereby the few computational studies at early ages. In this sense, for instance, the unmineralized state of bones physically complicates the model reconstruction due to the low grey gradient between the different parts, requiring a high cost of manual work. The computational models described in Chapter 2 required overcoming these limitations but, they produced biologically plausible results in comparison to in vivo data [220].

Mesh

The geometry is then transformed to a mesh dividing the model into a finite number of discrete subregions (elements) that are connected through nodal points [221]. By going back in time, first 2D FE models were manually meshed assuming plane-stress and plane-strain conditions [215]. Then, manual and semiautomatic meshing algorithms were gradually improved [221] to allow meshing 3D models. The mesh in these models was relatively large due to the immature meshing techniques and required a lot of time to build it [222]. Fortunately, current advances in FE software have automated the meshing methods, conducted rather dense meshes. However, the effectiveness of these algorithms highly depends on the shape and details of the volume to mesh, not being supported by all meshing techniques in every geometry. It is particularly difficult to mesh, for instance, some 3D anatomical regions with hexahedral elements. To solve it, in many 3D FE models, some operations as smoothing geometry, parameterizing surfaces [223], meshing with voxels [224], refining the mesh in complex regions or using tetrahedral elements [225] are performed. Unfortunately, the smoothing tools or voxel mesh algorithms lead to inaccurate geometry [226] and therefore to erroneous results. Besides, although finer mesh produces more accurate results, it increases also the computational cost [226]. By contrast, a smaller element size may cause excessive distortion of the element under large stretching efforts [227].

The automatic mesh generation requires, therefore, a careful oversight based on the specific analysis being performed [226] with greatly refined in the small geometry [34], in the areas of interest [228], in contact surfaces [169] and overstretched regions [229]. Manual partition of the parts also facilitates the meshing process [230] in complex regions, as will conduct to mesh the PDLs in the subsequent chapter.

Forces

Muscle forces in adults have often computed from EMG data [231] and the maximum muscle force obtained from the physiological muscle cross-sectional area (PCSA) of each muscle [232], [233]. Nevertheless, the signal noise and the variability of in vivo measurements [226] have hampered to establish reference values for each muscle, being both measurements strongly questioned in the literature. In children, the consensus of average muscular forces is even weaker than in adults since the ethical limitations of *in vivo* studies at this age [234]. As an alternative to experimental approaches, in the

last years, the MBD analysis has been extended to compute the muscular forces knowing the paths of some reference points. Musculoskeletal models allow the dynamic study of the chewing system under controlled conditions [203], [235], [236], but simplifying the tissues' behaviour as rigid bodies. For a study which computes the muscle forces by considering tissues deformations, it would be necessary the integration of both approaches, MBD and FE analyses.

Boundary conditions

In an idealized FE model of the chewing system, which includes all connective tissues and all contacts pairs, only those parts which have no relative movement should be restricted [202]. In chewing simulations, for instance, the upper region of the skull and the hyoid bone would be often fixed [202] because they are relatively far from the interest region of the model. The mandible movement is then constrained by the TMJ soft tissues, the chewing muscles, the TMJ contact surfaces and the occlusal surfaces of the teeth. However, most computational studies only considered a few soft tissues [218], [229], requiring to over constrain the model because of the non-convergence of the numerical problem. Computational studies often restrict mandibular movement by imposing condyle movements [237] or occlusal forces. This results in non-physiological movements of the joint [238], incorrect stress results [239], and unreal occlusal reactions [169]. Besides, many of the available studies [228], [240] do not mimic the contacts between the articular and occlusal surfaces to minimize the instability of the problem and help to the analysis convergence.

Materials

One of the key aspects of accurate FE modelling is the proper characterization of the material behaviour of the soft tissues involved [221]. The mandibular movement is highly dependent on the mechanical properties of the soft tissues. A well-defined behaviour of the TMJ tissues will lead to a correct mandibular restriction of the movement and therefore to a physiological movement of the mandible [229], [238]. On the other hand, a correct definition of the PDL behaviour contributes to determining the real occlusal pattern [169], [241], [242]. Nevertheless, the effect of them, i.e the PDL's behaviour, is often neglected in some studies [218], [243]–[245], since its complex modelling, leading to high occlusal contacts in a few teeth. In addition, as it will be later discussed, the complex nature of the soft tissues [37], [238], [239], [246] has

resulted in a large number of literature discrepancies about the most appropriate material model or mechanical properties [247] to describe their behaviour. Besides, the experimentation with tissues of species with a chewing system too much different than humans ones has produced contradictory results [248], [249]. This uncertain lead to no consensus about the most suitable properties [250]–[252] or about the real conditions supported by the soft tissues in the stomatognathic system-[253], [254].

In summary, despite the widespread development of modelling, meshing and FE software, the available studies have not been able to model the chewing system completely right [255]. Computational studies should accurately reproduce the system's anatomy, having a regular and appropriate mesh, real boundary conditions, and mimicking accurately the soft tissues' behaviour. Considering all these issues, in this dissertation, the mandibular movements during chewing have been simulated and the consequences of the craniofacial development in UXB patients are analysed.

1.6 Finite element method

In this section, a summary of the Continuum Mechanics is done with an emphasis on the hyperelastic material models used in this dissertation for the mechanical behaviour of soft tissues.

1.6.1 Kinematics

From a macroscopic point of view, a continuum body, Ω with a particle, P, embedded in the three-dimensional Euclidean space, $P\,\varepsilon\,\Omega \rightarrow \mathbb{R}^3$, at an instant of time t occupies different regions of the space denoted by $\Omega_0 \ldots, \Omega(t)$ at each instant of time. The region at initial time, Ω_0, is referred as **undeformed configuration**, while the other positions are referred as **deformed configurations.**

The position of the particle P in the underformed configuration may be defined by the position vector $\mathbf{X}$ relative the orthogonal coordinate origin, O. Meanwhile, the P position in the deformed configuration is defined by the spatial vector, $\mathbf{x}$. The characterization of any quantity with respect X and x is often referred as **Lagrangian** (or material) and **Eulerian** (or spacial) form, respectively.

For instance, Lagrangian description of displacement, $\boldsymbol{U}(\mathbf{X}, t)$, relates the position of P in an instant of time t with the position of the same particle in $t = 0$ as $\mathbf{U}(\mathbf{X}, t) = \mathbf{x}(\mathbf{X}, t) - \mathbf{X}$. Meanwhile, Eulerian description of displacement is given by $\mathbf{u}(\mathbf{x}, t) = \mathbf{x} - \mathbf{X}(\mathbf{x}, t)$.

Deformation gradient tensor

The **deformation gradient tensor F**, is an important quantity of the relative spatial position of particles of a body $\Omega(t)$ in terms of their relative material position before deformation Ω_0, defined as follows:

$$F_{ij} = \frac{\partial x_i}{\partial X_j} \qquad \text{being} \quad i, j = 1,2,3 \tag{1}$$

The $\mathbf{F}$ determinant, $|\mathbf{F}|$, is designated as **Jacobian determinant**, J, and quantifies the change of volume between the undeformed and deformed configuration.

The deformation gradient can be decomposed by the polar decomposition into the stretch and rotation tensors of the continuum body as follows:

$$\mathbf{F} = \mathbf{RU} = \mathbf{vR} \tag{2}$$

The rotation tensor $\mathbf{R}$ is an orthogonal tensor $\mathbf{R}^{\boldsymbol{T}}\,\mathbf{R} = \mathbf{I}$, while $\mathbf{U}$ and $\mathbf{v}$ referred to the right (or material) and left (or spatial) stretch tensor, respectively.

Strain tensors

The strain can be measured in the material and spatial coordinates through the **right Cauchy-Green tensor**, $\mathbf{C}$, and **left Cauchy-Green tensor**, $\mathbf{b}$, respectively.

$$\mathbf{C} = \mathbf{F}^T\mathbf{F} \quad \boldsymbol{and} \quad \mathbf{b} = \mathbf{F}\mathbf{F}^T \tag{3}$$

By easy mathematical transformation, $\mathbf{C}$ and $\mathbf{b}$ may be expressed by the stretch and rotation tensors as follows:

$$\mathbf{C} = \mathbf{UU} = \mathbf{U^2} \quad \boldsymbol{and} \quad \mathbf{b} = \mathbf{vv} = \mathbf{v^2} \tag{4}$$

Stress tensors

The **Cauchy stress tensor**, $\boldsymbol{\sigma}$, relates the force per unit area in the current configuration at time t. In a three-dimensional space it can be expressed as $\boldsymbol{\sigma} = \boldsymbol{\sigma}_{ij}$ for $i,j = 1,2,3$.

The **Kirchhoff stress tensor** ($\boldsymbol{\tau} = J\boldsymbol{\sigma}$), is a commonly used tensor to describe stresses of the solid by the Jacobian determinant J.

The **second Piola-Kirchhoff stress tensor S,** is a symmetric tensor that can be related to the Cauchy stress tensor by:

$$\boldsymbol{\sigma} = J^{-1}\mathbf{F}\mathbf{S}\mathbf{F}^{\boldsymbol{T}} \tag{5}$$

If it is defined by the pull-back operations on $\boldsymbol{\tau}$, it can be described as:

$$\mathbf{S} = \boldsymbol{\phi}^*[\boldsymbol{\tau}] = \mathbf{F}^{-1}\boldsymbol{\tau}\mathbf{F}^{-\mathrm{T}} \tag{6}$$

Finally, the **first Piola-Kirchhoff stress tensor, P,** relates the force in the current configuration with the unit area of the undeformed configuration by the following equation:

$$\mathbf{P} = \mathbf{FS} \tag{7}$$

1.6.2 Conservation laws

In the following section the conservation laws (mass, moment, energy and entropy inequality) are explained to relate the functional variables previously defined.

Conservation of mass

The basis of this law can be summarized as mass, m, cannot be produced or destroyed and can be written as:

$$m = \int_{\Omega_0} \rho dV = \int_{\Omega} \rho_c dv \tag{8}$$

where ρ and ρ_c are the reference and spatial mass density respectively. Through easy mathematical transformations, previous equation leads to $\rho = J\rho_c$. Therefore, conservation mass throughout the position at time t has to be zero, leading:

$$\frac{D}{Dt}m = \frac{D}{Dt}\int_{\Omega} \rho_c dv = \frac{D}{Dt}\int_{\Omega_0} \rho dV = \frac{D}{Dt}\int_{\Omega_0} J\rho_c dV = 0 \tag{9}$$

Considering that $\frac{DJ}{Dt} = J\nabla \cdot v$ and after some transformation, the previous equation can lead to the final form of the continuity equation, as a function of the spatial velocity, v:

$$\frac{D\rho}{Dt} + \rho_c \nabla \cdot v = 0 \tag{10}$$

Conservation of momentum

The balance of linear momentum can be written as:

$$\dot{\boldsymbol{L}}(t) = \frac{D\boldsymbol{L}}{Dt} = \frac{D}{Dt}\int_{\Omega} \rho_c v dv = \int_{\partial\Omega} \boldsymbol{t} ds + \int_{\Omega} \rho_c \hat{\boldsymbol{b}} dv \tag{11}$$

where $\boldsymbol{L}$ is the total linear momentum defined by the spatial mass density and spatial velocity, $\boldsymbol{t}$ is the Cauchy traction vector, $\boldsymbol{ds}$ is an infenitesimal spatial surface, $\boldsymbol{dv}$ is the infinitesimal spatial velocity and $\widehat{\boldsymbol{b}}$ is the body force per unit of mass.

Through the divergence and Cauchy's stress ($\mathbf{t} = \boldsymbol{\sigma} \cdot \mathbf{n}$) theorems, previous equation leads to:

$$\rho_c \frac{Dv}{Dt} = \boldsymbol{\nabla} \cdot \boldsymbol{\sigma} + \rho_c \widehat{\boldsymbol{b}} \tag{12}$$

On the other hand, the **balance of angular momentum** ($\dot{\boldsymbol{J}}$) can be written as:

$$\dot{\boldsymbol{J}}(t) = \frac{D\boldsymbol{J}}{Dt} = \frac{D}{Dt}\int_{\Omega} x \times (\rho_c \widehat{\boldsymbol{b}}) dv = \int_{\partial\Omega} x \times \mathbf{t} dS + \int_{\Omega} x \times (\rho_c \widehat{\boldsymbol{b}}) dv \tag{13}$$

As in the previous case, by the divergence and Cauchy's stress theorems the equation this equation is derived:

$$\int_{\Omega} \boldsymbol{\mathcal{E}} : \boldsymbol{\sigma}^{\boldsymbol{T}} + \boldsymbol{x} \times \left(\boldsymbol{\nabla} \cdot \boldsymbol{\sigma} + \rho_c \widehat{\boldsymbol{b}} - \rho_c \frac{Dv}{Dt} \right) dv = 0 \tag{14}$$

Replacing the second term by the balance of linear momentum, the previous equation leads $\int_{\Omega} \boldsymbol{\mathcal{E}} : \boldsymbol{\sigma}^{\boldsymbol{T}} = \mathbf{0}$ which is a demonstration of the symmetry of the Cauchy stress tensor.

Conservation of energy

The first law of thermodynamics ($D/Dt(K + \mathcal{E}) = W + U$) is defined by the kinetic energy (K), the internal energy ($\mathcal{E}$), the external mechanical work (W) and the thermal power (U) as follows:

$$\begin{aligned} &\overbrace{\frac{D}{Dt}\int_{\Omega} \rho_c \mathbf{v} \cdot \mathbf{v} dv}^{K} + \overbrace{\frac{D}{Dt}\int_{\Omega} e_c dv}^{\mathcal{E}} \\ &= \overbrace{\int_{\Omega} \widehat{\boldsymbol{b}} \cdot \mathbf{v} dv + \int_{\partial\Omega} \mathbf{t} \cdot \mathbf{v} ds}^{W} + \overbrace{\int_{\Omega} r dv - \int_{\partial\Omega} \boldsymbol{q} \cdot n ds}^{U} \end{aligned} \tag{15}$$

where e_c is the internal energy per unit of volume, $\boldsymbol{q}$ is the Cauchy heat flux vector and r is the heat source in the current volume. Then, applying Reynolds' transport theorem to the left term and the divergence theorem to the second and fourth integrals of the right term, previous equation can be result in the differential equation of the first law of thermodynamics:

$$\dot{e_c} + \boldsymbol{\nabla} \cdot \mathbf{q} = r + \boldsymbol{\sigma} : \mathbf{d} \tag{16}$$

where $\mathbf{d}$ is the deformation tensor rate, $\mathbf{d} = {}^{1}/_{2}\,(\boldsymbol{\nabla}\mathbf{v} + \boldsymbol{\nabla}\mathbf{v}^{\mathrm{T}})$.

Same equation can be rewritten in the Lagrangian form as:

$$\dot{e} + Div\mathbf{Q} = R + \mathbf{P} : \dot{\mathbf{F}} \tag{17}$$

where $\dot{e}$ is the internal energy rate per unit of volume, $\boldsymbol{Q}$ is the heat flux per unit of surface area and R is the heat source per unit ofg time and volume.

Entropy inequality principle

The second law of thermodynamics demonstrate the positive sign of the total entropy (Γ) production in all thermodynamic processes:

$$\Gamma(t) = \frac{D}{Dt}\int_{\Omega} \eta_c dv + \int_{\Omega} \frac{\boldsymbol{q}\cdot\boldsymbol{n}}{\theta} dS - \int_{\Omega} \frac{r}{\theta} dv \geq 0 \tag{18}$$

where η_c is the entropy per unit of volume, r is the entropy per unit of time and volume and θ is a scalar magnitude of the absolute temperature. Then, applying Reynolds' transport and divergence theorems to the first and the second integrals respectively, previous equation is rewritten as:

$$\int_{\Omega} \dot{\eta_c} dv \geq \int_{\Omega} \left[\frac{r}{\theta} - \nabla \cdot \left(\frac{\boldsymbol{q}}{\theta}\right)\right] dv \tag{19}$$

Therefore, $\dot{\eta_c} \geq \frac{1}{\theta} r - \nabla \cdot \left(\frac{\boldsymbol{q}}{\theta}\right)$ for any arbitrary volume. This inequation is known as the Eulerian description of the **Clausius-Duhem inequality**. In Lagrange description it is formulated as $\dot{\eta} \geq (1/\Theta) \cdot R - \mathrm{Div} \cdot (\mathbf{Q}/\Theta)$. Deleting the heat source and replacing $\mathbf{Q}$ divergence by the equation (17).

$$\mathbf{P}:\dot{\mathbf{F}} - \dot{e} + \Theta\dot{\eta} - \frac{1}{\Theta} Grad\Theta \geq 0 \tag{20}$$

Due to the direction of heat (from warmer to colder region), last term must be non-negative. This restriction introduces the **Clausius-Plank inequality** which determines that the internal dissipation or production of entropy, $\mathcal{D}_{int}$, must be nonnegative. In mechanical theory, it is common to use Helmholtz free-energy function (Ψ) or free energy to replace $e + \Theta\eta$, leading:

$$\mathcal{D}_{int} = \mathbf{P}:\dot{\mathbf{F}} - \dot{e} + \Theta\dot{\eta} = \mathbf{P}:\dot{\mathbf{F}} - \dot{\Psi} - \eta\dot{\Theta} \geq 0 \tag{21}$$

It is remarkable that the thermal effects ($-\eta\dot{\Theta}$) are neglected in the following sections of this thesis.

1.6.3 Hyperelasticity

An elastic material is characterized by a no internal dissipation ($\mathcal{D}_{int}$). Therefore, the **Clausius-Plank inequality** (Eq. 21) can be rewritten as follows:

$$\mathcal{D}_{int} = \mathbf{P}:\dot{\mathbf{F}} - \dot{\Psi} = 0; \quad \mathcal{D}_{int} = \left(\mathbf{P} - \frac{\partial\Psi(\mathbf{F})}{\partial\mathbf{F}}\right):\dot{\mathbf{F}} = 0 \tag{22}$$

For an arbitrary $\mathbf{F}$ and $\dot{\mathbf{F}}$, this equation can be expressed as:

$$\mathbf{P} = \frac{\partial\Psi(\mathbf{F})}{\partial\mathbf{F}} \tag{23}$$

Hence, the function of a **hyperelastic** or **Green-elastic** constitutive model is a scalar function whose derivate with respect the stretch tensor determines the stress tensor. By considering that Ψ is invariant of the current configuration, depends exclusively on $\mathbf{F}$ via the right stretch tensor ($\mathbf{U}$) and the right Cauchy-Green tensor ($\mathbf{C}$) is given by equation (4), $\Psi(\mathbf{F})$ can be expressed as a function of $\mathbf{C}$ as:

$$\Psi(\mathbf{F}) = \Psi(\mathbf{C}) = \Psi[I_1(\mathbf{C}), I_2(\mathbf{C}), I_3(\mathbf{C})] \tag{24}$$

where these invariants are defined according $\mathbf{C}$ eigenvalues $(\lambda_1, \lambda_2, \lambda_3)$ as follows:

$$I_1 = tr(\mathbf{C}) = \lambda_1^2 + \lambda_2^2 + \lambda_3^2 \tag{25}$$

$$I_2 = {}^1\!/_2 \left[tr(\mathbf{C})^2 - tr(\mathbf{C^2})\right] = \lambda_1^2\lambda_2^2 + \lambda_1^2\lambda_3^2 + \lambda_2^2\lambda_3^{\,2} \tag{26}$$

$$I_3 = det(\mathbf{C}) = \lambda_1^2\lambda_2^2\lambda_3^2 \tag{27}$$

Hence, from the equation (6) the second Piola-Kirchhoff stress tensor can be rewritten:

$$\mathbf{S} = 2\frac{\partial \Psi(\mathbf{C})}{\partial \mathbf{C}} = 2\left[\frac{\partial \Psi}{\partial I_1}\frac{\partial I_1}{\partial \mathbf{C}} + \frac{\partial \Psi}{\partial I_2}\frac{\partial I_2}{\partial \mathbf{C}} + \frac{\partial \Psi}{\partial I_3}\frac{\partial I_3}{\partial \mathbf{C}}\right] \tag{28}$$

According to equation (7) the First Piola-Kirchhoff stress tensor is:

$$\mathbf{P} = \mathbf{FS} = 2\mathbf{F}\frac{\partial \Psi(\mathbf{C})}{\partial \mathbf{C}} \tag{29}$$

And according equation (5) the Cauchy stress tensor is given by:

$$\begin{aligned} \boldsymbol{\sigma} &= 2J^{-1}\mathbf{b}\frac{\partial \Psi(\mathbf{b})}{\partial \mathbf{b}} \\ &= 2J^{-1}\left[I_3\frac{\partial \Psi}{\partial I_3}\mathbf{I} + \left(\frac{\partial \Psi}{\partial I_1} + I_1\frac{\partial \Psi}{\partial I_1}\right)\mathbf{b} - \frac{\partial \Psi}{\partial I_2}\mathbf{b^2}\right] \end{aligned} \tag{30}$$

In compressible materials, strain energy function can be decomposed into the deviatoric and volumetric responses of the material.

$$\Psi(\mathbf{C}) = \Psi_{dev}(\overline{\mathbf{C}}) + \Psi_{vol}(\mathbf{C}) = \Psi_{dev}[I_1(\mathbf{C}), I_2(\mathbf{C})] + \Psi_{vol}(J) \tag{31}$$

Therefore, the equation (28) of second Piola-Kirchhoff stress tensor can also split to:

$$\mathbf{S} = 2\frac{\partial \Psi_{dev}(\overline{\mathbf{C}})}{\partial \mathbf{C}} + 2\frac{\partial \Psi_{vol}(J)}{\partial \mathbf{C}} = \mathbf{S_{dev}} + \mathbf{S_{vol}} \tag{32}$$

where $\mathbf{S_{dev}} = J^{-2/3}\left(\mathbb{I} - \frac{\mathbf{1}}{\mathbf{3}}\mathbf{C^{-1}} \otimes \mathbf{C}\right) : \bar{\mathbf{S}}$ and $\mathbf{S_{vol}} = Jp\mathbf{C^{-1}}$, being p the hydrostatic pressure defined as $p = d\Psi_{\mathrm{vol}}(J)/dJ$.

Likewise, the Cauchy stress tensor of equation (30) can be split into deviatoric and volumetric components as follows:

$$\boldsymbol{\sigma} = 2J^{-1}\mathbf{b}\frac{\partial \Psi_{iso}(\mathbf{b})}{\partial I_{\mathbf{b}}} + 2J^{-1}\mathbf{b}\frac{\partial \Psi_{vol}(\mathbf{b})}{\partial I_{\mathbf{b}}} = \boldsymbol{\sigma_{dev}} + \boldsymbol{\sigma_{vol}} \tag{33}$$

where $\boldsymbol{\sigma_{dev}} = \left(\mathbb{I} - \frac{\mathbf{1}}{\mathbf{3}}\mathbf{I} \otimes \mathbf{I}\right) : \bar{\boldsymbol{\sigma}}$ and $\boldsymbol{\sigma_{dev}} = p\mathbf{I}$.

In computational mechanics is common to solve nonlinear problems through the linearization of the constitutive equations. To that end, the **elasticity tensor** is defined as:

$$\begin{aligned} \mathbb{C} &= \mathbb{C}_{dev} + \mathbb{C}_{vol} \\ &= 2\frac{\partial \mathbf{S_{dev}}(\bar{\mathbf{C}})}{\partial \mathbf{C}} + 2\frac{\partial \mathbf{S_{vol}}(\bar{\mathbf{C}})}{\partial \mathbf{C}} = 4\frac{\partial^2 \boldsymbol{\Psi}_{\boldsymbol{dev}}(\bar{\mathbf{C}})}{\partial \mathbf{C}\,\partial \mathbf{C}} + 4\frac{\partial^2 \boldsymbol{\Psi}_{\boldsymbol{vol}}(\bar{\mathbf{C}})}{\partial \mathbf{C}\,\partial \mathbf{C}} \end{aligned} \tag{34}$$

In Eulerian description, c is J^{-1} times the push-forward of $\mathbb{C}$. Hence, c is defined as:

$$c = c_{dev} + c_{vol} \tag{35}$$

where deviatoric and volumetric components are given from the following expressions:

$$\begin{aligned} Jc_{dev} &= 4b\frac{\partial^2 \boldsymbol{\Psi}_{\boldsymbol{dev}}(J)}{\partial \mathbf{b}\,\partial \mathbf{b}}\mathbf{b} = \\ &= \mathbb{P} : 4\bar{\mathbf{b}}\frac{\partial^2 \boldsymbol{\Psi}_{\boldsymbol{dev}}(\bar{\mathbf{b}})}{\partial \bar{\mathbf{b}}\,\partial \bar{\mathbf{b}}}\bar{\mathbf{b}} : \mathbb{P} + \frac{\mathbf{2}}{\mathbf{3}}\boldsymbol{tr}(J\bar{\boldsymbol{\sigma}})\mathbb{P} - \frac{\mathbf{2}}{\mathbf{3}}(\mathbf{I} \otimes J\bar{\boldsymbol{\sigma}} + J\bar{\boldsymbol{\sigma}} \otimes \mathbf{I}) \end{aligned} \tag{36}$$

Resulting in the following expression:

$$Jc_{vol} = 4b\frac{\partial^2 \boldsymbol{\Psi}_{\boldsymbol{vol}}(J)}{\partial \mathbf{b}\,\partial \mathbf{b}}\mathbf{b} = J\left[\left(p + J\frac{dp}{dJ}\right)\mathbf{I} \otimes \mathbf{I} - \mathbf{2}p\mathbb{I}\right] \tag{37}$$

1.6.4 Biphasic elastic models

The stress state in a porous solid matrix ($\boldsymbol{\sigma}^s$) has a double contribution: pressure due to the interstitial fluid and the internal stress state of the solid matrix called effective Cauchy stress tensor, $\boldsymbol{\sigma}_E^s$. The stress state is now defined by the following way:

$$\boldsymbol{\sigma}^s = -\phi^s p\boldsymbol{I} + \boldsymbol{\sigma}_E^s \tag{38}$$

where ϕ^s is the fraction of solid volume of the medium defined by the inherent density of the solid $\overline{\rho^s}$ and the physical density of the solid $\rho^s = \rho_0^s J^{-1}$ which is affected over time by the coupling between the solid and liquid phases. In a saturated tissue, the interstices of the tissue must be filled. Hence, the sum of the solid and liquid phase (ϕ^f) must satisfy $\phi^s + \phi^f = 1$. On the other hand, the effective Cauchy stress tensor $\boldsymbol{\sigma}_E^s$ is related to the second effective Piola-Kirchhoff tensor, $\mathbf{S}_E^s$, by:

$$\boldsymbol{\sigma}_E^s = \frac{1}{J^s}\mathbf{F}^{-1}\mathbf{S}_E^s\mathbf{F}^{-\mathrm{T}} \tag{39}$$

where $\mathbf{S}_E^s$ can be written in terms of the right Green stress tensor as:

$$\mathbf{S}_E^s = 2\frac{\partial\Psi^s(\overline{\mathbf{C}}^s)}{\partial\mathbf{C}^s} \tag{40}$$

In biphasic material models, the conservation laws previously explained in section 1.3.2 are rewritten as follows:

Conservation of mass [256]–[259]*:*

$$\nabla\cdot\left(\phi^s\boldsymbol{v}^s + \phi^f\boldsymbol{v}^f\right) = 0 \tag{41}$$

where $\boldsymbol{v}^s$ and $\boldsymbol{v}^f$ are the spatial velocities of the solid and fluid phases respectively.

Balance equations [257], [260], [261]*:*

$$\boldsymbol{\nabla}\cdot\boldsymbol{\sigma}_e^s - \phi^s\boldsymbol{\nabla}p - \mathbf{K}\cdot\left(\boldsymbol{v}^s - \boldsymbol{v}^f\right) = 0 \tag{42}$$

$$-\phi^f\boldsymbol{\nabla}p + \mathbf{K}\cdot\left(\boldsymbol{v}^s - \boldsymbol{v}^f\right) = 0 \tag{43}$$

where $\mathbf{K}$ is defined by $\rho^f\mathbf{q}^f = -\mathbf{K}\cdot\boldsymbol{v}^f + p\nabla\phi^f$, being $\mathbf{q}^f$ the interaction force applied by the solid phase per unit of fluid mass.

Clausius-Duhem inequality [262]*:*

$$\rho^s \mathbf{q}^s = -\rho^f \mathbf{q}^f = \mathbf{K} \cdot \left(\boldsymbol{v}^f - \boldsymbol{v}^s\right) + p\nabla\phi^s \tag{44}$$

$$\rho^f \mathbf{q}^f = -\mathbf{K} \cdot \left(\boldsymbol{v}^f - \boldsymbol{v}^s\right) + p\nabla\phi^f \tag{45}$$

where $\mathbf{q}^s$ is the interaction force applied by the fluid phase per unit of solid mass.

To integrate fluid contribution in the global stiffness matrix, the computational software used (Abaqus 6.14, Simulia, Rhode Island, USA) defines the scalar diffusion coefficient K as a function of tissues permeability, :

$$K = \frac{\phi^f}{k} \tag{46}$$

In this work, the exponential permeability function described by Argoubi and Shirazi-Adl, 1996 [263] for biphasic material is used:

$$k = k_0 \left[\frac{e(1+e_0)}{e_0(1+e)}\right]^2 exp\left[M\left(\frac{1+e}{1+e_0} - 1\right)\right] \tag{47}$$

where k_0 is the permeability at zero strain, M is a dimensionless material parameter, e is the void ratio defined as the ratio of the volume of fluid (V_f) to the total volume (V_t) by $n = dV_f/dV_t$ in the current time, and e_0 is the void ratio at zero strain.

1.6.5 Hyperelastic material models for biological tissues

Soft tissues are mainly composed by fibres embedded in a hyperelastic matrix that result in an isotropic or anisotropic mechanical response that is typically described by a hyperelastic constitutive equation. Some of the most used constitutive equations are summarized in this section.

Isotropic material models

Neo-Hookean model [264]:

$$\Psi = C_{10}(\overline{I_1} - 3) + \frac{1}{D_1}(J-3)^2 \tag{48}$$

where C_{10} is a temperature-dependent material parameter, and D_1 is a temperature dependent material parameter, which controls the compressibility of the material.

Polynomial model [265]:

$$\Psi = \sum_{i,j=0}^{n} C_{ij}(\bar{I}_1 - 3)^i (\bar{I}_2 - 3)^j + \sum_{i,j=0}^{n} \frac{1}{D_i}(J-3)^{2i} \tag{49}$$

where n describes the order of the function, C_{ij} is a temperature-dependent material parameter and D_i is again the compressibility of the tissue.

Ogden model [266]:

$$\Psi = \sum_{i=1}^{n} \frac{2\mu_i}{\alpha_i^2}\left(\bar{\lambda}_1^{\alpha_i} + \bar{\lambda}_3^{\alpha_i} + \bar{\lambda}_3^{\alpha_i} - 3\right) + (\bar{I}_2 - 3)^j + \sum_{i=1}^{n} \frac{1}{D_i}(J-3)^{2i} \tag{50}$$

where, λ_1, λ_2 and λ_3 are the eigenvalues of the right Cauchy-Green tensor, n is a material parameter, μ_i and α_i are temperature parameters and D_i is the compressibility parameter.

Elastic foam [267]

$$\Psi = \sum_{i,j=0}^{n} \frac{2\mu_i}{{\alpha_i}^2}\left[\bar{\lambda}_1^{\alpha_i} + \bar{\lambda}_2^{\alpha_i} + \bar{\lambda}_3^{\alpha_i} - 3 + \frac{1}{\beta_i}\left(J^{\alpha_i\beta_i} - 1\right)\right] \tag{51}$$

where μ and α are material parameters, and the coefficient β determines the degree of compression related to the Poisson's ratio, ν, by $\beta = \nu/(1-2\nu)$.

Transversely isotropic material models

Some material models incorporate the anisotropy behaviour that is caused by fibres bundles using the pseudo-invariants. The pseudo-invariants describe the relation between the vector that define the direction of the fibrous bundle, $\boldsymbol{a^0}$, and the deformation tensor as:

$$\bar{I}_4 = \boldsymbol{a}^0 \cdot \boldsymbol{C} \cdot \boldsymbol{a}^0 \quad \text{and} \quad \bar{I}_5 = \boldsymbol{a}^0 \cdot \boldsymbol{C^2} \cdot \boldsymbol{a}^0 \tag{52}$$

Therefore, the energy density function of a transversally isotropic material can be written in terms of the five invariants[1] as follows:

$$\Psi(\mathbf{F}) = \Psi(\mathbf{C}, \boldsymbol{a}^0) = \Psi\left[\bar{I}_1(\mathbf{C}), \bar{I}_2(\mathbf{C}), \bar{I}_3(\mathbf{C}), \bar{I}_4(\mathbf{C}, \boldsymbol{a}^0), \bar{I}_5(\mathbf{C}, \boldsymbol{a}^0)\right]$$

The most used material models that follows this approach are the Weiss [268], Humphrey and Na [269], Gasser [270] and Holzapfel [271] material models. In this section, the Holzapfel's material model is described due to it was implemented in the computational models later explained.

Holzapfel model [271]:

$$\begin{aligned}\Psi = \; & C_1 \cdot (\tilde{I}_1 - 3) + \frac{k_1}{2 \cdot k_2}\left\{exp\left[k_2 \cdot \left(\bar{I}_4 - 1\right)^2\right] - 1\right\} \\ & + \frac{1}{D}\left[\frac{(J)^2 - 1}{2} - lnJ\right]\end{aligned} \tag{53}$$

where C_1 is a material constant related to the matrix substance, $k_1 > 0$ and $k_2 > 0$ are the parameters which identify the exponential behaviour due to the presence of collagen fibres and D is the compressibility parameter related to bulk modulus K, by $K = 2/D$.

Therefore, the second Piola-Kirchhoff stress tensor can be expressed:

$$\mathbf{S} = 2\frac{\partial \Psi_{dev}(\bar{\mathbf{C}}, \boldsymbol{a}^0 \otimes \boldsymbol{a}^0)}{\partial \mathbf{C}} = 2\left[\frac{\partial \Psi}{\partial \bar{I}_1}\frac{\partial \bar{I}_1}{\partial \mathbf{C}} + \frac{\partial \Psi}{\partial \bar{I}_2}\frac{\partial \bar{I}_2}{\partial \mathbf{C}} + \frac{\partial \Psi}{\partial \bar{I}_3}\frac{\partial \bar{I}_3}{\partial \mathbf{C}} + \frac{\partial \Psi}{\partial \bar{I}_4}\frac{\partial \bar{I}_4}{\partial \mathbf{C}}\right] \tag{54}$$

Likewise, the Cauchy stress tensor is written as following:

$$\boldsymbol{\sigma} = 2J^{-1}\left[\tilde{I}_3\frac{\partial \Psi}{\partial \tilde{I}_3}\mathbf{I} + \left(\frac{\partial \Psi}{\partial \tilde{I}_1} + \tilde{I}_1\frac{\partial \Psi}{\partial \tilde{I}_2}\right)\mathbf{b} - \frac{\partial \Psi}{\partial \tilde{I}_2}\mathbf{b}^2 + \tilde{I}_4\frac{\partial \Psi}{\partial \tilde{I}_4}\boldsymbol{a}^0 \otimes \boldsymbol{a}^0\right] \tag{55}$$

Finally, the elasticity tensor $\mathbb{C}$ can be defined as:

$$\mathbb{C} = 2\frac{\partial \bar{\mathbf{S}}(\bar{\mathbf{C}})}{\partial \mathbf{C}} = 4\frac{\partial^2 \boldsymbol{\Psi}_{\boldsymbol{dev}}(I_1, I_2, I_4)}{\partial \mathbf{C}\,\partial \mathbf{C}} + 4\frac{\partial^2 \boldsymbol{\Psi}_{\boldsymbol{vol}}(\bar{\mathbf{C}})}{\partial \mathbf{C}\,\partial \mathbf{C}} \tag{56}$$

[1] The contribution of $\tilde{I}_5$ is often neglected since its effect is mostly reproduced by $\tilde{I}_4$.

1.7 Motivation

The main motivation of this research is founded on the high social and economic impact of the anomalous growth and development of the stomatognathic system due to malocclusions [272]. Malocclusions are considered by the World Health Organization the third dental problem [272]. In this sense, functional UXB is one of the main causes of the anomalous growth of the stomatognathic system in patients with no associated genetic problems. As introduced, UXB affects between 7.1% to 23.3% of the general population [77]–[80] and its rate is increasing in industrialized economies due to the breastfeeding habits [154], [156], the breathing problems [150] and the low-consistency diet [167], [168]. As a consequence of UXB, changes in tooth eruption [210] and in the normal growth of the skull and mandible [152] can occur, leading in the adulthood to occlusal problems [154], [156], periodontal diseases [35], TMDs [194], displacement of the articular disc [112], joint sounds [112], bone resorption [35], atrial or muscle pain [112], among others. That is why it is important to treat them early.

Nevertheless, although an early treatment of UXB could avoid further problems, it is difficult to identify the morphological abnormalities of the skull due to limitations such as: the correct definition of the sagittal midplane, the reconstruction of the unmineralized osseous regions or the ethical restrictions of use CT or CBCT scanning in paediatric patients, among others. More knowledge of the morphological abnormalities in paediatric patients may demonstrate the applicability of N.O.R in the early treatment of UXB.

Simultaneously to clinical researches, several computational studies have been conducted [200], [202], [213], [214] to demonstrate analytically the role of chewing in the development of craniofacial system [273], [274] and the role of UXB in the development of facial asymmetries [275]. Nonetheless, most of the available studies use simplified FE models because of the complex anatomy of the stomatognathic system, the biphasic behaviour of its tissues or the sophisticated movement of the mandible. Further investigations seem to be needed to provide an analytic explanation of the relationship between function and shape, as described in the FMH by Melvin Moss (1962) [64], [65].

1.8 Objectives

From the abovementioned motivation, the main goal of this dissertation is to explain how occlusion affects the development of the stomatognathic system during childhood using detailed computational models of the masticatory system. Hence, this Thesis attempts to answer the following questions. First, is there a significant relationship between craniofacial malformations and the functional UXB? Second, how can the neuro-stimulation of the PDLs and TMJs affect to the asymmetrical development of the stomatognathic system in patients with UXB, and in particular, to the mandible and maxilla growth? Finally, how does selective grinding modify the neuro-stimulation in the PDLs, TMJs and bony structures?

Although some previous studies have attempted to address these questions, their findings present some limitations, as was introduced in section 1.5. To respond to the initial question, for instance, the clinical studies [180], [181], [183] employed sagittal midplanes which were defined without compensating the asymmetric features, possibly leading to erroneous and subjective results [182]. Regarding the second issue, several computational studies [200], [276], [277] attempted to correlate their physical results with the growth theory proposed by Melvin, the Functional Matrix Hypothesis (discussed in section 1.2.3). Nonetheless, FE models are often simplified and cannot reproduce the biphasic nature of the soft tissues, or the complex geometry and motion of the TMJ (section 1.5.2). Thus, the analytical data available is not enough to demonstrate the basis of the FMH and even less about how UXB affects the asymmetrical development of the stomatognathic system during childhood. Finally, few studies have computationally examined [278], [279] the selective grinding treatment, and none have evaluated it using FE models of paediatric patients. Analytical results of the biomechanical effect of selective grinding would validate the principles of Neuro-Occlusal Rehabilitation as an early treatment of UXB.

Therefore, to achieve the main objective of this dissertation it is also necessary to reach the following partial objectives:

(O.1) To implement a computational algorithm for determining the sagittal midplane of the skull of patients with facial asymmetry, by compensating the morphological differences between both facial sides

(O.2) To develop accurate FE models of the paediatric craniofacial system which consider the irregular morphology of the craniofacial system, the activation of the elevator and depressor muscles, the occlusal contacts, the TMJ motion and the biphasic mechanical behaviour of the soft tissues, in particular, the PDL and TMJ disc responses.

(O.3) To characterize the PDL' biphasic behaviour and to evaluate its mechanical response under cyclic and/or traumatic loads that may occur on the patient. To this end, it will be necessary for the implementation of a porous transversally isotropic hyperelastic material model which considers the damage phenomena produced by the cyclic loading and the overstretching of the tissue. This model should be characterized by experimental data from the literature.

(O.4) To characterize the mechanical behaviour of the TMJ' soft tissues, in particular, the biphasic behaviour of the TMJ disc. It will, therefore, require the numerical approximation of hyperelastic material models to experimental data of the literature. The characterization of these tissues should be able to mimic the dynamic and static behaviour of the joint through FE models which include these material descriptions.

(O.5) To develop FE models of the craniofacial system of children with UXB or without malocclusions which incorporate the biphasic and hyperelastic behaviours studied previously for PDLs and TMJ' soft tissues.

(O.6) To in silico evaluate the physical changes which produce different alternatives of the selective grinding treatment under maximum intercuspation or chewing conditions.

We hope that this dissertation will help professionals in various sectors (including engineers, prosthetic developers, orthodontists, dentists, rehabilitation physicians, surgeons) to have a better understanding of how the mechanical occlusion can affect to the development of the stomatognathic system, in order to adapt and refine therapies that take both physiology and biology into consideration.

1.9 Thesis outline

This dissertation is presented under the modality of a thesis by a compendium of publications according to the requirements established by the University of Zaragoza following the agreement of 25th of June of 2020 of the Governing Council that approves the Regulations of the Doctoral Thesis. According to these specifications, this dissertation is composed of the following 3 chapters.

Summary presents a brief introduction of the issue covered, a summary of the work done and the main findings of this research.

In **chapter 1**, Introduction, the anatomy of the stomatognathic system is described, attending to the skeletal, muscular, neural and occlusal (teeth). subsystems. Then, the mechanisms of ossification and growth (sutural, cartilaginous or periosteal/endosteal) are also detailed, reviewing the main theories that have attempted to explain craniofacial growth. From this literature review, the FMH of Dr Melvin Moss and N.O.R concepts of Dr Pedro Planas are highlighted due to the biomechanical approach of this dissertation. Afterwards, the 3 main functional stimuli (breathing, breastfeeding and chewing) of the maxillofacial growth are explained and how some functional alterations in childhood may cause malocclusions such as UXB or severe disorders in adulthood. It is then highlighted the importance of early treatment to avoid further complications in adulthood. Almost at the end of this chapter, there is a review of the clinical and computational studies that have attempted to explain how occlusion or malocclusion affects the normal or abnormal development of the craniofacial system, respectively. Finally, the limitations of these studies are outlined, and the main objectives of this work are described.

In chapter 2, the nine manuscripts that constitute the main body of the Thesis are compiled. The manuscripts 1-6 and 9 are already published in high-impact journals, while manuscripts 7 and 8 are under review.

In manuscript 1, the morphological differences between both facial sides in five patients with UXB and five healthy patients are three-dimensionally analysed using a sagittal midplane which compensates the anatomical differences between both sides of the face. To that end, a computational algorithm which defines a real sagittal midplane is presented throughout this chapter, and some of the most characteristic facial features are statistically studied.

In manuscript 2, it is explained the characterization process of the porous transversally isotropic hyperelastic material properties of the PDL and the evaluation of the mechanical response in a detailed FE model of a tooth that was obtained through μCT.

In manuscript 3, the PDL damage phenomena caused by cyclical loading and tissue overstretching are analysed, by including them in the material model described in manuscript 1.

In manuscript 4, the damage of the PDL's porous-fibrous structure, which was characterized in chapter 3, is analysed subjecting the fine-detailed FE model of a tooth (manuscript 2) to the occlusal responses gathered from another FE model of the full dentition under normal, traumatic and parafunctional loading conditions.

In manuscript 5, it is presented the characterization and validation of the material models that describe the biphasic behaviour of the TMJ disc and the transversally isotropic hyperelastic response of remaining soft tissues in the TMJ such as the retrodiscal tissue, condylar cartilage, and collateral ligaments.

In manuscript 6, the TMJ's dynamic and damping responses are compared by using isotropic or transversally isotropic (characterized in manuscript 6) properties in detailed FE models of six TMJ, which were developed from the combination of MRI and CT databases.

In manuscript 7, it is related the craniofacial morphology with the physical results (in the PDLs, TMJs and bones) which are produced by the simulation of maximum intercuspation occlusion in ten FE models of the masticatory system of 5 children without malocclusions and other 5 with UXB. These in silico models are developed from the database used in manuscript 1 and incorporate the mechanical properties characterized and validated in manuscripts 2 -6.

In manuscript 8, it is computationally studied how different alternatives of the N.O.R treatments can affect to the occlusal rehabilitation and the correction of the mechanical stimulation on the PDLs, TMJs and bony structures of a paediatric patient with UXB, by simulating bilateral chewing. For this purpose, a patient-specific FE model is subjected to the muscle activations gathered from a MBD model, also explained throughout the chapter.

Additionally, **in manuscript 9**, a preliminary approach of the integration of biomechanical engineering in the diagnosis of craniofacial malformations is described by using shape recognition algorithms on panoramic radiographs and automatic generation of planar FE models.

Finally, **chapter 3**, *Conclusions and original contributions*, describes the main findings of this Thesis that are grouped into two categories according to their clinical relevance or their impact in the craniofacial system modelling. It is also summarized the original contributions published in scientific international journals and congresses as a result of the findings of this Thesis. It ends with the Bibliography section in which are summarised the main references of this dissertation and an Appendix which includes the details of scientist journals that published some of the results of this dissertation.

2. Manuscripts

Manuscript 1: Towards an early 3D-diagnosis of craniofacial asymmetry by computing the accurate midplane: A PCA-based method

Javier Ortún-Terrazas, Michael J. Fagan, José Cegoñino, Edson Illipronti-Filho, Amaya Pérez del Palomar

Abstract

Background and objective: Craniofacial asymmetry is a common growth disorder often caused by unilateral chewing. Although an early orthodontic treatment would avoid surgical procedures later in life, the uncertainty of defining the accurate sagittal midplane potentially leads to misdiagnosis and therefore inaccurate orthodontic treatment plans. This novel study aims to 3D-diagnose craniofacial complex malformations in children with unilateral crossbite (UXB) considering a midplane which compensates the asymmetric morphology. **Methods:** The sagittal midplane of 20 children, fifteen of whom exhibited UXB, was computed by a PCA-based method which compensates the asymmetry mirroring the 3D models obtained from cone-beam computed tomography data. Once determined, one side of the data was mirrored using the computed midplane to visualize the malformations on the hard and soft tissues by 3D-computing the distances between both halves. Additionally, 31 skull's landmarks were manually placed in each model to study the principal variation modes and the significant differences in the group of subjects with and without UXB through PCA and Mann-Whitney U test analyses respectively. **Results:** Morphological 3D-analysis showed pronounced deformities and esthetic implications for patients with severe asymmetry (jaw deviation > 0.8 mm) in whole craniofacial system, while initial signs of asymmetry were found indistinctly in the mandible or maxilla. We detected significant ($p < 0.05$) malformations for example in mandibular ramus length (0.0086), maxillary palate width (0.0481) and condylar head width (0.0408). Craniofacial malformations increased the landmarks' variability in the group of patients with UXB over the control group requiring 8 variation modes more to define 99% of the sample' variability. **Conclusions:** Our findings demonstrated the viability of early diagnosis of craniofacial asymmetry through computing the accurate sagittal midplane which compensates the individual's asymmetrical morphology. Furthermore, this study provides important computational insights into the determination of craniofacial deformities which are caused by UXB, following some empirical findings of previous clinical studies. Hence, this computational approach can be useful for the development of new software in craniofacial surgery or for its use in biomedical research and clinical practice.

Graphical abstract

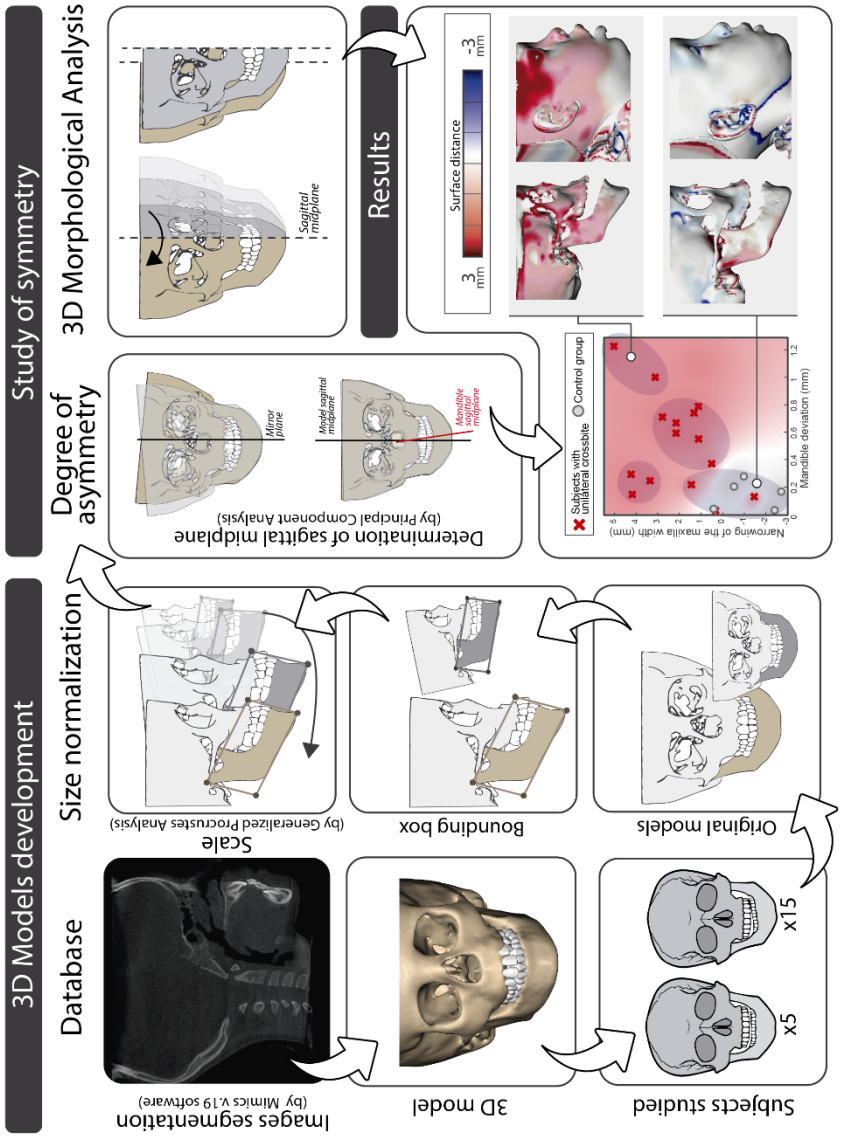

Computer Methods and Programs in Biomedicine 191 (2020) 105397

Contents lists available at ScienceDirect

Computer Methods and Programs in Biomedicine

journal homepage: www.elsevier.com/locate/cmpb

Towards an early 3D-diagnosis of craniofacial asymmetry by computing the accurate midplane: A PCA-based method

Javier Ortún-Terrazas[a,*], Michael J. Fagan[b], Jose Cegoñino[a], Edson Illipronti-Filho[c], Amaya Pérez del Palomar[a]

[a] Group of Biomaterials, Aragon Institute of Engineering Research (I3A), University of Zaragoza, Zaragoza, Spain
[b] Medical and Biological Engineering, School of Engineering and Computer Science, University of Hull, Hull, United Kingdom
[c] School of Dentistry, Department of Orthodontics and Pediatric Dentistry, University of São Paulo, São Paulo, Brazil

ARTICLE INFO

Article history:
Received 29 October 2019
Revised 11 January 2020
Accepted 13 February 2020

Keywords:
Sagittal midplane
Morphological analysis
Principal component analysis
Facial asymmetry
Unilateral crossbite
Children

ABSTRACT

Background and objective: Craniofacial asymmetry is a common growth disorder often caused by unilateral chewing. Although an early orthodontic treatment would avoid surgical procedures later in life, the uncertainty of defining the accurate sagittal midplane potentially leads to misdiagnosis and therefore inaccurate orthodontic treatment plans. This novel study aims to 3D-diagnose craniofacial complex malformations in children with unilateral crossbite (UXB) considering a midplane which compensates the asymmetric morphology.

Methods: The sagittal midplane of 20 children, fifteen of whom exhibited UXB, was computed by a PCA-based method which compensates the asymmetry mirroring the 3D models obtained from cone-beam computed tomography data. Once determined, one side of the data was mirrored using the computed midplane to visualize the malformations on the hard and soft tissues by 3D-computing the distances between both halves. Additionally, 31 skull's landmarks were manually placed in each model to study the principal variation modes and the significant differences in the group of subjects with and without UXB through PCA and Mann-Whitney U test analyses respectively.

Results: Morphological 3D-analysis showed pronounced deformities and aesthetic implications for patients with severe asymmetry (jaw deviation > 0.8 mm) in whole craniofacial system, while initial signs of asymmetry were found indistinctly in the mandible or maxilla. We detected significant ($p < 0.05$) malformations for example in mandibular ramus length (0.0086), maxillary palate width (0.0481) and condylar head width (0.0408). Craniofacial malformations increased the landmarks' variability in the group of patients with UXB over the control group requiring 8 variation modes more to define 99% of the sample' variability.

Conclusions: Our findings demonstrated the viability of early diagnosis of craniofacial asymmetry through computing the accurate sagittal midplane which compensates the individual's asymmetrical morphology. Furthermore, this study provides important computational insights into the determination of craniofacial deformities which are caused by UXB, following some empirical findings of previous clinical studies. Hence, this computational approach can be useful for the development of new software in craniofacial surgery or for its use in biomedical research and clinical practice.

1. Introduction

Everyone has some degree of facial asymmetry [1], however, severe asymmetrical growth may cause not only aesthetic but also functional problems [2] which are hardly treated in adulthood, such as temporomandibular joint (TMJ) disorders [2], cephalea [3], malocclusion [4], loss of periodontal support and even loss of teeth [5]. According to Claude Bernard's principle, the development of craniofacial complex is mainly experienced during growth and is conditioned by the paratypic stimulus [6] primarily produced during breathing and chewing [7,8]. Hence, some oral disorders, as mouth breathing syndrome (MBS) [9] or unilateral crossbite (UXB) [10], would be related to the narrowing of the

* Corresponding author at: Aragon Institute of Engineering Research (I3A), School of Engineering and Architecture, University of Zaragoza, Calle María de Luna 3, 50018 Zaragoza, Spain.
E-mail address: javierortun@unizar.es (J. Ortún-Terrazas).

https://doi.org/10.1016/j.cmpb.2020.105397

maxilla or the lateral shift of the mandible towards the crossbite side.

Biomechanically, these disorders result in an imbalanced craniofacial complex and therefore, in a potential factor of the asymmetrical growth [11]. Early treatments, such as simple selective grinding or maxilla expander [12], would correct the mechanical imbalance and avoid abnormal irreversible developments and surgical treatments later in life [11,13,14]. Unfortunately, early asymmetry is usually misdiagnosed due to the difficulty of identifying an accurate symmetrical reference which is a key step for pre-treatment evaluation, treatment planning and post-treatment evaluation [15,16]. In 2D-imaging methods, commonly 2D frontal photographs or 2D cephalometric images, the facial midline is estimated through the glabella and other craniofacial landmarks [17] which are generally affected by craniofacial malformations, image's magnifying errors or an inadequate subject posture, among other defects [18,19]. Against these limitations, the progress in imaging acquisition and computer methods has increase the use of 3D imaging techniques [18], such as Computed Tomography (CT), Cone-Beam CT (CBCT) or Magnetic Resonance Imaging (MRI). In this context, CBCT is the most recommended method for an early diagnosis due to its relatively low radiation levels and time required in comparison with the other approaches [20]. Nevertheless, the determination of the appropriate sagittal midplane is still complicated [15,16,21] and the conventional approaches used, such as landmark-based, voxel-based or morphometric midplane approach [21,22], do not compensate the asymmetrical morphology. Among them, the landmark-based method is the most used because it requires just 3 landmarks to define the sagittal midplane [23]. These landmarks are often defined by nasion, crista galli landmarks and cranial base features such as basion [24–26] which are apparently less affected by the facial asymmetry than mandibular ones. Nevertheless, the influence of the facial asymmetry in cranial structures is still unclear and there is no consensus on which landmarks produce more reproducible results [23,27].

Some recent studies [15,16] have proposed robust and easily applicable algorithms, based on Principal Component Analysis (PCA) to determine the accurate plane of symmetry in theoretical cases. In Pinheiro et al. study [16], for instance, the inherent asymmetry of a skull was compensated by mirroring the 3D model through a sagittal midplane defined by PCA. In addition, new approaches [28–30] have been developed to study the asymmetry in superficial soft tissues without a known reference plane for each patient. In Cho et al. study [30], this is achieved through the registration and transformation of a template model with known left and right point correspondences to each scan. Notwithstanding recent advances in 3D imaging and midplane identification methods, these protocols are rarely used in clinical practise and have not been used to diagnose facial asymmetry in real asymmetric patients yet.

The known relationships between malocclusions, as UXB, and asymmetrical malformations are mainly based on statistical 2D studies which used midplanes defined by the inaccurate landmark-based method. The craniofacial malformations are generally analyse [31,32] based on limited number of landmarks through PCA or statistical point distribution models (PDM) [33]. With the advance of 3D imaging techniques, new parametric [34–36] and non-parametric techniques [37,38] have emerged to study the entire shape variability through statistical shape models (SSMs). SSMs describe the shape of a model through the transformation of a template pattern according to its variation modes [39]. Nevertheless, despite the potential of those methods, parametric SSMs require a priori knowledge of the characteristic landmarks which define the shape [38] and non-parametric SSMs require a sufficient number of models to characterize adequately the transformation function [38,40].

Despite the unclear and uncertain relationships, some insights are generally accepted (shown in Fig 1) such as the increase of the mandibular thickness and the condyle of the cross side (XS) [41]. Moreover, there have been reports of an increase in the temporal fossa inclination [42], a reduction of the maxillary width [5,43,44] or the elevation of the ocular orbit and the half cranium [45–48] on the same side. On the other hand, several studies [41,49] agree than the mandibular ramus is longer in the non-cross side (NXS). Contrariwise, some studies did not find a strong correlation between UXB and facial asymmetry and some authors [50,51] even did not find significant differences between the shape of both mandibular halves.

This computational study aims to 3D-diagnose the craniofacial complex malformations that appear in 20 children through 3D cephalometric and midplane identification novel methods. To that end, firstly, the sagittal midplane of 3D models reconstructed from CBCT images was computed compensating the asymmetrical morphology through the mirroring technique and identifying the midplane by PCA. Based on the individual's midplane computed, the variation, differentiation and correlation of several bilateral measurements were statistically analysed by PCA, Mann–Whitney *U* test and Pearson's correlation coefficient, respectively. Deformities in hard and soft tissues were also evaluated by computing the 3D distances between the surfaces of NXS and XS mirrored.

2. Material and methods

2.1. 3D database

CBCT images were obtained from 20 paediatric subjects, fifteen of whom exhibited UXB, (see Table A of the supplementary material) with mixed dentition, which included 9 males (mean age 7.9 years) and 11 females (mean age 8.2 years). According UXB diagnosis, the subjects were classified into 2 groups: a UXB group ($n = 15$) and a control (non-cross bite) group ($n = 5$). The scans of the UXB patients were performed as a part of treatment planning and were classified into 3 categories (minor, moderate and marked) according to the degree of asymmetry by an expert on the diagnosis of facial asymmetry. The control group subjects were scanned for preventive reasons as part of a routine medical examination. The information from the medical images was used exclusively for scientific purposes and was approved by the Research Ethics Committee of the University of São Paulo – USP, School of Dentistry (numbers 200/06 and 16/2008).

All images were obtained with an i-CAT^{TM} CBCT imaging system (Imaging Sciences International, Hatfield, PA, USA) with a field of view (FOV) of 13 cm × 17 cm, an acquisition time of 5–26 s and pulse exposure. The images were output in a 14-bit grey scale and 16,384 shades of grey. The focal point was at 0.5 m with a 0.3 mm voxel, an effective dose of 36.74 uSv and cylindrical reconstruction. The data was digitalized by tomography sensors through reconstruction algorithms and converted to the Digital Imaging and Communication in Medicine (DICOM) format. The cylindrical reconstruction of the dataset consisted of 210 images with an interscan distance of 0.50 mm. More details about the scan protocol appear in a previous study [52].

DICOM images were initially filtered by a gradient filter to improve edge definition due to the unmineralized condition of the bones (Fig. 2a). Then, images were segmented by Mimics (Mimics, v.19.; Materialise, Leuven, Belgium) commercial software using threshold levels of 1688 [53] and 226 [54] Hounsfield unit (HU) for dental and osseous regions respectively. The incomplete 3D surfaces (Fig. 2b) were computed through an automated interpolation of the masks. In addition, the cavities of the dental follicles and periodontal ligaments (Fig. 2c and d) were defined through a Boolean subtraction operation with a 0.2 mm [55.56] clearance

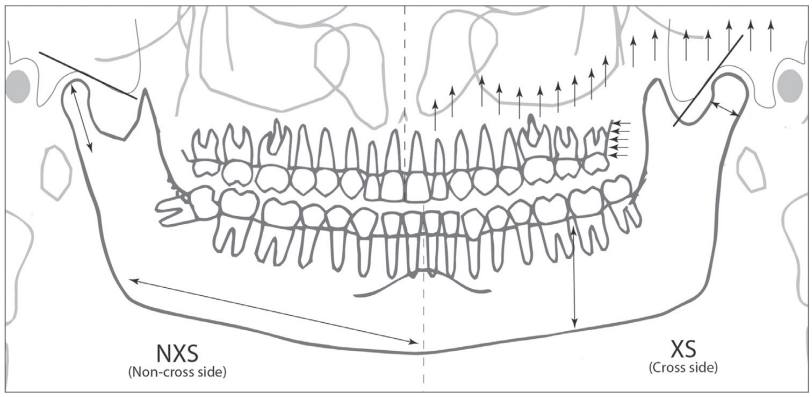

Fig. 1. Panoramic scheme of the morphological changes of the craniofacial complex in a patient with facial asymmetry.

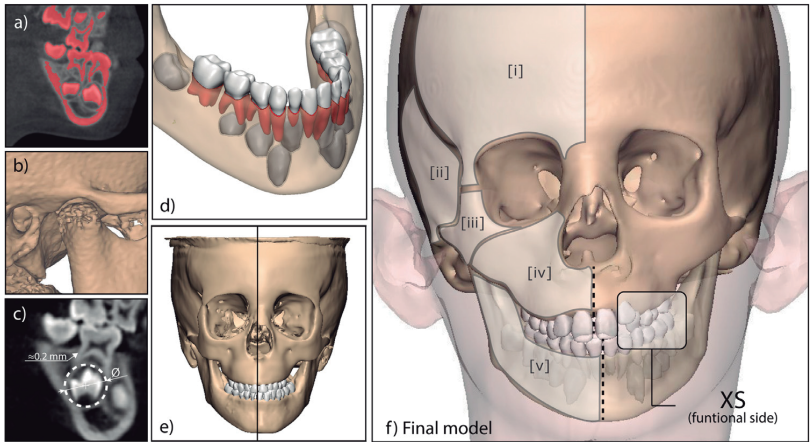

Fig. 2. (a) Small differences between the teeth and the cortical bone; (b) figure showing incomplete regions after automated bone segmentation; (c) approximation of dental follicles and periodontal ligaments as spheres and thin layers around each tooth; (d) detail of the inferior teeth, their periodontal ligaments and the unerupted teeth; (e) left side: model before smoothing operation, right: model after smoothing operation; and (f) model of a patient with UXB in the left side (i: frontal, ii: temporal, iii: zygomatic, iv: maxilla and v: mandible).

around each tooth. The result of the segmentation process is a 3D model composed of the skull, the mandible, the teeth and the superficial soft tissue of the face (Fig 2f). Analytically, each model is a set of N points $\mathcal{P}_N = \{\boldsymbol{p}_i | 1, \ldots, N\}$, where each point i is defined by a vector $\boldsymbol{p}_i = (x_i, y_i, z_i)^T$ in the Cartesian reference system Ω defined by three unitary and orthogonal vectors $\Omega = \{\boldsymbol{i}, \boldsymbol{j}, \boldsymbol{k}\}$. The origin of the reference system was set according to the factory default settings of the i-CAT™ CBCT imaging system. The noise of this point cloud was removed, and the surface was smoothed (Fig. 2e).

For further statistical analyses, thirty-one anthropometric reference points (Table 1) were placed on the hard tissues of 3D models (Fig 3). The soft tissue malformations will not be statistically studied due to the high variance in paediatric patients. The coordinates (x,y,z) of each landmark were reassessed three times by a radiologist expert in the diagnosis of facial asymmetries with a month gap between each assessment. The reliability of this procedure was determined by an Intra-Class Correlation Coefficient (ICC) of 0.91, which was considered enough for the study's scope. From these landmarks, 13 bilateral and 4 global measurements (Table 2) were defined to study statistically the asymmetry. The distance between two landmarks was calculated by the distance formula in 3D coordinate system, while the angle between two vectors was computed by the scalar product of both vectors.

2.2. Size normalization

To reduce the effect of size variations which are inevitable during childhood, the $\mathcal{P}_N$ of the entire volume of each model was uniformly scaled according to the size normalization of the minimum-volume bounding box of the mandible of each patient. The entire volume was not considered to compute the linear transformation matrix T since different cranial portions were scanned for each database. Besides, the minimum-volume oriented bounding boxes approach allows to determine the link among the vertices of the boxes from different patients with different meshes and thus perform the subsequent Generalized Procrustes Analysis (GPA) [57]. Then, a normalization method was developed to equalize the volume of each mandible's set of points, $\mathcal{V}_S$, with the volume of a reference set of points, $\mathcal{U}_R$ (Fig 4a). The reference set was composed by the points of the mandible of third subject (shown in Table A) because he had similar age as the mean age of all subjects and was apparently not affected by the asymmetry. To that end, the minimum-volume oriented bounding boxes (Fig 4b) which contain

Table 1
Definitions of landmarks.

Name	Abbr.	Description
Landmarks on sagittal midplane		
Glabella	G	Most prominent point in the median sagittal plane between the supraorbital ridges
Menton	Me	Most inferior point in symphysis
Pharyngeal tubercle	PhT	Point on the lower surface of the basioccipital region.
Bilateral landmarks (right and left)		
Condyle lateral	CoL	Most lateral point of condyle head
Condyle superior	CoS	Most superior point of condyle head
Gonion	Go	Point between mandibular plane and ramus
Infraorbitale	InfOr	Deepest point on infraorbital margin
Jugale	Ju	Intersection between the margin of the frontal and temporal processes with the zygomatic bone
Last molar	Mo	Most buccal point of the junction between the last molar and the mandible.
Last molar buccal	MoB	Most buccal point of the junction between the last superior molar and the maxilla.
Last molar inferior	MoI	Perpendicular projection of the point on the inferior edge of the jaw.
Last molar lingual	MoL	Most labial point of the junction between the last superior molar and the maxilla.
Porion	Po	Highest point on roof of external auditory meatus
Ramus anterior	RaA	Most posterior point of the intermediate section of the ramus
Ramus posterior	RaP	Most anterior point of the intermediate section of the ramus
Zygion	Zy	Most lateral point of the zygomatic arch
Zygomatic anterior	ZyA	Most anterior point of the intersection between the zygomatic root and the squama of the temporal bone

Table 2
Statistical variables.

Name	Abbr.	Description
Global measurements		
Coronal angle	CoAng	Vertical projection of the angle defined between M plane and sagittal midplane.
Frontal angle	FrAng	Frontal projection of the angle defined between M plane and sagittal midplane.
Mandible deviation	ManDev	Horizontal distance on the FH plane between sagittal midplane and the centre of mass of $\mathcal{V}_S + \mathcal{V}_S^*$.
Menton deviation	MeS	Shortest distance between Me and the sagittal midplane
Bilateral measurements (right and left)		
Body length	Go-Me	Distance between Go and Me
Body width	MoI-Mo	Distance between MoI and Mo
Condylar head height	CoH	Distance of CoS and CoL projections on the S plane
Condylar head width	CoW	Distance of CoS and CoL projections on the FH plane
Gonial angle	GoAng	Angle defined between Go-Me and Go-CoS
Laterality of the gonion	GoS	Shortest distance between Go and the S plane
Laterality of the zygomatic arch	ZyS	Shortest distance between Zy and the S plane
Maxilla height	JuFH	Shortest distance between Ju and the FH plane
Maxilla thickness	MoL-MoB	Distance between MoB and MoL
Maxilla width	MoLS	Shortest distance between MoL and the S plane
Ramus length	Go-CoS	Distance between Go and the CoS
Ramus width	RaA-RaP	Distance between RaA and RaP
Zygomatic arch height	ZyAFH	Shortest distance between ZyA and the FH plane

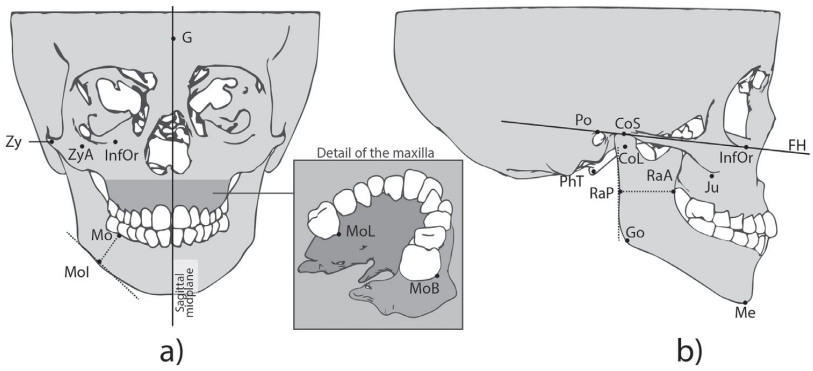

Fig. 3. Landmarks and reference planes in (a) frontal and (b) lateral views of a skull. (Note: Landmarks definitions appear in Table 1).

$\mathcal{V}_S$ and $\mathcal{U}_R$ were computed through O'Rourke's algorithm [58]. The vertices of these boxes were then used to compute the transformation matrix T which transforms $\mathcal{V}_S$ to a set of similar volumes to $\mathcal{U}_R$ through GPA [57] (Fig 4c). As a result of this procedure, the set of points $\mathcal{P}_N$ and of manual-marked landmarks of each subject were scaled by the transformation matrix T.

2.3. Sagittal midplane

For sagittal midplane determination, a computational algorithm [16] which uses interchangeably PCA and Iterative Closest Point (ICP) methods was implemented in the commercial software MATLAB (MATLAB 6.0 R12, The MathWorks Inc, Natick, Massachusetts,

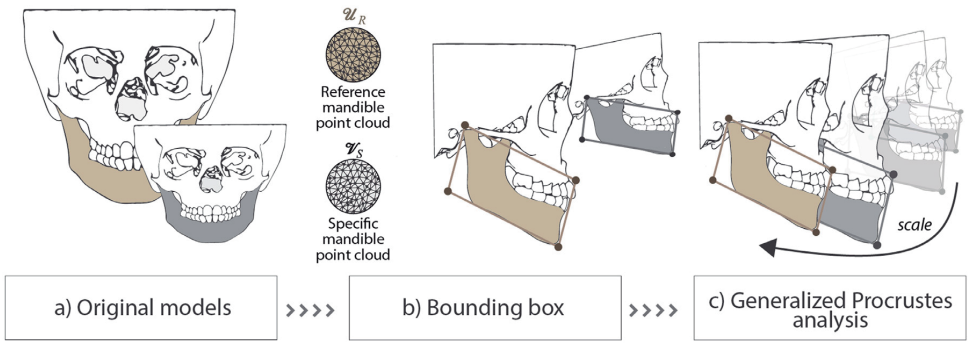

Fig. 4. Scheme of the process followed for the model normalization: (a) Non-scaled models of a specific patient (grey) and the reference subject (brown); (b) minimum-volume oriented bounding boxes of the mandible of each model and (c) linear transformation of the patient model through GPA. (For interpretation of the references to color in this figure legend, the reader is referred to the web version of this article.)

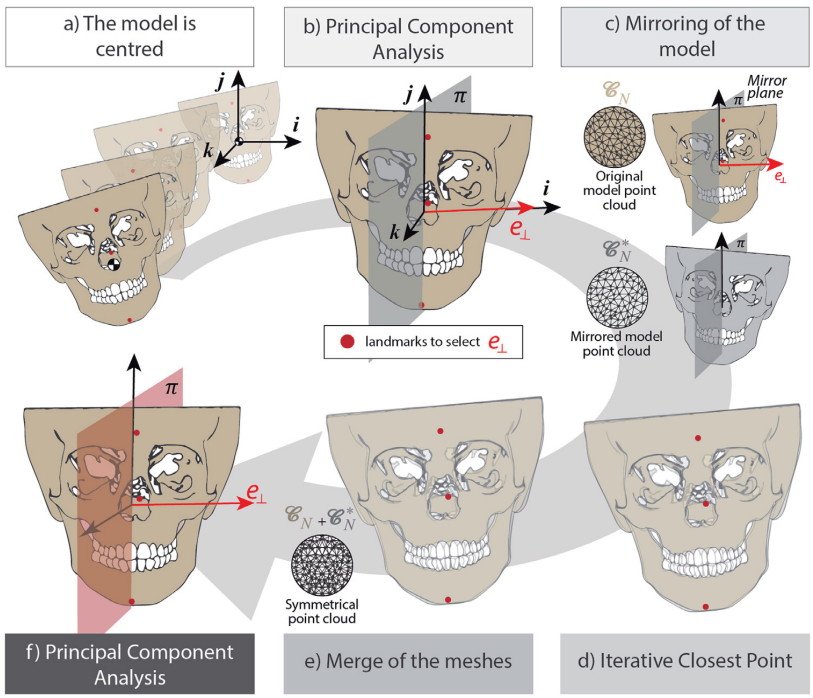

Fig. 5. Flowchart for the identification of the sagittal midplane: (a) the model is centred at the origin of coordinates using its centroid; (b) the initial eigenvectors and a preliminary sagittal plane is computed by PCA; (c) a mirrored model is created from the preliminary sagittal plane; (d) the position of the mirrored set of points is adjusted to the original ones by ICP; (e) both sets of points are merged and (f) the final sagittal midplane is computed by PCA.

2000). This algorithm computes the sagittal midplane of a set of points $\mathcal{C}_N$ which defines the mandible and skull of each patient, compensating for any asymmetric malformation. The PCA technique is widely used to find the eigenvectors $\boldsymbol{e_j}$ that minimize the sum of the projection of each point $\boldsymbol{p}_i \in \mathcal{C}_N$ onto $\boldsymbol{e_i}$ and the squared distances between $\boldsymbol{e_j}$ and $\boldsymbol{p_i}$. PCA requires firstly that the mean point, $\boldsymbol{o}$, of the bony structures $\mathcal{C}_N$ is centred to the origin of Ω which is the reference system from which the coordinates of all points are defined (Fig 5a). Therefore, if $\mathcal{C}_N$ is not centred, all points of the model ($\mathcal{P}_N$) and landmarks must be moved through the translation vector $\boldsymbol{v}_t$ defined by the centroid of $\mathcal{C}_N$ as $\boldsymbol{v}_t = (\frac{\sum_{i=1}^{N} x_i}{N}, \frac{\sum_{i=1}^{N} y_i}{N}, \frac{\sum_{i=1}^{N} z_i}{N})$.

As a result of PCA in $\mathcal{C}_N$, the first three eigenvectors ($\boldsymbol{e}_1$,$\boldsymbol{e}_2$,$\boldsymbol{e}_3$) depend on the portion of skull digitalized and the uniformity of the database. In a uniform set of points of a whole skull, the first principal direction tracks approximately the direction of the line that connects the chin with the parietal bone. Another frequent principal direction is a vector that follows the direction which connects the foramen magnum with the ethmoid bone. Both directions define the sagittal plane that is perpendicular to the undefined principal direction. However, these principal directions are sorted according to the scanned sample. To select the eigenvector that is perpendicular to the sagittal plane $\boldsymbol{e}_\perp$ (Fig 5b) within the principal directions computed, the algorithm employs three hand-

marked landmarks located on the mental protuberance (Me), on the pharyngeal tubercle (PhT) and on the glabella (G), by the procedure explained in Section 2.1. These landmarks define a plane π which is normal to a vector $\boldsymbol{t}$ and apparently parallel to the sagittal midplane searched. Then, the smallest scalar product of each principal directions ($\boldsymbol{e}_1$,$\boldsymbol{e}_2$,$\boldsymbol{e}_3$) with $\boldsymbol{t}$ identifies the $\boldsymbol{e}_\perp$ direction. This direction is used to calculate the rotation matrix Q that aligns $\boldsymbol{e}_\perp$ with the $\boldsymbol{i}$ orthogonal vectors of Ω. The new position of the points is computed by the multiplication of the landmarks and the set of points $\mathcal{P}_N$ by the rotation matrix Q.

To compensate for an individual's asymmetrical morphology, the mirror method was used, as it had already been used in other computational approaches [16,22,59]. This method consists of creating a new set of points $\mathcal{C}_N^*$ symmetrical to $\mathcal{C}_N$ with respect to the sagittal midplane which was previously generated (Fig 5c). Then, $\mathcal{C}_N^*$ is aligned to $\mathcal{C}_N$ by the Iterative Close Points algorithm [60] that minimizes the square of the errors of two sets of points (Fig 5d). The set of points $\mathcal{C}_N + \mathcal{C}_N^*$ represents an idealized symmetrical shape with an equal distribution of points in both halves (Fig 5e). Hence, applying again PCA to the idealized set of points $\mathcal{C}_N + \mathcal{C}_N^*$, (Fig 5f) the eigenvector, $\boldsymbol{e}_\perp$, which is normal to the sagittal plane searched, is obtained by compensating the morphological variations caused by the asymmetry. Finally, the models and their respective landmarks were rotated in that plane to align the horizontal plane with the Frankfort Horizontal (FH) plane, which was defined by the infraorbital and porion landmarks [61], thereby completing alignment of the models.

Although earlier studies have evaluated mandible deviation by the distance between the mental protuberance and the apparent sagittal midplane, the menton location might not be representative of the mandible midplane, as discussed below. Therefore, the algorithm explained previously was also applied only to the set of points that define the mandible $\mathcal{V}_S$, to compute the mandible' midplane, *M*. The angles between the sagittal midplane of the mandible and of the whole skull were then measured through their projection on to the frontal and coronal planes (global measurements, Table 2).

2.4. Statistical and morphological analyses

The morphological variability in UXB and control groups was analysed for each group by a PDM defined in an open-source code [62] written in Python (Python 2.7.3, Python Software Foundation) for morphometric analysis. The PDM is a statistical analysis which identified holistically the variation of a group of shapes considering the covariation of each point with every other point. The covariance matrix results in a set of eigenvalues and eigenvectors which define respectively the variation level and direction in which the landmarks tend to vary as a group. Sorting the eigenvectors, or modes of variation, in descending order of their eigenvalues, the most representative modes of variation of the thirty landmarks were obtained.

PCA can then be applied by ordering the eigenvectors, and retaining only the modes with the highest values, which represent the modes of variation that account for most of the variation seen in the training shapes. Each PDM consist therefore of a mean shape and principal variation modes whose variation is controlled by their eigenvalues (i.e. ±3 SD). Statistically, the differences between the 17 bilateral measurements of both halves were tested by a Mann-Whitney U test (significance level $P \leq 0.05$). Pearson's correlation coefficient, *r*, and its associated *p*-value were also computed to establish the different associations that could be presented between the bilateral and global variables of both groups and halves. All statistical analyses were performed using SPSS software (SPSS software, v. 16.0; SPSS Inc., Chicago, IL).

For 3D evaluation of asymmetric malformations, each 3D model was divided according to the symmetrical midplane previously defined and the left side (cross side in patients with UXB) was mirrored. The normal distance between both halves was then computed in MATLAB and plotted in Paraview software (Paraview v5.6, National Technology & Engineering Solutions of Sandia, New Mexico) to 3D evaluate the morphological differences between both facial sides.

3. Results

PDMs were generated within UXB and control group to define s variability. According to PDMs description, over 95% of the total landmarks' variability in the control and UXB groups is described by 5 and 11 principal variation modes, respectively (Fig 6a and b). The accumulative vector of the first five modes of variation (at −3 SD) in both groups is shown in Figs. 6c and d. While the variation of the landmarks' position was lower in UXB than in the control group, it was also more asymmetric. Alternatively, the landmarks variability for the first five modes of variation is displayed in the supplementary video.

From the statistical analysis, significant differences in the bilateral measurements of condylar head width (CoW), gonial angle (GoAng), ramus length (Go-CoS), maxilla height (JuFH), maxilla width (MoLS) and laterality of the zygomatic arch (ZyS) were found between the XS and NXS data for the UXB group of subjects (Fig 7). The distances measured in XS were greater for CoW and GoAng measurements compared to NXS, and shorter in Go-CoS, MoLS and ZyS. Moreover, the condyloid process width (CoH) and mandible body length (Go-Me) were shorter in XS, although they were not significantly different. Distances of JuFH were significantly greater in NXS than in XS which reflects a deeper position of the jugale landmark (Ju) with respect to the FH plane. Meanwhile, no significant differences were observed between the measurements of both sides in the control group.

From the comparison of the 2 groups (numerical results in Table B2 of the Supplementary material), the differences of the measurements were computed as the difference between the values of both halves, NXS-XS and Right-Left for UXB and control groups respectively. According to our findings, no significant differences were observed for the CoW and ZyS measurements in both groups (Fig 8). Differences in the measurements of GoAng, Go-CoS, JuFH, MoLS, laterality of the gonion (GoS) and ramus width (RaA-RaP) were significantly greater in the UXB group than in the control group. Nevertheless, no significative difference was found between the body width (MoI-Mo) of both groups. Interestingly, for those subjects with UXB, mandible deviation (ManDev) was more significative for UXB diagnoses than the conventional measurement of menton deviation (MeS).

The relationship between the 17 variables in XS, NXS and in the control group are displayed in Fig 9a and b (numerical data summarized in Tables C1-C3 of the Supplementary material). There was a significant positive relationship between the CoW and CoH measurements of the control group and in the NXS side of patients with UXB, but not on the XS. Moreover, a positive and significant correlation was found between Go-CoS and mandible body length (Go-ME) in the control group. On the other hand, the deviation in mandible position (ManDev) was closely related to the reduction of MoLS in XS of the UXB group.

Images a-d in Fig 10 show plots of the normal distance between the surfaces of NXS and XS mirrored through the sagittal midplane in four subjects. The positive (red) areas show where NXS protrudes, while the negative (blue) areas indicate protrusion of XS. The scatter plot in Fig 10e illustrates the positive relationship between the differences of the MoLS and ManDev measurements of both halves in UXB and in the control groups. Using the

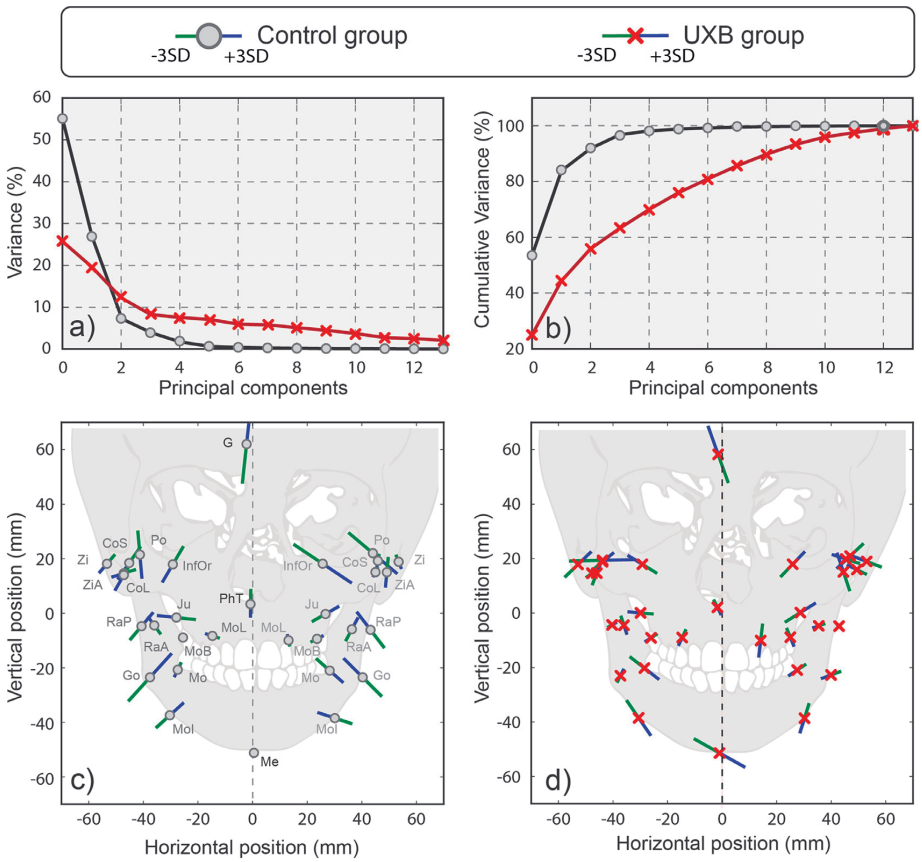

Fig. 6. (a) Percentage and (b) accumulative percentage of landmarks variance described by the principal variation modes. Bottom figures: total vector of the five main modes of variation (at ±3 SD) in the c) control and d) UXB groups.

classification of subjects according to the asymmetry severity (Table A1 of the supplementary material), Fig 10e was divided into 3 regions: minor, moderate and marked asymmetric patients. The minor asymmetric category (Fig 10a) was composed of subjects with short mandible deviation (<0.3 mm) and small differences in MoLS between both sides (±1.5 mm). The moderate asymmetrical subjects mainly presented 2 different malformations, either in the maxilla (Fig 10b) or in the mandible (Fig 10c), which can be differentiated through ManDev and MoLS values respectively. In the first group, the maxilla portion of the XS was less open and slightly higher than those of the NXS, which was also apparent in the cheeks of the superficial soft tissue. Meanwhile, half of the mandible of NXS was more open and longer (Fig 10c) in the case of subjects with mandible malformation. Finally, subjects with marked asymmetry show both maxilla and mandible deformities with a pronounced effect in the superficial soft tissue.

4. Discussion

Although 2D diagnostic tools have been widely used to diagnose asymmetry, their usefulness and associate concepts are recently being questioned because of the high variability, inconsistency and errors during image capture or landmark identification. To solve these limitations [63,64], the use of 3D cephalometric methods, specially CBCT, has increased in the last decade. Nevertheless, the improvement of 3D methods has not demonstrated yet and some studies [65,66]] have not even found significant differences between 2D and 3D methods. Normal approaches to define the midplane, do not compensate the asymmetric shape [67,68] and often use landmarks from areas which could be affected by the asymmetry [48,69], such as the cranial base region, possibly leading to misdiagnosis and inaccurate orthodontic treatments plans. Meanwhile, new methods [28–30] which do not require a specific sagittal midplane have recently been developed to study the asymmetry in soft tissues. As it was introduced, these techniques transform a template model to each model through known landmarks that define its shape. Nevertheless, despite the great potential of these methods, they are hardly applicable in the study of the asymmetry in irregular craniofacial structures because of the unknowledge of the landmarks that define their shape. On the other hand, the use of ionising CT scans and the continually changing state of paediatric bones makes 3D studies difficult in early years. Due to the uncertainties in the sagittal midplane determination and in the development of 3D models of children's craniofacial complex, the relationship between malocclusion and the asymmetric growth of the craniofacial complex is still unclear [70]. This lack of knowledge has complicated the early identification of the asymmetry and therefore its early treatment which is crucial to avoid irreversible abnormal developments [11,13,14].

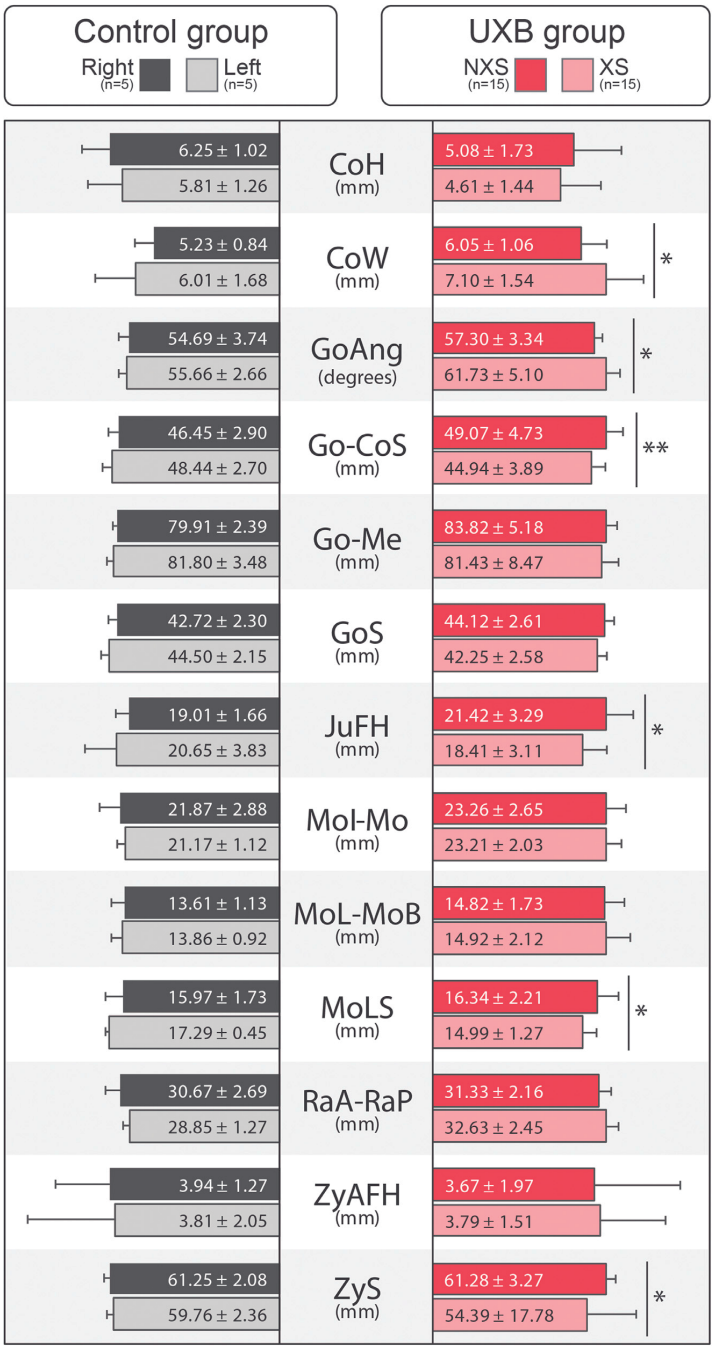

Fig. 7. Bar chart showing the mean ± SD values of the 13 bilateral variables measured in the control group (left) and in the UXB group (right). Significant difference at $p < 0.05$ (*); $p < 0.01$ (**).

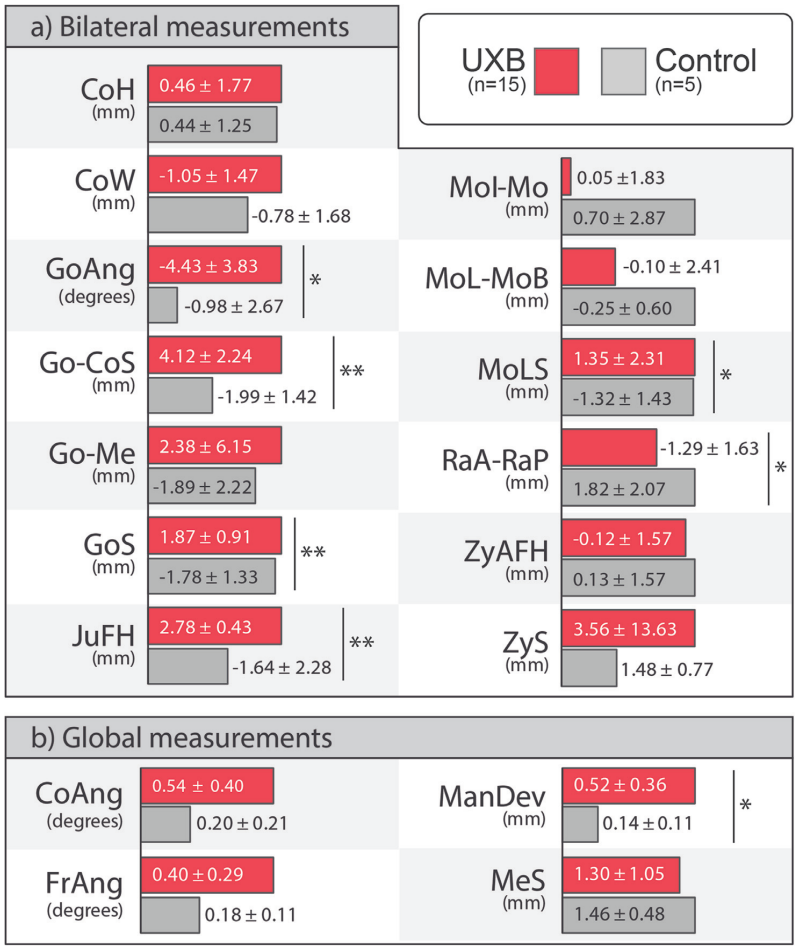

Fig. 8. Bar chart showing the mean value of (a) the difference between the measurements of both sides and (b) global measurements in the UXB group (red bars) and in the control group (grey bars). Significant difference at $p < 0.05$ (*); $p < 0.01$ (**). (For interpretation of the references to color in this figure legend, the reader is referred to the web version of this article.)

In this computational study, the early diagnosis of asymmetrical development in 20 paediatric subjects was 3D-evaluated through CBCT images reconstruction and the accurate identification of the sagittal midplane by a PCA-based method. Although this method was recently demonstrated and validated in a theoretical case of an induced growth pattern of a single skull [16], until now, it had not been evaluated in real paediatric patients with facial asymmetry. For the 3D-diagnosis, the surfaces of each halve of the craniofacial complex were compared. Moreover, the bilateral differences were statistically quantified computing the variability and significance of bilateral landmarks in UXB and control groups by PDMs and Mann-Whitney test respectively. Although a non-parametric SSM could describe the variability of the entire model, the reduced sample size would mischaracterize the transformation function leading to inaccurate results. Alternatively, PDMs identified the principal variation modes of the landmarks in both groups and the associated variability characterized. Although other morphometrics studies [31,71], in other oral disorders or congenital syndromes, have reported a relationship between the principal variation modes and some anatomical references, it was difficult to establish a clear relationship from our results. The relatively small size of our sample or the random differences in sample selection could have affected the high dispersion level of the sample. Nevertheless, our results demonstrated the higher variability and more asymmetrical variation of the landmarks in UXB group against in the control group. In UXB group, especially remarkable was the vertical direction of the landmarks in the infraorbital and maxilla regions of the XS, whereas they varied horizontally in NXS following Trpkova et al. [72] findings.

From 3D morphological analysis, our findings revealed that the head of the condyle was wider in XS, while the condyloid process and the mandible body length were longer in NXS being in agreement with the findings of Veli et al. [41]. As a result, a sizeable gonion angle was also found in the XS as reported by Nur et al. [18]. These results provide support to the hypothesis that mandible malformations are caused due to shear and compression effects in NXS and XS mandible halves, respectively. These findings seem to support the idea that chin deviation can be used as a tool for indicating facial asymmetry. In the current research, the mandibular deviation was evaluated by two variables, ManDev and MeS (shown in Table 2), which measured the distance from the midplane of the mandible (M) or from the menton (Me) to the

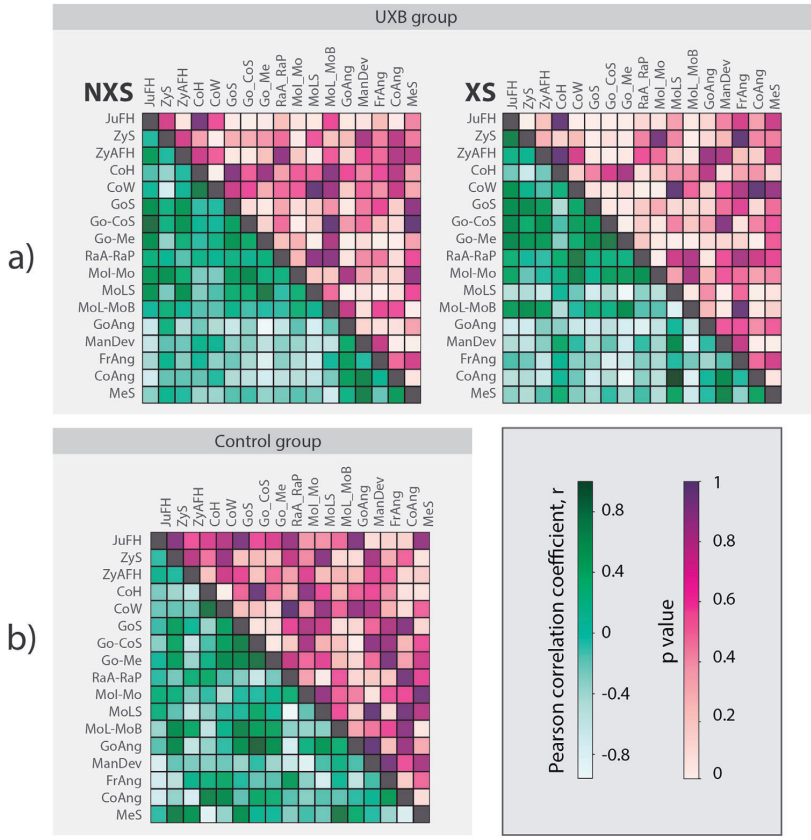

Fig. 9. Correlation matrices based on Pearson's correlation coefficient (green, below the diagonal), r, and its associated probabilistic value p (purple, above the diagonal) of the variables studied in: (a) both halves of the group of subjects with unilateral crossbite; and (b) in the control group. (For interpretation of the references to color in this figure legend, the reader is referred to the web version of this article.)

sagittal midplane. Our results suggested that the ManDev variable was more representative of the asymmetry than the MeS one. This difference may be caused because the asymmetry at early ages alters the whole shape of the mandible, but not necessarily leads to a chin displacement. This observation agrees with the conclusions of Fang et al. [73] who identified significant mandibular body deviations in patients with significant facial asymmetry despite acceptable symmetry of the mandibular contours.

Our results also reveal a morphological asymmetry of the maxilla, with the posterior maxillary region of XS being narrower than of NXS. This finding differs from those of Kwon et al. [68] who reported minor variations in the maxilla, but is broadly consistent with other clinical studies [5,43,44]. Many authors [9,74], in fact, have related breathing problems (as MBS) with UXB and facial asymmetry in accordance with Moss' functional matrix hypothesis [8], which states that nasal breathing promotes proper growth and development of the maxilla.

These results demonstrate the interrelationship between anomalies in the maxilla and its counterpart, the mandible, which was previously stated by Enlow's facial growth theory [75] and later by Kim et al. [47]. Therefore, these concurrent malformations emphasise the importance of a simultaneous assessment of maxilla and mandible. The current study found 2 groupings in subjects with moderate facial asymmetry (Fig 10b and c) that confirmed this proposition.

It is also interesting to note that malformations of the cranial base were detected in all UXB patients of this study (Fig 10b-d), with the largest effects observed in patients with severe facial asymmetry. Moreover, the differences in this region could be observed on the elevated portion of the jugale, the ocular orbit and on the narrower zygomatic arch of XS. These findings seem to be consistent with Sepahdari et al. [48] who showed an increase in cranial base and mandibular volumes on NXS.

The deviations in mandible, maxilla and cranium could be also observed in the morphological analysis of superficial soft tissues (Fig 10a-d). These results confirmed the same deviations in hard and soft tissues previously reported by Nur et al. [18] and Ryckman et al. [67], amongst others. Nevertheless, as it was aforementioned, soft tissue malformations were not statistically studied due to the high variance in paediatric patients. Our findings have therefore quantified the differences in the mandible, maxilla and skull on both sides of the face in patients with UXB and are in agreement with previous studies [5,43,44,76] and empirical theories [8,9,74,75].

4.1. Limitations

Despite the promising results of this work, some limitations need to be mentioned, such as its cross-sectional nature, i.e. different individuals with different ages and sex, which may have led to mixed results. Therefore, results should be interpreted with caution

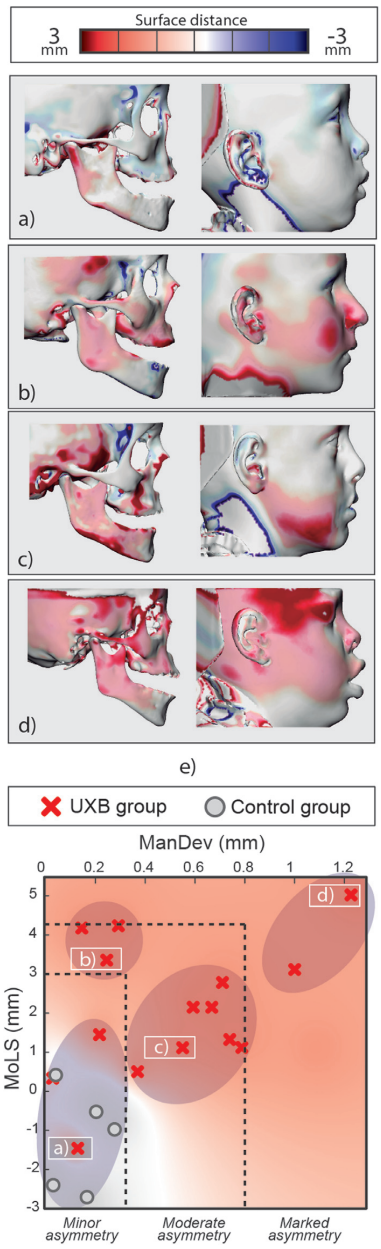

Fig. 10. Top: distance of the hard (left column) and soft (right column) tissues between the NXS region and their counterparts on XS in subjects with: (a) minor asymmetry, (b) moderate asymmetry located on the maxilla, (c) moderate asymmetry located on the mandible and (d) marked asymmetry. (e) scatter plot of ManDev global measurement and the difference of MoLS of both halves. The 3 rectangular areas divide the graph according to a pre-clinical evaluation of the degree of symmetry. The circles cluster the cases according to the obtained values of ManDev and MoLS.

since they could reflect random differences due to sample selection. Moreover, it might not be possible to extrapolate the findings to all patients, since the analysis has been carried with patients between 6 and 12 years old with no congenital disorders. Secondly, the size of our sample size was limited and the gender distribution in our sample was different in the control and UXB groups. Nevertheless, our sample size was based on the size of previous studies [20,52,77] which also evaluated the facial asymmetry in children by CBCT images. On the other and, the craniofacial growth differences in both genders seem not to be statistically significant [77] at ages before the puberty [78,79]. Additionally, the size differences due to gender or age variation had already been reduced after the size normalization procedure explained in Section 2.2. Nonetheless, we believe that a wider sample with equal gender distribution could result in more reliable and precise results. Future studies with a wider database could even study the shape variability of patients with facial asymmetry using SSMs. Finally, a more detailed list of anthropometric reference points could lead to new findings for the early diagnosis of facial asymmetry. We considered that 31 landmarks were enough to describe the application of this method in this computational framework. Notwithstanding this, we suggest addressing more points in further studies, especially clinical ones.

5. Conclusions

The results of this study help to elucidate the accuracy of applying computational methods in the early diagnosis of facial asymmetry providing a reliable and valuable 3D cephalometric workflow for the evaluation and quantification of asymmetrical development and planning subsequent orthodontic and surgical treatments. Within the limitations of this study, we summarize our findings by the following conclusions:

1 The PCA-based algorithm identified accurately and objectively the sagittal midplane in each subject, allowing the subsequent 3D-diagnosis workflow.
2 This 3D-method allowed to statistically demonstrate some traditional theories about the asymmetric development of the craniofacial complex in patients with UXB.
3 Morphometric analysis demonstrated greater variability and asymmetry among the patients with UXB than in the control group, requiring 8 variation modes more to define 99% of the variability.
4 The correlation analyses suggested that the degree of asymmetry could be related both with the maxillary width and mandibular deviation to the midplane identified.
5 3D diagnosis also revealed alterations in the cranial base and soft tissues which future studies should address.

Ethical approval

The study was approved by the Research Ethics Committee of the University of São Paulo – USP, School of Dentistry (numbers 200/06 and 16/2008) and medical images was used exclusively for scientific purposes.

Funding

This work was supported by the Spanish Ministry of Economy and Competitiveness (project DPI 2016-79302-R), the European Social Funds and Regional Government of Aragon (grant 2016/20) and Ibercaja- Cai Fundation(grant IT 4/18).

Declaration of Competing Interest

The authors have no conflicts of interest.

Acknowledgements

The authors would like to thank Dr. Ángel Sampietro Fuentes for his assistance in this research.

Supplementary materials

Supplementary material associated with this article can be found, in the online version, at doi:10.1016/j.cmpb.2020.105397.

References

[1] C. Baek, J.Y. Paeng, J.S. Lee, J. Hong, Morphologic evaluation and classification of facial asymmetry using 3-dimensional computed tomography, J. Oral Maxillofac. Surg. 70 (2012) 1161–1169, doi:10.1016/j.joms.2011.02.135.
[2] M. Inui, K. Fushima, S. Sato, Facial asymmetry in temporomandibular joint disorders., J. Oral Rehabil. 26 (1999) 402–406, doi:10.1111/j.1365-2842.2010.02087.x.
[3] R.P. Schokker, T.L. Hansson, B.J. Ansink, L.L. Habets, Craniomandibular asymmetry in headache patients., J. Craniomandib. Disord. 4 (1990) 205–209 http://www.ncbi.nlm.nih.gov/pubmed/2098397.
[4] Y.-W. Cheong, L.-J. Lo, Facial asymmetry: etiology, evaluation, and management, Chang Gung Med. J. 34 (2014) 341–351, doi:10.1590/0103-6440201300003.
[5] P. Ngan, Contemporary orthodontics, Am. J. Orthod. Dentofac. Orthop. 142 (2012) 425, doi:10.1016/j.ajodo.2012.07.004.
[6] A. Nanci, Oral histology: development, structure, and function, J. Oral Maxillofac. Surg. 48 (1990) 98–99, doi:10.1016/0278-2391(90)90217-P.
[7] S.-J. Yoon, R.-F. Wang, H.J. Na, J.M. Palomo, Normal range of facial asymmetry in spherical coordinates: a CBCT study, Imaging Sci. Dent. 43 (2013) 31, doi:10.5624/isd.2013.43.1.31.
[8] M.L. Moss, L. Salentijn, The primary role of functional matrices in facial growth, Am. J. Orthod. 55 (1969) 566–577, doi:10.1016/0002-9416(69)90034-7.
[9] D. Harari, M. Redlich, S. Miri, T. Hamud, M. Gross, The effect of mouth breathing versus nasal breathing on dentofacial and craniofacial development in orthodontic patients, Laryngoscope 120 (2010) 2089–2093, doi:10.1002/lary.20991.
[10] N. Tsanidis, G.S. Antonarakis, S. Kiliaridis, Functional changes after early treatment of unilateral posterior cross-bite associated with mandibular shift: a systematic review, J. Oral Rehabil. 43 (2016) 59–68, doi:10.1111/joor.12335.
[11] J. Zou, M. Meng, C.S. Law, Y. Rao, X. Zhou, Common dental diseases in children and malocclusion, Int. J. Oral Sci. 10 (2018) 7, doi:10.1038/s41368-018-0012-3.
[12] L. Kurol, J. Berglund, Longitudinal study and cost-benefit analysis of the effect of early treatment of posterior cross-bites in the primary dentition, Eur. J. Orthod. 14 (1992) 173–179.
[13] P. Planas, Neuro-Occlusal Rehabilitation: NOR, Second ed., España, Amolca, Barcelona, 2013.
[14] P. Prakash, B.H. Durgesh, Anterior Crossbite Correction in Early Mixed Dentition Period Using Catlan's Appliance: A Case Report, ISRN Dent 2011 (2011) 1–5, doi:10.5402/2011/298931.
[15] L. Zhang, A. Razdan, G. Farin, J. Femiani, M. Bae, C. Lockwood, 3D face authentication and recognition based on bilateral symmetry analysis, Vis. Comput. 22 (2006) 43–55, doi:10.1007/s00371-005-0352-9.
[16] M. Pinheiro, X. Ma, M.J. Fagan, G.T. McIntyre, P. Lin, G. Sivamurthy, P.A. Mossey, A 3D cephalometric protocol for the accurate quantification of the craniofacial symmetry and facial growth, J. Biol. Eng. 13 (2019) 42, doi:10.1186/s13036-019-0171-6.
[17] R. Nanda, M.J. Margolis, Treatment strategies for midline discrepancies, Semin. Orthod. 2 (1996) 84–89, doi:10.1016/S1073-8746(96)80046-6.
[18] R.B. Nur, D.G. Çakan, T. Arun, Evaluation of facial hard and soft tissue asymmetry using cone-beam computed tomography, Am. J. Orthod. Dentofac. Orthop. 149 (2016) 225–237, doi:10.1016/j.ajodo.2015.07.038.
[19] P. Berssenbrügge, N.F. Berlin, G. Kebeck, C. Runte, S. Jung, J. Kleinheinz, D. Dirksen, 2D and 3D analysis methods of facial asymmetry in comparison, J, Cranio-Maxillofacial Surg 42 (2014) e327–e334, doi:10.1016/j.jcms.2014.01.028.
[20] E. Huntjens, G. Kiss, C. Wouters, C. Carels, Condylar asymmetry in children with juvenile idiopathic arthritis assessed by cone-beam computed tomography, Eur. J. Orthod. 30 (2008) 545–551, doi:10.1093/ejo/cjn056.
[21] J. Damstra, Z. Fourie, M. De Wit, Y. Ren, A three-dimensional comparison of a morphometric and conventional cephalometric midsagittal planes for craniofacial asymmetry, Clin. Oral Investig. 16 (2012) 285–294, doi:10.1007/s00784-011-0512-4.
[22] S.M. Shin, Y.-M.Y.-I. Kim, N.-R. Kim, Y.-S. Choi, S.-B. Park, Y.-M.Y.-I. Kim, Statistical shape analysis-based determination of optimal midsagittal reference plane for evaluation of facial asymmetry, Am. J. Orthod. Dentofac. Orthop. 150 (2016) 252–260, doi:10.1016/j.ajodo.2016.01.017.
[23] A. Dobai, Z. Markella, T. Vízkelety, C. Fouquet, A. Rosta, J. Barabás, Landmark-based midsagittal plane analysis in patients with facial symmetry and asymmetry based on CBCT analysis tomography, J. Orofac. Orthop. / Fortschritte Der Kieferorthopädie. 79 (2018) 371–379, doi:10.1007/s00056-018-0151-3.
[24] H.-J. Kim, B.C. Kim, J.-G. Kim, P. Zhengguo, S.H. Kang, S.-H. Lee, Construction and validation of the midsagittal reference plane based on the skull base symmetry for three-dimensional cephalometric craniofacial analysis, J. Craniofac. Surg. 25 (2014) 338–342, doi:10.1097/SCS.0000000000000380.
[25] A. Katsumata, M. Fujishita, M. Maeda, Y. Ariji, E. Ariji, R.P. Langlais, 3D-CT evaluation of facial asymmetry, Oral Surg. Oral Med. Oral Pathol. Oral Radiol. Endodontol. 99 (2005) 212–220, doi:10.1016/j.tripleo.2004.06.072.
[26] T.-Y. Kim, J.-S. Baik, J.-Y. Park, H.-S. Chae, K.-H. Huh, S.-C. Choi, Determination of midsagittal plane for evaluation of facial asymmetry using three-dimensional computed tomography, Imaging Sci. Dent. 41 (2011) 79, doi:10.5624/isd.2011.41.2.79.
[27] A. Gong, J. Li, Z. Wang, Y. Li, F. Hu, Q. Li, D. Miao, L. Wang, Cranial base characteristics in anteroposterior malocclusions: a meta-analysis, Angle Orthod. 86 (2016) 668–680, doi:10.2319/032315-186.1.
[28] A.B. Lipira, S. Gordon, T.A. Darvann, N.V. Hermann, A.E. Van Pelt, S.D. Naidoo, D. Govier, A.A. Kane, Helmet versus active repositioning for plagiocephaly: a three-dimensional analysis, Pediatrics 126 (2010) e936–e945, doi:10.1542/peds.2009-1249.
[29] S. Lanche, T.A. Darvann, H. Ólafsdóttir, N.V Hermann, A.E. Van Pelt, D. Govier, M.J. Tenenbaum, S. Naidoo, P. Larsen, S. Kreiborg, A statistical model of head asymmetry in infants with deformational plagiocephaly, in: Scand. Conf. Image Anal., Springer, 2007, pp. 898–907.
[30] M.-J. Cho, R.R. Hallac, J. Ramesh, J.R. Seaward, N.V. Hermann, T.A. Darvann, A. Lipira, A.A. Kane, Quantifying normal craniofacial form and baseline craniofacial asymmetry in the pediatric population, Plast. Reconstr. Surg. 141 (2018) 380e–387e, doi:10.1097/PRS.0000000000004114.
[31] S.C. Schaal, C. Ruff, B.I. Pluijmers, E. Pauws, C.W.N. Looman, M.J. Koudstaal, D.J. Dunaway, Characterizing the skull base in craniofacial microsomia using principal component analysis, Int. J. Oral Maxillofac. Surg. 46 (2017) 1656–1663, doi:10.1016/j.ijom.2017.07.008.
[32] B.D.P.J. Maas, B.I. Pluijmers, P.G.M. Knoops, C. Ruff, M.J. Koudstaal, D. Dunaway, Using principal component analysis to describe the midfacial deformities in patients with craniofacial microsomia, J. Cranio-Maxillofacial Surg. 46 (2018) 2032–2041, doi:10.1016/j.jcms.2018.09.019.
[33] T.F. Cootes, C.J. TaylorM. Sonka, K.M. Hanson (Eds.), Statistical models of appearance for medical image analysis and computer vision, N. Engl. J. Med. (2001) 236–248, doi:10.1117/12.431093.
[34] W. Semper-Hogg, M.A. Fuessinger, S. Schwarz, E. Ellis, C.-P. Cornelius, F. Probst, M.C. Metzger, S. Schlager, Virtual reconstruction of midface defects using statistical shape models, J. Cranio-Maxillofacial Surg 45 (2017) 461–466, doi:10.1016/j.jcms.2016.12.020.
[35] M.A. Fuessinger, S. Schwarz, C.-P. Cornelius, M.C. Metzger, E. Ellis, F. Probst, W. Semper-Hogg, M. Gass, S. Schlager, Planning of skull reconstruction based on a statistical shape model combined with geometric morphometrics, Int. J. Comput. Assist. Radiol. Surg. 13 (2018) 519–529, doi:10.1007/s11548-017-1674-6.
[36] P. Mitteroecker, P. Gunz, Advances in Geometric Morphometrics, Evol. Biol. 36 (2009) 235–247, doi:10.1007/s11692-009-9055-x.
[37] A. Dall'Asta, S. Schievano, J.L. Bruse, G. Paramasivam, C.T. Kaihura, D. Dunaway, C.C. Lees, Quantitative analysis of fetal facial morphology using 3D ultrasound and statistical shape modeling: a feasibility study, Am. J. Obstet. Gynecol. 217 (2017) 76.e1–76.e8, doi:10.1016/j.ajog.2017.02.007.
[38] J.L. Bruse, K. McLeod, G. Biglino, H.N. Ntsinjana, C. Capelli, T.-Y. Hsia, M. Sermesant, X. Pennec, A.M. Taylor, S. Schievano, A statistical shape modelling framework to extract 3D shape biomarkers from medical imaging data: assessing arch morphology of repaired coarctation of the aorta, BMC Med. Imaging. 16 (2016) 40, doi:10.1186/s12880-016-0142-z.
[39] N. Sarkalkan, H. Weinans, A.A. Zadpoor, Statistical shape and appearance models of bones, Bone 60 (2014) 129–140, doi:10.1016/j.bone.2013.12.006.
[40] S. Durrleman, X. Pennec, A. Trouvé, N. Ayache, Measuring brain variability via sulcal lines registration: a diffeomorphic approach, in: Med. Image Comput. Comput. Interv. – MICCAI 2007, Springer Berlin Heidelberg, Berlin, Heidelberg, Heidelberg, n.d.: pp. 675–682. doi:10.1007/978-3-540-75757-3_82.
[41] I. Veli, T. Uysal, T. Ozer, F.I. Ucar, M. Eruz, Mandibular asymmetry in unilateral and bilateral posterior crossbite patients using cone-beam computed tomography, Angle Orthod. 81 (2011) 966–974, doi:10.2319/022011-122.1.
[42] P. Pirttiniemi, T. Kantomaa, P. Lahtela, Relationship between craniofacial and condyle path asymmetry in unilateral cross-bite patients, Eur. J. Orthod. 12 (1990) 408–413, doi:10.1093/ejo/12.4.408.
[43] C.A. Wong, P.M. Sinclair, R.G. Keim, D.B. Kennedy, Arch dimension changes from successful slow maxillary expansion of unilateral posterior crossbite, Angle Orthod 81 (2011) 616–623, doi:10.2319/072210-429.1.
[44] F. Ferro, P. Spinella, N. Lama, Transverse maxillary arch form and mandibular asymmetry in patients with posterior unilateral crossbite, Am. J. Orthod. Dentofac. Orthop. 140 (2011) 828–838, doi:10.1016/j.ajodo.2011.08.003.
[45] V. Katyal, Y. Pamula, C.N. Daynes, J. Martin, C.W. Dreyer, D. Kennedy, W.J. Sampson, Craniofacial and upper airway morphology in pediatric sleep-disordered breathing and changes in quality of life with rapid maxillary expansion, Am. J. Orthod. Dentofac. Orthop. 144 (2013) 860–871, doi:10.1016/j.ajodo.2013.08.015.
[46] H. Kapadia, P.R. Shetye, B.H. Grayson, J.G. McCarthy, Cephalometric assessment of craniofacial morphology in patients with treacher Collins syndrome., J. Craniofac. Surg. 24 (2013) 1141–1145, doi:10.1097/SCS.0b013e3182860541.
[47] S.-J. Kim, K.-J. Lee, S.-H. Lee, H.-S. Baik, Morphologic relationship between the cranial base and the mandible in patients with facial asymmetry and mandibular prognathism, Am. J. Orthod. Dentofacial Orthop. 144 (2013) 330–340, doi:10.1016/j.ajodo.2013.03.024.
[48] A.R. Sepahdari, S. Mong, Skull base CT: normative values for size and symmetry of the facial nerve canal, foramen ovale, pterygoid canal, and foramen rotundum, Surg. Radiol. Anat. 35 (2013) 19–24, doi:10.1007/s00276-012-1001-4.

[49] S. Hara, M. Mitsugi, T. Kanno, A. Nomachi, T. Wajima, Y. Tatemoto, Three-dimensional virtual operations can facilitate complicated surgical planning for the treatment of patients with jaw deformities associated with facial asymmetry: a case report, Int. J. Oral Sci. 5 (2013) 176–182, doi:10.1038/ijos.2013.48.
[50] I. Saitoh, C. Yamada, H. Hayasaki, T. Maruyama, Y. Iwase, Y. Yamasaki, Is the reverse cycle during chewing abnormal in children with primary dentition? J. Oral Rehabil 37 (2010) 26–33, doi:10.1111/j.1365-2842.2009.02006.x.
[51] L. Sonnesen, M. Bakke, Bite force in children with unilateral crossbite before and after orthodontic treatment. A prospective longitudinal study, Eur. J. Orthod. 29 (2007) 310–313, doi:10.1093/ejo/cjl082.
[52] E. Illipronti-Filho, S.M. de Fantini, I. Chilvarquer, Evaluation of mandibular condyles in children with unilateral posterior crossbite, Braz. Oral Res. 29 (2015) 49, doi:10.1590/1807-3107BOR-2015.vol29.0049.
[53] Y. Wang, S. He, L. Yu, J. Li, S. Chen, Accuracy of volumetric measurement of teeth in vivo based on cone beam computer tomography, Orthod. Craniofac. Res. 14 (2011) 206–212, doi:10.1111/j.1601-6343.2011.01525.x.
[54] H. Lin, P. Zhu, Y. Lin, S. Wan, X. Shu, Y. Xu, Y. Zheng, Mandibular asymmetry: A three-dimensional quantification of bilateral condyles, Head Face Med 9 (2013) 1–7, doi:10.1186/1746-160x-9-42.
[55] L. Keilig, M. Drolshagen, K.L. Tran, I. Hasan, S. Reimann, J. Deschner, K.T. Brinkmann, R. Krause, M. Favino, C. Bourauel, In vivo measurements and numerical analysis of the biomechanical characteristics of the human periodontal ligament, Ann. Anat. - Anat. Anzeiger. 206 (2016) 80–88, doi:10.1016/j.aanat.2015.08.004.
[56] B. Xu, Y. Wang, Q. Li, Modeling of damage driven fracture failure of fiber post-restored teeth, J. Mech. Behav. Biomed. Mater. 49 (2015) 277–289, doi:10.1016/j.jmbbm.2015.05.006.
[57] J.C. Gower, Generalized procrustes analysis, Psychometrika 40 (1975) 33–51, doi:10.1007/BF02291478.
[58] J. O'Rourke, Finding minimal enclosing boxes, Int. J. Comput. Inf. Sci. 14 (1985) 183–199, doi:10.1007/BF00991005.
[59] J. Damstra, B.C.M. Oosterkamp, J. Jansma, Y. Ren, Combined 3-dimensional and mirror-image analysis for the diagnosis of asymmetry, Am. J. Orthod. Dentofac. Orthop. 140 (2011) 886–894, doi:10.1016/j.ajodo.2010.03.032.
[60] P.J. Besl, N.D. McKay, Method for registration of 3-D shapes, in: P.S. Schenker (Ed.), Sens. Fusion IV Control Paradig. Data Struct., International Society for Optics and Photonics, 1992, pp. 586–606, doi:10.1117/12.57955.
[61] D. Lonic, A. Sundoro, H.-H. Lin, P.-J. Lin, L.-J. Lo, Selection of a horizontal reference plane in 3D evaluation: identifying facial asymmetry and occlusal cant in orthognathic surgery planning, Sci. Rep. 7 (2017) 2157, doi:10.1038/s41598-017-02250-w.
[62] J. Alabort-i-Medina, E. Antonakos, J. Booth, P. Snape, S. Zafeiriou, Menpo, in: Proc. ACM Int. Conf. Multimed. - MM '14, New York, New York, USA, ACM Press, 2014, pp. 679–682, doi:10.1145/2647868.2654890.
[63] B.F. Gribel, M.N. Gribel, D.C. Frazão, J.A. McNamara Jr, F.R. Manzi, Accuracy and reliability of craniometric measurements on lateral cephalometry and 3D measurements on CBCT scans, Angle Orthod. 81 (2011) 26–35.
[64] G. Akhil, K. Senthil Kumar, S. Raja, K. Janardhanan, Three-dimensional assessment of facial asymmetry: a systematic review, J. Pharm. Bioallied Sci. 7 (2015) 433, doi:10.4103/0975-7406.163491.
[65] N. Zamora, J.M. Llamas, R. Cibrián, J.L. Gandia, V. Paredes, Cephalometric measurements from 3D reconstructed images compared with conventional 2D images, Angle Orthod. 81 (2011) 856–864, doi:10.2319/121210-717.1.
[66] P. Pittayapat, M.M. Bornstein, T.S.N. Imada, W. Coucke, I. Lambrichts, R. Jacobs, Accuracy of linear measurements using three imaging modalities: two lateral cephalograms and one 3D model from CBCT data, Eur. J. Orthod. 37 (2015) 202–208, doi:10.1093/ejo/cju036.
[67] M.S. Ryckman, S. Harrison, D. Oliver, C. Sander, A.A. Boryor, A.A. Hohmann, F. Kilic, K.B. Kim, Soft-tissue changes after maxillomandibular advancement surgery assessed with cone-beam computed tomography, Am. J. Orthod. Dentofac. Orthop. 137 (2010) S86–S93, doi:10.1016/j.ajodo.2009.03.041.
[68] T.G. Kwon, H.S. Park, H.M. Ryoo, S.H. Lee, A comparison of craniofacial morphology in patients with and without facial asymmetry - A three-dimensional analysis with computed tomography, Int. J. Oral Maxillofac. Surg. 35 (2006) 43–48, doi:10.1016/j.ijom.2005.04.006.
[69] P.M. Pirttiniemi, Associations of mandibular and facial asymmetries—A review, Am. J. Orthod. Dentofac. Orthop. 106 (1994) 191–200, doi:10.1016/S0889-5406(94)70038-9.
[70] R.C. Solem, A. Ruellas, A. Miller, K. Kelly, J.L. Ricks-Oddie, L. Cevidanes, Congenital and acquired mandibular asymmetry: Mapping growth and remodeling in 3 dimensions, Am. J. Orthod. Dentofacial Orthop. 150 (2016) 238–251, doi:10.1016/j.ajodo.2016.02.015.
[71] G. Laganà, V. Di Fazio, V. Paoloni, L. Franchi, P. Cozza, R. Lione, Geometric morphometric analysis of the palatal morphology in growing subjects with skeletal open bite, Eur. J. Orthod. 41 (2019) 258–263, doi:10.1093/ejo/cjy055.
[72] B. Trpkova, N.G. Prasad, E.W.N. Lam, D. Raboud, K.E. Glover, P.W. Major, Assessment of facial asymmetries from posteroanterior cephalograms: validity of reference lines, Am. J. Orthod. Dentofac. Orthop. 123 (2003) 512–520, doi:10.1016/S0889-5406(02)57034-7.
[73] J.-J. Fang, Y.-H. Tu, T.-Y. Wong, J.-K. Liu, Y.-X. Zhang, I.-F. Leong, K.-C. Chen, Evaluation of mandibular contour in patients with significant facial asymmetry, Int. J. Oral Maxillofac. Surg. 45 (2016) 922–931, doi:10.1016/j.ijom.2016.02.008.
[74] C.E. Zambon, M.M. Ceccheti, E.R. Utumi, F.R. Pinna, G.G. Machado, M.P.S.M. Peres, R.L. Voegels, Orthodontic measurements and nasal respiratory function after surgically assisted rapid maxillary expansion: an acoustic rhinometry and rhinomanometry study, Int. J. Oral Maxillofac. Surg. 41 (2012) 1120–1126, doi:10.1016/j.ijom.2011.12.037.
[75] D.H. Enlow, Facial growth, WB Saunders Company, 1990.
[76] M.Y. Leung, Y.Y. Leung, Three-dimensional evaluation of mandibular asymmetry: a new classification and three-dimensional cephalometric analysis, Int. J. Oral Maxillofac. Surg. 47 (2018) 1043–1051, doi:10.1016/j.ijom.2018.03.021.
[77] L. Abad-Santamaría, A. López-de-Andrés, I. Jiménez-Trujillo, C. Ruíz, M. Romero, Effect of unilateral posterior crossbite and unilateral cleft lip and palate on vertical mandibular asymmetry, Ir. J. Med. Sci. 183 (2014) 357–362, doi:10.1007/s11845-013-1020-0.
[78] H.S. Matthews, A.J. Penington, R. Hardiman, Y. Fan, J.G. Clement, N.M. Kilpatrick, P.D. Claes, Modelling 3D craniofacial growth trajectories for population comparison and classification illustrated using sex-differences, Sci. Rep. 8 (2018) 4771, doi:10.1038/s41598-018-22752-5.
[79] S. Pirinen, Endocrine regulation of craniofacial growth, Acta Odontol. Scand. 53 (1995) 179–185, doi:10.3109/00016359509005969.

Manuscript 2: Approach towards the porous fibrous structure of the periodontal ligament using micro-computerized tomography and finite element analysis

Javier Ortún-Terrazas, José Cegoñino, Urbano Santana-Penín, Urbano Santana-Mora, Amaya Pérez del Palomar

Abstract

The periodontal ligament (PDL) is a porous and fibrous soft tissue situated around the tooth, which plays a key role in the transmission of loads from the tooth to the alveolar bone of the mandible. Although several studies have tried to characterize its mechanical properties, the behaviour of this tissue is not clear yet. In this study, a new simulation methodology based on a material model which considers the contribution of porous and fibrous structure with different material model formulations depending on the effort direction is proposed. The defined material model was characterized by a non-linear approximation of the porous fibrous matrix to experimental results obtained from samples of similar species and was validated by rigorous test simulations under tensile and compressive loads. The global PDL response was also validated using the parameters of the characterization in a finite element model of full human canine tooth obtained by micro-tomography. The results suggest that the porous contribution has high influence during compression because the bulk modulus of the material depends on the ability of interstitial fluid to drain. On the other hand, the collagen fibres running along the load direction are the main responsible of the ligament stiffness during tensile efforts. Thus, a material model with distinct responses depending of the load direction is proposed. Furthermore, the results suggest the importance of considering 3D finite element models based of the real morphology of human PDL for representing the irregular stress distribution caused by the coupling of complex material models and irregular morphologies.

Graphical abstract

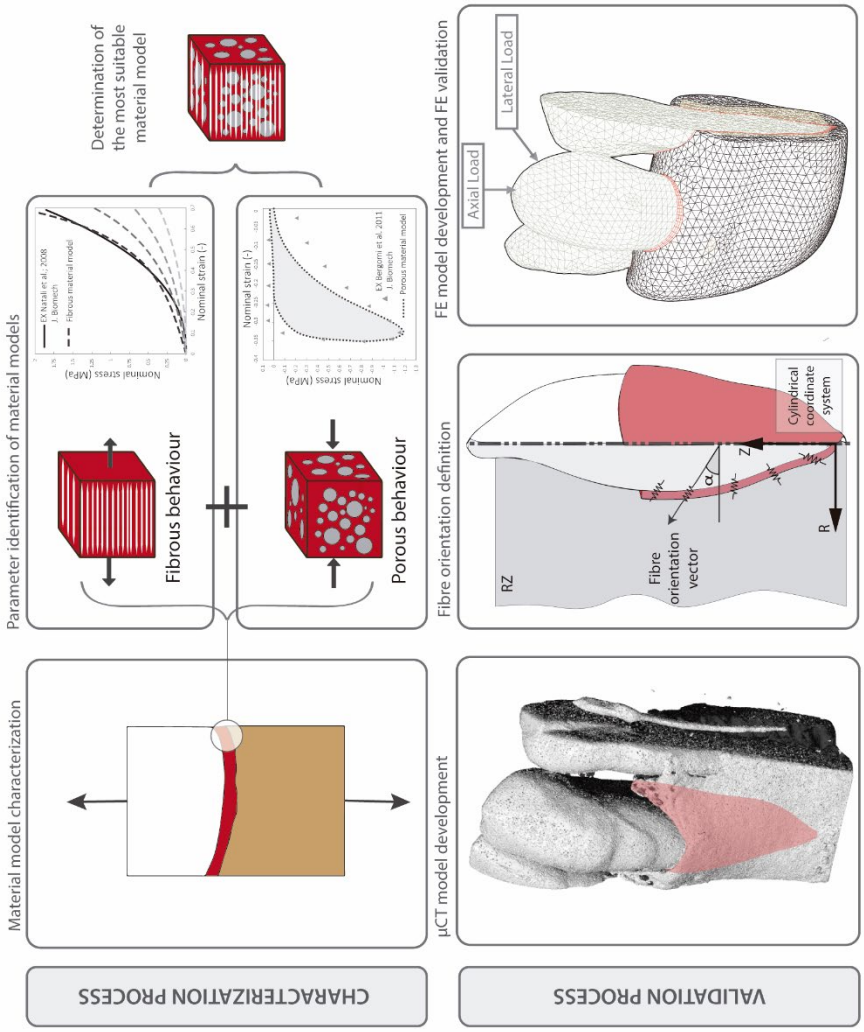

Journal of the Mechanical Behavior of Biomedical Materials 79 (2018) 135–149

Contents lists available at ScienceDirect

Journal of the Mechanical Behavior of Biomedical Materials

journal homepage: www.elsevier.com/locate/jmbbm

Approach towards the porous fibrous structure of the periodontal ligament using micro-computerized tomography and finite element analysis

J. Ortún-Terrazas[a,*], J. Cegoñino[a], U. Santana-Penín[b], U. Santana-Mora[b], A. Pérez del Palomar[a]

[a] Group of Biomaterials, Aragon Institute of Engineering Research (I3A), University of Zaragoza, Zaragoza, Spain
[b] School of Dentistry, Faculty of Medicine and Odontology, Santiago de Compostela University, Santiago de Compostela, Spain

ARTICLE INFO

Keywords:
Periodontal ligament
Fibrous structure
Hyperfoam
Porous elastic
Transversely isotropic hyperelastic
Microcomputed tomography

ABSTRACT

The periodontal ligament (PDL) is a porous and fibrous soft tissue situated around the tooth, which plays a key role in the transmission of loads from the tooth to the alveolar bone of the mandible. Although several studies have tried to characterize its mechanical properties, the behaviour of this tissue is not clear yet. In this study, a new simulation methodology based on a material model which considers the contribution of porous and fibrous structure with different material model formulations depending on the effort direction is proposed. The defined material model was characterized by a non-linear approximation of the porous fibrous matrix to experimental results obtained from samples of similar species and was validated by rigorous test simulations under tensile and compressive loads. The global PDL response was also validated using the parameters of the characterization in a finite element model of full human canine tooth obtained by micro-tomography. The results suggest that the porous contribution has high influence during compression because the bulk modulus of the material depends on the ability of interstitial fluid to drain. On the other hand, the collagen fibres running along the load direction are the main responsible of the ligament stiffness during tensile efforts. Thus, a material model with distinct responses depending of the load direction is proposed. Furthermore, the results suggest the importance of considering 3D finite element models based of the real morphology of human PDL for representing the irregular stress distribution caused by the coupling of complex material models and irregular morphologies.

1. Introduction

The periodontal ligament (PDL) plays an important role in transferring loads through the teeth to the alveolar bone (McCormack et al., 2014), and it is the physiological mechanism primarily responsible for tooth movement in response to force. When a tooth is subjected to an excessive force, the strain energy is dissipated by the viscous component of the porous tissue (Komatsu et al., 2007), and the interstitial fluid flows to the alveolar bone which is also a porous medium. Periodontal ligament without diseases contributes to the correct distribution of stresses from the tooth to the alveolar bone (Pihlstrom et al., 2005). However, the periodontal diseases are highly prevalent and could affect up to 90% of the worldwide population (Pihlstrom et al., 2005). Periodontitis, which results in the loss of connective tissue and bone support, is one of the most usual periodontal diseases. It is a major cause of tooth loss in adults (Pihlstrom et al., 2005). It can be ensured that the origin of this disease is multifactorial. Nevertheless, it has been proved (Preshaw et al., 2004) that mechanical loads contribute to the onset of a susceptible host to bacteria proliferation (Pihlstrom et al., 2005).

Biomechanically, the PDL is a kind of composite biological material that can be considered as a porous vasculature solid with a highly structured collagen network (Bergomi et al., 2010). Blood vessels occupy around 4–47% of its volume (Bergomi et al., 2011) containing a fluid (interstitial fluid, blood lymph) (Blaushild et al., 1992; Nyashin et al., 1999). The study of Pini et al. (2004), among others (Komatsu et al., 2007, 2004; McCormack et al., 2014), reveals that collagen fibre density and orientation are primary responsible for the differences observed in PDL mechanical response.

In the late 70 s, different researches started investigating experimentally the mechanical properties of the PDL by in vitro test in small PDL samples (a review of the literature is shown in Table 1). However, quantitative experimental data describing the complete behaviour of the PDL are still unavailable (Fill et al., 2011), as evidenced by the significant discrepancies that exist in published literature regarding mechanical properties of the PDL (Fill et al., 2011). For instance, elastic modulus and Poisson's ratio values can vary between 0.05 (Poppe et al., 2002) to 1 MPa (Jones et al., 2001), and between 0.086 (Bergomi et al.,

* Corresponding author.
E-mail address: javierortun@unizar.es (J. Ortún-Terrazas).

https://doi.org/10.1016/j.jmbbm.2017.12.022
Received 18 August 2017; Received in revised form 8 December 2017; Accepted 22 December 2017
Available online 28 December 2017
1751-6161/

Table 1
Review of published studies including finite element analysis and experimental tests sort by date. Left to right column: tooth that is involved in the analysis; specie; type of computational model; the scan method (if the model is based on real specimen geometry); PDL thickness of the computational model; material model used for the simulation; if experimental analysis is done; if strain rate dependence is analysed; type of loading. (Studies which appear in bold are studies that has been used in this study).

Ref.	Tooth	Specie	Computational model	Scan method	PDL thickness (mm)	Material model (MPa)	Exp. analysis	Velocity depended	Type
(Farah et al., 1973)	First molar	Human	2D	–	Uniform	Linear elastic	No	–	–
(Thresher and Saito, 1973)	First molar	Human	2D	–	Uniform	Linear elastic	No	–	–
(Daly et al., 1974)	Incisor	Human	No	–	Uniform	–	Yes	–	–
(Selna et al., 1975)	–	–	2D − 3D	–	Uniform	Linear elastic	No	–	–
(Widera et al., 1976)	Canine	Human	2D	–	0.4	Linear elastic	No	–	–
(Yettram et al., 1977)	Central incisor	Human	2D	–	Uniform	Linear elastic	No	–	–
(Atkinson and Ralph, 1977)	Various	Human	No	–	–	–	Yes	No	Intrusive test
(Weinstein et al., 1980)	Molar	Canine	2D-3D	–	0.125	Linear elastic	Yes	No	Intrusive test
(Takahashi et al., 1980)	Premolar, molar, incisor	Human	2D	–	0.2	Linear elastic	No	–	–
(Davy et al., 1981)	Central incisor	Human	2D	–	Uniform	Linear elastic	No	–	–
(Atmaram and Mohammed, 1981)	Molar	–	2D	–	Uniform	Linear elastic[a]	No	–	–
(Cook and Weinstein, 1982)	Molar	–	3D	–	Uniform	Linear elastic	No	–	–
(Ferrier and Dillon, 1983)	–	Old pigs	No	–	–	Viscoelastic	Yes	No	Water winding
(Reinhardt et al., 1984)	Central incisor	–	2D	–	Uniform	Linear elastic	No	–	–
(Williams and Edmundson, 1984)	Central incisor	–	2D	–	Uniform	Linear elastic	No	–	–
(Chen and Zhai, 1994)	Premolar	Human	No	–	–	–	Yes	No	Shear
(Tanne et al., 1987)	Premolar	–	3D	–	Uniform	Linear elastic	No	–	–
(Tanne et al., 1988)	Incisor	Animals	3D	–	Non-uniform	Linear elastic	Yes	No	Lateral load
(Farah et al., 1988)	Various	–	2D	–	Uniform	Linear elastic	No	–	–
(van Rossen et al., 1990)	–	–	2D axisymmetric	–	Uniform	Linear elastic	No	–	–
(Andersen et al., 1991)	Molar, first premolar and second premolar	Human	3D	Radiograph	Uniform	Linear elastic	Yes	No	Lateral load
(Cobo et al., 1993)	Canine	Human	3D	Photographs	0.2	Linear elastic	No	–	–
(Chiba and Komatsu, 1993)	Incisor	Rats	–	–	–	–	Yes	Yes	Shear
(Korioth and Hannam, 1994)	All mandible	Human	3D	CT	Non-uniform	Linear elastic (3 sections)	No	–	–
(Komatsu et al., 1996)	Incisor	Rat	–	–	–	–	Yes	Yes	Shear
(Middleton et al., 1996)	Canine	No	2D	–	Uniform	Viscoelastic	No		
(Rees and Jacobsen, 1997)	First premolar	Human	2D	Photographs	0.25	Linear elastic	Yes	No	Lateral load
(Tanne et al., 1998)	Incisor	Human	3D	Anatomic data	–	Linear elastic	Yes	Yes	Lateral load
(Rees, 2001)	Premolar	–	2D	Radiograph	0.3	Linear elastic	No	–	–
(Yoshida et al., 2001)	Incisor	Human	–	–	–	–	Yes	No	Lateral load
(Jones et al., 2001)	Incisor	Human	3D	–	Uniform	Linear elastic	Yes	No	Lateral load
(Qian et al., 2001)	Canine	Dog	3D	–	Non-uniform	Linear elastic[a]	Yes	No	Lateral load
(Poppe et al., 2002)	Incisor and canine	Human	3D	Photographs of sections	Non-uniform	Bilinear	Yes	No	Intrusive load
(Pietrzak et al., 2002)	Incisor	Human	3D	CT	0.2	Nonlinear isotropic	No	–	–
(Toms and Eberhardt, 2003)	Canine	Human	2D axisymmetric	Photograph	0.291	Linear elastic, nonlinear elastic	Yes	No	Shear
(Shimada et al., 2003)	Incisor	Rat	–	–	–	–	Yes	Yes	Intrusive load
(Natali et al., 2008)	–	Pig	–	–	–	–	Yes	Yes	Axial test
(Pini et al., 2004)	Incisor and molar	Bovine	–	–	–	–	Yes	Yes	Axial test
(Cattaneo et al., 2005)	Canine and premolar	Human	3D	μCT	Non-uniform	Nonlinear and linear elastic	No	–	–
(Coelho et al., 2009)	Incisor	Human	2D	–	–	Linear elastic	No	–	–

(*continued on next page*)

Table 1 (*continued*)

Ref.	Tooth	Specie	Computational model	Scan method	PDL thickness (mm)	Material model (MPa)	Exp. analysis	Velocity depended	Type
(Gonzales et al., 2009)	Molar	Rats	3D	μCT	Non-uniform (mean 0.15 mm)	Linear elastic	Yes	No	Extrusion test with spring
(Meyer et al., 2010)	Incisor	Dogs	3D	μCT	Non- uniform	Linear elastic[a]	No	–	–
(Bergomi et al., 2011)	Molars	Bovine	2D axisymmetric	–	Uniform	Porous hyperfoam	Yes	Yes	Axial test
(Wei et al., 2014)	Premolar, molar	Human	3D	CT	0.2	Elastic, hyperfoam, Ogden hyperelastic	No	–	–
(Boldt et al., 2012)	Incisor	Human	–	–	–	–	Yes	Yes	Intrusive and lateral load
(Xu et al., 2015)	Incisor	Human	3D	Laser-based 3D digitizing	0.3	Linear elastic	Yes	–	Fracture failure, Axial compressive and tensile tests
(Zhang et al., 2016)	Molar	Human	3D	μCT	Non-uniform 0.2–0.4	Linear elastic	No	–	–
(Oskui et al., 2016)	Molar	Bovine	Constitutive model	–	–	Visco-hyperelastic	Yes	Yes	Axial test
(Nikolaus et al., 2016)	Premolar	Human (3D) Pig (exp.data)	3D	μCT	Non-uniform	Ogden hyperelastic	Yes	No	Intrusion test
(Huang et al., 2017)	Molar	Pig	2D axisymmetric		Uniform	Visco-hyperelastic model	Yes	Yes	Nanoindentation

[a] Distinguish the fibrous and continuous structure.

2011) to 0.49 (Pietrzak et al., 2002), respectively. Lack of PDL mechanical properties consistency throughout the literature is a function of several, often interrelated, parameters. One of the main difficulties for obtaining PDL data is related with extracting small samples with regular geometry from its complex biological structure. Moreover, there is a great dispersion among data from different species (Komatsu et al., 1998). It is well-known that experimental data from porcine and bovine PDLs showed a possible better correlation with human PDL (Genna et al., 2008 and Nikolaus et al., 2016, among others), than others such as mouse (Afanador et al., 2005), hamster (Komatsu et al., 1998), rat (Shimada et al., 2003) or rabbit (Komatsu et al., 2007) tissue. In some cases, the experimental data was not measured correctly because the saturated fluid phase of the ligament was not taken into account (Genna et al., 2008). Another key aspect of a correct characterization of PDL biomechanical response is to measure the contribution of the fibre network to the overall behaviour of the tissue. Several authors (Berkovitz, 1990; Dorow and Krstin, 2002; Komatsu et al., 2007; Sanctuary, 2003) have demonstrated that collagen bundles are intimately related to the stress–strain behaviour of the tissue, mainly under tensile efforts. Later studies (Qian et al., 2009; Natali et al., 2008; Provatidis, 2000) have found that PDL has anisotropic behaviour, in which collagen fibres are a key factor. Finally, the different behaviour of the PDL under tensile and compressive loads is another aspect that has to be accurately solve too (Fill et al., 2012; Huang et al., 2017). Some authors (Fill et al., 2012; Natali et al., 2008) suggest that the PDL is quasi-incompressible when they performed tensile tests. On the other hand, other authors (Bergomi et al., 2009; Wei et al., 2014) suggest that the PDL is very compressible when they performed compressive tests. Because of its porous structure, the fluid phase and its highly vascular matrix (Sanctuary, 2003) several studies have revealed that PDL has significant time response behaviour (Bergomi et al., 2010; Natali et al., 2011; Nishihira et al., 2003; Papadopoulou et al., 2011; Wang et al., 2012). Although some of them (Natali et al., 2008) studied the viscoelastic phenomena at a wide range of time intervals, they did not analyse its permeability and the hysteresis behaviour at different strain-rates. Luckily, Bergomi et al., 2011 analysed cylindrical bovine specimens under sinusoidal tension-compression displacements at various frequencies in a fully saturated medium.

Regarding the numerical analysis, whether or not to include the PDL in finite element (FE) models is a subject of much debate throughout the literature (Gröning et al., 2011). Due to its complex nature, numerical studies have to be performed. Research in PDL biomechanics has been essentially focused on four specific types of constitutive modelling approaches (Fill et al., 2012): linear-elastic (Zhang et al., 2016), viscoelastic (Oskui et al., 2016), hyperelastic (Nikolaus et al., 2016) and visco-hyperelastic models (Huang et al., 2017). Several numerical studies have attempted to explain the anisotropic behaviour using 2D finite element models introducing collagen fibres bundles as 1D elements (Romeed et al., 2006). Nevertheless, a considerable amount of literature has stated that the use of 3D geometry is mandatory; plane models are inadequate and should not be used to simulate the tooth/bone mechanical system under loading (Fill et al., 2012). This point of view is supported by McCormack et al. (2014) who proposed to investigate the role of PDL fibres in morphologically accurate models based on micro-tomography (μCT) scans of human mandibles. Because of that, constructing accurate and suitable FE meshes to reproduce teeth geometry is essential since FE simulation results are highly sensitive to geometrical modelling assumptions (Hohmann et al., 2011; Nikolaus et al., 2016). However, the inclusion of PDL as a 3D body requires a dense FE mesh due to its geometric morphology, which implies that large models and time-consuming analysis are needed. Another way of simulating the PDL behaviour is using a contact model between the interface of tooth root and the alveolar process instead of a FE mesh (Tuna et al., 2014).

Due to the complex nonlinear behaviour, a rigorous material model parameters identification and validation were developed in this study.

For the validation, a μCT scan of a human canine was used to construct an accurate 3D finite element model. Thus, the purpose of this study was multiple: 1. To characterize the parameters which describe the fibrous and porous structure behaviour of the PDL under different loading directions. 2. To validate these material parameters by simulating different experimental tests from the literature. 3. To develop a FE model based on μCT of a human tooth able to predict PDL behaviour under distinct loading conditions considering the aforementioned material parameters.

To determine which constitutive material model explains better the periodontal ligament response under different types of forces, several nonlinear FE analyses were performed. (Purpose 1.) The material parameters of porous transversely isotropic (Por. Trans. Iso) and of transversely isotropic (Trans. Iso) were characterized using experimental data of the literature. The experimental results of PDL of porcine and bovine species were used due to their similarities with the human PDL anatomy (Fill et al., 2012) and collagen fibril diameter (Pini et al., 2004), among others. The validation process (Purpose 2.) was performed comparing the both aforementioned material models with hyperfoam (HFoam) and porous hyperfoam (Por. HFoam) material models of the literature. Finally, the material model which adjusted better to the experimental test curves was used for simulating the movement of the full human canine tooth FE model under intrusive and lateral loads (Purpose 3.).

2. Material and methods

2.1. Material parameters characterization

In this section, the characterization of the parameters to define a transversely isotropic material (Trans. Iso) and porous transversely isotropic material (Por. Trans. Iso) for the PDL are presented. Since the fluid contribution can be negligible under tensile loading (Bergomi et al., 2011; Natali et al., 2008), experimental data of tensile tests of the literature were used for this fitting. It was assumed that these parameters can be used for tensile and compressive behaviour and this validity was checked. The experimental test data performed by Natali et al. (2008) under tensile loads were used to characterize the transversely isotropic hyperelastic materials because human samples were used, and it is more suitable than others referred to animal species with a different bite system such as rat and rabbit (Fill et al., 2012). Moreover, it was used because it describes the PDL behaviour until its failure. For the fitting process, it was assumed that fibres in the samples experimentally tested by Natali et al. were oriented in the same direction that the traction load (shown in Fig. 2a), according to the experimental test specifications. Thus, the transversely isotropic hyperelastic material model of the solid matrix was defined by the Holzapfel strain energy function (Holzapfel, 2000):

$$W_s = W_m + W_f + W_{vol} \quad [1]$$

where W_m is the component of the hyperelastic matrix substance without fibres, W_f represents the fibrous term and W_{vol} is the volumetric component defined as:

$$W_m = C_1 \cdot (\widetilde{I}_1 - 3);$$
$$W_f = \frac{k_1}{2 \cdot k_2} \{exp[k_2 \cdot (\widetilde{I}_4 - 1)^2] - 1\};$$
$$W_{vol} = \frac{1}{D}\left(\frac{(J_{el})^2 - 1}{2} - lnJ_{el}\right) \quad [2]$$

Where C_1 is a material constant related to the matrix substance, $k_1 > 0$ and $k_2 > 0$ are the parameters which identify the exponential behaviour due to the presence of collagen fibres, D is related to bulk modulus K, by $K = 2/D$, and $J_{el} = \det \boldsymbol{F}$. The strain energy function (Eq. (1)) is written in terms of the modified invariants that arise from uncoupling the dilatational and deviatoric responses. These invariants are defined as:

$$\widetilde{I}_1 = tr\widetilde{\boldsymbol{C}} \cdot \widetilde{I}_4 = \boldsymbol{a}^0 \cdot \widetilde{\boldsymbol{C}} \cdot \boldsymbol{a}^0 \quad [3]$$

where $\boldsymbol{a}^0$ is unitary vector defining the orientation of the collagen fibres. If the stretch (λ) of the fibre at each time (t) is defined as the ratio between the lengths at the deformed ($\boldsymbol{X}$) and reference configurations ($\boldsymbol{x}$), the new fibre orientation is updated in the following way:

$$\lambda \cdot \boldsymbol{a}(\boldsymbol{x}, t) = \boldsymbol{F}(\boldsymbol{X}, t)\boldsymbol{a}^0(\boldsymbol{X}) \quad [4]$$

where $\boldsymbol{a}(\boldsymbol{x}, t)$ is the unit vector of the fibre in the deformed configuration ($\boldsymbol{x}$) at each time, t. Thus, it is assumed that the fibre moves with the material points of the continuum.

In equations (3 and 4), $\boldsymbol{F}$ is the deformation gradient and $\widetilde{\boldsymbol{C}}$ is the modified Green tensor in the reference configuration defined as:

$$\widetilde{\boldsymbol{C}} = \widetilde{\boldsymbol{F}}^T \widetilde{\boldsymbol{F}} \quad \text{with} \quad \widetilde{\boldsymbol{F}} = (J_{el})^{-1/3}\boldsymbol{F} \quad [5]$$

In this model, it is assumed that when the tissue is compressed ($\widetilde{I}_4 < 1$) the strain energy corresponding to collagen fibres is null. Therefore, they only contribute to the hyperelastic behaviour of the solid phase when they stretch, only the matrix being responsible for the hyperelastic behaviour in compression.

The non-linear fitting process of the analytical solution of the transversely isotropic hyperelastic material model [Eq. (1)] was implemented in MATLAB (MATLAB 6.0 R12 The MathWorks Inc., Natick, MA, 2000). The parameters were obtained by approximating the analytical solution to the experimental results obtained by Natali et al.. The fitting curve (shown in discontinuous line in Fig. 1.a) differs by 0.9% to the experimental results. The four parameters of transversely isotropic hyperelastic material model obtained by this procedure were: C_1 = 0.01 MPa, D = 9.078 MPa^{-1}, k_1 = 0.298 MPa and k_2 = 1.525.

On the other hand, to introduce the influence of the biphasic nature of the PDL, the porous contribution was added. Thus, the total stress, $\boldsymbol{\sigma}$, in a fully saturated tissue is defined as:

$$\boldsymbol{\sigma} = (1-n)\overline{\sigma_s} - n \cdot \overline{p_t} \cdot \boldsymbol{I} \quad [6]$$

Where $\overline{\sigma_s}$ is the stress component obtained from the second Piola -Kiorchhoff stress tensor of the strain energy function of solid phase, $\overline{p_t}$ is the average pressure stress of the interstitial fluid and n is the void ratio defined as the ratio of the volume of fluid (V_f) to the total volume (V_t) by $n = dV_f/dV_t$. The pressure stress, $\overline{p_t}$, is related to the Jacobian contribution from the permeability of the tissue by the nonlinear Forchheimer flow law. This law was employed in Abaqus (Abaqus 6.14, Simulia, Rhode Island, USA) to describe the fluid flow for a permeability that varies with the deformation by the exponential permeability function described by Argoubi and Shirazi-Adl (1996) for biphasic materials:

$$k = k_0 \left[\frac{e(1+e_0)}{e_0(1+e)}\right]^2 exp\left[M\left(\frac{1+e}{1+e_0} - 1\right)\right] \quad [7]$$

where k_0 and e_0 are the permeability and void ratio at zero strain; e is the strain dependent void ratio and M is a dimensionless material parameter. To compute the initial void ratio, a 0.7 porosity value was used such as other studies of the literature (Bergomi et al., 2011; Nishihira et al., 2003; Wei et al., 2014). On the other hand, k_0 and M were identified by an iterative process to fit the compression test results obtained by Bergomi et al. (2011). The iterative process was executed by a commercial software package (Python 3.5.2, Python Software Foundation). For the fitting process, the experimental results at 1 Hz strain rate were used. For this frequency, the poromechanical behaviour was more pronounced, and it is easier to characterize the porous mechanical response. The iterative simulation gives the permeability (k_0) and M values as results for Por. Trans. Iso material model. As it was expected, these parameters were different to the parameters obtained by Bergomi et al. (2011) for a different solid matrix formulation, in their case, hyperfoam material model formulation. The porous phase approximation to the Bergomi et al. (2011) experimental results at 1 Hz is shown in Fig. 1b. The interstitial fluid contribution was characterized

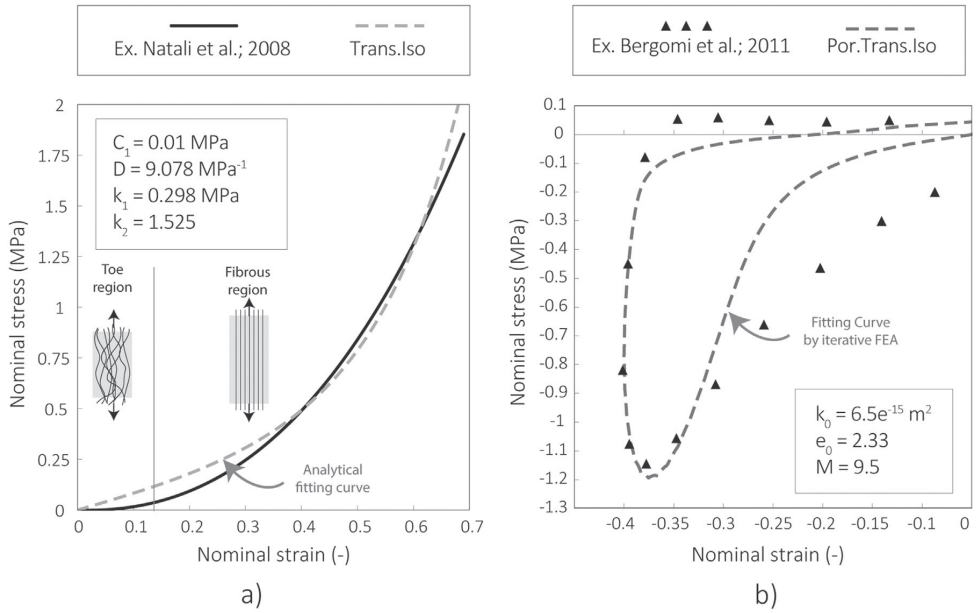

Fig. 1. a: Constitutive material model approximation of transversely isotropic hyperelastic material model to Natali et al. (2008) experimental results; b: Curve approximation of porous parameters to Bergomi et al. (2011) experimental results.

by permeability value, $k_0 = 6.5 \cdot 10^{-15}$ m^2, and of M = 9.5.

Finally, the aforementioned materials models (Trans. Iso and Por. Trans. Iso) were compared with hyperfoam (HFoam) and porous hyperfoam (Por. HFoam) material models. The HFoam material model considers only the contribution of the matrix without fluid, while the Por. HFoam considers both, porous and solid phases of the tissue. The parameters given by Bergomi et al. (2011) were used for HFoam and Por. HFoam material model description. The validity of these parameters was verified simulating the same compressive test mimicking their axisymmetric model (results are shown in Fig. 4.b in "3.1 FE Simulation of the specimens" section). Thus, HFoam and Por. HFoam were defined using the elastic foam energy function (Storakers, 1986) defined as:

$$W_s = \frac{2\mu}{\alpha^2}\left[\hat{\lambda}_1^{\alpha} + \hat{\lambda}_2^{\alpha} + \hat{\lambda}_3^{\alpha} - 3 + \frac{1}{\beta}(J_{el}^{-\alpha\beta} - 1)\right] \quad [8]$$

Where J_{el} is the elastic volume strain, μ and α are material parameters, λ_i is the stretch ratio at i principal direction (related with the strain, ε_i, by $\lambda_i = 1+\varepsilon_i$), and the coefficient β determines the degree of compression related to the Poisson's ratio, ν, by $\beta = \nu/(1-2\nu)$. All the hyperfoam and transversely isotropic material models parameters are summarized in Table 3.

2.2. FE simulation of the specimens

Both different material models defined in the previous section were compared with data from literature. Thus, 3D finite element models reproducing the test samples geometry used by Natali et al., (2008), and Bergomi et al. (2011) in their experimental tests (tension and compression respectively) were developed using Abaqus CAE 6.14 (Abaqus 6.14, Simulia, Rhode Island, USA). For tension analysis, a 3D finite element model was developed according to the geometry description given in Natali et al. (2003). For compression analysis, the axisymmetric model described by Bergomi et al. (2011) was used. To reach the ideal finite element mesh (shown in Fig. 2), the number of elements along PDL thickness of the FE model performed by Natali et al. and the axisymmetric FE model performed by Bergomi et al. was maintained. The element length was defined by a mesh refinement process, until verify mesh convergence. Thus, the number of elements was increased until the difference of the results was 3% or lower. The final length of the element obtained from this mesh refinement process was around 0.035 mm for both models.

For each simulation test, the periodontal ligament was defined according to the four following material models: hyperfoam (Por. HFoam) and transversely isotropic hyperelastic (Por. Trans. Iso) with porous coupling, and, hyperfoam (HFoam) and transversely isotropic hyperelastic (Trans. Iso) without porous coupling. The different parameters of the transversely isotropic hyperelastic models were obtained from the fitting procedure described previously. However, the parameters of hyperfoam (HFoam) and porous hyperfoam (Por. HFoam) material models were given by Bergomi et al. (2011) FE study. The alveolar bone and dentin were included to reproduce as similar as possible the experimental tests and to simulate the fluid exchange between PDL and these stiffer bodies, as it was demonstrated by Bergomi et al. (2011). Porous elastic material models were used for alveolar bone and dentine, (shown in Fig. 2) because they have enough porosity to be considered (Bergomi et al., 2011; Lacroix and Prendergast, 2002). Table 3 shows the material parameters used for bone, dentine and distinct PDL material models.

To reproduce the different experimental set up of the experiments the following boundary conditions and loads were considered. From the tensile behaviour a pure sinusoidal traction ($\lambda(t) = 1 + \lambda_{70\%} sin(2\pi ft)$) displacement equivalent to 70% PDL thickness (0.25 mm) at different frequencies (0.1, 0.5 and 1 Hz) was applied at the top of the bone of the 3D specimen model (shown in Fig. 2a). The bottom surface of tooth was restrained. With respect to the compression behaviour, an axisymmetric model was used (shown Fig. 2b). The simulation setup was equivalent to the traction test, but here a sinusoidal compressive displacement equivalent to 35% PDL thickness (0.60 mm) was applied. In both cases, two full cycles were simulated to provide time for model stabilization due to the transient phenomena. The second cycle was used for the comparison with experimental data. Also, to verify the influence of

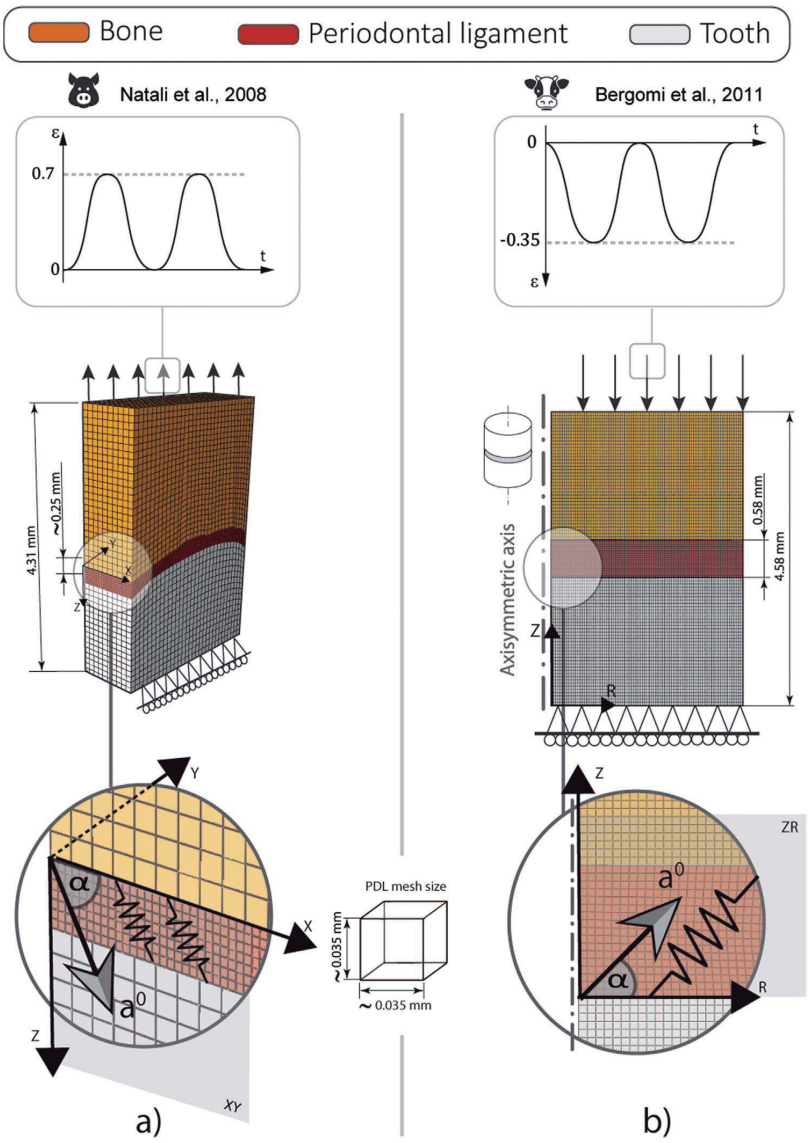

Fig. 2. Up to down: Loading conditions; Simulation conditions of test specimens FE models; Fibre direction scheme (rectangular coordinate system for tensile test specimen and cylindrical system for compressive test specimen) of Natali et al. (2008) specimen (a) and Bergomi et al. (2011) specimen (b), respectively.

collagen fibres direction, simulations at different α values in the undeformed state (0, 20, 45, 70 and 90 degrees) (shown in Fig. 2) were performed for the fibre reinforced models (Trans. Iso and Por. Trans. Iso).

2.3. FE model of a human canine based on a μct

The 3D finite element model which was used in this research was constructed based on a μCT of a portion of human mandible. This specimen was extracted from a 42 years old human cadaver with no periodontal disease and kept frozen (−20 °C). The sample was taken from the freezer and placed at room temperature to thawing. Then, the specimen was kept in Ringer's solution tube throughout the preparation period to avoid drying out phenomena. Soft tissues of the surrounding of the mandible were removed and a μCT scan (Skyscan 1172, Bruker μCT N.V., Kontich, Belgium) was used to scan the cleaned specimen. The tomograms obtained from the scanning were rebuilt by Feldkamp algorithm modified version 1.6.1.7 NRecon application (Bruker μCT N.V., Kontich, Belgium), executing reduced artefacts caused by beam hardening ring. Computed μCT was obtained with cross-sections of 13 μm distance to achieve improved resolution. The μCT model was parametrized using Rhinoceros v5 software (Robert McNeel & Associates, Seattle, USA), thereby making the transformation of non-parametric models into parametric models with Non-Uniform Rational Bases Splines (NURBS). Since soft tissues cannot be determined using a μCT scan (Nikolaus et al., 2016), the PDL was generated using computer-aided design (CAD) software (Rhinoceros v5, Robert McNeel & Associates, Seattle, USA). Thus, the free space between alveolar bone and tooth defined the PDL geometry.

To obtain the ideal size of the FE mesh (shown in Fig. 3), a process

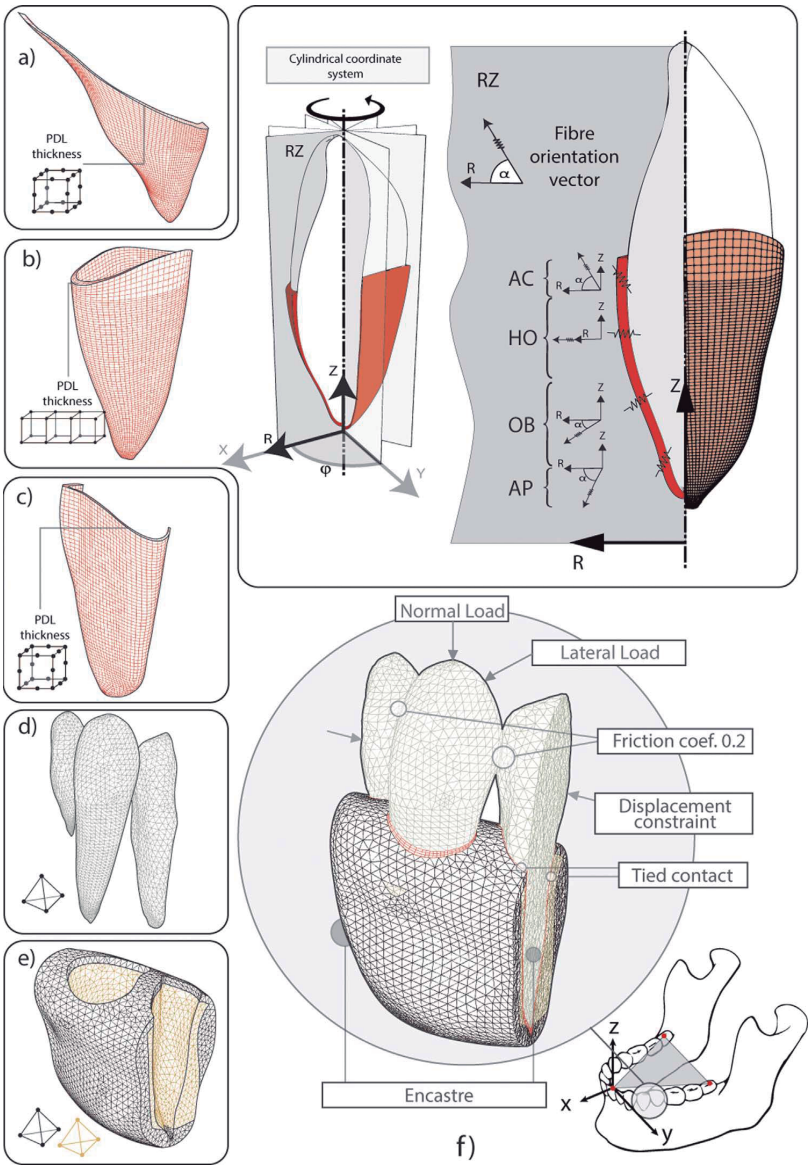

Fig. 3. Up to down: a) mesh of the lateral incisor PDL; b) mesh of the canine PDL and fibre distribution according to different direction of fibres bundles (AP: apical, OB: oblique, HO: horizontal and AC: alveolar crest), c) mesh of the premolar PDL, d) mesh of lateral incisive, canine and premolar teeth, e) mesh of the alveolar (yellow) and cortical (black) bones, f) scheme of the loading conditions where canine tooth is subjected to a normal force or a lateral force (The normal force was applied perpendicular to the plane which is represented in the corner of the figure, the lateral load was applied at labial-lingual direction). (For interpretation of the references to color in this figure legend, the reader is referred to the web version of this article.)

Table 2
Element and node numbers of the model.

Part	Type of element	Number of elements	Number of nodes
Cortical bone	C3D4	4.118	2.315
Alveolar bone	C3D4P	62.697	35.250
Canine tooth	C3D4P	48.499	27.267
Premolar tooth	C3D4P	52.819	29.696
Lateral incisor tooth	C3D4P	52.547	29.543
Canine PDL	C3D8RP	40.716	22.892
Premolar PDL	C3D20	3.360	1.889
Lateral incisor PDL	C3D20	3.157	1.776

of mesh refinement was executed until verifying mesh convergence. The mesh refinement process was stopped when the difference between the results was 5% or lower by Abaqus CAE 6.14 (Abaqus 6.14, Simulia, Rhode Island, USA). The periodontal ligament was meshed using three hexahedral elements of first order in its thickness. More elements in PDL thickness would exponentially increase the number of elements along the height to maintain the aspect proportion, and with it, the time of the analysis. Furthermore, a smaller element size would produce an excessive distortion of the elements making the convergence more difficult. A reduced integration scheme was used because full integration one has difficulty with volumetric locking in cases of incompressible materials. Furthermore, the use of this technique has been found to efficiently control the hourglass modes without affecting the precision of the numerical result. Therefore, the model consisted of

150.628 nodes, distributed as appear in Table 2. The other two ligaments were meshed using only one quadratic element along its thickness, because the geometry of these ligaments is not complete, and they are not the topic of analysis. Besides, these tissues underwent low stresses/strains and here mesh effects can be considered negligible.

As it will be seen in "*3.1 FE Simulation of the specimens*", the results of test specimens under tensile and compressive loads revealed that a complex material model is necessary to accurately describe the PDL behaviour. Thus, this tissue was simulated using the poroelastic theory and the behaviour of the solid phase matrix was implemented in a user subroutine. The UMAT subroutine was implemented in Abaqus 6.14 commercial software (Abaqus 6.14, Simulia, Rhode Island, USA). Different behaviour was considered in traction and compression. Thus, it was assumed that when the tissue is compressed ($\widetilde{I_4} \leq 1$) [Eq. (2)], the strain energy function corresponds to a porous hyperfoam material model (Eq. (8)). However, when the tissue is stretched ($\widetilde{I_4} > 1$) (Eq. (2)) the behaviour of the material is described by a porous transversely isotropic hyperelastic material model using the Holzapfel strain energy function described previously (Eq. (1)). This switch caused discontinuities around zero strain. However, these discontinuities were small because the low stiffness of the Neo-Hookean matrix at small tensile strains (small C_1 parameter) and the smooth slope of the Por. Hfoam material stress/strain curve at small compressive strains. Furthermore, the automatic stabilization method of ABAQUS/Standard was used by automatically adding a volume-proportional damping to the model.

For the last, the preferential direction of the fibres bundles (shown in Fig. 3b) were defined according to the experimental results of Lindhe et al. (2003). Thus, the human PDL of this study considered four principal groups of fibres bundles regarding their different orientations (apical, oblique, horizontal, and alveolar-crestal fibres). Transseptal, alveolo-gingival, dentogingival, dentoperiosteal, circular/semi-circular, intercircular, intergingival, transgingival, interpapillary, periosteo-gingival and inter-radicular fibres were not included because these bundles are in the gum, and they are hardly relevant in the mechanical support for the applied loading conditions (Natali et al., 2004).

The material constants of the remaining components of this model were defined on the basis of previous data (Bergomi et al., 2011; Lacroix and Prendergast, 2002) as shown in Table 3. It is remarkable that the cortical bone was not defined as a porous medium due to the distance to the ligament and its low porosity compared to other tissues.

Finally, the same material properties were used for every tooth part (dentine, enamel, pulp and tooth nerve) because they are significantly stiffer than the PDL tissue. Thus, the tooth was assumed as a homogeneous poroelastic material with dentin properties. The mechanical poroelastic properties to take into account the fluid interaction with the PDL.

Fig. 3.f shows the boundary and loading conditions of the model. Nodes of both lateral sections of the mandible were fixed according to the rest of mandible function (Qian, Chen, and Katona, 2001). The movement in the distal-mesial direction of the nodes of premolar and lateral incisor teeth was constrained to represent the restriction condition with the remaining teeth of the mandible. To define the interaction between the teeth and PDL, a tied contact condition was used since there are interstitial fibres that maintain them together (Huang et al., 2012; Schünke et al., 2010; Tuna et al., 2014). Moreover, a tied contact was used between the PDL and the alveolar bone. The interactions between the teeth were defined by a penalty contact formulation with a friction coefficient (value of 0.2), according to the studies by Zheng and Zhou (2006).

The validation of the FE model of the full human canine tooth was performed using the experimental data test performed by Boldt et al. (2012) for an intrusion load of 80 N and a lateral load of 35 N at an incisor tooth. The loads were applied at 250 N/s in a plane which was located at the occlusal plane position according to the studies from Hattori et al. (2009). The coordinate system with its origin was at the mandibular incisal point and the x–y plane coinciding with the occlusal plane was used (shown in Fig. 3.f).

3. Results

3.1. FE simulation of the specimens

A comparison between material models was performed. Fig. 4 shows the results for tensile and compressive simulation tests using different material models, loading at different strain-rates and changing the orientation of the fibre network.

With respect to the material model comparison (shown in Fig. 4.a) under tensile load, there is a significant positive correlation between the experimental data and transversely isotropic material models. Although the FE modelling tends to be stiffer at the initial part of the curve, there is a similar behaviour for strain values higher than 0.37. This concave shape at the beginning of the curve is caused by the Neo-Hookean term of the constitutive material model for the initial strain values. However, this model behaviour changes when the fibres begin to stretch. Not the same occurs for the hyperfoam material model defined by Bergomi et al. (2011). The behaviour of the hyperfoam material models are similar for the first curve values (shown in Fig. 4a), but it becomes stiffer than the experimental response for strains higher than 0.15. For Por. HFoam and Por. Trans. Iso material models, the porous contribution during the tensile test is insignificant, especially for the fibrous model in which the porous contribution could be only appreciated for strain values lower than 0.50. The negligible influence of the porous term during traction loading can be explained considering that when hen the tissue is stretched its volume increases (because Poisson effect). This causes an increment of the PDL porosity. Thus, the fluid flow (defined by Eq. (7)) increases exponentially making the influence of porous pressure not significative. That means that the bulk

Table 3
Mechanical properties assigned to each material.

	Matrix parameters				**Porous properties**				
	Young's Modulus (MPa)		**Poisson's Ratio (-)**		**k_0 (m^2)**	**M (-)**	**Porosity (-)**	**Void Radio (-)**	**Specif. weight of interstitial fluid (N/mm^3)**
Cortical bone	20000[b]		0.30[b]		–	–	–	–	–
Dentin	15000[a]		0.31[a]		$3.88 \cdot 10^{-17}$[a]	–	0.8[b]	4[b]	$9.8 \cdot 10^{-6}$
Alveolar bone	345[a]		0.31[a]		$5.29 \cdot 10^{-14}$[a]	–	0.8[b]	4[b]	$9.8 \cdot 10^{-6}$
	μ (MPa)	**α (-)**	**Poisson's Ratio (-)**						
PDL HFoam	0.03[a]	20.9[a]	0.257[a]		–	–	–	–	–
PDL Por. HFoam					$8.81 \cdot 10^{-15}$[a]	14.2[a]	0.7[a]	2.33[a]	$9.8 \cdot 10^{-6}$
	C_1 (MPa)	**D (MPa^{-1})**	**k_1 (MPa)**	**k_2 (-)**	**k_0 (m^2)**	**M (-)**	**Porosity (-)**	**Void Radio (-)**	**Specif. weight of interstitial fluid (N/mm^3)**
PDL Trans. Iso	0.01	9.078	0.298	1.525	–	–	–	–	–
PDL Por. Trans. Iso					$6.5 \cdot 10^{-15}$	9.5	0.7[a]	2.33[a]	$9.8 \cdot 10^{-6}$

[a] Bergomi et al. (2011).
[b] Lacroix and Prendergast (2002).

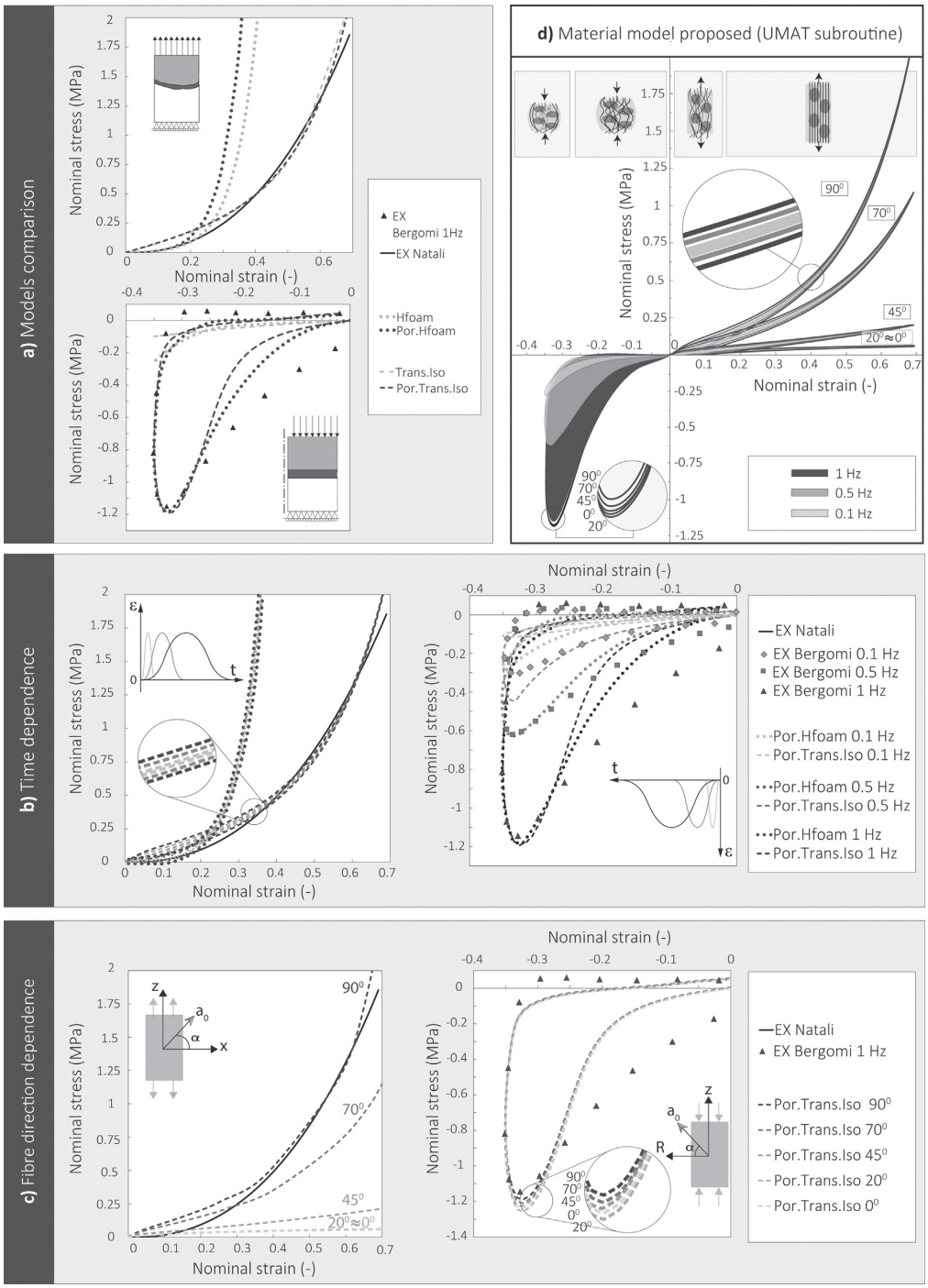

Fig. 4. Comparison between the experimental and numerically-simulated response for traction-compression loading. a) Comparison between the four material models; b) time response comparison of porous hyperfoam and porous transversely isotropic hyperelastic material models under 0.1, 0.5 and 1 Hz frequencies; c) fibre direction dependence of porous transversely isotropic hyperelastic material model response; d) Response of the material model proposed in full traction-compression cycles at different frequencies and fibre directions.

modulus of the PDL is not hardly related with porosity for traction efforts. On the other hand, a strong evidence of considering the porous coupling is found when compressive tests are simulated. The material models with no porous coupling have poor approximation for loading and relaxing responses. Furthermore, it is remarkable that the porous hyperfoam material model is more similar to the experimental data during loading process, than porous transversally isotropic hyperelastic material response.

In Fig. 4b both formulations, porous transversely isotropic and transversely isotropic, have similar time response during the tensile test, especially for low strain values. It can be seen that loading-relaxing curves for porous transversely isotropic formulation show higher hysteresis behaviour than those for porous hyperfoam at traction. But as it is aforementioned during the tensile test, the porous coupling has slight contribution. Not the same happens for the compression test simulation. For low strain rates, the fluid has enough time to flow while for higher strain rates, the fluid does not have enough time to leak. Therefore, the fluid in the matrix for the same strain is higher at 1 Hz frequency than at 0.1 Hz. This translates into a stiffer behaviour of the tissue for higher strain rates.

On the other hand, the high contribution of the fibrous structure is demonstrated in Fig. 4c. For tensile test, the PDL tissue is stiffer when fibres are aligned with loading direction. For low strain values (toe region in Fig. 1.a), fibres are not stretched and the matrix resists most of the stresses. However, for strain values higher than 0.13, fibres start stretching. Thus, the curves tend to the Neo-Hookean material model curve when fibres hardly contribute (fibres perpendicularly oriented to loading direction). Besides, an insignificant contribution of the fibres is obtained during the compression test for different fibres directions. However, it is remarkable that the stiffness of the tissue increases when fibres are perpendicular to the load direction. This could happen because the specimen has barrel shape in the deformed state, since fibres located in the middle of the test specimen are stretched.

In summary, the low contribution of the porous term and the key role of fibres during tensile loading suggest that Trans. Iso material model would be enough to characterize the behaviour of the ligament under tensile efforts. However, during compression, it has been demonstrated the importance of considering the porous term because the difference of stiffness according to the strain rate. Thus, Por. Trans. Iso should be considered as an option to represent the porous and fibrous behaviour. Nevertheless, this constitutive model (Por. Trans. Iso) fitted worse than Por. Hfoam response for compression experimental data. Therefore, the same material model cannot explain the complex nature of this tissue correctly. For this reason, a material model that combines Por. Trans. Iso and Por. HFoam responses has been proposed for this study (shown in Fig. 4d).

3.2. FE model of human canine based on A μCT

Figs. 5–7 and 8 compare numerical results obtained by this study and the experimental results obtained by Boldt et al. (2012) for 80 N intrusion load and 35 N lateral load, respectively. The load-displacement relationship of the canine as well as the PDL stresses along its height are shown. Furthermore, these figures compare the results obtained by using the proposed material model (porous hyperfoam behaviour for compression, and the porous transversely isotropic material model for traction) and the results obtained using the same formulation for both efforts.

For intrusive loading, the numerical curve which combines both material models shows a great similarity with the results of Por. HFoam material model for low strain rates (shown in Fig. 5). Concave shape of the tooth causes the PDL compression when the tooth is going down. This compression is mostly supported by the hyperfoam material model. When the fibres start to stretch, the tissue stiffness increases, and its behaviour is a combination of the transversely isotropic hyperelastic formulation and of the porous hyperfoam material model

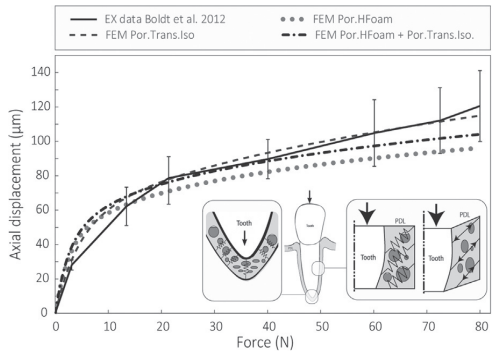

Fig. 5. Comparison between the experimental displacements given by Boldt et al. (2012) and numerical displacements obtained by model simulation under intrusive load.

(show the inferior label of Fig. 5). The middle region of the PDL is the most loaded part (shown in Fig. 6). The maximum principal stress is maximum in this area because the fibres run horizontally. Thus, they start stretching early. Besides, the minimum principal stresses has the maximun value in this region, because the shape of the tooth changes more abruptly. Although the three material models fit between the deviations obtained by Boldt et al. (2012), the Por. Trans. Iso formulation has the most similar behaviour. This fact corroborates that most of the stresses are absorbed by the fluid phase for intrusion load. On the other hand, the high values of stresses at distal and mesial direction are due to the extremely thin thickness at these regions. Furthermore, it is remarkable that both, the maximum and minimum principal stresses, are compressive at the apical region in labial direction where the tooth is wider.

The results of the lateral loading (shown in Fig. 7) support the idea of considering different behaviour in traction and compression. Although the porous transversely isotropic hyperelastic material performs better for intrusive load, the response for lateral load is not so good. It could be possible because the fluid contribution during lateral loads is lower than during intrusion loads. When lateral load is applied, the tooth rotates. Thus, this rotation causes a matrix compression at some areas, and fibres stretch on the opposite areas, causing the combination of porous hyperfoam and transversely isotropic hyperelastic material models, respectively. On the other hand, the porous transversely isotropic material is stiffer than the experimental values obtained by Boldt et al. (2012). Regarding the stresses (shown in Fig. 8), the PDL is compressed at the alveolar-crest region in lingual direction and at the apical region in labial direction. It could be caused due to tooth rotation. Conversely, the maximum principal stresses are located at the opposite region, at the apical region in lingual direction and at the alveolar-crest region in labial direction.

In summary, it is not adequate to define the PDL behaviour only considering the fibrous structure or the porous time response. The model which combines both material models has the best relationship for intrusion and lateral tests. This topic is extensively discussed in “4.2 FE simulation of the specimens” at discussion section.

4. Discussion

4.1. Material parameters characterization

In the first part of this study, the parameters of transversely isotropic material model were obtained by a fitting procedure. The parameters characterization was done using Holzapfel strain energy formulation (Holzapfel, 2000). This constitutive model formulation describes two different contributions, the non-fibrous hyperelastic and the fibrous hyperelastic. However, it is not only the collagen structure

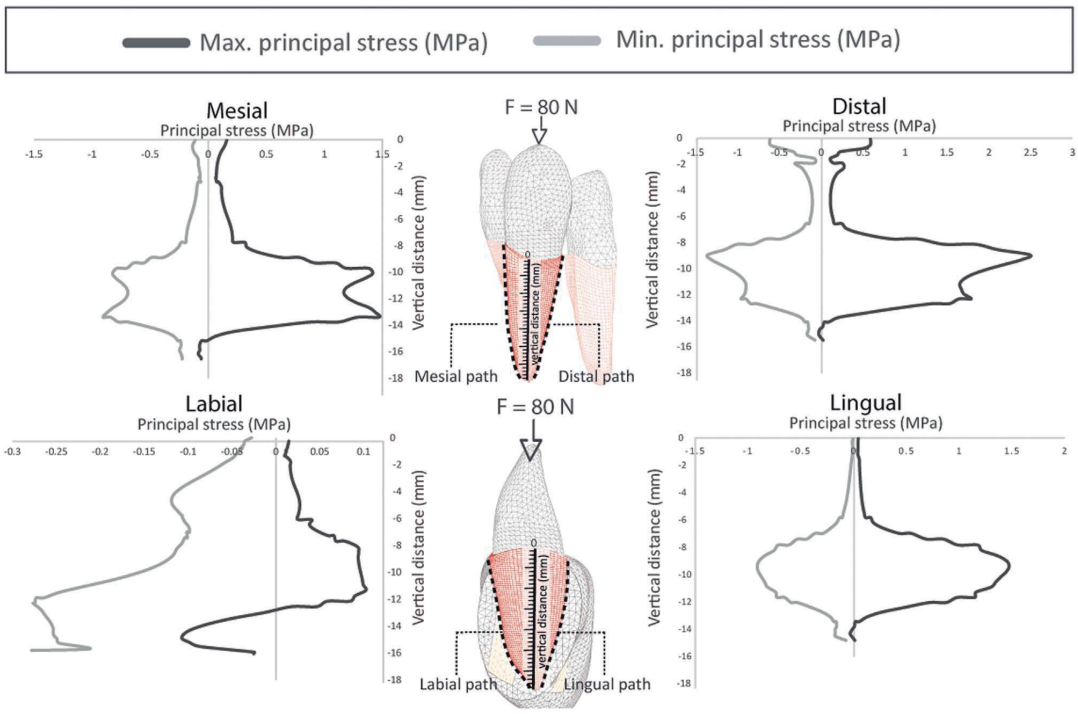

Fig. 6. Maximum and minimum principal stresses at the mesial, distal, labial and lingual sides of the periodontal ligament for 80 N axial loading. The graphs relate stresses to the vertical distance away from the top of the ligament at the paths drawn (Up: mesial-distal; Down: labial-lingual).

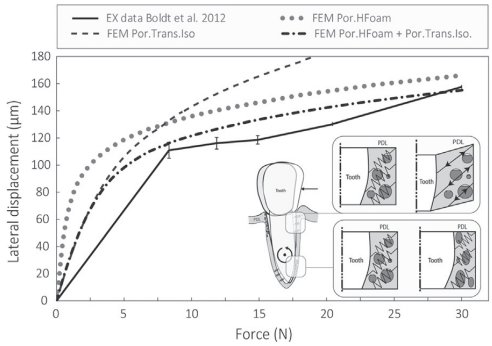

Fig. 7. Comparison between the experimental displacements given by Boldt et al. (2012) and numerical displacements obtained by model simulation under lateral load.

which determines the behaviour of the periodontal ligament but also hydrodynamic effects. Thus, Trans. Iso and Por. Trans. Iso material models were characterized. Trans. Iso material model only considered the collagen network, and Por. Trans. Iso considered both, fibrous and hydrodynamic effects.

The results of the material model parameter characterization showed a high value of the initial elastic tensor, D, that denotes high vascularity. This high vascularity behaviour was suggested by Bergomi et al. (2009) in their experimental test. Regarding C_1 parameter value, it was shown that the PDL is extremely soft at low strain values. It is remarkable the relevant relation between C_1 and D, because high D parameter of the matrix causes an extension of the toe region of the matrix (shown in Fig. 1a). Although these parameters have good correlation with the experimental results given by Natali et al. (2008) for tension, not the same occurs for compression in which the curve for the porous transversely isotropic model shows significant differences (shown Fig. 1b), specially at low strain values. It could be due to the low parameter of Neo-Hooke's hyperelastic constant, C_1. For low strain values, the permeability [Eq. (7)] is high, causing high flow velocities. Thus, the hyperelastic matrix (defined by C_1 parameter) has to resist most of the load. However, a higher C_1 value would mean worse approximation in the first part for the traction curve. Thus, it is not numerically possible to obtain other parameters that adjust the curve both for tension and compression.

On the other hand, the permeability obtained for Por. Trans. Iso material model is slightly different from the parameters given by Bergomi et al. (2011). The permeability value of this study is near to the results obtained by Natali et al. (2002) who established that PDL permeability lies between $1{\cdot}10^{-14}$ and $1{\cdot}10^{-13}$ m^2.

4.2. FE simulation of the specimens

As mentioned in the literature review (Fill et al., 2012), a real time observation of the PDL tissue deformation indicates that collagen network plays an important role in the mechanical response. In compression, the behaviour of the PDL seems to be influenced by interstitial fluid flow. Thus, a biphasic material with solid and fluid phases would have to be considered.

For tensile test, the FE sample fit as well as the analytical curve to the experimental data (shown Figs. 1a and 4a). For compressive test, the result of the characterization and the results of specimens FE model not differs. This fact is due to porous properties were obtained from an iterative process with the same FE model used for compression test.

One question that wanted to be solved was to evaluate the importance of considering different species to characterized the human PDL. Although, few studies have been performed (Drolshagen et al.,

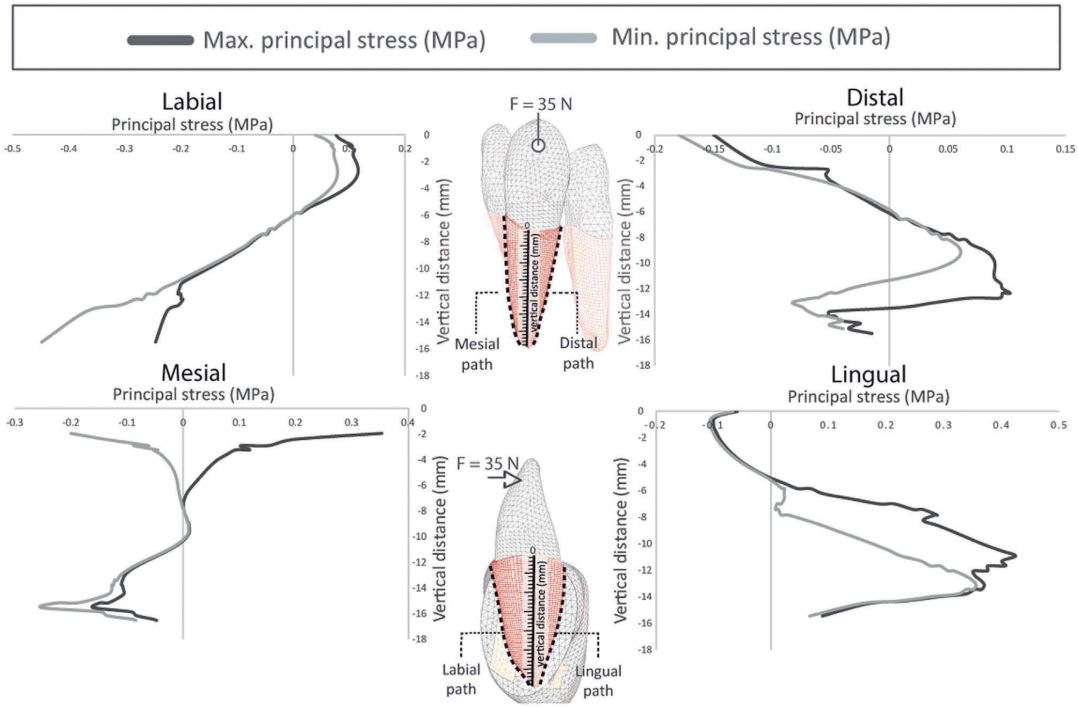

Fig. 8. Maximum and minimum principal stresses at the mesial, distal, labial and lingual sides of the periodontal ligament for 35 N lateral loading. The graphs relate stresses to the vertical distance away from the top of the ligament at the paths drawn (Up: mesial-distal; Down: labial-lingual).

2011; Genna et al., 2008; Wood et al., 2011), the few that have been made show that the biology of porcine PDL does not differ largely from human PDL. The results shown in Fig. 4a indicate a good numerical approximation of the porous transversally isotropic material model with the experimental results proposed by Natali et al. (2008) for porcine specimen under tensile load. The results revealed that the parameters used by Bergomi for describing the PDL behaviour are not adequate to represent the porcine behaviour under tensile load. The material model described by Bergomi et al. (2011) is stiffer than the experimental results obtained by Natali et al. (2008) with porcine samples. It could be possible, because the bitting system of cows are more different from the human ones than of pigs (Bergomi et al., 2010). In the current study, comparing the porous with the no porous material models (shown in Fig. 4b) it can be seen that the porous coupling has not significant influence in the results for traction load. This finding supports the idea of Bergomi et al. (2010) of no dissipation process during tension loading. Another important finding was the relevance of considering the fibrous structure (shown in Fig. 4c). The PDL stiffness shows a high dependence of the fibrous structure. This finding could explain the high variation of the PDL properties that appear in the literature, as it is described by Fill et al. (2012). Furthermore, it is in agreement with McCormack et al. (2014) who investigated the effect of including the fibrous structure in FE models when applying either occlusal or orthodontic loads.

Moreover, some authors suggest there is not so much difference in considering different species for compression load (Natali et al., 2008). The results shown in Fig. 4a, indicate that it is possible to couple the porous contribution into the transversely isotropic material model. However, Por. Trans. Iso material model is not fit good, especially at the initial strain values. As it was aforementioned in results sections, it could be due to the low stiffness of the matrix. As far as it can be seen in Fig. 4b, the curve defined by hyperfoam material model shows a better agreement for compressive test, specially for high strain rates. One unanticipated finding was that the PDL stiffness increased when the fibre direction tends to be perpendicular to the load direction (shown in Fig. 4c). However, the influence of the fibrous term during compressive specimen test was less than 2% of the total stress between both extreme configurations (fibres oriented at 0 and 90 degrees of the compressive load direction). This might be due to the fact that when the tissue is compressed, some elements are in traction and therefore some fibres are stretched. It is remarkable, that some difficulties were found during the convergence process when fibres were perpendicular to the load direction.

This study was designed to the aim of evaluating the importance of using a material that responses in two distinct modes depending of the loading. When PDL is pulled in tension, it acts like a fibre reinforced hyperelastic material (little or no dissipative process can be noticed). Conversely, when it is pushed in compression, clear inelastic phenomena is observed and large dissipation of energy occurs. As Favino et al. (2013) formulated, our findings suggested that PDL has to be defined as a fibrous-porous material. Thus, PDL structure has to be composed by a fibrous network of collagen, and an hyperelastic matrix by interstitial fluid.

4.3. FE model of human canine based on a μCT

To verify the complex behaviour of PDL, a FE model of a portion of a human mandible has been developed. The portion of the mandible includes the PDL of a canine tooth. The mechanical properties of the PDL have been defined by the aforementioned porous-fiborus properties. The results of this study support the hypothesis that simple material models are definitely inadequate for predicting the biomechanical response of the PDL for different loading scenarios.

On the question of whether or not to include the PDL in finite

element (FE) models, this study found that including the ligament is mandatory when the transmission of loads between the tooth and bone is analysed. Moreover, it is difficult to explain the PDL behaviour only using one material model, specially if we want to know the tooth response during short time periods, such as biting or parafuntional habits. In these cases, the most appropriate material should be one which combines the anisotropic behaviour caused by the collagen network and the time-dependence response produced by the interstitial fluid. Furthermore, the loading direction is another key factor to be considered to choose the best material model to reproduce the PDL behaviour. For intrusion loads, the tooth movements can be reproduced using a simplier material model (shown in Fig. 5). Our study, as Nikolaus et al. (2017) study, supports that considering fibres effect is mandatory (shown in Fig. 7). Other simplifications relating to microstructural and property details are of minor importance. The results shown in Fig. 7 suggest that tooth rotation movement produces the fluid drainage in compressed regions. This flow contributes to energy dissipation. On the other hand, the regions under tensile stresses suggest higher stress values due to the stretch of the fibres. It is now possible to state that this model could explain the "stretched fibre hypothesis" suggested by Melsen (2001). This hypothesis does not consider whether the bone is in compression or tension, but it regards whether the bone is in higher or lower stress level. According to the results shown in Fig. 8, the maximum principal stresses should be high on this side due to the stretching of the PDL fibres. The fibres of the PDL only apply force to the surrounding bone where they are in tension, not when they are in compression. Thus, the regions where the fibres are in tension causes more bone formation than the regions where the tissue of the PDL is in compression. These finding could answer the future lines of some recent studies (Nikolaus et al., 2016; Oskui et al., 2016) which proposed new studies considering the biphasic behaviour.

In the case of intrusive load, almost symmetrical stresses were obtained in distal-mesial direction (shown in Fig. 6). In an idealized case, the stresses should be the same in all directions. However, in this case, the stresses are not similar in lingual and labial sides. The middle regions of PDL at mesial, distal and lingual sides underwent positive maximum principal stresses and negative minimum principal stresses, respectively. Thus, these regions are mainly subjected to shear stress. However, the labial side of the PDL is mostly under compressive effort, with a mean value of − 0.15 MPa. This value is less than in the other sides, with a mean value of − 1.25 MPa. This phenomenon can be caused because the PDL is mainly compressed in this region, and the fluid flow dissipates more energy than in the regions which are under shear stresses. On the other hand, under lateral load (shown in Fig. 8) the signs of the first and third principal stresses are the same in most of the points along PDL height. This fact suggests that few regions are subjected to shear efforts. The null combination of traction and compressive efforts in the same area could remark the differences between material models.

Another fact that has been confirmed is the need of using microtomography scans as a tool for the PDL study. As it is shown in Figs. 6 and 8, the PDL morphology determines the maximum and minimum principal stresses along the tooth. The irregular profile of principal stresses along PDL height in Figs. 6 and 8 could be explained by the combination of two effects, the fibres orientation and the differences of PDL geometry.

According to the orientation of the fibres bundles, the horizontal family of fibres (HO fibres family in Fig. 3b) stretched more under intrusive load (shown in Fig. 6). Thus, these regions were subjected to higher stresses. On the other hand, the minimum principal stresses appeared in the apical region where the fibres run in the loading direction. Therefore, the hyperelastic matrix underwent low stresses because its low stiffness. Similar behaviour was shown in Fig. 8 for lateral loading. The tooth rotation centre (RC) can be defined at 7 mm depth of the upper border of the ligament. Thus, the region which is upper than RC in labial direction and the region which is lower than RC in lingual direction were only under traction efforts. It is remarkable that the maximum principal stresses appeared in lingual direction. This fact could be produced since fibres run horizontally in this region. Contrary, the stresses were lower at labial direction because in this region, the fibres were oriented obliquely.

On the other hand, in Fig. 6 it can be seen how the geometry affects the stress distribution. It is remarkable that the maximum and minimum stresses are compressive at the apical region in labial direction. This can be produced because the differences of the cross-section of the tooth compress the PDL with the alveolar bone face, when the tooth is going down. The morphological differences between variable and uniform PDL geometries lead to markedly different contact areas between tooth and bone. However, the inclusion of μCT PDL model requires a dense FE mesh because its irregular geometric morphology. This results in the need of large FE models and time-consuming analysis. For that purpose, a reduced integration scheme was used because full integration has long time requirements (shown in Table 2). Furthermore, the use of this technique found to control efficiently the hourglass modes without affecting the precision of the numerical results. In all cases, the stability of the solution and the convergence process were precise.

4.4. Study limitations

The findings in this paper are subjected to at least three limitations. The most important limitation lies in the fact that different animal species were considered for the material parameters characterization. And although the porcine bite system has mechanical similarities with the human bite system, it is better to consider human experimental data. Also, the use of porcine test samples for the characterization of compressive behaviour, should be better than the use of bovine samples. Another major source of uncertainty is in the experimental datum used to approximate the Holzapfel material model, because the direction of the fibres of the specimen could not be verified in the experimental tests used. Another limitation is that the model does not include the transseptal, alveolo-gingivial, dentino-gingibial, circumferential and inter-radicular fibres, which interact with the adjacent teeth. And although for an analysis of one tooth these fibres are not relevant, they should be considered for PDL analysis if the interaction of more teeth is considered. Finally, this study only considers the geometric morphometric of a canine tooth from a particular patient, and there are several differences between the teeth of patients and the way they bite. The stress distribution cannot be extrapolated to all patients but it can represent the PDL stresses appropriately in adult patients with no periodontal disease. Further research could be oriented to investigate the effect that the periodontal ligament has on patients with parafunctional habits, as bruxism.

Despite the limitations of this model, this research will serve as a base for future studies and will help to understand the role of the PDL. An implication of these findings is that both, porous-fibrous structure and the real geometry, should be taken into account when the tooth movement is being analysed. These results have thrown many questions that need further research, as the reabsorption of bone, or the periodontal ligament damage with occlusal traumatic loads. Future researchs could approach these issues.

5. Conclusion

In this study, an accurate 3D finite element model of a human canine PDL obtained by micro-CT was used to determine an appropriate material model that could describe the PDL behaviour. For a correct PDL behaviour characterization, a methodology based on the correlation between numerical results and literature experimental data was performed. Within the limitations of this study, the following conclusions were drawn:

1. The experimental data test is an important uncertainly factor for the material parameters characterization of the PDL. Bovine and porcine experimental data for tensile loading are extremely different, and this could be an important source of error.
2. The collagen network has a key effect on the PDL response when it is in traction. Not considering the fibrous contribution causes significant differences in the PDL response. Also, the high permeability of the tissue has to be considered, especially under compressive loading when most of the stresses are supported by the fluid phase.
3. A complex material model (with porous transversely isotropic hyperelastic material model for traction and porous hyperfoam material model for compression) should be used for accurate characterization of PDL behaviour.
4. A simpler material model can be used if a pure loading direction is applied. For instance, porous transversely isotropic material model could be used if only an intrusion load is simulated.
5. Large 3D models based in μ-CT scan should be used to obtain accurate results of the PDL response. Considering uniform thickness is definitely not appropriate if the aim is to study the PDL behaviour.

Acknowledgements

This work was supported by the Spanish Ministry of Economy and Competitiveness through project DPI 2016–79302-R.

References

Afanador, E., Yokozeki, M., Oba, Y., Kitase, Y., Takahashi, T., Kudo, A., Moriyama, K., 2005. Messenger RNA expression of periostin and Twist transiently decrease by occlusal hypofunction in mouse periodontal ligament. Arch. Oral Biol. 50, 1023–1031. http://dx.doi.org/10.1016/j.archoralbio.2005.04.002.

Andersen, K.L., Pedersen, E.H., Melsen, B., 1991. Material parameters and stress profiles within the periodontal ligament. Am. J. Orthod. Dentofac. Orthop. 99, 427–440. http://dx.doi.org/10.1016/S0889-5406(05)81576-8.

Argoubi, M., Shirazi-Adl, A., 1996. Poroelastic creep response analysis of a lumbar motion segment in compression. J. Biomech. 29, 1331–1339. http://dx.doi.org/10.1016/0021-9290(96)00035-8.

Atkinson, H.F., Ralph, W.J., 1977. In vitro strength of the human periodontal ligament. J. Dent. Res. 56, 48–52. http://dx.doi.org/10.1177/00220345770560011001.

Atmaram, G.H., Mohammed, H., 1981. Estimation of physiologic stresses with a natural tooth considering fibrous PDL structure. J. Dent. Res. 60, 873–877. http://dx.doi.org/10.1177/00220345810600050301.

Bergomi, M., Wiskott, H.W.A., Botsis, J., Mellal, A., Belser, U.C., 2009. Load response of periodontal ligament: assessment of fluid flow, compressibility, and effect of pore pressure. J. Biomech. Eng. 132, 14504. http://dx.doi.org/10.1115/1.4000154.

Bergomi, M., Cugnoni, J., Botsis, J., Belser, U.C., Anselm Wiskott, H.W., 2010. The role of the fluid phase in the viscous response of bovine periodontal ligament. J. Biomech. 43, 1146–1152. http://dx.doi.org/10.1016/j.jbiomech.2009.12.020.

Bergomi, M., Cugnoni, J., Galli, M., Botsis, J., Belser, U.C., Wiskott, H.W.A., 2011. Hydromechanical coupling in the periodontal ligament: a porohyperelastic finite element model. J. Biomech. 44, 34–38. http://dx.doi.org/10.1016/j.jbiomech.2010.08.019.

Berkovitz, B.K., 1990. The structure of the periodontal ligament: an update. Eur. J. Orthod. 12, 51–76.

Blaushild, N., Michaeli, Y., Steigman, S., 1992. Histomorphometric study of the periodontal vasculature of the rat incisor. J. Dent. Res 71, 1908–1912. http://dx.doi.org/10.1177/00220345920710121001.

Boldt, J., Knapp, W., Proff, P., Rottner, K., Richter, E.J., 2012. Measurement of tooth and implant mobility under physiological loading conditions. Ann. Anat. 194, 185–189. http://dx.doi.org/10.1016/j.aanat.2011.09.007.

C. Dorow, N. Krstin, F.G.S., 2002. Experiments to determine the material properties of the periodontal ligament. J. Orofac. Orthop. 63 (2002), 94–104.

Cattaneo, P.M., Dalstra, M., Melsen, B., 2005. The finite element method: a tool to study orthodontic tooth movement. J. Dent. Res. 84, 428–433. http://dx.doi.org/10.1177/154405910508400506.

Chen, X.M., Zhai, Y.F., 1994. A biomechanical study of the human periodontal ligament. Shanghai Kou Qiang Yi Xue 3, 30–33.

Chiba, M., Komatsu, K., 1993. Mechanical responses of the periodontal ligament in the transverse section of the rat mandibular incisor at various velocities of loading in vitro. J. Biomech. 26, 561–570. http://dx.doi.org/10.1016/0021-9290(93)90017-9.

Cobo, J., Sicilia, A., Argüelles, J., Suárez, D., Vijande, M., 1993. Initial stress induced in periodontal tissue with diverse degrees of bone loss by an orthodontic force: tridimensional analysis by means of the finite element method. Am. J. Orthod. Dentofac. Orthop. 104, 448–454. http://dx.doi.org/10.1016/0889-5406(93)70071-U.

Coelho, C.S., de, M., Biffi, J.C.G., Silva, G.R., da, Abrahão, A., Campos, R.E., Soares, C.J., 2009. Finite element analysis of weakened roots restored with composite resin and posts. Dent. Mater. J. 28, 671–678. http://dx.doi.org/10.4012/dmj.28.671.

Daly, C.H., Nicholls, J.I., Kydd, W.L., Nansen, P.D., 1974. The response of the human periodontal ligament to torsional loading—I. Experimental methods. J. Biomech. 7, 517–522. http://dx.doi.org/10.1016/0021-9290(74)90086-4.

Davy, D.T., Dilley, G.L., Krejci, R.F., 1981. Determination of stress patterns in root-filled teeth incorporating various dowel designs. J. Dent. Res. 60, 1301–1310. http://dx.doi.org/10.1177/00220345810600070301.

Drolshagen, M., Keilig, L., Hasan, I., Reimann, S., Deschner, J., Brinkmann, K.T., Krause, R., Favino, M., Bourauel, C., 2011. Development of a novel intraoral measurement device to determine the biomechanical characteristics of the human periodontal ligament. J. Biomech. 44, 2136–2143. http://dx.doi.org/10.1016/j.jbiomech.2011.05.025.

Farah, J.W., Craig, R.G., Sikarskie, D.L., 1973. Photoelastic and finite element stress analysis of a restored axisymmetric first molar. J. Biomech. 6, 511–520. http://dx.doi.org/10.1016/0021-9290(73)90009-2.

Farah, J.W., Craig, R.G., Meroueh, K.A., 1988. Finite element analysis of a mandibular model. J. Oral Rehabil. 15, 615–624. http://dx.doi.org/10.1111/j.1365-2842.1988.tb00199.x.

Favino, M., Gross, C., Drolshagen, M., Keilig, L., Deschner, J., Bourauel, C., Krause, R., 2013. Validation of a heterogeneous elastic-biphasic model for the numerical simulation of the PDL. Comput. Methods Biomech. Biomed. Eng. 16, 544–553. http://dx.doi.org/10.1080/10255842.2011.628660.

Ferrier, J.M., Dillon, E., 1983. The water binding capacity of the periodontal ligament and its role in mechanical function. J. Dent. Res. 5, 469–473. http://dx.doi.org/10.1111/j.1600-0765.1983.tb00384.x.

Fill, T.S., Carey, J.P., Toogood, R.W., Major, P.W., 2011. Experimentally determined mechanical properties of, and models for, the periodontal ligament: critical review of current literature (312980). J. Dent. Biomech. 2, 312980. http://dx.doi.org/10.4061/2011/312980.

Fill, T.S., Toogood, R.W., Major, P.W., Carey, J.P., 2012. Analytically determined mechanical properties of, and models for the periodontal ligament: critical review of literature. J. Biomech. 45, 9–16. http://dx.doi.org/10.1016/j.jbiomech.2011.09.020.

Genna, F., Annovazzi, L., Bonesi, C., Fogazzi, P., Paganelli, C., 2008. On the experimental determination of some mechanical properties of porcine periodontal ligament. Meccanica 43, 55–73. http://dx.doi.org/10.1007/s11012-007-9094-2.

Gonzales, C., Hotokezaka, H., Arai, Y., Ninomiya, T., Tominaga, J., Jang, I., Hotokezaka, Y., Tanaka, M., Yoshida, N., 2009. An in vivo 3D micro-CT evaluation of tooth movement after the application of different force magnitudes in rat molar. Angle Orthod. 79, 703–714. http://dx.doi.org/10.2319/071308-366.1.

Gröning, F., Fagan, M.J., O'Higgins, P., 2011. The effects of the periodontal ligament on mandibular stiffness: a study combining finite element analysis and geometric morphometrics. J. Biomech. 44, 1304–1312. http://dx.doi.org/10.1016/j.jbiomech.2011.01.008.

Hattori, Y., Satoh, C., Kunieda, T., Endoh, R., Hisamatsu, H., Watanabe, M., 2009. Bite forces and their resultants during forceful intercuspal clenching in humans. J. Biomech. 42, 1533–1538. http://dx.doi.org/10.1016/j.jbiomech.2009.03.040.

Hohmann, A., Kober, C., Young, P., Dorow, C., Geiger, M., Boryor, A., Sander, F.M., Sander, C., Sander, F.G., 2011. Influence of different modeling strategies for the periodontal ligament on finite element simulation results. Am. J. Orthod. Dentofac. Orthop. 139, 775–783. http://dx.doi.org/10.1016/j.ajodo.2009.11.014.

Holzapfel, G., 2000. Nonlinear Solid Mechanics. Wiley, New York.

Huang, H., Tang, W., Yan, B., Wu, B., 2012. Mechanical responses of periodontal ligament under a realistic orthodontic loading. Procedia Eng. 31, 828–833. http://dx.doi.org/10.1016/j.proeng.2012.01.1108.

Huang, H., Tang, W., Tan, Q., Yan, B., 2017. Development and parameter identification of a visco-hyperelastic model for the periodontal ligament. J. Mech. Behav. Biomed. Mater. 68, 210–215. http://dx.doi.org/10.1016/j.jmbbm.2017.01.035.

Jones, M.L., Hickman, J., Middleton, J., Knox, J., Volp, C., 2001. A validated finite element method study of orthodontic tooth movement in the human subject. J. Orthod. 28, 29–38. http://dx.doi.org/10.1093/ortho/28.1.29.

Komatsu, K., Tsurumi, P., Medicine, D., Accepted, R.Y., 1996. Analysis of stress-strain curves and histological observations on the periodontal ligament of impeded and unimpeded rat incisors at low velocities of loading. 192–202. Jpn. J. Oral Biol. http://dx.doi.org/10.2330/joralbiosci1965.38.192.

Komatsu, K., Yamazaki, Y., Yamaguchi, S., Chiba, M., 1998. Comparison of biomechanical properties of the incisor periodontal ligament among different species. Anat. Rec. 250, 408–417. http://dx.doi.org/10.1002/(SICI)1097-0185(199804)250:4<408::AID-AR3>3.0.CO;2-T.

Komatsu, K., Kanazashi, M., Shimada, A., Shibata, T., Viidik, A., Chiba, M., 2004. Effects of age on the stress-strain and stress-relaxation properties of the rat molar periodontal ligament. Arch. Oral Biol. 49, 817–824. http://dx.doi.org/10.1016/j.archoralbio.2004.04.002.

Komatsu, K., Sanctuary, C., Shibata, T., Shimada, A., Botsis, J., 2007. Stress–relaxation and microscopic dynamics of rabbit periodontal ligament. J. Biomech. 40, 634–644. http://dx.doi.org/10.1016/j.jbiomech.2006.01.026.

Korioth, T.W.P., Hannam, A.G., 1994. Deformation of the human mandible during simulated tooth clenching. J. Dent. Res. 73, 56–66. http://dx.doi.org/10.1177/00220345940730010801.

Lacroix, D., Prendergast, P.J., 2002. A mechano-regulation model for tissue differentiation during fracture healing: analysis of gap size and loading. J. Biomech. 35, 1163–1171. http://dx.doi.org/10.1016/S0021-9290(02)00086-6.

Lindhe, J., Karring, T., Niklaus, P.L., 2003. Clinical Periodontology and Implant Dentistry, 4th ed. Blackwell, Oxford.

Mathworks Inc, 2000. 2000a. MATLAB Mathworks Inc, Natick, MA, USA.

McCormack, S.W., Witzel, U., Watson, P.J., Fagan, M.J., Gröning, F., 2014. The biomechanical function of periodontal ligament fibres in orthodontic tooth movement. PLoS One 9, e102387. http://dx.doi.org/10.1371/journal.pone.0102387.

Melsen, B., 2001. Tissue reaction to orthodontic tooth movement-a new paradigm. Eur. J.

Orthod. 23, 671–681 (doi: 11890063).
Meyer, B.N., Chen, J., Katona, T.R., 2010. Does the center of resistance depend on the direction of tooth movement. Am. J. Orthod. Dentofac. Orthop. 137, 354–361. http://dx.doi.org/10.1016/j.ajodo.2008.03.029.
Middleton, J., Jones, M., Wilson, A., 1996. The role of the periodontal ligament in bone modeling: the initial development of a time-dependent finite element model. Am. J. Orthod. Dentofac. Orthop. 109, 155–162. http://dx.doi.org/10.1016/S0889-5406(96)70176-2.
Natali, A.N., Pavan, P.G., Carniel, E.L., Dorow, C., 2003. A transversally isotropic elasto-damage constitutive model for the periodontal ligament. Comput. Methods Biomech. Biomed. Eng. 6, 329–336. http://dx.doi.org/10.1080/1025584031000163984O.
Natali, A.N., Pavan, P.G., Scarpa, C., 2004. Numerical analysis of tooth mobility: formulation of a non-linear constitutive law for the periodontal ligament. Dent. Mater. 20, 623–629. http://dx.doi.org/10.1016/j.dental.2003.08.003.
Natali, A.N, Pavan, P.G., Schrefler, B.A., Secchi, S., 2002. A multi-phase media formulation for biomechanical analysis of periodontal ligament. Meccanica 37, 407–418. http://dx.doi.org/10.1023/A:1020895906292.
Natali, A.N., Carniel, E.L., Pavan, P.G., Sander, F.G., Dorow, C., Geiger, M., 2008. A visco-hyperelastic-damage constitutive model for the analysis of the biomechanical response of the periodontal ligament. J. Biomech. Eng. 130, 31004. http://dx.doi.org/10.1115/1.2900415.
Natali, A.N., Pavan, P.G., Venturato, C., Komatsu, K., 2011. Constitutive modeling of the non-linear visco-elasticity of the periodontal ligament. Comput. Methods Prog. Biomed. 104, 193–198. http://dx.doi.org/10.1016/j.cmpb.2011.03.014.
Nikolaus, A., Fleck, C., Lindtner, T., Currey, J., Zaslansky, P., 2016. Importance of the variable periodontal ligament geometry for whole tooth mechanical function: a validated numerical study. J. Mech. Behav. Biomed. Mater. 67, 61–73. http://dx.doi.org/10.1016/j.jmbbm.2016.11.020.
Nishihira, M., Yamamoto, K., Sato, Y., Ishikawa, H., Natali, A., 2003. Mechanics of periodontal ligament. Dent. Biomech. 20–32.
Nyashin, M.Y., Osipov, A.P., Bolotova, M.P., Nyashin, Y.I., Simanovskaya, E.Y., 1999. Periodontal ligament may be viewed as a porous material filled by free fluid: experimental proof. Russ. J. Biomech. 3, 89–95.
Oskui, I.Z., Hashemi, A., Jafarzadeh, H., 2016. Biomechanical behavior of bovine periodontal ligament: experimental tests and constitutive model. J. Mech. Behav. Biomed. Mater. 62, 599–606. http://dx.doi.org/10.1016/j.jmbbm.2016.05.036.
Papadopoulou, K., Keilig, L., Eliades, T., Krause, R., Jäger, A., B, C., 2011. The time-dependent biomechanical behavior of the periodontal ligament—an in vitro experimental study in minipig mandibular two-rooted premolars. Eur. J. Orthod. http://dx.doi.org/10.1093/ejo/cjr134.
Pietrzak, G., Curnier, A., Botsis, J., Scherrer, S., Wiskott, A., Belser, U., 2002. A nonlinear elastic model of the periodontal ligament and its numerical calibration for the study of tooth mobility. Comput. Methods Biomech. Biomed. Eng. 5, 91–100. http://dx.doi.org/10.1080/10255840290032117.
Pihlstrom, B.L., Michalowicz, B.S., Johnson, N.W., 2005. Periodontal diseases. Lancet (Lond., Engl.) 366, 1809–1820. http://dx.doi.org/10.1016/S0140-6736(05)67728-8.
Pini, M., Zysset, P., Botsis, J., Contro, R., 2004. Tensile and compressive behaviour of the bovine periodontal ligament. J. Biomech. 37, 111–119. http://dx.doi.org/10.1016/S0021-9290(03)00234-3.
Poppe, M., Bourauel, C., Jäger, A., 2002. Determination of the elasticity parameters of the human periodontal ligament and the location of the center of resistance of single-rooted teeth. J. Orofac. Orthop. der Kiefer. 63, 358–370. http://dx.doi.org/10.1007/s00056-002-0067-8.
Preshaw, P.M., Seymour, R.A., Heasman, P.A., 2004. Current concepts in periodontal pathogenesis. Dent. Update 31 (570–572), 574–578.
Provatidis, C.G., 2000. A comparative FEM-study of tooth mobility using isotropic and anisotropic models of the periodontal ligament. Med. Eng. Phys. 22, 359–370. http://dx.doi.org/10.1016/S1350-4533(00)00055-2.
Qian, H., Chen, J., Katona, T.R., 2001. The influence of PDL principal fibers in a 3-dimensional analysis of orthodontic tooth movement. Am. J. Orthod. Dentofac. Orthop. 120, 272–279. http://dx.doi.org/10.1067/mod.2001.116085.
Qian, L., Todo, M., Morita, Y., Matsushita, Y., Koyano, K., 2009. Deformation analysis of the periodontium considering the viscoelasticity of the periodontal ligament. Dent. Mater. 25, 1285–1292. http://dx.doi.org/10.1016/j.dental.2009.03.014.
Rees, J.S., 2001. An investigation into the importance of the periodontal ligament and alveolar bone as supporting structures in finite element studies. J. Oral Rehabil. 28, 425–432.
Rees, J.S., Jacobsen, P.H., 1997. Elastic modulus of the periodontal ligament. Biomaterials 18, 995–999. http://dx.doi.org/10.1016/S0142-9612(97)00021-5.
Reinhardt, R.A., Pao, Y.C., Krejci, R.F., 1984. Periodontal ligament stresses in the initiation of occlusal traumatism. J. Periodontal Res. 19, 238–246. http://dx.doi.org/10.1111/j.1600-0765.1984.tb00815.x.
Romeed, S.A., Fok, S.L., Wilson, N.H.F., 2006. A comparison of 2D and 3D finite element analysis of a restored tooth. J. Oral Rehabil. 33, 209–215. http://dx.doi.org/10.1111/j.1365-2842.2005.01552.x.
S.D. Cook, A.M. Weinstein, J.J.K., 1982. Parameters affecting the stress-distribution around LTI carbon and aluminum-oxide dental implants. J. Biomed. Mater. Res. 16 (1982), 875–885 (16, 875–885).
Sanctuary, C., 2003. Experimental Investigation of the Mechanical Behaviour and Structure of the Bovine Periodontal Ligament (Ph.D. Thesis). École Politecniche Fédérale de Lausanne, Lausanne.
Schünke, M., Schulte, E., Schumacher, U., 2010. PROMETHEUS.
Selna, L.G., Shillingburg, H.T., Kerr, P.A., 1975. Finite element analysis of dental structures? Axisymmetric and plane stress idealizations. J. Biomed. Mater. Res. 9, 237–252. http://dx.doi.org/10.1002/jbm.820090212.
Shimada, A., Shibata, T., Komatsu, K., Chiba, M., 2003. The effects of intrusive loading on axial movements of impeded and unimpeded rat incisors: estimation of eruptive force. Arch. Oral Biol. 48, 345–351. http://dx.doi.org/10.1016/S0003-9969(03)00010-4.
Storakers, B., 1986. On material representation and constitutive branching in finite compressible elasticity. J. Mech. Phys. Solids 34, 125–145. http://dx.doi.org/10.1016/0022-5096(86)90033-5.
Takahashi, N., Kitagami, T., Komori, T., 1980. Behaviour of teeth under various loading conditions with finite element method. J. Oral Rehabil. 7, 453–461 (doi: 0305-182X/80/1100-0453).
Tanne, K., Sakuda, M., Burstone, C., 1987. Three-dimensional finite element analysis for stress in the periodontal tissue by orthodontic forces. Am. J. Orthod. Dentofac. Orthop. 92, 499–505.
Tanne, K., Koenig, H.A., Burstone, C.J., 1988. Moment to force ratios and the center of rotation. Am. J. Orthod. Dentofac. Orthop. 94, 426–431. http://dx.doi.org/10.1016/0889-5406(88)90133-3.
Tanne, K., Yoshida, S., Kawata, T., Sasaki, A., Knox, J., Jones, M.L., 1998. An evaluation of the biomechanical response of the tooth and periodontium to orthodontic forces in adolescent and adult subjects. Br. J. Orthod. 25, 109–115. http://dx.doi.org/10.1093/ortho/25.2.109.
Thresher, R.W., Saito, G.E., 1973. The stress analysis of human teeth. J. Biomech. 6, 443–449. http://dx.doi.org/10.1016/0021-9290(73)90003-1.
Toms, S.R., Eberhardt, A.W., 2003. A nonlinear finite element analysis of the periodontal ligament under orthodontic tooth loading. Am. J. Orthod. Dentofac. Orthop. 123, 657–665. http://dx.doi.org/10.1016/S0889540603001641.
Tuna, M., Sunbuloglu, E., Bozdag, E., 2014. Finite element simulation of the behavior of the periodontal ligament: a validated nonlinear contact model. J. Biomech. 47, 2883–2890. http://dx.doi.org/10.1016/j.jbiomech.2014.07.023.
van Rossen, I.P., Braak, L.H., de Putter, C., de Groot, K., 1990. Stress-absorbing elements in dental implants. J. Prosthet. Dent. 64, 198–205. http://dx.doi.org/10.1016/0022-3913(90)90179-G.
Wang, C.-Y., Su, M.-Z., Chang, H.-H., Chiang, Y.-C., Tao, S.-H., Cheng, J.-H., Fuh, L.-J., Lin, C.-P., 2012. Tension-compression viscoelastic behaviors of the periodontal ligament. J. Formos. Med. Assoc. 111, 471–481. http://dx.doi.org/10.1016/j.jfma.2011.06.009.
Wei, Z., Yu, X., Xu, X., Chen, X., 2014. Experiment and hydro-mechanical coupling simulation study on the human periodontal ligament. Comput. Methods Prog. Biomed. 113, 749–756. http://dx.doi.org/10.1016/j.cmpb.2013.12.011.
Weinstein, A.M., Klawitter, J.J., Cook, S.D., 1980. Implant-bone interface characteristics of bioglass dental implants. J. Biomed. Mater. Res. 14, 23–29. http://dx.doi.org/10.1002/jbm.820140104.
Widera, G.E.O., Tesk, J.A., Privitzer, E., 1976. Interaction effects among cortical bone, cancellous bone, and periodontal membrane of natural teeth and implants. J. Biomed. Mater. Res. 10, 613–623. http://dx.doi.org/10.1002/jbm.820100418.
Williams, K.R., Edmundson, J.T., 1984. Orthodontic tooth movement analysed by the finite element method. Biomaterials 5, 347–351. http://dx.doi.org/10.1016/0142-9612(84)90033-4.
Wood, S.A., Strait, D.S., Dumont, E.R., Ross, C.F., Grosse, I.R., 2011. The effects of modeling simplifications on craniofacial finite element models: the alveoli (tooth sockets) and periodontal ligaments. J. Biomech. 44, 1831–1838. http://dx.doi.org/10.1016/j.jbiomech.2011.03.022.
Xu, B., Wang, Y., Li, Q., 2015. Modeling of damage driven fracture failure of fiber post-restored teeth. J. Mech. Behav. Biomed. Mater. 49, 277–289. http://dx.doi.org/10.1016/j.jmbbm.2015.05.006.
Yettram, A.L., Wright, K.W.J., Houston, W.J.B., 1977. Centre of rotation of a maxillary central incisor under orthodontic loading. Br. J. Orthod. 4, 23–27. http://dx.doi.org/10.1179/bjo.4.1.23.
Yoshida, N., Koga, Y., Peng, C.-L., Tanaka, E., Kobayashi, K., 2001. In vivo measurement of the elastic modulus of the human periodontal ligament. Med. Eng. Phys. 23, 567–572. http://dx.doi.org/10.1016/S1350-4533(01)00073-X.
Zhang, Z., Zheng, K., Li, E., Li, W., Li, Q., Swain, M.V., 2016. Mechanical benefits of conservative restoration for dental fissure caries. J. Mech. Behav. Biomed. Mater. 53, 11–20. http://dx.doi.org/10.1016/j.jmbbm.2015.08.010.
Zheng, J., Zhou, Z.R., 2006. Effect of age on the friction and wear behaviors of human teeth. Tribol. Int. 39, 266–273. http://dx.doi.org/10.1016/j.triboint.2004.09.004.

Manuscript 3: A porous fibrous hyperelastic damage model for human periodontal ligament: Application of a micro-computerized tomography finite element model.

Javier Ortún-Terrazas, José Cegoñino, Urbano Santana-Penín, Urbano Santana-Mora, Amaya Pérez del Palomar

Abstract

The periodontal ligament (PDL) is a soft biological tissue that connects the tooth with the trabecular bone of the mandible. It plays a key role in load transmission and is primarily responsible for bone resorption and most common periodontal diseases. Although several numerical studies have analysed the biomechanical response of the PDL, most did not consider its porous fibrous structure, and only a few analysed damage to the PDL. This study presents an innovative numerical formulation of a porous fibrous hyperelastic damage material model for the PDL. The model considers two separate softening phenomena: fibre alignment during loading and fibre rupture. The parameters for the material model characterization were fitted using experimental data from the literature. Furthermore, the experimental tests used for characterization were computationally modelled to verify the material parameters. A finite element model of a portion of a human mandible, obtained by micro-computerized tomography, was developed, and the proposed constitutive model was implemented for the PDL. Our results confirm that damage to the PDL may occur mainly due to overpressure of the interstitial fluid, while large forces must be applied to damage the PDL fibrous network. Moreover, this study clarifies some aspects of the relationship between PDL damage and the bone remodelling process.

Graphical abstract

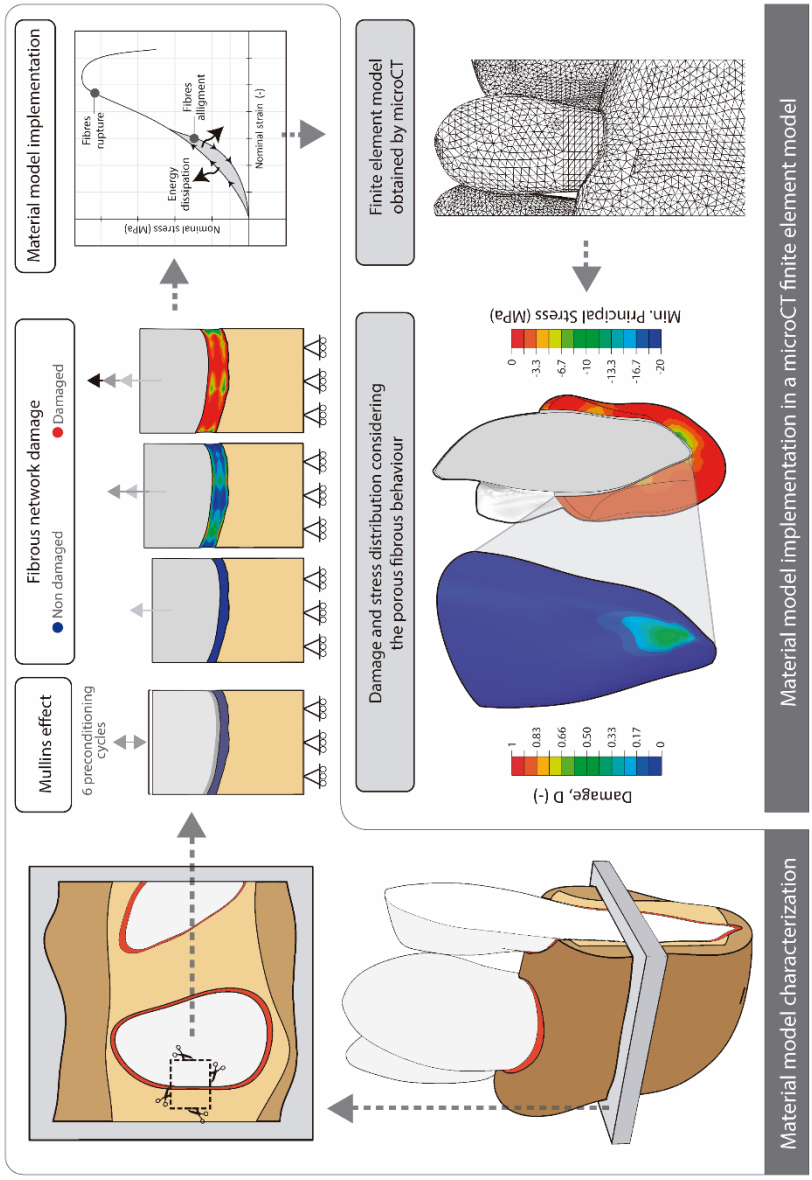

Received: 28 July 2018 | Revised: 21 November 2018 | Accepted: 16 December 2018

DOI: 10.1002/cnm.3176

RESEARCH ARTICLE - APPLICATION

WILEY

A porous fibrous hyperelastic damage model for human periodontal ligament: Application of a microcomputerized tomography finite element model

Javier Ortún-Terrazas[1] | José Cegoñino[1] | Urbano Santana-Penín[2] | Urbano Santana-Mora[2] | Amaya Pérez del Palomar[1]

[1]Group of Biomaterials, Aragon Institute of Engineering Research (I3A), Department of Mechanical Engineering, University of Zaragoza, Zaragoza, Spain

[2]School of Dentistry, Faculty of Medicine and Odontology, Santiago de Compostela University, Santiago de Compostela, Spain

Correspondence
Javier Ortún-Terrazas, Department of Mechanical Engineering, University of Zaragoza, María de Luna No. 3, Betancourt Building, 50018 Zaragoza, Spain.
Email: javierortun@unizar.es

Funding information
Spanish Ministry of Economy and Competitiveness, Grant/Award Number: DPI 2016-79302-R

Abstract

The periodontal ligament (PDL) is a soft biological tissue that connects the tooth with the trabecular bone of the mandible. It plays a key role in load transmission and is primarily responsible for bone resorption and most common periodontal diseases. Although several numerical studies have analysed the biomechanical response of the PDL, most did not consider its porous fibrous structure, and only a few analysed damage to the PDL. This study presents an innovative numerical formulation of a porous fibrous hyperelastic damage material model for the PDL. The model considers two separate softening phenomena: fibre alignment during loading and fibre rupture. The parameters for the material model characterization were fitted using experimental data from the literature. Furthermore, the experimental tests used for characterization were computationally modelled to verify the material parameters. A finite element model of a portion of a human mandible, obtained by microcomputerized tomography, was developed, and the proposed constitutive model was implemented for the PDL. Our results confirm that damage to the PDL may occur mainly because of overpressure of the interstitial fluid, while large forces must be applied to damage the PDL fibrous network. Moreover, this study clarifies some aspects of the relationship between PDL damage and the bone remodelling process.

KEYWORDS

damage model, fibrous network, microcomputed tomography, Mullins effect, periodontal ligament, porous elasticity

1 | INTRODUCTION

The periodontal ligament (PDL) is a soft connective tissue that absorbs and distributes chewing loads. A healthy PDL contributes to homogeneous transmission of loads to the trabecular bone of the mandible. However, several mechanical factors may affect periodontal health and cause destruction of the connective matrix, loss of fibrous attachment, or bone remodelling.[1]

Anatomically, the human periodontium is composed of the gum (G), the trabecular bone (TB), the cortical bone (CB), the tooth, and the PDL. The tooth is mainly formed of enamel (E), dentin (D), pulp (P), and cementum root (CR) (Figure 1A). The gum is the main responsible for periodontal diseases produced by bacterial action, although the gum is less relevant from a biomechanical point of view.[2] In contrast, dentin, bone, and the PDL are the main agents for load transmission, and some of the most common periodontal diseases are related to an abnormal mechanical role of these elements.[3]

Biomechanically, the PDL is a soft biological tissue that can be considered a porous vasculature solid with a highly structured collagen network.[4-6] Approximately 50% to 75% of the PDL volume is formed by collagen fibres,[7] primarily type I,[7] III,[8] and XII fibres (Figure 1B).[9] The fibres are primarily responsible for the differences observed in PDL reactions under tensile force. On the other hand, the high vascular density of the PDL confers the tissue a viscoelastic behaviour, which has been extensively studied in the literature.[10-12] Thus, the tissue behaves as an incompressible material under fast strains and as a highly compressible material under slow strains due to this viscoelastic phenomenon.[5,13-15] Neglecting the fibrous and time-dependent behaviour of the PDL is a typical source of error in experimental studies found in the literature.[14,16,17] Thus, large variations in both the elastic modulus (0.01-1750 MPa) and Poisson ratio (0.28-0.49) have been reported.[17] Furthermore, these values are often experimentally obtained using rodent PDL samples,[17-19] which have a masticatory system that is extremely different from that in humans.[20] Fortunately, the number of studies that used porcine or bovine samples has increased in recent years. Moreover, the experimental protocol is another common source of error.[17]

Because of the difficulty obtaining accurate experimental measurements, finite element analysis (FEA) has been extensively used. Some authors[21-24] have recently used finite element (FE) models obtained by microcomputerized tomography (microCT). The authors of these studies assert the importance of considering the irregular geometry of the PDL to obtain reliable results. Some FE studies use isotropic hyperelastic or elastic properties[23,25,26] for the ligament or viscoelastic material models.[27,28] Instead of defining the PDL as an isotropic tissue without fluid coupling, we considered the porous and fibrous components of the PDL in our previous study.[24] Thus, a complex material model that takes into account different behaviours for tensile and compressive effects was developed. However, damage to the PDL tissue has been poorly analysed, and our previous study[24] only explained the PDL response under a nontraumatic loading scenario. The viscohyperelastic damage model proposed by Natali et al[16,28] is one of the most comprehensive studies of PDL damage. They proposed a material model that considers anisotropy, an almost-incompressible behaviour, time dependence and the damage phenomenon for large strains. Nevertheless, the softening phenomena due to repetitive loads or fibrous network rupture remain unknown. The experimental results reported by Natali et al[29] show a softening phenomenon of the tissue under load repetition that may be caused by rearrangement of fibres.[16,26,30] In the nonloading state, the fibrous network is partially disorganized with interweaved collagen fibres.[31] This organization leads to a stiffer behaviour of the matrix than if the fibres were not interconnected. When the tissue is stretched, the local movement of the collagen fibres causes the fibrous network to become untangled, resulting in a softening phenomenon[31] that has been observed in other soft tissues, such as the arteries,[32] veins,[33] vaginal tissues,[34] and oesophageal tissues.[35] No numerical study of PDL damage has considered softening effects due to fibre alignment or fibrous network failure. Furthermore, the damage phenomena have not yet been implemented in a full FE model of the PDL, considering its nonuniform thickness and porous fibrous structure.

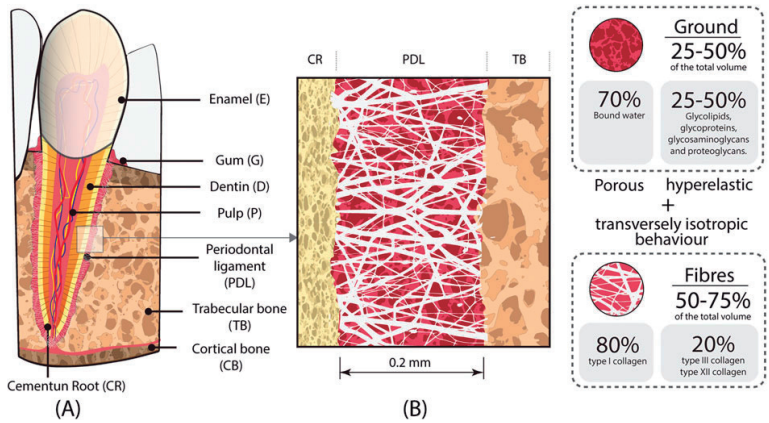

FIGURE 1 A, Schematic of human canine tooth anatomy. B, Details of the periodontal ligament structure and relationship between its composition and a porous hyperelastic and transversely isotropic material model

The main objective of this study was to analyse the mechanical response of the PDL under traumatic conditions considering the softening phenomena caused by fibre alignment and rupture. A constitutive damage model was developed and incorporated into our previous material model.[24] This damage model of PDL tissue was then implemented into an FE model of a human periodontium obtained by microCT. This FE model was subjected to three theoretical traumatic loads along intrusive, mesial-distal, and labial-lingual directions.

This paper is organized as follows. First, we introduce the material model used to mimic the porous fibrous response of the PDL without damage. Then, the softening effect due to fibrous network alignment is formulated according to Mullins effect theory. The mechanical response caused by fibrous network failure is described and incorporated into the constitutive model. Then, the parameters of the material model are obtained by an iterative process until good fitting of experimental data from the literature is achieved. The porous fibrous hyperelastic damage material model is implemented in a user material subroutine in Abaqus (Abaqus 6.14, Simulia, Rhode Island, USA) and applied to PDL tissue in a microCT 3D FE model. Finally, the results of fibrous alignment and fibrous failure and their effects on PDL behaviour under traumatic loading are extensively discussed.

2 | MATERIAL AND METHODS

2.1 | Material model characterization

In this section, first, the nondamage material model, which takes into account the different behaviours under tensile and compressive forces, is explained. Second, the formulation of the softening phenomenon due to fibre alignment is presented, and the characterization process is explained. Finally, the damage mechanism due to fibre rupture is developed.

2.1.1 | Porous fibrous material model without damage

It is well known that the PDL undergoes large deformation when the tooth is loaded. Thus, hyperelastic material models are useful to simulate large nonlinear strains under constant strain rates. However, the PDL is a porous tissue filled with interstitial fluid, which causes a viscoelastic response, especially under compressive forces. To consider this effect, viscoelastic or porous-elastic material models should be used. Moreover, the collagen fibre network produces a directional dependence behaviour when the fibres are stretched. Consequently, a transversely isotropic hyperelastic material model should be used to simulate the fibrous behaviour of the ligament.

Because of these porous fibrous effects, we proposed in a previous paper[24] a material model that considered both contributions. This material model combines the transversely isotropic hyperelastic behaviour caused by the collagen network and the time-dependent response produced by the interstitial fluid. However, it is not possible to correctly simulate the PDL response using a porous transversely isotropic hyperelastic material model for all loading conditions. Thus, we proposed a material model with different behaviours depending on the stretch direction. The material behaviour was defined by a porous transversely isotropic hyperelastic model or by a porous Ogden hyperfoam model if the region of the PDL was under tensile or compressive forces, respectively. The Ogden hyperfoam material model was developed for describing the behaviour of highly compressible elastomers.[36] It was used by Bergomi et al[14] to describe the behaviour of the PDL according to the high compressibility (a Poisson ratio of 0.086) observed in their previous experimental study.[6] The energy density function (ψ) of the constitutive material model can be defined by the deviatoric (ψ_{dev}) and volumetric (ψ_{vol}) components as follows:

$$\psi\left(\widetilde{\boldsymbol{C}}, \mathbf{M}\right) = \psi_{dev}\left(\widetilde{I}_1, \widetilde{I}_4\right) + \psi_{vol}(J_{\mathrm{el}}); \qquad \psi_{dev}\left(\widetilde{I}_1, \widetilde{I}_4\right) = \psi_m\left(\widetilde{I}_1\right) + \psi_f\left(\widetilde{I}_4\right), \tag{1}$$

where ψ_m is the component of the hyperelastic matrix and ψ_f is the component related to the fibrous network. Equation 1 is written in terms of the modified invariants $\widetilde{I}_1$ and $\widetilde{I}_4$, which are dilatational and deviatoric responses, respectively. These invariants are defined as follows:

$$\widetilde{I}_1 = tr\widetilde{\boldsymbol{C}} \qquad \widetilde{I}_4 = \mathbf{m}\cdot\widetilde{\boldsymbol{C}}\cdot\mathbf{m}, \tag{2}$$

where $\mathbf{m}$ is a unitary vector defining the orientation of the collagen fibres in the reference configuration and $\widetilde{\boldsymbol{C}}$ is the modified right Cauchy-Green tensor, defined by the modified deformation gradient $\widetilde{\boldsymbol{F}}$ as $\widetilde{\boldsymbol{C}} = \widetilde{\boldsymbol{F}}^T\widetilde{\boldsymbol{F}}$. The modified deformation gradient can be expressed as $\widetilde{\boldsymbol{F}} = J_{el}{}^{-\frac{1}{3}}\boldsymbol{F}$, where J_{el} is the Jacobian of the deformation gradient and $\boldsymbol{F}$ is the associated deformation gradient defined by $\boldsymbol{F} = \dfrac{\partial \boldsymbol{x}}{\partial \boldsymbol{X}}$, where $\boldsymbol{X}$ and $\boldsymbol{x}$ define the respective position of a particle in the reference Ω_0 and current Ω configurations. [Correction added on 01 March 2019, after first online publication: Equation 7 has been corrected] The terms of the energy density function can be written depending on $\widetilde{I}_4$ as follows:

$$\psi_m = \begin{cases} \dfrac{2\mu}{\alpha^2}\left[\widehat{\lambda}_1^{\alpha} + \widehat{\lambda}_2^{\alpha} + \widehat{\lambda}_3^{\alpha}\right] & if \ \left(\widetilde{I}_4 < 1\right) \\ C_1 \cdot \left(\widetilde{I}_1 - 3\right) & if \ \left(\widetilde{I}_4 \geq 1\right) \end{cases}, \tag{3,4}$$

$$\psi_f = \begin{cases} 0 & if \ \left(\widetilde{I}_4 < 1\right) \\ \dfrac{k_1}{2 \cdot k_2}\left\{exp\left[k_2 \cdot \left(\widetilde{I}_4 - 1\right)^2\right] - 1\right\} & if \ \left(\widetilde{I}_4 \geq 1\right) \end{cases}, \tag{5,6}$$

$$\psi_{vol} = \begin{cases} \dfrac{2\mu}{\alpha^2\beta}\left[(J_{el})^{-\alpha\beta} - 1\right] & if \ \left(\widetilde{I}_4 < 1\right) \\ \dfrac{1}{D}\left[\dfrac{(J_{el})^2 - 1}{2} - lnJ_{\mathrm{el}}\right] & \text{if } \left(\widetilde{I}_4 \geq 1\right) \end{cases}. \tag{7,8}$$

In Equation 3, μ and α are material parameters for a hyperfoam material model. The stretch $\left(\widehat{\lambda}_i\right)$ is defined as the ratio between the lengths at the deformed ($\boldsymbol{X}$) and reference configurations ($\boldsymbol{x}$) in the i direction. In Equation 4, C_1 is a material constant related to the ground substance of the transversely isotropic material model. In Equation 5, the fibrous term is 0 when the tissue is compressed. If not (Equation 6), $k_1 > 0$ and $k_2 > 0$ are the parameters that describe the exponential behaviour due to the presence of the collagen fibres. For the volumetric part of the strain energy function (ψ_{vol}), in Equation 7, β determines the degree of porous hyperfoam material compressibility related to Poisson ratio, by $\beta = \nu/(1 - 2\nu)$, and α is the aforementioned material parameter in Equation 3. Finally, in Equation 8, D is related to the bulk modulus, K, by $K = 2/D$.

The biphasic behaviour of the PDL was introduced by adding the porous contribution. Thus, the total stress in a point, $\boldsymbol{\sigma}$, in the fully saturated tissue is defined[37] as follows:

$$\boldsymbol{\sigma} = (1 - e) \cdot \overline{\boldsymbol{\sigma}} - e \cdot \overline{p}_t \cdot \boldsymbol{I} - \zeta \cdot \overline{p}_t \cdot \boldsymbol{I}, \tag{9}$$

where ζ is a factor that depends on saturation (in this case, $\zeta = 1.0$ because the PDL is a fully saturated tissue), e is the void ratio defined as the ratio of the volume of fluid (V_f) to the total volume (V_t) by $e = dV_f/dV_t$, $\overline{\boldsymbol{\sigma}}$ is the effective stress of the solid matrix obtained from the second Piola-Kirchhoff stress tensor of the strain energy function of the solid phase, and $\overline{p}_t$ is the average pressure stress of the fluid. The pressure stress, $\overline{p_t}$, is related to the Jacobian contribution from the permeability of the tissue by the nonlinear Forchheimer flow law. It was employed in Abaqus (Abaqus 6.14, Simulia, Rhode Island, USA) to describe the fluid flow for permeability. The exponential permeability function described by Argoubi and Shirazi-Adl[38] for biphasic materials was used to relate the fluid flow permeability dependence with the deformation as follows:

$$\overline{k} = k_0\left[\frac{e(1 + e_0)}{e_0(1 + e)}\right]^2 exp\left[M\left(\frac{1 + e}{1 + e_0} - 1\right)\right], \tag{10}$$

where k_0 and e_0 are the permeability and void ratio at zero strain, respectively, and M is a dimensionless material parameter.

To fit the material parameters that describe the tensile and compressive response, two iterative processes were executed by a script written in Python ("Python 3.5.2, Python Software Foundation"). The material behaviour under

tensile force was characterized by the experimental data obtained by Natali et al.[28] In this experiment, the specimen was extracted from the mandible of an adult pig. It was cut into a rectangular shape containing a portion of both bone and tooth, with the PDL between the bone and the tooth (schematically shown in Figure 3A), and its geometry was measured by a reflecting microscope. Then, the sample was stretched along the fibre direction until rupture using a material testing machine (Zwick Z005/TN29). The compressive response was obtained by fitting experimental data obtained by Bergomi et al[14] using bovine samples. The experimental results were obtained by Bergomi et al from a cylindrical specimen extracted from bovine first molar. The specimen was composed of a portion of a molar, bone, and PDL (shown in Figure 3B). It was subjected to sinusoidal compressive displacement equivalent to 35% PDL thickness (0.60 mm) at three different frequencies (0.1, 0.5, and 1 Hz) using a displacement-controlled actuator (Microtester 5848, Instron, Norwood, Massachusetts). Although porcine data are considered more optimal,[17] some authors suggest that there is not a marked difference in considering different species for compression loads.[28] The similarity between the compressive responses of different species will be verified later in Section 3.1.1, comparing the response of the material model (characterized with bovine experimental data) with the compressive response of PDL samples from cats.

The material parameters were obtained in separate steps. First, C_1 was obtained by fitting the first region of the experimental curve[28] using the neo-Hookean hyperelastic model response. Afterwards, k_2 and k_1 were determined by mimicking the curvature and fitting the rest of the experimental tensile curve.[28] Figure 4A shows the material response variation for different values of C_1, k_1, and k_2. The permeability (k_0) was defined by fitting the experimental compressive behaviour[14] at 1 Hz using the proposed material model. To avoid unreal k_0 values, the permeability was constrained between (10^{-15}m^2) and (10^{-13}m^2) according to the permeability dimension order of other studies.[14,42] The dependence of the compressive behaviour on the permeability value is shown in Figure 4C. The fitting procedures were widely explained in our previous work.[24] Finally, the material model described was implemented in the UMAT user subroutine in Abaqus 6.14 commercial software.

2.1.2 | Softening due to fibre alignment

Several authors[19,29,43-45] experimentally observed a softening behaviour of the PDL during preconditioning loading-unloading cycles. This effect was shown in experimental studies for both bovine[44,45] and porcine[29,43] samples. This stress softening phenomenon is commonly referred to as the Mullins effect.[46] Although this effect was formulated to represent the preconditioning response in synthetic rubbers, it has been extensively used for soft tissues.[47] Microscopically, the softening phenomenon allows for multiple interpretations, such as fibre slipping, fibrous network reorganization, or fibre separation from the ground substance. Some of these softening mechanisms are illustrated in Figure 2A-C.

To represent the softening phenomenon, an anisotropic extension of the pseudo-elastic model proposed by Ogden and Roxburgh[48] and Horgan et al[49] was used. The energy density function defined in Equation 1 by the deviatoric and volumetric components was modified in the following form:

$$\psi\left(\widetilde{I}_1,\widetilde{I}_4,\eta\right)=\eta\psi_{dev}\left(\widetilde{I}_1,\widetilde{I}_4\right)+\Phi(\eta)+\psi_{vol}(J_{\mathrm{el}}), \tag{11}$$

where $\Phi(\eta)$ and η are the damage continuous function and the damage variable, respectively. The continuous function Φ is defined by the expression of the Ogden-Roxburgh model as follows:

$$\Phi(\eta)=\frac{\left(m+\beta_m\psi^m_{dev}\right)}{r\sqrt{\pi}}\left\{exp\left[-\left(\frac{\psi^m_{dev}-\psi_{dev}}{m+\beta_m\psi^m_{dev}}\right)\right]^2-1\right\}+(1-\eta)\psi^m_{dev}, \tag{12}$$

where r and β_m are dimensionless material parameters, m has the dimensions of energy, and ψ^m_{dev} is the maximum value of the deviatoric strain energy density experienced by the material during its deformation. The damage variable η varies with the deformation according to

$$\eta=1-\frac{1}{r}errf\left(\frac{\psi^m_{dev}-\psi_{dev}}{m+\beta_m\psi^m_{dev}}\right), \tag{13}$$

where the error function ($errf$) is defined as $errf(x)=\frac{2}{\sqrt{\pi}}\int_0^x\exp(-\omega^2)d\omega$.

To obtain the different parameters of the Mullins effect damage model, a nonlinear regression procedure was implemented in MATLAB (MATLAB 6.0 R12, The MathWorks Inc, Natick, Massachusetts, 2000). Although the experimental

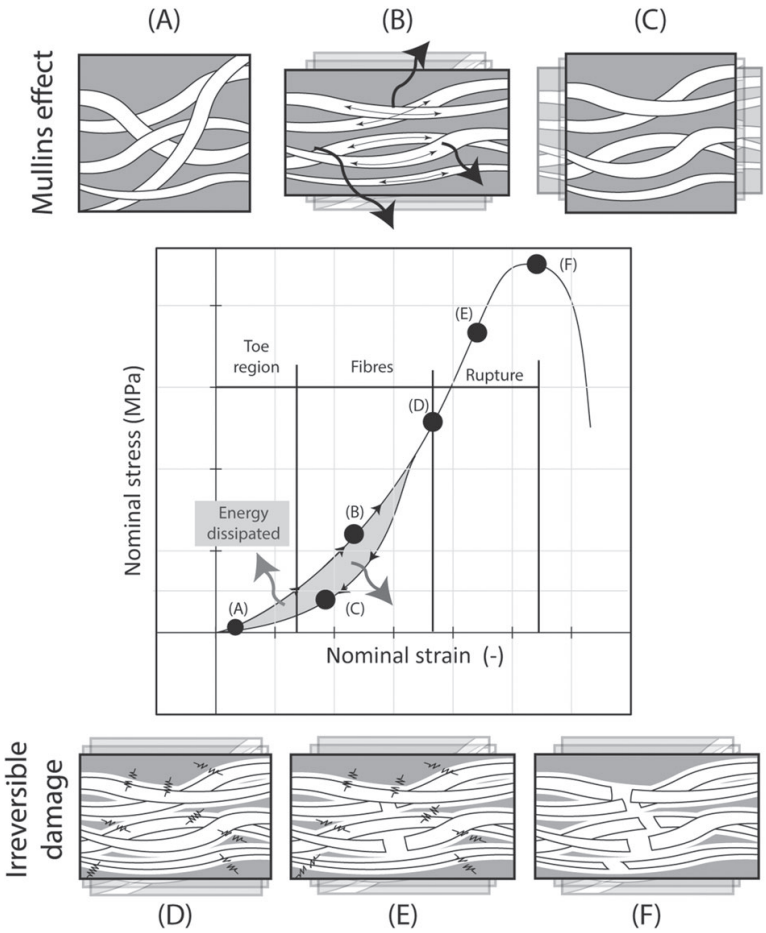

FIGURE 2 Schematic of the periodontal ligament (PDL) tensile response. A, Disorganized fibrous network at the initial state. B, Fibre alignment and energy dissipation due to the friction between fibres during tensile loading. C, Organized fibrous network after load removal. D, Damage to the ties between the fibres and the matrix beginning at higher strains. E, Fibre rupture at strains higher than the fibre elongation. F, Rupture of the entire fibrous network and tissue failure

data of Natali et al[28] were used in the previous section, the experimental data of one of their previous studies[29] were used for the characterization of this softening phenomenon. Although the same animal species was used for both tests, there are significant differences in the results of both studies. These differences could be because different regions of the PDL were tested or because different strain rates were imposed. Nevertheless, it was assumed that Natali et al utilized similar experimental protocols in both studies, obtaining a similar softening response with the preconditioning cycles. According to the test data of Natali et al,[29] the preconditioning of the tissue was defined as a change in the hysteresis curve until a steady condition was reached. The hysteresis indicates an energy loss within the PDL between cycles that is defined in this manuscript as a softening phenomenon caused by the fibrous network reorganization. Therefore, the softening phenomenon was characterized by preconditioning the experimental data from Natali et al.[29] The extraction protocol and the geometric registration procedure followed by Natali et al[29] were the same as that explained in Section 2.1.1 for the experimental test described in the previous experimental study by Natali et al.[28] However, the specimen of this study was subjected to loading and unloading cycles of 40% PDL thickness at a constant elongation rate of 0.5 mm/s. The parameters obtained (r, β_m, and m) were then implemented in our material model. As described previously, the behaviour of our material model was characterized by the data in Natali et al.[28] The softening phenomenon was then added to the aforementioned user subroutine in Abaqus. The complete strain energy function is detailed in Equation 20.

2.1.3 | Damage due to fibre over-elongation

In addition to the softening phenomenon due to loading-unloading cycles, PDL damage can be caused by the rupture of collagen fibres or damage to the fibre attachments to the ground matrix.[50] Under physiological loads, the waviness of the fibres makes the tissue softer for low strains (see the region in Figure 2) and stiffer for high strains. However, the damage phenomenon starts when the strain exceeds a specific limit (Figure 2D). This damage leads to a decrease in tissue stiffness. Any further increase in loading (Figure 2E) leads to progressive failure of the collagen fibre network until its complete rupture (Figure 2F).

Several authors have used FE models to determine the PDL stress state.[23,51,52] However, few of them[16,28] described the PDL behaviour in the failure region. As previously mentioned, the study of Natali et al[28] is one of the most relevant. Nevertheless, their study did not consider softening behaviour due to fibre alignment, the pressure of the interstitial fluid, or its effect on a full PDL. To include these aspects, a porous transversely isotropic hyperelastic damage constitutive model is developed in the present work. Thus, continuum damage mechanic was used to describe the irreversible damage under finite deformation.

To establish the law of evolution, the equivalent strain[53] of the fibrous term $\boldsymbol{\Xi_s}$ at any time s of the loading process is defined as follows:

$$\Xi_s\left(\widetilde{\boldsymbol{C}}\right) = \sqrt{2\cdot\psi_f\left(\widetilde{I_4}\right)\cdot\widetilde{\boldsymbol{C}}(s)}. \tag{14}$$

On the other hand, Ξ_t^m is the maximum value of Ξ_s over the past up to the current time s, which can be mathematically expressed as follows:

$$\Xi_t^m = \max_{s\in(0,t)}\left\{\sqrt{2\cdot\psi_f\left(\widetilde{I_4}\right)\cdot\widetilde{\boldsymbol{C}}(s)}\right\}, \tag{15}$$

where t is the time when the damage starts. With Ξ_s and Ξ_t^{max} defined, the damage criterion in the strain space can be expressed for any time t when the following expression is fulfilled:

$$\Xi_s - \Xi_t^m \le 0. \tag{16}$$

Equation 16 represents the damage surface in the strain space whose evolution is determined by the rate of the damage parameter $D_f\left(\Xi_t^m\right) \in [0,1]$:

$$\frac{dD_f}{dt} = \begin{cases} 0 & \text{if } \Xi_s < \Xi_t^m \\ \overline{h}\left(\Xi_t^m\right)\cdot\dot{\Xi_t^m} & \text{if } \Xi_s \ge \Xi_t^m \end{cases}, \tag{17}$$

where $\overline{h}\left(\Xi_t^m\right)$ is the function that characterizes the damage process of the fibrous network. In this model, we adopted the damage function used by Rodríguez et al,[54] as follows:

$$\overline{h}\left(\Xi_t^m\right) = \frac{\alpha_f}{\beta_f}\frac{\left(4\Xi_t^m\alpha_f + \beta_f\right)e^{2\alpha_f\left[\left(2\Xi_t^m/\beta_f\right)-1\right]}}{\left\{1+\alpha_f\Xi_t^m e^{2\alpha_f\left[\left(2\Xi_t^m/\beta_f\right)-1\right]}\right\}^2}. \tag{18}$$

After integration of Equation 17, the damage parameter (D_f) can be expressed as a function of two material parameters, α_f and β_f, as follows:

$$D_f\left(\Xi_t^m\right) = \frac{1}{2}\left\{1 + \frac{\alpha_f\Xi_t^m e^{2\alpha_f\left[\left(2\Xi_t^m/\beta_f\right)-1\right]} - 1}{\alpha_f\Xi_t^m e^{2\alpha_f\left[\left(2\Xi_t^m/\beta_f\right)-1\right]} + 1}\right\}. \tag{19}$$

This damage function allows control of the exponential damage at the beginning, the close constant damage propagation, and the end of damage. The $(1 - D_f)$ term multiplies the fibrous term of the deviatoric component (Equation 20). Thus, the porous transversely isotropic hyperelastic damage constitutive model can be summarized as follows:

$$\psi = \overbrace{\eta}^{\substack{\text{Mullins}\\ \text{variable}}} \cdot \overbrace{\left[\overbrace{\psi_m\left(\widetilde{I}_1\right)}^{\substack{\text{Matrix}\\ \text{term}}} + \overbrace{\left(1-D_f\right)\cdot\psi_f\left(\widetilde{I}_4\right)}^{\substack{\text{Fibres}\\ \text{damage}}}\right]}^{\substack{\text{Fibrous}\\ \text{term}}} + \overbrace{\Phi(\eta)}^{W.\ \text{dissipated}} + \overbrace{\psi_{vol}(J_{\text{el}})}^{\substack{\text{Volumetric}\\ \text{term}}}. \tag{20}$$

Desviatoric term with Mullins effect

To obtain the parameters that describe the material model damage, the constitutive formulation presented (Equation 20) was implemented in a UMAT user subroutine. The scheme of the FE program used to implement the porous fibrous hyperelastic damage material model is described in Appendix B. An iterative process was used to fit the tensile test results obtained by Natali et al.[28] The iterative process was executed in Python 3.5.2 and was stopped when the deviation between the numerical and experimental curves was lower than 2%. It was considered that the tissue damage starts at a strain value of 0.6 (corresponding to an equivalent strain value, Ξ_t, of 0.28).

2.2 | FE simulations of the test specimens

In this section, the material model described previously was implemented using an FEA to mimic the experimental test performed by Natali et al under tensile forces.[28] Moreover, the experimental tests performed by Bergomi et al[14] and Nishihira et al[39] were simulated to analyse the material response under compressive forces.

A 3D FE model reproducing the test sample geometry used experimentally by Natali et al[16] was developed using Abaqus CAE 6.14 (Abaqus 6.14, Simulia, Rhode Island, USA). Development of the FE model (Figure 3A) was extensively explained in our previous work.[24] After a mesh refinement process, the average size of the elements was approximately 0.035 mm. The material parameters of the transversely isotropic hyperelastic contribution (Equations 4 and 6) were obtained by mimicking the experimental dataset reported by Natali et al.[28] The specimen was extracted from the mandible of an adult pig. It was cut into a rectangular shape containing a portion of both bone and tooth with the PDL between the bone and the tooth (shown schematically in Figure 3A), and its geometry was measured by a reflecting microscope. Then, the sample was stretched along the fibre direction until rupture using a material testing machine (Zwick Z005/TN29). Therefore, the characterization process presented in Section 2.1.1 considers that PDL fibres run in the direction of the load (90°). To mimic the specific clamping fixture used in the experimental test, the bottom surface of the tooth was fixed, and a displacement equivalent to 70% PDL thickness (0.25 mm) was applied at the top surface of the bone. The displacement was computed from the experimental data reported by Natali et al.[28] It was assumed that the stress-stretch curve data were only caused by the PDL stretch because bone and teeth were considered practically rigid.[14,28] Furthermore, the response of the test sample was evaluated for different fibre orientations (90°, 70°, 45°, 20°, and 0°) (Figure 3A). The material parameters for the different FE model regions appear in Table 1.

For softening phenomenon verification during the tensile preconditioning cycles, the 3D FE model based on the dataset of Natali et al was used.[16] The experiment included six pure sinusoidal traction displacements equivalent to 20%, 24%, 28%, 32%, 36%, and 40% PDL thickness (0.25 mm) at 1.0 Hz (Figure 5A). These strain values correspond to the nondamaged strain region of the fibrous network, according to the experimental results of Natali et al[28] (higher strain than 60% of the PDL thickness). Moreover, the dependency of the softening effect on the fibre direction was analysed. Thus, several simulations for different α values in the undeformed state (0°, 20°, 45°, 70°, and 90°) (Figure 5C) were performed.

On the other hand, the 3D FE model was subjected to a displacement equivalent to 135% of the PDL thickness to determine the material parameters that define fibrous network damage. According to the experimental results of Natali et al,[28] the test sample failed before this strain value. The material damage parameters were obtained by an iterative process executed by a script written in Python until good agreement with the experimental results was achieved.

For characterization of the compressive material parameters, the axisymmetric FE model (Figure 3B) developed by Bergomi et al[14] was used. The response of the tissue without softening phenomena was evaluated at 0.1, 0.5, and 1 Hz frequencies (Figure 4B).

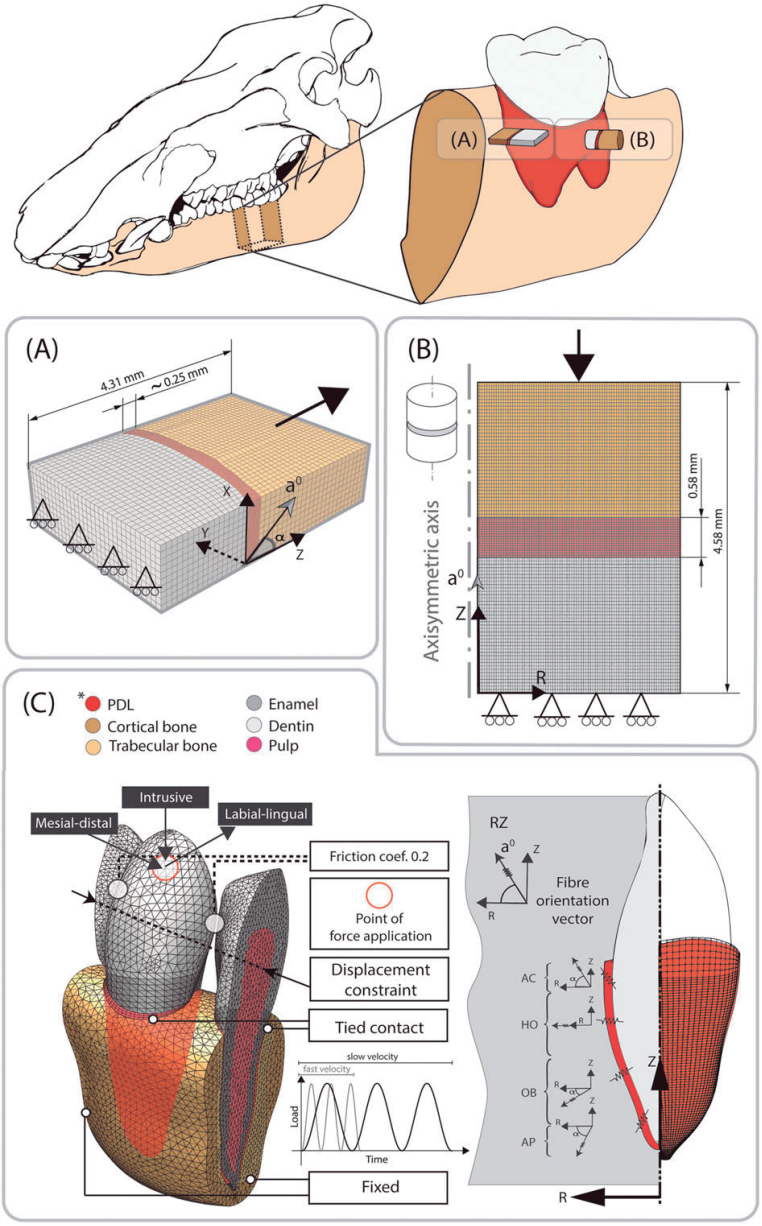

FIGURE 3 Top: Schematic of the acquisition of the experimental samples by Natali et al[16] and Bergomi et al.[14] A, A 3D finite element (FE) model that mimics the sample used by Natali et al[16] in their experimental test and boundary conditions applied. B, An axisymmetric FE model that mimics the samples used by Bergomi et al[14] in their experiments and the boundary conditions applied. C, Left: The FE model based on a microcomputerized tomography (microCT) scan with the boundary conditions and loading cycles. Right: Mesh of the canine periodontal ligament (PDL) and fibre distribution according to the different directions of fibre bundles (AP, apical; OB, oblique; HO, horizontal; and AC, alveolar crest). *For colour interpretation, see the web version of this article

To verify the softening phenomenon due to fibrous alignment, the axisymmetric FE model was subjected to three compressive cycles equivalent to 15%, 25%, and 30% of the PDL thickness (0.58 mm). Moreover, to understand the dependency of this effect on the strain rate, a previous test was performed at 0.1, 0.5, and 1.0 Hz frequencies.

TABLE 1 Mechanical properties assigned to each region

	Ground Parameters		Porous Properties			
	Young Modulus, MPa	Poisson Ratio	k_0, m^2	M	Void Ratio e_0	Specif Weight of Interstitial Fluid, N/mm^3
Pulp	2[a]	0.45[b]	–	–	–	–
Enamel	80 000[c]	0.31[b]	–	–	–	–
Cortical bone	20 000[e]	0.30[e]				
Trabecular bone	345[d]	0.31[d]	$5.29{\cdot}10^{-14}$[d]	–	4[d]	$9.8{\cdot}10^{-6}$
Dentin	15 000[d]	0.31[d]	$3.88{\cdot}10^{-17}$[d]	–	4[d]	$9.8{\cdot}10^{-6}$

	μ, MPa	α	Poisson Ratio	k_0, m^2	M	Void Ratio e_0	Specif Weight of Interstitial Fluid, N/mm^3
PDL if $\left(\tilde{I}_4 < 1\right)$	0.03[d]	20.9[d]	0.257[d]	$8.81{\cdot}10^{-15}$[d]	14.2[d]	2.33[d]	$9.8{\cdot}10^{-6}$

	C_1, MPa	D, MPa^{-1}	k_1, MPa	k_2	k_0, m^2	M	Void Ratio e_0	Specif Weight of Interstitial Fluid, N/mm^3
PDL if $\left(\tilde{I}_4 \geq 1\right)$	0.01[f]	9.078[f]	0.298[f]	1.525[f]	$6.5{\cdot}10^{-15}$[f]	9.5[f]	2.33[d]	$9.8{\cdot}10^{-6}$

Softening Phenomena	Due to Fibre Alignment			Due to Fibre Over-elongation		
	r	m, mJ	β_m	α_f	β_f	Ξ_t^{max}
PDL damage	1.492	0.064	0.1	1.0	0.25	0.28

[a]Wang et al.[12]

[b]Belli et al.[40]

[c]Nikolaus et al.[23]

[d]Bergomi et al.[14]

[e]Lacroix and Prendergast.[41]

[f]Ortún-Terrazas et al.[24]

As mentioned above, few differences exist between the compressive behaviour of the PDL from different species. This fact was verified by numerically mimicking the experimental data of adult cat samples[39] with a material model based on bovine experimental data. Thus, the 3D FE model of Natali et al[28] was compressed at the same strain rates of 260%, 63%, 6.7%, 0.55%, and 0.0052% of PDL thickness per second, as used by Nishihira et al,[39] and the results were compared.

2.3 | PDL material model application to a canine microCT FE model

After characterization and validation of the porous transversely isotropic hyperelastic damage material model, this material model was implemented for the PDL tissue in an FE model of a portion of a human mandible obtained by microCT. In this section, the FE model and the boundary conditions are explained.

A portion of a human mandible was extracted from a cadaver, and it was conserved under stable conditions until it was scanned. The tomograms obtained from the scanning were rebuilt, the noise was reduced, and the point cloud was converted into nonuniform rational basis splines (NURBSs). This model was composed of a full canine tooth with its PDL, two portions of lateral teeth (premolar and lateral incisor) with their respective ligaments, and portions of the cortical and trabecular bones of the mandible (shown in Figure 3C). In addition, the teeth were divided into pulp, enamel, and cement regions (shown in the tooth section of Figure 3C). The microCT FE model was meshed using a commercial software program (Abaqus 6.14, Simulia, Rhode Island, USA) until mesh convergence. More details of the model are provided in our previous paper.[24] The material properties applied to each region of the model are summarized in Table 1. The influence of the softening effects was analysed in the complete FE model.

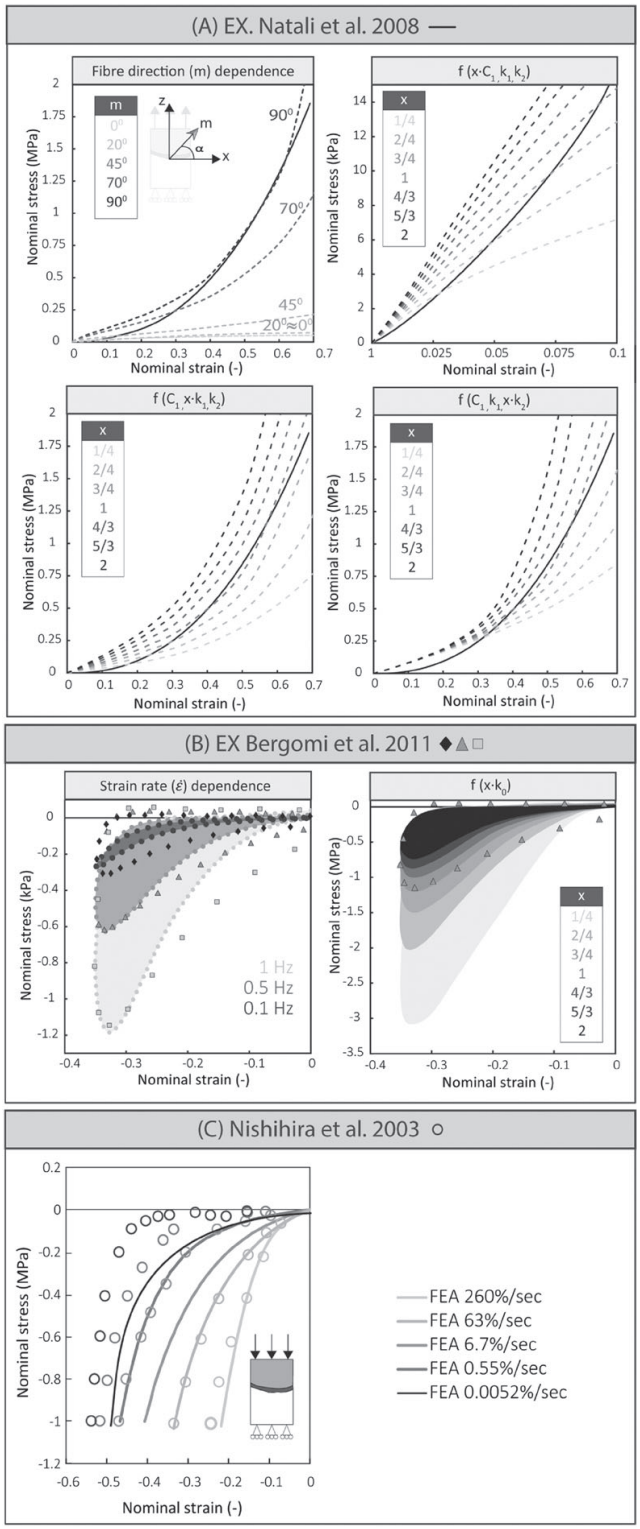

FIGURE 4 A, Porous fibrous material model approximation to the experimental results of Natali et al[28] and its dependence on fibre direction and different parameter values (C_1, k_1, and k_2). B, Porous fibrous material model approximation to the experimental results of Bergomi et al[14] under 0.1, 0.5, and 1 Hz frequencies and its behaviour dependence on different k permeability values. C, Comparison between the porous fibrous material model response and the experimental results obtained by Nishihira et al[39] at 260%/s, 63%/s, 6.7%/s, 0.55%/s, and 0.0052%/s strain rates. The variation in the material parameters and permeability values was defined as the fraction x of the values listed in Table 1

Regarding the loading conditions, the FE model was subjected to three theoretical loads of 360 N along intrusive, labial-lingual, and mesial-distal directions (see the load point application in Figure 3C). The intrusive load is a vertical load defined by the main longitudinal axis of the teeth and oriented along the direction from the tooth cuspid to the tooth root. The magnitude of this load was defined according to different studies of adult human teeth under possible damage conditions.[1,40,55] There are significant discrepancies in the literature regarding the magnitude of the physiological occlusal load, which can vary between 14.5 N[56] and 100 N.[1] In comparison with normal chewing conditions, a 360-N load would represent a large load that may cause damage to the ligament, which is demonstrated in Section 3. However, this magnitude does not represent a real traumatic load of an occlusal trauma scenario. Loads were applied by three sinusoidal cycles (see the detail of Figure 3C) to analyse the damage due to load repetition. Moreover, each case was studied considering a physiological chewing velocity (1.33 Hz)[57] and a theoretical slow velocity (0.0166 Hz). The results at fast (physiological) and slow velocities allow us to separately study the residual strains due to the porous coupling and the softening phenomena. The lateral nodes of the mandible were constrained considering fixation with the rest of the mandible. Moreover, the nodes of the cut planes of the premolar and incisal teeth were constrained at the mesial-distal direction to represent the restriction imposed by the remaining teeth. The contact between teeth was defined by a penalty contact term with a friction coefficient (value of 0.2), according to the studies by Zheng and Zhou.[58] Figure 3C shows the boundary and loading conditions applied. On the other hand, the PDLs were considered to be attached to the trabecular bone and the teeth by a tied contact due to the presence of interstitial fibres.[4,51,59]

3 | RESULTS

3.1 | Material model characterization and validation

This section shows the material parameter characterization and the numerical results for the mimicked experimental test (previously defined in Section 2.2). First, the mechanical response of the material model without damage is presented. Then, the Mullins effect is evaluated in compression and tension tests, modifying the fibre bundle direction and the strain rate. Finally, the fibrous network damage is analysed using experimental data.[28]

3.1.1 | Porous fibrous material model without damage

Figure 4 shows the responses of the material model without damage defined in Section 2.1.1. The results of mimicking the experimental tests performed by Natali et al,[28] Bergomi et al,[14] and Nishihira et al[39] are summarized in Figure 4A-C, respectively.

Figure 4A shows a good approximation between the FEA at 90° and the experimental responses under tensile efforts less than 0.7 strain. The higher deviation appears in the first part of the curve due to the concave shape of the neo-Hookean material response. The dependence of the material behaviour response on the direction of the fibres is also shown (Figure 4A). The stiffness of the PDL increases when the fibre bundles run along the direction of the traction load. The values of k_1 and k_2 modify the curvature and exponential growth of the curve, respectively (as shown in Figure 4A). For a region in which fibres are aligned at 20° or 0°, the material response is mainly defined by the porous hyperelastic behaviour of the matrix (Equation 4). Increasing the C_1 parameter leads to stiffer behaviour of the porous hyperelastic matrix (as shown in Figure 4A).

The energy dissipation due to the porous term is clearly presented in Figure 4B. Despite the difficulties in predicting the permeability effects, the FEA curves closely follow the experimental data of Bergomi et al.[14] For higher strain rates, the fluid phase does not have enough time to flow, and consequently, the tissue becomes stiffer. An increase in the initial permeability value k_0 leads to softer behaviour of the tissue because the fluid can more easily flow out (as shown in Figure 4B).

Although different samples from species were used for tensile (porcine samples) and compressive (bovine samples) material behaviour characterization, it was demonstrated that the different species have similar compressive responses. Figure 4C compares the numerical results using our material model (characterized by data from bovine samples) and the experimental data of adult cat samples.[39] It can be appreciated that no significant differences exist between the compressive responses of the PDL of each species. The similarity for high strain rates is especially remarkable when the fluid phase contributes more.

3.1.2 | Softening due to fibre alignment

Figure 5 shows the FEA curves using the porous fibrous material model, which includes the softening behaviour caused by the fibre alignment (described in Section 2.1.2) for different situations. Figure 5A shows the tensile response considering the Mullins effect characterized by the experimental data of Natali et al.[29] By introducing the Mullins effect, the numerical response after the preconditioning cycles (Figure 5A) better fits the experimental data for the first part of

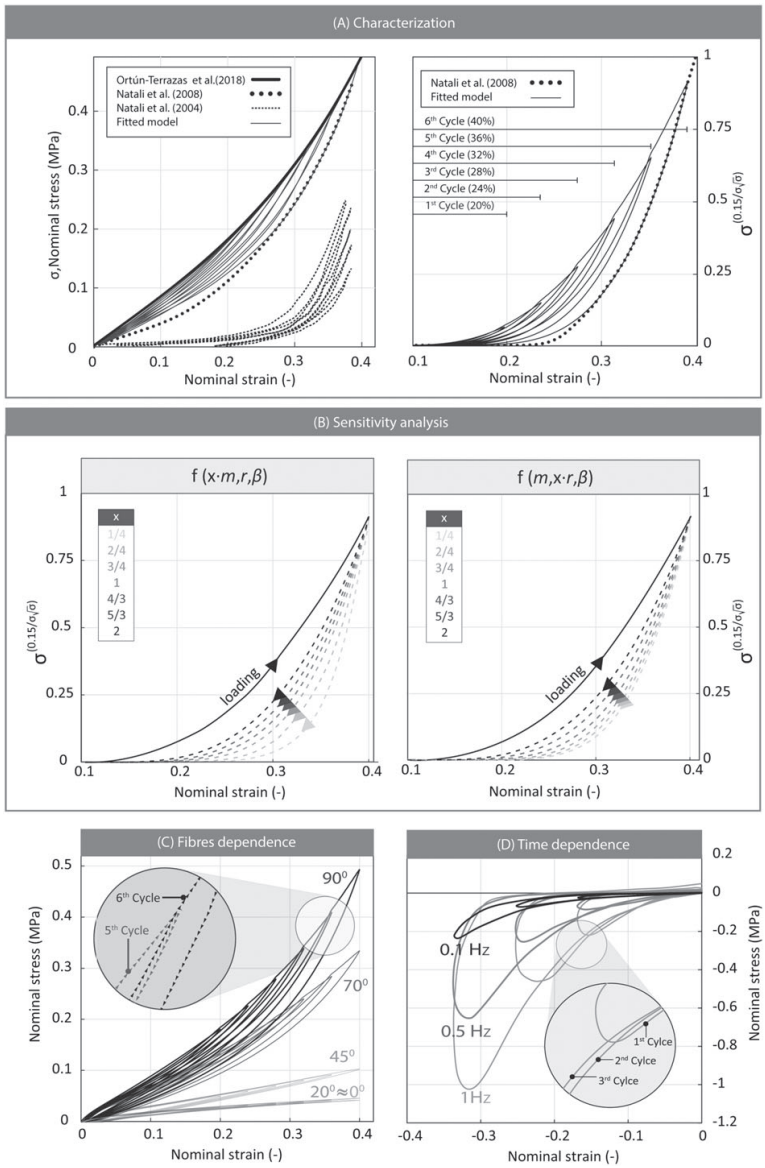

FIGURE 5 A, Left: Comparison between the two previous studies of Natali et al.[28,29] Right: Representation of the theoretical Mullins effect using a magnification variable of the nominal stress ($\sigma^{0.15/\sigma\sqrt{\sigma}}$). B, Dependence of the softer unloading response with different m and r material parameters. C, Mullins effect for different fibre directions using the 3D finite element (FE) model of the Natali et al[16] experiment. D, Mullins effect for different strain rates using the axisymmetric FE model of the Bergomi et al[14] experiment

the curve, where the porous fibrous material model without damage exhibited poor fitting. Modifying the m and r parameters leads to different energy loss and curvature, respectively, of the unloading curve (as shown in Figure 5B).

The dependence of the softening effect on the fibre bundle orientation and its behaviour under compressive effort is presented in Figure 5C and 5D, respectively. The Mullins effect at different fibre orientations is shown in Figure 5C. The effect of the fibre alignment is more noticeable when the fibres are aligned along the loading direction. Moreover, the porous and Mullins effects are coupled, as shown in the graphical detail of Figure 5C. In a pure Mullins effect response, the unloading and subsequent loading curves must be the same. However, a deviation occurs when the porous effect is added. This effect was also observed during compression, revealing a softening phenomenon when the loading process is repeated (Figure 5C).

3.1.3 | Damage due to fibre over-elongation

Figure 6 shows several aspects of the damage function (described in Section 2.1.3). The dependence of the damage function on different damage parameters and the curve fitted to the experimental results of Natali et al[28] are shown in Figure 6B. Figure 6C shows the damage evolution of the elements of the PDL mesh.

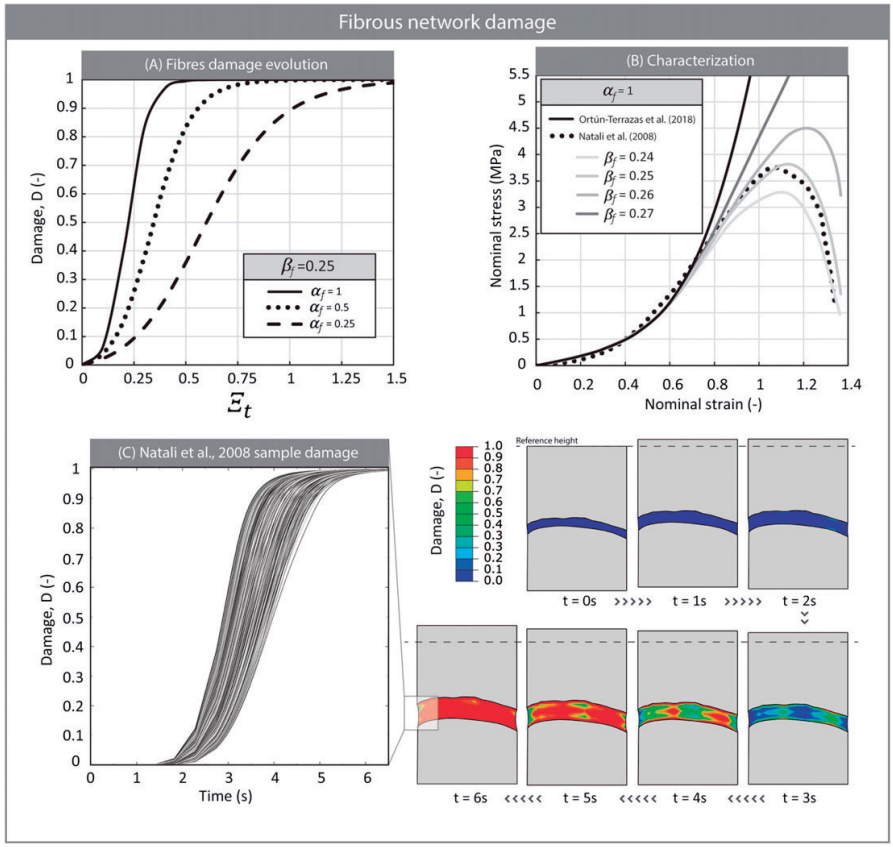

FIGURE 6 A, Evolution of the damage function (Equation 19) modifying α_f and β_f parameters. B, Influence of α_f and β_f damage parameters on the material model response and characterization of the fibrous network damage using the 3D finite element (FE) model of the experimental dataset in Natali et al.[16] C, Left: Damage evolution of the integration points of the 3D FE sample. Right: Damage evolution of the fibrous network during the tensile test using the 3D FE model of the experimental sample of Natali et al[16]

Varying the parameters α_f and β_f can increase the damage initiation velocity, the gradient of damage evolution in the quasilinear zone, and the final failure evolution (Figure 6A). Moreover, extension of the damage region is a function of these parameters. The PDL begins to become damaged at strains higher than 0.6 (0.28 equivalent strain of the fibrous term), and at a strain of 1.05, the tissue has completely failed. Therefore, PDL rupture occurs in a small strain range. Thus, similar parameters cause significant differences in tissue damage behaviour, as shown in Figure 6B. As mentioned, an iterative process was executed in Python to fit the damage parameters. For the iterative analysis, the 3D FE model mimicked the geometry of the sample used in Natali et al.[16] The best adjustment was obtained for $\alpha_f = 1$ and $\beta_f = 0.25$ damage parameters values. The deviation between the experimental curve and the computational material response was lower than 2%. Damage to the fibrous network starts to appear in two regions near the midplane (Figure 6C, time = 3 s), which are the thinnest regions, and continues to the closest regions until its complete failure (Figure 6C, time = 6 s).

3.2 | PDL material model application to a canine microCT FE model

After characterization of the PDL tissue behaviour, the porous fibrous hyperelastic damage model was implemented into the periodontium of a human canine FE model. In this section, the results of the FE model under three loading conditions are explained. Figure 7 shows the minimum principal stresses in the bone, the void ratio, damage of the fibrous network, and the minimum principal stresses in the ligament after the first cycle under high strain rate. The damage evolution with the cycles is negligible in a damage-time curve at high strain rates (Figure 8A). Therefore, a local magnification of each damage-time curve is shown in detail in Figure 8A. Furthermore, the difference between the initial and final positions of the tooth (named residual displacement) is shown in Figure 8B. In this figure, the differences regarding whether the damage phenomenon is considered at high or low strain rates are shown. The complete information of the stress distribution for the different tissues involved is provided in the available supporting information.

3.2.1 | Intrusive loading

It is well known that the physiological role of the PDL is to absorb intrusive loads. When the intrusive load is applied, the tooth is displaced downward (see Figure A1C), and the apical region of the PDL is compressed towards the bone (Figure 7A). Compression of the ligament causes the fluid to flow to the bone, decreasing the void ratio in this region (Figure 7B). The dissipation of fluid partially relaxes the ligament and contributes to bone loading. However, a large compression of the PDL may cause a reduction in the fluid content and an increase in the load supported by the solid phase. Because of the high loss of fluid in the apical region, the maximum value of the minimum principal stress is located in this region (Figure 7D). On the other hand, the void ratio of the alveolar crest region increases because the PDL is stretched in this region (Figure 7B).

Regarding the fibrous network role, the PDL is subjected to shear forces. The regions where the fibre bundles run horizontally and obliquely become more stretched, causing higher maximum principal stress in these areas (see Figure A2A). This effect increases the strain level in this region, causing damage to the fibrous network on the mesial side of the PDL (Figure 7C). Curiously, no fibrous damage appears at the top region of the ligament. Despite the excessive magnitude of the load, the maximum damage value is 0.29 and minimally increases by load repetition (see the continuous line in Figure 8A). In the case of slow load application, the fluid does not absorb the load, and the solid matrix supports most of it. In this case, the residual displacement increases (shown percentage differences in Figure 8B legend) because of greater damage to the fibrous network. However, the PDL matrix is the least damaged of the three cases (Figure 8B) because fibres are primarily oriented to resist intrusive loads.

3.2.2 | Labial-lingual loading

The results of the FEA suggest that the tooth rotates when a lateral labial-lingual load is applied (see Figure A1C). For this particular model, the rotation centre (RC) is at a depth of approximately 7 mm from the upper border of the ligament. This rotation movement causes compression efforts in the upper region of the opposite side of the bone (Figure 7A). Thus, the top region of the lingual side and the bottom region of the labial side of the ligament are compressed (Figure 7D), while the opposite regions are stretched (see Figure A2A). The compression reduces the void ratio

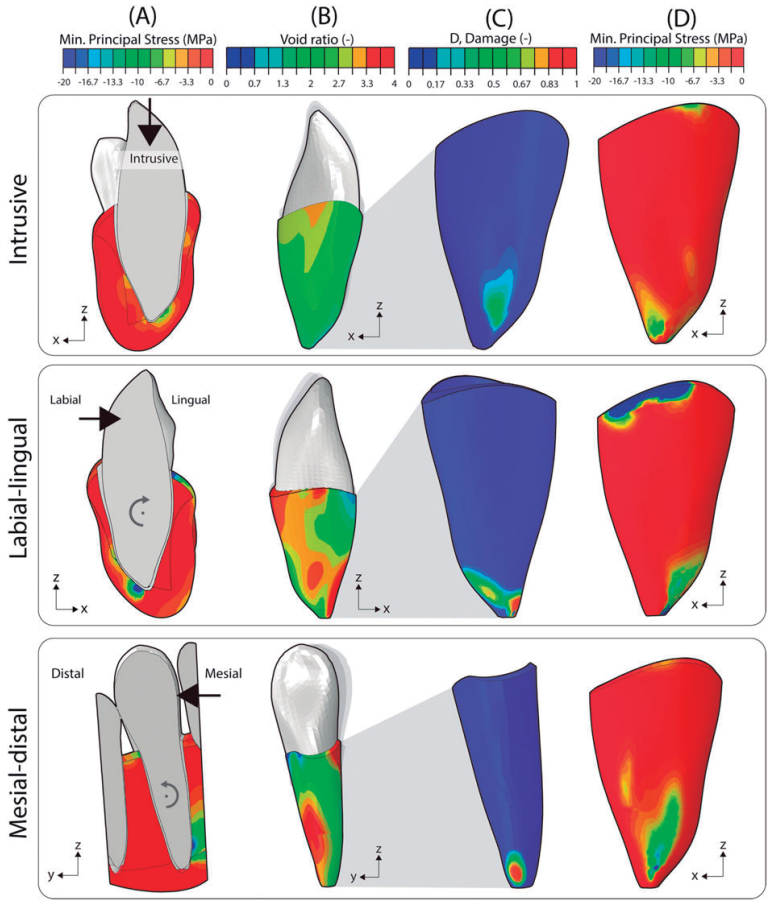

FIGURE 7 Top to bottom: Finite element (FE) results corresponding to the first cycle of applying a 360-N load in intrusive, labial-lingual, and mesial-distal directions. A, Minimum principal stresses in the cortical and trabecular bone portions. B, Void ratio in the canine periodontal ligament (PDL). C, Damage of the fibrous network of the PDL due to excessive stretch. D, Minimum principal stresses in the canine PDL

(Figure 7B) in these sections, which increases the value of the minimum principal stresses in the solid matrix (Figure 7 D) and the pressure of the interstitial fluid (see Figure A2C).

On the other hand, the highest values of the maximum principal stresses are located at the top region of the labial side and at the bottom region of the lingual side (see Figure A2B). Although similar displacement occurs in both regions, the apical region experiences higher stresses due to the small thickness of the PDL in this region. Thus, the damage of the fibres network starts at this region (Figure 7C). In this case, the maximum damage values (83%) are similar to the total damage of the tissue. However, the damage evolution increases slowly within the cycles (Figure 8A) because the porous term continues to support much of the stress. For low strain rates, the fluid phase only minimally contributes, and the irreversible displacement due to fibrous damage increases (Figure 8B). This residual displacement percentage is related to the maximum damage value.

3.2.3 | Mesial-distal loading

Loading along the mesial-distal direction is probably the most unusual loading scenario. The thinnest region of the PDL is located at the mesial-distal sides of the top region of the ligament since this region is minimally loaded under

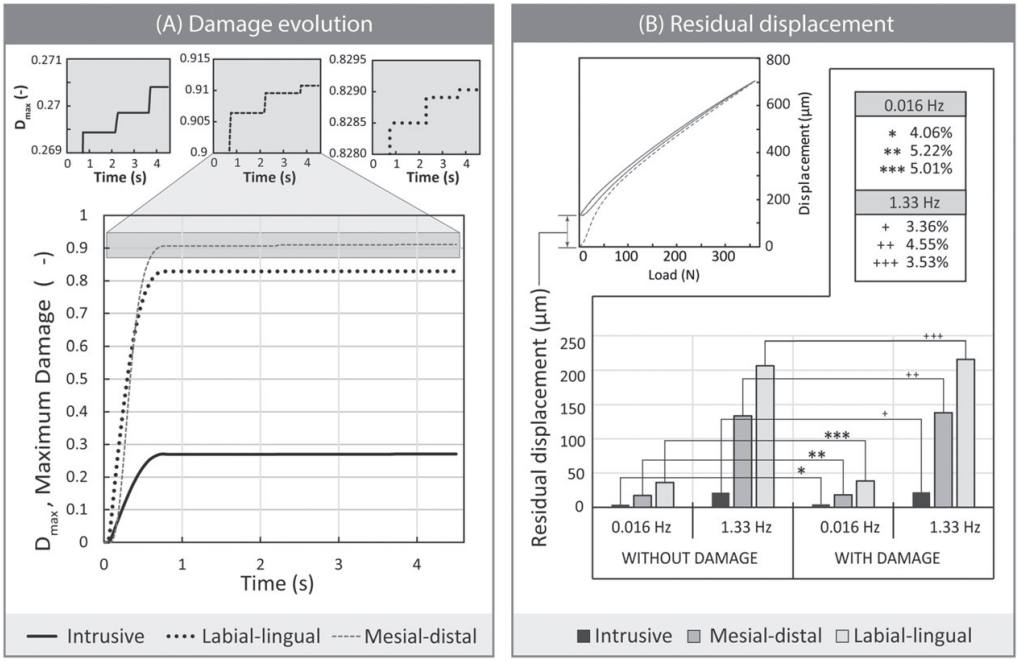

FIGURE 8 A, Top: Details of the damage evolution due to repetitive traumatic loading. Bottom: Damage evolution of the maximum damaged element for each loading scenario at 1.33 Hz. B, Top: Load-displacement curve obtained by applying the load in the mesial-distal direction to show the concept of residual displacement. Bottom: Comparison of residual displacement at slow (0.0166 Hz) and fast (1.33 Hz) velocities, considering the nondamage or damage phenomenon. *Difference percentages at slow velocity. +Difference percentages at fast velocity

physiological conditions. As mentioned, the main role of the ligament is to resist the intrusive loads produced during chewing. When the tooth is subjected to loads along the mesial-distal direction, the tooth rotates (see Figure A1C). This movement causes compression of the alveolar crest and apical regions of the distal and mesial sides, respectively (Figure 7B). Therefore, it reduces the fluid volume (Figure 7B) and increases the pressure of the fluid in the areas mainly compressed (see Figure A2C). In addition, the fluid flow contributes to loading the underlying trabecular bone (Figure 7A). It is remarkable that the top region of the PDL at the distal side evacuates all the interstitial fluid of the PDL (Figure 7B). Thus, the maximum value of minimum principal stresses is located at the top region of the bone. On the other hand, the maximum value of maximum principal stresses is located at the apical region of the PDL distal side (see Figure A2A). The apical fibres must support high stress values in this region, causing damage to its fibrous structure. The damage value during mesial-distal loading is the highest of the three performed tests (Figure 8A) and may be caused by the unusual direction of the load.

4 | DISCUSSION

4.1 | Characterization and validation of the material model

As mentioned in Section 1, several studies have explained PDL behaviour using elastic isotropic or hyperelastic material formulations.[23,25,26] Moreover, some computational studies have attempted to explain the nonlinear anisotropic behaviour by introducing collagen fibres as 1D FE elements.[60] On the other hand, some researchers have explained the effect of the PDL interstitial fluid by means of viscoelastic material formulations.[12,27,28] We recently proposed a new model that combines the porous and fibrous properties of the PDL.[24] However, the role of the PDL in some of the most common periodontal diseases is unknown. This work is the first to study the porous fibrous behaviour of

the PDL under traumatic loads. We suggest an innovative material model, namely, a porous fibrous material model, that considers the PDL softening behaviour due to fibre alignment and damage due to fibre rupture.

The first part of Section 2.1 summarizes the material model without damage mechanism proposed in our previous work. As shown in Figure 4, good correlation exists between the numerical and experimental data under tensile and compressive efforts (Figure 4A and 4B, respectively). The tensile response of the PDL was characterized using experimental data of porcine samples from the literature,[28] while the compressive behaviour was defined by data of bovine samples.[14] Although the porcine PDL seems more similar to the human PDL, it has been suggested that no significant differences exist among the compressive responses of different species.[28] This similarity was verified by subjecting the 3D FE model (which reproduces the experimental sample geometry in the study of Natali et al) to Nishihira et al[39] loading scenarios where samples of an adult cat PDL were tested. The computational compressive response (characterized by bovine experimental data) was not significantly different from the experimental results of Nishihira et al (Figure 4C). Remarkably, higher differences appeared at low strain rates (0.0052%/s and 0.55%/s), when the porous component has minimal contributions. Thus, it can be assumed that the porous component is similar among different species and plays a key role under compressive efforts. In summary, the findings of the material model without damage demonstrated the biphasic behaviour of the tissue, as suggested by other authors.[5,6,61] This study suggests that the stiffness highly depends on the fibrous structure (Figure 4A) under tensile forces and on the strain rate under compressive forces (Figure 4B).

Regarding the softening mechanisms, this study numerically demonstrated the softening effect due to fibre alignment and damage due to fibre rupture (Figure 2). The softening behaviour observed in Natali et al[29] was extrapolated to the experimental data of their later study.[28] The Mullins effect was characterized using this theoretical assumption. Thus, the numerical results suggested a small softening effect of the fibrous network due to the alignment of fibres with repetitive loading (Figure 5A). The dissipated energy increased when the fibres ran along the loading direction (Figure 5C) because the fibrous term has a greater influence on the PDL behaviour. Additionally, the softening effect under compressive forces can be seen in Figure 5C. Because "n" is a loading-unloading cycle, the unloading curve of the "n" cycle did not fit with the loading curve of the "$n + 1$" cycle (see details in Figure 5C and 5D) because of the viscoelastic contribution. Interestingly, the material model without a damage criterion did not fit well with the experimental data for strains lower than 0.4 (Figure 4A). However, the softening phenomenon improved the fitting of the experimental data (Figure 5A). This improvement could mean that the specimens tested by Natali et al[28] were also previously preconditioned.

Regarding fibrous network damage, the experimental test performed by Natali et al[28] was computationally mimicked (Figure 6B). For strains higher than 0.6, the numerical response of the material model without damage was stiffer than the experimental data. According to our material description, this deviation could be caused by fibrous network damage.

4.2 | PDL material model application to the microCT FE model

The causes of chronic periodontitis have been mainly explained from an infectious point of view. The infection can begin with an inflammatory response due to a repetitive traumatic load. Thus, interest in studying the role of the mechanical response of the PDL in periodontitis diseases has increased in recent years.[2,3,61] The PDL plays two roles under traumatic loading conditions. First, it works as a mechanical stimulus receptor and informs the chewing system when overload occurs; then, the chewing muscles immediately reduce the loads. On the other hand, the PDL releases inflammatory mediators that cause bone remodelling. Therefore, several authors[4,43] suggest that the PDL plays a key role in tooth movement, and some studies have sought to explain bone resorption according to its mechanical response.[62,63]

Figure 7A shows the regions of the cortical and trabecular bones that are mainly compressed. For lateral loads (labial-lingual and mesial-distal directions), the highest minimum principal stresses were observed at the alveolar crestal and apical regions of the PDL. The compressive stresses in the alveolar crest zone are caused by rotation of the tooth and coincide with the middle region of the tooth (see Figures A1C). On the other hand, the value of the minimum principal stresses is maximum in the apical zone due to the interaction of two effects. First, compression of the PDL decreases the fluid volume in that area, causing an increase in the load supported by the fibrous network. This overloading state damages the matrix and causes a weakening of the PDL. This fact can be seen in Figure 8B, which shows greater damage for low strain rates due to the small influence of the fluid. Second, the maximum value of the

minimum principal stress in the apical region is caused by the increase in fluid pressure with cycles and by the softening phenomena.

Both softening phenomena reduce the stiffness of the solid matrix. This fact increases the interstitial liquid pressure at the regions that are mainly compressed (see Figure A2C). Some of the most common bone remodelling hypotheses of tooth movement are that tensile strain of the ligament causes the formation of bone tissue, while compressive strain causes the resorption of bone tissue. We refer to the "pressure-tension hypothesis," [64,65] "alveolar bending hypothesis,"[66] or "stretched fibre hypothesis,"[67] among others. This study suggests that mandibular bone remodelling cannot be explained in simple terms of tension or compression regions. We considered that a complete study of the porous fibrous structure of the PDL should be performed to explain the bone remodelling mechanism. On the basis of our numerical results, we predict that the bone remodelling mechanics may be a combination of the "stretched fibre hypothesis," damage to the fibrous network, and overpressure of the interstitial fluid.

From a cellular point of view, recent studies have considered that bone resorption could be caused by the combination of three mechanisms.[68,69] First, the fibres compressed at the alveolar crest or apical regions (Figure 7A) could release some cytokines and prostaglandins to form leucocytes, macrophages, and monocytes.[69] Then, the chemical changes at these compressive regions may recruit and differentiate cells into osteoclasts. These osteoclasts would reabsorb the adjacent bone and destroy the necrotic hyalinized tissue.[70] On the other hand, overpressure of the interstitial fluid (Figure 7B) can produce inflammatory cytokines.[71] Cytokines also stimulate bone resorption.[72] Finally, it is well known that the adjacent bone contains fenestrations,[73] which can detect whether the PDL fluid is compressed.[74,75] Stimulation by fenestrations reduces the bone density.[74-76]

By contrast, the formation of bone tissue can be explained by fibre stretching.[77-79] The maximum value of the maximal principal stresses can be found in the apical region of the PDL (see Figure A2A). The over-elongation of fibres in this region causes fibrous network damage (Figure 7C), local vascularization,[69] and mechanobiological signals (arachidonic acid metabolites, neuropeptides, or cytokines).[80-82] These signals can translate to bone formation around these sides of the ligament. However, excessive stretching of fibres can cause PDL deterioration (Figure 7C)[16] and trigger inflammatory processes.[83] In this case, cytokines may initiate the bone resorption process.

Furthermore, the fibre contribution under intrusive loads causes a well-balanced stress distribution along the PDL (Figure 7A).[4] This uniform stress state can prevent bone resorption, especially in the middle region. Biologically, fenestrations of the bone in this region may not receive enough mechanical signals to initiate bone formation.[73] In our simulations, only a small area of the ligament experiences damage to the fibrous network (Figure 7C), and the maximum damage value in this case is smaller than that in the other two cases. According to the bone remodelling principles followed in this study ("stretched fibre theory," fluid pressure, and PDL damage mechanism), bone resorption can begin at the apical region since the previously mentioned rules are satisfied. However, the uniform mechanical stress state maintains stability of the bone density.

4.3 | Study limitations

There are several limitations of the current study, which future research should address. The most important limitation lies in the fact that experimental data of human PDL samples were not used. Nevertheless, experimental data of porcine and bovine PDL samples have been extensively used because their bite systems have mechanical similarities with the human bite system. Moreover, the same animal species was not used for the compressive and tensile behaviour characterization. Future experimental studies should test porcine samples under compressive and tensile efforts, considering the fibrous network and the permeability of the tissue.

Second, the Mullins effect and the tensile material response were characterized using experimental data from different studies (Natali et al[16] and Natali et al,[28] respectively). Although both studies were performed by the same authors, the Mullins effect was characterized by a theoretical curve. On the other hand, this material model only uses one function to describe both the matrix and fibre alignment softening phenomena. Experimental tests should be performed to separately determine the effects of repetitive loading on the matrix and the fibrous network.

Another major source of uncertainty is the experimental data used to characterize the damage of the fibrous network. It was assumed that the damage process started at 0.6 strain, but this assumption is not based on histological experimental studies. Fibrous damage should be studied by a combination of microscopic and macroscopic analysis. Advances in these two areas would improve our knowledge of the complex degradation mechanism of the PDL.

Although this study verifies the important effect of fibrous damage, damage due to overpressure of the interstitial fluid was not considered. To take into account this effect, other authors[84] have simplified the fluid pressure by the volume averaged hydrostatic pressure, $\overline{\sigma}_h$, defined as $\overline{\sigma}_H = \frac{\sum_e \sigma_H^e V^e}{\sum_e V^e}$, where σ_H^e and V^e are the hydrostatic stress and volume of each element, respectively. They consider that bone regeneration occurs for higher $\overline{\sigma}_h$ values than the capillary blood pressure $\overline{\sigma}_h = 4.7$ kPa (35 mm Hg). However, this is a severe assumption because it does not consider the real viscoelastic effect of the fluid phase. We have to remark that the fluid effect must be considered in future studies to acquire complete knowledge of the PDL. On the basis of mechanobiological studies of PDL degeneration, the fluid phase likely plays the most significant role in PDL diseases.

Finally, using FE models to study patient-specific periodontal diseases from a practical point of view will require extensive further development. This study was developed using a computational model for a specific patient tooth, and the numerical results cannot be directly extrapolated to other cases. However, the FE model presented in this manuscript contributes to improving our knowledge of the role of the PDL in supporting loads.

5 | CONCLUSIONS

The present results demonstrate the applicability of a porous fibrous damage hyperelastic material model to describe the mechanical response of the PDL and its damage under traumatic conditions. Within the limitations of this study, we summarize our findings by the following conclusions:

(1) Both porous and fibrous effects must be considered in numerical studies of periodontium diseases. In particular, these contributions must be included in studies that analyse the stress state of the ligament and its effect on bone remodelling.
(2) The preconditioning process modifies the ligament response, reducing its stiffness in mechanical experimental tests. Furthermore, this softening effect increases the residual displacement of the tooth under intrusive and lateral loads, which are common loads during chewing or parafunctional clenching.
(3) The damage produced by fibre stretching occurs at high strains (upper than 60%). The PDL fibrous network is not damaged under physiological loading scenarios. However, it may suffer small deterioration under traumatic loads, as studied in this manuscript.
(4) The fluid pressure in the alveolar crest and apical regions may cause a deterioration process due to the interstitial fluid overpressure under lateral and intrusive traumatic loads, respectively. The effect of overpressure may be the main cause of deterioration of a healthy PDL under nonphysiological loads.
(5) The interstitial fluid effect, the collagen bundles and the softening phenomena should be simultaneously considered to explain the bone remodelling mechanism.

This study demonstrates the key roles of interstitial fluid and collagen fibres in the tissue mechanical response, the softening phenomenon due to fibre alignment or fibrous network damage, and the effect of considering a non-uniform thickness of the PDL by microCT scan techniques. The results presented here will serve as a basis for future studies and will help elucidate the role of the PDL in some of the most common periodontal diseases or bone remodelling processes. This FE model marks the beginning of potential research on PDL mechanical behaviour. Future studies should consider PDL damage due to overpressure of the interstitial fluid, the role of the PDL in real chewing cases, its deterioration under parafunctional loads, or the rates of bone remodelling in the mandible.

ACKNOWLEDGEMENT

This work was supported by the Spanish Ministry of Economy and Competitiveness through project DPI 2016-79302-R.

CONFLICT OF INTEREST

The authors have no conflicts of interest related to the present work.

ORCID

Javier Ortún-Terrazas https://orcid.org/0000-0002-6186-5695

REFERENCES

1. Poiate IAVP, de Vasconcellos AB, de Santana RB, Poiate E. Three-dimensional stress distribution in the human periodontal ligament in masticatory, parafunctional, and trauma loads: finite element analysis. *J Periodontol*. 2009;80(11):1859-1867. https://doi.org/10.1902/jop.2009.090220.
2. Pihlstrom BL, Michalowicz BS, Johnson NW. Periodontal diseases. *Lancet (London, England)*. 2005;366(9499):1809-1820. https://doi.org/10.1016/S0140-6736(05)67728-8.
3. Drolshagen M, Keilig L, Hasan I, et al. Development of a novel intraoral measurement device to determine the biomechanical characteristics of the human periodontal ligament. *J Biomech*. 2011;44(11):2136-2143. https://doi.org/10.1016/j.jbiomech.2011.05.025.
4. Tuna M, Sunbuloglu E, Bozdag E. Finite element simulation of the behavior of the periodontal ligament: a validated nonlinear contact model. *J Biomech*. 2014;47(12):2883-2890. https://doi.org/10.1016/j.jbiomech.2014.07.023.
5. Favino M, Gross C, Drolshagen M, et al. Validation of a heterogeneous elastic-biphasic model for the numerical simulation of the PDL. *Comput Methods Biomech Biomed Engin*. 2013;16(5):544-553. https://doi.org/10.1080/10255842.2011.628660.
6. Bergomi M, Cugnoni J, Botsis J, Belser UC, Anselm Wiskott HW. The role of the fluid phase in the viscous response of bovine periodontal ligament. *J Biomech*. 2010;43(6):1146-1152. https://doi.org/10.1016/j.jbiomech.2009.12.020.
7. Daly CH, Nicholls JI, Kydd WL, Nansen PD. The response of the human periodontal ligament to torsional loading—I. Experimental methods. *J Biomech*. 1974;7(6):517-522. https://doi.org/10.1016/0021-9290(74)90086-4.
8. Berkovitz BKB, Weaver ME, Shore RC, Moxham BJ. Fibril diameters in the extracellular matrix of the periodontal connective tissues of the rat. *Connect Tissue Res*. 1981;8(2):127-132. https://doi.org/10.3109/03008208109152132.
9. Tsuzuki T, Kajiya H, T-goto K, Tsutsumi T. Hyperocclusion stimulates the expression of collagen type XII in periodontal ligament. *Arch Oral Biol*. 2016;66:86-91. https://doi.org/10.1016/j.archoralbio.2016.02.009
10. Qian L, Todo M, Morita Y, Matsushita Y, Koyano K. Deformation analysis of the periodontium considering the viscoelasticity of the periodontal ligament. *Dent Mater*. 2009;25(10):1285-1292. https://doi.org/10.1016/j.dental.2009.03.014.
11. Toms SR, Dakin GJ, Lemons JE, Eberhardt AW. Quasi-linear viscoelastic behavior of the human periodontal ligament. *J Biomech*. 2002;35(10):1411-1415. https://doi.org/10.1016/S0021-9290(02)00166-5.
12. Wang C-Y, Su M-Z, Chang H-H, et al. Tension-compression viscoelastic behaviors of the periodontal ligament. *J Formos Med Assoc*. 2012;111(9):471-481. https://doi.org/10.1016/j.jfma.2011.06.009.
13. Nyashin MY, Osipov AP, Bolotova MP, Nyashin YI, Simanovskaya EY. Periodontal ligament may be viewed as a porous material filled by free fluid: experimental proof. *Russian Journal Biomechanics*. 1999;3:89-95. 89–95
14. Bergomi M, Cugnoni J, Galli M, Botsis J, Belser UC, Wiskott HW. Hydro-mechanical coupling in the periodontal ligament: a porohyperelastic finite element model. *J Biomech*. 2011;44(1):34-38. https://doi.org/10.1016/j.jbiomech.2010.08.019.
15. Natali AN, Pavan PG, Venturato C, Komatsu K. Constitutive modeling of the non-linear visco-elasticity of the periodontal ligament. *Comput Methods Programs Biomed*. 2011;104:193-198. https://doi.org/10.1016/j.cmpb.2011.03.014
16. Natali AN, Pavan PG, Carniel EL, Dorow C. A transversally isotropic elasto-damage constitutive model for the periodontal ligament. *Comput Methods Biomech Biomed Engin*. 2003;6:329-336. https://doi.org/10.1080/10255840310001639840
17. Fill TS, Carey JP, Toogood RW, Major PW. Experimentally determined mechanical properties of, and models for, the periodontal ligament: critical review of current literature. *J Dent Biomech*. 2011;2(1):312980-312980. https://doi.org/10.4061/2011/312980.
18. Detamore MS, Athanasiou KA. Tensile properties of the porcine temporomandibular joint disc. *J Biomech Eng*. 2003;125:558-565. https://doi.org/10.1115/1.1589778
19. Genna F, Annovazzi L, Bonesi C, Fogazzi P, Paganelli C. On the experimental determination of some mechanical properties of porcine periodontal ligament. *Mec Dent*. 2008;43:55-73. https://doi.org/10.1007/s11012-007-9094-2
20. Kalpakci KN, Willard VP, Wong ME, Athanasiou KA. An interspecies comparison of the temporomandibular joint disc. *J Dent Res*. 2011;90:193-198. https://doi.org/10.1177/0022034510381501
21. Chang C, Lei Y, Ho Y, Sung Y, Lin T. Predicting the holistic force-displacement relation of the periodontal ligament: in-vitro experiments and finite element analysis. *Biomed Eng Online*. 2014;13(1):107. https://doi.org/10.1186/1475-925X-13-107
22. Benazzi S, Nguyen HN, Kullmer O, Kupczik K. Dynamic modelling of tooth deformation using occlusal kinematics and finite element analysis. *Plos One*. 2016;1-17. https://doi.org/10.1371/journal.pone.0152663
23. Nikolaus A, Fleck C, Lindtner T, Currey J, Zaslansky P. Importance of the variable periodontal ligament geometry for whole tooth mechanical function: a validated numerical study. *J Mech Behav Biomed Mater*. 2016;67:61-73. https://doi.org/10.1016/j.jmbbm.2016.11.020

24. Ortún-Terrazas J, Cegoñino J, Santana-Penín U, Santana-Mora U, Pérez del Palomar A. Approach towards the porous fibrous structure of the periodontal ligament using micro-computerized tomography and finite element analysis. *J Mech Behav Biomed Mater*. 2018;79:135-149. https://doi.org/10.1016/j.jmbbm.2017.12.022
25. Zhang Z, Zheng K, Li E, Li W, Li Q, Swain MV. Mechanical benefits of conservative restoration for dental fissure caries. *J Mech Behav Biomed Mater*. 2016;53:11-20. https://doi.org/10.1016/j.jmbbm.2015.08.010
26. Oskui IZ, Hashemi A, Jafarzadeh H. Biomechanical behavior of bovine periodontal ligament: experimental tests and constitutive model. *J Mech Behav Biomed Mater*. 2016;62:599-606. https://doi.org/10.1016/j.jmbbm.2016.05.036
27. Huang H, Tang W, Tan Q, Yan B. Development and parameter identification of a visco-hyperelastic model for the periodontal ligament. *J Mech Behav Biomed Mater*. 2017;68:210-215. https://doi.org/10.1016/j.jmbbm.2017.01.035
28. Natali AN, Carniel EL, Pavan PG, Sander FG, Dorow C, Geiger M. A visco-hyperelastic-damage constitutive model for the analysis of the biomechanical response of the periodontal ligament. *J Biomech Eng*. 2008;130(3):31004. https://doi.org/10.1115/1.2900415.
29. Natali AN, Pavan PG, Carniel EL, Dorow C. Viscoelastic response of the periodontal ligament: an experimental—numerical analysis. *Connect Tissue Res*. 2004;45(4-5):222-230. https://doi.org/10.1080/03008200490885742.
30. Fill TS, Toogood RW, Major PW, Carey JP. Analytically determined mechanical properties of, and models for the periodontal ligament: critical review of literature. *J Biomech*. 2012;45(1):9-16. https://doi.org/10.1016/j.jbiomech.2011.09.020.
31. Hirashima S, Ohta K, Kanazawa T, et al. Three-dimensional ultrastructural analysis and histomorphometry of collagen bundles in the periodontal ligament using focused ion beam/scanning electron microscope tomography. *J Periodontal Res*. 2018;1-9. https://doi.org/10.1111/jre.12592
32. Maher E, Creane A, Lally C, Kelly DJ. An anisotropic inelastic constitutive model to describe stress softening and permanent deformation in arterial tissue. *J Mech Behav Biomed Mater*. 2012;12:9-19. https://doi.org/10.1016/j.jmbbm.2012.03.001
33. Alastrué V, Peña E, Martínez MA, Doblaré M. Experimental study and constitutive modelling of the passive mechanical properties of the ovine infrarenal vena cava tissue. *J Biomech*. 2008;41:3038-3045. https://doi.org/10.1016/j.jbiomech.2008.07.008
34. Peña E, Calvo B, Martínez MA, et al. Experimental study and constitutive modeling of the viscoelastic mechanical properties of the human prolapsed vaginal tissue. *Biomech Model Mechanobiol*. 2010;9(1):35-44. https://doi.org/10.1007/s10237-009-0157-2.
35. Natali AN, Carniel EL, Gregersen H. Biomechanical behaviour of oesophageal tissues: material and structural configuration, experimental data and constitutive analysis. *Med Eng Phys*. 2009;31:1056-1062. https://doi.org/10.1016/j.medengphy.2009.07.003
36. Storakers B. On material representation and constitutive branching in finite compressible elasticity. *J Mech Phys Solids*. 1986;34:125-145. https://doi.org/10.1016/0022-5096(86)90033-5
37. Wu, T. H. Soil mechanics. 1967.
38. Argoubi M, Shirazi-Adl A. Poroelastic creep response analysis of a lumbar motion segment in compression. *J Biomech*. 1996;29:1331-1339. https://doi.org/10.1016/0021-9290(96)00035-8
39. Nishihira M, Yamamoto K, Sato Y, Ishikawa H, Natali A. Mechanics of periodontal ligament. *In Dental Biomechanics*. 2003. 1st ed;20:-32.
40. Belli S, Eraslan O, Eskitaşcioğlu G. Effect of different treatment options on biomechanics of immature teeth: a finite element stress analysis study. *J Endod*. 2017. https://doi.org/10.1016/j.joen.2017.08.037;44(3):475-479.
41. Lacroix D, Prendergast PJ. A mechano-regulation model for tissue differentiation during fracture healing: analysis of gap size and loading. *J Biomech*. 2002;35(9):1163-1171. https://doi.org/10.1016/S0021-9290(02)00086-6.
42. Natali AN, Pavan PG, Schrefler BA, Secchi S. A multi-phase media formulation for biomechanical analysis of periodontal ligament. *Mec Dent*. 2002;37:407-418. https://doi.org/10.1023/A:1020895906292
43. Dorow C, Krstin N, Sander F-G. Experiments to determine the material properties of the periodontal ligament. *J Orofac Orthop/Fortschritte der Kieferorthopädie*. 2002;63(2):94-104. https://doi.org/10.1007/s00056-002-0107-4.
44. Pini M, Zysset P, Botsis J, Contro R. Tensile and compressive behaviour of the bovine periodontal ligament. *J Biomech*. 2004;37:111-119. https://doi.org/10.1016/S0021-9290(03)00234-3
45. Bergomi M, Anselm Wiskott HW, Botsis J, Shibata T, Belser UC. Mechanical response of periodontal ligament: effects of specimen geometry, preconditioning cycles and time lapse. *J Biomech*. 2009;42:2410-2414. https://doi.org/10.1016/j.jbiomech.2009.06.031
46. Mullins L. Effect of stretching on the properties of rubber. *Rubber Chem Technol*. 1948;21(2):281-300. https://doi.org/10.5254/1.3546914.
47. Ehret AE, Itskov M. Modeling of anisotropic softening phenomena: application to soft biological tissues. *Int J Plast*. 2009;25(5):901-919. https://doi.org/10.1016/j.ijplas.2008.06.001.
48. Ogden RW, Roxburgh DG. A pseudo-elastic model for the Mullins effect in filled rubber. *Proceedings of the Royal Society A: Mathematical, Physical and Engineering Sciences*. 1999;455(1988):2861-2877. https://doi.org/10.1098/rspa.1999.0431.
49. Horgan CO, Ogden RW, Saccomandi G. A theory of stress softening of elastomers based on finite chain extensibility. *Proceedings of the Royal Society A: Mathematical, Physical and Engineering Sciences*. 2004;460:1737-1754. https://doi.org/10.1098/rspa.2003.1248

50. Provenzano PP, Heisey D, Hayashi K, Lakes R, Vanderby R. Subfailure damage in ligament: a structural and cellular evaluation. *J Appl Physiol*. 2002;92:362-371. https://doi.org/10.1152/jappl.2002.92.1.362
51. Huang H, Tang W, Yan B, Wu B. Mechanical responses of periodontal ligament under a realistic orthodontic loading. *Procedia Engineering*. 2012;31:828-833. https://doi.org/10.1016/j.proeng.2012.01.1108
52. Boryor A, Hohmann A, Geiger M, Wolfram U, Sander C, Sander FG. A downloadable meshed human canine tooth model with PDL and bone for finite element simulations. *Dent Mater*. 2009;25(9):57-62. https://doi.org/10.1016/j.dental.2009.05.002.
53. Peña E, Calvo B, Martínez MA, Doblaré M. On finite-strain damage of viscoelastic-fibred materials. Application to soft biological tissues. *Int J Numer Methods Eng*. 2008;74:1198-1218. https://doi.org/10.1002/nme.2212
54. Rodríguez JF, Cacho F, Bea JA, Doblaré M. A stochastic-structurally based three dimensional finite-strain damage model for fibrous soft tissue. *J Mech Phys Solids*. 2006;54:864-886. https://doi.org/10.1016/j.jmps.2005.10.005
55. Razaghi R, Biglari H, Karimi A. Dynamic finite element simulation of dental prostheses during chewing using muscle equivalent force and trajectory approaches. *J Med Eng Technol*. 2017;41:314-324. https://doi.org/10.1080/03091902.2017.1299231
56. Hattori Y, Satoh C, Kunieda T, Endoh R, Hisamatsu H, Watanabe M. Bite forces and their resultants during forceful intercuspal clenching in humans. *J Biomech*. 2009;42(10):1533-1538. https://doi.org/10.1016/j.jbiomech.2009.03.040
57. Kerstein RB, Radke J. Average chewing pattern improvements following disclusion time reduction. *Cranio*. 2017;35:135-151. https://doi.org/10.1080/08869634.2016.1190526
58. Zheng J, Zhou ZR. Effect of age on the friction and wear behaviors of human teeth. *Tribology International*. 2006;39:266-273. https://doi.org/10.1016/j.triboint.2004.09.004
59. Schünke, M. Prometheus-Lernatlas der Anatomie: Innere Organe; 118 Tabellen (Vol. 2). 2009 Georg Thieme Verlag.
60. Freitas AC, Rocha EP, dos Santos PH, Ko CC, Martín M, de Almeida EO. Mechanics of the maxillary central incisor. Influence of the periodontal ligament represented by beam elements. *Comput Methods Biomech Biomed Engin*. 2010;13:515-521. https://doi.org/10.1080/10255840903273175
61. Keilig L, Drolshagen M, Tran KL, et al. In vivo measurements and numerical analysis of the biomechanical characteristics of the human periodontal ligament. *Annals of Anatomy—Anatomischer Anzeiger*. 2016;206:80-88. https://doi.org/10.1016/j.aanat.2015.08.004
62. Qian H, Chen J, Katona TR. The influence of PDL principal fibers in a 3-dimensional analysis of orthodontic tooth movement. *Am J Orthod Dentofacial Orthop*. 2001;120:272-279. https://doi.org/10.1067/mod.2001.116085
63. Zargham A, Geramy A, Rouhi G. Evaluation of long-term orthodontic tooth movement considering bone remodeling process and in the presence of alveolar bone loss using finite element method. *Orthodontic Waves*. 2016;5:1-12. https://doi.org/10.1016/j.odw.2016.09.001
64. Schwarz AM. Tissue changes incidental to orthodontic tooth movement. *Int J Orthod, Oral Surgery and Radiography*. 1932;18(4):331-352. https://doi.org/10.1016/S0099-6963(32)80074-8.
65. Reitan K. The initial tissue reaction incident to orthodontic tooth movement as related to the influence of function; an experimental histologic study on animal and human material. *Acta Odontol Scand*. 1951;6:1-240.
66. Baumrind S. A reconsideration of the propriety of the 'pressure-tension' hypothesis. *Am J Orthod*. 1969;55(1):12-22. https://doi.org/10.1016/S0002-9416(69)90170-5.
67. Melsen B. Tissue reaction to orthodontic tooth movement—a new paradigm. *Eur J Orthod*. 2001;23:671-681.
68. Kim S-J, Park K-H, Park Y-G, Lee S-W, Kang Y-G. Compressive stress induced the up-regulation of M-CSF, RANKL, TNF-α expression and the down-regulation of OPG expression in PDL cells via the integrin-FAK pathway. *Arch Oral Biol*. 2013;58:707-716. https://doi.org/10.1016/j.archoralbio.2012.11.003
69. Dutra EH, Nanda R, Yadav S. Bone response of loaded periodontal ligament. *Curr Osteoporos Rep*. 2016;14:280-283. https://doi.org/10.1007/s11914-016-0328-x
70. Rosenstiel SF, Land MF, Fujimoto J. Contemporary fixed prosthodontics-e-book. Elsevier Health Sciences 2015. ISBN: 0323112889.
71. Goto H, Osaki M, Fukushima T, et al. Human bone marrow adipocytes support dexamethasone-induced osteoclast differentiation and function through RANKL expression. *Biomedical Research (Tokyo, Japan)*. 2011;32:37-44. https://doi.org/10.2220/biomedres.32.37
72. Kapoor P, Kharbanda OP, Monga N, Miglani R, Kapila S. Effect of orthodontic forces on cytokine and receptor levels in gingival crevicular fluid: a systematic review. *Prog Orthod*. 2014;15:65. https://doi.org/10.1186/s40510-014-0065-6
73. Bright R, Hynes K, Gronthos S, Bartold PM. Periodontal ligament-derived cells for periodontal regeneration in animal models: a systematic review. *J Periodontal Res*. 2015;50:160-172. https://doi.org/10.1111/jre.12205
74. Bien SM. Hydrodynamic damping of tooth movement. *J Dent Res*. 1966;45(3):907-914. https://doi.org/10.1177/00220345660450036701
75. Bergomi M, Wiskott HWA, Botsis J, Mellal A, Belser UC. Load response of periodontal ligament: assessment of fluid flow, compressibility, and effect of pore pressure. *J Biomech Eng*. 2010;132:14504. https://doi.org/10.1115/1.4000154
76. Guo Z, Bo D, He P, et al. Sequential controlled-released dual-drug loaded scaffold for guided bone regeneration in a rat fenestration defect model. *J Mater Chem B*. 2017;5(37):7701-7710. https://doi.org/10.1039/C7TB00909G

77. McCormack SW, Witzel U, Watson PJ, Fagan MJ, Gröning F. Inclusion of periodontal ligament fibres in mandibular finite element models leads to an increase in alveolar bone strains. *PLoS One*. 2017;12:1-23. https://doi.org/10.1371/journal.pone.0188707

78. Bernick S. The organization of the periodontal membrane fibres of the developing molars of rats. *Arch Oral Biol*. 1960;2:57-63. https://doi.org/10.1016/0003-9969(60)90038-8

79. McCormack SW, Witzel U, Watson PJ, Fagan MJ, Gröning F. The biomechanical function of periodontal ligament fibres in orthodontic tooth movement. *Plos One*. 2014;9(7):e102387. https://doi.org/10.1371/journal.pone.0102387

80. Yamamoto TT. Orthodontic tooth movement and expression of calcium regulating hormone. *Clin Calcium*. 2012;22:91-98.

81. Kashyap S. Current concepts in the biology of orthodontic tooth movement: a brief overview. *NJDSR*. 2006;1(4):28-31. https://doi.org/10.1016/j.ajodo.2005.12.013.

82. Yamaguchi M, Shimizu N, Goseki T, et al. Effect of different magnitudes of tension force on prostaglandin E2 production by human periodontal ligament cells. *Arch Oral Biol*. 1994;39(10):877-884. https://doi.org/10.1016/0003-9969(94)90019-1

83. Hallmon WW. Occlusal trauma: effect and impact on the periodontium. *Ann Periodontol*. 1999;4(1):102-108. https://doi.org/10.1902/annals.1999.4.1.102.

84. Chen J, Li W, Swain MV, Ali Darendeliler M, Li Q. A periodontal ligament driven remodeling algorithm for orthodontic tooth movement. *J Biomech*. 2014;47:1689-1695. https://doi.org/10.1016/j.jbiomech.2014.02.030

85. Holzapfel GA. Nonlinear solid mechanics: a continuum approach for engineering science. *Mec Dent*. 2002;37(4):489-490.

86. Marsden, Jerrold E., and Thomas, JR Hughes. Mathematical foundations of elasticity. Courier Corporation, 1994.

SUPPORTING INFORMATION

Additional supporting information may be found online in the Supporting Information section at the end of the article.

How to cite this article: Ortún-Terrazas J, Cegoñino J, Santana-Penín U, Santana-Mora U, Pérez del Palomar A. A porous fibrous hyperelastic damage model for human periodontal ligament: Application of a microcomputerized tomography finite element model. *Int J Numer Meth Biomed Engng*. 2019;35:e3176. https://doi.org/10.1002/cnm.3176

APPENDIX A

BIOMECHANICAL ANALYSIS OF THE TEETH, PDL, AND MANDIBULAR BONE

As it was introduced, the PDL works as a stress absorber to transmit loads from the tooth to the alveolar bone. Our numerical results verify that the PDL distributes intrusive loads better than lateral loads to the teeth and the mandibular bone. Under an intrusive load, the tooth moves vertically (Figure A1C), and homogeneous maximum and minimum principal stress distributions are generated along the tooth (Figure A1A and A1B, respectively). On the other hand, the lateral loads cause tooth rotation (Figure A1C). This movement concentrates the higher stresses in the middle region of the tooth.

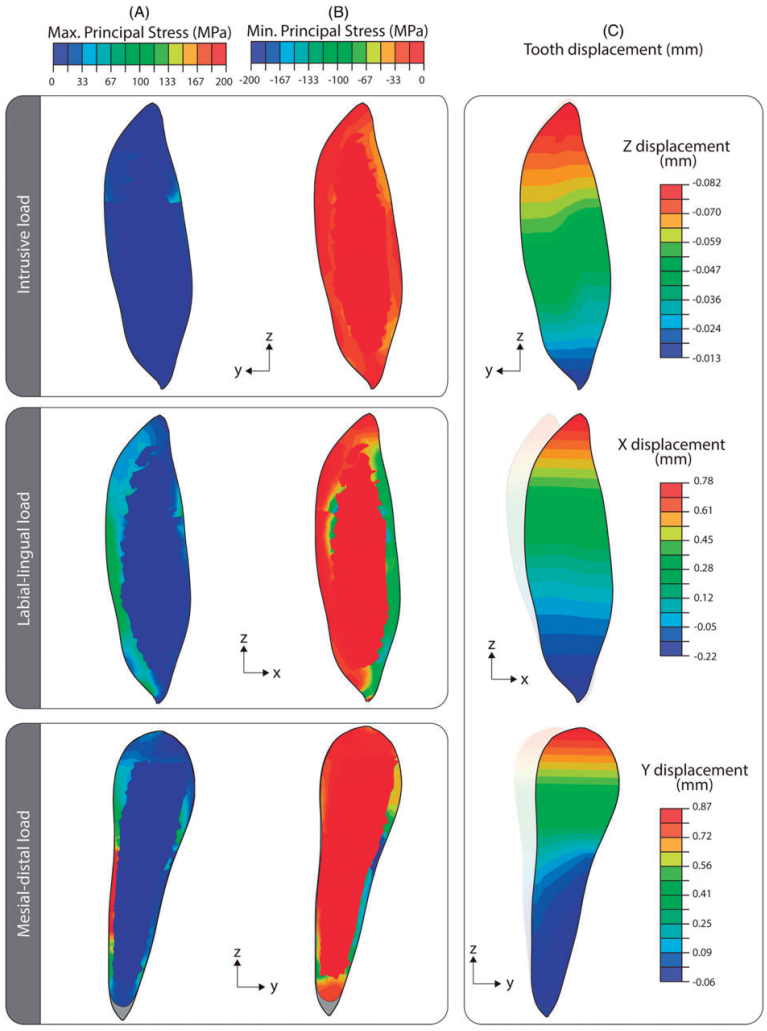

FIGURE A1 A, Maximum principal stress, B, minimum principal stress, and C, displacement of the canine tooth after applying a 360-N load at intrusive, labial-lingual, and mesial-distal directions (ordered from top to bottom)

Tooth movement is directly related to the PDL stress distribution. Under intrusive loading, the liquid phase of the ligament partially reduces the minimum principal stress (Figure A2B) of the solid matrix of the PDL. Conversely, the porous pressure of the interstitial fluid increases (Figure A2C) and the volume of fluid decreases (Figure A2D) in the areas mainly compressed (Figure A2B). On the other hand, the apical fibres of the PDL try to support tooth rotation when lateral loads are applied. This role of the fibres increases the maximum principal stress of the solid matrix in the apical region (Figure A2A). As shown in Figure 5C, over-elongation of the apical fibres leads to irreversible damage to the fibrous network in this area. Furthermore, the compressive force evacuates most of the fluid (Figure A2D), causing overpressure of the remaining interstitial fluid, mainly in the alveolar crest region (Figure A2C).

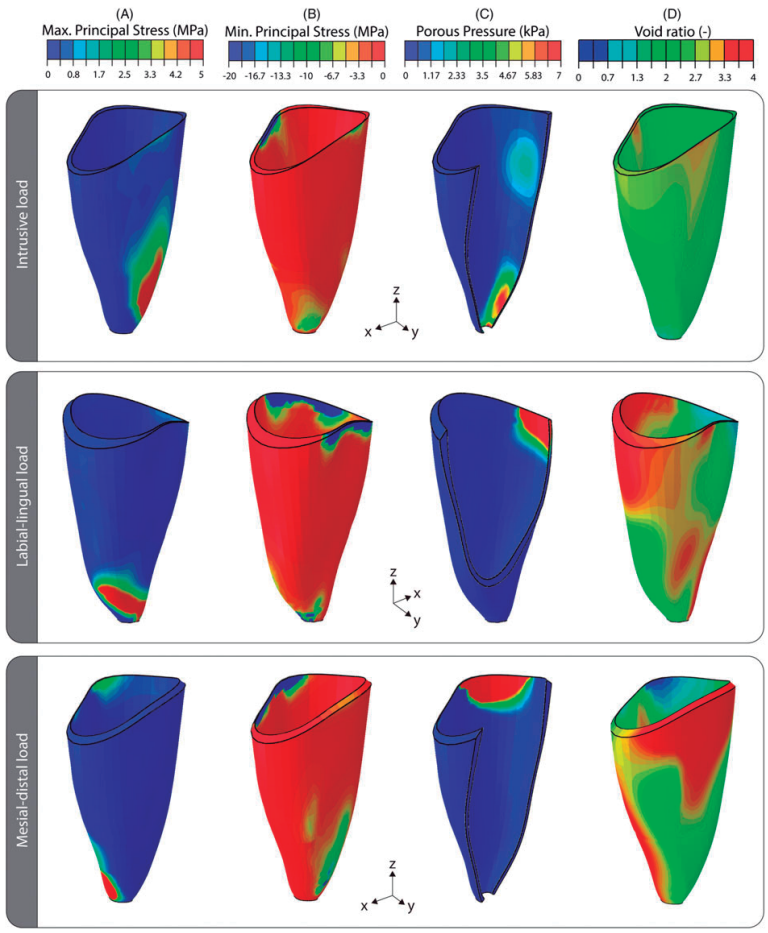

FIGURE A2 Distribution of A, maximum principal stress, B, minimum principal stress, C, porous pressure, and D, void ratio in the periodontal ligament (PDL) after the first cycle of applying a 360-N load at intrusive, labial-lingual, and mesial-distal directions (ordered from top to bottom)

As mentioned in Section 3, the apical region of the bone is mainly compressed when an intrusive load is applied (Figure A3). Moreover, the curved shape of the canine tooth compresses the bone at the middle and alveolar crest regions. On the other hand, lateral forces cause compressive stresses on two opposite areas of the apical and alveolar crest regions of the bone (Figure A3). The stress values on the bone are higher for lateral loads than for intrusive loads, especially in the layer of the apical region.

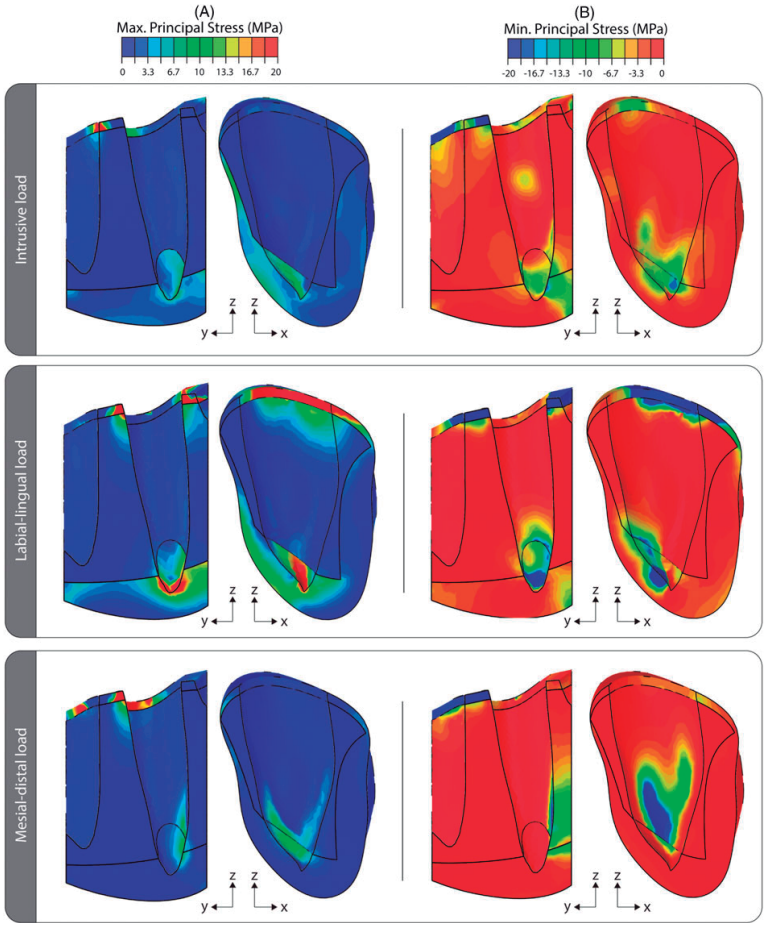

FIGURE A3 A, Maximum and B minimum principal stress distributions in the cortical and trabecular portions of the mandibular bone after the first cycle of applying a 360-N load at intrusive, labial-lingual, and mesial-distal directions (ordered from top to bottom)

APPENDIX B

ALGORITHMIC PROCEDURE FOR IMPLEMENTATION OF THE POROUS FIBROUS HYPERELASTIC DAMAGE MATERIAL MODEL

1. A database with the mechanical variables and $D_f|^k$, $\eta|^k$ and $\Xi_t^m\big|^k$ at k time point is created.
2. The initial elastic stress tensor is computed.
3. The value of the fourth invariant $\widetilde{I_4}$ is obtained by Equation 2.
   3.1. If $\widetilde{I_4} < 1$:

$$\psi_m = \frac{2\mu}{\alpha^2}\left[\widehat{\lambda}_1^{\alpha} + \widehat{\lambda}_2^{\alpha} + \widehat{\lambda}_3^{\alpha}\right) \; and \; \psi_f = 0$$

   3.2. Otherwise, if $\widetilde{I_4} \geq 1$:

$$\psi_m = C_1 \cdot \left(\widetilde{I}_1 - 3\right) \; and \; \psi_f = \frac{k_1}{2 \cdot k_2}\left\{ \exp\left[k_2 \cdot \left(\widetilde{I}_4 - 1\right)^2\right] - 1\right\}$$

      3.2.1. The equivalent strain of the fibrous term is defined by Equation 14.
      3.2.2. The damage is checked:
         3.2.2.1. If $\Xi_s\big|^k > \Xi_t^m\big|^k$, the $D_f|^{k+1}$ parameter is computed by Equation 19, and its value is updated.
         3.2.2.2. Otherwise, if $\Xi_s\big|^k \geq \Xi_t^m\big|^k$, the damage is not updated $D_f|^{k+1} = D_f|^k$.
4. The damage variable η and the continuous function $\Phi(\eta)$ are defined by Equations 12 and 13.
   4.1. If $\psi_{dev}\big|^k > \psi_{dev}^m\big|^k$ update $\psi_{dev}^m\big|^{k+1}$ with $\psi_{dev}|^k$ value.
   4.2. Otherwise, if $\psi_{dev}\big|^k \leq \psi_{dev}^m\big|^k$, not update $\psi_{dev}^m\big|^k$ value.
5. The Cauchy stress tensor of the solid matrix is computed as $1/J_{el}$ times the push-forward of $\boldsymbol{S}$ [86,87] by the following expression:

$$\overline{\boldsymbol{\sigma}}\big|^{k+1} = J^{-1}\boldsymbol{\chi}_*(\boldsymbol{S})$$

where the second Piola–Kirchhoff stress $\boldsymbol{S}$ tensor consists of the deviatoric and volumetric contributions ($\boldsymbol{S}_{dev}$ and $\boldsymbol{S}_{vol}$, respectively) for the following strain energy density function:

$$\begin{aligned}\psi\left(\widetilde{\boldsymbol{C}}, \mathbf{M}, D_f, \eta\right) &= \psi_{dev}\left(\widetilde{\boldsymbol{C}}, \mathbf{M}, D_f, \eta\right) + \psi_{vol}(J_{el}) = \psi_{dev}\left(\widetilde{I}_1, \widetilde{I}_4, D_f, \eta\right) + \psi_{vol}(J_{el}) \\ &= \eta\psi_m\left(\widetilde{I}_1\right) + \eta(1 - D_f)\psi_f\left(\widetilde{I}_4\right) + \psi_{vol}(J_{el}) + \Phi(\eta)\end{aligned}$$

Therefore:

$$\boldsymbol{S}(\boldsymbol{C}, \mathbf{M}) = \boldsymbol{S}_{dev} + \boldsymbol{S}_{vol} = 2\left[\frac{\partial \psi_{dev}}{\partial \boldsymbol{C}} + \frac{\partial \psi_{vol}}{\partial \boldsymbol{C}}\right];$$

$$\boldsymbol{S}(\boldsymbol{C}, \mathbf{M}) = 2\left[\eta\frac{\partial \psi_m\left(\widetilde{I}_1\right)}{\partial \widetilde{I}_1} \cdot \frac{\partial \widetilde{I}_1}{\partial \widetilde{\boldsymbol{C}}} \cdot \frac{\partial \widetilde{\boldsymbol{C}}}{\partial \boldsymbol{C}} + \psi_m\frac{\partial \eta}{\partial \boldsymbol{C}} + \eta(1 - D_f)\frac{\partial \psi_f\left(\widetilde{I}_4\right)}{\partial \widetilde{I}_4} \cdot \frac{\partial \widetilde{I}_4}{\partial \widetilde{\boldsymbol{C}}} \cdot \frac{\partial \widetilde{\boldsymbol{C}}}{\partial \boldsymbol{C}} + \; (1 - D_f)\psi_f\frac{\partial \eta}{\partial \boldsymbol{C}} - \eta\psi_f\frac{\partial D_f}{\partial \boldsymbol{C}} + \frac{\psi_{vol}(J_{el})\partial J_{el}}{\partial J_{el} \quad \partial \boldsymbol{C}} + \frac{\partial \Phi \partial \eta}{\partial \eta \partial \boldsymbol{C}}\right]$$

6. The total stress, $\boldsymbol{\sigma}$, in the fully saturated tissue with the porous contribution coupled is defined by Equation 12.
7. The initial elastic modulus [86,87] is calculated as $1/J_{el}$ times the push-forward of the elasticity tensor $\mathbf{C}$ by:

$$\mathbf{c}\big|^{k+1} = J^{-1}\boldsymbol{\chi}_*(\mathbf{C})$$

where the elasticity tensor is obtained from the second Piola–Kirchhoff stress tensor by:

$$\mathbf{C} = \mathbf{C}_{des} + \mathbf{C}_{vol} = 2\frac{\partial \boldsymbol{S}(\boldsymbol{C}, \mathbf{M})}{\partial \boldsymbol{C}} = 4\left[\frac{\partial^2 \psi_{dev}(\boldsymbol{C}, \mathbf{M})}{\partial \boldsymbol{C} \otimes \partial \boldsymbol{C}} + \frac{\partial^2 \psi_{vol}(J_{el})}{\partial \boldsymbol{C} \otimes \partial \boldsymbol{C}}\right]$$

Manuscript 4: In silico study of cuspid' periodontal ligament damage under parafunctional and traumatic conditions of whole-mouth occlusions. A patient-specific evaluation

Javier Ortún-Terrazas, José Cegoñino, Amaya Pérez del Palomar

Abstract

Background and objective: Although traumatic loading has been associated with periodontal ligament (PDL) damage and therefore with several oral disorders, the damage phenomena and the traumatic loads involved are still unclear. The complex and weakness structure of the PDL difficulties its experimental study, requiring of multiscale simulations. In this study, a new multiscale methodology to analyse the damage phenomena in the collagen network and the extracellular matrix of the PDL caused by parafunctional and traumatic occlusal forces was proposed. **Methods:** The entire human mandible and a portion thereof containing a full cuspid tooth were separately modelled using finite element analysis based on computed tomography and micro-computed tomography images, respectively. The first model was experimentally validated by occlusion analysis and subjected to the muscle loads produced during hard and soft chewing, traumatic cuspid occlusion, grinding, clenching, and simultaneous grinding and clenching. The occlusal forces computed by the first model were subsequently applied to the micro-sized model to evaluate damage to the collagen network and the extracellular matrix of the PDL. **Results:** Early occlusal contact on the left cuspid tooth guided the mandible to the more occluded side (16.5% greater) and absorbing most of the lateral load. The intrusive occlusal loads on the posterior teeth were 0.77–13.3% greater than those on the cuspid. Damage to the collagen network and the extracellular matrix of the PDL was observed in traumatic and grinding conditions, mainly due to fibre overstretching (>60%) and interstitial fluid overpressure (>4.7 kPa), respectively. **Conclusions:** Our findings provide important biomechanical insights into the determination of damage mechanisms and the key role of the porous-fibrous of the PDL in parafunctional and traumatic loading scenarios. Besides, the 3D loading conditions computed will help to future researches in the design of new orthodontics appliances and encourage the application of computing methods in medical practice.

Graphical abstract

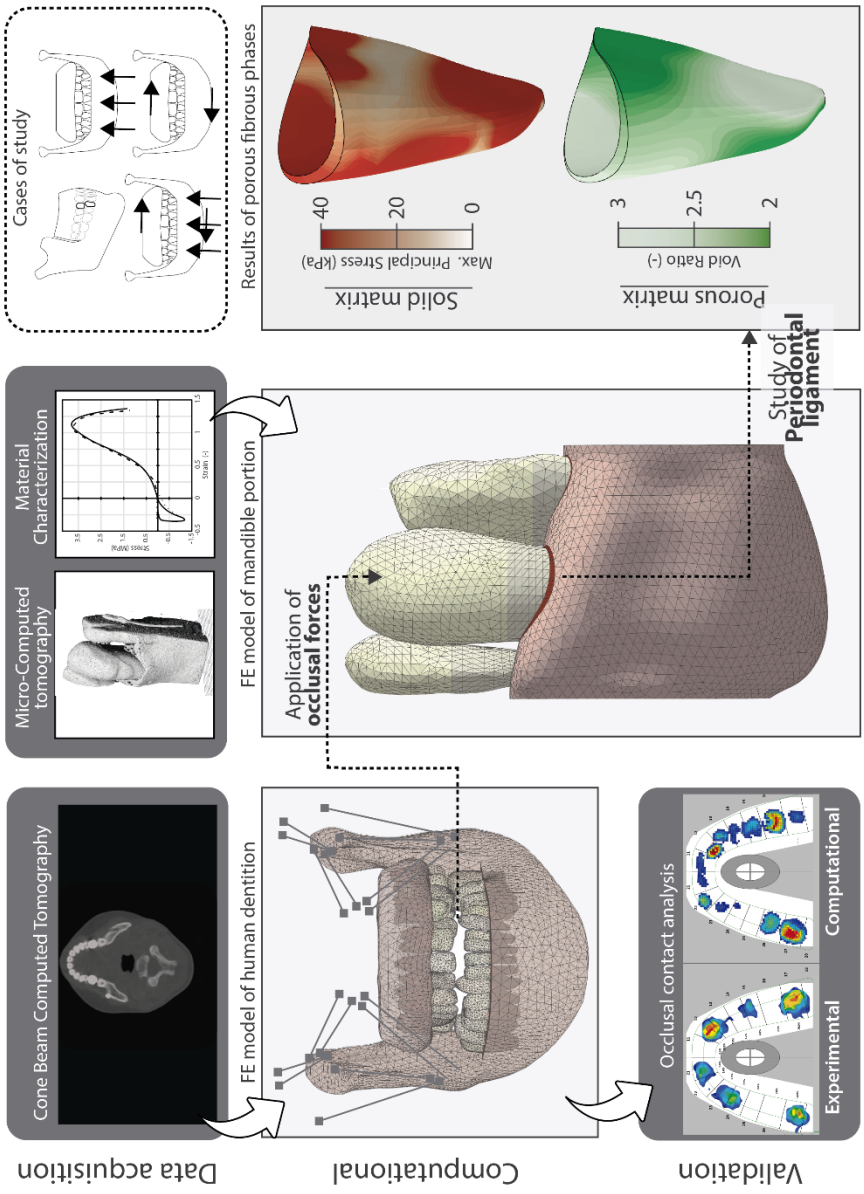

Computer Methods and Programs in Biomedicine 184 (2020) 105107

Contents lists available at ScienceDirect

Computer Methods and Programs in Biomedicine

journal homepage: www.elsevier.com/locate/cmpb

In silico study of cuspid' periodontal ligament damage under parafunctional and traumatic conditions of whole-mouth occlusions. A patient-specific evaluation

Javier Ortún-Terrazas*, José Cegoñino, Amaya Pérez del Palomar

Group of Biomaterials, Aragon Institute of Engineering Research (I3A), University of Zaragoza, Zaragoza, Spain

ARTICLE INFO

Article history:
Received 17 July 2019
Revised 28 September 2019
Accepted 1 October 2019

Keywords:
Periodontal ligament damage
Multiscale analysis
Occlusal trauma
Porous fibrous behaviour
Finite element method
Micro-computed tomography

ABSTRACT

Background and objective: Although traumatic loading has been associated with periodontal ligament (PDL) damage and therefore with several oral disorders, the damage phenomena and the traumatic loads involved are still unclear. The complex composition and extremely thin size of the PDL make experimentation difficult, requiring computational studies that consider the macroscopic loading conditions, the microscopic composition and fine detailed geometry of the tissue. In this study, a new methodology to analyse the damage phenomena in the collagen network and the extracellular matrix of the PDL caused by parafunctional and traumatic occlusal forces was proposed.

Methods: The entire human mandible and a portion thereof containing a full cuspid tooth were separately modelled using finite element analysis based on computed tomography and micro-computed tomography images, respectively. The first model was experimentally validated by occlusion analysis and subjected to the muscle loads produced during hard and soft chewing, traumatic cuspid occlusion, grinding, clenching, and simultaneous grinding and clenching. The occlusal forces computed by the first model were subsequently applied to the single tooth model to evaluate damage to the collagen network and the extracellular matrix of the PDL.

Results: Early occlusal contact on the left cuspid tooth guided the mandible to the more occluded side (16.5% greater in the right side) and absorbed most of the lateral load. The intrusive occlusal loads on the posterior teeth were 0.77–13.3% greater than those on the cuspid. According to our findings, damage to the collagen network and the extracellular matrix of the PDL could occur in traumatic and grinding conditions, mainly due to fibre overstretching (>60%) and interstitial fluid overpressure (>4.7 kPa), respectively.

Conclusions: Our findings provide important biomechanical insights into the determination of damage mechanisms which are caused by mechanical loading and the key role of the porous-fibrous behaviour of the PDL in parafunctional and traumatic loading scenarios. Besides, the 3D loading conditions computed from occlusal contacts will help future studies in the design of new orthodontics appliances and encourage the application of computing methods in medical practice.

1. Introduction

The stomatognathic system provides the complex function of chewing by the synergic activity of the elevator and depressor muscles that moves the mandible along the contact surfaces of the temporomandibular joints (TMJs) and that is limited by the occlusal surfaces of the teeth [1]. The occlusal reaction forces are meanwhile absorbed by the periodontal ligaments (PDLs) which play a key role in transferring them to the surrounding bone. Hence, PDL damage can result in a variety of disorders ranging from lesser to greater severity, including loss of the connective matrix, pathologic tooth movement, bone resorption, malocclusions, TMJ disorders, and myalgia [2,3]. Understanding the biomechanical

* Corresponding author at: Aragon Institute of Engineering Research (I3A), School of Engineering and Architecture, University of Zaragoza, Calle María de Luna 3, Zaragoza 50018, Spain.
E-mail address: javierortun@unizar.es (J. Ortún-Terrazas).

https://doi.org/10.1016/j.cmpb.2019.105107

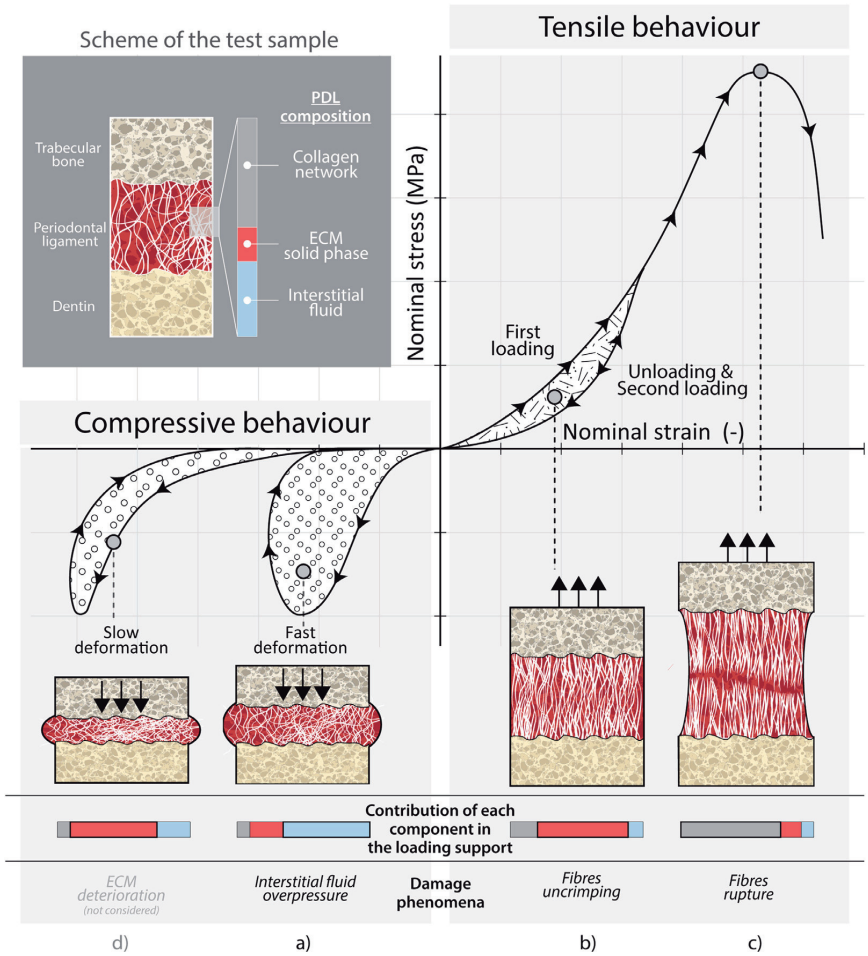

Fig. 1. Top grey box: tissue sample in relaxed state with crimped collagen fibres and scheme of the PDL composition. Below: an schematic showing an axial tensile-compressive test of a PDL until rupture with the representation of the fibres and the interstitial fluid of the tissue at different stages of the tension/compression test: a) tissue compressed with significant interstitial fluid contribution to the loading support; b) tissue partially stretched with fewer fibre entanglements and a high ECM solid phase contribution to the loading support; c) tissue overstretched and fibrous network almost completely ruptured; d) overcompression resulting in complete fluid extrusion and damage to the PDL's dry ECM. (This damage phenomenon was not considered in this study).

response of the PDL is crucial in order to elucidate its role in the development of these disorders [4–7]. Although several experimental [8,9] and computational [9–11] studies have attempted to describe the processes involved in PDL damage, it is still unclear how mechanical loading under traumatic and parafunctional conditions affects the health of the PDL. Moreover, study of the PDL is complicated by its complex mechanical and anatomical composition.

Anatomically, the PDL is a soft connective tissue composed of an extracellular matrix (ECM) in which a fibrous collagen network is embedded [12] and elastin fibrils are randomly distributed [13] (Fig. 1). The collagen network is mainly composed of collagen types I (approximately 80%) and III (about 15%), but also of types IV, V, VI, XII and XIV in small quantities [14]. The non-fibrous component of ECM is composed by lymph vessels, blood vessels and the ground substance which includes proteoglycans, glycoproteins, hyaluronan and mainly, the interstitial fluid (about 70% of the ground substance) [14,15]. Biomechanically, the fibrous network architecture has a key role in the transversally isotropic tensile behaviour of the PDL [9,16], while the rest of the ECM components cause an almost viscous-hyperelastic isotropic behaviour. Elastin fibrils contribute to ECM consistency and the fluid phase of the ECM generates a viscoelastic response to compression, absorbing most of the compressive load [15–17]. The viscoelastic behaviour confers the ligament with an almost incompressible response at fast strain rates and a highly compressible behaviour at slow strain rates [16,18]. Furthermore, excessive compression or fast strain-rates can hinder interstitial fluid flow, leading to damage of the ECM (Fig. 1a) [19]. In the unloaded state, the collagen fibres are wavy and partially disorganized [9,11,20] (Fig. 1b). Stretching of the tissue results in progressive uncrimping and alignment of the fibres, leading to a stiffer PDL response when the fibres are geometrically aligned (Fig. 1b) [9,16]. Thus, if the tissue is unloaded and immediately loaded again, the fibre entanglements

become disentangled [10,21] and some fibres are ruptured [22], softening the tissue mainly at the toe region. The network's architecture plays, therefore, a key role in the fatigue behaviour of the network, as it was recently demonstrated in Dhume et al. multiscale study [22]. When fibres are uncrimped and the tissue continues being stretched under its stretching limit, the tissue stiffness become almost linear due to fibre are already aligned and uncrimped. Any further stretching causes complete rupture of the tissue (Fig. 1c). In summary, fast compressive strain rates and cyclic loads/overstretching of the PDL can lead to progressive damage of the ECM and the collagen network, respectively.

These complex damage phenomena significantly complicate attempts to perform *in vivo* and non-destructive experimental analyses [23]. Fortunately, computational methods such as finite element (FE) analysis enable non-destructive evaluation of PDL damage. However, most FE models are simplified by assuming that tooth's occlusal forces are almost oriented along tooth's long axis; simplified PDL geometry; and homogeneous or non-time dependent behaviour of the PDL.

The assumption of tooth's occlusal forces almost aligned with the tooth axis is mainly due to that fact that current devices do not enable measurement of the direction of occlusal forces in 3 dimensions [24]. FE models that include accurate definitions of tooth surfaces and of PDL damping behaviour would allow successful computation of occlusal loads on the dentition of a specific patient. Some authors [25–27] have used micro-computed tomography (μCT) scanning to avoid simplifying the occlusal surfaces and to take into account the irregular thickness of the PDL. Although some computational studies have characterized the viscous [4,10,28,29], fibrous [5,9] or porous-fibrous [16] behaviour of the PDL, few have considered the softening caused by the disentangled of the fibres entanglements, the alignment of the fibres and the damage of the chemical crosslinks at low strains or the damage caused by the rupture of the tissue at higher strains [9,10,21]. Consequently, the relationship between PDL damage and mechanical overload in realistic traumatic conditions remains unknown. No previous *in silico* study has analysed the PDL damage response under different 3D loading scenarios, taking into account the non-uniform thickness, the porous-fibrous structure of the PDL and the damage phenomena to which it was subjected.

In this study, we evaluated the mechanical response of the PDL and the damage it sustains when subjected to normal, parafunctional, and traumatic occlusal forces using an *in silico* approach that considers the 3D loading conditions, micromorphology, and porous-fibrous biological composition of the PDL through models of different scales. To this end, a FE model of a full dentition was subjected to various combinations of muscular forces that produced different occlusal conditions. Next, the occlusal responses gathered from the full dentition model were applied to a single tooth model of the left cuspid with fine detail that took into account the non-uniform thickness and porous-fibrous structure of the PDL and the damage phenomena to which it is subjected.

2. Material and methods

2.1. FE model of the full dentition

A 3D model of a complete dentition was developed from data of a 44-year-old male with a functional crossbite but with no periodontal diseases and with no facial asymmetry (chin deviation < 4 mm from the facial midline). The data was obtained as a part of an orthodontic treatment planning for the correction of the malocclusion and to push forward the left lateral incisor of the superior arch. It was digitalized by cone beam computed tomography (CBCT) (Vatech PaX-i 3D Green, Vatech Spain) using a 90-kVp tube voltage, tube current of 4 mA, field of view (FOV) of 20 cm $\times$ 19 cm, an acquisition time of 24 s and a voxel size of 0.6 mm. The images were output in a 14-bit grey scale and 16,384 shades of grey. The cylindrical reconstruction of the dataset consisted of 210 images with an interscan distance of 0.60 mm. The hard tissues were automatically segmented by Mimics software (Mimics, v.19.; Materialise, Leuven, Belgium) using threshold levels of 226 [30] and 1688 [31] Hounsfield unit (HU) for osseous and dental regions respectively .The PDL was defined as a 0.2-mm-thick layer around each tooth [32,33] (Fig. 2a). Next, the model was meshed via a mesh convergence process using 1,120,179 elements in Abaqus software (Abaqus 6.14, Simulia, Rhode Island, USA).

Linear elastic properties were assigned to all tissues, except for the PDLs of this model, to which non-linear hyperelastic properties [34] were assigned (Table A.2). In the full dentition model, the porous fibrous properties were not considered for the definition of PDLs' behaviour in order to avoid excessively increasing the computational cost in Abaqus. Whereas in the single tooth model which will be later explained, porous and fibrous properties were considered.

The upper nodes of the maxilla were fixed, and the nodes of the condyles were linked to the point at which both condylar long axes are intersected (point P in Fig. 2a) by rigid beam elements. Although the displacements of this point were fixed, the beam elements could rotate, allowing the rotation of the mandible along the condylar axes, following the TMJ fulcrum theory [35]. By contrast, the condylar paths were neglected since the slight translation of the condyles from the initial position of the mandible (resting position) to its position in centric occlusion (CO). The occlusal contacts were defined using a friction coefficient of 0.2 [25,36], and a penalty contact formulation. The PDLs were attached to the surrounding hard tissues by tied connections. Multiple loading conditions were simulated: hard and soft normal chewing by the right side (chewing side in Fig. 2a), traumatic cuspid-cuspid occlusion, and parafunctional conditions (grinding, clenching, and a combination of both). For each loading condition, the masticatory muscles were mimicked by connector elements that simulate the passive, active, and dampening responses of the muscles. To simulate hard and soft chewing tasks the muscles activation data of the study of Farella and coworkers [37] was used, when a piece ($1 \times 1 \times 1$ cm) of dried meat and a commercially available gum (Spearmint, Migros, Zurich, Switzerland) were respectively chewed. In the occlusal trauma simulation, only cuspid-cuspid contact was allowed.

To compare the simulation with a real voluntary clenching scenario, the patient's occlusion was experimentally recorded by piezoelectric film sensor using a T-Scan III system (Tek-Scan South Boston, MA, USA) and visualized in T-Scan v10 software. The occlusal contacts of the simulation were then compared with the experimental measurements in a common visualization environment. Additional information on the mesh, material properties, muscle forces, and occlusal analysis is provided in Appendix A.

2.2. FE model of the single cuspid tooth

A portion of a human mandible with the entire left cuspid was scanned *ex vivo* using a μCT scanner (Skyscan 1172, Bruker μCT N.V., Kontich, Belgium). The resulting tomographic images were rebuilt using a modified Feldkamp algorithm in NRecon 1.6.1.7, applying reduced artifact. The model was meshed in Abaqus using 267,913 elements (Fig. 2b).

In contrast to the FE model of the full dentition, the porous-fibrous component of the PDL [16] was accounted for by means of a porous transversally isotropic hyperelastic material model, which also incorporated damage phenomena caused by fibre uncrimping and rupture [21]. The fibres were distributed cylindrically using a cylindrical coordinate system with the Z-axis running along

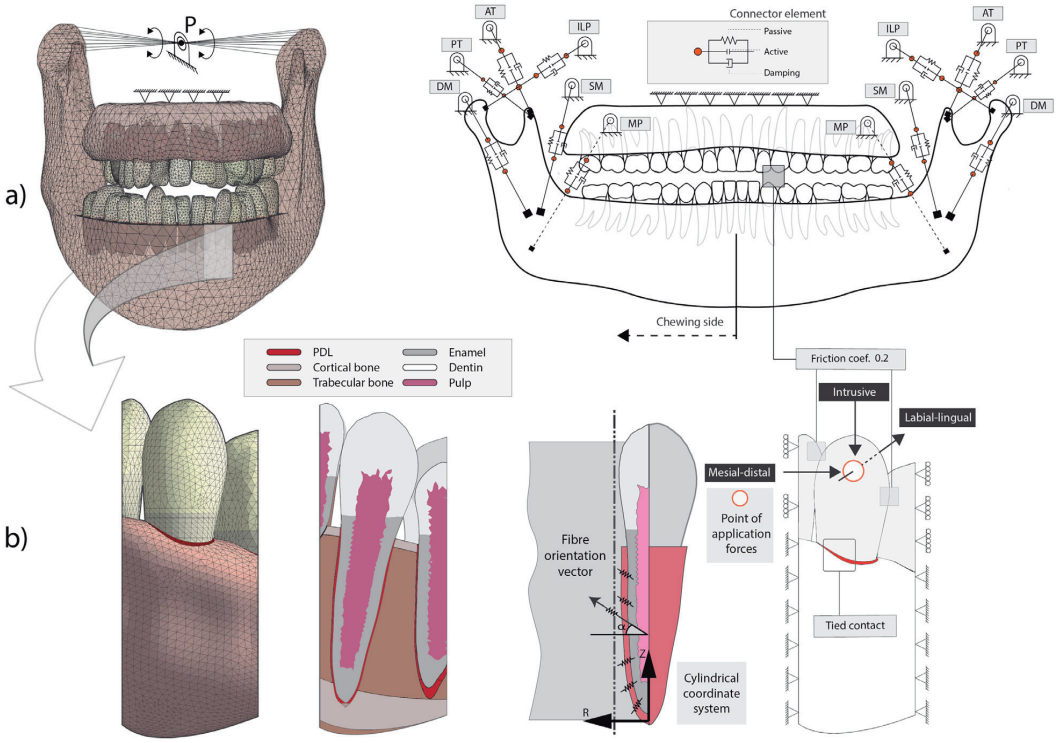

Fig. 2. a) Left: mesh of the full dentition model obtained by CBCT scan with mandible, maxilla, teeth, and PDLs. Right: schematic showing the boundary conditions applied to the model and the muscle system modelled. SM, superficial masseter; DM, deep masseter; ILP, inferior lateral pterygoid; AT, anterior temporalis; PT, posterior temporalis; MP, medial pterygoid. b) Left to right: mesh of the portion of a human mandible obtained by μCT; section of the model with color-coded components; schematic showing of the cylindrical coordinate system used to describe the orientation of the fibres bundles, and boundary conditions applied to the model.

the length of each tooth (Fig. 2b). For each fibre bundles, apical, oblique, horizontal, and alveolar crest, the preferential direction of the fibres (α vector in Fig. 2b) was defined varying α along Z-axis between 0 to −20, −20 to 55, 55 to 0, and 0 to 60° for each fibre bundles respectively, in accordance to a previous study of the literature [38]. Porous behaviour was also considered in the dentin and trabecular bone regions. The remaining tissues were defined using only elastic or hyperelastic properties, without considering viscoelastic effects. Additional information on the model, the validity of which has been previously demonstrated [16], is provided in the Appendix C.

To mimic the boundary conditions of the full mandible, the nodes located in the cutting planes of the mandible were fixed, and the movement of the cut surfaces of the lateral teeth was constrained to the mesial-distal direction (Fig. 2a). The properties of the occlusal contacts and the occlusal forces of the full dentition model were mirrored in this model. To establish the loading conditions, the occlusal reaction forces on the lower left cuspid tooth of the full dentition model were deconstructed into intrusive, labial-lingual, and mesial-distal components. The single tooth model was then loaded two times with these reaction forces with an unloading period of 1.12 s (sec) between each loading (show "opening" interval in Fig. 3b). Based on T-Scan measurements, normal chewing cycles were simulated for 1.58 s and maintained for 2.76 s to simulate parafunctional clenching (Fig. 3b). Grinding cycles lasted 0.95 s (Fig. 3c). To simulate spontaneous trauma, load was applied 25% faster than in hard and soft chewing tasks (2.70 s), in which the load was applied in 1.58 s and was removed in 1.12 s [39].

3. Results

3.1. Occlusal contacts

The occlusal analysis yielded quantifiable contact pressures for each tooth when the patient clenched with maximum voluntary force. Initially, the contacts predominantly centred on the left lower cuspid, guiding the mandible to the right (Fig. 3b). Posterior occlusion mainly occurred in teeth 16–17 and 26–27 (Fig. 3a). The full occlusion cycle ended with slightly greater loading on the right than the left side (58.2 and 41.7% of the total reaction forces, respectively) (Fig. 3a). The FE simulation yielded a similar occlusal pattern (Fig. 3a), with early contact on the left cuspid tooth (Fig. 4e) that guided the mandible slightly to the right.

3.2. Occlusal forces

Fig. 4 shows the reaction loads on the lower left cuspid and the premolars and molars of the right-hand side for different loading conditions. All simulations revealed an early cuspid-cuspid contact that decreased when the posterior teeth occluded, expect in occlusal trauma where posterior teeth did not contact. In hard and soft clenching tasks, the tangential friction on the cuspid tooth was maximum at the beginning of loading and decreased when the mandible was guided to the chewing side and posterior teeth began to occlude. Thus, the tangential friction forces on the posterior teeth were more uniform than on the cuspid tooth due to the excursive movement decreased and the occlusion is more stable at the end of the chewing cycle.

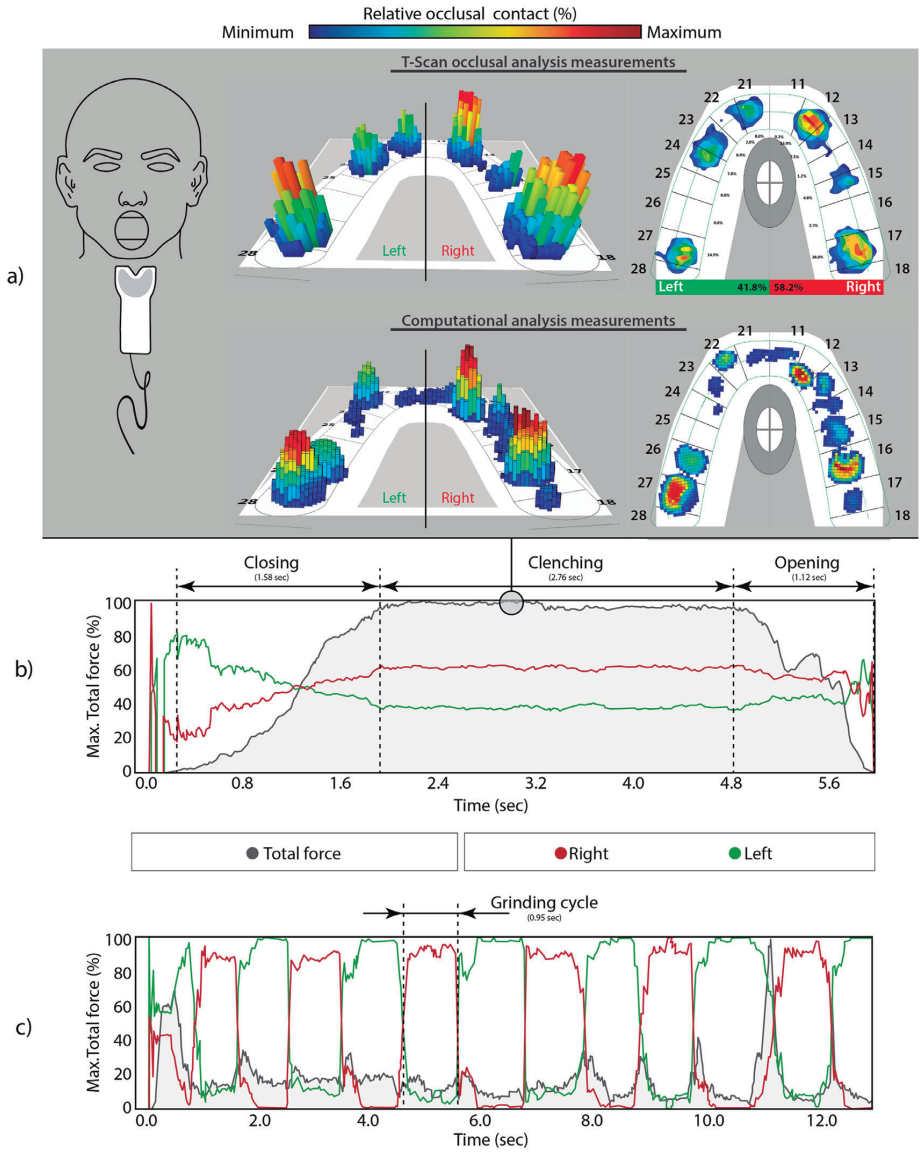

Fig. 3. a) Occlusal contacts at maximum intercuspation (MI) clenching measured by T-scan occlusal analysis sensor (top) and in a computational simulation (bottom), with maximum occlusal loads in teeth 16–17 and 26–27. Evolution of the relative percentage of the total occlusal force (black line) produced by the contacts on the teeth of the right (red line) or left (green line) dentition halves during clenching (b) and grinding (c).

In the 2 normal chewing scenarios (Fig. 4a and b), the normal reaction forces on the cuspid tooth were lower than 9 N and ranged from 17 to 120 N for the posterior teeth. The low tangential friction between posterior teeth may have been due to the fact that the lateral movements were mainly supported by the cuspid.

Maximum reaction force in the cuspid was obtained when traumatic loads were applied (Fig. 4c). In this loading scenario, 2 different slopes were observed: the first was caused by sliding of the upper canine along the mesiolingual fossa of the lower cuspid. The second slope occurred when the mesial cusp ridge of the lower cuspid contacted with the cingulum of the upper cuspid.

During grinding movement, the reaction forces on the cuspid tooth were more than 3 times greater than normal occlusal reaction forces (Fig. 4d), but were similar to those observed for clenching (Fig. 4e), during which most of the occlusion was supported by the posterior teeth.

3.3. PDL reactions

Occlusal forces (black lines in Fig. 5) were applied twice to the single tooth model to induce a reaction movement (grey discontinuous lines in Fig. 5) of the cuspid tooth for each loading.

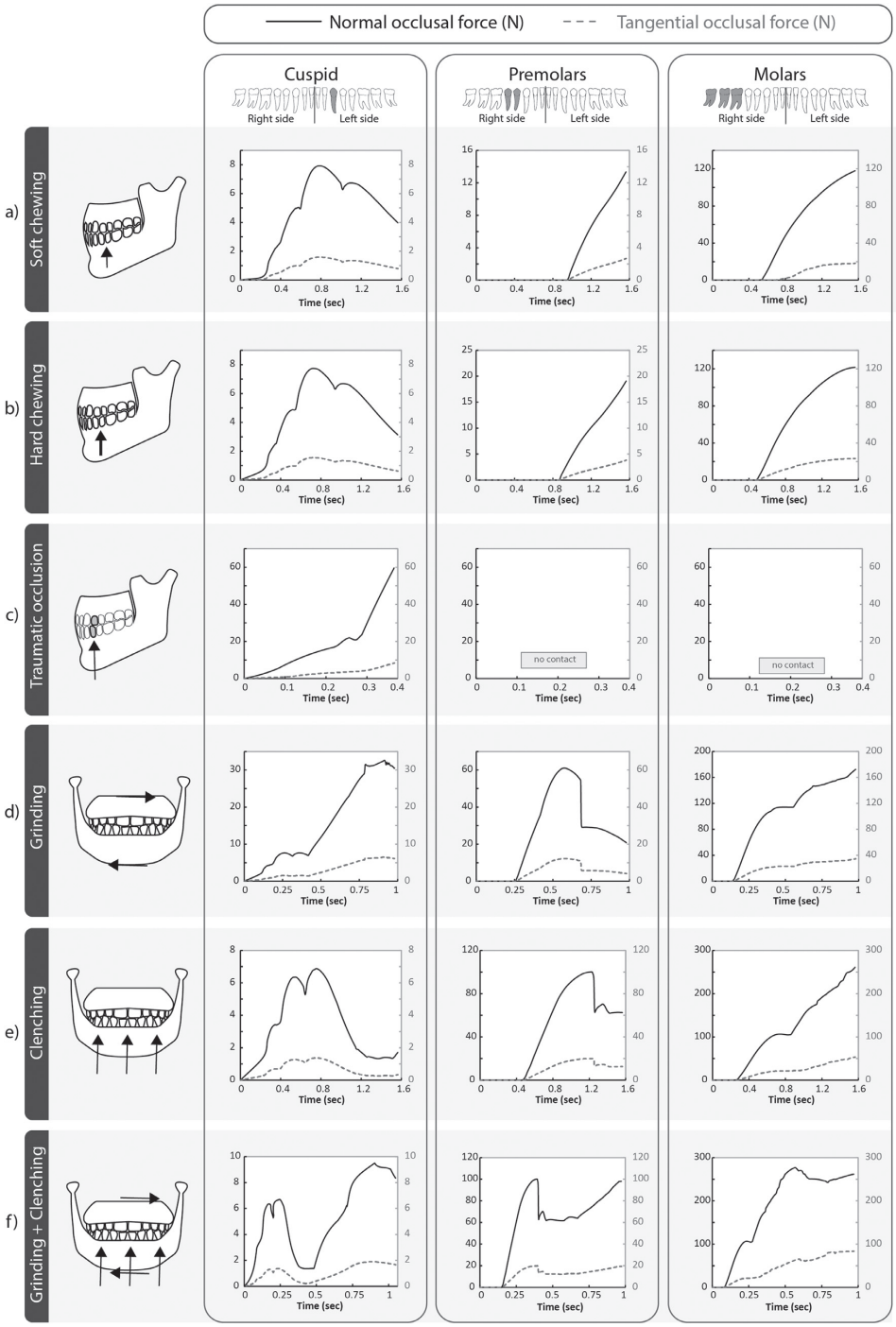

Fig. 4. Normal (black lines) and tangential (grey discontinuous lines) occlusal forces on the left cuspid, both right premolars, and the 3 right molars during a) soft chewing; b) hard chewing; c) traumatic cuspid-cuspid occlusion; d) grinding; e) involuntary clenching; and f) combined grinding and clenching.

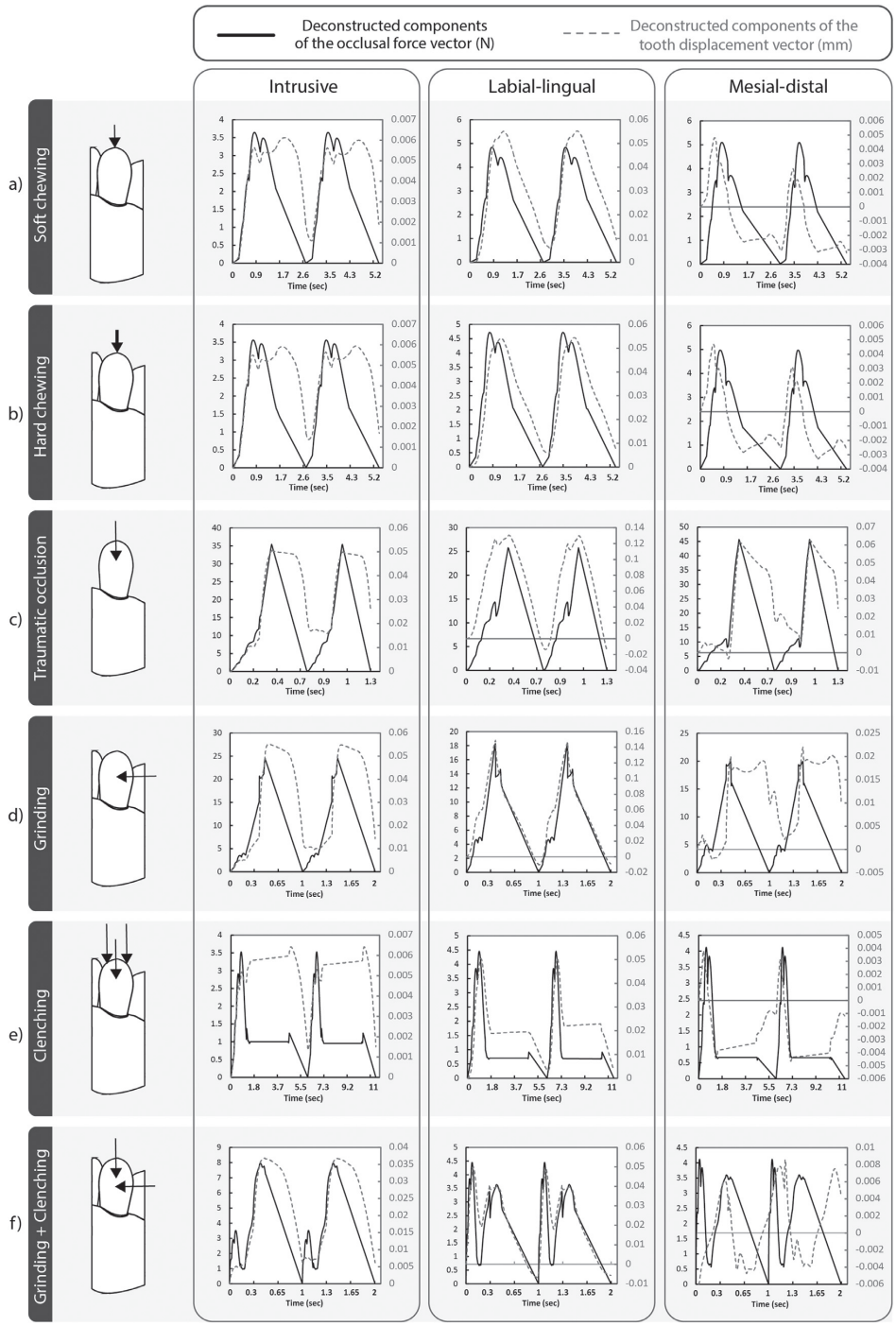

Fig. 5. Deconstructed vectors (black lines) of the occlusal force gathered from the cuspid tooth in the full dentition model and resulting displacement (grey discontinuous lines) of the cuspid tooth in intrusive, labial-lingual, and mesial-distal directions during a) soft chewing; b) hard chewing; c) traumatic cuspid-cuspid occlusion; d) grinding; e) involuntary clenching; and f) combined grinding and clenching.

Remarkably, the residual displacements observed after the first cycle due to the combination of the viscous effect of the fluid phase with the softening phenomena of the fibre uncrimping.

Normal chewing forces (Fig. 5a and b) cause the cuspid tooth to rotate, leading to compressive loads in the alveolar-crest and in the apical regions of the bone in distal and mesial directions, respectively (Fig. 6a and b). These compressive loads resulted in energy dissipation (third column in Fig. 6a and b) and therefore an increase in hydrostatic pressure (Fig. 7a and b) due to fluid flow in these areas. Nonetheless, overstretching of the fibrous network only occurred when traumatic loads were applied (Fig. 5c). Damage of the fibrous network (Fig. 6c) resulted in an abrupt increase in fluid overpressure (Fig. 7c) at the 80–100% of the first loading cycle which correspond to the 0.32–0.40 s time period. On the other hand, excessive tooth rotation in response to grinding (Fig. 5d) resulted in local stress distribution on the alveolar bone (Fig. 6d) and an interstitial fluid pressure (Fig. 7d) that was greater than the capillary blood pressure $\bar{\sigma}_h = 4.7\ kPa (35\text{mm Hg})$, which is considered by some authors [19,40] as the limit of the non-damage state. Curiously, no damage or overpressure phenomena occurred in the PDL when clenching loads were applied (Figs. 5d and 6e). Support of most of the occlusal forces by the posterior teeth likely explains the low stress state observed in these scenarios.

4. Discussion

PDL damage plays a key role in the development of many oral diseases, occlusal disorders, and the loss of bone and teeth [41]. Despite great effort by researchers studying the biomechanical responses of the PDL [9,15,21,23], the mechanisms underlying PDL damage remain unclear. Most previous studies have failed to adequately simulate the biomechanical response of the PDL by neglecting its irregular thickness and porous fibrous structure, or the variable direction of the tooth's occlusal forces during the mandibular movement.

In this *in silico* study, we studied porous-fibrous damage phenomena in the PDL using a fine detail model of a single tooth that was subjected to 3D normal, traumatic, and parafunctional loads that were first evaluated in a larger sized FE model of a full dentition.

The literature reveals several discrepancies regarding the magnitude of occlusal forces to which the PDL is subjected, with reported values ranging from 1 N [6,42,43] to over 100 N [44–46] for the same tooth. This lack of consistency is mainly due to patient-specific variations in number of contacts and the type of chewing activity analysed. Moreover, most studies do not consider viscoelastic phenomena. In the present study, we computed the magnitude and duration of occlusal forces using a macroscale model of a full dentition of a specific patient. The results of the occlusal analysis revealed a close correspondence between the computational findings and the contacts measured experimentally during clenching, with slight differences observed for the occlusion of premolar teeth on the right side (Fig. 3a) which could be caused by variations in the film' position or by tongue movements. Additionally, the gaps in the T-Scan measurements could be the result of a coarse adjustment of the device sensitivity since they coincide with the less occluded regions, or because an excessively soft material was used to simulate the film in the computational analysis. A previous study in which occlusion was analysed using T-Scan measurements [47] reported reliability errors of 2.8%. Possible explanations for the differences between our T-Scan measurements and the results produced by the model include the activation of different muscles in physiological versus modelled scenarios and deviations that may arise during image segmentation and modelling. Despite these differences, our simulations successfully mimicked the occlusal pattern, with an early contact on the left lower cuspid (Fig. 4) that partially guided the mandible to the right (Fig. 3b). This occlusal pattern is a key feature of canine protected occlusion (CPO) [48], the main premise of which is that only cuspid-cuspid contact occurs during excursive movements of the mandible, and therefore that cuspid occlusion protects the posterior teeth from lateral loads. The T-Scan data (Fig. 3b) showed that the cuspid tooth plays a key role in orienting the mandible towards maximum intercuspation position at the beginning of the chewing cycle (0.8 s). When the occlusal reaction force was decomposed into the intrusive, labial-lingual, and mesial-distal directions (Fig. 5), it was noted that the occlusal force on the cuspid tooth was mainly applied laterally (labial-lingual and mesial-distal), promoting the tooth rotation around its centre of rotation (CR) [49]. The PDL stress values produced by our model were significantly higher than those reported in previous studies [50–52], in which the lateral directions of the tooth's occlusion force vector were not considered.

As expected, no signs of collagen network damage or ECM overpressure were observed in normal chewing conditions. However, in traumatic occlusion conditions damage of the fibrous network was caused by the high occlusal load in the intrusive direction (> 60 N), resulting in partial rupture of the collagen fibres and interstitial fluid overpressure in the apical region of the PDL. Although some biological studies have empirically analysed fibrous network damage [7,53] and ECM loss [19,54] caused by overstretching of the PDL or interstitial fluid overpressure, our study is the first to provide numerical evidence of these phenomena using a material model that consider fluid and solid phase of the PDL. One unexpected result was the low reaction forces on the cuspid observed in response to parafunctional occlusal forces such as clenching or clenching/grinding. In these scenarios, the posterior teeth supported most of the chewing load, resulting in force reactions of over 300 N, in agreement with previously reported values [24]. Meanwhile, the stress state of the bone adjacent to the cuspid was slightly higher than that observed in normal chewing conditions. Future studies should consider the damage caused to the PDLs of the posterior teeth in these loading conditions. In the grinding condition, the lateral occlusal forces on the cuspid were similar to those observed for traumatic occlusion (around 20 N). Although these loads did not cause damage to the fibrous matrix, there were certain areas in which the hydrostatic pressure of the interstitial fluid was higher than that of capillary blood, indicating the potential for ECM damage. This state of overpressure could account for PDL attachment and bone loss in patients with teeth grinding habits [55].

In summary, in this *in silico* study we evaluated biological damage phenomena in a cuspid PDL under normal, traumatic, and parafunctional 3D loading conditions, using a model that took into account the non-uniform thickness and fluid-fibrous composition of the PDL. Based on our findings we hypothesize that the mechanical stimuli produced during grinding and traumatic occlusion of the cuspid lead to damage of the fibrous network and ECM of the cuspid PDL caused by fibre overstretching and high hydrostatic pressures, respectively. Our data also point to PDL damage in the posterior teeth during clenching as an emerging issue that should be investigated further in future studies.

4.1. Limitations

Our results should be interpreted bearing in mind four main limitations. First, the occlusal loads computed in this study are valid only for the specific patient studied and cannot be directly extrapolated to occlusal models corresponding to other clinical cases. Second, although PDL properties were based on experimental data from animals with chewing systems similar to those of humans, the mechanical properties of the respective

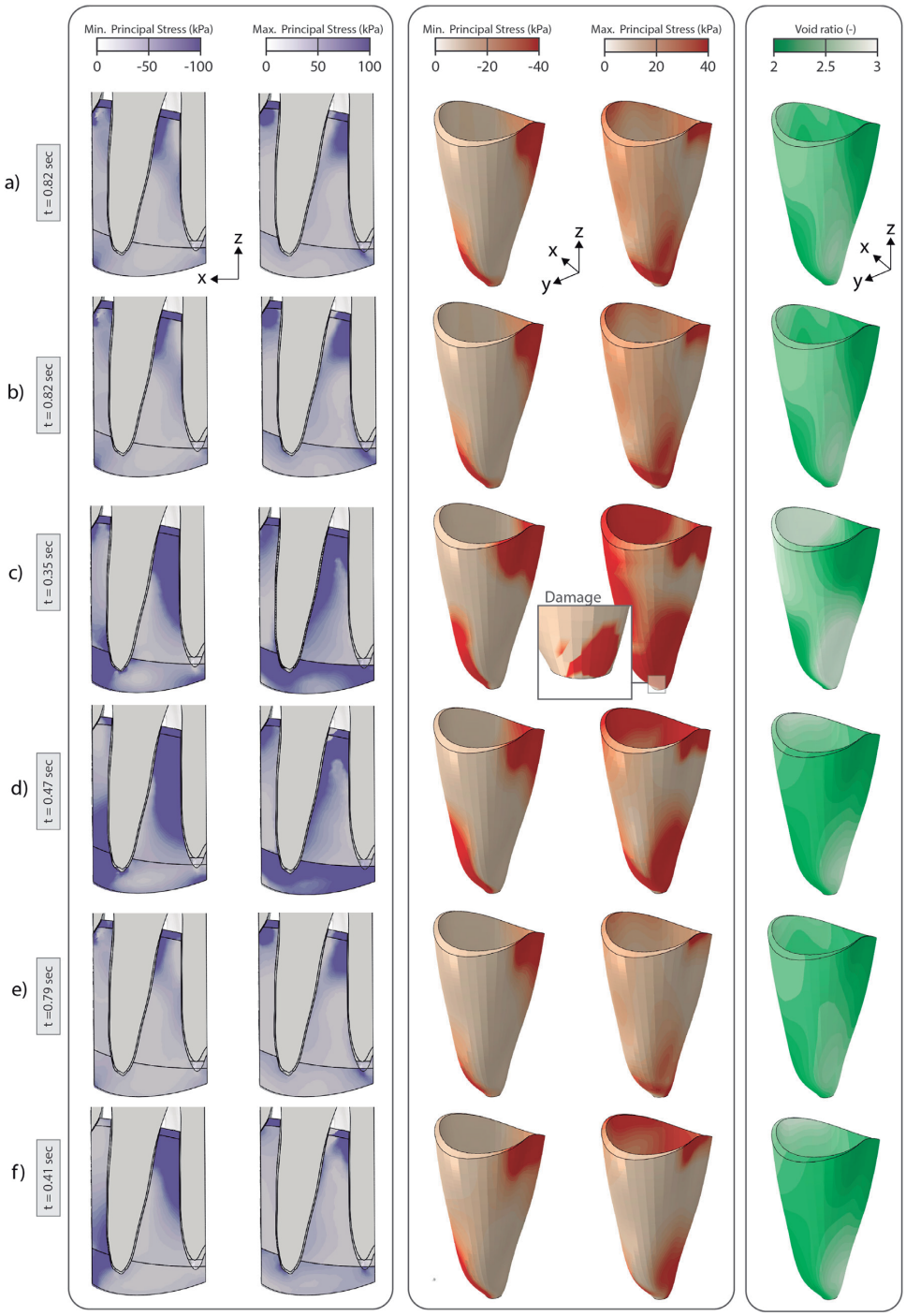

Fig. 6. Minimum (3rd principal stress) and maximum (1st principal stress) principal stresses in bone regions (first column) and in the PDL of the cuspid tooth (second column) and void ratio in the PDL (third column) at maximum loading time during a) soft chewing; b) hard chewing; c) traumatic cuspid-cuspid occlusion; d) grinding; e) involuntary clenching; and f) combined grinding and clenching.

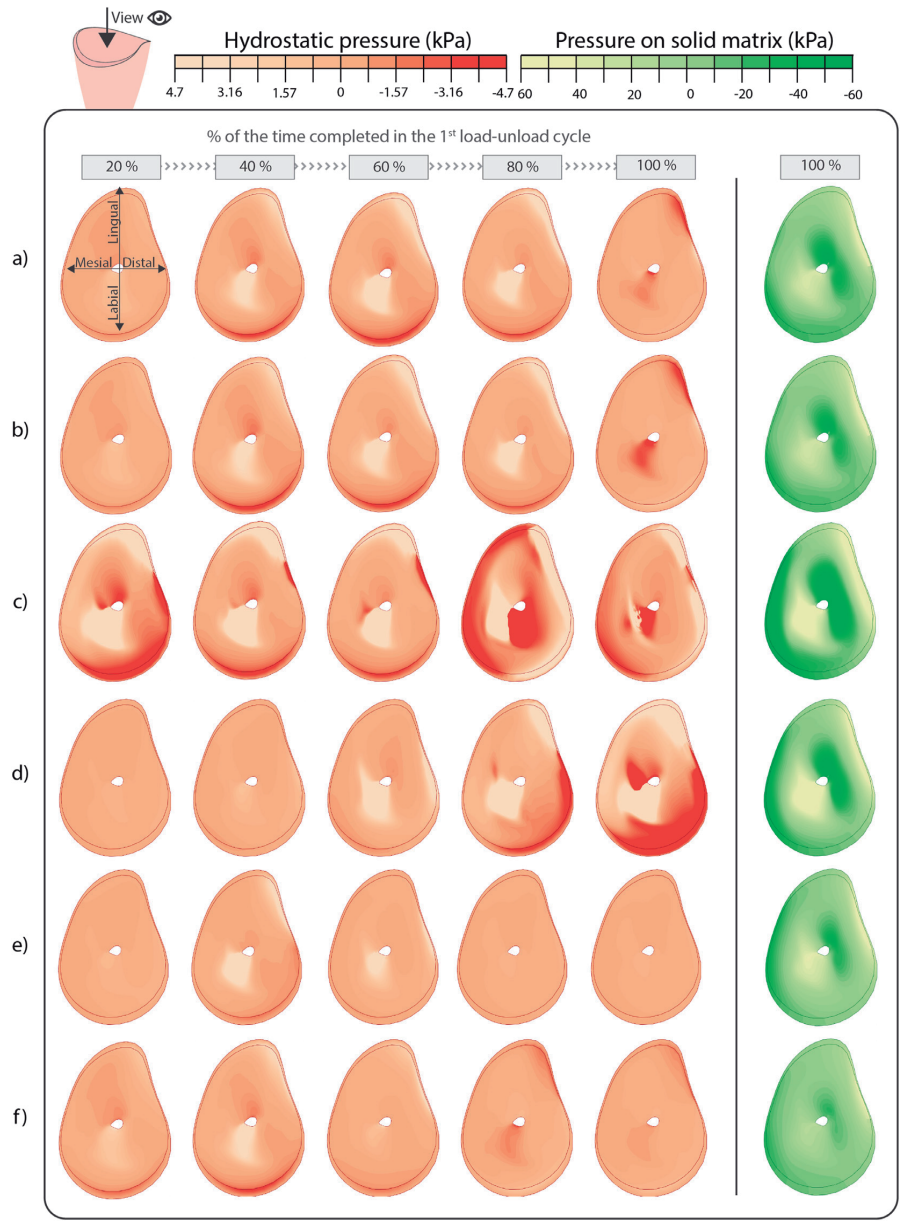

Fig. 7. Evolution (expressed as percentage of the total duration of the 1st loading-unloading cycle) of the interstitial fluid hydrostatic pressure (left) and of the pressure in the solid matrix (right) under the following load conditions: a) soft chewing; b) hard chewing; c) traumatic cuspid-cuspid occlusion; d) grinding; e) involuntary clenching; and f) combined grinding and clenching. (*Note:* PDL images show axial views).

systems may differ. Thirdly, as other studies of the literature [56–58], our model did not allow the condylar translation which is a key factor for the simulation of anteroposterior and mediolateral movements of the mandible. Finally, owing to the scarcity of data on the magnitude and sequence of muscle forces in deep muscles, we were obliged to estimate the contractile forces for each activity based on the anatomical relationships between muscles.

Bearing these limitations in mind, our results nonetheless could serve to demonstrate a role of the PDL in the origin of oral disorders and serve as a useful basis for the future design and evaluation of dental prostheses and implants. Moreover, our findings highlight several issues that could be addressed in future studies, including the relationship between the mechanobiological responses of the PDL, PDL damage, and the evolution of tooth movement.

5. Conclusion

Within the limitations of this study, we can draw the following conclusions:

1. Early contact of the cuspid tooth could be the main responsible for absorbing lateral occlusal forces, which may serve to validate the basic premise of canine protected occlusion.
2. The response of the PDL to occlusal forces seems to be highly dependent on time and it could be characterised by a persisting stress state between cycles of occlusal forces and residual displacement.
3. In grinding conditions, the PDL of the cuspid tooth seems to be subjected to high lateral compressive loads that could cause ECM damage.
4. Traumatic cuspid-cuspid occlusion could result in deterioration of the fibrous network and the ECM of the PDL which could be caused by fibre overstretching and interstitial fluid overpressure, respectively.

Funding

This work was supported by the Spanish Ministry of Economy and Competitiveness (project DPI 2016–79302-R), the European Social Funds and Regional Government of Aragon (grant 2016/20) and Ibercaja- Cai Fundation (grant IT 4/18).

Declaration of Competing Interest

The authors have no conflicts of interest.

Appendix A. Details of the FE model of the full dentition

The 3D model of the full dentition consisted of a portion of the superior maxilla, the mandible, and the 16 teeth of each arch with their respective periodontal ligaments (PDLs) (Fig. 2a). Hard tissues were segmented by Mimics software (Mimics, v.19.; Materialise, Leuven, Belgium). Firstly, osseous and dental regions of the model were separated through the respective segmentation of the database with threshold levels of 226 HU [1] and 1688 HU [2]. Then, the trabecular bone and the enamel of each tooth were respectively segmented by Mimics default threshold levels of 148 HU and 1553 HU. The results of enamel and trabecular bone segmentation was subtracted from the original segmentation mask to differentiate the cortical and dentin regions. Finally, the pulp of each tooth was defined by the gap inside each tooth.

Mesh

The finite element (FE) mesh was generated using a free meshing technique of 3D solid elements and was refined until further refinement resulted in differences of less than 7%. Except for the PDL, all tissues were meshed using second order tetrahedral elements with mean dimensions of 0.20 mm in all directions and a maximum deviation factor of 0.1. Each PDL was meshed using a second order hexahedral hybrid element along its thickness to avoid excessively increasing the computational cost (Table A.1). Hybrid formulation was required to simulate the incompressible behaviour of the PDL.

Mechanical behaviour of the PDL

The behaviour of the PDL was defined by a nonlinear hyperelastic material model using the fifth order Ogden strain energy function [3], as follows:

$$\psi = \sum_{i=1}^{5} \frac{2\mu_i}{{\alpha_i}^2}\left(\bar{\lambda}_1^{\alpha_i} + \bar{\lambda}_2^{\alpha_i} + \bar{\lambda}_3^{\alpha_i} - 3\right) + \sum_{i=1}^{5} \frac{1}{D_i}(J_{el} - 1)^{2i} \qquad (A.1)$$

Table A.1
Types of elements, number of elements, and number of nodes used in each part of the FE model of the full dentition.

FE model of the full dentition			
Region	Element type	No. of elements	No. of nodes
Maxillary cortical bone	C3D10	3,434	15,753
Maxillary trabecular bone	C3D10	67,715	104,042
Mandibular cortical bone	C3D10	28,334	117,933
Mandibular trabecular bone	C3D10	265,566	418,354
PDLs	C3D20H	390,160	2,117,913
Teeth	C3D10	364,970	241,338

where J_{el} is the elastic volume strain, μ and α are material parameters, λ_j is the stretch ratio at principal direction j (related to the strain, ε_j, by $\lambda_i = \varepsilon_j + 1$), and D is related to the bulk modulus. For almost incompressible materials ($D \simeq 0$ and $J_{el} \simeq 1$), the resolution of Eq. (A.1) leads a numerical problem which is solved in Abaqus using hybrid elements formulation. Material parameters were computed by non-linear fitting in MATLAB commercial software (MATLAB 6.0 R12 The MathWorks Inc., Natick, MA, 2000) of the analytical solution (Eq. (A.1)) to experimental compression [4] and stretch [5] data from the literature. Material parameters and the fitted curve for the characterized material model are shown in Table A.2 and Fig. A.1a, respectively.

Modelling of the muscle system

The active (F_a), passive (F_p), and damping (F_d) responses of each chewing muscle were defined through the actuator, spring, and damper components of the connector elements (CONN3D2-type element in Abaqus), respectively. The active force ($F_a = MVC \cdot F_{max}$) of each muscle depended on the activity studied and was determined by multiplying the maximum voluntary clench (MVC) percentage by the maximum force of each muscle (F_{max}) (Table A.3). Due to the lack of available data on the responses of deep muscles, we were obliged to estimate their MVC percentages for each activity based on available values for superficial muscles. For instance, for occlusal trauma the MVC percentages for deep muscles were computed by multiplying MVC values in normal chewing conditions (MVC^{HC}) by c_{OT}, a coefficient of 1.44, which was calculated as the ratio of the MVC percentages for the left superficial masseter in each condition (56.0/38.8). Likewise, the MVC percentages for grinding and involuntary clenching activities were respectively calculated by multiplying by the coefficients c_{Gr} (0.30 [11.6/38.8]) and c_{Cl} (1.72 [67/38.8]). For the grinding condition, only the activity of the muscles of the working side [6] were considered.

Passive muscle stiffness was related to muscle elongation (ε) by $F_p = k\varepsilon/(1 - \varepsilon/a) \cdot PCSA$, where k is the estimated force-length stiffness of the muscles ($k = 40\ N/cm^2$) [7], a is the passive force-length asymptote ($a = 0.7$) [8], and $PCSA$ is the cross-sectional area of the muscle.

Finally, the damping reaction ($F_d = C \cdot \dot{\Delta}l$) was defined as a function of the critical damping coefficient (C) and the stretch velocity in the longitudinal direction, $\dot{\Delta}l = \frac{d(l_F - l_0)}{dt}$ where l_F and l_0 were the instant and initial lengths of the connector respectively. All the parameters for each connector are summarized in Table A.3.

Appendix B. Occlusal analysis by T-scan

The same patient who underwent computed tomography scanning was seated in an upright position to record occlusal contacts using a piezoelectric film sensor. The sensor was inserted into a plastic U-shaped device that was previously selected to match the patient's dentition arch and shape. The U-shaped device was positioned parallel to the upper occlusal plane and was centred along

Table A.2
Mechanical properties assigned to each region of the FE model of the full dentition. E, elastic modulus; ν, Poisson coefficient.

Elastic material properties					
Region	*E (MPa)*		ν (−)		
Cortical bone	20000[a]		0.30[a]		
Dentin	15000[b]		0.31[b]		
Enamel	80000[c]		0.31[d]		
Pulp	2[e]		0.45[d]		
Trabecular bone	345[b]		0.31[b]		
Hyperelastic material properties					
PDL	μ_1 (*MPa*)	μ_2 (*MPa*)	μ_3 (*MPa*)	μ_4 (*MPa*)	μ_5 (*MPa*)
	−3420.83	1434.35	−5.56E-04	3345.65	−1365.88
	α_1 (−)	α_2 (−)	α_3 (−)	α_4 (−)	α_5 (−)
	−0.506	−0.134	13.708	−1.029	−1.397
	D_1 (MPa^{-1})	D_2 (MPa^{-1})	D_3 (MPa^{-1})	D_4 (MPa^{-1})	D_5 (MPa^{-1})
	0	0	0	0	0

[a] Lacroix and Prendergast, 2002 [9].
[b] Bergomi et al., 2011 [4].
[c] Nikolaus et al., 2016 [10].
[d] Belli et al., 2017 [11].
[e] Lin et al., 2014 [12].
[f] Ortún-Terrazas et al., 2018 [13].
[g] Ortún-Terrazas et al., 2019 [14].

Table A.3
Parameters used to compute F_a, F_p, and F_d values for each muscle on the right (R) and left (L) sides during hard (HC) and soft (SC) chewing, occlusal trauma (OT), grinding (Gr), and involuntary clenching (Cl). SM, superficial masseter; AT, anterior temporalis; DM, deep masseter; PT, posterior temporalis; IHLP, inferior head of lateral pterygoid; MP, medial pterygoid; R, right side; L, left side.

Muscle ID	$F_{max}(N)$	$PCSA\,(cm^2)$	$C\,(N/\mu m)$	*Side*	$L_0(mm)$	*MVC (%)*				
						HC	SC	OT	Gr	Cl
SM	272.8[a]	4.76[b]	0.053[c]	L	52.8	38.8[d]	35.9[d]	56.0[e]	11.6[d]	67.0[f]
				R	54.5	31.6[d]	20.3[d]	46.8 [e]	6.9[d]	66.0[f]
AT	308.0[a]	3.95[b]	0.035[c]	L	57.9	34.5[d]	29.4[d]	46.3[e]	12.9[d]	84.0[f]
				R	74.1	25.2[d]	22.5[d]	32.2[e]	8.3[d]	83.0[f]
DM	73.8[a]	2.04[b]	0.038[c]	L	55.0	23.4[g]		33.8[h]	7.0[i]	40.5[j]
				R	74.1	12.9[g]		18.6[h]	–	22.2[j]
PT	222.0[a]	1.89[b]	0.023[c]	L	70.1	8.4[g]		12.1[h]	2.5[i]	14.5[j]
				R	85.8	9.7[g]		14.0[h]	–	16.8[j]
ILP	112.8[a]	1.67[b]	0.021[c]	L	32.0	1.9[g]		2.7[h]	–	3.2[j]
				R	46.0	1.9[g]		2.8[h]	0.6[i]	3.4[j]
MP	240[a]	4.37[b]	0.060[c]	L	46.3	11.8[g]		17.1[h]	–	20.4[j]
				R	47.8	13.5[g]		19.5[h]	4.1[i]	23.4[j]

[a] Koolstra and van Eijden [15].
[b] Peck et al. [7].
[c] Langenbach and Hannam [16].
[d] Farella et al. [17].
[e] Pérez del Palomar et al. [18].
[f] Cecílio et al. [19].
[g] Computed based on the muscles forces reported by Langenbach and Hannam [16] and the F_{max} of the muscle.
[h] Computed using $MVC^{HC} \bullet c_{OT}$.
[i] Computed using $MVC^{HC} \bullet c_{Gr}$.
[j] Computed using $MVC^{HC} \bullet c_{Cl}$.

the midline between the central incisor teeth by a dentist with expertise in the occlusal analysis. The film consisted of a 100-µm-thick mylar-encased recording sensor with 1500 compressible sensitive receptor points. The sensitivity range of the film was established before recording.

The patient was instructed to chew the pressure-sensitive film, applying maximum voluntary force. The analysis was repeated 3 times and the analysis with the most balanced occlusion (Fig. 3b) was selected for comparison with the occlusal contacts produced by the FE model (Fig. 3a). The patient was also instructed to grind their teeth to record the relative percentage of the total bite force, and its distribution across both halves of the dentition (Fig. 3c).

The contact pressures in our simulations were recorded using a virtual square-shape film with a thickness of 0.1 mm. The virtual film body was manually centred along the central incisor teeth midpoint. The film was composed of 11,200 s-order quadrilateral membrane elements (M3D8-type element in Abaqus) and its behaviour was defined based on the linear elastic properties of Mylar840 (DuPont; $E = 5\,GPa$ and $\nu = 0.3$). To plot the contact results shown in Fig. 3a, the contact reaction forces of the centroid node of each element were extracted using a Python script ("Python 3.5.2, Python Software Foundation") and the values plotted on a 3D bars graph in MATLAB.

Appendix C. Details of the single tooth FE model

A portion of a human mandible was extracted from a cadaver within 4 h after death and stored frozen (−20 °C) until it was scanned. Prior to scanning, the sample was taken from the freezer and allowed to thaw at room temperature (17 °C). The soft tissues attached to the mandible were carefully removed and the cleaned

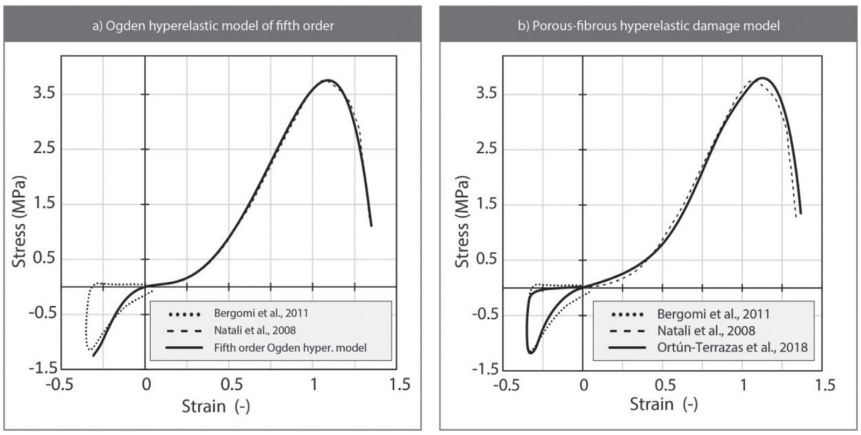

Fig. A.1. Fitted curve obtained by approximation to the experimental data published by Natali et al. (2008) and Bergomi et al. (2011) using a) fifth order Ogden hyperelastic model and b) a porous-fibrous hyperelastic damage model previously characterized by our group [14].

specimen was scanned by μCT scan (Skyscan 1172, Bruker μCT N.V., Kontich, Bélgica). μCT data was collected using 13-μm cross-sections to ensure resolution. Next, the tomographic images generated after scanning were rebuilt, the noise was reduced, and the point cloud was converted into Non-Uniform Rational Bases Splines (NURBS) using Rhinoceros software (Rhinoceros v.5, Robert McNeel & Associates, Seattle, USA). Because PDLs could not be detected by μCT, they were defined within the free space between the trabecular bone and the teeth. The model was composed of an entire cuspid tooth and 2 partial teeth (a premolar and a lateral incisal) with their respective PDLs embedded in the mandibular bone (Fig. 2b). Further information on the development of this model is provided in a previous publication by our group [13].

Mesh

Mesh refinement was performed until further refinement resulted in differences of 5% or less. The PDL of the cuspid tooth was meshed throughout its thickness using 3 first-order hexahedral elements. The other 2 PDLs were meshed along their thickness using a quadratic element; while the incomplete shape of these ligaments complicated the mesh refinement process, the data obtained from these ligaments were not the main goal of this study. Regardless, the effect of the mesh size on these PDLs was negligible given the low stress/strain values to which they were subjected. The remaining regions were meshed by tetrahedral linear elements with mean dimensions of 0.2 mm in all directions and a maximum deviation factor of 0.15. Further information on the meshing process is provided in Table C.1.

Table C.1
Types of elements, number of elements, and number of nodes used in each region of the FE model of a single tooth.

FE model of the single tooth			
Region	Element type	No. elements	No. nodes
Cortical bone	C3D4	4,118	2,315
Cuspid tooth	C3D4P	48,499	27,267
Cuspid PDL	C3D8RP	40,716	22,892
Lateral incisor PDL	C3D20	3,157	1,776
Lateral incisor tooth	C3D4P	52,547	29,543
Premolar PDL	C3D20	3,360	1,889
Premolar tooth	C3D4P	52,819	29,696
Trabecular bone	C3D4P	62,697	35,250

Mechanical behaviour of the PDL

According to previous findings [5,13,14,20,21], the PDL undergoes 2 types of softening phenomena caused by fibre uncrimping and rupture, and displays 2 different behaviours owing to its porous-fibrous structure. Therefore, energy density function (ψ) of the porous transversely-isotropic-hyperelastic-damage material model was formulated as follows:

$$\psi = \eta \cdot \left[\psi_m\left(\widetilde{I_1}\right) + \left(1 - D_f\right) \cdot \psi_f\left(\widetilde{I_4}\right)\right] + \Phi(\eta) + \psi_{vol}(J_{el}) \qquad \text{(C.1)}$$

Where ψ_m and ψ_f are the ground matrix and fibrous terms of the deviatoric component (ψ_{dev}), $D_f \in [0,1]$ is the damage parameter that explains the evolution of damage due to fibre rupture, Φ is the energy dissipated, ψ_{vol} is the volumetric term and η is the damage variable for softening due to fibre uncrimping which varies with deformation, as follows:

$$\eta = 1 - \frac{1}{r} errf\left(\frac{\psi^m_{dev} - \psi_{dev}}{m + \beta_m \psi^m_{dev}}\right) \qquad \text{(C.2)}$$

where r and β_m are dimensionless material parameters, m is a parameter with the dimensions of energy, ψ^m_{dev} is the maximum value of the deviatoric strain energy density experienced by the material during its deformation history, and *errf* is the error function defined by $errf(x) = \frac{2}{\sqrt{\pi}} \int_0^x \exp(-\omega^2) d\omega$.

The energy dissipation term Φ was defined by the Ogden-Roxburgh model as follows:

$$\Phi(\eta) = \frac{\left(m + \beta_m \psi^m_{dev}\right)}{r\sqrt{\pi}} \left\{ \exp\left[-\left(\frac{\psi^m_{dev} - \psi_{dev}}{m + \beta_m \psi^m_{dev}} \right) \right]^2 - 1 \right\} + (1 - \eta)\psi^m_{dev} \qquad \text{(C.3)}$$

To consider porous-fibrous different contributions, the terms ψ_{dev} and ψ_{vol} were described by 2 different material models according to the direction of fibre stretch. Therefore, ψ_{dev} and ψ_{vol} are described by a porous hyperfoam material formulation [22] when PDL was compressed ($\widetilde{I_4} \leq 1$), and by a porous transversely isotropic hyperelastic damage material model [23] when the tissue is stretched ($\widetilde{I_4} > 1$).

The dilatational ($\tilde{I}_1$) and deviatoric ($\tilde{I}_4$) invariants are defined as follows:

$$\tilde{I}_1 = tr\tilde{\boldsymbol{C}}; \quad \tilde{I}_4 = \boldsymbol{a}^0 \cdot \tilde{\boldsymbol{C}} \cdot \boldsymbol{a}^0 \tag{C.4}$$

where $\boldsymbol{a}^0$ is a unitary vector defining the orientation of the collagen fibres and $\tilde{\boldsymbol{C}}$ is the modified Green tensor in the reference configuration, defined by the deformation gradient $\tilde{\boldsymbol{F}}$, as $\tilde{\boldsymbol{C}}(\hat{\lambda}_i) = \tilde{\boldsymbol{F}}^T\tilde{\boldsymbol{F}}$. The stretch ($\hat{\lambda}_i$) is determined as the ratio between fibre lengths in deformed ($\boldsymbol{X}$) and reference ($\boldsymbol{x}$) configurations in direction i. The deformation gradient is therefore expressed by the Jacobian elastic tensor as $\tilde{\boldsymbol{F}} = {J_{el}}^{-\frac{1}{3}}\boldsymbol{F}$. The terms ψ_{vol} and ψ_{dev} of the energy density function are written as follows:

$$\psi_{vol} = \begin{cases} \frac{1}{\beta}\left[(J_{el})^{-\alpha\beta} - 1\right] & if\ \left(\tilde{I}_4 < 1\right) \quad (C.5) \\ \frac{1}{D}\left[\frac{(J_{el})^2-1}{2} - \ln J_{el}\right] & if\ \left(\tilde{I}_4 \geq 1\right) \quad (C.6) \end{cases}$$

$$\psi_{dev} = \begin{cases} \frac{2\mu}{\alpha^2}\left[\hat{\lambda}_1^{\alpha} + \hat{\lambda}_2^{\alpha} + \hat{\lambda}_3^{\alpha}\right] & if\ \left(\tilde{I}_4 < 1\right) \quad (C.7) \\ C_1 \cdot \left(\tilde{I}_1 - 3\right) + \left(1 - D_f\right) \cdot \frac{k_1}{2 \cdot k_2}\left\{exp\left[k_2 \cdot \left(\tilde{I}_4 - 1\right)^2\right] - 1\right\} & if\ \left(\tilde{I}_4 \geq 1\right) \quad (C.8) \end{cases}$$

In Eq. C.5, α is a dimensionless material parameter of the porous hyperfoam material, and β determines the degree of compressibility related to the Poisson ratio by $\beta = \nu/(1 - 2\nu)$. The parameter D of Eq. C.6 is related to the bulk modulus, K, by $K = 2/D$. μ and α are material parameters of the deviatoric term of the hyperfoam material model (Eq. C.7). In Eq. C.8, C_1 is a material constant related to the ground substance of the transversely isotropic material model, $k_1 > 0$ and $k_2 > 0$ are the parameters that identify the exponential behaviour due to the presence of the collagen fibres, and the damage parameter, D_f, explains the evolution of damage due to fibre rupture as follows:

$$D_f(\Xi_t^m) = \frac{1}{2}\left\{1 + \frac{\alpha_f \Xi_t^m e^{2\alpha_f\left[\left(2\Xi_t^m/\beta_f\right)-1\right]} - 1}{\alpha_f \Xi_t^m e^{2\alpha_f\left[\left(2\Xi_t^m/\beta_f\right)-1\right]} + 1}\right\} \tag{C.9}$$

where α_f and β_f are 2 material parameters and Ξ_t^m is the maximum value of Ξ_s over past history up to the current time s. Ξ_s is the equivalent strain [24] at any time s defined by $\Xi_s(\tilde{\boldsymbol{C}}) = \sqrt{2 \cdot \psi_f(\tilde{I}_4) \cdot \tilde{\boldsymbol{C}}(s)}$ where the fibrous term ψ_f corresponds to the second term of Eq. C.8.

To account for the biphasic behaviour of the PDL a porous contribution was added to the model. In the fully saturated tissue, total stress at a given point $\boldsymbol{\sigma}$ is defined [25] as follows:

$$\boldsymbol{\sigma} = (1 - e) \cdot \bar{\boldsymbol{\sigma}} - e \cdot \bar{p}_t \cdot \boldsymbol{I} - \zeta \cdot \bar{p}_t \cdot \boldsymbol{I} \tag{C.10}$$

where e is the void ratio related to the porosity of a tissue (n) by $e = n/(1-n)$, being n defined by the volume of the fluid phase V_f in the total volume of the tissue V_t, ζ is a factor that depends on

Table C.2
Mechanical properties assigned to each region of the FE model of a single tooth. E, elastic modulus; $\boldsymbol{\nu}$, Poisson coefficient; $\boldsymbol{\Upsilon_w}$, specific weight of interstitial fluid.

Elastic material model

Region	$E\,(MPa)$	$\nu\,(-)$
Pulp[a]	3	0.45
Enamel[b]	80000	0.31
Cortical bone[c]	20000	0.30

Porous elastic material model

Region	$E\,(MPa)$	$\nu\,(-)$	$k_0 \cdot 10^{-15}\ (m^2)$	$M\,(-)$	$e_0(-)$	$\Upsilon_w \cdot 10^{-6}\ (N/mm^3)$
Trabecular bone[d]	345	0.31	52.9	–	4	9.8
Dentin[d]	15000	0.31	0.038	–	4	9.8

Transversally isotropic material model

Region	$C_1(MPa)$	$D(MPa^{-1})$	$k_1(MPa)$	$k_2(-)$
Premolar PDL[e]	0.01	9.078	0.298	1.525
Incisor PDL[e]	0.01	9.078	0.298	1.525

Porous transversally isotropic material model

Region	$C_1(MPa)$	$D(MPa^{-1})$	$k_1(MPa)$	$k_2(-)$	$k_0 \cdot 10^{-15}(m^2)$	$M\,(-)$	$e_0(-)$	$\Upsilon_w \cdot 10^{-6}\ (N/mm^3)$
Cuspid PDL ($\tilde{I}_4 \geq 1$)	0.01[e]	9.078[e]	0.298[e]	1.525[e]	6.5[e]	9.5[e]	2.33[d]	9.8

Porous hyperfoam material model

Region	$\mu\,(MPa)$	$\alpha\,(-)$	$\nu\,(-)$	$k_0 \cdot 10^{-15}(m^2)$	$M\,(-)$	$e_0(-)$	$\Upsilon_w \cdot 10^{-6}(N/mm^3)$
Cuspid PDL ($\tilde{I}_4 < 1$)[d]	0.03	20.9	0.257	8.81	14.2	2.33	9.8

Fibre uncrimping

Region	$r\,(-)$	$m\,(mJ)$	$\beta_m\,(-)$
Cuspid PDL[g]	1.492	0.064	0.1

Fibres rupture

Region	$\alpha_f\,(-)$	$\beta_f\,(-)$	$\Xi_s^{max}\ (-)$
Cuspid PDL[g]	1.0	0.25	0.28

[a] Belli et al., 2017 [11].
[b] Nikolaus et al., 2016 [10].
[c] Lacroix and Prendergast, 2002 [9].
[d] Bergomi et al., 2011 [4].
[e] Ortún-Terrazas et al., 2018 [13].
[g] Ortún-Terrazas et al., 2019 [14].
[h] Wei et al. 2014 [28].

saturation, $\bar{\sigma}$ is the effective stress of the solid matrix, and $\bar{p}_t$ is the average pressure stress related to tissue permeability by the non-linear Forchheimer flow law and implemented in Abaqus. To relate permeability to deformation, the exponential function described by Argoubi and Shirazi-Adl [26] was used as follows:

$$\bar{k} = k_0\left[\frac{e(1+e_0)}{e_0(1+e)}\right]^2 exp\left[M\left(\frac{1+e}{1+e_0}-1\right)\right] \quad (C.11)$$

where k_0 and e_0 are the permeability and void ratio at zero strain, and M is a dimensionless material parameter.

The damage parameters m, r and β_m of Eq. (C.2) were defined based on the experimental data of Natali et al. [27]. Material parameters C_1, k_1, k_2, D, α_f and β_f were defined based on later experimental data published by Natali et al. [5]. Finally, parameters μ, α, β, and M were defined based on experimental compression test data from Bergomi et al. [4]. The material formulation and the characterization of aforementioned parameters have been fully described in our previous publications [13,14]. The material parameters and the material response mimicked are shown in Table C.2 and Fig. A.1b, respectively.

Appendixes references

[1] H. Lin, P. Zhu, Y. Lin, S. Wan, X. Shu, Y. Xu, Y. Zheng, Mandibular asymmetry: A three-dimensional quantification of bilateral condyles, Head Face Med. 9 (2013) 1–7. doi:10.1186/1746–160x-9–42.

[2] Y. Wang, S. He, L. Yu, J. Li, S. Chen, Accuracy of volumetric measurement of teeth *in vivo* based on cone beam computer tomography, Orthod. Craniofac. Res. 14 (2011) 206–212. doi:10.1111/j.1601–6343.2011.01525.x.

[3] R.W. Ogden, Non linear elastic deformations, 1997.

[4] M. Bergomi, J. Cugnoni, M. Galli, J. Botsis, U.C. Belser, H.W.A. Wiskott, Hydro-mechanical coupling in the periodontal ligament: A porohyperelastic finite element model, J. Biomech. 44 (2011) 34–38. doi:10.1016/j.jbiomech.2010.08.019.

[5] A.N. Natali, E.L. Carniel, P.G. Pavan, F.G. Sander, C. Dorow, M. Geiger, A visco-hyperelastic-damage constitutive model for the analysis of the biomechanical response of the periodontal ligament., J. Biomech. Eng. 130 (2008) 31004. doi:10.1115/1.2900415.

[6] A.J. Miller, Craniomandibular muscles: Their role in function and form, CRC Press, 2017. doi:10.4324/9781315150550.

[7] C.C. Peck, G.E.J. Langenbach, A.G. Hannam, Dynamic simulation of muscle and articular properties during human wide jaw opening, Arch. Oral Biol. 45 (2000) 963–982. doi:10.1016/S0003-9969(00)00071–6.

[8] van der M.J. Horst, Human Head Neck Response in Frontal, Lateral and Rear End Impact Loading - modelling and validation -, 2002. doi:10.6100/IR554047.

[9] D. Lacroix, P.J. Prendergast, A mechano-regulation model for tissue differentiation during fracture healing: analysis of gap size and loading, J. Biomech. 35 (2002) 1163–1171. doi:10.1016/S0021-9290(02)00086–6.

[10] A. Nikolaus, C. Fleck, T. Lindtner, J. Currey, P. Zaslansky, Importance of the variable periodontal ligament geometry for whole tooth mechanical function: A validated numerical study, J. Mech. Behav. Biomed. Mater. 67 (2016) 61–73. doi:10.1016/j.jmbbm.2016.11.020.

[11] S. Belli, O. Eraslan, G. Eskitaşcioğlu, Effect of Different Treatment Options on Biomechanics of Immature Teeth: A Finite Element Stress Analysis Study, J. Endod. (2017). doi:10.1016/j.joen.2017.08.037.

[12] S.-L. Lin, S.-Y. Lee, Y.-C. Lin, Y.-H. Huang, J.-C. Yang, H.-M. Huang, Evaluation of mechanical and histological properties of cryopreserved human premolars under short-term preservation: A preliminary study, J. Dent. Sci. 9 (2014) 244–248. doi:10.1016/j.jds.2013.04.010.

[13] J. Ortún-Terrazas, J. Cegoñino, U. Santana-Penín, U. Santana-Mora, A. Pérez del Palomar, Approach towards the porous fibrous structure of the periodontal ligament using micro-computerized tomography and finite element analysis, J. Mech. Behav. Biomed. Mater. 79 (2018) 135–149. doi:10.1016/j.jmbbm.2017.12.022.

[14] J. Ortún-Terrazas, J. Cegoñino, U. Santana-Penín, U. Santana-Mora, A. Pérez del Palomar, A porous fibrous hyperelastic damage model for human periodontal ligament: Application of a micro-computerized tomography finite element model., Int. j. Numer. Method. Biomed. Eng. (2019) e3176. doi:10.1002/cnm.3176.

[15] J.H.H. Koolstra, T.M.G.J.M.G.J. van Eijden, Combined finite-element and rigid-body analysis of human jaw joint dynamics, J. Biomech. 38 (2005) 2431–2439. doi:10.1016/j.jbiomech.2004.10.014.

[16] G.E.J. Langenbach, A.G. Hannam, The role of passive muscle tensions in a three-dimensional dynamic model of the human jaw, Arch. Oral Biol. 44 (1999) 557–573. doi:10.1016/S0003-9969(99)00034–5.

[17] M. Farella, S. Palla, S. Erni, A. Michelotti, L.M. Gallo, Masticatory muscle activity during deliberately performed oral tasks, Physiol. Meas. 29 (2008) 1397–1410. doi:10.1088/0967–3334/29/12/004.

[18] A. Pérez del Palomar, U. Santana-Penín, M.J. Mora-Bermúdez, M. Doblaré, Clenching TMJs-Loads Increases in Partial Edentates: A 3D Finite Element Study, Ann. Biomed. Eng. 36 (2008) 1014–1023. doi:10.1007/s10439-008–9487-y.

[19] F.A. Cecílio, S.C.H.H. Regalo, M. Palinkas, J.P.M.M. Issa, S. Siéssere, J.E.C.C. Hallak, J.P. Machado-de-sousa, M. Semprini, Ageing and surface EMG activity patterns of masticatory muscles, J. Oral Rehabil. 37 (2010) 248–255. doi:10.1111/j.1365–2842.2010.02051.x.

[20] M. Bergomi, H.W.A. Wiskott, J. Botsis, A. Mellal, U.C. Belser, Load Response of Periodontal Ligament: Assessment of Fluid Flow, Compressibility, and Effect of Pore Pressure, J. Biomech. Eng. 132 (2009) 014504. doi:10.1115/1.4000154.

[21] A.N. Natali, P.G. Pavan, E.L. Carniel, C. Dorow, A Transversally Isotropic Elasto-damage Constitutive Model for the Periodontal Ligament, Comput. Methods Biomech. Biomed. Engin. 6 (2003) 329–336. doi:10.1080/1025584031000163984 0.

[22] B. Storakers, On material representation and constitutive branching in finite compressible elasticity, J. Mech. Phys. Solids. 34 (1986) 125–145. doi:10.1016/0022–5096(86)90033–5.

[23] J.F. Rodríguez, F. Cacho, J.A. Bea, M. Doblaré, A stochastic-structurally based three dimensional finite-strain damage model for fibrous soft tissue, J. Mech. Phys. Solids. 54 (2006) 864–886. doi:10.1016/j.jmps.2005.10.005.

[24] E. Peña, B. Calvo, M.A. Martínez, M. Doblaré, On finite-strain damage of viscoelastic-fibred materials. Application to soft biological tissues, Int. J. Numer. Methods Eng. 74 (2008) 1198–1218. doi:10.1002/nme.2212.

[25] T.H. Wu, Soil mechanics, (1967).

[26] M. Argoubi, A. Shirazi-Adl, Poroelastic creep response analysis of a lumbar motion segment in compression, J. Biomech. 29 (1996) 1331–1339. doi:10.1016/0021–9290(96)00035–8.

[27] A.N. Natali, P.G. Pavan, E.L. Carniel, C. Dorow, Viscoelastic response of the periodontal ligament: An experimental-numerical analysis, Connect. Tissue Res. 45 (2004) 222–230. doi:10.1080/03008200490885742.

[28] Z. Wei, X. Yu, X. Xu, X. Chen, Experiment and hydro-mechanical coupling simulation study on the human periodontal ligament, Comput. Methods Programs Biomed. 113 (2014) 749–756. doi:10.1016/j.cmpb.2013.12.011.

References

[1] C.C. Peck, A.G. Hannam, Human jaw and muscle modelling, Arch. Oral Biol. 52 (2007) 300–304, doi:10.1016/j.archoralbio.2006.11.004.

[2] J.P. Hatch, R.S.A. Shinkai, S. Sakai, J.D. Rugh, E.D. Paunovich, Determinants of masticatory performance in dentate adults, Arch. Oral Biol. 46 (2001) 641–648.
[3] W.H. Organization, Oral Health Surveys: Basic Methods, World Health Organization, 2013.
[4] A.N. Natali, P.G. Pavan, C. Scarpa, Numerical analysis of tooth mobility: formulation of a non-linear constitutive law for the periodontal ligament, Dent. Mater. 20 (2004) 623–629, doi:10.1016/j.dental.2003.08.003.
[5] C.G. Provatidis, A comparative FEM-study of tooth mobility using isotropic and anisotropic models of the periodontal ligament, Med. Eng. Phys. 22 (2000) 359–370, doi:10.1016/S1350-4533(00)00055-2.
[6] K. Reitan, The initial tissue reaction incident to orthodontic tooth movement as related to the influence of function, Acta Odonto. Scand. 6 (1951) 1–240.
[7] S. Nakatsu, Y. Yoshinaga, A. Kuramoto, F. Nagano, I. Ichimura, K. Oshino, A. Yoshimura, Y. Yano, Y. Hara, Occlusal trauma accelerates attachment loss at the onset of experimental periodontitis in rats, J. Periodontal Res. 49 (2014) 314–322, doi:10.1111/jre.12109.
[8] I.Z. Oskui, A. Hashemi, H. Jafarzadeh, Biomechanical behavior of bovine periodontal ligament: experimental tests and constitutive model, J. Mech. Behav. Biomed. Mater. 62 (2016) 599–606, doi:10.1016/j.jmbbm.2016.05.036.
[9] A.N. Natali, P.G. Pavan, E.L. Carniel, C. Dorow, A transversally isotropic elasto-damage constitutive model for the periodontal ligament, Comput. Methods Biomech. Biomed. Engin. 6 (2003) 329–336, doi:10.1080/10255840310001639840.
[10] A.N. Natali, E.L. Carniel, P.G. Pavan, F.G. Sander, C. Dorow, M. Geiger, A visco-hyperelastic-damage constitutive model for the analysis of the biomechanical response of the periodontal ligament., J. Biomech. Eng. 130 (2008) 31004, doi:10.1115/1.2900415.
[11] F. Genna, L. Annovazzi, C. Bonesi, P. Fogazzi, C. Paganelli, On the experimental determination of some mechanical properties of porcine periodontal ligament, Meccanica 43 (2008) 55–73, doi:10.1007/s11012-007-9094-2.
[12] T. Tsuzuki, H. Kajiya, K. T-Goto, T. Tsutsumi, T. Nemoto, K. Okabe, Y. Takahashi, Hyperocclusion stimulates the expression of collagen type XII in periodontal ligament, Arch. Oral Biol. 66 (2016) 86–91, doi:10.1016/j.archoralbio.2016.02.009.
[13] Y. Ujiie, A. Shimada, K. Komatsu, K. Gomi, S. Oida, T. Arai, M. Fukae, Degradation of noncollagenous components by neutrophil elastase reduces the mechanical strength of rat periodontal ligament, J. Periodontal Res. (2007) 070508213437001-???, doi:10.1111/j.1600-0765.2007.00990.x.
[14] B.K.B. Berkovitz, G.R. Holland, B.J. Moxham, Oral Anatomy, Histology and Embryology E-Book, Elsevier Health Sciences, 2017.
[15] M. Bergomi, J. Cugnoni, M. Galli, J. Botsis, U.C. Belser, H.W.A. Wiskott, Hydro-mechanical coupling in the periodontal ligament: a porohyperelastic finite element model, J. Biomech. 44 (2011) 34–38, doi:10.1016/j.jbiomech.2010.08.019.
[16] J. Ortún-Terrazas, J. Cegoñino, U. Santana-Penín, U. Santana-Mora, A. Pérez del Palomar, Approach towards the porous fibrous structure of the periodontal ligament using micro-computerized tomography and finite element analysis, J. Mech. Behav. Biomed. Mater. 79 (2018) 135–149, doi:10.1016/j.jmbbm.2017.12.022.
[17] Z. Wei, X. Yu, X. Xu, X. Chen, Experiment and hydro-mechanical coupling simulation study on the human periodontal ligament, Comput. Methods Programs Biomed. 113 (2014) 749–756, doi:10.1016/j.cmpb.2013.12.011.
[18] M. Bergomi, H.W.A. Wiskott, J. Botsis, A. Mellal, U.C. Belser, Load response of periodontal ligament: assessment of fluid flow, compressibility, and effect of pore pressure, J. Biomech. Eng. 132 (2009) 014504, doi:10.1115/1.4000154.
[19] J. Chen, W. Li, M.V. Swain, M. Ali Darendeliler, Q. Li, M.A. Darendeliler, Q. Li, A periodontal ligament driven remodeling algorithm for orthodontic tooth movement, J. Biomech. 47 (2014) 1689–1695, doi:10.1016/j.jbiomech.2014.02.030.
[20] M. Pini, P. Zysset, J. Botsis, R. Contro, Tensile and compressive behaviour of the bovine periodontal ligament, J. Biomech. 37 (2004) 111–119, doi:10.1016/S0021-9290(03)00234-3.
[21] J. Ortún-Terrazas, J. Cegoñino, U. Santana-Penín, U. Santana-Mora, A. Pérez del Palomar, A porous fibrous hyperelastic damage model for human periodontal ligament: application of a micro-computerized tomography finite element model, Int. J. Numer. Method. Biomed. Eng. (2019) e3176, doi:10.1002/cnm.3176.
[22] R.Y. Dhume, E.D. Shih, V.H. Barocas, Multiscale model of fatigue of collagen gels, Biomech. Model. Mechanobiol. 18 (2019) 175–187, doi:10.1007/s10237-018-1075-y.
[23] T.S. Fill, J.P. Carey, R.W. Toogood, P.W. Major, Experimentally determined mechanical properties of, and models for, the periodontal ligament: critical review of current literature, J. Dent. Biomech. 2 (2011) 312980–312980, doi:10.4061/2011/312980.
[24] O. Röhrle, H. Saini, D.C. Ackland, Occlusal loading during biting from an experimental and simulation point of view, Dent. Mater. 34 (2018) 58–68, doi:10.1016/j.dental.2017.09.005.
[25] S. Benazzi, H.N. Nguyen, O. Kullmer, K. Kupczik, Dynamic modelling of tooth deformation using occlusal kinematics and finite element analysis, PLoS ONE 11 (2016) 1–17, doi:10.1371/journal.pone.0152663.
[26] A. Nikolaus, C. Fleck, T. Lindtner, J. Currey, P. Zaslansky, Importance of the variable periodontal ligament geometry for whole tooth mechanical function: a validated numerical study, J. Mech. Behav. Biomed. Mater. 67 (2016) 61–73, doi:10.1016/j.jmbbm.2016.11.020.
[27] G.R.S. Naveh, V. Brumfeld, R. Shahar, S. Weiner, Tooth periodontal ligament: direct 3D microCT visualization of the collagen network and how the network changes when the tooth is loaded, J. Struct. Biol. 181 (2013) 108–115, doi:10.1016/j.jsb.2012.10.008.
[28] A.N. Natali, P.G. Pavan, C. Venturato, K. Komatsu, Constitutive modeling of the non-linear visco-elasticity of the periodontal ligament, Comput. Methods Programs Biomed. 104 (2011) 193–198, doi:10.1016/j.cmpb.2011.03.014.
[29] H. Huang, W. Tang, Q. Tan, B. Yan, Development and parameter identification of a visco-hyperelastic model for the periodontal ligament, J. Mech. Behav. Biomed. Mater. 68 (2017) 210–215, doi:10.1016/j.jmbbm.2017.01.035.
[30] H. Lin, P. Zhu, Y. Lin, S. Wan, X. Shu, Y. Xu, Y. Zheng, Mandibular asymmetry: a three-dimensional quantification of bilateral condyles, Head Face Med. 9 (2013) 1–7, doi:10.1186/1746-160x-9-42.
[31] Y. Wang, S. He, L. Yu, J. Li, S. Chen, Accuracy of volumetric measurement of teeth *in vivo* based on cone beam computer tomography, Orthod. Craniofac. Res. 14 (2011) 206–212, doi:10.1111/j.1601-6343.2011.01525.x.
[32] L. Keilig, M. Drolshagen, K.L. Tran, I. Hasan, S. Reimann, J. Deschner, K.T. Brinkmann, R. Krause, M. Favino, C. Bourauel, *In vivo* measurements and numerical analysis of the biomechanical characteristics of the human periodontal ligament, Ann. Anat. - Anat. Anzeiger. 206 (2016) 80–88, doi:10.1016/j.aanat.2015.08.004.
[33] B. Xu, Y. Wang, Q. Li, Modeling of damage driven fracture failure of fiber post-restored teeth, J. Mech. Behav. Biomed. Mater. 49 (2015) 277–289, doi:10.1016/j.jmbbm.2015.05.006.
[34] R.W. Ogden, Large deformation isotropic elasticity: on the correlation of theory and experiment for compressible rubberlike solids, Proc. R. Soc. A Math. Phys. Eng. Sci. 328 (1972) 567–583, doi:10.1098/rspa.1972.0096.
[35] L.A. Weinberg, Temporomandibular joint function and its effect on concepts of occlusion, J. Prosthet. Dent. 35 (1976) 553–566, doi:10.1016/0022-3913(76)90051-2.
[36] W.H. Douglas, R.L. Sakaguchi, R. DeLong, Frictional effects between natural teeth in an artificial mouth, Dent. Mater. 1 (1985) 115–119, doi:10.1016/S0109-5641(85)80040-3.
[37] M. Farella, S. Palla, S. Erni, A. Michelotti, L.M. Gallo, Masticatory muscle activity during deliberately performed oral tasks, Physiol. Meas. 29 (2008) 1397–1410, doi:10.1088/0967-3334/29/12/004.
[38] A.C. Freitas, E.P. Rocha, P.H. dos Santos, C.-C. Ko, M. Martín, E.O. de Almeida, Mechanics of the maxillary central incisor. Influence of the periodontal ligament represented by beam elements., Comput. Methods Biomech. Biomed. Engin. 13 (2010) 515–521, doi:10.1080/10255840903273175.
[39] A. Oppenheim, Human tissue response to orthodontic intervention of short and long duration, Am. J. Orthod. Oral Surg. 28 (1942) 263–301, doi:10.1016/S0096-6347(42)90492-7.
[40] A. Hohmann, U. Wolfram, M. Geiger, A. Boryor, C. Kober, C. Sander, F.G. Sander, Correspondences of hydrostatic pressure in periodontal ligament with regions of root resorption: a clinical and a finite element study of the same human teeth, Comput. Methods Programs Biomed. 93 (2009) 155–161, doi:10.1016/j.cmpb.2008.09.004.
[41] I.A.V.P. Poiate, A.B. Vasconcellos, R.B. Santana, E. Poiate Jr, Three-dimensional stress distribution in the human periodontal ligament in masticatory, parafunctional, and trauma loads: finite element analysis., J. Periodontol. 80 (2009) 1859–1867, doi:10.1902/jop.2009.090220.
[42] P. Rygh, P. Brudvik, Root resorption and new wire qualities, Eur. J. Orthod. 15 (1993) 343.
[43] F. Weiland, Constant versus dissipating forces in orthodontics: the effect on initial tooth movement and root resorption, Eur. J. Orthod. 25 (2003) 335–342.
[44] T. Van Eijden, Three-dimensional analyses of human bite-force magnitude and moment, Arch. Oral Biol. 36 (1991) 535–539.
[45] J.D. Lin, H. Özcoban, J.P. Greene, A.T. Jang, S.I. Djomehri, K.P. Fahey, L.L. Hunter, G.A. Schneider, S.P. Ho, Biomechanics of a bone–periodontal ligament–tooth fibrous joint, J. Biomech. 46 (2013) 443–449.
[46] Y. Hattori, C. Satoh, T. Kunieda, R. Endoh, H. Hisamatsu, M. Watanabe, Bite forces and their resultants during forceful intercuspal clenching in humans, J. Biomech. 42 (2009) 1533–1538, doi:10.1016/j.jbiomech.2009.03.040.
[47] B. Koos, A. Godt, C. Schille, G. Göz, Precision of an instrumentation-based method of analyzing occlusion and its resulting distribution of forces in the dental arch, J. Orofac. Orthop. / Fortschritte Der Kieferorthopädie 71 (2010) 403–410, doi:10.1007/s00056-010-1023-7.
[48] K. Francová, M. Eber, J. Zapletalová, Functional occlusal patterns during lateral excursions in young adults, J. Prosthet. Dent. 113 (2015) 571–577, doi:10.1016/j.prosdent.2014.12.004.
[49] D. Vollmer, C. Bourauel, K. Maier, A. Jäger, Determination of the centre of resistance in an upper human canine and idealized tooth model, Eur. J. Orthod. 21 (1999) 633–648, doi:10.1093/ejo/21.6.633.
[50] H.T. Shillingburg, D.A. Sather, E.L. Wilson, J.R. Cain, D.L. Mitchell, L.J. Blanco, J.C. Kessler, Fundamentals of Fixed Prosthodontics (2012).
[51] C.-L. Lin, J.-C. Wang, Nonlinear finite element analysis of a splinted implant with various connectors and occlusal forces, Int. J. Oral Maxillofac. Implants 18 (2003).
[52] S.F. Rosenstiel, M.F. Land, J. Fujimoto, Contemporary Fixed Prosthodontics-E-Book, Elsevier Health Sciences, 2015.
[53] W.W. Hallmon, Occlusal trauma: effect and impact on the periodontium, Ann. Periodontol. 4 (1999) 102–108, doi:10.1902/annals.1999.4.1.102.
[54] Z. Liao, J. Chen, W. Li, M.A. Darendeliler, M. Swain, Q. Li, Biomechanical investigation into the role of the periodontal ligament in optimising orthodontic force: a finite element case study, Arch. Oral Biol. 66 (2016) 98–107.
[55] B. Melsen, Tissue reaction to orthodontic tooth movement–a new paradigm, Eur. J. Orthod. 23 (2001) 671–681 doi:11890063.

[56] R. Razaghi, H. Biglari, A. Karimi, Dynamic finite element simulation of dental prostheses during chewing using muscle equivalent force and trajectory approaches, J. Med. Eng. Technol. 41 (2017) 314–324, doi:10.1080/03091902.2017.1299231.

[57] J. Żmudzki, K. Panek, G. Chladek, M. Adamiak, P. Lipinski, Finite element analysis of adolescent mandible fracture occurring during accidents, (2018).

[58] L. Borák, Z. Florian, S. Bartáková, P. Prachár, N. Murakami, M. Ona, Y. Igarashi, N. Wakabayashi, Bilinear elastic property of the periodontal ligament for simulation using a finite element mandible model, Dent. Mater. J. 30 (2011) 448–454, doi:10.4012/dmj.2010-170.

Manuscript 5: Computational characterization of the porous-fibrous behaviour of the soft tissues in the temporomandibular joint

Javier Ortún-Terrazas, José Cegoñino, Amaya Pérez del Palomar

Abstract

The prevalence and severity of temporomandibular joint (TMJ) disorders have led to growing research interest in the development of new biomaterials and medical devices for TMJ implant designs. In computational designs, however, the time and stretch direction dependences of the TMJ soft tissues behaviour are not considered and they are frequently based on measurements taken from non-human species or from joints that differ markedly from the human TMJ. The aim of this study was to accurately characterize the porous-fibrous properties of the TMJ soft tissues by simulating previously published experimental tests, to assist professionals in the design of new TMJ implants. To that end, material parameters were determined assuming a uniform fibre orientation throughout the entire sample. This assumption was then tested by comparing these results with those of considering multiple regions and distinct fibre orientations in each sample. Our findings validated the use of a transversely isotropic hyperelastic material model to characterize the direction dependent behaviour of TMJ soft tissues and its combination with porous hyperfoam material models to mimic the compressive response of the TMJ disc. In conclusion, constitutive model proposed accurately reproduce the mechanical response of the TMJ soft tissues at different strain rates and stretch directions.

Graphical abstract

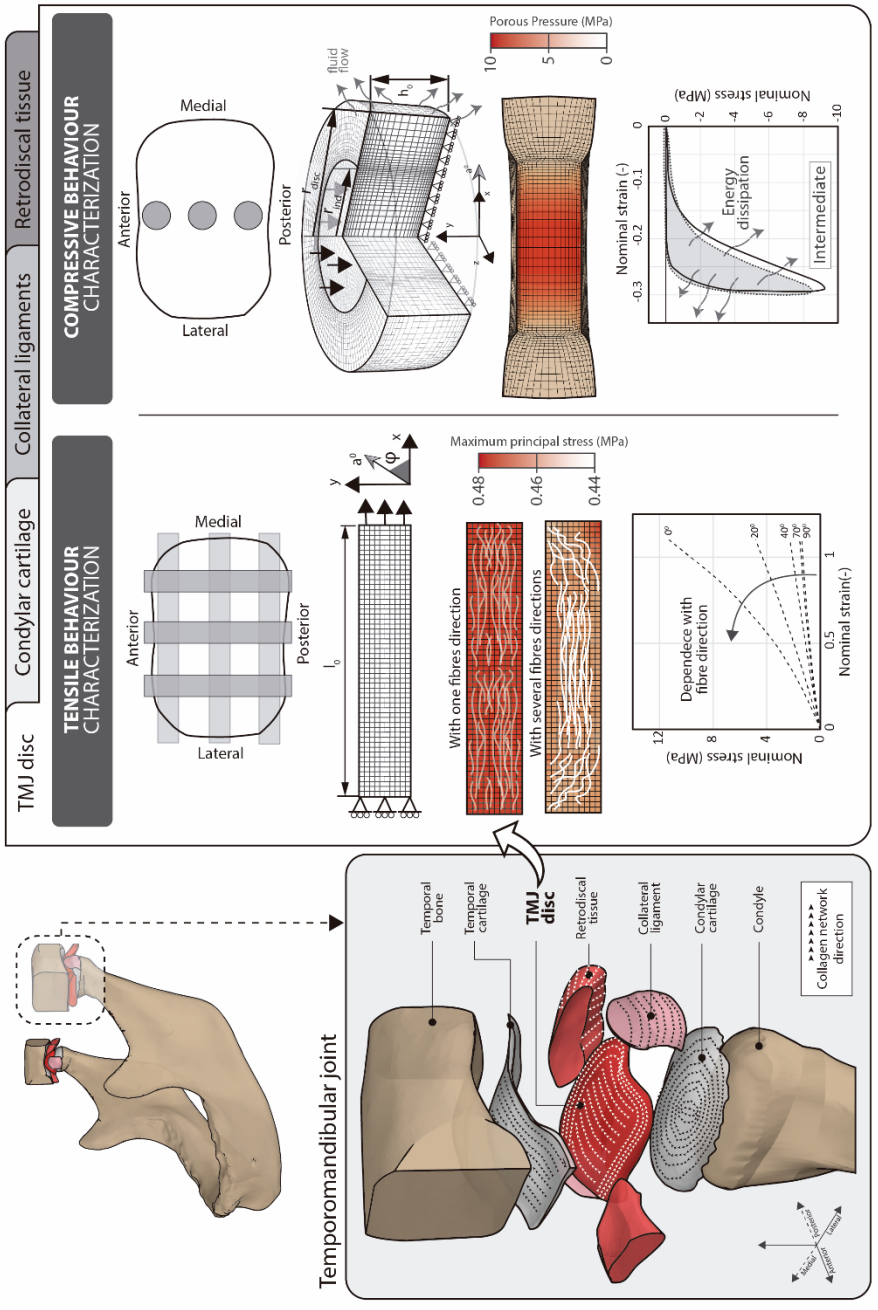

Received: 3 July 2019 | Revised: 26 November 2019 | Accepted: 6 January 2020

DOI: 10.1002/jbm.b.34558

ORIGINAL RESEARCH REPORT

Computational characterization of the porous-fibrous behavior of the soft tissues in the temporomandibular joint

Javier Ortún-Terrazas | José Cegoñino | Amaya Pérez del Palomar

Group of Biomaterials, Aragón Institute of Engineering Research (I3A), University of Zaragoza, Zaragoza, Spain

Correspondence
Javier Ortún-Terrazas, Aragon Institute of Engineering Research (I3A), School of Engineering and Architecture, University of Zaragoza, Zaragoza, Spain, Calle María de Luna 3, 50018 Zaragoza, Spain.
Email: javierortun@unizar.es

Funding information
European Social Funds and Regional Government of Aragon, Grant/Award Number: 2016/20; Ibercaja- Cai Fundation, Grant/Award Number: IT 4/18; Spanish Ministry of Economy and Competitiveness, Grant/Award Number: DPI 2016-79302-R

Abstract

The prevalence and severity of temporomandibular joint (TMJ) disorders have led to growing research interest in the development of new biomaterials and medical devices for TMJ implant designs. In computational designs, however, the time and stretch direction dependences of the TMJ soft tissues behavior are not considered and they are frequently based on measurements taken from non-human species or from joints that differ markedly from the human TMJ. The aim of this study was to accurately characterize the porous-fibrous properties of the TMJ soft tissues by simulating previously published experimental tests, to assist professionals in the design of new TMJ implants. To that end, material parameters were determined assuming a uniform fiber orientation throughout the entire sample. This assumption was then tested by comparing these results with those of considering multiple regions and distinct fiber orientations in each sample. Our findings validated the use of a transversely isotropic hyperelastic material model to characterize the direction dependent behavior of TMJ soft tissues and its combination with porous hyperfoam material models to mimic the compressive response of the TMJ disc. In conclusion, constitutive model proposed accurately reproduce the mechanical response of the TMJ soft tissues at different strain rates and stretch directions.

KEYWORDS

hyperfoam constitutive model, porohyperelastic behavior, soft tissues, temporomandibular joint, transversely isotropic hyperelastic constitutive model

1 | INTRODUCTION

The temporomandibular joint (TMJ) is an articular joint that connects the mandible to the skull and enables jaw movement. From a biomechanical point of view, some of the most important tissues in this joint are the articular disc, the condylar and temporal cartilage, the retrodiscal tissue, and the collateral ligaments (Figure 1). These soft tissues constrain jaw movement and are the tissues most commonly implicated in temporomandibular joint disorders (TMDs). Although TMDs have a multifactorial etiology, approximately 70% of TMDs (Detamore & Athanasiou, 2005) and/or TMJ malformations are closely linked to biomechanical anomalies (Allen & Athanasiou, 2006) that end up being resolved through joint replacements. A deeper knowledge of the biomechanical behavior of the soft tissues of the TMJ would facilitate the development of more accurate finite element (FE) models, more effective treatments and designs of implants closer to human joint.

The TMJ disc is a biconcave, elliptical, fibrocartilaginous tissue located in the glenoid fossa of the temporal bone (Figure 1). This

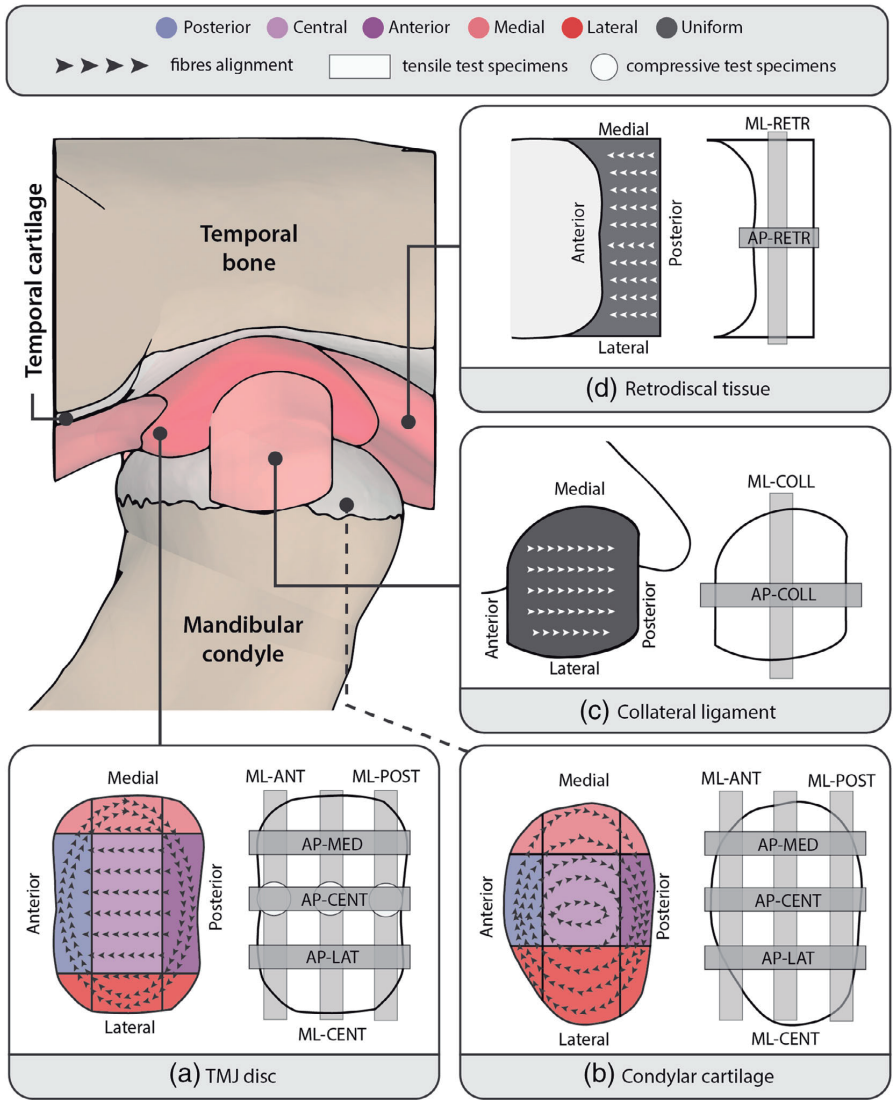

FIGURE 1 Schematic showing the anatomy of the temporomandibular joint. (a) TMJ disc, (b) condylar cartilage, (c) collateral ligament, and (d) retrodiscal tissue. In each panel, the alignment of collagen networks is shown on the left, and the samples analyzed in this study are indicated on the right

tissue distributes load and absorbs shock, preventing stress concentration on the articulating surfaces of the TMJ (condylar and temporal cartilage). The TMJ disc slides between the articular surfaces of the temporal and condylar bone regions which are covered by hyaline cartilage (Singh & Detamore, 2009) (Figure 1). In normal conditions, the condylar cartilage is mainly subjected to compression stress and the shear stress is often neglected due to extremely low friction (Nickel & McLachlan, 1994) between the contact surfaces which are lubricated by the synovial fluid. The retrodiscal tissue contains collagen and elastic fibers and connects the posterior band of the disc to the mandibular fossa (Tanaka, Del Pozo, Sugiyama, & Tanne, 2002). Finally, the medial and lateral collateral ligaments connect the medial and lateral sides of the TMJ disc to the condyle, thereby contributing to joint stabilization during TMJ movement.

Structurally and biomechanically, the TMJ disc (Wright et al., 2016) and fibrous region of the condylar cartilage (Singh & Detamore, 2009) can be divided in five regions (Figure 1a,b): the anterior band (ANT), posterior band (POST), central zone (CENT), lateral zone (LAT), and medial zone (MED). Experimental studies (Singh & Detamore, 2008; Wright et al., 2016) have shown that collagen fiber density and orientation account for mechanical differences between these regions. In the disc attachments (retrodiscal and collateral ligaments),

the fibrous network is particularly dense and is oriented in an anteroposterior direction (Murphy, Arzi, Hu, & Athanasiou, 2013).

Because experimental manipulation of the TMJ is hampered by the fragility of this joint's soft tissues, the last decade has seen an increase in the number of computational studies of the TMJ (Ingawalé & Goswami, 2009) (shown in Table S1). However, the mechanical properties of the soft tissues of the TMJ remain to be fully characterized (Ingawalé & Goswami, 2009), as underscored by the many contrasting findings in the published literature. This variability may be due to viscoelastic behavior is not considered; the dependence of biomechanical behavior on fiber orientation is not considered; and mechanical tests are performed using animal species with a very different masticatory system to that of the human. Therefore, experimental studies that have considered the influence of fibrous network (Murphy et al., 2013; Singh & Detamore, 2008; Wright et al., 2016) and the time-dependence behavior (Beek, Aarnts, Koolstra, Feilzer, & Van Eijden, 2001) are particularly important for the present work.

Moreover, few of the computational studies have included all TMJ soft tissues in their FE models (shown in Table S1) and only a few have examined the behavior of the collagen network. Furthermore, no studies have characterized the biomechanical contributions of both, the fibrous network and the interstitial fluid of the TMJ disc, using experimental data obtained from a species with a masticatory system similar to that of the human (Ingawalé & Goswami, 2009; Wright et al., 2016).

Given the discrepancies in the literature regarding some of the key biomechanical properties of the soft tissues of the TMJ, we sought to identify and rigorously validate material model parameters for the characterization of the soft tissues of the TMJ. The aims of this study were: (a) to characterize the mechanical parameters that describe the fibrous and porous behavior of the TMJ disc and the role of the fibrous network in other soft tissues of the TMJ (condylar cartilages, retrodiscal tissue, and collateral ligaments); (b) to validate the material properties by comparing our numerical results with experimental data from the literature; (c) to evaluate the simplifications performed during the material model characterization by considering different configurations of the fibrous network. In this study, firstly the characterization of the fibrous network of the TMJ disc, retrodiscal tissue, condylar cartilage, and collateral ligaments is explained. The behavior of the temporal cartilage was not characterized owing to a lack of sufficient data. Next, the contribution of TMJ disc fluid is evaluated by reproducing compression tests described in the literature. Based on the respective contributions of the fibrous network and the TMJ disc fluid, a material model is proposed. Finally, we describe the evaluation of TMJ soft tissue responses for different directions, configurations, and strain rates.

2 | MATERIALS AND METHODS

2.1 | Characterization of the fibrous matrix

In soft tissues studied, the collagen network is the main component responsible for tensile stiffness, while the interstitial fluid resists most of the compressive load (Beek et al., 2001; Wright et al., 2016). The tensile stiffness of the tissue varies according to the preferential direction of fiber orientation. Thus, collagen fibers contribute significantly to tissue stiffness when stretched, but make little contribution when transverse loads are applied. In this latter situation, the majority of the load must be borne by the hyperelastic isotropic matrix.

Considering $\boldsymbol{x}$ and $\boldsymbol{X}$, the respective positions of a particle in a current (Ω) and reference configurations (Ω_0), the deformation gradient $\boldsymbol{F}$ is defined by $\boldsymbol{F} = \partial\boldsymbol{x}/\partial\boldsymbol{X}$. Alternatively, the modified deformation gradient $\left(\tilde{\boldsymbol{F}}\right)$ can be expressed by the Jacobian deformation gradient ($J_{el} = det\boldsymbol{F}$) and the deformation gradient ($\boldsymbol{F}$) by the formula $\tilde{\boldsymbol{F}} = J_{el}^{-(1/3)}\boldsymbol{F}$. The right Cauchy-Green tensor $\left(\tilde{\boldsymbol{C}}\right)$ can therefore be defined by the modified deformation gradient, $\tilde{\boldsymbol{F}}$, as $\tilde{\boldsymbol{C}} = \tilde{\boldsymbol{F}}^T\tilde{\boldsymbol{F}}$. To account for the aforementioned behaviors of the matrix and the fibrous network, we used a transversely isotropic hyperelastic material model (Holzapfel, 2000) which is expressed by the following strain energy density function (W):

$$W\left(\tilde{\boldsymbol{C}}, \tilde{I}_1, \tilde{I}_4\right) = W_m\left(\tilde{I}_1\right) + W_f\left(\tilde{I}_4\right) + W_{vol}(J_{el}) \tag{1}$$

where W_m is the component of the hyperelastic matrix substance without fibers, W_f represents the fibrous term, and W_{vol} is the volumetric term. W_m is defined according to the deviatoric invariant which can be expressed in term of $\tilde{\boldsymbol{C}}$ eigenvalues $(\hat{\lambda}_1, \hat{\lambda}_2, \hat{\lambda}_3)$ as follows:

$$\tilde{I}_1 = tr\tilde{\boldsymbol{C}} = \hat{\lambda}_1^2 + \hat{\lambda}_2^2 + \hat{\lambda}_3^2 \tag{2}$$

On the other hand, W_f is a function of the dilatational invariant which is defined as:

$$\tilde{I}_4 = \boldsymbol{a}^0 \cdot \tilde{\boldsymbol{C}} \cdot \boldsymbol{a}^0 \tag{3}$$

where $\boldsymbol{a}^0$ is the unitary vector defining the orientation of the collagen fibers in the reference configuration. Therefore, the terms of the energy density function (Equation (1) can be reformulated as follows:

$$W_m = C_1 \cdot \left(\tilde{I}_1 - 3\right); \tag{4a}$$

$$W_f = \frac{k_1}{2 \cdot k_2}\left\{exp\left[k_2 \cdot \left(\tilde{I}_4 - 1\right)^2\right] - 1\right\} \tag{4b}$$

$$W_{vol} = \frac{1}{D}\left(\frac{(J_{el})^2 - 1}{2} - lnJ_{el}\right) \tag{4c}$$

where W_m is defined by the Neo-Hookean hyperelastic material formulation and C_1 is the material constant related to the matrix substance. $k_1 > 0$ and $k_2 > 0$ are the parameters which identify the exponential behavior due to the presence of collagen fibers, and D is related to bulk modulus K, by $D = 2/K$ being zero for an incompressible material. For quasi-incompressible materials ($J_{el} \approx 1$), the volumetric term can be underestimated.

In an uniaxial stretch test, axial stretch ratio λ_u can be defined by the $\tilde{\boldsymbol{C}}$ eigenvalues as $\lambda_1 = \lambda_u$ and $\lambda_2 = \lambda_3 = 1/\sqrt{\lambda_u}$ due to incompressible condition ($J_{el} = \lambda_u\lambda_2^2 = 1$). Hence, the nominal stress-stretch relation

(Holzapfel, 2000) for the transversely isotropic material model can be expressed as follows:

$$\sigma_u = \frac{\partial W}{\partial \lambda_u} = {\lambda_u}^2 \left\{ C_1 \left(1 - \frac{1}{{\lambda_u}^3} \right) + 2 \cdot k_1 \left(\bar{I}_4 - 1 \right) \cdot exp\left[k_2 \cdot \left(\bar{I}_4 - 1 \right)^2 \right] \right\} \quad (5)$$

When the collagen fibers are almost not stretched $\left(\bar{I}_4 \lesssim 1\right)$ the contribution of the fibrous network is practically null and the hyperelastic matrix (first term of Equation (5)) must support most of the load. Conversely, most of the load is supported by the fibers if the tissue is stretched in the direction of the fibrous network ($\bar{I}_4 > 1$). Therefore, it is possible to determine separately the material parameters that define both terms (W_m and W_f) by fitting the stretch experimental response of samples tested longitudinal and transversal to the direction of fibers network. The parameters of Equation (5) were adjusted through a nonlinear least-squares fitting procedure using MATLAB commercial software (MATLAB 6.0 R12, The MathWorks Inc., Natick, MA, 2000), which minimizes the relative error between the analytical values of Equation (5) and the experimental fitted curves. The toe region (strain <6%) (Singh & Detamore, 2008) of the fitted curves was defined by the transversal elastic modulus and was used to the characterization of C_1. Meanwhile, k_1 and k_2 parameters were obtained by fitting the near-linear region (strain >6%) which was defined based on the longitudinal elastic modulus of the experimental studies that are described below.

For characterization of the TMJ disc, we used the experimental data of Wright et al. (2016) in which 24 human TMJ discs were tested in anteroposterior and mediolateral directions, analyzing the effects of loading direction, region, and sex. Their histological findings revealed that collagen fibers are oriented to form a peripheral ring (Figure 1a). Given that central fibers run in the anteroposterior direction, the matrix parameters can be computed from the elastic modulus of central region tested mediolaterally. Therefore, we defined W_m based on the elastic modulus of the ML-CENT sample. The parameters of the fibrous term (W_f) of each region were characterized using samples that were stretched along the preferred direction of the fibrous network of each region. The elastic modulus of AP-MED, AP-CENT, AP-LAT, ML-POST, and ML-ANT samples was used for the characterization of the fibrous term in medial, central, lateral, posterior, and anterior regions, respectively. Furthermore, the parameters for each region were characterized separately for men and women using experimental data taken from Wright et al. (2016).

To characterize the behavior of condylar cartilage, we used experimental data from a study by Singh and Detamore (2008), who tested seven samples of porcine condylar cartilage in anteroposterior and mediolateral directions. Based on the orientation of the cartilage fibers (Figure 1b), W_m parameters were computed from the ML-CENT elastic modulus. W_f parameters for each of the five regions of the condylar cartilage were computed from the elastic modulus of the samples tested in the direction of fiber orientation.

Finally, the material parameters of collateral ligaments and retrodiscal tissue were computed based on experimental data from Murphy et al. (2013). That study quantified the elastic modulus of porcine TMJ disc attachments in both anteroposterior and mediolateral directions (Figure 1c,d). In both tissues the fibers are mainly oriented in the anteroposterior direction. Therefore, W_m and W_f were computed based on the results obtained from samples that were tested mediolaterally and anteroposteriorly, respectively. The material parameters obtained are summarized in Table 1.

2.2 | Characterization of the porous parameters of the TMJ disc

To account for the biphasic nature of the TMJ disc, the poroelastic contribution was added in Abaqus software (Abaqus 6.14, Simulia, Rhode Island) to the transversely isotropic material model defined in Equation (1). In a biphasic material (Holmes & Mow, 1990), as here studied, media is composed of solid (ϕ^s) and fluid phases (ϕ^f). The sum of both phases in fully saturated media, ζ, must satisfy $\zeta = \phi^s + \phi^f = 1$. Abaqus provides capabilities for modelling a biphasic material when the media is completely saturated with an incompressible fluid by the conventional poroelastic theory which considers the medium as a multiphase media with the interaction between the solid and the fluid phases. The balanced equations for mass, linear momentum and energy in soil mechanics (Wu, 1967) are additionally provided in the supplementary material. This approach uses the principle of effective stress which states that the total stress acting in a mixture can be decomposed into two components. The neutral stress, also called pore pressure, p, which acts in every direction and the effective stress, $\bar{\boldsymbol{\sigma}}$, whose effect is exclusively on the solid matrix. Therefore, the total stress acting at a point, $\boldsymbol{\sigma}$, is defined from the Clausius-Duhem entropy inequality as follows:

$$\boldsymbol{\sigma} = (1-e)\bar{\boldsymbol{\sigma}} - e \cdot p \cdot \boldsymbol{I} - \zeta \cdot p \cdot \boldsymbol{I} \quad (6)$$

where $\boldsymbol{I}$ is the identity tensor, p is the pore pressure, and $\bar{\boldsymbol{\sigma}}$ is the effective stress tensor which is determined from the strain energy density function for a hyperelastic materials by (Systèmes, 2014):

$$\bar{\boldsymbol{\sigma}} = \frac{2}{J_{el}} \tilde{\boldsymbol{F}} \frac{\partial W}{\partial \tilde{\boldsymbol{C}}} \tilde{\boldsymbol{F}}^{\mathrm{T}} \quad (7)$$

To compute p, Abaqus requires to specify the permeability, $\bar{k}$, as a function of the void ratio which is the ratio of fluid volume to total volume of the element ($e = dV_f/dV_t$). In our simulations, the exponential permeability function for biphasic materials (Argoubi & Shirazi-Adl, 1996) was used:

$$\bar{k} = k_0 \left[\frac{e(1+e_0)}{e_0(1+e)} \right]^2 exp\left[M\left(\frac{1+e}{1+e_0} - 1 \right) \right] \quad (8)$$

where e is the strain-dependent void ratio, M is a dimensionless material parameter and, k_0 and e_0 are the permeability and the void ratio at zero strain (shown in Table 1). The initial void ratio in each region of the disc, $e_0 = \phi_0^f / \left(1 - \phi_0^f\right)$, was computed from the porosity values at

TABLE 1 Left to right: parameters for the transversely isotropic hyperelastic material model for the TMJ disc (man and woman), condylar cartilage, medial and lateral collateral ligaments, and retrodiscal tissue; parameters for the hyperfoam material model, which characterizes the compressive response of the solid phase of the TMJ disc; parameters for biphasic characterization of the TMJ disc. Note: (a) Kuo et al. (2010)

	Solid phase							Porous phase			
	Trans. Iso. Hype. mat. model				Hyperfoam mat. model			Permeability function parameters			
	C_1 (MPa)	D (MPa^{-1})	k_1 (MPa)	k_2 (–)	ν (–)	μ (MPa)	α (–)	k_0 (10^{-15} m^2)	M (–)	φ (–)	γ_w (N/m^3)
TMJ disc (man)											
ANT	1.45	0	0.43	0.34	0.1667	1.72	75	8.95 ± 1.17 (a)	49	0.80 (a)	9800
LAT	1.45	0	0.69	0.43	0.1667	3.86	78	3.64 ± 0.65 (a)	45	0.79 (a)	9800
CENT	1.45	0	0.97	0.17							
MED	1.45	0	0.17	1.68							
POST	1.45	0	1.25	0.16	0.1667	0.86	75	8.07 ± 1.55 (a)	43	0.83 (a)	9800
TMJ disc (woman)											
ANT	2.4	0	0.05	3.72	0.1667	1.72	75	8.95 ± 1.17 (a)	49	0.81 (a)	9800
LAT	2.4	0	0.11	2.52	0.1667	3.86	78	3.64 ± 0.65 (a)	45	0.79 (a)	9800
CENT	2.4	0	0.75	0.87							
MED	2.4	0	0.08	2.93							
POST	2.4	0	0.31	1.44	0.1667	0.86	75	8.07 ± 1.55 (a)	43	0.83 (a)	9800
Condylar cartilage (porcine)											
ANT	1.65	0	0.24	1.95	–	–	–	–	–	–	–
LAT	1.65	0	2.58	0.43	–	–	–	–	–	–	–
CENT	1.65	0	3.77	0.21	–	–	–	–	–	–	–
MED	1.65	0	2.52	0.42	–	–	–	–	–	–	–
POST	1.65	0	0.16	1.92	–	–	–	–	–	–	–
Medial collateral ligaments (porcine)											
UNIF.	0.38	0	0.68	10^{-5}	–	–	–	–	–	–	–
Lateral collateral ligaments (porcine)											
UNIF.	0.41	0	0.35	10^{-5}	–	–	–	–	–	–	–
Retrodiscal tissue (porcine)											
UNIF.	1.05	0	0.27	10^{-5}	–	–	–	–	–	–	–

zero strain proposed in the literature (Kuo, Zhang, Bacro, & Yao, 2010). The initial permeabilities of each region were also determined from this experimental study (Kuo et al., 2010). The void ratio at each instant of time, e, is dependent on the deformation (Systèmes, 2014) and was obtained from the computational results of our simulations according to the following equation:

$$e = \frac{1 - {J_{el}}^{-1}\left(1 - \phi_0^f\right)}{{J_{el}}^{-1}\left(1 - \phi_0^f\right)} \tag{9}$$

On the other hand, M parameter was iteratively determined through a least-squares fitting procedure, minimizing the relative error between the nominal stress obtained from our compressive simulations and the experimental compressive response. The computational nominal stress values in each fitting-iteration were obtained through an iterative compression test of the cylindrical 3D model which is subsequently explained. This iterative process was executed in Python (Python 3.5.2, Python Software Foundation). Meanwhile, the experimental data was obtained from Beek et al. (2001) study in which human samples were tested considering both strain-rate and region dependencies.

As it will show in Section 3 (Figure 6a), the porous transversely isotropic material model did not fit well the compression data. This incompatibility has been previously reported for other soft tissues of the masticatory system, such as the periodontal ligament (Ortún-Terrazas, Cegoñino, & Pérez del Palomar, 2020; Ortún-Terrazas, Cegoñino, Santana-Penín, Santana-Mora, & Pérez del Palomar, 2018; Ortún-Terrazas, Cegoñino, Santana-Penín, Santana-Mora, & Pérez del Palomar, 2019). This poor fit is largely due to the fact that a Neo-Hookean hyperelastic material formulation is not valid for high compressive stretch values (Ogden, 1972; Yeoh, 1993). Consequently, we developed a new material model defined by a porous transversely isotropic hyperelastic material description for tensile efforts $\left(\tilde{I}_4 > 1\right)$, and a porous hyperfoam material description for compressive efforts $\left(\tilde{I}_4 \leq 1\right)$. This constitutive material model was implemented in a UMAT user subroutine, as previously described (Ortún-Terrazas et al., 2018).

The hyperfoam strain energy density function (Storakers, 1986) is defined as follows:

$$W = \frac{2\mu}{\alpha^2}\left[\hat{\lambda}_1^{\alpha} + \hat{\lambda}_2^{\alpha} + \hat{\lambda}_3^{\alpha} - 3 + \frac{1}{\beta}\left(J_{el}^{-\alpha\beta} - 1\right)\right] \quad (10)$$

Where μ and α are material parameters and the coefficient β determines the degree of compressibility being related to Poisson's ratio, ν, by $\beta = \nu/(1 - 2\nu)$. In an uniaxial compression test of a compressible isotropic material ($J_{el} \neq 1$), the Jacobian deformation gradient can be then defined as leading the following nominal stress-stretch relation (Systèmes, 2014):

$$\sigma_u = \frac{\partial W}{\partial \lambda_u} = \frac{2\mu}{\lambda_u \alpha}\left(\hat{\lambda}_u^{\alpha} - J_{el}^{-\alpha\beta}\right) \quad (11)$$

In our model, the coefficient β was computed through a Poisson ratio, ν = 0.1667, suggested in Beek, Koolstra, and van Eijden (2003) for the whole disc. Meanwhile, μ and α parameters were defined for each region through a nonlinear least-squares fitting procedure in MATLAB, which minimizes the relative error between the analytical values of Equation (11) and the experimental fitted curves. The input experimental data for fitting procedure were obtained from the unloading curves of anterior, intermediate and posterior tests at 0.05 Hz performed by Beek et al. (2001). Additionally, the upper limit of μ variation range was limited to the shear modulus of maximum stretch value because of the relation between μ and the shear modulus (Systèmes, 2014).

2.3 | FE models for validation tests

To validate the material parameters computed previously, the experimental data taken from the literature and used for the characterization were mimicked numerically in Abaqus. In this section, we first summarize the geometry of the test samples and then describe the FE models used by us to simulate the experimental tests. We simulated the tensile tests (Murphy et al., 2013; Singh & Detamore, 2008; Wright et al., 2016) using a rectangular 2D FE model (Figure 2a), and the compressive test (Beek et al., 2001) using a cylindrical 3D model (Figure 2b).

In the stress-relaxation tests described in Wright et al. (2016), rectangular specimens from six female and six male human TMJ discs were stretched (Figure 1a). The mean thickness of the samples was 2.2 mm in the anteroposterior (AP) direction and 2.5 mm in the mediolateral (ML) direction. In our simulations, sample width (w) (Figure 2a) was set at 2 mm and mean lengths (l_0) at 7.1 mm and 10.6 mm for samples tested in the anteroposterior and mediolateral directions, respectively.

In the study by Beek et al., several cylindrical samples of human TMJ discs were compressed (Beek et al., 2001) by two impermeable indenters with a radius of 1.97 mm (r_{ind}). In a subsequent computational study (Beek et al., 2003), the authors calculated that the cylindrical samples had an external radius of 3.49 mm (r_{disc}) and a thickness of 2.14 mm (h_0) (Figure 2b).

In experiments performed by Singh and Detamore (2008), the mean dimensions of the condylar cartilage samples tested in mediolateral and anteroposterior directions, respectively, were as follows: thickness, 0.47 and 0.49 mm; length, 9.6 and 9.1 mm; width, 2.0 and 1.9 mm.

Regarding the dimensions of the samples stretched by Murphy et al. (2013), they reported a mean thickness of 1.7 mm for both retrodiscal tissue and collateral ligaments. Width (1.9 mm) and length (12 mm) values were the same in the anteroposterior and mediolateral directions.

To simulate tensile experimental tests, rectangular samples were 2D modeled because they were less thick than they were long/wide. To define different fiber orientations, each FE model was divided into 10 sections by making five cuts along the length of the sample and one along the midline. The preferential direction of the fiber bundles, $\boldsymbol{a}^0$, was defined using a rectangular reference system (Figure 2a). Each sample was meshed by applying a mesh convergence process. This process evaluates changes in the mesh in samples with the largest and smallest geometric dimensions (i.e., geometry of TMJ disc attachments and AP samples of the TMJ disc, respectively). After the mesh convergence analysis, the FE model consisted of 550 second-order quadrilateral elements (S8-type element in Abaqus). In all cases, the longitudinal movement of one end of the sample was restricted in the direction of the load. The opposite side was displaced by 20, 30, 100, and 110% of the sample length, in accordance with the maximum stretch values described in the experimental test mimicked.

To evaluate the sensibility of considering different fibers properties and orientations in the same sample, two different scenarios were simulated for the samples of TMJ disc and the condylar cartilage. The first modeled a single preferential direction of fiber orientation in whole sample (direction of the central sections of the samples shown in Figure 2a), while the second assumed that each sample consisted of three different regions with distinct fiber properties and orientations (Figure 2a). The sections with an oblique orientation shown in Figure 2a were defined with a mean angle φ of 30° for vector $\boldsymbol{a}^0$. The mean angle was computed based on polarized light microscopy images from studies by Wright et al. (2016) and Singh and Detamore (2008). Owing to a lack of published experimental data, we made no distinction between regions for collateral ligaments and retrodiscal tissue. Nonetheless, the dependence of their mechanical behavior on fibrous network direction was evaluated by considering different fiber orientations (0, 20, 40, 70, and 90°). The material parameters shown in Table 1 were assigned to each section according to the color code shown in Figure 2a.

Regarding the cylindrical 3D model used to mimic the compressive experimental test, it was meshed with 53,940 porous second-order elements (C3D20P-type element in Abaqus). The mesh size was also determined based on a mesh convergence analysis, as described above, and was finer in the intermediate region (Figure 2b). The response of the test sample was recorded for both the porous

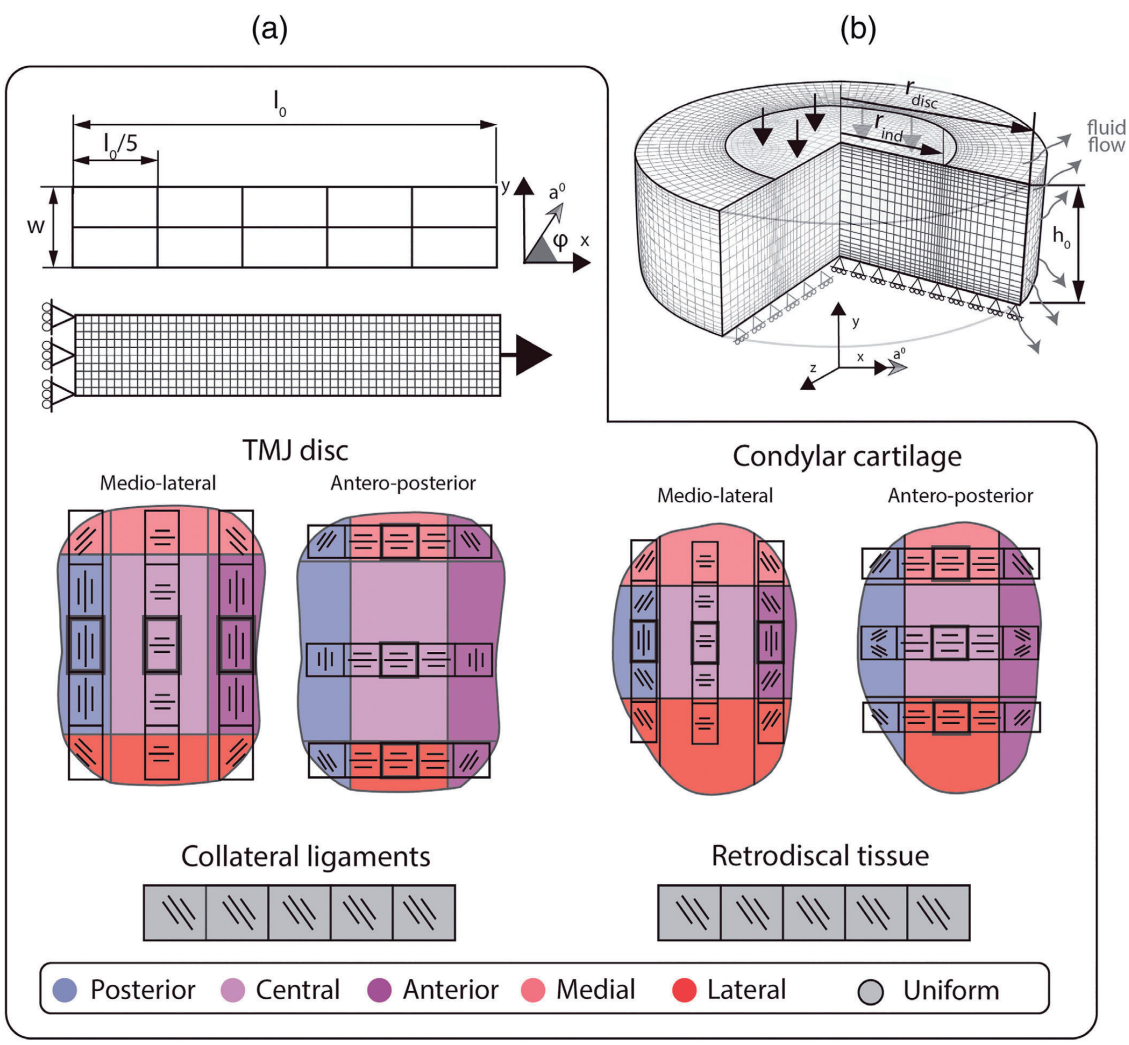

FIGURE 2 (a) Top: geometry and FE model mesh of the rectangular specimen used to mimic tensile tests. Bottom: schematic showing fiber orientation and the regions of the TMJ disc, condylar cartilage, collateral ligaments, and retrodiscal tissue. (b) 3D FE model of the cylindrical test sample used for compression analysis and schematic showing the boundary conditions applied

transversely isotropic hyperelastic material model and the porous hyperfoam material model. In the case of the porous transversely isotropic hyperelastic material model, the orientation of the fiber network was considered perpendicular to the load ($\varphi = 0^0$).

To reproduce Beek et al. (2001) experimental compression test, of interstitial fluid through the free sides of the disc was allowed and the nodes of the upper surface of the computational sample were thus subjected to a sinusoidal ($\varepsilon(t) = \varepsilon \cdot \sin(2\pi ft)$) compressive displacement equivalent to 35, 30, and 25% strain (ε). The compressive displacement cycle was evaluated at 0.02, 0.05, and 0.1 Hz. Two full cycles were simulated to allow time for model stabilization (Bergomi et al., 2011). The second cycle was used for comparison with the experimental data. The compression test was performed for the anterior, posterior, and intermediate regions of the TMJ disc.

3 | RESULTS

The results of the numerical mimicking of the selected experimental data are presented here. As aforementioned, in our study, the properties of the transversely isotropic hyperelastic material model were characterized assuming the orientation of all fibers in the same direction throughout the whole sample. This assumption was computationally evaluated by comparing results obtained considering

one or several concurrent fibrous network orientations and region properties. Figures 3–5 show the different outcomes obtained for models defined with a single fiber orientation versus with multiple regions with distinct fiber orientations. Numerical tensile responses and Normalized Root Mean Squared Error (NRMSE) from data of Wright et al. (2016), Singh and Detamore (2008) and Murphy et al. (2013) are respectively shown in Figures 3–5. On the other hand, the results of the evaluation of the compressive response and its associated NRMSEs are shown in Figure 6. Figure 6a shows the fitted curve for the experimental data of Beek et al. (2001), at 0.05 Hz, while Figure 6b–d) shown the different mechanical responses obtained using the porous transversely isotropic hyperelastic and porous hyperfoam material models. Additionally, Figure S1 shows the minimum principal stress values of our simulations and Beek et al. (2001) experimental results for different compressive strain values (35, 30, and 25%) and frequencies (0.1, 0.05, and 0.02 Hz).

As shown in Figure 3, in both cases the numerical responses fall within the experimental deviation with NRMSEs between 0.88–3.46% and 0.95–9.61% for simulations with singular and multiple fiber orientations, respectively. For both sexes, the greatest deviation between both approaches is observed for the AP-CENT sample. No differences were observed for the ML-CENT sample, the fibers were not stretched and the C_1 parameter in all regions was characterized using data from the same sample (ML-CENT).

In the case of the condylar cartilage sample under tensile load, marked differences were observed between the two sample types (Figure 4). These differences were particularly significant for the three

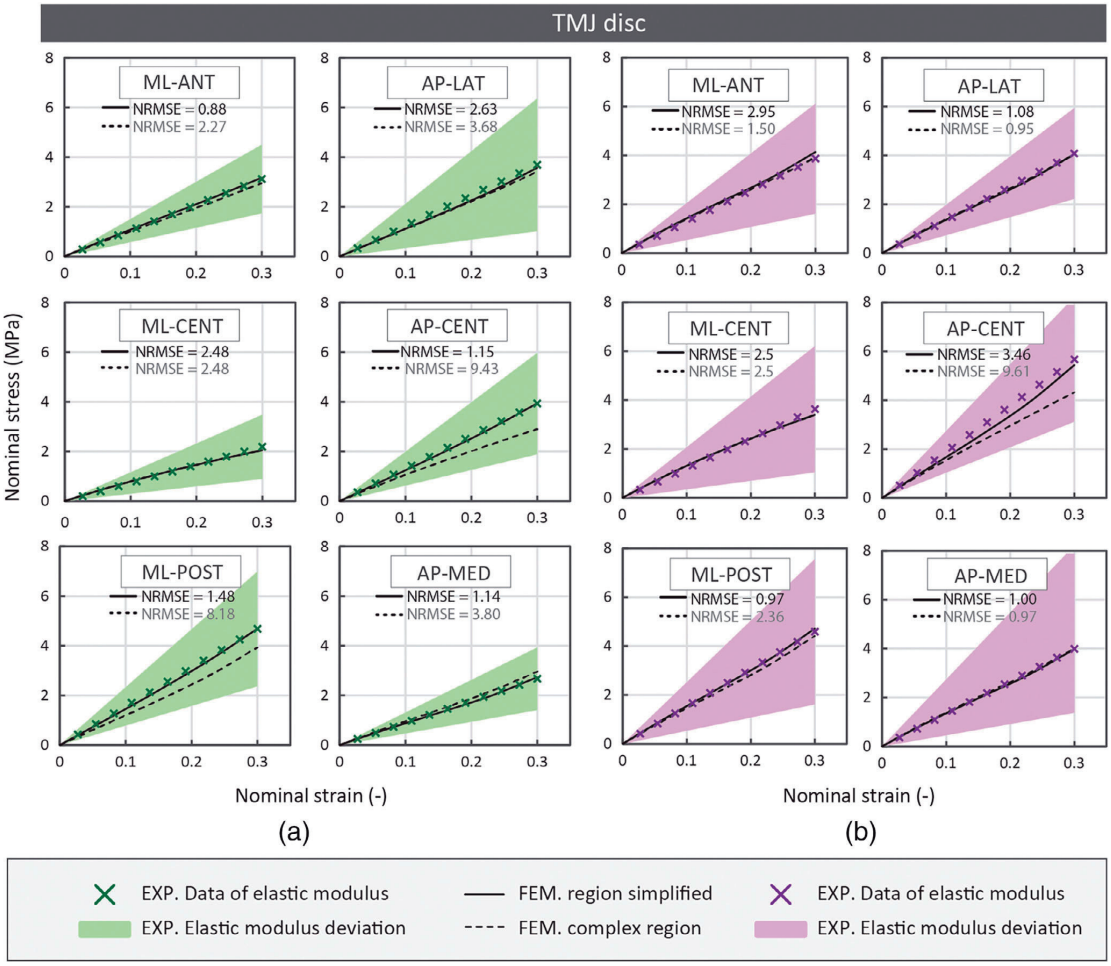

FIGURE 3 Comparison of the tensile response computed from the planar FE model sample by using a single (continuous line) or multiple (discontinuous line) fibers orientations regarding the experimental data (Wright et al., 2016) for the TMJ disc of man (green) and woman (purple). Regions: ANT, anterior; CENT, central; POST, posterior; LAT, lateral; MED, medial; Directions: AP, anteroposterior; ML, mediolateral

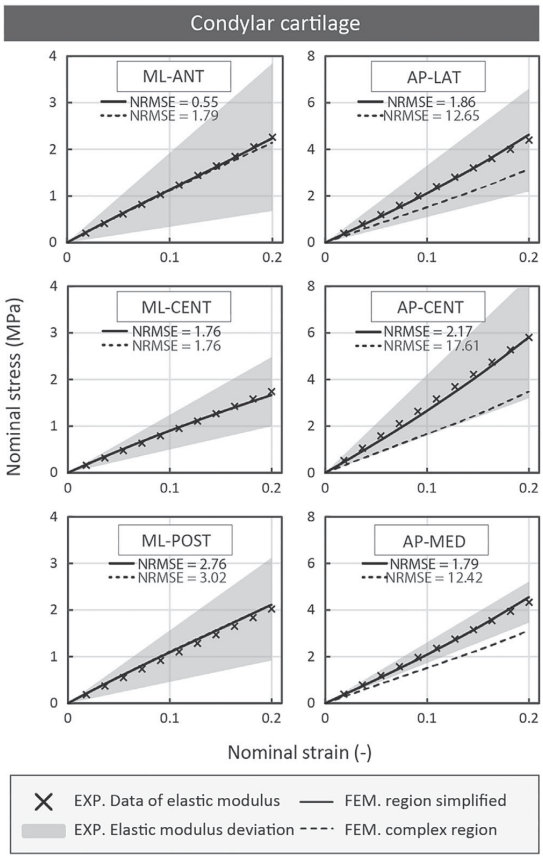

FIGURE 4 Comparison of the tensile response computed from the planar FE model sample by using a single (continuous line) or multiple (discontinuous line) fibers orientations regarding the experimental data (Singh & Detamore, 2008) for the condylar cartilage. Regions: ANT, anterior; CENT, central; POST, posterior; LAT, lateral; MED, medial; Directions: AP, anteroposterior; ML, mediolateral

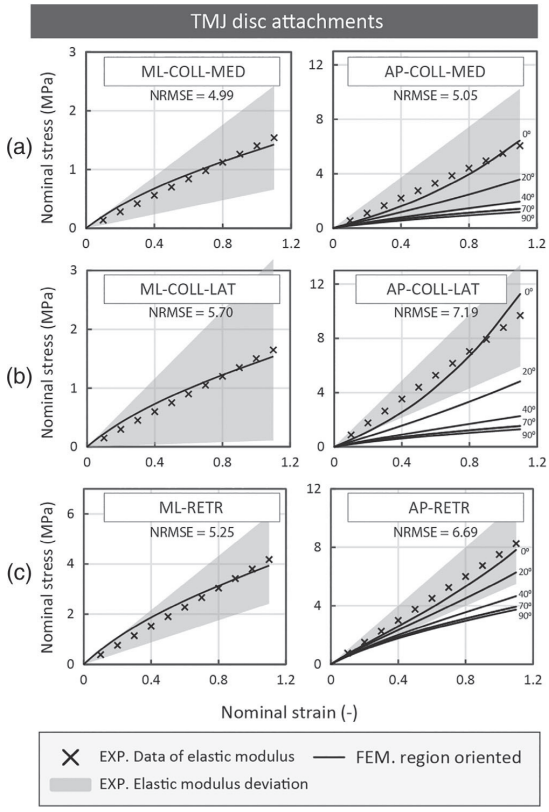

FIGURE 5 Comparison of the tensile response computed from the planar FE model sample by using a single (continuous line) or multiple (discontinuous line) fibers orientations regarding the experimental data (Murphy et al., 2013) for the (a) medial collateral ligament; (b) lateral collateral ligament, and (c) retrodiscal tissue. Directions: AP, anteroposterior; ML, mediolateral

samples that were stretched in the anteroposterior direction (AP-LAT, AP-CENT, and AP-MED) with NRMSE values higher than 10%. As a result of the orientation of the fibrous network in these three samples, the anterior and posterior regions are stretched more than the central region. The fibers of the anterior and posterior regions pose almost no resistance because they are not oriented in the direction in which the sample is stretched. Consequently, the degree of stretching in these two bands is greater, leading to a reduction in the stiffness of the sample.

The effect of fiber network orientation on the tensile mechanical response of disc attachments is illustrated in Figure 5. As its analytical statement describes, tissue stiffness increases when the fibers are oriented in the direction of the load. Conversely, when the fibers are oriented transversally relative to the direction of load, the resulting behavior resembles that observed for the hyperelastic material model.

Despite the differences between both approaches, the NRMSEs are lower than 7.2% for all simulations that considered singular orientation of the collagen network and all material responses fall within the experimental deviation.

Figure 6 shows the compressive response of the TMJ disc obtained using the cylindrical FE model. An unfitted compressive response was obtained using the porous transversely isotropic hyperelastic material description to describe the experimental data of Beek et al. (2001). In this scenario, energy dissipation during the loading–unloading cycle (known as hysteresis) was almost inappreciable, possibly owing to the quasi-incompressible behavior of the tissue and the minimal contribution of the fluid phase. Meanwhile, the porous hyperfoam model produced a better curve fit, and more marked hysteresis, as illustrated in the color maps in Figure 6b–d. Comparison of the two models reveals that the minimum principal stress of the solid matrix (Figure 6b) is greater for the porous transversely isotropic material model, while the interstitial fluid pressure

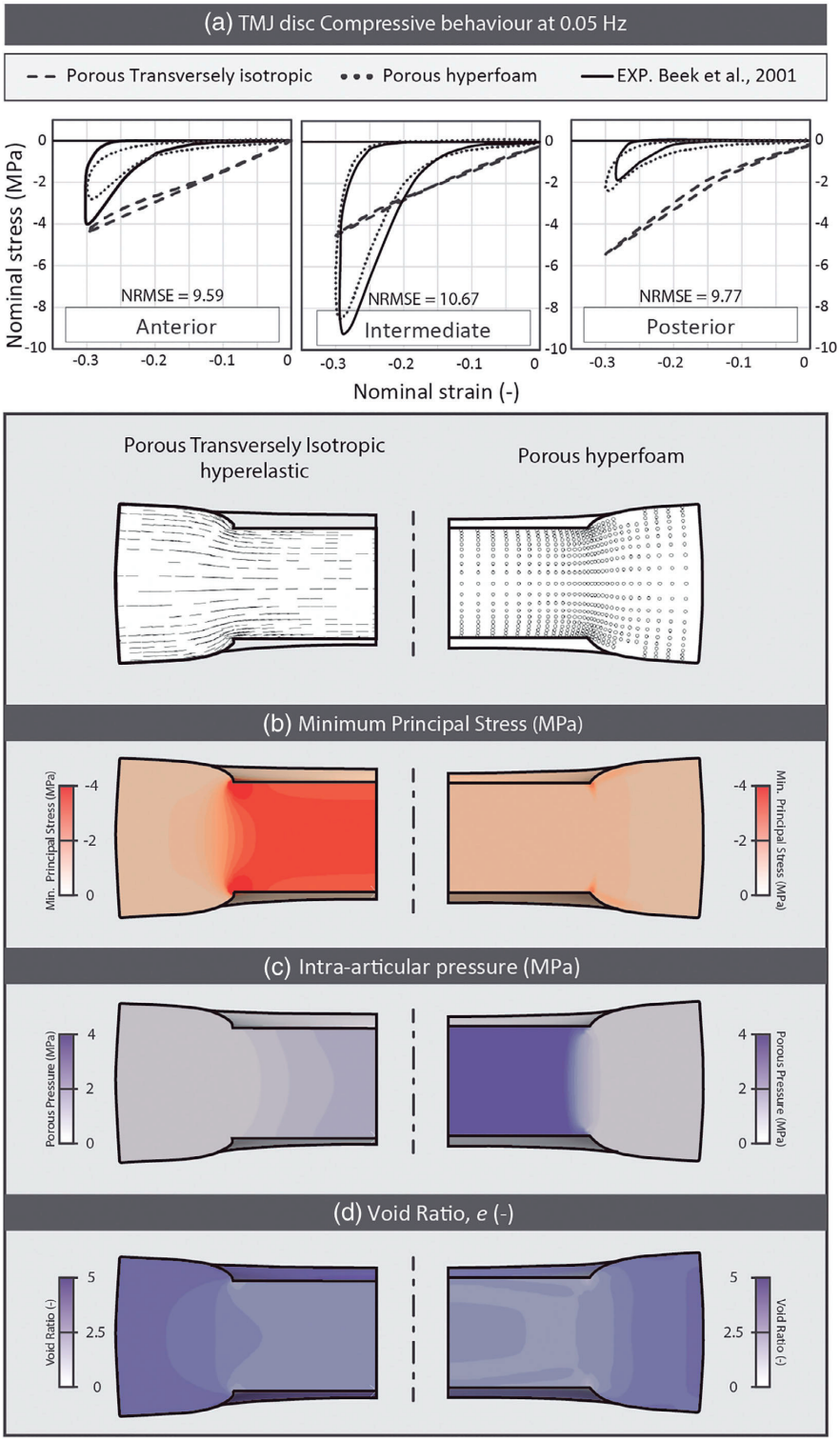

FIGURE 6 Legend on next page.

is greater for the porous hyperfoam material model (Figure 6c). This outcome demonstrates the marked contribution of the fluid phase in the porous hyperfoam model. This contribution is also reflected in the capacity of the fluid to fill surrounding areas, resulting in a higher void ratio gradient in the porous hyperfoam model (Figure 6d). To verify the porous effect using the porous hyperfoam model, we also compared results obtained at different frequencies (Figure S1) with those of Beek et al. (2001). Although, the computed response of the intermediate region at a high strain rate (0.05 Hz) and strain (35%) is the most deviated from the experimental results of Beek and coworkers, all values fell within the experimental deviation.

4 | DISCUSSION

The first part of this study describes the characterization of the fibrous properties of the soft tissues of the TMJ using a transversely isotropic hyperelastic material model (Holzapfel, 2000). The material parameters were computed for the collateral ligaments, the retrodiscal tissue, the five regions of the TMJ disc, and the condylar cartilage. While many studies have sought to characterize these tissues (see Table S2), the existing literature contains many conflicting findings, owing to the complex behavior of these tissues.

Several experimental studies have investigated the biomechanical behavior of the TMJ disc. While most of these studies take into account the biomechanical differences between different regions of the disc (shown in Table S2), few consider the influence of fiber orientation on the outcomes obtained (shown in Table S2). Thus, in the present study, we examined the biomechanical responses of the TMJ disc in the context of the different potential orientations of the collagen fiber network. The anterior and posterior bands of the TMJ disc are stiffer in the mediolateral direction because of the ring-like distribution of the collagen fibers in these regions. By contrast, the remaining regions are stiffer in the anteroposterior direction owing to the anteroposterior orientation of the fibers. These properties can be related to the physiological function of the disc. When the disc is compressed against the mandibular fossa by the chewing muscles, the ring-shaped fibers help maintain the shape of the disc (Angelo et al., 2016; Detamore & Athanasiou, 2003). On the other hand, the fibers of the central region (mainly anteroposteriorly oriented) support protrusion and retrusion movements (Palla, Gallo, & Gossi, 2003) of the mandible. The fact that both the non-fibrous hyperelastic matrix and the collagen network are stiffer in women than in men may have etiological implications for the onset and progression of TMDs in women (Wright et al., 2016).

Despite inconsistencies in the literature regarding the compressive properties of the TMJ disc, it is clear that the disc response is softer in compression than in tension (Allen & Athanasiou, 2006). The study by Beek et al. (2001) is one of the most important experimental studies of the compressive response of the TMJ published to date. In that study, the authors demonstrated that the compressive response is dependent on strain-rate, a relationship they propose may help explain some of the discrepancies in the literature. They examined the effects of compression in different regions (intermediate, anterior, and posterior bands) of seven human TMJ discs. When the tissue is compressed, the fibers are not stretched, and the tissue softens, resulting in the absorption of most of the stress by the interstitial fluid. In the present study, we included the porous contribution in a transversely isotropic hyperelastic material model in order to quantify the contribution of the interstitial fluid. However, the porous formulation of the fiberless matrix defined by a Neo-Hookean hyperelastic material formulation does not fit well with the compressive experimental data of Beek et al. (2001). We therefore assessed the compressive response of the tissue using a porous hyperfoam material model, which allowed us to characterize the hysteresis behavior generated by the viscoelastic effects of the interstitial fluid. Using this material model, we also correctly mimicked the compressive responses of the TMJ disc at different frequencies and strain rates.

We propose therefore a complex model for TMJ soft tissues that considers the contribution of collagen fibers and the compression of the interstitial fluid. This model is based on a model generated by our group for another soft tissue, the periodontal ligament (Ortún-Terrazas et al., 2018, 2019). When the tissue is compressed $\left(\tilde{I}_4 \leq 1\right)$ the strain energy function is defined by the porous hyperfoam material model (Equation (10)). When the tissue is stretched $\left(\tilde{I}_4 > 1\right)$, its behavior is defined by the porous transversely isotropic hyperelastic material model (Equation (1)). Therefore, the behavior of the disc can be described as quasi-incompressible for tensile loading (Beek et al., 2001; Tanaka et al., 2004) but highly compressible under slow compressive loads (Hagandora, Chase, & Almarza, 2011; Spilker, Nickel, & Iwasaki, 2009).

Few experimental studies have analyzed the biomechanical response of condylar cartilage, and almost none have evaluated the temporal cartilage (shown in Table S2). This dearth of information is largely due to the complex structure of this hyaline articular cartilage, which differs to that of other forms of hyaline cartilages in the appendicular skeleton (Milam, 2003). The distribution of collagen fibers suggests that the fibrous zone is mainly subjected to tensile load, while the mature and hypertrophic zones support compressive loads (Singh & Detamore, 2009). The zones proximal to the subchondral bone are rich in aggrecan and poor in collagen fibers. Therefore, the mature and hypertrophic zones of condylar cartilage primarily serve to resist compressive load. On the other hand, the collagen fibers of the fibrous region are predominantly oriented in the anteroposterior direction (Singh & Detamore, 2008) following the main sliding

FIGURE 6 (a) Compressive response of the anterior, intermediate, and posterior regions of the TMJ (0.05 Hz) evaluated using a porous transversely isotropic hyperelastic model (narrow discontinuous line) and a porous hyperfoam material model (dotted line); distribution of (b) minimum principal stress; (c) porous pressure, and (d) void ratio in the cylindrical FE model using the porous transversely isotropic hyperelastic material model (left) and the porous hyperfoam material model (right)

direction of the condyle. The condylar cartilage is likely subjected to anteroposterior shear stress (Singh & Detamore, 2009), which results in a preferred anteroposterior collagen fiber alignment in the fibrous zone (Singh & Detamore, 2008). This study was based on the aforementioned relationship between shear/tensile stresses and the fibrous region of the cartilage. Even though the specimens stretched by Singh and Detamore (2008) were cartilage samples with fibrous and hyaline-like cartilage regions, the authors assumed that the fibrous region was the only part that supported tensile stress. Consistent with this simplification, this tissue shows greater stiffness when stretched anteroposteriorly as a result of the significant contribution of the fibrous network. Furthermore, the deviation between the results obtained for single versus multiple fiber orientations was greater for the condylar cartilage than any other soft tissues of the TMJ. This can be explained by the greater differences in stiffness between the fiberless and fibrous matrices of this tissue than the other TMJ soft tissues.

Regarding the tissues that attach the TMJ disc to the surrounding tissue, although they are extremely important for coordinated movements of the joint (Willard, Arzi, & Athanasiou, 2012), little is known about their mechanical properties. Most studies performed to date have focused on identifying the functional requirements of the lateral and posterior attachments (Liu & Herring, 2000; Sun, Liu, & Herring, 2002; Tanaka et al., 2002, 2003). Although these studies consider the composition of the fibrous tissue, they do not account for fiber orientation. However, in their study Murphy and coworkers tested the response of discal attachments to tension in two different directions (Murphy et al., 2013). By using those data, we were able to separately characterize the contributions of the hyperelastic matrix and the fibrous network in collateral ligaments and retrodiscal tissue.

The collateral ligaments join the disc to the head of the condyle, where they combine with the joint capsule. These lateral attachments keep the disc fixed to the condyle during retrusion and protrusion movements. The fiber bundles in the collateral ligaments are mainly oriented in an anteroposterior direction to withstand anteroposterior sliding movement of the condyle, maintaining the TMJ disc positioning (Murphy et al., 2013). To date, the few computational studies that have modelled the collateral ligament (Commisso, Martínez-Reina, & Mayo, 2014; Pérez del Palomar & Doblaré, 2006) have simulated its behavior based on the known properties of the knee ligament. However, Murphy et al. (2013) did conduct some experimental studies of porcine collateral ligament. By using those data, which were generated from samples that closely resemble the human collateral ligament, we can separately consider the properties of the hyperelastic fiberless matrix and the fibrous network.

Our numerical data corroborate this function–orientation relationship, demonstrating greater stiffness of the collateral ligament in the anteroposterior direction. Remarkably, our data indicate that the medial collateral ligament is softer than the lateral ligament. This may be due to the lower collagen fiber content of the medial region (Willard et al., 2012). According to our results, the response of the collateral ligaments is highly dependent on the orientation of the fibrous network. Thus, the connection formed by the collateral ligaments between the TMJ disc and the condyle is less stiff when the fibers in these ligaments are oriented mediolaterally. This phenomenon may be implicated in the progression from normal to abnormal joint motion observed in patients with TMDs.

In their study of the mechanical properties of the posterior attachment, Tanaka and coworkers examined the viscoelastic response to compressive efforts of bovine retrodiscal tissue, but did not consider fibrous reinforcement (Tanaka et al., 2002). However, a 2013 analysis (Murphy et al., 2013) of the response of porcine retrodiscal tissue to tensile stress did consider the influence of fiber orientation. Thus, by using those data we were able to characterize the parameters of the transversely isotropic hyperelastic material model. Our results show that greater stiffness is associated with fiber orientation in the anteroposterior direction. Moreover, we found that the stiffness of the fiberless matrix was similar to that of the fibrous network, possibly because fibers are more randomly dispersed in this tissue, resulting in stiffer isotropic behavior.

4.1 | Study limitations

The findings presented here constitute an important step toward characterizing the fibrous properties of the soft tissues of the TMJ and the porous-fibrous properties of the TMJ disc. Nonetheless, several limitations of the study should be considered. First, for the material characterization of each sample, we assumed a preferential direction of fiber orientation. Although, the consideration of different regions and fibers orientations did not cause several differences, it is better to characterize the properties of the samples based on specific histological studies for each sample and biaxial mechanical test. Another limitation is that the experimental data derived from different species were used to test the computational models described here. Furthermore, the study from which we obtained the data used to characterize the compressive behavior of the TMJ disc (Beek et al., 2001) did not test the medial and lateral regions of the TMJ disc. Therefore, the compression parameters characterized in this study are also applied to the anterior, intermediate, and posterior bands of the disc in part 2 of this study (without distinguishing between medial and lateral regions). Future experimental studies should test samples from the same species and separately analyze all five regions of the TMJ disc. It should be noted that we did not consider the hyaline-like cartilage region in our characterization of the properties of condylar cartilage owing to a lack of sufficient reliable experimental data to describe permeability functions. Finally, the specific test protocols used in this study most likely influenced our findings. The establishment of standard protocols for future experimental tests would considerably facilitate the comparison of results across studies.

5 | CONCLUSION

This study describes the characterization of the porous fibrous properties of the TMJ disc and the fibrous properties of the condylar cartilage,

collateral ligaments, and retrodiscal tissue. The transversely isotropic hyperelastic material model showed limited validity for the characterization of the compressive behavior of the TMJ disc. Consequently, we evaluated the validity of a porous hyperfoam material model for this purpose. These two material models were combined, building upon an existing material model proposed by Ortún-Terrazas et al. (2018) and later validated (Ortún-Terrazas et al., 2019, 2020). The present study further develops the approach proposed by Pérez del Palomar and Doblaré (2006) by considering the fibrous-porous properties of the TMJ disc, and extends this approach to the other soft tissues of the TMJ. Based on our findings, the following conclusions can be drawn:

1. Transversely isotropic hyperelastic material models can be used to explain the differences in the behavior of the TMJ disc, condylar cartilage, collateral ligaments and retrodiscal tissue associated with loading direction.
2. The porous component of the TMJ disc mediates reduced disc stiffness at low rates of deformation and increased stiffness at higher rates.
3. Complex material models are required for characterization of the biomechanical properties of the TMJ disc. The behavior of the collagen fibers and the contribution of the interstitial fluid cannot be defined using a single material model. This study demonstrates that the biphasic nature of the TMJ disc can be defined by combining porous transversely isotropic and porous hyperfoam material models.
4. Compared with other TMJ soft tissues, the assumption of a preferential orientation of fiber direction resulted in poorer fitting of experimental data for the condylar cartilage.
5. Fibers play a fundamental role in connecting the TMJ attachments to the movements of the condyle-disc system, modifying their stiffness according to load direction. Collateral ligaments are less stiff when the condyle compresses the disc against the fossa, but are stiffer, facilitating guidance of the disc, during protrusion and retrusion movements.

Conflict of interests

The authors have no conflicts of interest related to the present work.

ACKNOWLEDGEMENTS

This work was supported by the Spanish Ministry of Economy and Competitiveness (project DPI 2016-79302-R), the European Social Funds and Regional Government of Aragon (grant 2016/20) and Ibercaja-Cai Fundation (grant IT 4/18).

ORCID

Javier Ortún-Terrazas https://orcid.org/0000-0002-6186-5695

REFERENCES

Allen, K. D., & Athanasiou, K. A. (2006). Tissue engineering of the TMJ disc: A review. *Tissue Engineering*, *12*, 060509063358001 Available from: http://www.liebertonline.com/doi/abs/10.1089/ten.2006.12.ft-62

Angelo, D. F., Morouço, P., Alves, N., Viana, T., Santos, F., González, R., … Pinho, M. (2016). Choosing sheep (*Ovis aries*) as animal model for temporomandibular joint research: Morphological, histological and biomechanical characterization of the joint disc. *Morphologie*, *100*, 223–233 Available from: http://linkinghub.elsevier.com/retrieve/pii/S1286011516300261

Argoubi, M., & Shirazi-Adl, A. (1996). Poroelastic creep response analysis of a lumbar motion segment in compression. *Journal of Biomechanics*, *29*, 1331–1339 Available from: http://linkinghub.elsevier.com/retrieve/pii/0021929096000358

Beek, M., Aarnts, M. P., Koolstra, J. H., Feilzer, A. J., & Van Eijden, T. M. G. J. (2001). Dynamic properties of the human Temporomandibular joint disc. *Journal of Dental Research*, *80*, 876–880 Available from: http://jdr.sagepub.com/content/80/3/876.abstract

Beek, M., Koolstra, J. H., & van Eijden, T. M. G. J. (2003). Human temporomandibular joint disc cartilage as a poroelastic material. *Clinical Biomechanics*, *18*, 69–76 Available from:http://linkinghub.elsevier.com/retrieve/pii/S0268003302001353

Bergomi, M., Cugnoni, J., Galli, M., Botsis, J., Belser, U. C., & Wiskott, H. W. A. (2011). Hydro-mechanical coupling in the periodontal ligament: A porohyperelastic finite element model. *Journal of Biomechanics*, *44*, 34–38.

Commisso, M. S., Martínez-Reina, J., & Mayo, J. (2014). A study of the temporomandibular joint during bruxism. *International Journal of Oral Science*, *6*, 116–123 Available from: http://www.nature.com/ijos/journal/v6/n2/full/ijos20144a.html%5Cnhttp://www.nature.com/ijos/journal/v6/n2/pdf/ijos20144a.pdf

Detamore, M. S., & Athanasiou, K. A. (2003). Motivation, characterization, and strategy for tissue engineering the temporomandibular joint disc. *Tissue Engineering*, *9*, 1065–1087 Available from: http://www.liebertonline.com/doi/abs/10.1089/10763270360727991

Detamore, M. S., & Athanasiou, K. A. (2005). Evaluation of three growth factors for TMJ disc tissue engineering. *Annals of Biomedical Engineering*, *33*, 383–390 Available from: http://link.springer.com/10.1007/s10439-005-1741-y

Hagandora, C. K., Chase, T. W., & Almarza, A. J. (2011). A comparison of the mechanical properties of the goat temporomandibular joint disc to the mandibular condylar cartilage in unconfined compression. *Journal of Dental Biomechanics*, *2011*, 212385 Available from: http://www.pubmedcentral.nih.gov/articlerender.fcgi?artid=3134092&tool=pmcentrez&rendertype=abstract

Holmes, M. H., & Mow, V. C. (1990). The nonlinear characteristics of soft gels and hydrated connective tissues in ultrafiltration. *Journal of Biomechanics*, *23*, 1145–1156 Available from: https://linkinghub.elsevier.com/retrieve/pii/002192909090007P

Holzapfel, G. (2000). *Nonlinear solid mechanics: A continuum approach for engineering*. New York: Wiley.

Ingawalé, S., & Goswami, T. (2009). Temporomandibular joint: Disorders, treatments, and biomechanics. *Annals of Biomedical Engineering*, *37*, 976–996 Available from: http://journals.sagepub.com/doi/10.1177/154405910808701101

Kuo, J., Zhang, L., Bacro, T., & Yao, H. (2010). The region-dependent biphasic viscoelastic properties of human temporomandibular joint discs under confined compression. *Journal of Biomechanics*, *43*, 1316–1321 Available from: https://doi.org/10.1016/j.jbiomech.2010.01.020

Liu, Z.-J., & Herring, S. W. (2000). Masticatory strains on osseous and ligamentous components of the temporomandibular joint in miniature pigs. *Journal of Orofacial Pain*, *14*, 265–278.

Milam, S. B. (2003). Pathophysiology and epidemiology of TMJ. *Journal of Musculoskeletal & Neuronal Interactions*, *3*, 382–390.

Murphy, M. K., Arzi, B., Hu, J. C., & Athanasiou, K. A. (2013). Tensile characterization of porcine temporomandibular joint disc attachments. *Journal of Dental Research*, *92*, 753–758 Available from: http://www.ncbi.nlm.nih.gov/pubmed/23783320

Nickel, J. C., & McLachlan, K. R. (1994). In vitro measurement of the stress-distribution properties of the pig temporomandibular joint disc.

Archives of Oral Biology [Internet, *39*, 439–448 Available from: https://linkinghub.elsevier.com/retrieve/pii/0003996994901759

Ogden, R. W. (1972). Large deformation isotropic elasticity: On the correlation of theory and experiment for compressible rubberlike solids. *Proceedings: Mathematical, Physical and Engineering Sciences*, *328*, 567–583 Available from: http://rspa.royalsocietypublishing.org/cgi/doi/10.1098/rspa.1972.0096

Ortún-Terrazas, J., Cegoñino, J., & Pérez del Palomar, A. (2020). In silico study of cuspid' periodontal ligament damage under parafunctional and traumatic conditions of whole-mouth occlusions. A patient-specific evaluation. *Computer Methods and Programs in Biomedicine*, *184*, 105107 Available from: https://linkinghub.elsevier.com/retrieve/pii/S0169260719311599

Ortún-Terrazas, J., Cegoñino, J., Santana-Penín, U., Santana-Mora, U., & Pérez del Palomar, A. (2018). Approach towards the porous fibrous structure of the periodontal ligament using micro-computerized tomography and finite element analysis. *Journal of the Mechanical Behavior of Biomedical Materials*, *79*, 135–149 Available from: https://doi.org/10.1016/j.jmbbm.2017.12.022

Ortún-Terrazas, J., Cegoñino, J., Santana-Penín, U., Santana-Mora, U., & Pérez del Palomar, A. (2019). A porous fibrous hyperelastic damage model for human periodontal ligament: Application of a micro-computerized tomography finite element model. *International Journal of Numerical Methods in Biomedical Engineering*, *35*, e3176. Available from: http://doi.wiley.com/10.1002/cnm.3176

Palla, S., Gallo, L., & Gossi, D. (2003). Dynamic stereometry of the temporomandibular joint. *Orthodontics and Craniofacial Research*, *6*, 37–47.

Pérez del Palomar, A., & Doblaré, M. (2006). 3D finite element simulation of the opening movement of the mandible in healthy and pathologic situations. *Journal of Biomechanical Engineering*, *128*, 242 Available from: http://biomechanical.asmedigitalcollection.asme.org/article.aspx?articleid=1415491

Singh, M., & Detamore, M. S. (2008). Tensile properties of the mandibular condylar cartilage. *Journal of Biomechanical Engineering*, *130*, 011009 Available from: http://biomechanical.asmedigitalcollection.asme.org/article.aspx?doi=10.1115/1.283e8062

Singh, M., & Detamore, M. S. (2009). Biomechanical properties of the mandibular condylar cartilage and their relevance to the TMJ disc. *Journal of Biomechanics*, *42*, 405–417 Available from: http://linkinghub.elsevier.com/retrieve/pii/S0021929008006623

Spilker, R. L., Nickel, J. C., & Iwasaki, L. R. (2009). A biphasic finite element model of in vitro plowing tests of the temporomandibular joint disc. *Annals of Biomedical Engineering*, *37*, 1152–1164 Available from: http://link.springer.com/10.1007/s10439-009-9685-2

Storakers, B. (1986). On material representation and constitutive branching in finite compressible elasticity. *Journal of the Mechanics and Physics of Solids*, *34*, 125–145 Available from: http://linkinghub.elsevier.com/retrieve/pii/0022509686900335

Sun, Z., Liu, Z.-J., & Herring, S. W. (2002). Movement of temporomandibular joint tissues during mastication and passive manipulation in miniature pigs. *Archives of Oral Biology*, *47*, 293–305.

Systèmes, D. (2014). Abaqus analysis user's guide, version 6.14. In *Dassault Systèmes*. Simulia: Rhode Island, United States.

Tanaka, E., Del Pozo, R., Sugiyama, M., & Tanne, K. (2002). Biomechanical response of retrodiscal tissue in the temporomandibular joint under compression. *Journal of Oral and Maxillofacial Surgery* [Internet, *60*, 546–551 Available from: http://linkinghub.elsevier.com/retrieve/pii/S0278239102844792

Tanaka, E., Del Pozo, R., Tanaka, M., Asai, D., Hirose, M., Iwabe, T., & Tanne, K. (2004). Three-dimensional finite element analysis of human temporomandibular joint with and without disc displacement during jaw opening. *Medical Engineering & Physics*, *26*, 503–511 Available from: http://linkinghub.elsevier.com/retrieve/pii/S1350453304000414

Tanaka, E., Hanaoka, K., Tanaka, M., Van Eijden, T., Iwabe, T., Ishino, Y., … Tanne, K. (2003). Viscoelastic properties of bovine retrodiscal tissue under tensile stress-relaxation. *European Journal of Oral Sciences*, *111*, 518–522 Available from: http://doi.wiley.com/10.1111/j.0909-8836.2003.00081.x

Willard, V. P., Arzi, B., & Athanasiou, K. A. (2012). The attachments of the temporomandibular joint disc: A biochemical and histological investigation. *Archives of Oral Biology*, *57*, 599–606 Available from: https://doi.org/10.1016/j.archoralbio.2011.10.004

Wright, G. J., Coombs, M. C., Hepfer, R. G., Damon, B. J., Bacro, T. H., Lecholop, M. K., … Yao, H. (2016). Tensile biomechanical properties of human temporomandibular joint disc: Effects of direction, region and sex. *Journal of Biomechanics*, *49*, 3762–3769 Available from: https://doi.org/10.1016/j.jbiomech.2016.09.033

Wu TH. *Soil mechanics*. 1967. Allyn and Bacon, Inc: Boston, MA, United States.

Yeoh, O. H. (1993). Some forms of the strain energy function for rubber. *Rubber Chemistry and Technology*, *66*, 754–771 Available from: http://rubberchemtechnol.org/doi/abs/10.5254/1.3538343

SUPPORTING INFORMATION

Additional supporting information may be found online in the Supporting Information section at the end of this article.

How to cite this article: Ortún-Terrazas J, Cegoñino J, Pérez del Palomar A. Computational characterization of the porous-fibrous behavior of the soft tissues in the temporomandibular joint. *J Biomed Mater Res*. 2020;1–14. https://doi.org/10.1002/jbm.b.34558

Manuscript 6: Biomechanical impact of the porous-fibrous tissue behaviour in the temporomandibular joint movements. An in silico approach

Javier Ortún-Terrazas, José Cegoñino, Amaya Pérez del Palomar

Abstract

The movement of the temporomandibular joint (TMJ) is a function of its complex geometry and its interaction with the surrounding soft tissues. Owing to an increase in the prevalence of temporomandibular joint disorders (TMDs), many computational studies have attempted to characterize its biomechanical behaviour in the last 2 decades. However, most such studies are based on a single computational model that markedly simplifies the complex geometry and mechanical properties of the TMJ's soft tissues. The present study aims to computationally evaluate in a wider sample the importance of considering their complex anatomy and behaviour for simulating both damping and motion responses of this joint. Hence, 6 finite element models of healthy volunteers' TMJ were developed and subjected to both conditions in two different behavioural scenarios. In one, the soft tissues' behaviour was modelled by considering the porous-fibrous properties, whereas in the other case they were simplified assuming isotropic-hyperelastic response, as had been traditionally considered. The damping analysis, which mimic the conditions of an experimental test of the literature, consisted of subject the jaw to 2 distinct compressive loads, while the motion analysis evaluated the condylar path during the mandible centric depression by the action of muscular forces. From the results of both analyses, the contact pressures, intra-articular fluid pressure, path features, and stress/strain values were compared using the porous-fibrous and isotropic-hyperelastic models. Besides the great differences observed between patients due patient-specific morphology, the porous-fibrous approach yielded results closer to the reference experimental values and to the outcomes of other computational studies of the literature. Our findings underscore, therefore, the importance of considering realistic joint geometries and porous-fibrous contribution in the computational modelling of the TMJ, but also in the design of further joint replacements or in the development of new biomaterials for this joint.

Graphical abstract

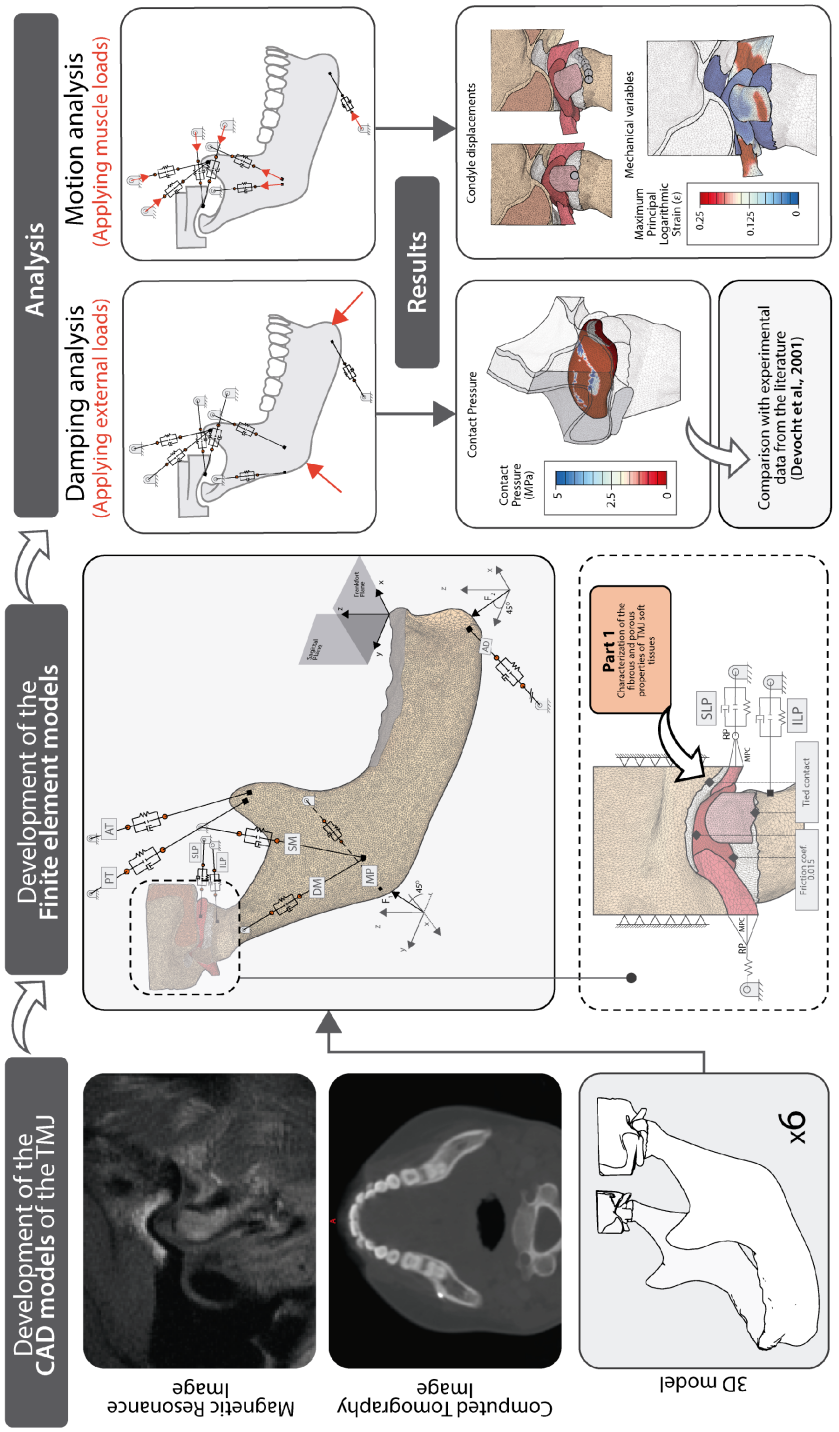

journal of the mechanical behavior of biomedical materials 120 (2021) 104542

Contents lists available at ScienceDirect

Journal of the Mechanical Behavior of Biomedical Materials

journal homepage: www.elsevier.com/locate/jmbbm

Biomechanical impact of the porous-fibrous tissue behaviour in the temporomandibular joint movements. An *in silico* approach

Javier Ortún-Terrazas *, José Cegoñino, Amaya Pérez del Palomar

Group of Biomaterials, Aragon Institute of Engineering Research (I3A), University of Zaragoza, Zaragoza, Spain

ARTICLE INFO

Keywords:
Fibrous structure
Transversely isotropic hyperelastic material model
Poroelastic behaviour
Temporomandibular joint
Magnetic resonance imaging
Computed tomography

ABSTRACT

The movement of the temporomandibular joint (TMJ) is a function of its complex geometry and its interaction with the surrounding soft tissues. Owing to an increase in the prevalence of temporomandibular joint disorders (TMDs), many computational studies have attempted to characterize its biomechanical behaviour in the last 2 decades. However, most such studies are based on a single computational model that markedly simplifies the complex geometry and mechanical properties of the TMJ's soft tissues. The present study aims to computationally evaluate in a wider sample the importance of considering their complex anatomy and behaviour for simulating both damping and motion responses of this joint. Hence, 6 finite element models of healthy volunteers' TMJ were developed and subjected to both conditions in two different behavioural scenarios. In one, the soft tissues' behaviour was modelled by considering the porous-fibrous properties, whereas in the other case they were simplified assuming isotropic-hyperelastic response, as had been traditionally considered. The damping analysis, which mimic the conditions of an experimental test of the literature, consisted of applying two different compressive loads to the jaw. The motion analysis evaluated the condylar path during the mandible centric depression by the action of muscular forces. From the results of both analyses, the contact pressures, intra-articular fluid pressure, path features, and stress/strain values were compared using the porous-fibrous and isotropic-hyperelastic models. Besides the great differences observed between patients due patient-specific morphology, the porous-fibrous approach yielded results closer to the reference experimental values and to the outcomes of other computational studies of the literature. Our findings underscore, therefore, the importance of considering realistic joint geometries and porous-fibrous contribution in the computational modelling of the TMJ, but also in the design of further joint replacements or in the development of new biomaterials for this joint.

1. Introduction

The temporomandibular joint (TMJ) is a load-bearing organ and a profusely operational joint. Temporomandibular joint disorders (TMDs) are thought to affect 20–25% of the world's population (Detamore et al., 2007; Ingawalé and Goswami, 2009), and are often caused by functional anomalies of the components of the TMJ (Fig. 1), including the articular cartilage (temporal and condylar cartilages), TMJ disc, muscles of the masticatory system, retrodiscal tissue, collateral ligaments, and teeth. Located between the condyle and the mandibular fossa, the TMJ disc acts as a shock absorber while ensuring ease of movement of the condyle. The contact surfaces of the condyle and the mandibular fossa are covered by thin layers of cartilage that ensure even distribution of contact pressure on the disc. The friction between the disc and these cartilages is minimized by the surrounding synovial fluid. TMJ disc is moreover connect laterally to the condyle by the collateral ligaments. More posteriorly, the retrodiscal tissue constrains disc movement in the anterior-posterior direction, acting as a volumetric compensatory mechanism for pressure equilibration. Disc is finally stretched anteriorly by the lateral pterygoid muscle. Although the role of this muscle remains a topic of unfinished debate in the literature (DeVocht et al., 1996), it is known to play a key role in advancing the TMJ disc during mandible depression.

A better understanding of the biomechanical behaviour of all these tissues would facilitate the development of treatments for TMDs and the design of more effective implants. However, because the in vivo placement of sensing devices inside the TMJ can cause soft tissue damage, experimental analysis of the TMJ is particularly challenging. To avoid

* Corresponding author. Aragon Institute of Engineering Research (I3A), School of Engineering and Architecture, University of Zaragoza, Calle María de Luna 3, 50018, Zaragoza, Spain.
E-mail address: javierortun@unizar.es (J. Ortún-Terrazas).

https://doi.org/10.1016/j.jmbbm.2021.104542
Received 12 January 2021; Received in revised form 13 April 2021; Accepted 16 April 2021
Available online 27 April 2021

this problem, many researchers use finite element (FE) analysis to study the biomechanical response in this joint. Nevertheless, although many such studies of the TMJ have been published (see Table 1), the accuracy of their outcomes remains unclear, owing to the irregular geometry and complex structure of the TMJ, a lack of knowledge regarding its response to different loading conditions, and difficulties in modelling the mechanical properties of the soft tissues of the joint, among other factors. In this sense, computational studies have typically made several fundamental assumptions: the biomechanical behaviour of the soft tissues of the TMJ is assumed to be linear and isotropic (neither porous nor fibrous contributions are considered), limiting the model to 2 dimensions; or omitting several regions of the TMJ (e.g., collateral ligaments, retrodiscal tissues) in the *in silico* models. Fortunately, more recent studies have attempted to address these oversimplifications, generating detailed 3D models based on images acquired by magnetic resonance images (MRI) (Commisso et al., 2014; Mori et al., 2010) or including nonlinear and time-dependent mechanical behaviours in their computational analyses (Koolstra and van Eijden, 2007; Mori et al., 2010; Pérez del Palomar and Doblaré, 2006a). Nonetheless, most computational studies still assume static loading scenarios or limited displacement of the condyle (Mori et al., 2010; Pérez del Palomar and Doblaré, 2006a), giving rise to unrealistic loading scenarios with high reaction forces (Commisso et al., 2014). Furthermore, these FE models have not proved in both damping and motion conditions and until now no *in silico* database of TMJ models has been compiled.

The present study aimed, therefore, to evaluate computationally patient-specific geometries and porous-fibrous contribution of TMJ's soft tissues in the simulation of joint's movements. Hence, based on the combination of MRI and computed tomography (CT) images, we first developed 6 detailed FE models of the TMJ (one per volunteer), each of which included the temporal and condylar bone, the TMJ disc, the temporal and condylar cartilages, the retrodiscal tissue, the collateral ligaments, and a portion of the pterygoid muscle (Fig. 1). Each model was then subjected to damping and motion loading conditions in two different behavioural scenarios, one considering porous-fibrous mechanical properties and the other without considering them for the soft tissues within this joint. Therefore, both analyses were performed twice, applying either a porous-fibrous material model or an isotropic hyperelastic material model in the behavioural descriptions of these tissues. Physical properties of these material models had already been characterized in a previous study (Ortún-Terrazas et al., 2020), but never before had they been implemented in detailed joint models at both loading conditions. As a result, for both behavioural approaches, the damping response within the TMJ was evaluated and the results were compared with experimental measurements and other computational studies of the literature. On the other hand, the motion response of the TMJ during mandible depression was evaluated by comparing the condylar paths computed with those reported in previously published experimental and computational studies. Finally, we discuss the importance of considering the biphasic nature of the joint's soft tissues in its computational modelling, but also the limitations of simplifying their geometry. Furthermore, at the end of the manuscript, the limitations and future research that could be derived from this research are stated.

2. Material and methods

2.1. Development of the TMJ models

Six TMD-free volunteers (4 women, 2 men) aged 28–41 years (mean age, 33.27 ± 4.79 years) participated in this study (see patient data in Table A1 of the Appendix). All volunteers were fully informed and provided written consent to participate in the study. MRI were captured in a supine position using a multi-channel 12-element head array coil in a 1.5-Tesla scanner (Siemens Syngo MRB17, Erlangen, Germany). Images were obtained in a closed mouth position, with an interslice gap of 0.3 mm, a slice thickness of 1 mm (approximately 24 slices per TMJ). Contiguous sagittal and coronal images of the TMJ were captured. The rest geometry of the mandible was determined based on a series of 1500 images captured by a CT scan in the sagittal, coronal, and axial planes and separated by intervals of 0.01 mm. Only half of the mandible and a TMJ eminence were reconstructed from the databases since symmetrical boundary conditions were considered (Beldie et al., 2010; Fričová et al., 2006; Kim et al., 2012; Alkhiary et al., 2012; Ramos et al., 2009; Shrivastava et al., 2015). The assumption of symmetry was made to reduce the size of the model and the instabilities due to contacts, and consequently, reduce the computational time. Although it was recognized that this assumption introduces a limitation to the model, as is later discussed in the limitations section, this was deemed as acceptable for this study (Beldie et al., 2010).

For both MRI and CT images, greyscale image segmentation (Fig. 1a) based on Hounsfield Unit (HU) was performed using Mimics commercial software (Mimics, v.19.; Materialise, Leuven, Belgium). First, from CT images, the cortical and cancellous portions of the bones were

Table 1
Studies of the TMJ using finite-element models, indicating the number of samples simulated (Cases); the dimensionality of the finite element analysis conducted (2D or 3D); the TMJ regions considered in the model; the material model used for the soft tissues in the simulation; and the type of analysis. (AD, articular disc; AL, anterior ligament; CB, condylar bone; CC, condylar cartilage; CL, collateral ligament; DA, discal attachments; JC, joint capsule; PL, posterior ligament; PT, pterygoid muscle; RT, retrodiscal tissue; T, teeth; TB, temporal bone; TC, temporal cartilage, TML, temporomandibular ligament). * Note: Considers different areas within this region.

Reference	Cases	Dim.	Regions	Material model	Analysis
Chen and Xu (1994)	1	2D	AD, AL, CB, TB, PL	Linear elastic	Motion
Tanaka et al. (1994)	1	3D	AD, CB, CC, TB	Linear elastic	Static
DeVocht et al. (1996)	1	2D	AD, CB, DA, TB	Linear elastic	Motion
Chen et al. (1998)	1	2D	AD, AL, CB, CC, PL	Hyperelastic (Mooney–Rivlin) Linear elastic	Motion
Hu et al. (2003)	1	3D	AC, CB, CC*, TB	Linear elastic	Motion
Detamore and Athanasiou (2003)	1	3D	AD, CB, TB	Linear elastic	Static
Donzelli et al. (2004)	1	3D	AD, CB, TB	Porous linear elastic	Motion
Koolstra and van Eijden (2005)	1	3D	AD, CB, CC, TB, TC	Hyperelastic (Mooney–Rivlin) Linear elastic	Motion
Pérez del Palomar and Doblaré (2006b)	1	3D	AD*, CB, CL, LL, TL	Fibre-reinforced poroelastic	Motion
Pérez del Palomar and Doblaré (2006a)	1	3D	AD*, CB, CL, LL, TL	Fibre-reinforced poroelastic	Motion
Koolstra and van Eijden (2007)	1	3D	AD, CB, CC, TB, TC	Non-linear viscoelastic (Maxwell)	Motion
Tanaka et al. (2008)	1	3D	AD, CB, JC, RT, TB	Non-linear viscoelastic (Kelvin)	Almost Static
Mori et al. (2010)	1	3D	AD, CB, CC, JC, RT, TB, TC	Non-linear viscoelastic (Kelvin)	Almost Static
Commisso et al. (2014)	1	3D	AD, CB, CL, TB, TML, JC	Quasi-linear viscoelastic	Motion
Aoun et al. (2014)	1	3D	AD	Marlow model	Motion
Present study	6	3D	AD*, CB, CC*, CL, PT, RT, TB, TC*	Fibre-reinforced poroelastic	Almost static Motion

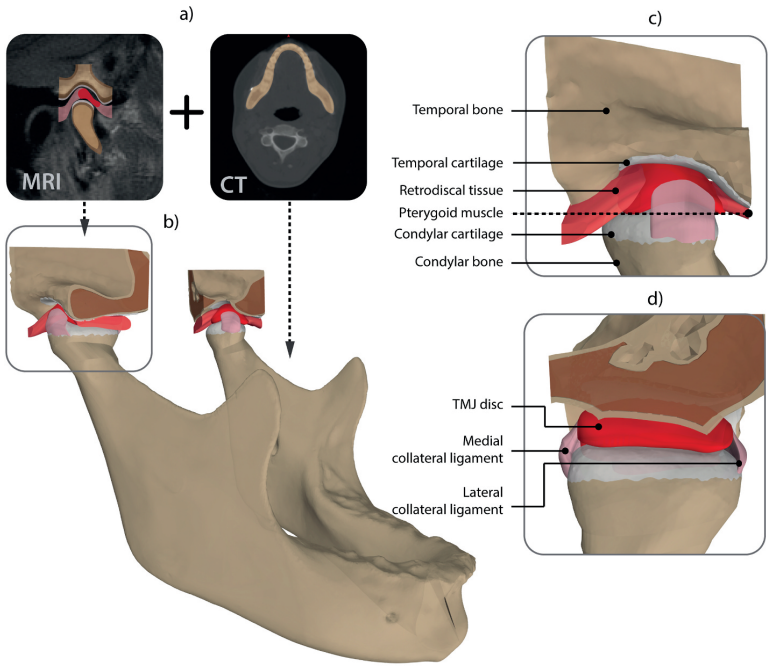

Fig. 1. a) Image acquisition (Left: Segmentation of TMJ soft tissues from MRI; Right: segmentation of mandible from CT images). b) Computer-aided design model combining both models. c) Lateral view of the TMJ. d) Posterior view of the TMJ.

automatically segmented with threshold levels of 662–1988 HU and 148–661 HU, respectively. Next, manual segmentation was performed for regions with less dense bone and for defining the geometry of the soft tissues from MRI. Subsequently, the components of the models were parametrized using Rhinoceros v5 software (Rhinoceros v5, Robert McNeel & Associates, Seattle, United States), thereby transforming non-parametric models into parametric models with non-uniform rational bases splines (NURBS). The 3D parts reconstructed from both scanning techniques were aligned through a script based on the iterative closest point algorithm developed in MATLAB (MATLAB 6.0 R12, The MathWorks Inc., Natick, Massachusetts, United States).

Each model consisted of 9 distinct parts (shown in Fig. 1): the temporal and mandible bones which are subdivided into cortical and alveolar regions; the TMJ disc, situated in the space between the mandibular fossa and the condyle; the collateral ligaments at the medial and lateral sides of the disc; the pterygoid muscle and retrodiscal tissue, located respectively in the anterior and posterior regions of the TMJ disc (Fig. 1c and d); and the temporal and condylar cartilages. The temporal cartilages were modelled in the upper region of the articular surface as thin layers of 0.406, 0.256 and 0.106 mm mean thickness in the anterior, central and posterior regions respectively (see Table A1 of the Appendix). Meanwhile, the condylar cartilages were defined in the lower region of the articular surface as variable thickness layers of 0.393, 0.473 and 0.321 mm mean thickness in the anterior, central and posterior regions respectively (see Table A1 of the Appendix). From the superior view, the TMJ disc appears as an ellipse (longer in the mediolateral direction than the anteroposterior direction), with mean lengths of 12.15 ± 2.56 mm and 9.05 ± 1.21 mm, respectively (see Table A1 of the Appendix). Cartilages and disc attachments were connected respectively to bony structures and TMJ disc by tied contacts, whereas the contact between the disc and the cartilage was defined by a friction coefficient of 0.015 (Tanaka et al., 2004) using a penalty formulation (shown in Fig. 2b).

Each FE model was meshed in Abaqus software (Abaqus 6.14, Simulia, Rhode Island, United States) by approximately 200,954 nodes and 196,419 second-order elements, distributed as shown in Table 2. The edge length of each element was approximately 0.25 mm in all directions and was defined as a result of a mesh converge analysis which consisted of refining iteratively the whole mesh of the model until further mesh refinement produces changes in the result below 5% (Anderson et al., 2005; Schmidt et al., 2009). The iterative mesh refinement process was executed in Abaqus 6.14 through a script written in Python (Python 3.5.2, Python Software Foundation), and started with 0.5 mm element size, decreasing 0.05 mm per iteration. Regarding the element's description, disc attachments and cartilage were meshed using tetrahedral elements with hybrid formulation (C3D10H-type element in Abaqus). For meshing of bony structures, the porous contribution was included in the degree of freedom of the tetrahedral elements (C3D10MP-type element in Abaqus). As for TMJ disc, which was meshed with second-order hexahedral elements of second order with porous coupling (C3D20P-type element in Abaqus). Finally, muscles were modelled by connector-type element (CONN3D2-type element in Abaqus) which are unidirectional deformable elements (shown in Fig. 2a) capable to describe their passive, active, and dampening responses.

Hence, the increase of passive stiffness (F_p^i) of a muscle, i, according

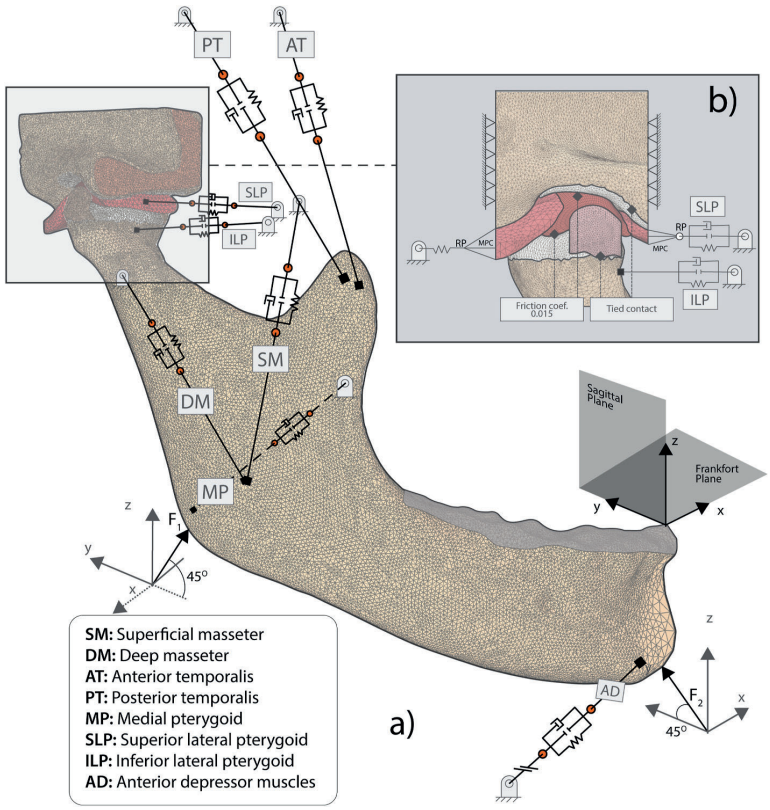

Fig. 2. a) Schematic showing the boundary conditions applied to the FE models and muscle positions. b) Detail of TMJ boundary conditions (RP, reference point; MPC, general multi-point constraints).

Table 2
Types and mean number of elements and nodes for each region of the FE model.

Part	Type of Element	Mean No. of Elements	Mean No. of Nodes
Collateral ligaments			
Lateral	C3D10H	12152	19463
Medial	C3D10H	11622	17336
Condylar cartilage	C3D10H	10580	20524
Mandible bone			
Cancellous portion	C3D10MP	69342	17271
Cortical portion	C3D10	11046	10215
Pterygoid muscle	C3D10H	4160	7038
Retrodiscal tissue	C3D10H	5778	9640
Temporal cartilage	C3D10H	8265	16407
Temporal bone			
Cancellous portion	C3D10MP	10740	18946
Cortical portion	C3D10	23120	32232
TMJ disc	C3D20P	29614	31882
Whole model		196419	200954

to its stretch, ε^i was defined by the following stress-strain non-linear expression (Pérez del Palomar and Doblaré, 2008):

$$F_p^i(t) = \frac{K \cdot \varepsilon^i(t)}{[1 - \varepsilon^i(t)/a]} \cdot PCSA^i \quad (1)$$

where K is the estimated force-length stiffness of the muscles ($K = 40N/cm^2$) (Peck et al., 2000), a is the passive force-length asymptote ($a = 0.7$) (Horst, 2002), $PCSA^i$ is the cross-sectional area of the muscle and ε^i is the ratio between muscle's stretch ($l_t^i - l_f^i$) at instant t and the length of the muscle at the free state, l_f^i. Free state's length is frequently estimated through the length of the muscle in the optimum state (l_0^i) and the lengths of the sarcomeres in a free (S_f^i) and relaxed states ($S_r = 2.73$ μm) (Van Ruijven and Weijs, 1990) as $l_f^i = l_0^i \cdot S_f^i / S_r$.

The damping response (F_d^i) was otherwise defined as a function of the critical damping coefficient (C) and the stretch rate ($\dot{\varepsilon} = d\varepsilon/dt$) along with the muscle longitudinal direction by the following expression:

$$F_d^i(t) = C^i \cdot \dot{\varepsilon}^i(t) \quad (2)$$

Finally, the contractile force exerted by each muscle (F_a^i) was modelled as a function of the maximum force in isometric contraction, F_{max}^i and the activation level, a, at each time of the simulation by the following equation (Commisso et al., 2015; Pérez del Palomar and Doblaré, 2008):

$$F_a^i(t) = a^i(t) \cdot F_{max}^i \quad (3)$$

All the parameters used to define passive, active, and dampening response of the muscle shown in Fig. 2 are summarized in Table 3, but also those reference values used to compute them. It is also remarkable the use of multipoint constraint elements (MPC) (shown in detail in Fig. 2b) to limit the anterior and posterior disc attachments over-stretching. Thereby, the external nodes of the retrodiscal tissue and the superior portion of lateral pterygoid were connected to 2 reference points by MPCs which allow partial rotation of the nodes, reducing

Table 3
Parameters used to compute the active, passive, and damping responses of the muscles of the masticatory system. (SM, superficial masseter; DM, deep masseter; AT, anterior temporalis; PT, posterior temporalis; MP, medial pterygoid; SLP, superior lateral pterygoid; ILP, inferior lateral pterygoid; AD, anterior depressors). Note: $^{*}F_{max}$ computed as the combined maximum physiological forces of grouped muscles of first column; $^{\dagger}S_f^i$ computed as the average of the S_f^i values of the muscles of first column.

Literature data					Model variables				
Muscle	F^i_{max} (N)[a]	l^i_0 (mm)[b]	S^i_f (μm)[c]	$PCSA^i$ (cm^2)	Ref.	F^i_{max} (N)	$PCSA^i$ (cm^2)	S^i_f (μm)	C^i (N/μm)[d]
Superficial masseter	190.4	48.0	2.47	4.76 [d]	SM	190.4	4.76	2.47	53
Deep masseter	81.6	30.9	2.44	2.04 [d]	DM	81.6	2.04	2.44	38
Anterior temporalis	158	57.4	2.35	3.95 [d]	AT	158	3.95	2.35	35
Posterior temporalis	75.6	62.9	2.31	1.89 [d]	PT	75.6	1.89	2.31	23
Medial pterygoid	174.8	43.3	2.48	4.37 [d]	MP	174.8	4.37	2.48	60
Sup. lat. pterygoid	17	29.1	2.72	0.95 [c]	SLP	17	0.95	2.72	–
Inf. lat. pterygoid	50	27.2	2.83	1.67 [c]	ILP	50	1.67	2.83	21
Anterior digastric	50	51.9	2.75	1.16 [c]	AD	110*	4.25*	3.02†	19
Geniohyoid	20	48.5	2.65	0.97 [c]					
Anterior mylohyoid	20	21.8	2.80	2.12 [c]					
Posterior mylohyoid	20	44.8	3.89						

[a] Hannam, Alan G., et al. (2008).
[b] Koolstra and van Eijden (2005).
[c] Van Eijden, T. M. G. J., et al. (1997).
[d] Langenbach, G. E. J., et al. (1999).

potential distortion of border elements. The retrodiscal tissue was moreover prolonged using a spring element (Fig. 2b) of 0.008 N/mm stiffness, according to the specifications of DeVocht et al. (1996).

Regarding the stiffness of the TMJ's soft tissues in our FE models, following several studies' outcomes (Ingawalé and Goswami, 2009; Ruggiero et al., 2015; Singh and Detamore, 2008), the transversely isotropic behaviour produced due to the presence of a collagen network within them was considered. This fibrous behaviour was therefore defined using the Holzapfel strain energy function (Holzapfel, 2000), as follows:

$$W = C_1 \cdot \left(\widetilde{I}_1 - 3\right) + \frac{k_1}{2 \cdot k_2}\left\{exp\left[k_2 \cdot \left(\widetilde{I}_4 - 1\right)^2\right] - 1\right\} + \frac{1}{D}\left(\frac{(J_{el})^2 - 1}{2} - lnJ_{el}\right) \tag{4}$$

where C_1 is a material constant related to the ground substance; $k_1 > 0$ and $k_2 > 0$ are the parameters that identify the exponential behaviour due to the presence of collagen fibres; D is the compressibility modulus; $\widetilde{I}_1$ and $\widetilde{I}_4$ are terms of the modified invariants that arise from uncoupling the dilatational and deviatoric responses, respectively; and J_{el} is the elastic volume strain. Aforementioned fibre-reinforced hyperelastic material model, whose parameter had already been characterized and validated in a previous study (Ortún-Terrazas et al., 2020), was used to describe the mechanical responses of the condylar cartilage, collateral ligaments, and retrodiscal tissue. Table 4 summarizes the material parameters (C_1, k_1, k_2 and D) that define the mechanical behaviour of each tissue. In the case of temporal cartilage, however, condylar cartilage properties were used to describe its behaviour, owing to the lack of published biomechanical data about the fibrous properties in this tissue. Fibre-reinforced TMJ disc, whereas, required a more complex material description with distinct responses to compression and tension, in agreement with previous outcomes (Ortún-Terrazas et al., 2020). Hence, tensile response was defined using the aforementioned constitutive material model (Eq. (4)) while the compressive response was defined using the following material description (Storakers, 1986):

$$W = \frac{2\mu}{\alpha^2}\left[\widehat{\lambda}_1^{\alpha} + \widehat{\lambda}_2^{\alpha} + \widehat{\lambda}_3^{\alpha} - 3 + \frac{1}{\beta}\left(J_{el}^{-\alpha\beta} - 1\right)\right] \tag{5}$$

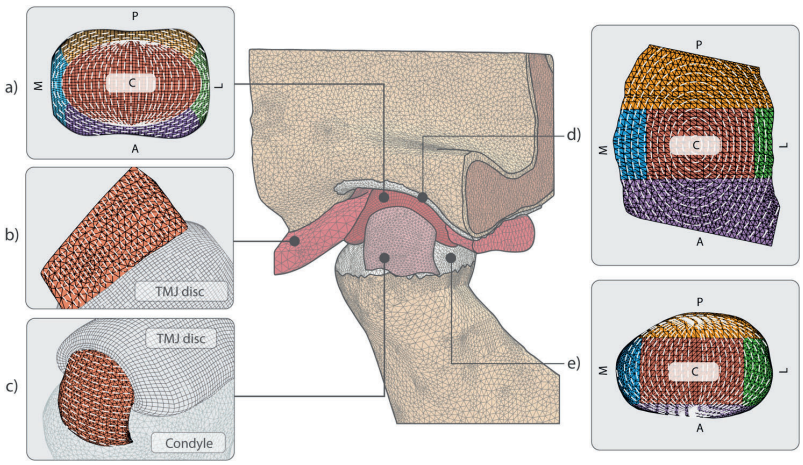

Fig. 3. Mesh of one of the FE models. Image shows fibre orientation in a) the TMJ disc, b) retrodiscal tissue, c) collateral ligament, d) temporal cartilage, and e) the condylar cartilage. A, anterior; L, lateral; M, medial; P, posterior; and C, central region. White discontinuous lines indicate the preferential direction of the fibre network.

where μ and α are material parameters, and the coefficient β determines the degree of compressibility and is related to the Poisson's ratio ν, by $\beta = \nu/(1-2\nu)$. The poroelastic contribution of the TMJ disc was added using the exponential permeability function described by Argoubi and Shirazi-Adl (1996) for biphasic materials: $k = k_0\left[\frac{e(1+e_0)}{e_0(1+e)}\right]^2 exp\left[M\left(\frac{1+e}{1+e_0}-1\right)\right]$ where k_0 and e_0 represent the permeability and void ratio at zero strain, respectively; e is the strain-dependent void ratio; and M is a dimensionless material parameter. The aforementioned properties, which are summarized in Table 4, were introduced into a user material subroutine in Abaqus CAE.

Experimental data from the literature was used to establish the preferential direction of the fibre bundles (shown in Fig. 3a–e) for the main regions of the TMJ disc (Wright et al., 2016), the regions of condylar cartilage (Singh and Detamore, 2008), and the retrodiscal tissue and collateral ligaments (Murphy et al., 2013). Hence, articular disc (Fig. 3a) and cartilages' fibres (Fig. 3d and e) follow a ring-like distribution that can be approximated by the ellipse equation ($x^2/a^2 + y^2/b^2 = 1$) (Detamore and Athanasiou, 2003a–c). Hence, the fibre orientation at each node was approximated from the ellipse function derivative at the coordinates of each node, and then implemented in the aforementioned subroutine in Abaqus. A schematic showing the preferential orientation of fibre direction in each of the different regions of the TMJ disc, the cartilage, and the disc attachments is shown in Fig. 3.

To evaluate the effect of incorporating porous-fibrous properties for the different tissues into our model, the analysis described below was simulated twice. In the first case, we modelled the tissue as an isotropic transversally hyperelastic material, considering the fibrous network by the previous material model. In the second analysis, we expressed the mechanical behaviour of the material using the energy density function of the neo-Hookean material model as follows:

$$W = C_1 \cdot \left(\tilde{I}_1 - 3\right) + \frac{1}{D}(J_{el} - 1)^2 \quad (6)$$

where C_1 is a material constant and the second term is the volumetric component. In scenarios involving a high degree of incompressible behaviour, the volumetric term (second term of Equation (6)) is practically negligible and C_1 can be computed from the elastic modulus (E) in an uniaxial tensile test as follows: $C_1 = E/6$. The elastic modulus of each section was defined based on the same experimental data that was used for the characterization of parameters of fibrous material model (Murphy et al., 2013; Singh and Detamore, 2008; Wright et al., 2016). Otherwise, to examine the biomechanical behaviour of bony structures, the cortical and cancellous portions were defined using poroelastic properties, according to previous studies (Bergomi et al., 2011; Ramos et al., 2015). The parameters that describe the material models are summarized in Table 4.

2.2. Damping and motion analyses

To evaluate the contribution of porous-fibrous properties in the simulation of TMJ's movements, each model was subjected to 2 loading

Table 4
Material model parameters assigned to each region of the model. ANT, anterior; LAT, lateral; CENT, central; MED, medial; POST, posterior; UNIF, tissue considered as uniform (no distinction between regions).

	Solid phase								Porous phase			
	Neo-Hookean mat. model	Trans. Iso. Hype. mat. model				Hyperfoam mat. model			Permeability function parameters			
	C_1 (MPa)	C_1 (MPa)	D (MPa^{-1})	k_1 (MPa)	k_2 (−)	ν (−)	μ (MPa)	α (−)	$k_0 \cdot 10^{-15}$ (m^2)	M (−)	ϕ (−)	γ_w (N/m^3)
TMJ Disc (man) [a]												
ANT	1.73	1.45	0	0.43	0.34	0.1667	1.72	75	8.95	49	0.80	9800
LAT	2.05	1.45	0	0.69	0.43	0.1667	3.86	78	3.64	45	0.79	9800
CENT	2.18	1.45	0	0.97	0.17							
MED	1.48	1.45	0	0.17	1.68							
POST	2.60	1.45	0	1.25	0.16	0.1667	0.86	75	8.07	43	0.83	9800
TMJ Disc (woman) [a]												
ANT	2.15	2.4	0	0.05	3.72	0.1667	1.72	75	8.95	49	0.81	9800
LAT	2.27	2.4	0	0.11	2.52	0.1667	3.86	78	3.64	45	0.79	9800
CENT	3.15	2.4	0	0.75	0.87							
MED	2.22	2.4	0	0.08	2.93							
POST	2.55	2.4	0	0.31	1.44	0.1667	0.86	75	8.07	43	0.83	9800
Condylar cartilage (porcine) [a]												
ANT	1.88	1.65	0	0.24	1.95	-	-	-	-	-	-	-
LAT	3.67	1.65	0	2.58	0.43	-	-	-	-	-	-	-
CENT	4.83	1.65	0	3.77	0.21	-	-	-	-	-	-	-
MED	3.62	1.65	0	2.52	0.42	-	-	-	-	-	-	-
POST	1.68	1.65	0	0.16	1.92	-	-	-	-	-	-	-
Medial Collateral ligaments (porcine) [a]												
UNIF.	0.92	0.38	0	0.68	10^{-5}	-	-	-	-	-	-	-
Lateral Collateral ligaments (porcine) [a]												
UNIF.	1.47	0.41	0	0.35	10^{-5}	-	-	-	-	-	-	-
Retrodiscal tissue (porcine) [a]												
UNIF.	1.25	1.05	0	0.27	10^{-5}	-	-	-	-	-	-	-

	Elastic material model		Permeability function parameters			
	E (MPa)	ν (−)	$k_0 \cdot 10^{-15}$ (m^2)	M (−)	ϕ (−)	γ_w (N/m^3)
Trabecular bone [b]	345	0.31	52.9	-	0.8	9800
Cortical bone [c]	13000	0.30	-	-	-	-
Pterygoid muscle [d]	$6.2 \cdot 10^{-3}$	0.49	-	-	-	-

(a) Ortún-Terrazas et al. (2020)
(b) Bergomi et al. (2011)
(c) Ramos et al. (2015)
(d) Beldie et al. (2010)

Table 5
Forces applied to the model for each of the 4 loading cases simulated and contact stress values obtained experimentally by DeVocht et al. (2001).

Loading cases	A	B	C	D
Loads				
F1 (N)	72	46	57	43
F2 (N)	163	132	155	181
Experimental results				
Max. Contact Stress (MPa)	5.6	8.6	6.4	9.9

probes: in the first test the disc remained in the temporal cavity, while in the second the condyle moved along the articular eminence. Throughout this article, we will refer to these probes as "damping" and "motion" analyses, respectively, according to the main role of the articular disc in each scenario.

For the damping analysis, we simulated experimental tests conducted by Devocht and coworkers (DeVocht et al., 2001) in which the authors subjected the mandible of a human cadaver to 4 loading cases (see Table 5). Each load case consisted of 2 forces applied manually to the gonial angle and the chin (F1 and F2, respectively, in Fig. 2a). Both loads were applied parallel to sagittal plane, forming an angle of 45° with the Frankfort mandibular plane. The loads were applied for 13 seconds to avoid an overpressure effect on the interstitial fluid. In establishing boundary conditions, the anterior and posterior surfaces of the temporal bone were fixed and the movement of the cut section of the mandible in the mediolateral direction was restricted, following the symmetry assumption of the model (Kim et al., 2012). The vertical movement of the nodes of the alveolar region of the mandible (grey area in Fig. 2a) was restricted to simulate the restriction caused by the upper teeth.

For the motion analysis, non-painful mouth centric opening of a healthy patient was simulated (interincisor point downwards approximately 10 mm). The activation response was considered linear (Tuijt et al., 2010) and was applied for 260 msec, in accordance with the duration of physiological mouth opening (Langenbach and Hannam, 1999). Only the cut plane of the mandible was restricted in the mediolateral direction, and the surfaces of the temporal bone were fixed, as in the previous analysis.

3. Results

The results are divided into 2 sub-sections describing the 2 types of analyses performed. Section 3.1 describes the results shown in Figs. 4–6 for the damping simulations, while section 3.2 describes the results of the motion analysis, which are presented in Figs. 7–9. Data were processed and plotted using Matplotlib library (Hunter, 2007) in Python (Python 3.5.2, Python Software Foundation).

3.1. Damping analysis

As discussed in the previous section, the 6 TMJ models with both behavioural approaches were subjected to the 4 different loading scenarios performed by DeVocht and coworkers, who measured the contact pressure of the articular disc in the upper cavity using pressure-sensitive Fujifilm (Inteque Resources Corp, Fort Lee, New Jersey).

Based on the reference experimental values (shown in Table 5), the computed contacts in each model were evaluated in Fig. 4 by plotting the percentage of the contact surface in a range of pressure. The upper limit of the figure's thresholds (blue region) corresponds to the experimental values in each loading case (shown in Table 5), whereas the lower, is half of this value. The computed data was plotted after excluding atypical and null values produced by the concentration or absence of contact in the nodes.

As shown in Fig. 4, the porous-fibrous approach produced greater contact pressures than those obtained through the neo-Hookean approach, which could be potentially cause due to the stiffer behaviour of the biphasic material model. The computed values in porous-fibrous approach were, in addition, closer to the experimental values obtained by DeVocht et al. (2001) (see blue ranges in Fig. 4), being about 5–25% of the contact surface subjected to this levels of pressure.

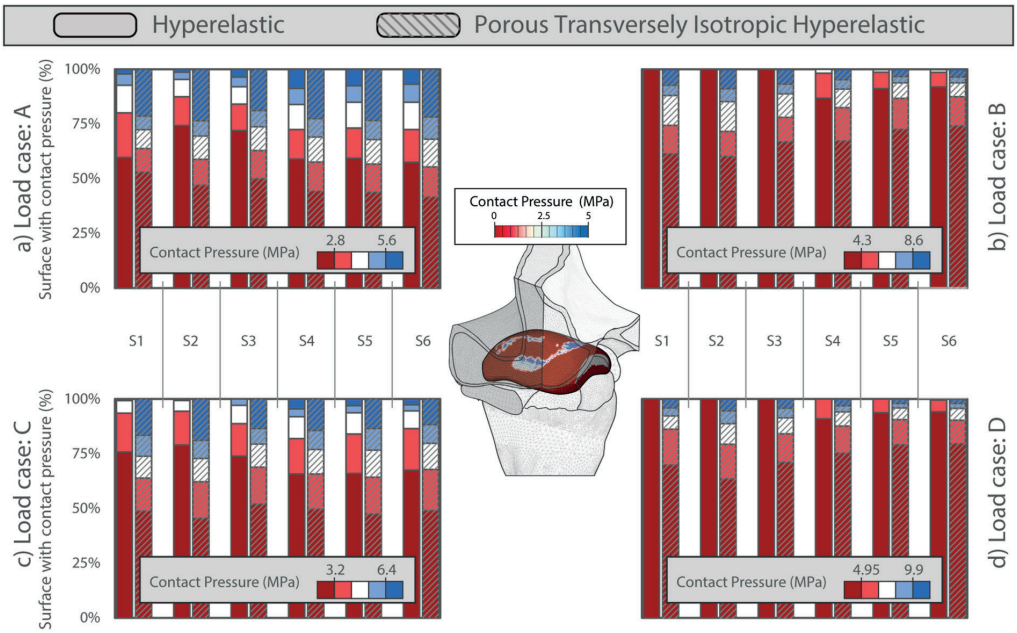

Fig. 4. Percentage on the solid surface of the TMJ's disc under a certain level of pressure for the 6 FE models (S1–S6) using porous transversely isotropic hyperelastic properties (smooth area) and hyperelastic properties (grated area) for load case A (a), case B (b), case C (c), and case D (d).

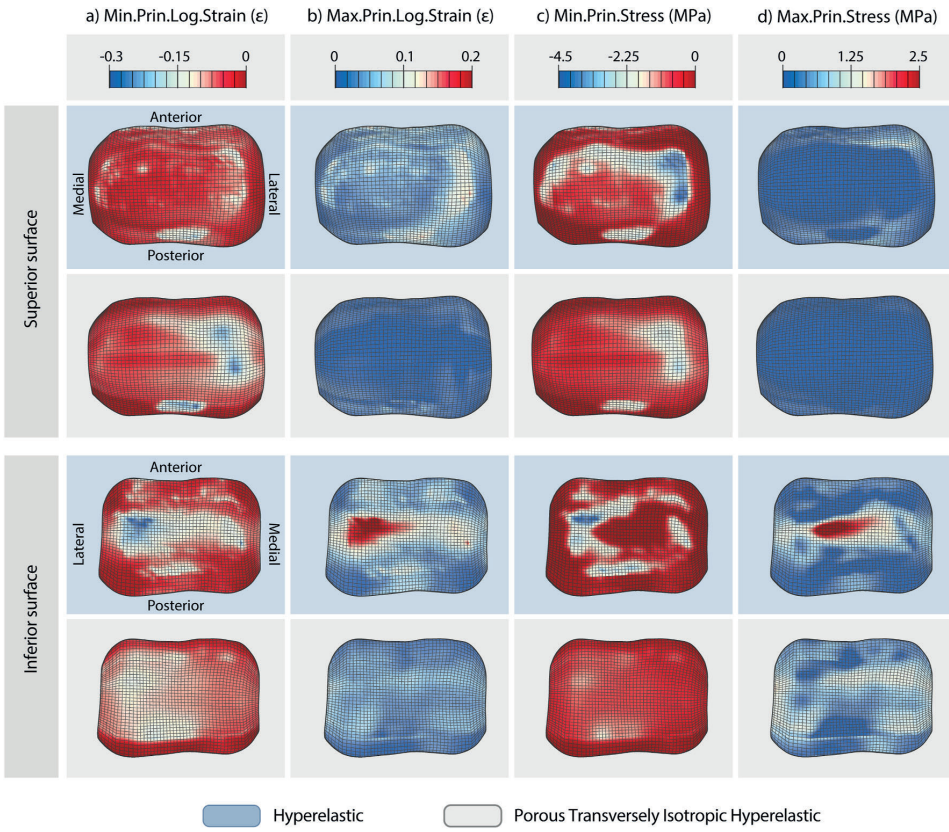

Fig. 5. a) Minimum principal logarithmic strain, b) maximum principal logarithmic strain, c) minimum principal stress, and d) maximum principal stress distribution on the superior (top rows) and inferior (bottom rows) surfaces of the articular disc using hyperelastic properties (blue background) and porous transversely isotropic hyperelastic properties (grey background).

Meanwhile, hyperelastic approach yielded results significantly lower than those obtained experimentally, which were achieved on only 5% of the total contact surface. This difference was especially pronounced in B and D cases, where not even the reference values were reached. Besides these quantitative differences, the pressure distribution on the disc was more similar in those discs with porous-fibrous properties than for those without them.

The contact between the articular disc and the condylar and temporal articular surfaces produced stresses on the disc, which were mainly compressive (see Fig. 5c). To illustrate the distribution of the principal logarithmic strains (Fig. 5a and b) and stresses (Fig. 5c and d) in the disc of subject 2 under the A loading conditions were plotted in Fig. 5. As mentioned above, the porous-fibrous approach resulted in a smoother response throughout the disc than the hyperelastic one. Hence, while the neo-Hookean behaviour concentrated the minimum principal logarithmic strains and stresses in the lateral posterior regions of the disc, the biphasic approach distributed them across the central band (shown in Fig. 5a and c).

From the fluid-solid interaction viewpoint, the central region of the porous-fibrous disc was the most compressed (see Fig. 5a), whereas the peripheral ones were most stretched (Fig. 5b). These outcomes were mainly caused because, when the condyle compresses the central region of the disc (see Fig. 5a), the fluid phase flows, leading to the swelling in the disc periphery. The ring-shaped fibres (Fig. 3a) constrain this expansion effect, leading to maximum stress levels around the disc' periphery (shown in Fig. 5d). Likewise, the collagen fibres of the central region are stretched (shown Fig. 5b) for maintaining the disc shape.

To a further study of the minimum principal logarithmic strains and stresses in the disc of each subject, the radial distribution of the mean values of both variables was respectively plotted in Fig. 6a and b, for both behavioural approaches. The plots were generated through a Python script, by first centring the disc in the polar reference system, then excluding the atypical and null values from the analysis, and finally computing and plotting the mean values of the mechanical variable for each revolution degree.

As it can be seen, although the mean values of the compressive logarithmic strain were quite similar for both approaches, ranging between −0.05 and −0.12ε (shown Fig. 6a), the compressive stress values were significantly different. Thereby, while the non-biphasic approach yielded mean values of compressive stress within −0.8 to −1.2 MPa, the biphasic behaviour reduced the average stress in the solid matrix of the disc below −0.5 MPa. As was previously noted, the stress relaxation in the two-phasic disc was mainly caused by the contribution of the fluid phase (shown in Fig. 6c), distributing and supporting a considerable portion of the load. Because of this support, the intra-articular fluid pressure achieves values of up to 57.8 mmHg in the lateral posterior regions of the discs (shown in Fig. 6c). The reader is hereby reminded that the intra-articular pressure has only been plotted for the porous-fibrous approach since the hyperelastic approach has no fluid phase.

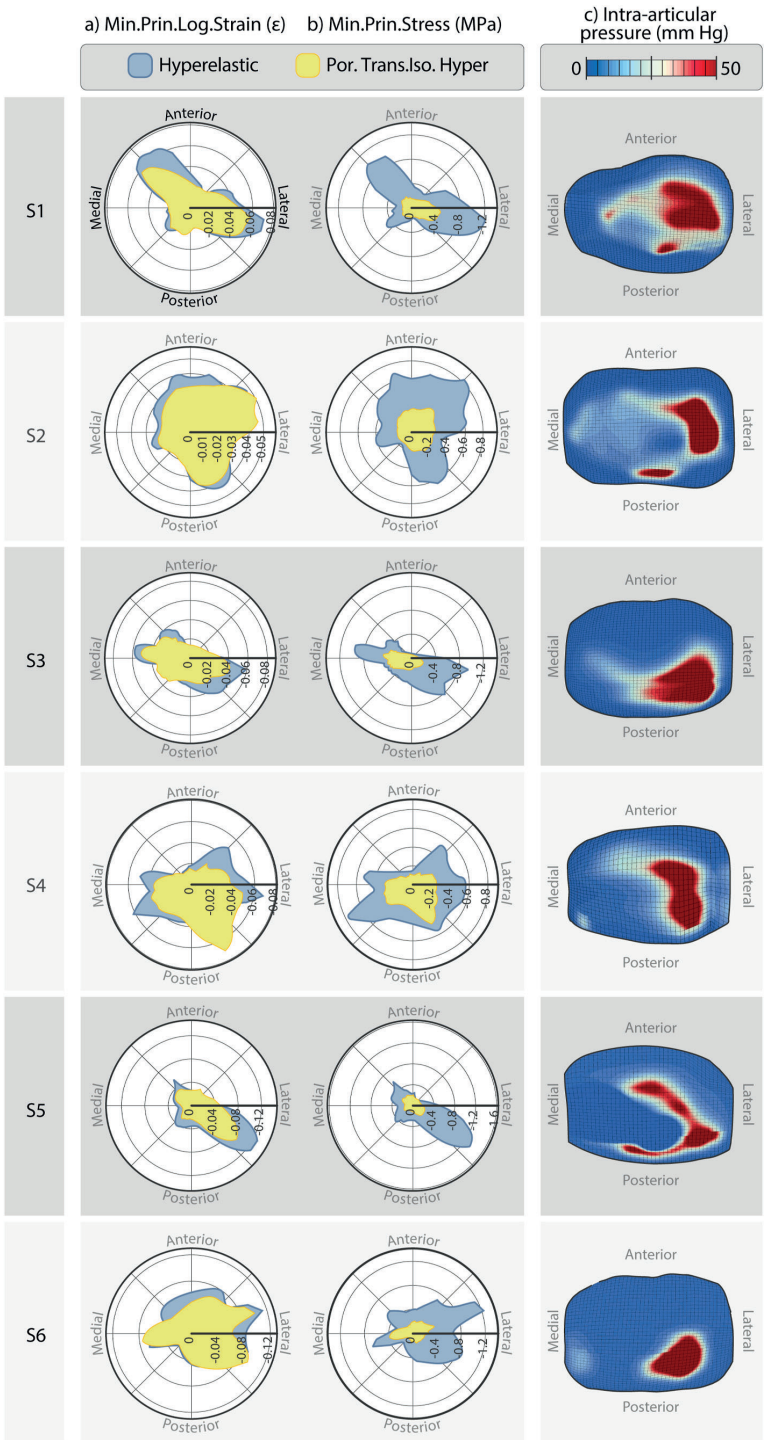

Fig. 6. Mean values (less than 1.5 times the interquartile range of the mean) of the a) minimum principal logarithmic strain and b) minimum principal stress around the disc of the 6 FE models in case A using hyperelastic properties (blue areas) and porous transversely isotropic hyperelastic properties (yellow areas). c) Intra-articular pressure distribution of the disc' fluid phase when the porous contribution is added.

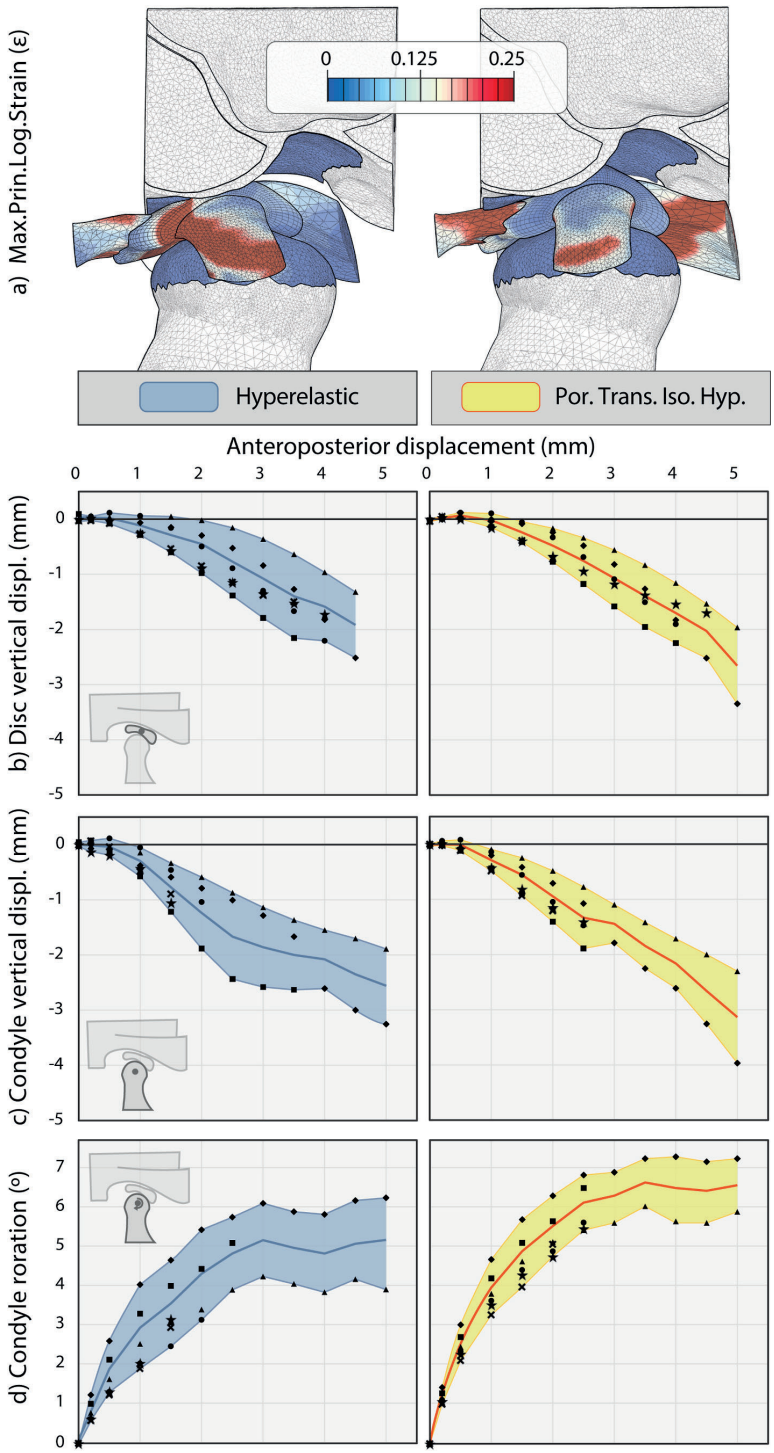

Fig. 7. a) Maximum principal logarithmic strain, b) vertical displacement of the centre of mass of the TMJ disc, and vertical displacement (c) and rotation (d) of the centre of the condyle computed from FE simulation using isotropic hyperelastic (left column) and porous transversely isotropic hyperelastic (right column) properties.

3.2. Motion analysis

For the motion analysis, the action of the depressor muscles during mouth centric opening was simulated for each of the 6 FE models. Table 6 summarizes the maximum values of the vertical (z-axis in Fig. 2) and anteroposterior (y-axis) displacements of the condyle, its rotation (x-axis), and the mean inclination of the condylar path (path in yz plane) obtained from the simulations under both behavioural approaches. Additionally, to discriminate amongst subjects and isolate samples based on the relative contribution of the translation and rotation measurements (Coutant et al., 2008), the C_p coefficient was computed as the ratio between the condyle rotation expressed in degrees and the condyle anteroposterior translation in mm.

As shown in Table 6, the porous-fibrous material model, in comparison with the hyperelastic approach, facilitated both rotation and translation movements of the condyle. Moreover, they resulted in higher translation-rotation ratios (C_p) in the biphasic approach, nearing the 2.13 reference value for common subjects (Coutant et al., 2008). It should be noted, however, that no significant difference was observed between the inclinations of the condylar path (approximately 33°) in both behavioural approaches, although the standard deviation was greater in the neo-Hookean approach. A graphical representation of these results can be seen in Fig. 7c and d, which respectively represent the mean path and rotation of the condyles' centre of mass.

Likewise, Fig. 7b shows the path of the mass centre of the disc for each behavioural scenario. As it can be noted, the absence of a fibrous component, especially in the retrodiscal and collateral ligaments, yielded a reduced forward movement of the disc. This disc-condylar misalignment in the hyperelastic approach also resulted in an overstretching of the collateral ligaments (shown in Fig. 7a), which tried to maintain the condyle and disc together. Whereas, the porous-fibrous approach resulted in a near-simultaneous movement of the condylar-disc joint, with maximum stretch rates (shown in Fig. 7a) in the anteroposterior disc attachments, which are the main responsible for anteroposterior movements.

A deeper analysis of the minimum and maximum principal logarithmic strains in the soft tissues of both behavioural approaches is presented in the box plots of Fig. 8. As was previously stated, the lack of a fibrous component produced a more retracted position of the disc with the condyle, which resulted in greater values of the maximum principal deformation in the collateral ligaments. Meanwhile, the retrodiscal tissue of the non-fibrous approach was stretched less than in the porous-fibrous approach, since the less forwarded position of the disc. Condyle-disc misalignment also reduced the normal reactions on the cartilaginous and disc surfaces, leading to lower compressive strains in the condylar cartilage (see minimum principal logarithmic strains in Fig. 8a and c). Meanwhile, the motion resistance in the neo-Hookean approach increased the shear loads on the cartilaginous surfaces, producing greater stretch values in these tissues (see maximal principal logarithmic strains in Fig. 8a and c). On the other hand, in the biphasic approach, both the fibrous matrix and the fluid phase increase the stiffness of the disc, decreasing the mean stretch and compression in the disc (see Fig. 8a).

For wider examination of the stress-strain distribution around the disc, their mean values were cylindrically plotted in Fig. 9 following the procedure described for Fig. 6. In this case, the plotted data was obtained after the load application (time equal to 260msec) and with the disc on the articular eminence. As can be seen in this figure, although the discs were subjected to both compressive and tensile loads (Fig. 9c and d, respectively), traction forces were predominant in this case. The compressive stresses were mainly located in the anterolateral region of the disc (shown in Fig. 9c), due to the contact of the disc with the temporal eminence.

As in the damping analysis, although the mean values of the minimum principal logarithmic strain are similar in both behavioural approaches, the fluid component distributes more uniformly the compressive strains (Fig. 9a) in the disc of the biphasic approach, reducing the minimum principal stress (Fig. 9c) in its solid phase. Concerning the fibrous matrix, it reduces the disc' stretching (Fig. 9b) because of two main sources. Firstly, the ring-shaped distribution of fibres (Fig. 3a) provides consistency against the disc collapse. Secondly, the anteroposteriorly oriented fibres (Fig. 3a) increase the tissue' stiffness along the tensile direction, which is primarily guided by the pterygoid muscle and the retrodiscal ligament. Hence, for similar values of stress (Fig. 9d), the biphasic behavioural approach yielded lower values of the maximum principal logarithmic strain than those obtained by the non-fibrous approach (Fig. 9b).

4. Discussion

The high and growing incidence of TMDs in the world's population (Detamore et al., 2007; Ingawalé and Goswami, 2009) had increased the number of in vivo studies about the TMJ in the last decades, but also *in silico* ones. Unfortunately, their results remain inconclusive owing to a lack of experimental data and differences across studies in terms of the experimental simplifications applied, among other factors. A better knowledge of TMJ's biomechanical response, however, would help future researchers and clinical experts in the modelling and the study of TMDs, but also in the development of new replacements or biomaterials for this joint. Notwithstanding it, the purpose of this *in silico* study was to evaluate the impact of include patient-specific geometries and porous-fibrous properties in the simulation of TMJ movements. To that end, we evaluated the biomechanical response of 6 patient-specific FE models, which were subjected to damp and dynamic loads in two different behavioural scenarios: with or without considering the porous-fibrous nature of the TMJ's soft tissues.

For evaluating the damping response of the joint, an experimental test of the literature (DeVocht et al., 2001) was mimicked by applying

Table 6
From left to right: vertical and anteroposterior displacement of the condyle, condyle rotation, condyle path inclination, and ratio between rotation and anteroposterior displacement (C_p) of the condyle computed from the simulation of each FE models (S1–S6) considering isotropic hyperelastic (Hyp.) or porous transversely isotropic hyperelastic (P.Trans.Iso.Hyp.) properties.

	Vertical displ. (mm)		Anteroposterior displ. (mm)		Condyle rotation (°)		Path Inclination (°)		C_p (°/mm)	
	Hyp.	P.Trans. Iso. Hyp	Hyp.	P.Trans. Iso. Hyp	Hyp.	P.Trans. Iso. Hyp	Hyp.	P.Trans. Iso. Hyp	Hyp.	P.Trans. Iso. Hyp
S1	2.4	1.9	2.6	2.6	5.1	6.5	47.6	38.9	2.0	2.5
S2	0.9	1.2	1.6	2.1	2.9	5.1	34.9	34.4	1.8	2.5
S3	1.1	1.4	1.6	2.5	3.2	5.5	34.7	32.0	2.0	2.2
S4	3.3	4.0	5.1	5.1	6.2	7.2	31.4	33.1	1.2	1.4
S5	1.9	2.3	5.1	5.1	3.9	5.9	22.9	25.6	0.8	1.1
S6	1.0	1.5	2.1	2.6	3.1	5.9	29.9	33.8	1.5	2.3
Mean	1.8	2.1	3.0	3.3	4.1	6.0	33.6	33.0	1.6	2.0
SD	1.0	1.0	1.7	1.4	1.3	0.8	8.1	4.3	0.5	0.6

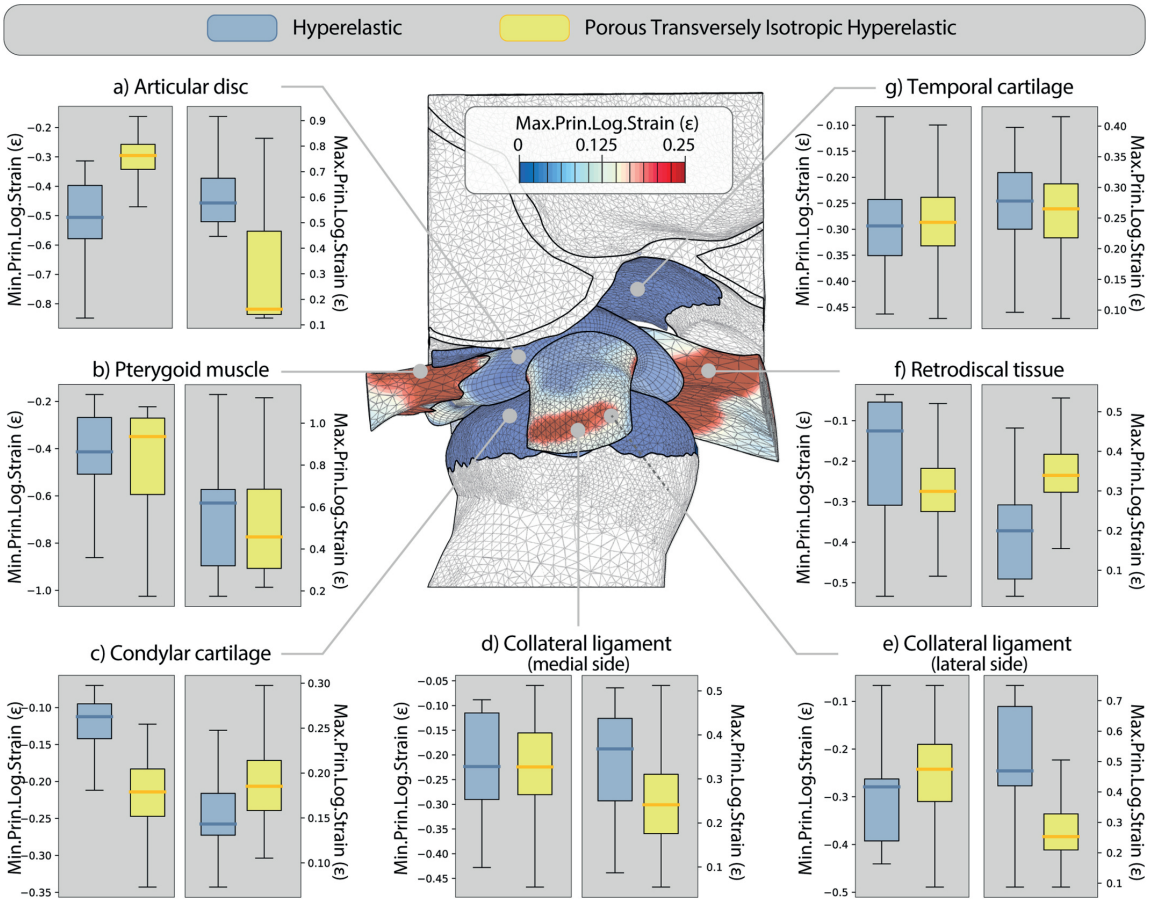

Fig. 8. Box plots of the minimum (left) and maximum (right) principal logarithmic strain distribution in the a) articular disc, b) pterygoid muscle, c) condylar cartilage, d) collateral ligament of the medial side, e) collateral ligament of the lateral side, f) retrodiscal tissue, and g) temporal cartilage using isotropic hyperelastic (blue boxes) and transversely isotropic hyperelastic (yellow boxes) properties.

two forces (Fig. 2) to the virtual mandibles and constraining the displacements of the occlusal region. As in clenching, the applied loads produced the condyle elevation and the subsequent contact between the disc and the articular cartilages, which led to the disc compression. As previously reported (Hattori-Hara et al., 2014; Liu et al., 2008), the contact in our simulations was mainly founded on the lateral-posterior region of the disc, leading to an increase of the strain (Fig. 5a) and intra-articular pressure in that area (Fig. 6c).

In the neo-Hookean approach, the computed contact pressures on the disc surface (Fig. 4) were lower than those measured experimentally (Table 5), achieving similar pressure levels only in cases A and C. These results are consistent with those obtained computationally by DeVocht and coworkers (DeVocht et al., 2001) who have also followed a non-biphasic approach for mimicking the disc response. With the biphasic behavioural approach here presented, we had been able to reproduce the experimental contact values in at least 5% of the contact surface of all models.

The greater contact pressure computed through the porous-fibrous properties could be attributable to the stiffer compressive behaviour of the disc in this case. As was already discussed, the stiffer response was mainly caused due peripheral fibres limit the disc' expansion and the fluid phase makes it almost incompressible. According to this point, 2D studies, which neglect the effect of the fibres perpendicular to the plane, could be yielding unrealistic results with a softer TMJ disc. This effect seems to be also neglected in those 3D simulations that have no consider the biphasic nature of these tissues. Hence, many of them (Abe et al., 2013; Tanaka et al., 2008) evaluated inaccurately the disc mechanical response through equivalent Von Mises stresses, which are not the most appropriate variable to evaluate the mechanical response of non-homogeneous soft tissues.

For predominantly compressive conditions, it is possible, however, to assume the Von Mises stress as an approximate value of the compressive stress. Understanding this assumption, the −4.5 MPa minimum principal stress values (see Fig. 5c) computed in our models would agree with the maximum Von Mises stress values reported in the literature, ranging from 4.9 MPa (Abe et al., 2013; Pileicikiene et al., 2007) to 7.05 MPa (Hattori-Hara et al., 2014). Furthermore, they are within the minimum principal stress ranges reported in the literature, which vary from −2.58 MPa (Liu et al., 2008) to −5 MPa (Mori et al., 2010). As could be noted in Fig. 5c, the distribution of the minimum principal stresses on the disc was not uniform, with mean principal stress values below −0.4 and −1.2 MPa for the neo-Hookean and porous-fibrous approaches respectively. Related studies from the literature reported similar mean values of the minimum principal stresses,

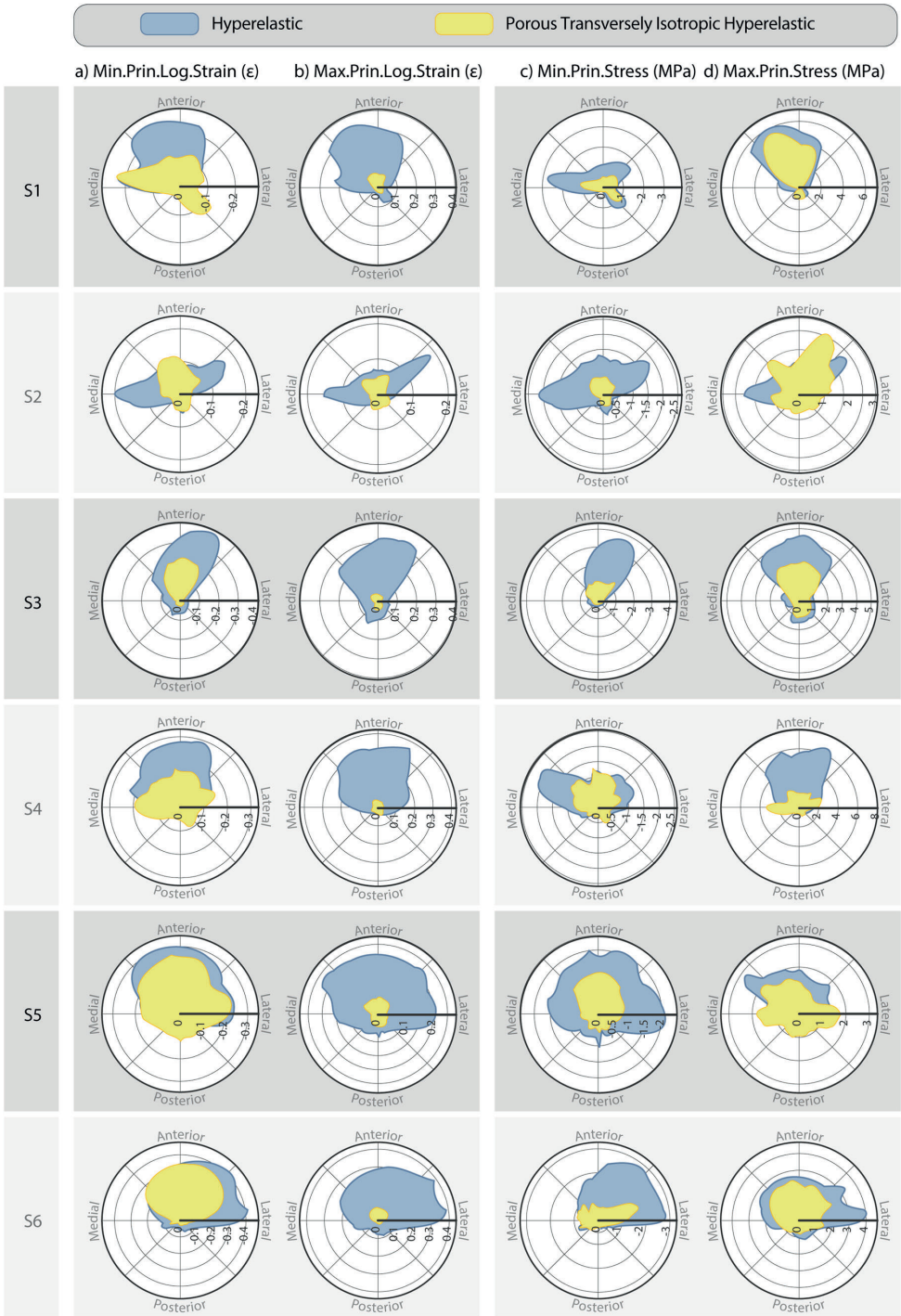

Fig. 9. Mean values (less than 1.5 times the interquartile range) of the a) minimum and b) maximum principal logarithmic strains, and c) minimum and d) maximum principal stresses around the TMJ disc for each of the 6 FE models using isotropic hyperelastic (blue areas) and porous transversely isotropic hyperelastic (yellow areas) properties under the motion test's conditions.

varying from −1 MPa (Pérez del Palomar et al., 2008) to −0.403 MPa (Tanaka et al., 1994). Concerning deformations, the discs in our simulations suffered minimum principal logarithmic strain of up to −0.3ε (shown in Fig. 5a), in agreement with the −0.15, −0.274 and −0.40ε reported respectively by Mori et al. (2010), Duarte et al. (2014), and de Aoun et al. (2014).

Meanwhile, in the porous-fibrous behavioural approach, the compressive strains also drained interstitial fluid to the remaining disc, which could allow a smoother distribution of stresses throughout the disc, as was shown in our results (Fig. 5c and d and 6b). In this sense, the intra-articular pressure values calculated computationally (Fig. 6c) were close to the experimental value of 58.56 ± 24.90 mmHg reported by Casares and coworkers (Casares et al., 2014) for the maximal intercuspidal position.

Regarding the motion analysis, the mandible of the computational models was subjected to the forces of the depressor muscles, which produced the forward movement of the condyle-disc joint along with the temporal eminence. The study of Tanaka and coworkers (Tanaka et al., 2001), which studied a similar joint movement, found that the condyle and disc move aligned, with 4 and 1.8 mm maximum displacement in anteroposterior and vertical displacement, respectively. These results agreed with those obtained in the two approaches of this study, in which mean displacements of 3–3.3 and 1.8–2.1 mm in the anteroposterior and vertical directions were respectively reported for the centre of mass of the condyle (Table 6). These displacements also showed condylar paths with an inclination between 22.9° and 47.6° (shown in Table 6), which were in line with the experimental values (26.1–61.8°) reported by Alshali and colleagues (Alshali et al., 2013). Likewise, the mean condylar path inclination values obtained from both isotropic and fibrous approaches (33.6° and 33°, respectively) are close to the 32.9° reported by Wieckiewicz and coworkers (Wieckiewicz et al., 2014).

Despite the good correlation of both approaches' results with published data, the biphasic approximation reproduced more accurately the alignment between the disc and condylar paths (Fig. 7b and c, respectively), which had been described by Tanaka and coworkers (Tanaka et al., 2001). Moreover, the C_p value computed in the porous-fibrous approach (2.0 ± 0.6°/mm) was closer to the reference mean value given by Coutant et al. (2008) for standard subjects (2.13°/mm), in comparison to that in the neo-Hookean one (1.6 ± 0.5°/mm). The similarity in the C_p coefficient was mainly due to the smoother disc rotation in the biphasic approach than in the neo-Hookean approach, with mean rotation values of 6° and 4.1° respectively.

As was introduced, in this loading, the upper portion of the lateral pterygoid stretches the anterior band of the disc, while the retrodiscal ligament constrains the movement of the disc in the anteroposterior direction. As shown in Fig. 7a, the exclusion of the fibrous component, when the isotropic hyperelastic material model is used, resulted in greater stretch of the collateral ligaments (shown in Fig. 8d and e) that try to maintain the condyle and disc attached. When the fibrous component is added, however, the collateral ligament stretching was reduced (shown in Fig. 8d and e). This was mainly because, firstly, the fibres of the retrodiscal tissue prevent excessive anteroposterior displacement of the disc (shown in Fig. 8f). And secondly, because the union between the condyle and disc is maintained by the fibres of the collateral ligaments. The fibres within these lateral attachments seem to play a key role in joint stabilization by improving the relative motion between the disc and the condyle. By contrast, in other tissues, such as temporal cartilage (Fig. 8g), no significant differences were observed between deformations of both behavioural approaches. Even softer response was obtained in the condylar cartilage when the fibrous component was added. This softer behaviour could be caused due to the cartilages are primarily subjected to compressive efforts, in which the fibrous region of the cartilage poses almost no resistance to compressive efforts. Moreover, the better distribution of the contact pressure contributes also to reduce the deformation of this tissue.

The traction system composed by the pterygoid, disc and retrodiscal tissue produces high stresses in the anterior region of the disc (shown in Fig. 9d) with maximum principal stress values up to 2.8 MPa and 6.1 MPa for those cases with and without porous-fibrous properties (shown in Fig. 9d). For 10° centric openings, as the one simulated here, Koolstra and van Eijden (2007) reported maximum Von Mises stress up to 5 MPa in the disc, which is within our reported results. Likewise, Tanaka et al. (2001) also reported maximum Von Mises stress values in the anterior disc region, with values up to 2.5 MPa, being similar to the values computed in the biphasic approach. By contrast, some studies in the literature (Donzelli et al., 2004) reported values in the disc much lower than those obtained in our simulation, ranging between 0.72 and 0.38 MPa, although all of them found maximum values in the anterior band of the disc. Several factors could account for these lower levels of stress, such as the consideration of extremely low young modulus for the articular disc, compared to other studies in the literature (M.S. Detamore and Athanasiou, 2003a,b,c).

As was previously noted, the collagen fibres of the central region connect the anterior and posterior bands of the disc and reinforce the disc anteroposteriorly. This increment of disc's stiffness in anteroposterior direction leads also to greater load distribution across the different regions of the disc (Fig. 9d) and a reduction of the minimum principal logarithmic strain value of the anterior band (Fig. 9b) to less than −0.1 ε. This deformation value had already been reported by Koolstra and van Eijden (2005), who indicated a mean disc deformation between −0.1 and −0.15 ε.

Despite all the limitations of working with computational models and differences between subjects with different geometries, the results of this study have demonstrated the key role of biphasic behaviour in the computational modelling of the TMJ. On the one hand, at damping conditions, the ring-shaped distribution of the collagen fibres and the fluid phase contribution seem to be crucial for maintaining the disc shape and supporting compressive stresses up to −4.5 MPa in its lateral-posterior region. On the other hand, during motion, the collagen fibres of the disc' central region and disc attachments seem to be keys to maintaining the condyle and disc aligned, limiting the overstretching of lateral attachments and reducing the stresses in the anterior band of the disc.

This study represents, therefore, a step forward in the computational modelling of the TMJ and in the computational study of TMDs, which should be considered in further *in silico*, and experimental studies. Common features of FE analysis studies include single FE models, simplified geometries, static loading conditions, and isotropic material formulations. Importantly, our study presents accurate patient-specific FE models that use porous-fibrous material properties and enable analysis of TMJ motion and damping responses.

4.1. Study limitations

Despite the careful development of the computational models presented here, several limitations of the present study should be noted. First, our models were only modelled by an articular eminence and half lower mandible, because symmetrical conditions were assumed. Although this simplification is widely accepted in TMJ (Beldie et al., 2010; Fričová et al., 2006; Kim et al., 2012; Alkhiary et al., 2012; Ramos et al., 2009; Shrivastava et al., 2015) studies, the mandibular aperture produces asymmetrical deviation of the mandible that should be considered in further studies (Coutant et al., 2008; Palla et al., 2003). On the other hand, the result presented here are specific to these models and other FE analysis might give slightly different values, because of the considerable different geometry of articular surfaces between subjects (Savoldelli et al., 2012), amongst other factors. Subject-specific characteristics and different testing procedures complicate an accurate comparison between computer-based studies in the literature, which could differ up to 25% (Anderson et al., 2010; Dreischarf et al., 2014; Périé and Hobatho, 1998). Future research should define testing standards that enable more accurate comparisons between other studies of

the literature. This limitation is also identifiable in the material parameters used here, which were obtained from other studies of the literature with different geometries and conditions. Hence, although the results produced by our computational models were consistent with those of published experimental studies, it would be more appropriate to obtain experimental measurements from each participating subject. Moreover, fibre orientation was estimated based on published anatomical data. Histological analyses of the samples modelled could improve the anisotropic tissue response. Furthermore, the mechanical behaviour of cartilage was simplified by considering only the fibrous zone, owing to a lack of data pertaining to other zones. Several authors (Athanasiou et al., 2009; Singh and Detamore, 2009) have recommended, further study of the hypertrophic zone of the cartilage. In this region, crimping of the fibres and cartilage interstitial fluid could result in increased matrix compressive stiffness (Singh and Detamore, 2009). Cartilage stiffness could be also increased if the liquid phase of cartilage was added. Finally, 3D reconstruction of the muscles of the TMJ was not possible due to the limited MRI field of view. This necessitated the use of 2D connectors based on properties described in the literature, which may have introduced a certain degree of error.

Despite the aforementioned limitations, our study proves the importance of considering the porous-fibrous properties within the computational modelling of the TMJ. *In silico* models presented here were carefully developed by recent advances in computer modelling techniques and findings in experimental (DeVocht et al., 2001; Murphy et al., 2013; Singh and Detamore, 2008; Wright et al., 2016) and computation studies (Ortún-Terrazas et al., 2020). Nevertheless, further investigations about the biphasic nature of the tissues, as well as more modern methods for the validation of the computational models, are needed. This study may also provide an approach towards such investigations, helping in the development of new procedures for experimentation and biomechanical evaluation of this joint.

5. Conclusion

In this *in silico* study, a careful evaluation of how the porous-fibrous properties affect the simulation of TMJ's movements was developed. Such methodology was assessed in 6 detailed FE models of the TMJ under compression and dynamic loadings. Within the limitations of this study, findings presented here have demonstrated the benefit of including porous-fibrous properties when modelling the soft tissues of the TMJ, leading the following conclusions:

1. The fluid phase of the disc, although valuable in both approaches, has a crucial role in the damping of the TMJ, since; on the one hand, it reduces the minimum principal stress in the solid phase of the disc. On the other hand, when the disc is compressed, the fluid flow towards the disc's periphery transforms the compressive loads into traction forces in the fibres of the periphery.
2. The fibrous matrix plays a key role in the dynamic and damping responses of the TMJ. The fibres in the periphery, which are ring-shaped distributed, are the main responsible for maintaining the elliptical shape of the disc during compression, while the fibres of the central region are key to the anteroposterior movement of the condylar-disc joint.
3. The activity of the fibres of the disc attachments results in unpredictable equilibration of the TMJ, and the interstitial fluid distributes stress across the disc. Disc attachments play a key role in disc stabilization during motion. Exclusion of these attachments from the modelling process or oversimplification of their fibrous structure can result in asynchronous movements of the disc and the condyle.
4. This study demonstrated that the porous transversely isotropic hyperelastic approach (characterized in Ortún-Terrazas et al., 2020) reproduces more properly the damping and motion TMJ's responses than the neo-Hookean approach. Thus, from the above results' discussion, a better correspondence of the biphasic approach with the published results has been observed.
5. Our results also demonstrate that differences in TMJ shape give rise to significant mechanical variation. Accordingly, multiple TMJ computational models must be developed for general joint analyses. Single FE models should only be used for patient-specific analyses.

This study demonstrates the importance of include collagen network and interstitial fluid for a realistic simulation of TMJ's responses. The results presented shed light on the role of the soft tissues in some of the most common TMDs and will serve as a basis for future studies of the porous-fibrous behaviour of the TMJ. Our findings underscore the importance of considering the time- and fibre-dependent nature of the TMJ response in future experiments. In particular, further investigation of the hypertrophic zone of the TMJ cartilage is warranted to clarify the role of this region in joint lubrication and stress distribution. Future studies will need to improve upon the computational simulations presented here by accounting for complex material behaviours and generating more accurate models.

Author statements

Javier Ortún-Terrazas: Data curation; Investigation; Methodology; Formal analysis; Software; Visualization; Writing - Original Draft. Jose Cegoñino: Project administration; Resources; Validation; Software; Supervisor; Visualization; Writing - Review & Editing. Amaya Perez del Palomar: Conceptualization; Validation; Funding acquisition; Project administration; Supervisor; Visualization; Writing - Review & Editing.

Funding

This work was supported by the Spanish Ministry of Economy and Competitiveness (project DPI, 2016-79302-R), the European Social Funds and Regional Government of Aragon (grant 2016/20) and Ibercaja-Cai Foundation (grant IT 4/18).

Author statement

Javier Ortún-Terrazas: Data curation; Investigation; Methodology; Formal analysis; Software; Visualization; Writing - Original Draft. *José Cegoñino*: Project administration; Resources; Validation; Software; Supervisor; Visualization; Writing - Review & Editing. *Amaya Pérez del Palomar*: Conceptualization; Validation; Funding acquisition; Project administration; Supervisor; Visualization; Writing - Review & Editing.

Declaration of competing interest

The authors declare that they have no known competing financial interests or personal relationships that could have appeared to influence the work reported in this paper.

Acknowledgements

The authors would like to thank Dr. Ángel Sampietro Fuentes for his assistance in this research.

Appendix A. Supplementary data

Supplementary data to this article can be found online at https://doi.org/10.1016/j.jmbbm.2021.104542.

References

Abaqus, 2014. Abaqus 6.14, Simulia. Rhode Island, United States.

Abe, S., Kawano, F., Kohge, K., Kawaoka, T., Ueda, K., Hattori-Hara, E., Mori, H., Kuroda, S., Tanaka, E., 2013. Stress analysis in human temporomandibular joint

affected by anterior disc displacement during prolonged clenching. J. Oral Rehabil. 40, 239–246. https://doi.org/10.1111/joor.12036.
Alkhiary, M., Nassef, Y.M., Yassine, T.A., Tayel, I.B., S, Ezzat, A.ElSalam kh., 2012. A new numerical model to analyze stress distribution of TMJ disc from 2-D MRI scans. Adv. Comput. 2, 66–75. https://doi.org/10.5923/j.ac.20120205.01.
Alshali, R.Z., Yar, R., Barclay, C., Satterthwaite, J.D., 2013. Sagittal condylar angle and gender differences. J. Prosthodont. 22, 561–565. https://doi.org/10.1111/jopr.12047.
Anderson, A.E., Peters, C.L., Tuttle, B.D., Weiss, J.A., 2005. Subject-specific finite element model of the pelvis: development, validation and sensitivity studies. J. Biomech. Eng. 127, 364–373. https://doi.org/10.1115/1.1894148.
Anderson, A.E., Ellis, B.J., Maas, S.A., Weiss, J.A., 2010. Effects of idealized joint geometry on finite element predictions of cartilage contact stresses in the hip. J. Biomech. 43, 1351–1357. https://doi.org/10.1016/j.jbiomech.2010.01.010.
Aoun, M., Mesnard, M., Monède-Hocquard, L., Ramos, A., 2014. Stress analysis of temporomandibular joint disc during maintained clenching using a viscohyperelastic finite element model. J. Oral Maxillofac. Surg. 72, 1070–1077. https://doi.org/10.1016/j.joms.2013.11.031.
Argoubi, M., Shirazi-Adl, A., 1996. Poroelastic creep response analysis of a lumbar motion segment in compression. J. Biomech. 29, 1331–1339. https://doi.org/10.1016/0021-9290(96)00035-8.
Athanasiou, K.a., Almarza, A.J., Detamore, M.S., Kalpakci, K.N., 2009. Tissue engineering of temporomandibular joint cartilage. Synth. Lect. Tissue Eng. 1, 1–122. https://doi.org/10.2200/S00198ED1V01Y200906TIS002.
Beldie, L., Walker, B., Lu, Y., Richmond, S., Middleton, J., 2010. Finite element modelling of maxillofacial surgery and facial expressions-a preliminary study. Int. J. Med. Robot. Comput. Assist. Surg. 6, 422–430. https://doi.org/10.1002/rcs.352.
Bergomi, M., Cugnoni, J., Galli, M., Botsis, J., Belser, U.C., Wiskott, H.W.A., 2011. Hydro-mechanical coupling in the periodontal ligament: a porohyperelastic finite element model. J. Biomech. 44, 34–38. https://doi.org/10.1016/j.jbiomech.2010.08.019.
Casares, G., Thomas, A., Carmona, J., Acero, J., Vila, C.N., 2014. Influence of oral stabilization appliances in intra-articular pressure of the temporomandibular joint. CRANIO® 32, 219–223. https://doi.org/10.1179/0886963413Z.00000000030.
Chen, J., Xu, L., 1994. A finite element analysis of the human temporomandibular joint. J. Biomech. Eng. 116, 401–407. https://doi.org/10.1115/1.2895790.
Chen, J., Akyuz, U., Xu, L., Pidaparti, R.M.V., 1998. Stress analysis of the human temporomandibular joint. Med. Eng. Phys. 20, 565–572. https://doi.org/10.1016/S1350-4533(98)00070-8.
Commisso, M.S., Martínez-Reina, J., Mayo, J., 2014. A study of the temporomandibular joint during bruxism. Int. J. Oral Sci. 6, 116–123. https://doi.org/10.1038/ijos.2014.4.
Commisso, M.S., Martínez-Reina, J., Ojeda, J., Mayo, J., 2015. Finite element analysis of the human mastication cycle. J. Mech. Behav. Biomed. Mater. 41, 23–35. https://doi.org/10.1016/j.jmbbm.2014.09.022.
Coutant, J.-C., Mesnard, M., Morlier, J., Ballu, A., Cid, M., 2008. Discrimination of objective kinematic characters in temporomandibular joint displacements. Arch. Oral Biol. 53, 453–461. https://doi.org/10.1016/j.archoralbio.2007.11.010.
Detamore, M.S., Athanasiou, K.A., 2003a. Tensile properties of the porcine temporomandibular joint disc. J. Biomech. Eng. 125, 558–565. https://doi.org/10.1115/1.1589778.
Detamore, M.S., Athanasiou, K.A., 2003b. Motivation, characterization, and strategy for tissue engineering the temporomandibular joint disc. Tissue Eng. 9, 1065–1087. https://doi.org/10.1089/10763270360727991.
Detamore, M.S., Athanasiou, K.A., 2003c. Biomechanical behavior of the temporomandibular joint disc. In: Proceedings of the Second Joint 24th Annual Conference and the Annual Fall Meeting of the Biomedical Engineering Society] [Engineering in Medicine and Biology. IEEE, pp. 440–441. https://doi.org/10.1109/IEMBS.2002.1136885.
Detamore, M.S., Athanasiou, K.A., Mao, J., 2007. A call to action for bioengineers and dental professionals: directives for the future of TMJ bioengineering. Ann. Biomed. Eng. 35, 1301–1311. https://doi.org/10.1007/s10439-007-9298-6.
DeVocht, J.W., Goel, V.K., Zeitler, D.L., Lew, D., 1996. A study of the control of disc movement within the temporomandibular joint using the finite element technique. J. Oral Maxillofac. Surg. 54, 1431–1437. https://doi.org/10.1016/S0278-2391(96)90259-1.
DeVocht, J.W., Goel, V.K., Zeitler, D.L., Lew, D., 2001. Experimental validation of a finite element model of the temporomandibular joint. J. Oral Maxillofac. Surg. 59, 775–778. https://doi.org/10.1053/joms.2001.24292.
Donzelli, P.S., Gallo, L.M., Spilker, R.L., Palla, S., 2004. Biphasic finite element simulation of the TMJ disc from in vivo kinematic and geometric measurements. J. Biomech. 37, 1787–1791. https://doi.org/10.1016/j.jbiomech.2004.01.029.
Dreischarf, M., Zander, T., Shirazi-Adl, A., Puttlitz, C.M., Adam, C.J., Chen, C.S., Goel, V. K., Kiapour, A., Kim, Y.H., Labus, K.M., Little, J.P., Park, W.M., Wang, Y.H., Wilke, H.J., Rohlmann, A., Schmidt, H., 2014. Comparison of eight published static finite element models of the intact lumbar spine: predictive power of models improves when combined together. J. Biomech. 47, 1757–1766. https://doi.org/10.1016/j.jbiomech.2014.04.002.
Duarte, R.J., Ramos, A., Mesnard, M., 2014. The influence of disc wear on the behavior of the temporomandibular joint: a finite element analysis in a specific case. Adv. Biomech. Appl. 1, 159–167. https://doi.org/10.12989/aba.2014.1.3.159.
Fričová, M., Horák, Z., Konvičková, S., Jirman, R., 2006. Modelling of temporomandibular joint and FEM analysis. Acta Bioeng. Biomech. 8, 35–43.
Hannam, A.G., Stavness, I., Lloyd, J.E., Fels, S., 2008. A dynamic model of jaw and hyoid biomechanics during chewing. J. Biomech. 41, 1069–1076. https://doi.org/10.1016/j.jbiomech.2007.12.001.
Hattori-Hara, E., Mitsui, S.N., Mori, H., Arafurue, K., Kawaoka, T., Ueda, K., Yasue, A., Kuroda, S., Koolstra, J.H., Tanaka, E., 2014. The influence of unilateral disc displacement on stress in the contralateral joint with a normally positioned disc in a human temporomandibular joint: an analytic approach using the finite element method. J. Cranio-Maxillofacial Surg. 42 https://doi.org/10.1016/j.jcms.2014.09.008, 2018–2024.
Holzapfel, G.A., 2000. Nonlinear Solid Mechanics: A Continuum Approach for Engineering. Wiley, New York.
Horst, van der M.J., 2002. Human Head Neck Response in Frontal , Lateral and Rear End Impact Loading - Modelling and Validation -. https://doi.org/10.6100/IR554047.
Hu, K., Qiguo, R., Fang, J., Mao, J.J., 2003. Effects of condylar fibrocartilage on the biomechanical loading of the human temporomandibular joint in a three-dimensional, nonlinear finite element model. Med. Eng. Phys. 25, 107–113. https://doi.org/10.1016/S1350-4533(02)00191-1.
Hunter, J.D., 2007. Matplotlib: a 2D graphics environment. Comput. Sci. Eng. 9, 90–95. https://doi.org/10.1109/MCSE.2007.55.
Ingawalé, S., Goswami, T., 2009. Temporomandibular joint: disorders, treatments, and biomechanics. Ann. Biomed. Eng. 37, 976–996. https://doi.org/10.1007/s10439-009-9659-4.
Kim, K.-N., Cha, B.-K., Choi, D.-S., Jang, I., Yi, Y.-J., Jost-Brinkmann, P.-G., 2012. A finite element study on the effects of midsymphyseal distraction osteogenesis on the mandible and articular disc. Angle Orthod. 82, 464–471. https://doi.org/10.2319/041211-262.1.
Koolstra, J.H., van Eijden, T.M.G.J., 2005. Combined finite-element and rigid-body analysis of human jaw joint dynamics. J. Biomech. 38, 2431–2439. https://doi.org/10.1016/j.jbiomech.2004.10.014.
Koolstra, J.H., van Eijden, T.M.G.J., 2007. Consequences of viscoelastic behavior in the human temporomandibular joint disc. J. Dent. Res. 86, 1198–1202. https://doi.org/10.1177/154405910708601211.
Langenbach, G.E.J., Hannam, A.G., 1999. The role of passive muscle tensions in a three-dimensional dynamic model of the human jaw. Arch. Oral Biol. 44, 557–573. https://doi.org/10.1016/S0003-9969(99)00034-5.
Liu, Z., Fan, Y., Qian, Y., 2008. Comparative evaluation on three-dimensional finite element models of the temporomandibular joint. Clin. Biomech. 23, S53–S58. https://doi.org/10.1016/j.clinbiomech.2007.12.011.
Matlab, 2000. MATLAB 6.0 R12. The MathWorks Inc., Natick, Massachusetts, United States.
Mimics, 2016. Mimics, v.19. Materialise, Leuven, Belgium. Mimics, 2016. Mimics, v.19.; Materialise, Leuven, Belgium.
Mori, H., Horiuchi, S., Nishimura, S., Nikawa, H., Murayama, T., Ueda, K., Ogawa, D., Kuroda, S., Kawano, F., Naito, H., Tanaka, M., Koolstra, J.H., Tanaka, E., 2010. Three-dimensional finite element analysis of cartilaginous tissues in human temporomandibular joint during prolonged clenching. Arch. Oral Biol. 55, 879–886. https://doi.org/10.1016/j.archoralbio.2010.07.011.
Murphy, M.K., Arzi, B., Hu, J.C., Athanasiou, K.A., 2013. Tensile characterization of porcine temporomandibular joint disc attachments. J. Dent. Res. 92, 753–758. https://doi.org/10.1177/0022034513494817.
Ortún-Terrazas, J., Cegoñino, J., Pérez del Palomar, A., 2020. Computational characterization of the porous-fibrous behavior of the soft tissues in the temporomandibular joint. J. Biomed. Mater. Res. Part B Appl. Biomater. jbm.b.34558 https://doi.org/10.1002/jbm.b.34558.
Palla, S., Gallo, L., Gossi, D., 2003. Dynamic stereometry of the temporomandibular joint. Orthod. Craniofac. Res. 6, 37–47. https://doi.org/10.1034/j.1600-0544.2003.233.x.
Peck, C.C., Langenbach, G.E.J., Hannam, A.G., 2000. Dynamic simulation of muscle and articular properties during human wide jaw opening. Arch. Oral Biol. 45, 963–982. https://doi.org/10.1016/S0003-9969(00)00071-6.
Pérez del Palomar, A., Doblaré, M., 2006a. The effect of collagen reinforcement in the behaviour of the temporomandibular joint disc. J. Biomech. 39, 1075–1085. https://doi.org/10.1016/j.jbiomech.2005.02.009.
Pérez del Palomar, A., Doblaré, M., 2006b. Finite element analysis of the temporomandibular joint during lateral excursions of the mandible. J. Biomech. 39, 2153–2163. https://doi.org/10.1016/j.jbiomech.2005.06.020.
Pérez del Palomar, A., Doblaré, M., 2008. Dynamic 3D FE modelling of the human temporomandibular joint during whiplash. Med. Eng. Phys. 30, 700–709. https://doi.org/10.1016/j.medengphy.2007.07.009.
Pérez del Palomar, A., Santana-Penín, U., Mora-Bermúdez, M.J., Doblaré, M., 2008. Clenching TMJs-loads increases in partial edentates: a 3D finite element study. Ann. Biomed. Eng. 36, 1014–1023. https://doi.org/10.1007/s10439-008-9487-y.
Périé, D., Hobatho, M.C., 1998. In vivo determination of contact areas and pressure of the femorotibial joint using non-linear finite element analysis. Clin. Biomech. 13, 394–402. https://doi.org/10.1016/S0268-0033(98)00091-6.
Pileicikiene, G., Surna, A., Barauskas, R., Surna, R., Basevicius, A., 2007. Finite element analysis of stresses in the maxillary and mandibular dental arches and TMJ articular discs during clenching into maximum intercuspation, anterior and unilateral posterior occlusion. Stomatol. 9, 121–128, 074-05 [pii].
Python, 2016. Python 3.5.2. Python Software Foundation.
Ramos, A., Relvas, C., Mesnard, M., Ballu, A., Simões, J.A., 2009. Numerical study of the mandible geometry influences using two different TMJ implants. Comput. Methods Biomech. Biomed. Eng. 12, 209–210. https://doi.org/10.1080/10255840903093433.
Ramos, A., Duarte, R.J., Mesnard, M., 2015. Prediction at long-term condyle screw fixation of temporomandibular joint implant: a numerical study. J. Cranio-Maxillofacial Surg. 43, 469–474. https://doi.org/10.1016/j.jcms.2015.02.013.
Rhinoceros, 2012. Rhinoceros V5. Robert McNeel & Associates, Seattle, United States.

Ruggiero, L., Zimmerman, B.K., Park, M., Han, L., Wang, L., Burris, D.L., Lu, X.L., 2015. Roles of the fibrous superficial zone in the mechanical behavior of TMJ condylar cartilage. Ann. Biomed. Eng. 43, 2652–2662. https://doi.org/10.1007/s10439-015-1320-9.

Savoldelli, C., Bouchard, P.-O., Loudad, R., Baque, P., Tillier, Y., 2012. Stress distribution in the temporo-mandibular joint discs during jaw closing: a high-resolution three-dimensional finite-element model analysis. Surg. Radiol. Anat. 34, 405–413. https://doi.org/10.1007/s00276-011-0917-4.

Schmidt, H., Alber, T., Wehner, T., Blakytny, R., Wilke, H.-J., 2009. Discretization error when using finite element models: analysis and evaluation of an underestimated problem. J. Biomech. 42, 1926–1934. https://doi.org/10.1016/j.jbiomech.2009.05.005.

Shrivastava, A., Hazarey, P.V., Kharbanda, O.P., Gupta, A., 2015. Stress distribution in the temporomandibular joint after mandibular protraction: a three-dimensional finite element study. Angle Orthod. 85, 196–205. https://doi.org/10.2319/091913-690.1.

Singh, M., Detamore, M.S., 2008. Tensile properties of the mandibular condylar cartilage. J. Biomech. Eng. 130, 011009 https://doi.org/10.1115/1.2838062.

Singh, M., Detamore, M.S., 2009. Biomechanical properties of the mandibular condylar cartilage and their relevance to the TMJ disc. J. Biomech. 42, 405–417. https://doi.org/10.1016/j.jbiomech.2008.12.012.

Storakers, B., 1986. On material representation and constitutive branching in finite compressible elasticity. J. Mech. Phys. Solid. 34, 125–145. https://doi.org/10.1016/0022-5096(86)90033-5.

Tanaka, E., Tanne, K., Sakuda, M., 1994. A three-dimensional finite element model of the mandible including the TMJ and its application to stress analysis in the TMJ during clenching. Med. Eng. Phys. 16, 316–322. https://doi.org/10.1016/1350-4533(94)90058-2.

Tanaka, E., Rodrigo, D.P., Tanaka, M., Kawaguchi, A., Shibazaki, T., Tanne, K., 2001. Stress analysis in the TMJ during jaw opening by use of a three-dimensional finite element model based on magnetic resonance images. Int. J. Oral Maxillofac. Surg. 30, 421–430. https://doi.org/10.1054/ijom.2001.0132.

Tanaka, E., Kawai, N., Tanaka, M., Todoh, M., van Eijden, T., Hanaoka, K., Dalla-Bona, D. A., Takata, T., Tanne, K., 2004. The frictional coefficient of the temporomandibular joint and its dependency on the magnitude and duration of joint loading. J. Dent. Res. 83, 404–407. https://doi.org/10.1177/154405910408300510.

Tanaka, E., Irose, M., Koolstra, J.H., van Eijden, T.M.G.J., Iwabuchi, Y., Fujita, R., Tanaka, M., Tanne, K., 2008. Modeling of the effect of friction in the temporomandibular joint on displacement of its disc during prolonged clenching. J. Oral Maxillofac. Surg. 66, 462–468. https://doi.org/10.1016/j.joms.2007.06.640.

Tuijt, M., Koolstra, J.H., Lobbezoo, F., Naeije, M., 2010. Differences in loading of the temporomandibular joint during opening and closing of the jaw. J. Biomech. 43, 1048–1054. https://doi.org/10.1016/j.jbiomech.2009.12.013.

Van Eijden, T.M.G.J., Korfage, J.A.M., Brugman, P., 1997. Architecture of the human jaw-closing and jaw-opening muscles. Anat. Rec. 248, 464–474. https://doi.org/10.1002/(sici)1097-0185(199707)248:3<464::aid-ar20>3.3.co;2-4.

Van Ruijven, L.J., Weijs, W.A., 1990. A new model for calculating muscle forces from electromyograms. Eur. J. Appl. Physiol. Occup. Physiol. 61, 479–485. https://doi.org/10.1007/BF00236071.

Wieckiewicz, M., Zietek, M., Nowakowska, D., Wieckiewicz, W., 2014. Comparison of selected kinematic facebows applied to mandibular tracing. BioMed Res. Int. https://doi.org/10.1155/2014/818694, 1–5.

Wright, G.J., Coombs, M.C., Hepfer, R.G., Damon, B.J., Bacro, T.H., Lecholop, M.K., Slate, E.H., Yao, H., 2016. Tensile biomechanical properties of human temporomandibular joint disc: effects of direction, region and sex. J. Biomech. 49, 3762–3769. https://doi.org/10.1016/j.jbiomech.2016.09.033.

Manuscript 7: Evaluation of the unilateral crossbite on the craniofacial complex asymmetrical development. A mechano-morphological approach.

Javier Ortún-Terrazas, Michael J. Fagan, Edson Illipronti-Filho, Amaya Pérez del Palomar

Abstract

The occlusion effect on the craniofacial development is a controversial topic that has attracted the interest of many researchers but that remains unclear, mainly due to the difficulties on measure its mechanical response experimentally. This mechano-morphological relationship of the craniofacial growth is often explained by the periosteal and capsular matrices of the functional matrix hypothesis (FMH); however, its outcomes have not been analytically demonstrated yet.

This computational study aims, therefore, to analytically demonstrate the mechano-morphological relationship in the craniofacial development of children with unilateral crossbite (UXB) using the finite element (FE) method. To this end, the craniofacial complex asymmetry of ten children, five of whom exhibit UXB, was 3D-analysed and compared with the biomechanical response computed from a FE analysis of each patient's occlusion. Due to the complexity of the geometry and the multitude of contacts involved, the inherent limitations of the model were evaluated by comparing computed occlusal patterns with those recorded by an occlusal analysis on 3D printed copies. Comparison's outcomes proved the reliability of our models with just a deviation error below 6% between both approaches.

Out of validation process, computational results showed that the mandibular advance on the crossed side, and particularly of the posterior region, could be associated with periodontal overpressure (>4.7kPa) and mandibular over deformation ($0.002\mu\varepsilon$) in that side, in agreement with the periosteal matrix's principles. Furthermore, the maxilla's transversal narrowing and the elevation of the maxillary and zygomatic regions on the crossed side seems to be related with their respective micro displacements at occlusion, as accounted by their specific capsule matrices.

Our results were consistent with those reported clinically and demonstrated analytically the mechano-morphological relationship of children's craniofacial development based on the FMH's functional matrices. This study is, therefore, a first step in the understanding of the occlusion's effect on the craniofacial development by computational methods. Our approach could help future engineers, researchers and clinicians to understand better the etiology of some dental malocclusions and functional disorders improve the diagnosis or even predict the craniofacial development.

Graphical abstract

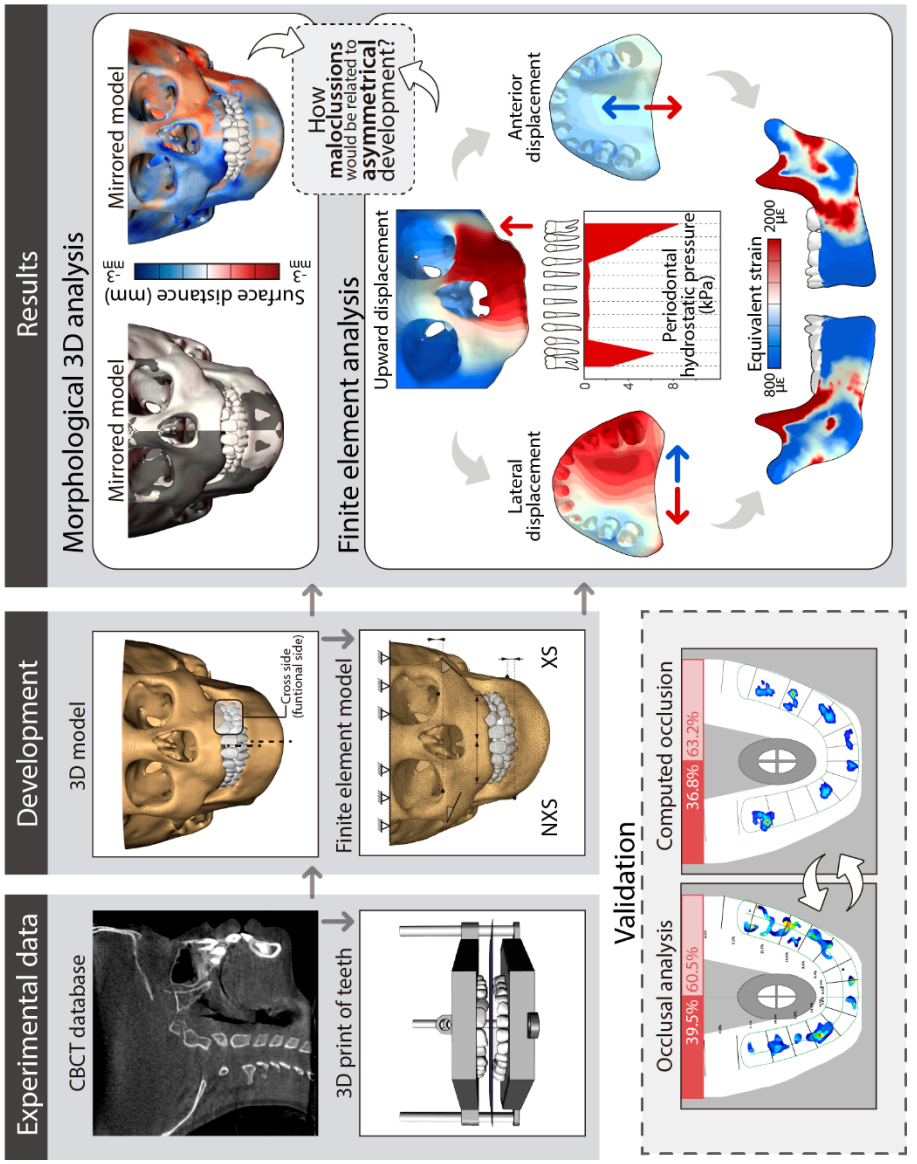

Evaluation of the unilateral crossbite on the craniofacial complex asymmetrical development. A mechano-morphological approach.

Javier Ortún-Terrazas[a*], Michael J. Fagan[b], José Cegoñino[a], Edson Illipronti-Filho[c], Amaya Pérez del Palomar[a]

[a] *Group of Biomaterials, Aragon Institute of Engineering Research (I3A), University of Zaragoza, Zaragoza, Spain*
[b] *Medical and Biological Engineering, School of Engineering and Computer Science, University of Hull, Hull, United Kingdom*
[c] *School of Dentistry, Department of Stomatology, University of São Paulo, São Paulo, Brazil*

Abstract

The occlusion effect on the craniofacial development is a controversial topic that has attracted the interest of many researchers but that remains unclear, mainly due to the difficulties on measure its mechanical response experimentally. This mechano-morphological relationship of the craniofacial growth is often explained by the periosteal and capsular matrices of the functional matrix hypothesis (FMH); however, its outcomes have not been analytically demonstrated yet.

This computational study aims, therefore, to analytically demonstrate the mechano-morphological relationship in the craniofacial development of children with unilateral crossbite (UXB) using the finite element (FE) method. To this end, the craniofacial complex asymmetry of ten children, five of whom exhibit UXB, was 3D-analysed and compared with the biomechanical response computed from a FE analysis of each patient's occlusion. Due to the complexity of the geometry and the multitude of contacts involved, the inherent limitations of the model were evaluated by comparing computed occlusal patterns with those recorded by an occlusal analysis on 3D printed copies. Comparison's outcomes proved the reliability of our models with just a deviation error below 6% between both approaches.

Out of validation process, computational results showed that the mandibular advance on the crossed side, and particularly of the posterior region, could be associated with periodontal overpressure (>4.7kPa) and mandibular over deformation ($0.002\mu\varepsilon$) in that side, in agreement with the periosteal matrix's principles. Furthermore, the maxilla's transversal narrowing and the elevation of the maxillary and zygomatic regions on the crossed side seems to be related with their respective micro displacements at occlusion, as accounted by their specific capsule matrices.

Our results were consistent with those reported clinically and demonstrated analytically the mechano-morphological relationship of children's craniofacial development based on the FMH's functional matrices. This study is, therefore, a first step in the understanding of the occlusion's effect on the craniofacial development by computational methods. Our approach could help future engineers, researchers and clinicians to understand better the etiology of some dental malocclusions and functional disorders improve the diagnosis or even predict the craniofacial development.

Keywords: cranio-facial development, facial asymmetry, finite element method, occlusal imbalance, unilateral crossbite

1. Introduction

The craniofacial complex is mainly composed of the cranial bones and the mandible that is bilaterally connected to the skull by the temporomandibular joints (TMJs) (Figure 1.D), the masticatory muscles (Figure 1.A) and the neurological tissues (shown in Figure 1.C). From the 1930s several theories have described the growth of the different regions of the craniofacial complex (Castaldo and Cerritelli, 2015; Ranly, 2000) basically according to three growth mechanisms (sutural, endochondral and intramembranous) and two conditioning factors (genetic and environmental). Despite none theories is totally valid (Castaldo and Cerritelli, 2015), the functional matrix hypothesis (FMH) proposed by Melvin Moss (1962) (Moss, 1970; Moss and Rankow, 1968) is widely used in dental and in maxillofacial disciplines since it seems to relate the craniofacial development with the mechanical stimulus produced at the environmental activity of chewing.

Anatomically, the occlusion is guided by both TMJs and occlusal planes and its maximum force is limited by the mechanical stimuli sensed by the neural receptors, both in the soft tissues of the TMJs and in the periodontal ligaments (PDLs) (shown Figures 1.D and F). In a well-balanced occlusion, the centric occlusion coincides with the

*Corresponding author at: Aragon Institute of Engineering Research (I3A), School of Engineering and Architecture, University of Zaragoza, Calle María de Luna 3, 50018 Zaragoza, Spain.

E-mail address: javierortun@unizar.es (J. Ortún-Terrazas).

maximum intercuspation position (Hodge and Mahan, 1967) and distributes the maximum bite force almost homogeneously along all occlusal plane, avoiding harmful overloading in some regions (Martinez-Gomis et al., 2009). The mechanical stimulus is therefore perceived by both mandibular nerves (shown in Figure 1.C), causing a normal and symmetrical growth. By contrast, malocclusions, such as unilateral crossbite (UXB), unbalance and gradually produce functional problems which lead to abnormal development of dental and craniofacial structures (Piancino and Kyrkanides, 2016; Thilander and Lennartsson, 2002; Thilandera, 2000) (shown Figures 1.B and E).

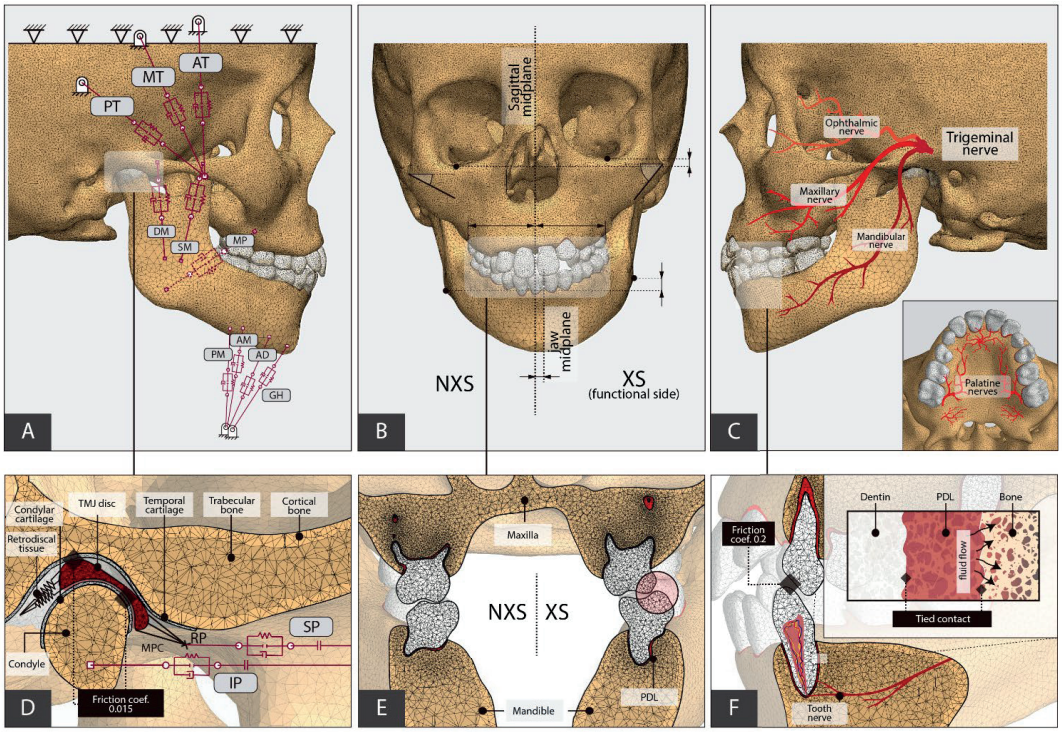

Figure 1. Captures from one of the FE models developed which show: A) the external boundary conditions of the model and the modelling of the chewing muscles (SM, superficial masseter; DM, deep masseter; AT, anterior temporalis; MT, middle temporalis; PT, posterior temporalis; MP, medial pterygoid; IP, inferior lateral pterygoid; SP, superior lateral pterygoid; AM, anterior mylohyoid, PM, posterior mylohyoid; AD, anterior digastric and GH, geniohyoids muscle); B) some of the main morphological differences between the crossed (XS) and non-crossed side (NXS); C) a scheme of the trigeminal nerve branches; D) the boundary conditions in the TMJ; E) the malocclusion associated to the unilateral crossbite; and F) the boundary conditions applied to the tooth-periodontal ligament (PDL)-bone attachment.

UXB is characterized by the lingual occlusion of the buccal cusps of the maxillary teeth with the buccal cusps of the corresponding mandibular teeth (Björk et al., 1964) in one of the two halves (shown in Figure 1.E). Henceforth, we are going to refer to this side as the crossed side (XS), and to the opposite side as the non-crossed (NXS) side (shown in Figure 1.B). Based on the aforementioned FMH, early correction of UXB would avoid irreversible unusual development of the craniofacial complex (Malandris and Mahoney, 2004; Planas, 2013) and painful, expensive and complex surgical treatments later in life (Petrén et al., 2003). Following this trend, some case reports and statistical studies (Agostino et al., 2014; Kennedy and Osepchook, 2005) have tried to relate UXB with the asymmetrical adaptation of soft and hard tissues at early ages. Amongst others morphological changes observed, these studies agree in the deviation of the chin to the XS (Gazit-Rappaport et al., 2003; Ishizaki et al., 2010; Primožič et al., 2009) and the width increment of the mandibular body (Veli et al., 2011) and ramus (Planas, 2013; Ramirez-Yanez et al., 2011) of the same side (shown Figure 1.B). But also, the asymmetrical morphology of the maxilla (Melink et al., 2010), the abnormal development of the glenoid fosses (Defraia et al., 2007; Langberg et al., 2005) or the asymmetrical height of the ocular orbits and the cranial halves (Kim et al., 2014; Sepahdari and Mong, 2013) were

recognized. Nevertheless, none of these clinical studies have been able to establish a function-shape relationship between UXB and the asymmetrical growth (O'Higgins et al., 2012) since they could not evaluate the mechanical stimulus sensed.

As an alternative, computational techniques (Cattaneo et al., 2005; Kofod et al., 2005), specially finite element (FE) method, have been extensively used to analyze the biomechanical effect of the occlusion into the craniofacial growth. Unfortunately, despite the numerous computational studies (Koolstra and van Eijden, 2005; Libby et al., 2017; Marghoub et al., 2017; O'Higgins et al., 2012) performed, the mechano-morphological relation of the craniofacial complex is still a controversial topic. Amongst others, the unmineralized state of bones at childhood, the complex anatomy and behavior of the tissues involved (Donzelli et al., 2004) or the several contacts involucrated (Benazzi et al., 2016) complicate the developing of accurate FE models at early ages. Fortunately, recent advances in 3D cephalometric methods, modelling commercial software, tissues engineering, and computerized occlusal analysis systems have improved its development, and consequently the knowledge about the craniofacial growth. A better knowledge of it could clarify the etiology of some dental malocclusions and functional disorders, improve the diagnosis and treatment selection, or even help to predict the reaction after treatment.

This study aims therefore to relate the craniofacial asymmetrical growth with the mechanical stimulation computed through FE analyses of the unilateral occlusion, following the FMH's principles and using the latest advances in scanning, modelling and occlusal analysis. Hence, the maximum intercuspation occlusion was simulated in 10 detailed patient-specific FE models developed from the segmentation of Cone Beam Computed Tomography (CBCT) images of children with and without UXBs. The accuracy of these computational models was firstly checked by the comparison of the occlusal patterns computed with those recorded experimentally by an occlusal analysis system in 3D printed copies of the full dentitions. Afterwards, the occlusal patterns, the mechanical response of the tissues and the bony regions' displacements were presented and related to the asymmetrical malformations identified through the 3D-comparison of both craniofacial halves. Our findings were then discussed and compared with those observed clinically in other studies of children with UXB, with a special focus on the fundamentals of the FMH. Finally, at the end of this manuscript, the potential of using FE models for the study of craniofacial growth was discussed based on our findings.

Table 1. Subject characteristics (F, female; M, male; XS, side of the unilateral crossbite; R, right; L, left) and FE model details.

Subject	Sex	Age (years)	Group	XS	No. of elements	No. of nodes
1	F	6	Control	-	2,879,238	6,120,296
2	F	7	Control	-	2,538,347	5,321,617
3	M	8	Control	-	3,166,195	6,577,722
4	F	9	Control	-	2,308,835	4,705,625
5	F	12	Control	-	3,176,348	6,370,546
6	F	6	UXB	R	3,659,199	7,154,101
7	F	7	UXB	L	4,161,445	8,008,087
8	M	8	UXB	L	3,170,809	6,283,733
9	F	9	UXB	L	3,986,407	8,032,221
10	F	12	UXB	R	1,977,934	4,025,711

2. Material and methods

2.1. FE models

Ten 3D models of the masticatory system were developed from the 3D-cephalometric images of 10 pediatric subjects (see Table 1) with mixed dentition, three of whom exhibited left UXB and other two that have right UXB according to the diagnosis performed by an expert. To facilitate the subsequent interpretation of results, the 3D models of those patients with right UXB were mirrored with respect to the sagittal midplane, achieving to have the XS on the left side in all the subjects. The other five models, which constitutes the control group of this study, did not show any malocclusion or asymmetry defects. The images of UXB and control groups were respectively obtained as a part of treatment planning or of a routine medical examination through a CBCT scan system (i-CAT™; Imaging Sciences International, Hatfield, PA, USA) and all of them were scanned in a maximum intercuspation position. Data

acquisition was approved by the Research Ethics Committee of the University of São Paulo – USP, School of Dentistry (numbers 200/06 and 16/2008) and was used exclusively for scientific purposes. All datasets were obtained with an acquisition time of 5-26 s and field of view (FOV) of 13 cm × 17 cm and were output in a 14-bit greyscale and 16,384 shades of grey to a Digital Imaging and Communication in Medicine (DICOM) file through cylindrical reconstruction algorithms. The output file of each subject was composed of 210 images with an interscan distance of 0.50 mm.

To improve the limiting contours of each part in the model, a gradient filter was initially applied to each database. For the modelling of hard tissues, the images were then automatically segmented in Mimics software (Mimics, v.19.; Materialise, Leuven, Belgium) using a masking technique. Meanwhile, cartilaginous structures, such as the fibrocartilage layers which cover condyle and temporal fossa surfaces, were manually segmented as 0.2 and 0.5 mm thickness layers, respectively (Pullinger et al., 1990) (shown in Figure 1.D). TMJ discs were modelled by the free space between the fibrocartilage layers having a variable thickness of about 1, 2 and 2.7 mm in intermediate, anterior and posterior regions, in agreement with the measurements of previous studies (Hansson and Nordström, 1977) (shown in Figure 1.D). On the other hand, PDLs were modelled through a Boolean subtraction operation of a 0.2 mm (Keilig et al., 2016; Ortún-Terrazas et al., 2018; Xu et al., 2015) clearance around each tooth (Figure 1.F). Thereafter, the geometry of each tissue was parametrized using non-uniform rational bases splines-based transformation in Rhinoceros v5 software (Robert McNeel & Associates, Seattle, USA).

For the posterior comparison of results among different subjects, 3D models were uniform scaled in order to compensate the craniofacial size differences between subjects. Hence, a linear transformation matrix (Ortún-Terrazas et al., 2020b) resulted from a Generalized Procrustes Analysis (GPA) of the patient' mandible was applied to each database. It is remarkable that the whole model's volume was not considered for the matrix computation since different cranial portions were scanned in each database, as it was widely explained in our previous publication (Ortún-Terrazas et al., 2020b).

The 3D-domain of each model was meshed via a free meshing technique in Abaqus software (Abaqus 6.14, Simulia, Rhode Island, USA), resulting in meshes of around 3,102,476 second-order tetrahedral elements (C3D10-type element in Abaqus) and 6,259,966 nodes (see Table 1). Mesh size was determined after a mesh convergence process in which further refinement of the mesh resulted in differences of the results less than 7%. As a result of this convergence test, hard and soft tissues were respectively discretized by elements whose mean dimensions were 0.20 and 0.1 mm, respectively in all directions. In those tissues with almost incompressible behavior, such as TMJ discs and fibrocartilage layers, hybrid formulation (C3D10H-type element in Abaqus) was included, whereas for PDLs and their adjacent trabecular tissue, the porous contribution (C3D10MP-type element in Abaqus) was added.

Following previous studies' recommendations (Ingawalé and Goswami, 2009; Ruggiero et al., 2015; Singh and Detamore, 2008), the effect of a collagen network embedded in the tissue's matrix was considered in the definition of TMJ discs and cartilaginous layers behaviors, following previous studies' recommendations (Ingawalé and Goswami, 2009; Ruggiero et al., 2015; Singh and Detamore, 2008). Hence, the collagen fibers in these tissues were oriented anteroposteriorly in the central region and forming a ring on the periphery, dividing these tissues in five different regions (anterior, posterior, central, medial and lateral) with particular mechanical properties and fibers orientations. This complex fibers embedded behavior was characterized by a transversally isotropic hyperelastic material model whose strain energy density function (Holzapfel, 2000) is defined as follows:

$$W = C_1 \cdot (\tilde{I}_1 - 3) + \frac{k_1}{2 \cdot k_2}\{exp[k_2 \cdot (\tilde{I}_4 - 1)^2] - 1\} + \frac{1}{\mathrm{D}}\left(\frac{(J_{el})^2 - 1}{2} - lnJ_{el}\right) \quad (1)$$

where C_1 is a material constant related to the ground substance; $k_1 > 0$ and $k_2 > 0$ are the parameters that identify the exponential behavior due to the presence of collagen fibers; D is the compressibility modulus; J_{el} is the elastic volume strain, and $\tilde{I}_1$ and $\tilde{I}_4$ are terms of the modified invariants that arise from uncoupling the dilatational and deviatoric responses, respectively. These invariants are defined as:

$$\tilde{I}_1 = tr\tilde{\boldsymbol{C}} \;\; \tilde{I}_4 = \boldsymbol{a}^0 \cdot \tilde{\boldsymbol{C}} \cdot \boldsymbol{a}^0 \quad (2)$$

where $\boldsymbol{a}^0$ is unitary vector defining the orientation of the collagen fibres and $\tilde{\boldsymbol{C}}$ is the modified Green tensor in the reference configuration defined by the deformation gradient $\tilde{\boldsymbol{F}}$, as $\tilde{\boldsymbol{C}}\,(\hat{\lambda}_{\mathrm{i}}) = \tilde{\boldsymbol{F}}^T\tilde{\boldsymbol{F}}$. The stretch $(\hat{\lambda}_{\mathrm{i}})$ is defined as the ratio between fibre length in deformed $(\boldsymbol{X})$ and in reference configurations $(\boldsymbol{x})$ in direction i.

Whereas, in the PDLs, the transversely isotropic behavior caused by collagen fibers was neglected since the centric occlusion simulated produced mainly intrusive forces which hardly stretched the collagen fibers (Ortún-Terrazas et al., 2018). This compressive loading produce a viscoelastic response of the tissue, which was described in our previous models by the strain energy density function of a highly compressible isotropic hyperelastic material (Storakers, 1986) as follows:

$$W = \frac{2\mu}{\alpha^2}\left[\hat{\lambda}_1^{\alpha} + \hat{\lambda}_2^{\alpha} + \hat{\lambda}_3^{\alpha} - 3 + \frac{1}{\beta}\left(J_{el}^{-\alpha\beta} - 1\right)\right] \quad (3)$$

where μ and α are material parameters and the coefficient β determines the degree of compressibility being related to Poisson's ratio, ν, by $\beta = \nu/(1-2\nu)$. Considering that the PDL is a fully saturated porous tissue (Figure 1.F), the total stress, $\boldsymbol{\sigma}$, is then defined by the second Piola-Kirchhoff stress tensor of the solid phase of the aforementioned hyperelastic material model, $\bar{\boldsymbol{\sigma}}_s$, and the coupling of the fluid phase pressure (Storakers, 1986) as follows:

$$\boldsymbol{\sigma} = (1-n)\cdot\bar{\boldsymbol{\sigma}}_s - n\cdot\bar{p_t}\cdot\boldsymbol{I} \quad (4)$$

where n is the porosity defined as the ratio of trapped fluid volume (V_f) to total volume (V_t) and $\bar{p_t}$ is the average pressure stress of the interstitial fluid which is related to the Jacobian contribution from the permeability of the tissue by the nonlinear Forchheimer flow law. This law was employed in Abaqus to describe the fluid flow for a permeability, k, which varies with the deformation by the exponential permeability function described by Argoubi and Shirazi-Adl, 1996 for biphasic materials:

$$k = k_0\left[\frac{e(1+e_0)}{e_0(1+e)}\right]^2 exp\left[M\left(\frac{1+e}{1+e_0} - 1\right)\right] \quad (5)$$

where e is the void ratio related to the tissue's porosity by $e = n/(1-n)$, k_0 and e_0 are the permeability and the void ratio at zero strain, and M is a dimensionless material parameter. To allow the fluid interaction between PDL and bone, a fluid pressure of 0.0 MPa (Bergomi et al., 2011) was set on the surface where PDLs are attached to the bone (shown in Figure 1.F). Table 2 summarizes the parameters of the above-mentioned material models and those that define the elastic and porous-elastic behavior of the hard tissues.

Regarding the external boundary conditions, as it is often assumed in this kind of simulations, the upper nodes of the skull were fixed (shown in Figure 1.B) and both PDLs and cartilages were connected to the adjacent bony structures by tied contacts (Figure 1.D and F, respectively).

Muscular loads were applied as contractile forces using connector elements (CONN3D2-type element in Abaqus) which reproduced the passive, active and damping behavior of the muscles (shown in Figure 1.A). For the infant participants of this study, these forces were approximated from adult measurements by considering a lower maximum bite force at childhood than at adulthood. Moreover, for those subjects with UXB, a-20% (Frongia et al., 2013) asymmetry index was considered for mimicking the muscular imbalance between both sides. The full process to compute muscular components and the resultant contractile forces are fully detailed in the supplementary material. These contractile forces were gradually applied for 1.6 seconds mimicking the muscles contraction at maximum intercuspation occlusion. However, the numerical results were not been captured until 2.76 seconds in order to simulate the time dependent reactions of the soft tissues at clenching (Ortún-Terrazas et al., 2020a).

It is also noteworthy that the insertion of the superior portion of lateral pterygoid in a unique node of the TMJ disc would cause an excessive distortion of the adjacent elements of the disc. For avoiding it, the superficial nodes of the anterior disc band were connected to an intermediate reference point by several multipoint constraint elements (MPC) and then to the muscle insertion (shown in Figure 1.D). On the other hand, the TMJ disc posterior attachment was modelled by spring elements (shown in Figure 1.D) of 0.008 N/mm stiffness, as in an elsewhere study (DeVocht et al., 1996). Finally, the sliding contacts between teeth and disc-cartilages were defined respectively by friction coefficients of 0.2 (Zheng et al., 2003), and 0.015 (Tanaka et al., 2004) using a penalty formulation (Figures 1.D and F).

2.2. Occlusal analysis by T-Scan

From the above segmentation procedure, the 3D geometry of the teeth cusps was extracted by applying a threshold level of 1688 HU (Wang et al., 2011) to each image database in Mimics software. For those pairs of teeth segmented as a single part, a manual detachment was conducted by considering the tooth's contour. The dental cusps reconstructed were then assembled on two thin sheets of 0.5 mm thickness (shown in supplementary Figure 1) and exported through the slicer software (Ultimaker Cura 3.6.0, Geldermalsen, Netherlands) to the desktop printer Ultimaker 3 (Ultimaker B.V., the Netherlands) for 3D-printing (layer height: 0.06 mm; wall thickness: 1 mm; infill density: 40%; speed: 60 mm/s; temperature: 195 °C). For printing the dental arches and their respective external holders, Polylactic Acid (PLA-Ultimaker BV, Geldermalsen, Netherlands) material ($E = 2346.5\ MPa$) was used. The inferior holder was fixed in the assembly, while the superior one could just move vertically (shown in Figure 1.A of the supplementary material) since, as described in the previous section, the initial position of the model was already situated at maximum intercuspation and it is just necessary a minimal vertical displacement to contact both dental arches.

Table 2. Mechanical properties assigned to each region of the FE model. E, elastic modulus; ν, Poisson coefficient; Υ_w, specific weight of the interstitial fluid.

Elastic material model

Region	E (MPa)	ν (-)
Cortical bone[(a)]	20000	0.30
Dentin[(b)]	15000	0.31

Transversally isotropic material model

Region	C_1 (MPa)	D (MPa^{-1})	k_1 (MPa)	k_2 (-)
TMJ disc (boys)[(c)]				
Anterior	1.45	0	0.43	0.34
Lateral	1.45	0	0.69	0.43
Central	1.45	0	0.97	0.17
Medial	1.45	0	0.17	1.68
Posterior	1.45	0	1.25	0.16
TMJ disc (girls)[(c)]				
Anterior	2.4	0	0.05	3.72
Lateral	2.4	0	0.11	2.52
Central	2.4	0	0.75	0.87
Medial	2.4	0	0.08	2.93
Posterior	2.4	0	0.31	1.44
Cartilages[(c)]				
Anterior	1.65	0	0.24	1.95
Lateral	1.65	0	2.58	0.43
Central	1.65	0	3.77	0.21
Medial	1.65	0	2.52	0.42
Posterior	1.65	0	0.16	1.92

Porous elastic material model

	Solid phase		*Porous phase*			
Region	E (MPa)	ν (-)	$k_0 \cdot 10^{-15}$ (m^2)	M (-)	e_0 (-)	Υ_w (N/m^3)
Trabecular bone[(b)]	345	0.31	52.9	-	4	9800

Porous hyperfoam material model

	Solid phase			*Porous phase*			
Region	μ (MPa)	α (-)	ν (-)	$k_0 \cdot 10^{-15}$ (m^2)	M (-)	e_0 (-)	Υ_w (N/m^3)
PDLs[(b)]	0.03	20.9	0.257	8.81	14.2	2.33	9800

a) Lacroix and Prendergast, 2002 (Lacroix and Prendergast, 2002).
b) Bergomi et al., 2011 (Bergomi et al., 2011).
c) Ortún-Terrazas et al., 2020 (Ortún-Terrazas et al., 2017).

To perform the experimental test, a piezoelectric film sensor was introduced between the 3D printed superior and inferior teeth arcades. This sensor records the occlusal contacts at maximum intercuspation by means of a T-Scan III system (Tek-Scan South Boston, MA, USA) (the assembly can be seen in Figure 1.B of the supplementary material). The piezoelectric film was a 100-µm-thick mylar-encased recording sensor with 1500 compressible sensitive receptor points and was inserted into a plastic U-shaped device. The U-shaped device was positioned parallel to the upper occlusal plane and centered along the midline between the upper central incisor teeth by a dentist with expertise in occlusal analysis. Then, a 2-kg-weight was applied to the superior component of the assembly to record the normalized contact pressures. The load value was computed by an inverse FE analysis in a way that the stress did not produce a noticeable deformation (minimum principal strain < 0.01 ε) on the printed samples which could modify the occlusal plane. Apart from avoiding occlusal malformations, the load's magnitude had not a quantifiable effect on the results recorded by the T-Scan III system, since the system computed just the relative percentage of the total

contact load recorded. This procedure was repeated three times for each case in order to check the sensitivity of the test. Afterwards, the occlusal patterns recorded were plotted in the T-Scan v10 software, as can be seen in Figure 2.

On the other hand, as it had been conducted in our previous study (Ortún-Terrazas et al., 2020a), the contact pressures in the computational models were recorded using a virtual square-shape film of 0.1 mm thickness positioned as in the experimental test. This virtual film was composed of 7,200 second-order quadrilateral membrane elements (M3D8-type element in Abaqus) and its behavior was defined based on the linear elastic properties of Mylar840 material (DuPont; $E = 5\ GPa$ and $\nu = 0.3$). With the upper nodes of the skull fixed, the contractile forces described in section 2.1 were applied to the model. Although the models were initially placed in the maximum intercuspation position, muscular forces were needed to engage the occlusal pattern on the virtual film. Finally, to display the relative percentages computed as those measured by the T-Scan III system, a 3D bars graph was developed in MATLAB (MATLAB 6.0 R12 The MathWorks Inc., Natick, MA, 2000). The height of the bars in this graph shows the contact pressure in the centroid of each film-element, while the width and depth represent its location in the reticule of the virtual film (80 x 90 elements). Both contact and location data were firstly extracted from Abaqus' output file through a Python script ("Python 3.5.2, Python Software Foundation").

2.3. Morphological 3D-analysis

As introduced, this study aims to relate the mechanical stimulation with the asymmetrical development of the craniofacial system. Therefore, in addition to the computational simulations explained above, a 3D evaluation of the morphological differences between both hemifacial sides was performed.

The first step of this morphological analysis was, therefore, to define an appropriate sagittal midplane (Pinheiro et al., 2019) which divides the craniofacial complex by compensating any asymmetrical variations. Thus, a new model was symmetrically copied from an approximate midplane which had been defined by the midpoints of the glabella, menton and pharyngeal tubercle. The mirrored model was then aligned to the original one through applying the Iterative Closest Point (ICP) algorithm. The combination of these point clouds, original and mirrored ones, provided an ideal symmetrical model of the patient whose first three eigenvectors established the desired sagittal midplane (Ortún-Terrazas et al., 2020b). Eigenvectors of this idealized model were then computed through Principal Component Analysis (PCA) of the points that constituted the 3D model. As a result, this midplane was used to build a new mirrored model which serve to compute the normal distance with the original model, i.e. to compute the morphological differences between both hemifacial sides. All these operations were performed in MATLAB, while the plotting of normal distances was displayed in Paraview software (Paraview v5.6, National Technology & Engineering Solutions of Sandia, New Mexico). More details about this procedure for 3D morphological-analysis can be found in our previous publication (Ortún-Terrazas et al., 2020b).

3. Results

In this section, firstly, the results of the occlusal analysis and those computed from FE simulations are displayed in Figure 2. Afterwards, it is presented the distribution of some mechanical variables that could be helpful in the explanation of the craniofacial development according the FMH's principles, such as the pressure of the PDL's interstitial fluid (Figure 3), the mandibular deformation (Figure 4), and the displacement patterns of the maxilla (Figure 5) and the skull (Figure 6). Finally, the results of the morphological analysis (Figure 7) are commented.

3.1. Occlusal contacts

Figure 2 displays both the bar graphs and the colored mapping generated by the T-Scan, and those pressures computed by the FE simulation on the contact surfaces of each subject in both groups. The color maps show the relative occlusal contact for each patient and the relative occlusion percentages on each hemiarch. In supplementary Table 2, the numerical values of the mean, standard deviations, relative errors and asymmetrical index (AI) of both groups are summarized. Basically, a positive score of AI indicates superiority of the occlusal force on the right side, whereas a negative score indicates superiority on the left side. In all cases of the control group, the percentage difference between the measured occlusal contacts of both sides was below 12 %, with mean values (± SD) of 46.8 % and 53.2% (± 3.7) Whereas, in the UXB group , the difference between the pressures in both halves exceeds even 42% (S10), being always greater on the XS (mean value 62%) than on the NXS (mean value 38%). This imbalance produces a negative IA in all cases. Similar results were obtained by the FE approach, with also a greater percentage of occlusion on the XS (61%) than on the NXS (39%). As a result of the comparison between the numerical and experimental results, percent errors between both approaches were lower than 3.5 % for the control group and below 6 % for the UXB group. Furthermore, as can be seen in Figure 2, the occlusal pattern in both approaches was quite similar, with maximum values (red regions in Figure 2) on the same pairs of teeth. Meanwhile, the greatest differences occur in those contacts of low level (blue regions in Figure 2), resulting in almost negligible differences in the total occlusal percentages on both halves.

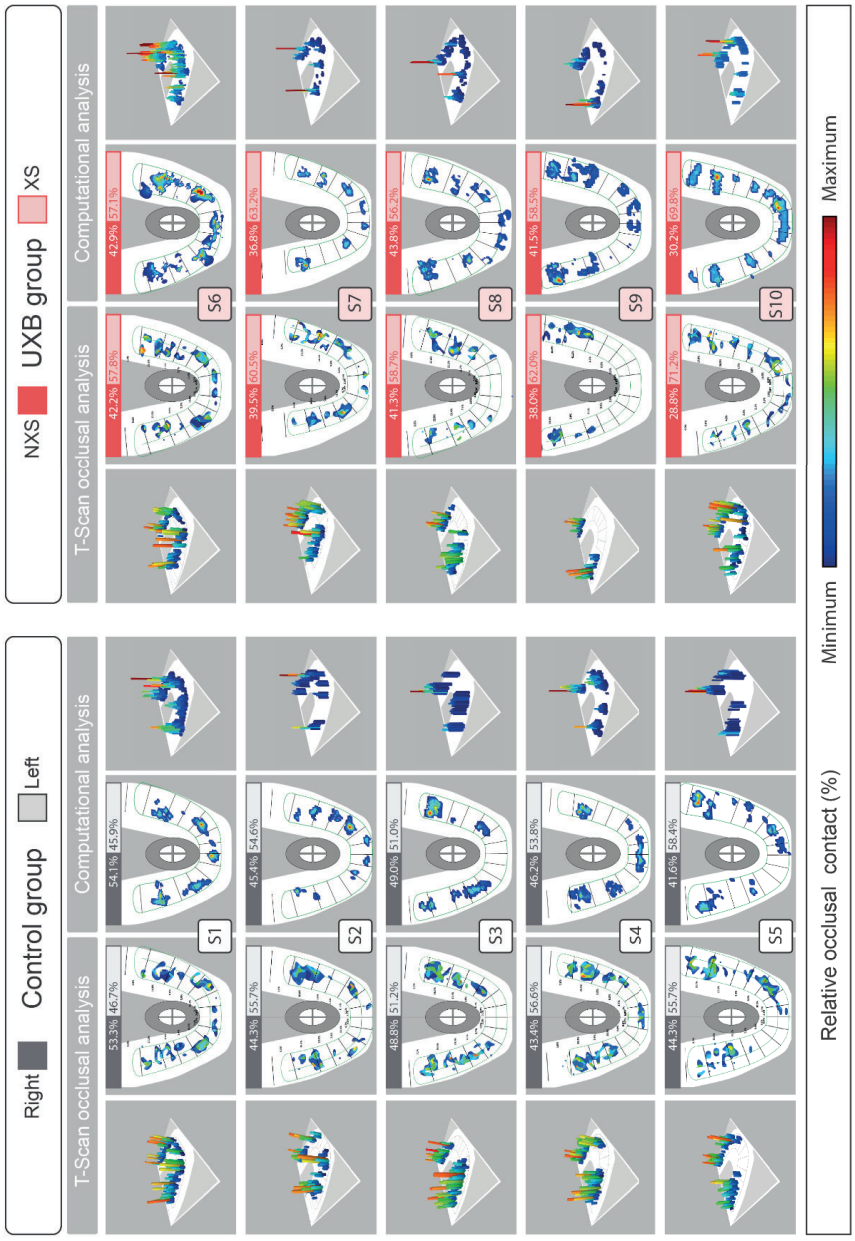

Figure 2. Perspective and top views of the occlusal records by the T-Scan III system and those computed through the FE analysis in each patient of the control group (left box) and the UXB group (right box).

3.2. Mechanical results

As was introduced, the occlusal forces subject PDLs to compressive stresses and strains, increasing, therefore, the hydrostatic pressure in the PDL's interstitial fluid. For many researchers (Chen et al., 2014; Dorow and Sander, 2005; Hohmann et al., 2009), this increment is the main responsible of the tooth movement and bone remodeling process as it was first introduced by Schwarz in 1932 (Schwarz, 1932). According to this "pressure-tension" theory, the overpressure could collapse the PDL's capillaries partially or completely, leading to a bone remodeling processes which may cause dental movement (Chen et al., 2014). Physiologically, the range of capillary blood pressure has been stated to be within 2–4.7 kPa (15-35 mmHg) (Hohmann et al., 2007). From this point of view, it is generally accepted (Chen et al., 2014) that bone remodeling occurs for values higher than 4.7 kPa of the volume-averaged hydrostatic pressure $\bar{\sigma}_H$. In our study, this variable was plotted for each PDL of the mandibular teeth in Figure 3, computing in each PDL element the $\bar{\sigma}_H$ as $\bar{\sigma}_H = (\sum_e \sigma_H^e \cdot V^e)/\sum_e V^e$ where σ_H^e and V^e are respectively the hydrostatic pressure and the volume of an element, e(Chen et al., 2014).

Hence, in the control group, the hydrostatic pressure was uniformly distributed along the PDLs of both halves, being greater in the posterior teeth than in the anterior ones. In those cases (i.e see S2 in Figure 3) where the PDL's hydrostatic pressure overcame the maximum capillary blood pressure ($\bar{\sigma}_H^*$ = 4.7kPa) in one of the hemiarches, the hydrostatic reaction in the PDL of the other side was similar, potentially leading to symmetrical growth of both halves. Contrariwise, in the UXB group, the PDL's reactions were unbalanced in agreement with the occlusal analysis results, being always greater in the XS than in the NXS. In fact, in almost three of UXB subjects, $\bar{\sigma}_H$ exceeded the capillary blood in the XS. Finally, it is also noticeable that older subjects (S5 and S10) showed PDL's reactions in the second molar' ligaments due to the eruption of these teeth.

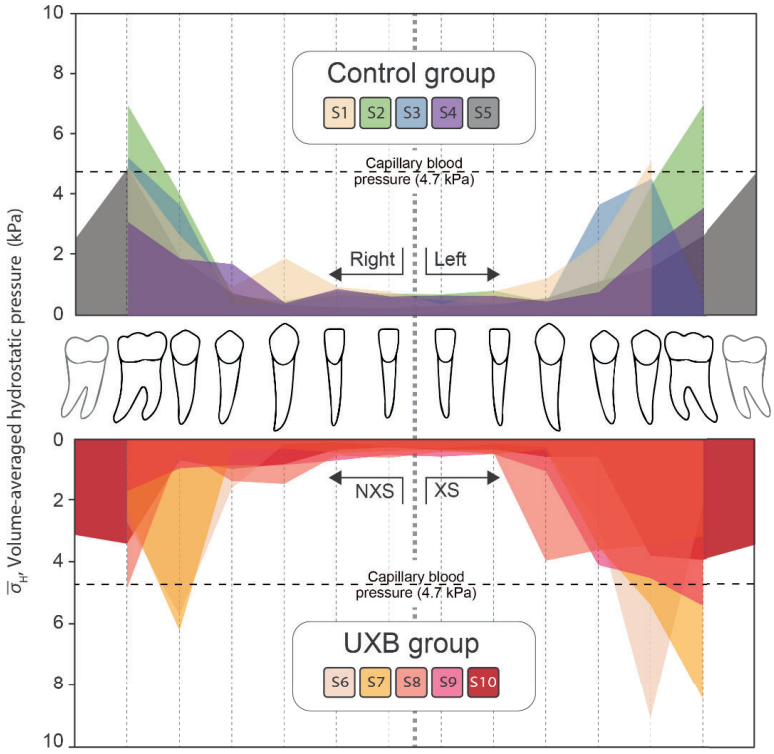

Figure 3. Volume-averaged hydrostatic pressure in each PDL of the inferior teeth of the patients of the Control (top) and UXB (bottom) groups. (For interpretation of the references to colour in this figure legend, the reader is referred to the web version of this article).

Besides the pressure-tension theory (Schwarz, 1932), mandibular bone remodeling is often explained through the distortion or bending of the alveolar bone by the Frost mechanostat theory (Frost, 1987, 1983). Regarding this, the minimum effective strain ε_e is generally used as a measure of the overall tissue deformation gradient, being expressed from components of principal strains (e_1, e_2, e_3) by $\varepsilon_e = \sqrt{0.5 \cdot [(e_1 - e_2)^2 + (e_2 - e_3)^2 + (e_3 - e_1)^2]}$. During physiological activities, osteoblasts and osteoclasts work synchronously in a range between 0.0008 to 0.002-unit bone surface strain, which is often referred to lazy region. For ε_e above this range, however, it is generally assumed that the bone volume could increase (Field et al., 2010; Frost, 2004, 1983). To evaluate the mandibular growth in our models according to this rule, the distribution of ε_e in both mandibular halves of each model was shown in Figure 4. Red regions represented those areas in which bone apposition may occur following this mechanostat theory. As can be shown, higher strains were obtained at the coronoid processes and in the middle of the mandibular ramus as a result of the temporal and masseter muscle insertions respectively. Apart from these regions, it is also remarkable ε_e values in the mandibular angle region, which are particularly pronounced on the XS side of the UXB patients. By contrast, in the control patients, the ε_e distribution was more balanced in both halves with maximum ε_e values in both molar regions.

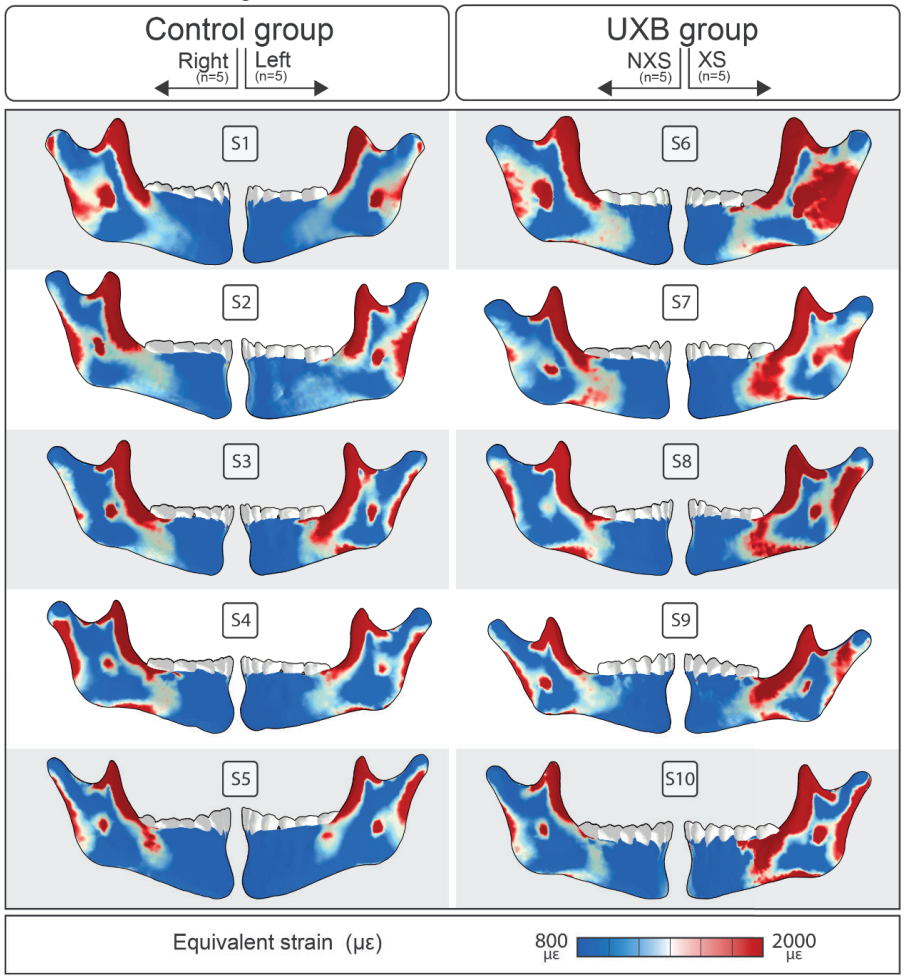

Figure 4. Distribution of the equivalent strain in both mandibular halves of those subjects of the control (left) and UXB groups (right).

In addition to the stress and strain results, the micro displacement patterns of the craniofacial structures were gathered from the FE analysis. Figure 5.A shows the maxilla displacements in the sagittal direction (x-direction) while Figure 5.B shows its displacements in the anteroposterior direction (y-direction). Note that most control patients (S1, S4 and S5) show a symmetrical forward movement of the maxilla. The sagittal displacement of each hemiarch was produced symmetrically towards a labial direction, potentially blending the maxilla around its sagittal midplane as part of a physiological expansion. In other cases (S2 and S3), maxilla's displacements were less pronounced and symmetric but always moves towards the anterior- labial direction. In UXB subjects, however, a non-symmetrical lateral displacement was observed, being mainly oriented towards the NXS. In fact, S7's maxilla experienced just the opposite movement that the observed in the control group, i.e. a displacement in labial direction. Likewise, the anterior displacement was neither symmetrical, being it greater on the NXS than on the opposite side. In the S9's maxilla, indeed, the hemiarch of the XS was posteriorly displaced.

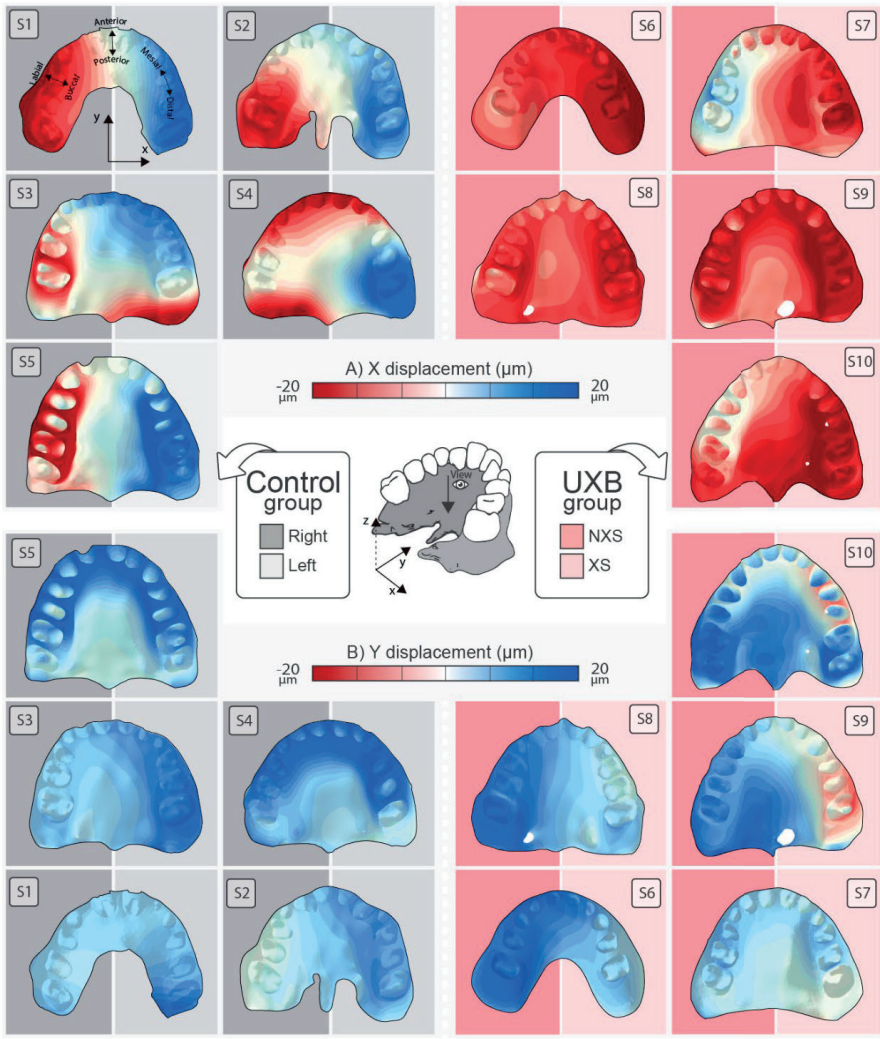

Figure 5. A) Lateral and B) anterior displacements of the maxilla in those subjects of the control (left) and UXB groups (right). Blue colour means positive displacement while red colour refers to negative displacements.

These differences were also noted on the upward displacement of craniofacial structures (shown in Figure 6). Whereas in control subjects, the occlusion moves the zygomatic and maxillary regions symmetrically and upward, in UXB subjects, this movement was just experimented by the XS' halve.

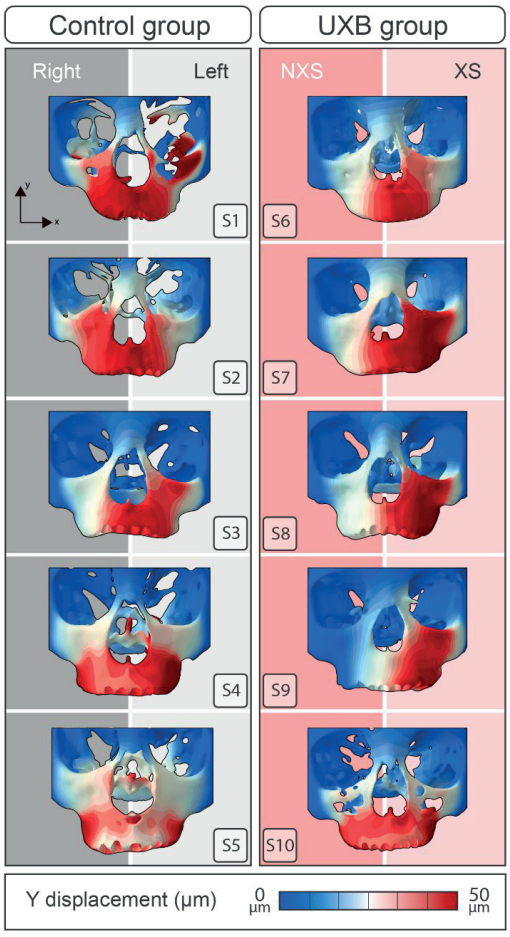

Figure 6. Coronal displacements of the skull in those subjects of the control (left) and UXB (right) groups. Red colour indicates upward movement, whereas blue colour denotes no displacement.

3.3. Morphological results

Finally, the normal distances between the surfaces of the original model and the mirrored one in each model of both groups were presented in Figure 7. From these results, as might be anticipated, the morphological difference between both halves was greater in UXB patients (out of ±3 mm range) than in the control subjects (within ± 2 mm range). A common aspect in all UXS patients was the backward position of the maxilla in the XS in comparison with its counterpart. Moreover, the mandible of these subjects was more forward on the XS side than on the NXS, except for S8 where just the contrary effect was obtained.

Figure 7. Normal distance between the original model and a mirrored model of the subjects of the control (left) and UXB (right) groups. Positive values (blue) means a forward position of this region against its counterpart, while negative values (red) indicate the backward position of the region.

The morphological variations between both sides were also noticeable in the temporal and zygomatic regions which were in a more posterior and upward position in the XS than in the NXS.

4. Discussion

As was previously introduced, many clinical (Agostino et al., 2014; Kennedy and Osepchook, 2005) and computational (Koolstra and van Eijden, 2005; Libby et al., 2017; Marghoub et al., 2017; O'Higgins et al., 2012) studies have attempted to understand the influence of the dental occlusion in the craniofacial development, and consequently, the influence of dental malocclusions in the craniofacial malformations. Nevertheless, the mechano-morphological relationship of craniofacial development during childhood is still uncertain (Testa et al., 2017).This uncertainty is mainly caused by the difficulty of evaluating biomechanically the craniofacial complex through the conventional experimental techniques (O'Higgins et al., 2012) and because of the limitations of the computational methods, such as the developing of accurate FE models (Benazzi et al., 2016; Donzelli et al., 2004) of pediatric subjects. Fortunately, recent technological advances in 3D cephalometric images acquisition have allowed reducing the radiation for the patient in diagnosis, facilitating the craniofacial 3D modelling also in children. Moreover, the extended use of new devices for non-invasive occlusal analyses has encouraged checking the accuracy of these computational models. The aim of this study was, therefore, to demonstrate, the relationship between their craniofacial morphology with the occlusion, or rather between the asymmetrical morphology and the unilateral occlusion, through the development of complex and accurate FE models of pediatric subjects. Hence, the stress, strain and displacements computed from FE analyses at maximum intercuspation occlusion were compared with the asymmetrical morphology identified after a morphological 3D-analysis (Ortún-Terrazas et al., 2020b). Although most of the population has a preferential chewing side, just in the most severe cases an unbalance in the occlusion occurs. Likewise, our occlusal analysis' outcomes (Figure 2) showed that the occlusal pattern in the control subjects was almost symmetrical with AI below 13.5 %. Consequently, it could be indicated that in these subjects the maximum intercuspation position coincides almost with the centric occlusion. According to the AI sign, however, our results suggest also that left side could be the referenced one in no pathological cases, in contrast with other studies (Martinez-Gomis et al., 2009; Nissan et al., 2004; Paphangkorakit et al., 2006) in which right side was found as preferential chewing side. This inconsistency with literature, however, could be explained by the modest size of our sample, in comparison with other clinical studies (Martinez-Gomis et al., 2009; Paphangkorakit et al., 2006). Furthermore, the low AI does not necessary mean an anomaly in the centered position of the occlusion (Martinez-Gomis et al., 2009) for these patients. On the contrary, in most UXB patients, the AI was greater than 20%, being in all cases the crossed side the one with the major occlusion. The occlusion patterns were also accurately simulated by our FE analyses, with an average relative error below 6%, which was close to the reliability errors of the T-Scan measurements (Koos et al., 2010). These results prove, therefore, the truthfulness of our computational approach and its applicability to the goal of this study.

Besides the noticeable occlusal imbalance, UXB resulted also to an asymmetric distribution of the mechanical variables in the craniofacial complex, which could account some shape, size and position alterations that have been clinically observed previously (Kennedy and Osepchook, 2005; Lee and Baek, 2012; Veli et al., 2011). In the case of the subjects of our study, these skeletal malformations were clearly highlighted through the 3D morphological analysis explained in section 3.3. Hence, apart from the specific variations of each subject, UXB patients displayed a common asymmetrical development on the mandible, maxilla and zygomatic region (shown in Figure 7). These variations, according to the FMH, could be explained by two different functional matrices: the periosteal and the capsular ones (Moss, 2007). The first mainly modified the size and shape of the mandible, while the second altered the spatial position of the maxilla and cranial regions (Moss and Salentijn, 1969).

From the periosteal matrix perspective, our numerical results (shown in Figures 3 and 4) could explain some of the mandibular malformations founded in those subjects with UXB, such as the more advanced position of the mandibular half of the XS than ones of NXS (shown in Figure 7). Hence, following the approach of other computational studies (Hohmann et al., 2009; Sarrafpour et al., 2013), we studied the periosteal functional matrix by the PDL's hydrostatic pressure (shown in Figure 3) and the mandibular deformation (shown in Figure 4) following the principles of the pressure-tension (Schwarz, 1932) and Frost mechanostat (Frost, 1987, 1983) theories respectively. Applying them to our numerical results, bone remodeling and apposition patterns in the mandible could be described.

Hence, according to our results, the occlusion in those subjects with no UXB produced almost a symmetrical distribution of the hydrostatic pressure in the PDL's of both mandible's body halves. The symmetry was also found in those PDLs that exceeded the capillary blood pressure. According to the principles of the pressure-tension (Schwarz, 1932), this overpressure in both sides would lead to an almost symmetrical bone remodeling (Chen et al., 2014) of the mandible. Contrariwise, in the case of patients with UXB, an imbalance in the periodontal reaction was observed. Because of this imbalance, the hydrostatic pressure in several PDLs of the XS, mainly in the posterior PDLs, was higher than in those of the NXS, leading to a potentially overdevelopment of the mandible's XS side, as the observed in the morphological analysis (shown in Figure 7). Furthermore, as a result of periodontal overpressure, the bone remodeling around those teeth could occur, potentially leading to dental movements in the teeth of the XS (Sarrafpour et al., 2013). This movement of XS' teeth would therefore aggravate and be responsible for UXB worsening

over time. Thereby, our outcomes could serve as an analytical demonstration of the need of early treatments to correct malocclusions during childhood, as has already been empirically supported in several clinical studies (Agostino et al., 2014; Kennedy and Osepchook, 2005; Malandris and Mahoney, 2004; Planas, 2013).

Besides the effect of the periodontal stimulation on the development of the mandibular body, the principles of the Frost mechanostat theory (Frost, 1987, 1983) were also used to study the development of other mandibular regions, such as the mandibular branch or the posterior alveolar region. Results in Figure 4 display how centric occlusion leads to an almost-symmetric ε_e distribution in the mandibles of non-UXB patients. Based on mechanostat theory principles, this balanced distribution leads to an almost symmetrical mandible's development. In addition to the symmetrical distribution of ε_e, it is noteworthy that ε_e values above the upper limit of the lazy region (red regions in Figure 4) are only produced in those areas where the temporal and masseter muscles are inserted. Nevertheless, the strain state in these areas has not a useful meaning since it is caused by the concentration of local deformations on connector elements' attachments. By contrast, in UXB patients the ε_e distribution was non-symmetric, which could lead to an asymmetrical development of the mandible, according to the mechanostat theory (Frost, 1987, 1983). Besides, in all UXB's cases, it was also found that effective minimum strain in the molar and posterior regions of the mandibular half of the XS deformed is greater 0.002. This finding could provide an analytical proof of the periosteal matrix's' role in the craniofacial development and could supply an analytical evidence of a possible bone apposition in these regions, in agreement with previous clinical observations (Ramirez-Yanez et al., 2011; Veli et al., 2011).

On the other hand, according to the FMH, the capsular matrix (Moss and Salentijn, 1969) is responsible for the spatial transformations in the craniofacial regions, such as the more retracted and elevated position of the maxilla or zygomatic regions in the XS (Moss, 2007). These spatial micro displacements, however, are difficult to measure experimentally because of their small size. Fortunately, computational approach, as the followed here, allowed us to identify the relative movements of these parts (Kumar et al., 2016; Lee and Baek, 2012) through the nodes' displacements (shown in Figures 5 and 6). Therefore, it was found that the upper maxilla moved almost symmetrically along labial direction (shown in Figure 5.A) when the occlusion of non-UXB subjects was simulated. This movement could be interpreted according to its functional matrix as normal opening movement of it to the sagittal midplane (Enlow, 1990). In UXB patients, however, this movement was only followed by the NXS, whereas the counterpart moved towards the buccal direction (shown in Figure 5.A). In this case, the maxilla displacement could indicate just an inverse growth pattern, i.e. a narrowed development, as it was already noted in some clinical studies (Kecik et al., 2007; Melink et al., 2010). Likewise, this result was consistent with the displacement patterns and with the narrowing of its transverse dimension reported in our 3D morphological analysis (shown in Figure 7).

Regarding the anterior-posterior displacements of the maxilla (shown in Figure 5.B), it was found that non-UXB patients experienced a slight forward movement of the whole maxilla, while UXB patients experienced only the forward movement on the NXS. Indeed, in subjects S9 and S10, there was even a backward movement of the half maxilla of XS, which could represent the maxilla rotation around the sagittal axis, as had been previously reported (Kecik et al., 2007).

As a consequence of the reaction of upper teeth, the occlusion causes the upward movement of the maxilla and consequently of the adjacent zygomatic region (shown in Figure 6). In non-UXB patients, this upward movement was practically symmetrical throughout the whole maxilla (see red regions in Figure 6). Nevertheless, in those patients with UXB, the unilateral occlusion caused just this effect in the XS (shown in Figure 6). This result is in agreement with recent clinical findings (Brin et al., 1996), which have found a significant elevation of the zygomatic region of the XS in patients with UXB. This finding was also consistent with the results of our 3D morphological analysis (see Figure 7), which displayed a clear asymmetry in the maxillary-zygomatic regions possibly caused by the upward movement of these regions at the unilateral occlusion. In some cases, such as S6 and S7 ones, the spatial asymmetry was even extended to the temporal region of the skull, which could additionally be influenced by the functional asymmetry of the chewing muscles. From our results, therefore, it is possible to establish a relationship between the craniofacial structures' movements with their spatial positioning, in agreement with their capsule matrixes.

This computational approach is, therefore, an important step in the study of FMH by computational models since it allows relating the mechanical stimulation of unilateral occlusion with the craniofacial development in children with UXB. Furthermore, up to now, this study presents the widest sample of craniofacial complex's FE models of children to study the FMH. It is also remarkable that the mechanical properties, muscular forces and modelling techniques here summarized could be a good reference for future engineers, researchers and clinical experts in the modelling of the pediatric craniofacial complex.

4.1. Study limitations

This study presents, however, several limitations that must be considered for the interpretation of the results and that future studies should address. Firstly, the sample size used was smaller than those used in other computational studies which studied, for instance, the femur's development (Gong et al., 2012; Klein et al., 2015). In our work, the sample size

was conditioned by the difficulties of obtaining CBCT images in pediatric patient, such as the radiation exposure, the scanning time or the natural nervousness of children. Despite the challenge of doing CBCT scans, our findings have demonstrated their potential in the assessment of the UXB, encouraging to further researchers to perform larger databases that improve the understanding of the effect of UXB on the craniofacial development. Moreover, despite the normalization of all models' size, the sample was not homogeneous and involved individuals of different ages (6-12 years old) and both sexes, which may have led to mixed results. Regarding the modelling procedure, the use of intraoral scanners and magnetic resonance imaging (MRI) images could improve respectively the geometrical definition of the occlusal plane and the soft tissues. However, it is important also to consider the challenge of performing these procedures in children without sedation. Likewise, a not superficial electromyography (EMG) study of the muscle activation in each patient would allow a more precise definition of the muscular activity, which is particularly important for defining the functional asymmetry in patients with UXB. Notwithstanding this, non-superficial EMGs are misadvised for the study of muscular activations in childhood because of the potential risks and implications for the child. Moreover, avoiding the challenge of treating children, other experimental tests such as in vivo occlusal analysis would yield more reliable occlusion patterns than those obtained using 3D printed pieces. The occlusal analyses could also be improved quantifying the specific reaction on each tooth, which could contribute to validate the computational models more precisely. Finally, our results suggested some possible morphological alterations based on the mechanical reactions in some tissues, but without applying any bone remodeling algorithm. We consider that current bone remodeling algorithms (Reina et al., 2007; Sarrafpour et al., 2013) should be carefully applied to the craniofacial complex since its development is conditioned by several interrelated factors such as the teeth eruption, the hormonal growth, the diet's consistency, breathing habits, amongst others. Notwithstanding all these limitations, this study is a first step in the understanding of the occlusion's effect on children's craniofacial development following the FMH principles. Future studies should address genetic and hormonal factors, or other functions effects on craniofacial development to describe then bone remodeling algorithms that integrate all these aspects.

5. Conclusion

This study computationally relates the biomechanical outcomes caused by unilateral occlusion with the morphological variations detected in pediatric patients with UXB according to the FMH's principles, leading the following conclusions:

- FE analysis is an effective tool for the biomechanical evaluation of unilateral crossbite, mimicking faithfully the occlusal patterns with a mean error below 6 %.
- Patients with unilateral crossbite showed a functional imbalance of up to 42% at both occlusal and periodontal levels.
- The interstitial fluid overpressure (> 4.7 kPa) in the periodontium of the crossed side could be responsible for the malocclusion worsening over time, based on the pressure-tension theory. It is crucial, therefore, to perform early treatments that compensate for the mechanical stimulation of the periodontium in both hemiarches.
- Mandibular over deformation (>2000 $\mu\varepsilon$) could explain the thickening of the molar region in the crossed side's mandibular body.
- Periodontal overpressure and mandibular over deformation are great predictors of asymmetric mandibular development in pediatric patients with unilateral crossbite, being consistent with the periosteal matrix principles of the FMH.
- Maxilla and zygomatic region movements reproduce the misplacement of these structures in patients with unilateral crossbite, in agreement with their capsular matrices.
- FE analysis is an effective tool for evaluating the effect of periosteal and capsular matrices on the craniofacial development, supporting the FMH's principles.

Conflict of interests

The authors declare that the research was conducted in the absence of any commercial or financial relationships that could be construed as a potential conflict of interest.

Author Contributions

Javier Ortún-Terrazas: Data curation; Investigation; Methodology; Formal analysis; Software; Visualization; Writing - Original Draft.

Michael J. Fagan: Methodology; Formal analysis; Supervisor; Writing - Original Draft.

José Cegoñino: Project administration; Resources; Validation; Software; Visualization; Writing - Review & Editing.

Edson Illipronti-Filho: Data curation; Investigation; Resources; Visualization.

Amaya Perez del Palomar: Conceptualization; Validation; Funding acquisition; Project administration; Supervisor; Writing - Review & Editing.

Funding

This work was supported by the Spanish Ministry of Economy and Competitiveness (project DPI 2016-79302-R), the European Social Funds and Regional Government of Aragon (grant 2016/20) and Ibercaja-Cai Foundation (grant IT 4/18).

Acknowledgements

The authors would like to thank Dr. Ángel Sampietro Fuentes for his assistance in this research

References

Agostino, P., Ugolini, A., Signori, A., Silvestrini-Biavati, A., Harrison, J.E., Riley, P., 2014. Orthodontic treatment for posterior crossbites. Cochrane Database Syst. Rev.

Argoubi, M., Shirazi-Adl, A., 1996. Poroelastic creep response analysis of a lumbar motion segment in compression. J. Biomech. 29, 1331–1339. https://doi.org/10.1016/0021-9290(96)00035-8

Benazzi, S., Nguyen, H.N., Kullmer, O., Kupczik, K., 2016. Dynamic modelling of tooth deformation using occlusal kinematics and finite element analysis. PLoS One 11, 1–17. https://doi.org/10.1371/journal.pone.0152663

Bergomi, M., Cugnoni, J., Galli, M., Botsis, J., Belser, U.C., Wiskott, H.W.A., 2011. Hydro-mechanical coupling in the periodontal ligament: A porohyperelastic finite element model. J. Biomech. 44, 34–38. https://doi.org/10.1016/j.jbiomech.2010.08.019

Björk, A., Krebs, A.A., Solow, B., 1964. A Method for Epidemiological Registration of Malocculusion. Acta Odontol. Scand. 22, 27–41.

Brin, I., Ben-Bassat, Y., Blustein, Y., Ehrlich, J., Hochman, N., Marmary, Y., Yaffe, A., 1996. Skeletal and functional effects of treatment for unilateral posterior crossbite. Am. J. Orthod. Dentofac. Orthop. 109, 173–179. https://doi.org/10.1016/S0889-5406(96)70178-6

Castaldo, G., Cerritelli, F., 2015. Craniofacial growth: evolving paradigms. CRANIO® 33, 23–31. https://doi.org/10.1179/0886963414Z.00000000042

Cattaneo, P.M., Kofod, T., Dalstra, M., Melsen, B., 2005. Using the finite element method to model the biomechanics of the asymmetric mandible before, during and after skeletal correction by distraction osteogenesis. Comput. Methods Biomech. Biomed. Engin. 8, 157–65. https://doi.org/10.1080/10255840512331388731

Chen, J., Li, W., Swain, M. V., Ali Darendeliler, M., Li, Q., Darendeliler, M.A., Li, Q., 2014. A periodontal ligament driven remodeling algorithm for orthodontic tooth movement. J. Biomech. 47, 1689–1695. https://doi.org/10.1016/j.jbiomech.2014.02.030

Defraia, E., Marinelli, A., Baroni, G., Tollaro, I., 2007. Dentoskeletal effects of a removable appliance for expansion of the maxillary arch: a postero-anterior cephalometric study. Eur. J. Orthod. 30, 57–60.

DeVocht, J.W., Goel, V.K., Zeitler, D.L., Lew, D., 1996. A study of the control of disc movement within the temporomandibular joint using the finite element technique. J. Oral Maxillofac. Surg. 54, 1431–1437. https://doi.org/10.1016/S0278-2391(96)90259-1

Donzelli, P.S., Gallo, L.M., Spilker, R.L., Palla, S., 2004. Biphasic finite element simulation of the TMJ disc from in vivo kinematic and geometric measurements. J. Biomech. 37, 1787–91. https://doi.org/10.1016/j.jbiomech.2004.01.029

Dorow, C., Sander, F.-G., 2005. Development of a Model for the Simulation of Orthodontic Load on Lower First Premolars Using the Finite Element Method. J. Orofac. Orthop. / Fortschritte der Kieferorthopädie 66, 208–218. https://doi.org/10.1007/s00056-005-0416-5

Enlow, D.H., 1990. Facial growth. WB Saunders Company.

Field, C., Li, Q., Li, W., Swain, M., 2010. Biomechanical Response in Mandibular Bone due to Mastication Loading on 3-Unit Fixed Partial Dentures. J. Dent. Biomech. 1. https://doi.org/10.4061/2010/902537

Frongia, G., Ramieri, G., De Biase, C., Bracco, P., Piancino, M.G., 2013. Changes in electric activity of masseter and anterior temporalis muscles before and after orthognathic surgery in skeletal class III patients. Oral Surg. Oral Med. Oral Pathol. Oral Radiol. 116, 398–401. https://doi.org/10.1016/j.oooo.2013.06.008

Frost, H.M., 2004. A 2003 update of bone physiology and Wolff's Law for clinicians. Angle Orthod. 74, 3–15. https://doi.org/10.1043/0003-3219(2004)074<0003:AUOBPA>2.0.CO;2

Frost, H.M., 1987. Bone "mass" and the "mechanostat": A proposal. Anat. Rec. 219, 1–9. https://doi.org/10.1002/ar.1092190104

Frost, H.M., 1983. A determinant of bone architecture. The minimum effective strain. Clin. Orthop. Relat. Res. 286–92.

Gazit-Rappaport, T., Weinreb, M., Gazit, E., 2003. Quantitative evaluation of lip symmetry in functional asymmetry. Eur. J. Orthod. 25, 443–450.

Gong, H., Zhang, M., Fan, Y., Kwok, W.L., Leung, P.C., 2012. Relationships Between Femoral Strength Evaluated by Nonlinear Finite Element Analysis and BMD, Material Distribution and Geometric Morphology. Ann. Biomed. Eng. 40, 1575–1585. https://doi.org/10.1007/s10439-012-0514-7

Hansson, T., Nordström, B., 1977. Thickness of the soft tissue layers and articular disk in temporomandibular joints with deviations in form. Acta Odontol. Scand. 35, 281–288. https://doi.org/10.3109/00016357709064126

Hodge, L.C., Mahan, P.E., 1967. A study of mandibular movement from centric occlusion to maximum intercuspation. J. Prosthet. Dent. 18, 19–30. https://doi.org/10.1016/0022-3913(67)90107-2

Hohmann, A., Wolfram, U., Geiger, M., Boryor, A., Kober, C., Sander, C., Sander, F.G., 2009. Correspondences of hydrostatic pressure in periodontal ligament with regions of root resorption: A clinical and a finite element study of the same human teeth. Comput. Methods Programs Biomed. 93, 155–161. https://doi.org/10.1016/j.cmpb.2008.09.004

Hohmann, A., Wolfram, U., Geiger, M., Boryor, A., Sander, C., Faltin, R., Faltin, K., Sander, F.G., 2007. Periodontal Ligament Hydrostatic Pressure with Areas of Root Resorption after Application of a Continuous Torque Moment. Angle Orthod. 77, 653–659. https://doi.org/10.2319/060806-234

Holzapfel, G., 2000. Nonlinear Solid Mechanics: A Continuum Approach for Engineering. Wiley, New York.

Ingawalé, S., Goswami, T., 2009. Temporomandibular Joint: Disorders, Treatments, and Biomechanics. Ann. Biomed. Eng. 37, 976–996. https://doi.org/10.1007/s10439-009-9659-4

Ishizaki, K., Suzuki, K., Mito, T., Tanaka, E.M., Sato, S., 2010. Morphologic, functional, and occlusal characterization of mandibular lateral displacement malocclusion. Am. J. Orthod. Dentofac. Orthop. 137, 454-e1.

Kecik, D., Kocadereli, I., Saatci, I., 2007. Evaluation of the treatment changes of functional posterior crossbite in the mixed dentition. Am. J. Orthod. Dentofac. Orthop. 131, 202–215.

Keilig, L., Drolshagen, M., Tran, K.L., Hasan, I., Reimann, S., Deschner, J., Brinkmann, K.T., Krause, R., Favino, M., Bourauel, C., 2016. In vivo measurements and numerical analysis of the biomechanical characteristics of the human periodontal ligament. Ann. Anat. -

Anat. Anzeiger 206, 80–88. https://doi.org/10.1016/j.aanat.2015.08.004

Kennedy, D.B., Osepchook, M., 2005. Unilateral posterior crossbite with mandibular shift: a review. Journal-Canadian Dent. Assoc. 71, 569.

Kim, J.-Y., Jung, H.-D., Jung, Y.-S., Hwang, C.-J., Park, H.-S., 2014. A simple classification of facial asymmetry by TML system. J. Craniomaxillofac. Surg. 42, 313–20. https://doi.org/10.1016/j.jcms.2013.05.019

Klein, K.F., Hu, J., Reed, M.P., Hoff, C.N., Rupp, J.D., 2015. Development and Validation of Statistical Models of Femur Geometry for Use with Parametric Finite Element Models. Ann. Biomed. Eng. 43, 2503–2514. https://doi.org/10.1007/s10439-015-1307-6

Kofod, T., Cattaneo, P.M., Dalstra, M., Melsen, B., 2005. Three-Dimensional Finite Element Analysis of the Mandible and Temporomandibular Joint During Vertical Ramus Elongation by Distraction Osteogenesis. J. Craniofac. Surg. 16, 586–593. https://doi.org/10.1097/01.SCS.0000157305.60505.B5

Koolstra, J.H.H., van Eijden, T.M.G.J.M.G.J., 2005. Combined finite-element and rigid-body analysis of human jaw joint dynamics. J. Biomech. 38, 2431–2439. https://doi.org/10.1016/j.jbiomech.2004.10.014

Koos, B., Godt, A., Schille, C., Göz, G., 2010. Precision of an Instrumentation-based Method of Analyzing Occlusion and its Resulting Distribution of Forces in the Dental Arch. J. Orofac. Orthop. / Fortschritte der Kieferorthopädie 71, 403–410. https://doi.org/10.1007/s00056-010-1023-7

Kumar, A., Ghafoor, H., Khanam, A., 2016. A comparison of three-dimensional stress distribution and displacement of naso-maxillary complex on application of forces using quad-helix and nickel titanium palatal expander 2 (NPE2): a FEM study. Prog. Orthod. 17, 17. https://doi.org/10.1186/s40510-016-0131-3

Lacroix, D., Prendergast, P.J., 2002. A mechano-regulation model for tissue differentiation during fracture healing: analysis of gap size and loading. J. Biomech. 35, 1163–1171. https://doi.org/10.1016/S0021-9290(02)00086-6

Langberg, B.J., Arai, K., Miner, R.M., 2005. Transverse skeletal and dental asymmetry in adults with unilateral lingual posterior crossbite. Am. J. Orthod. Dentofac. Orthop. 127, 6–15. https://doi.org/10.1016/j.ajodo.2003.10.044

Lee, N.-K., Baek, S.-H., 2012. Stress and displacement between maxillary protraction with miniplates placed at the infrazygomatic crest and the lateral nasal wall: A 3-dimensional finite element analysis. Am. J. Orthod. Dentofac. Orthop. 141, 345–351. https://doi.org/10.1016/j.ajodo.2011.07.021

Libby, J., Marghoub, A., Johnson, D., Khonsari, R.H., Fagan, M.J., Moazen, M., 2017. Modelling human skull growth: a validated computational model. J. R. Soc. Interface 14, 20170202. https://doi.org/10.1098/rsif.2017.0202

Malandris, M., Mahoney, E.K., 2004. Aetiology, diagnosis and treatment of posterior cross-bites in the primary dentition. Int. J. Paediatr. Dent. 14, 155–166.

Marghoub, A., Libby, J., Babbs, C., Pauws, E., Fagan, M.J., Moazen, M., 2017. Predicting calvarial growth in normal and craniosynostotic mice using a computational approach. J. Anat. 10, 440–448. https://doi.org/10.1111/joa.12764

Martinez-Gomis, J., Lujan-Climent, M., Palau, S., Bizar, J., Salsench, J., Peraire, M., 2009. Relationship between chewing side preference and handedness and lateral asymmetry of peripheral factors. Arch. Oral Biol. 54, 101–107. https://doi.org/10.1016/j.archoralbio.2008.09.006

Melink, S., Vagner, M.V., Hocevar-Boltezar, I., Ovsenik, M., 2010. Posterior crossbite in the deciduous dentition period, its relation with sucking habits, irregular orofacial functions, and otolaryngological findings. Am. J. Orthod. Dentofac. Orthop. 138, 32–40. https://doi.org/10.1016/j.ajodo.2008.09.029

Moss, M.L., 2007. The differential roles of periosteal and capsular functional matrices in orofacial growth. Eur. J. Orthod. 29, i96–i101. https://doi.org/10.1093/ejo/cjl097

Moss, M.L., 1970. The role of muscular functional matrices in development and maintenance of occlusion. Bull. Pac. Coast Soc. Orthod. 45, 29–30.

Moss, M.L., Rankow, R.M., 1968. The role of the functional matrix in mandibular growth. Angle Orthod. 38, 95–103.

Moss, M.L., Salentijn, L., 1969. The capsular matrix. Am. J. Orthod. 56, 474–490. https://doi.org/10.1016/0002-9416(69)90209-7

Nissan, J., Gross, M.D., Shifman, A., Tzadok, L., Assif, D., 2004. Chewing side preference as a type of hemispheric laterality. J. Oral Rehabil. 31, 412–416. https://doi.org/10.1111/j.1365-2842.2004.01256.x

O'Higgins, P., Fitton, L.C., Phillips, R., Shi, J., Liu, J., Gröning, F., Cobb, S.N., Fagan, M.J., 2012. Virtual Functional Morphology: Novel Approaches to the Study of Craniofacial Form and Function. Evol. Biol. 39, 521–535. https://doi.org/10.1007/s11692-012-9173-8

Ortún-Terrazas, J., Cegoñino, J., Pérez del Palomar, A., 2020a. In silico study of cuspid' periodontal ligament damage under parafunctional and traumatic conditions of whole-mouth occlusions. A patient-specific evaluation. Comput. Methods Programs Biomed. 184, 105107. https://doi.org/10.1016/j.cmpb.2019.105107

Ortún-Terrazas, J., Cegoñino, J., Santana-Penín, U., Santana-Mora, U., Pérez del Palomar, A., 2018. Approach towards the porous fibrous structure of the periodontal ligament using micro-computerized tomography and finite element analysis. J. Mech. Behav. Biomed. Mater. 79, 135–149. https://doi.org/10.1016/j.jmbbm.2017.12.022

Ortún-Terrazas, J., Cegoñino, J., Santana-Penín, U., Santana-Mora, U., Pérez del Palomar, A., 2017. Computational analysis of craniomandibular tissues for the correction of mandibular asymmetries in childhood. 23rd Congr. Eur. Soc. Biomech. https://doi.org/10.5281/zenodo.3775321

Ortún-Terrazas, J., Fagan, M.J., Cegoñino, J., Illipronti-Filho, E., Pérez del Palomar, A., 2020b. Towards an early 3D-diagnosis of craniofacial asymmetry by computing the accurate midplane: A PCA-based method. Comput. Methods Programs Biomed. 191, 105397. https://doi.org/10.1016/j.cmpb.2020.105397

Paphangkorakit, J., Thothongkam, N., Supanont, N., 2006. Chewing-side determination of three food textures. J. Oral Rehabil. 33, 2–7. https://doi.org/10.1111/j.1365-2842.2006.01535.x

Petrén, S., Bondemark, L., Söderfeldt, B., 2003. A systematic review concerning early orthodontic treatment of unilateral posterior crossbite. Angle Orthod. 73, 588–596.

Piancino, M.G., Kyrkanides, S., 2016. Understanding Masticatory Function in Unilateral Crossbites, Understanding Masticatory Function in Unilateral Crossbites. John Wiley & Sons, Inc., Oxford, UK. https://doi.org/10.1002/9781118971901

Pinheiro, M., Ma, X., Fagan, M.J., McIntyre, G.T., Lin, P., Sivamurthy, G., Mossey, P.A., 2019. A 3D cephalometric protocol for the accurate quantification of the craniofacial symmetry and facial growth. J. Biol. Eng. 13, 42. https://doi.org/10.1186/s13036-019-0171-6

Planas, P., 2013. Neuro-occlusal rehabilitation: NOR, 2nd ed. Amolca, Barcelona, España.

Primožič, J., Ovsenik, M., Richmond, S., Kau, C.H., Zhurov, A., 2009. Early crossbite correction: a three-dimensional evaluation. Eur. J. Orthod. 31, 352–356.

Pullinger, A.G.A.A.G., Baldioceda, F., Bibb, C.A.C.A., 1990. Relationship of TMJ Articular Soft Tissue to Underlying Bone in Young Adult Condyles. J. Dent. Res. 69, 1512–1518.

https://doi.org/10.1177/00220345900690081301

Ramirez-Yanez, G.O., Stewart, A., Franken, E., Campos, K., 2011. Prevalence of mandibular asymmetries in growing patients. Eur. J. Orthod. 33, 236–242. https://doi.org/10.1093/ejo/cjq057

Ranly, D.M., 2000. Craniofacial growth. Dent. Clin. North Am. 44, 457–70, v.

Reina, J.M., García-Aznar, J.M., Domínguez, J., Doblaré, M., 2007. Numerical estimation of bone density and elastic constants distribution in a human mandible. J. Biomech. 40, 828–836. https://doi.org/10.1016/j.jbiomech.2006.03.007

Ruggiero, L., Zimmerman, B.K., Park, M., Han, L., Wang, L., Burris, D.L., Lu, X.L., 2015. Roles of the Fibrous Superficial Zone in the Mechanical Behavior of TMJ Condylar Cartilage. Ann. Biomed. Eng. 43, 2652–2662. https://doi.org/10.1007/s10439-015-1320-9

Sarrafpour, B., Swain, M., Li, Q., Zoellner, H., 2013. Tooth Eruption Results from Bone Remodelling Driven by Bite Forces Sensed by Soft Tissue Dental Follicles: A Finite Element Analysis. PLoS One 8, e58803. https://doi.org/10.1371/journal.pone.0058803

Schwarz, A.M., 1932. Tissue changes incidental to orthodontic tooth movement. Int. J. Orthod. Oral Surg. Radiogr. 18, 331–352. https://doi.org/10.1016/S0099-6963(32)80074-8

Sepahdari, A.R., Mong, S., 2013. Skull base CT: normative values for size and symmetry of the facial nerve canal, foramen ovale, pterygoid canal, and foramen rotundum. Surg. Radiol. Anat. 35, 19–24. https://doi.org/10.1007/s00276-012-1001-4

Singh, M., Detamore, M.S., 2008. Tensile properties of the mandibular condylar cartilage. J. Biomech. Eng. 130, 011009. https://doi.org/10.1115/1.2838062

Storakers, B., 1986. On material representation and constitutive branching in finite compressible elasticity. J. Mech. Phys. Solids 34, 125–145. https://doi.org/10.1016/0022-5096(86)90033-5

Tanaka, E., Kawai, N., Tanaka, M., Todoh, M., van Eijden, T., Hanaoka, K., Dalla-Bona, D.A., Takata, T., Tanne, K., 2004. The Frictional Coefficient of the Temporomandibular Joint and Its Dependency on the Magnitude and Duration of Joint Loading. J. Dent. Res. 83, 404–407. https://doi.org/10.1177/154405910408300510

Testa, M., Geri, T., Gizzi, L., Falla, D., 2017. High-density EMG Reveals Novel Evidence of Altered Masseter Muscle Activity During Symmetrical and Asymmetrical Bilateral Jaw Clenching Tasks in People With Chronic Nonspecific Neck Pain. Clin. J. Pain 33, 148–159. https://doi.org/10.1097/AJP.0000000000000381

Thilander, B., Lennartsson, B., 2002. A Study of Children with Unilateral Posterior Crossbite, Treated and Untreated, in the Deciduous Dentition. J. Orofac. Orthop. / Fortschritte der Kieferorthopädie 63, 371–383. https://doi.org/10.1007/s00056-002-0210-6

Thilandera, B., 2000. Orthodontic relapse versus natural development. Am. J. Orthod. Dentofac. Orthop. 117, 562–563. https://doi.org/10.1016/S0889-5406(00)70200-9

Veli, I., Uysal, T., Ozer, T., Ucar, F.I., Eruz, M., 2011. Mandibular asymmetry in unilateral and bilateral posterior crossbite patients using cone-beam computed tomography. Angle Orthod. 81, 966–974. https://doi.org/10.2319/022011-122.1

Wang, Y., He, S., Yu, L., Li, J., Chen, S., 2011. Accuracy of volumetric measurement of teeth in vivo based on cone beam computer tomography. Orthod. Craniofac. Res. 14, 206–212. https://doi.org/10.1111/j.1601-6343.2011.01525.x

Xu, B., Wang, Y., Li, Q., 2015. Modeling of damage driven fracture failure of fiber post-restored teeth. J. Mech. Behav. Biomed. Mater. 49, 277–289. https://doi.org/10.1016/j.jmbbm.2015.05.006

Zheng, J., Zhou, Z.R., Zhang, J., Li, H., Yu, H.Y., 2003. On the friction and wear behaviour of human tooth enamel and dentin. Wear 255, 967–974. https://doi.org/10.1016/S0043-1648(03)00079-6

Supplementary Material

Muscular forces

The active behavior of a muscle, i, was modelled as a function of the maximum force in isometric contraction, $F^i_{\max}$ and the activation level, a, as follows (Pérez del Palomar and Doblaré, 2008; Commisso et al., 2015):

$$F^i_a = a^i \cdot F^i_{max} \quad (1)$$

The stress-strain passive behavior in an instant of time, t, was defined according to the muscle strain, ε^i by the following non-linear expression (Pérez del Palomar and Doblaré, 2008):

$$F^i_p(t) = \frac{K \cdot \varepsilon^i(t)}{[1-\varepsilon^i(t)/a]} \cdot PCSA^i, \text{ where } \varepsilon^i = \frac{l^i_t(t) - l^i_f}{l^i_f}, \quad (2)$$

$$\text{being } l^i_f = l^i_0 \cdot \frac{S^i_f}{S_r}$$

where K is the estimated force-length stiffness of the muscles ($K = 40\ N/cm^2$) (Peck et al., 2000), a is the passive force-length asymptote ($a = 0.7$) (Horst, 2002), $PCSA^i$ is the muscle's cross-sectional area, l^i_t and l^i_f are respectively the muscle's lengths at t instant and at the free state, and l^i_0 is the length of the muscle at the optimum state computed by the sarcomeres lengths in a free and relaxed state, S^i_f and S_r (2.73 μm according to Van Ruijven and Weijs, 1990), respectively.

The dynamic damping behavior of the muscle was defined as a function of the critical damping coefficient (C) and the stretch velocity ($\dot{\varepsilon} = d\varepsilon/dt$), as follows:

$$F^i_d(t) = C^i \cdot \dot{\varepsilon}^i(t) \quad (3)$$

Due to limited data available on pediatric subjects, some values had to be estimated from the reference values of an adult. Thus, F^i_{max} values were computed by multiplying the F^i_{max} values of an adult by a 0.657 coefficient, which was calculated as the ratio of the maximum bite force of a child (347 N) to that of an adult (528 N) (Palinkas et al., 2010). On the other hand, a^i values were defined by the normalized electromyographic values (EMG) of children of the same age range (Cecílio et al., 2010), being 1 for elevator and 0 for depressor muscles of the control group. In the UXB group, however, different a^i value was considered for the elevator muscles of both halves. Hence, to account an asymmetry index of -20% (Frongia et al., 2013), we use 0.8 and 1.2 values for NXS and XS elevator muscles, respectively. Likewise, $PCSA^i$ values were obtained by multiplying the $PCSA^i$ of an adult by 0.689 coefficient which was defined as the ratio between the mean $PCSA^{SM}$ of the superficial masseter in a group of children (Chan et al., 2008) and adults (Peck et al., 2000). Moreover, to consider the asymmetry of the muscles' shape in patients with UXB, $PCSA^i$ values of NXS y XS were multiplied respectively by 0.95 and 1.05, accounting for a -5% (Martín et al., 2012) asymmetry index. The reference values of the adult and those computed for our models are summarized in Supplementary Table 1.

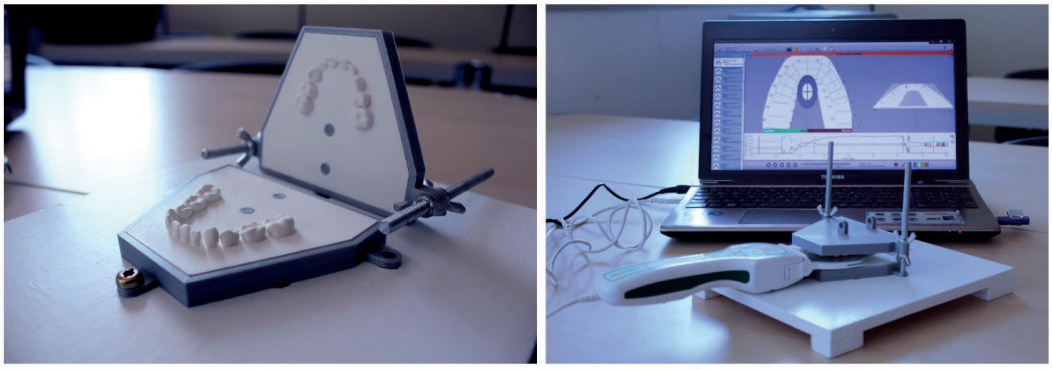

A B

Supplementary Figure 2 A) Dental arches assembly and their respective external holders; B) Experimental record of the occlusal contacts through the T-Scan III system at maximum intercuspation position.

Supplementary Table 1. Parameters used to compute F_a^i, F_p^i, and F_d^i for the right and left superficial masseters (SM); deep masseters (DM); anterior temporals (AT); middle temporals (MT); posterior temporals (PT); medial pterygoids (MP); inferior lateral pterygoids (IP); superior lateral pterygoids (SP); anterior mylohyoids (AM); posterior mylohyoids (PM); anterior digastrics (AD) and geniohyoids (GH) muscles.

	Adult		Control group				UXB group					
Ref.	F_{max}^i (N)[(a)]	$PCSA^i$ (cm^2)	F_a^i (N)		$PCSA^i$ (cm^2)		F_a^i (N)		$PCSA^i$ (cm^2)		S_f^i (μm)[(c)]	C^i (N/mm)[(b)]
			R	L	R	L	NXS	XS	NXS	XS		
SM	190.4	4.76[(b)]	125.1	125.1	3.28	3.28	100.08	150.12	3.12	3.44	2.47	0.053
DM	81.6	2.04[(b)]	53.6	53.6	1.41	1.41	42.88	64.32	1.34	1.48	2.44	0.038
AT	158	3.95[(b)]	103.8	103.8	2.72	2.72	83.04	124.56	2.58	2.86	2.35	0.035
MT	95.6	2.39[(b)]	62.8	62.8	1.65	1.65	50.24	75.36	1.57	1.73		0.029
PT	75.6	1.89[(b)]	49.7	49.7	1.30	1.30	39.76	59.64	1.24	1.37	2.31	0.023
MP	174.8	4.37[(b)]	114.8	114.8	3.01	3.01	91.84	137.76	2.86	3.16	2.48	0.060
IP	50	1.67[(b)]	-	-	1.15	1.15	-	-	1.09	1.21	2.83	0.021
SP	17	0.95[(c)]	-	-	0.65	0.65	-	-	0.62	0.68	2.72	0.019
AM	20	2.12[(c)]	-	-	1.46	1.46	-	-	1.39	1.53	2.80	
PM	20		-	-			-	-			3.89	
AD	50	1.16[(c)]	-	-	0.80	0.80	-	-	0.76	0.84	2.75	
GH	20	0.97[(c)]	-	-	0.67	0.67	-	-	0.64	0.70	2.65	

a) Hannam, Alan G., et al., 2008 (Hannam et al., 2008).
b) Langenbach, G. E. J., et al.,1999 (Langenbach and Hannam, 1999).
c) Van Eijden, T. M. G. J., et al., 1997 (Van Eijden et al., 1997).

Supplementary Table 2. Occlusal pressure percentages and asymmetry index (AI) computed from the outcomes of the T-Scan III system and FE simulations in both dental hemiarch of each subject, and the mean ± SD values in both groups. On the right, percent error of each case.

Control group

	T-Scan occlusal analysis			Computational analysis			Percent error (%)	
Subject	Right (%)	Left (%)	AI	Right (%)	Left (%)	AI	Right	Left
S1	53.3	46.7	6.6	54.1	45.9	8.2	1.5	1.7
S2	44.3	55.7	-11.4	45.4	54.6	-9.2	2.5	2.0
S3	48.8	51.2	-2.4	49.0	51.0	-2.0	0.4	0.4
S4	43.4	56.6	-13.2	46.2	53.8	-7.6	6.5	4.9
S5	44.3	55.7	-11.4	41.6	58.4	-16.8	6.1	4.8
Mean (±SD)	46.8 ± 3.7	º53.2 ± 3.7		47.3 ± 4.2	52.7 ± 4.2		3.4	2.8

UXB group

Subject	NXS (%)	XS (%)	AI	NXS (%)	XS (%)	AI	NXS	XS
S6	42.2	57.8	-15.6	42.9	57.1	-14.2	1.7	1.2
S7	39.5	60.5	-21.0	36.8	63.2	-26.4	6.8	4.5
S8	41.3	58.7	-17.4	43.8	56.2	-12.4	6.1	4.3
S9	38.0	62.0	-24.0	41.5	58.5	-17.0	9.2	5.6
S10	28.8	71.2	-42.4	30.2	69.8	-39.6	4.9	2.0
Mean (±SD)	38.0 ± 5.4	62.0 ± 5.4		39.0 ± 5.6	61.0 ± 5.6		5.7	3.5

References

Cecílio, F. A., Regalo, S. C. H. H., Palinkas, M., Issa, J. P. M. M., Siéssere, S., Hallak, J. E. C. C., et al. (2010). Ageing and surface EMG activity patterns of masticatory muscles. J. Oral Rehabil. 37, 248–255. doi:10.1111/j.1365-2842.2010.02051.x.

Chan, H. J., Woods, M., and Stella, D. (2008). Mandibular muscle morphology in children with different vertical facial patterns: A 3-dimensional computed tomography study. Am. J. Orthod. Dentofac. Orthop. 133, 1–13. doi:10.1016/j.ajodo.2007.05.013.

Commisso, M. S., Martínez-Reina, J., Ojeda, J., and Mayo, J. (2015). Finite element analysis of the human mastication cycle. J. Mech. Behav. Biomed. Mater. 41, 23–35. doi:10.1016/j.jmbbm.2014.09.022.

Frongia, G., Ramieri, G., De Biase, C., Bracco, P., and Piancino, M. G. (2013). Changes in electric activity of masseter and anterior temporalis muscles before and after orthognathic surgery in skeletal class III patients. Oral Surg. Oral Med. Oral Pathol. Oral Radiol. 116, 398–401. doi:10.1016/j.oooo.2013.06.008.

Hannam, A. G., Stavness, I., Lloyd, J. E., and Fels, S. (2008). A dynamic model of jaw and hyoid biomechanics during chewing. J. Biomech. 41, 1069–1076. doi:10.1016/j.jbiomech.2007.12.001.

Horst, van der M. J. (2002). Human Head Neck Response in Frontal , Lateral and Rear End Impact Loading - modelling and validation - . doi:10.6100/IR554047.

Langenbach, G. E. J., and Hannam, A. G. (1999). The role of passive muscle tensions in a three-dimensional dynamic model of the human jaw. Arch. Oral Biol. 44, 557–573. doi:10.1016/S0003-9969(99)00034-5.

Martín, C., Palma, J. C., Alamán, J. M., Lopez-Quiñones, J. M., and Alarcón, J. A. (2012). Longitudinal evaluation of sEMG of masticatory muscles and kinematics of mandible changes in children treated for unilateral cross-bite. J. Electromyogr. Kinesiol. 22, 620–628. doi:10.1016/j.jelekin.2012.01.002.

Palinkas, M., Nassar, M. S. P., Cecílio, F. A., Siéssere, S., Semprini, M., MacHado-De-Sousa, J. P., et al. (2010). Age and gender influence on maximal bite force and masticatory muscles thickness. Arch. Oral Biol. 55, 797–802. doi:10.1016/j.archoralbio.2010.06.016.

Peck, C. C., Langenbach, G. E. J., and Hannam, A. G. (2000). Dynamic simulation of muscle and articular properties during human wide jaw opening. Arch. Oral Biol. 45, 963–982. doi:10.1016/S0003-9969(00)00071-6.

Pérez del Palomar, A., and Doblaré, M. (2008). Dynamic 3D FE modelling of the human temporomandibular joint during whiplash. Med. Eng. Phys. 30, 700–709. doi:10.1016/j.medengphy.2007.07.009.

Van Eijden, T. M., Korfage, J. A., and Brugman, P. (1997). Architecture of the human jaw-closing and jaw-opening muscles. Anat. Rec. 248, 464–74. doi:10.1002/(sici)1097-0185(199707)248:3<464::aid-ar20>3.3.co;2-4.

Van Ruijven, L. J., and Weijs, W. A. (1990). A new model for calculating muscle forces from electromyograms. Eur. J. Appl. Physiol. Occup. Physiol. 61, 479–485. doi:10.1007/BF00236071.

Manuscript 8: In silico approach towards Neuro-Occlusal Rehabilitation for the early correction of asymmetrical development in a unilateral crossbite patient.

Javier Ortún-Terrazas, José Cegoñino, Amaya Pérez del Palomar

Abstract

Unilateral crossbite affects around 11.7% of children in deciduous dentition, potentially leading to an asymmetrical development of the stomatognathic system, which is hardly correctable in adulthood. To avoid surgical procedures later in life, Neuro-occlusal Rehabilitation (N.O.R.) aims to treat this malocclusion as soon as possible by minimum invasive treatments, such as the combination of composite resin occlusal guidance with selective grinding. Nevertheless, N.O.R.'s treatments are frequently questioned due to their outcomes and the system's development mechanisms are still uncertain. This study aims to evaluate computationally the effect of N.O.R.'s treatments for the early correction of unilateral crossbite, verifying its impact in the system's function and development. Therefore, bilateral chewing and maximum intercuspation occlusion were computationally modelled through a detailed finite element model of a paediatric craniofacial complex, before and after different selective grinding-alternatives. This model was subjected to the muscular forces derived from a musculoskeletal model and was validated by the occlusal contacts recorded experimentally on a piezoelectric film sensor. This approach yielded errors below 2% and reproduced successfully the occlusal, muscular, functional and mechanical imbalance before the therapies. Treatment strategies balanced the occlusal plane and reduced the periodontal overpressure (>4.7 kPa) and the mandibular over deformation (>0.002 $\mu\varepsilon$) on the crossed side. Based on the principles of the mechanostat theory of bone remodelling and the pressure-tension theory of tooth movement, these findings could demonstrate respectively how N.O.R.'s treatments correct the malocclusion and the asymmetrical development of the craniofacial complex. Besides, N.O.R.'s treatments slightly modified the stress state and functions of the temporomandibular joints, facilitating the chewing by the unaccustomed side and shifting the jaw to non-crossed side. These findings provide important biomechanical insights into the use of N.O.R.'s treatments for the correction of unilateral crossbites, but also encourage the application of computing methods in biomedical research and clinical practice.

Graphical abstract

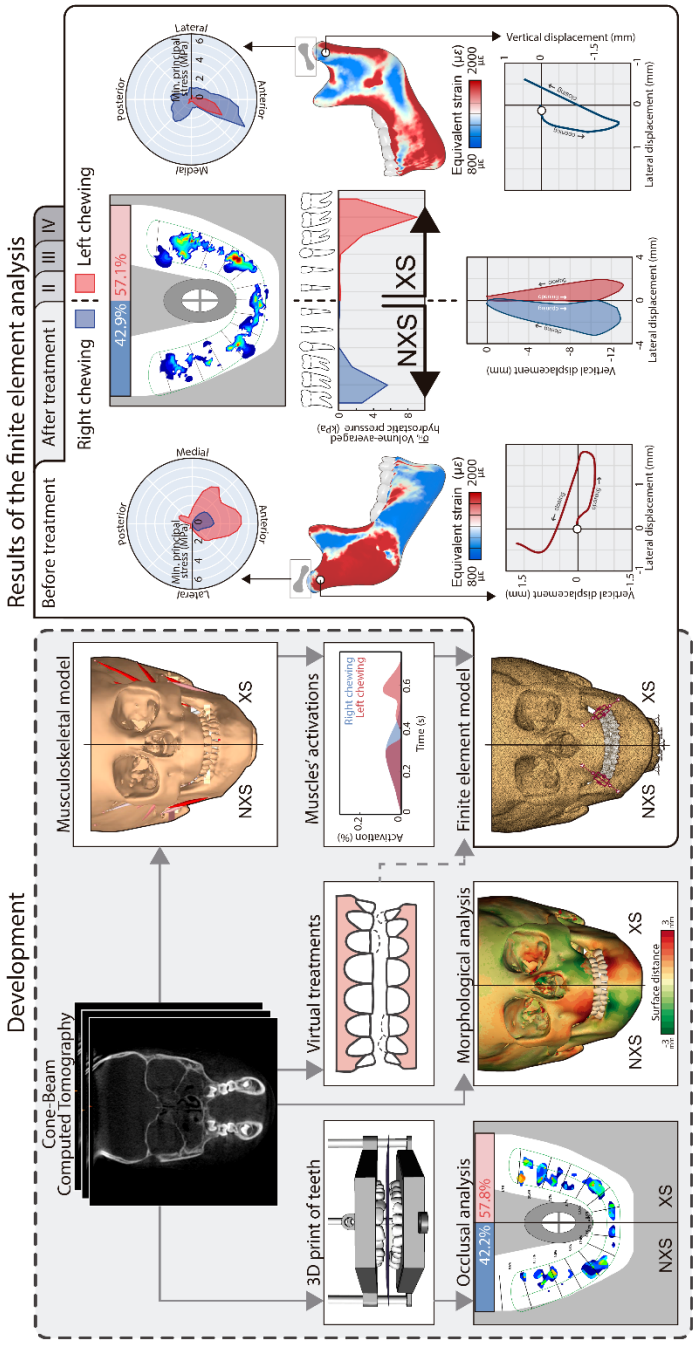

In silico approach towards Neuro-Occlusal Rehabilitation for the early correction of asymmetrical development in a unilateral crossbite patient.

Javier Ortún-Terrazas[a*], José Cegoñino[a], Amaya Pérez del Palomar[a]

[a] *Group of Biomaterials, Aragon Institute of Engineering Research (I3A), University of Zaragoza, Zaragoza, Spain*

Abstract

Unilateral crossbite affects around 11.7% of children in deciduous dentition, potentially leading to an asymmetrical development of the stomatognathic system, which is hardly correctable in adulthood. To avoid surgical procedures later in life, Neuro-occlusal Rehabilitation (N.O.R.) aims to treat this malocclusion as soon as possible by minimum invasive treatments, such as the combination of composite resin occlusal guidance with selective grinding. Nevertheless, N.O.R.'s treatments are frequently questioned due to their outcomes and the system's development mechanisms are still uncertain. This study aims to evaluate computationally the effect of N.O.R.'s treatments for the early correction of unilateral crossbite, verifying its impact in the system's function and development. Therefore, bilateral chewing and maximum intercuspation occlusion were computationally modelled through a detailed finite element model of a paediatric craniofacial complex, before and after different selective grinding-alternatives. This model was subjected to the muscular forces derived from a musculoskeletal model and was validated by the occlusal contacts recorded experimentally on a piezoelectric film sensor. This approach yielded errors below 2% and reproduced successfully the occlusal, muscular, functional and mechanical imbalance before the therapies. Treatment strategies balanced the occlusal plane and reduced the periodontal overpressure (>4.7 kPa) and the mandibular over deformation (>0.002 $\mu\varepsilon$) on the crossed side. Based on the principles of the mechanostat theory of bone remodelling and the pressure-tension theory of tooth movement, these findings could demonstrate respectively how N.O.R.'s treatments correct the malocclusion and the asymmetrical development of the craniofacial complex. Besides, N.O.R.'s treatments slightly modified the stress state and functions of the temporomandibular joints, facilitating the chewing by the unaccustomed side and shifting the jaw to non-crossed side. These findings provide important biomechanical insights into the use of N.O.R.'s treatments for the correction of unilateral crossbites, but also encourage the application of computing methods in biomedical research and clinical practice.

Keywords: Craniofacial development; finite element method; musculoskeletal model; selective grinding; unilateral crossbite

1. Introduction

The stomatognathic system is a morpho-functional system composed by a group of bony, muscular and neurological tissues (Nanci, 1990) whose development depends on several genetic and functional factors. The system's functional, sensorial and anatomical complexity has been difficult to understand the role of these factors in its development. Nevertheless, despite the uncertainness (Castaldo and Cerritelli, 2015), the functional matrix hypothesis (FMH) proposed by Prof. Melvin Moss in 1962 (Moss, 1970; Moss and Rankow, 1968) is generally accepted as a basis to explain how system's functions could influence to its development, i. e. the well-known function-shape relationship.

Based on the application of FMH principles in dentistry, in 1987, Dr Pedro Planas proposed the Neuro-occlusal Rehabilitation (N.O.R.) (Planas, 1987) in which an empirical relationship between functional malocclusions with bone malformations was suggested. According to N.O.R., out of breastfeeding period and genetic factors, the stomatognathic system's development is mainly conditioned by the mechanical stimulation produced at chewing. During chewing, the skeletal system moves bilaterally by the synergic activity of the depressor and elevator muscles (Piancino and Kyrkanides, 2016) to chew the food bolus. Henceforth, we will refer to the side with food bolus as "w*orking side*" and by the "*balancing side*" term to the opposite side (Palla et al., 2003). This alternative movement is mainly driven by the temporomandibular joints (TMJs) of both sides (Figure 1b-c) and the occlusal plane (Figure 1a) and is limited by the mechanical stimulus sensed by both neural receptors, in the TMJ's soft tissues and the periodontal ligaments (PDLs), amongst others (Piancino and Kyrkanides, 2016; Planas, 2013). From N.O.R. point of view, in conditions of well-balanced occlusion, the mechanical stimulation is alternatively sensed by the mechanoreceptors of both mandibular halves, leading to normal and symmetrical development of the system. Nevertheless, malocclusions can alter this symmetrical movement, creating a serious imbalance and gradually producing an abnormal and asymmetrical development, which will be hard to correct in adulthood.

*Corresponding author at: Aragon Institute of Engineering Research (I3A), School of Engineering and Architecture, University of Zaragoza, Calle María de Luna 3, 50018 Zaragoza, Spain.

E-mail address: javierortun@unizar.es (J. Ortún-Terrazas).

The basic rule of N.O.R. is, therefore, to treat these malocclusions as soon as possible, avoiding an irreversible and abnormal development of the system that will require complex and surgical treatment later in life.

Within all malocclusions, the posterior unilateral crossbite (UXB) is one of the most prevalent affecting between 7.1% to 23.3% of the general population (Kennedy and Osepchook, 2005; Keski-Nisula et al., 2003; Lippold et al., 2008; Peres et al., 2007) and around 11.7% of children in deciduous dentition (da Silva Filho et al., 2007). UXB is characterized by the lingual occlusion of the buccal cusps of the maxillary teeth with the buccal cusps of the corresponding mandibular teeth (Björk et al., 1964) in one of the two halves (Figure 1a). Henceforth, in UXB patients, we will refer to this side as the "crossed side" (XS), and to the opposite side as "non-crossed side" (NXS) (Figure 1a). Besides the evident alterations of the occlusion, UXB affects also to the neuromuscular coordination, skeletal development and TMJ functions (Alarcón et al., 2000; Piancino et al., 2016).In patients with UXB, for instance, the path of the lower interincisor point at chewing shows that the closing angle, which measures the bilateral movement and efficiency of chewing, is more pronounced in XS than in NXS (shown in Figure 1a). Likewise, the Planas' Masticatory Functional Angle (M.F.A.), which measures the trajectory performed by the mandible during bilateral excursions (Figure 1d-e), is often used to UXB evaluation. According to the law of minimum vertical dimension of N.O.R., the usual or functional chewing side in UXB patients is the one with lower M.F.A. (Neto et al., 2007; Planas, 2013)

To equalize both M.F.A.s and achieve a balanced occlusion, N.O.R. suggests the combination of composite resin occlusal guidance with the selective grinding (coronoplasty) of some occlusal cusps, preferably on the deciduous teeth. However, despite it is a low-invasive treatment, its application during childhood is frequently questioned due to the lack of scientific evidence about treatment's outcomes, the lack of knowledge about the system's development or the possibility of a spontaneous correction with growth (Chate, 2000; Leighton, 2007; William et al., 2007). Until now, these issues could not be analytically demonstrated since the traditional experimental techniques were unable to study the complex interactions during chewing in which bony structures, TMJ's, the occlusal planes, and the muscular and neurological systems work together to guide, slide, move, and limit the chewing movement. Consequently, for an integrated assessment of all these factors, it is required new approaches which can simulate the chewing movement in controlled conditions.

.

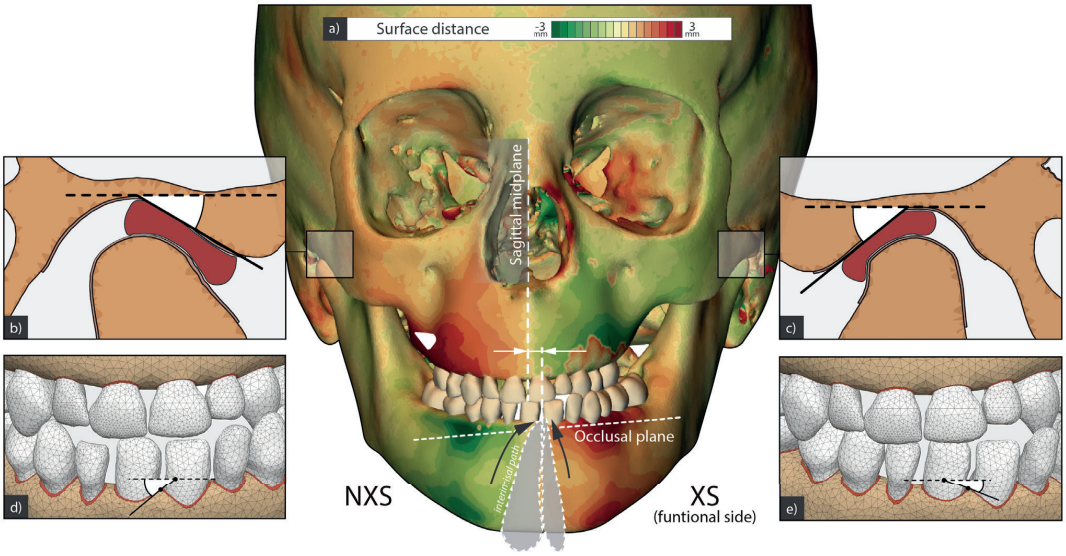

Figure 1 a) Craniofacial complex of the studied patient with left crossbite (the colour map displays the morphological differences between both halves of the craniofacial complex) (NXS: none-crossed side; XS: crossed side), TMJs of the b) non-crossed side and c) crossed side, M.F.A.s on the d) non-crossed side and e) on the crossed side.

In 1985, the FMH ideologue already insisted on the role of computational modelling for an integrated study of chewing function and craniofacial growth (Moss et al., 1985). Since then, many computational studies (Koolstra and van Eijden, 2005; Libby et al., 2017; Marghoub et al., 2017; O'Higgins et al., 2012) have tried to explain its development and some of them (Pileičikienė et al., 2010; Zhang et al., 2005) have even studied the selective grinding treatment in adulthood. From a computational point of view, the multibody dynamic (MBD) and the finite element (FE) analyses are the two leading computational approaches to study the system's function and development. MBD is mainly used (Hannam, 2003; Koolstra and van Eijden, 2005; Kupczik et al., 2007) for determining the muscles forces in a musculoskeletal model, knowing the relative motion, degrees of freedom, mass and inertia of its rigid bodies (O'Higgins et al., 2012). On the other hand, FE method has been used to compute the stress and strains of each part of the model (Geng et al., 2018) solving integral equations and partial differential equations that describe the physics of the craniofacial tissues (O'Higgins et al., 2012).

Nevertheless, despite the numerous computational studies performed, it has not yet been demonstrated how early treatments of UXB could correct the asymmetric development of the craniofacial system and avoid surgical procedures later in life. This lack of knowledge is partially caused by the limitations of the computational models in modelling, meshing, during the tissues' behaviour characterization, or at the definition of the boundary conditions (O'Higgins et al., 2012), among others. Fortunately, some recent advances in 3D cephalometric methods, modelling commercial software, tissues engineering, and computerized occlusal analysis systems have improved the computational models' development and therefore, the knowledge about the stomatognathic system growth.

Using all these advances, the computational approach here presented aims to evaluate the effect of N.O.R., and the selective grinding in particular, for the early correction of UXB, verifying its impact in the system's function and development. For this purpose, the maximum intercuspation occlusion and the bilateral chewing before and after four different treatments were evaluated through a computational model of a child with UXB. Model's geometry was reconstructed from Cone Beam Computed Tomography (CBCT) images of the patient before the treatment. This 3D-model was firstly used in a MBD analysis to compute the muscular forces produced at the bilateral chewing, which will be then applied to a FE model. Besides, to check the accuracy of this FE model description, the occlusal pattern was additionally compared with the ones recorded experimentally by an occlusal analysis system in 3D printed copies of the full dentition. As a result of these simulations, the muscular activation patterns, the paths of the condyles and the interincisor point, the mechanical responses in the PDLs and TMJs, as well as the bone deformations, before and after the alternatives of treatment were analysed. These results allowed us to check the effectiveness of N.O.R. treatments, and the selective grinding in particular, for the early correction of UXB. Moreover, at the end of the manuscript, the implications of our results to understand the craniofacial abnormal development are widely discussed.

2. Material and methods

2.1. Asymmetric 3D model

A 3D model of a craniofacial complex was developed from 3D-cephalometric images of a 6-year-old girl with a functional UXB on the left side. The images were obtained as a part of an orthodontic treatment planning and were digitalized by a CBCT scan system (i-CAT™; Imaging Sciences International, Hatfield, PA, USA), whose acquisition protocol was widely explained in an elsewhere study (Ortún-Terrazas et al., 2020). Afterwards, as a result of a cylindrical reconstruction algorithm, a Digital Imaging and Communication in Medicine (DICOM) file was obtained for the subsequent segmentation process.

Firstly, osseous and dental regions were automatically segmented by Mimics software (Mimics, v.19.; Materialise, Leuven, Belgium) using threshold levels of 226 (Lin et al., 2013) and 1688 (Wang et al., 2011) Hounsfield unit (HU), respectively. Trabecular bone regions were additionally identified by Mimics default threshold levels of 148 HU and separated from the mask of osseous tissue by Boolean operations. The condylar and temporal cartilages were manually segmented as two fibrocartilage layers of 0.2 and 0.5 mm thickness, respectively (Pullinger et al., 1990). Between these two layers, the TMJ discs were manually modelled as a tissue with variable thickness, around 1, 2 and 2.7 mm in anterior, intermediate and posterior regions (Hansson and Nordström, 1977), respectively. On the other hand, PDLs were modelled as a 0.2 mm (Keilig et al., 2016; Ortún-Terrazas et al., 2018; Xu et al., 2015) thickness layer around each tooth. All these parts were then parametrized using non-uniform rational bases splines-based transformation in Rhinoceros v5 software (Robert McNeel & Associates, Seattle, USA). Henceforth, this pre-treatment model will be referred to as "base model".

2.1.1. 3D Morphological diagnosis

The base model was firstly used in a 3D-evaluation of the craniofacial asymmetry by an expert in the diagnosis of skeletal malformations in patients with UXB. The evaluation was performed by comparing the normal distances between the original model and a copy of it, which was mirrored according to its sagittal midplane (Ortún-Terrazas et al., 2020; Pinheiro et al., 2019) (shown the colour map of Figure 1a). Normal distances between both models were computed in MATLAB software (MATLAB

6.0 R12 The MathWorks Inc., Natick, MA, 2000) and plotted in Paraview software (Paraview v5.6, National Technology & Engineering Solutions of Sandia, New Mexico). To identify the sagittal midplane, it was used an algorithm (Pinheiro et al., 2019) in MATLAB which compensated the differences between both craniofacial halves. More details about this procedure are available in the supplementary material.

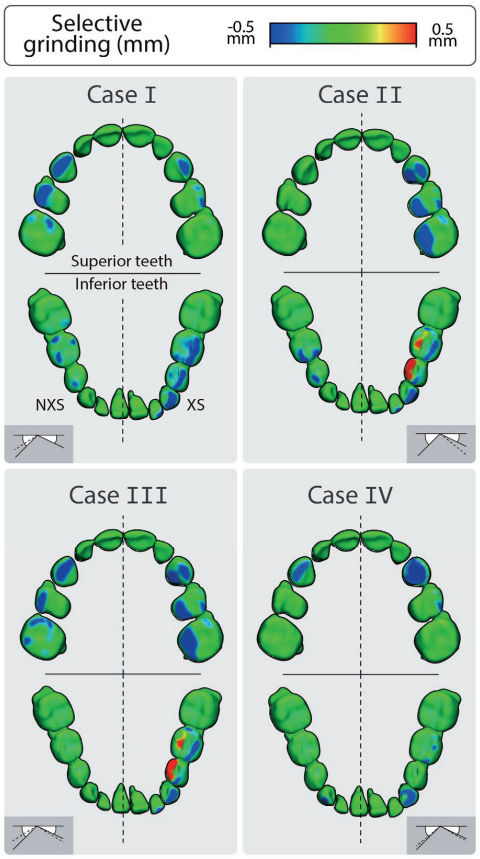

Figure 2 Alternatives of the selective grinding performed virtually on the 3D model's teeth. On the bottom-left, a diagram of the M.F.A.s before (continuous line) and after (dashed line) the treatment is shown.

2.1.2. N.O.R. treatment alternatives

The same expert in the UXB diagnostics modified virtually the cusps on teeth of the basic model by smoothing or protruding their geometry, to mimic respectively the selective grinding or the composite addiction procedures. Based on the occlusal analysis which will be then described in section 2.3, the expert performed four different alternatives of treatment to achieve a balanced occlusion (Figure 2). In case I, for instance, the practitioner removed the early contact between canines and conducted a selective grinding on the mandibular teeth of the XS and the maxilla's teeth of the NXS. Meanwhile, in case II, he protruded the medial cusps of the inferior teeth of XS and depressed the mesial planes of the upper teeth on the same side. Likewise, in case III, it was conducted a similar grinding pattern as in the case I with an additional protrusion of the medial cusps in the inferior teeth of XS. Lastly, in case IV, the expert addressed the UXB correction by grinding just the canines' cusps. In summary, in case II only the teeth of XS were treated, while in the other cases both sides were treated, grinding just the cuspid teeth in case IV or several teeth in cases I and III. Table 1 reported the volume grinded or added in each therapeutic solution. As a result, the geometry after these shape variations were then used to update the base FE model, which will be explained below.

2.1.3. FE model

The 3D-domain of the base model (Figure 3a) was discretized in 3,659,199 second-order tetrahedral elements (C3D10-type element in Abaqus) after a mesh converge process executed in Abaqus software (Abaqus 6.14, Simulia, Rhode Island, USA). Hard and soft tissues were respectively meshed by elements of 0.2 and 0.1-mm dimensions in all directions. Regarding the element formulation, in those incompressible tissues, such as in TMJ disc or cartilages, hybrid formulation was used (C3D10H-type element in Abaqus). On the other hand, for the elements which compose the PDLs, an additional degree of freedom (C3D10MP-type element in Abaqus) was added to consider the poroelastic behaviour (Bergomi et al., 2011; Natali et al., 2002; Ortún-Terrazas et al., 2018) of this tissue. Table 2 summarizes the details about the mesh of the base model.

Although the poroelastic behaviour of TMJ's discs and fibrocartilages was not considered, the incompressible response caused by the fluid confinement under the fast deformations experimented was already considered in their material description. Moreover, following previous studies (Ingawalé and Goswami, 2009; Ruggiero et al., 2015; Singh and Detamore, 2008) suggestions, the transversally isotropic behaviour caused by the collagen fibres embedded in these tissues was also considered. Hence, according to their collagen network (Singh and Detamore, 2008; Wright et al., 2016), each tissue was divided into five regions (anterior, central, posterior, medial, and lateral) with

different mechanical properties and fibres' orientations: anteroposterior in the central region and forming a ring on the periphery. Hence, the effect of the collagen network embedded in the hyperelastic ground matrix was defined by a transversely isotropic hyperelastic material model whose strain energy density function (Holzapfel, 2000) is written as follow::

$$\Psi = C_1 \cdot \left(\tilde{I}_1 - 3\right) + \frac{k_1}{2 \cdot k_2}\left\{exp\left[k_2 \cdot \left(\tilde{I}_4 - 1\right)^2\right]\right. + \frac{1}{D}\left(\frac{(J_{el})^2 - 1}{2} - lnJ_{el}\right) \quad (1)$$

where C_1 is a material constant related to the ground matrix; $k_1 > 0$ and $k_2 > 0$ are the parameters which define the effect of the collagen fibres, D is the compressibility modulus and J_{el} is the elastic volume strain. For an incompressible hyperelastic response, as was described above, the last two parameters are 0 and 1 respectively. On the other hand, $\tilde{I}_1$ and $\tilde{I}_4$ are the well-known modified invariants. terms of that arise from uncoupling the dilatational and deviatoric responses, respectively.

	Total volume (mm^3)		Volume visible (mm^3)		Grinding (mm^3)		Composite (mm^3)		Grinding (% visible)	
Situation	Inferior	Superior	Inf.	Sup.	Inf.	Inf.	Inf.	Sup.	Inf.	Sup.
Before	4429.24	2346.88	2572.83	1586.93	-	-	-	-	-	-
Case I	4381.32	2298.48	2524.90	1538.53	47.92	48.40	-	-	1.86	3.05
Case II	4415.56	2293.70	2559.15	1533.75	26.15	53.18	12.47	-	1.02	3.35
Case III	4417.94	2253.01	2561.53	1493.06	23.77	93.87	12.47	-	0.92	5.92
Case IV	4420.17	2308.15	2563.76	1548.20	9.07	38.73	-	-	0.35	2.44

Table 1 Total, visible, grinded and added volume to the inferior and superior teeth. Alternatively, the last column shows the percentage of the visible volume grinded in each arch.

Tissue	Type of element	Number of elements	Number of nodes
Cortical bone of the skull	C3D10	411,955	1,761,620
Trabecular bone of the skull	C3D10MP	2,288,343	3,769,578
Cortical bone of mandible	C3D10	35,347	154,402
Trabecular bone of the skull	C3D10MP	422,469	633,733
Teeth	C3D10	217,243	332,363
PDLs	C3D10MP	134,605	263,736
TMJ discs	C3D10H	110,386	161,141
Condylar cartilages	C3D10H	33,454	66,365
Temporal cartilages	C3D10H	5,397	11,163
Hyoid	C3D10	196,250	453,402

Table 2 Details of the mesh of the different tissues of the base model.

Whereas, for the PDL's material description, the contribution of the fluid phase was considered since it seems to plays a key role in the energy dissipation of the solid ground matrix and in the bone remodelling processes (Chen et al., 2014; Hohmann et al., 2009), which will be later discussed. The response of the solid matrix in this tissue was therefore described by the following strain energy density function of a highly compressible isotropic hyperelastic material (Storakers, 1986):

$$\Psi = \frac{2\mu}{\alpha^2}\left[\hat{\lambda}_1^{\alpha} + \hat{\lambda}_2^{\alpha} + \hat{\lambda}_3^{\alpha} - 3 + \frac{1}{\beta}\left(\bar{J}_{el}^{-\alpha\beta} - 1\right)\right] \quad (2)$$

where μ and α are material parameters and β is a coefficient related to Poisson's ratio, ν, by $\beta = \nu/(1-2\nu)$.To account for the biphasic behaviour of the PDL, the effective stress, $\boldsymbol{\sigma}$, in this tissue was defined by the second Piola -Kirchhoff stress tensor of the solid phase of the aforementioned hyperelastic material model, $\bar{\boldsymbol{\sigma}}_s$, and the coupling of the fluid phase pressure (Storakers, 1986) as follows::

$$\boldsymbol{\sigma} = (1-n)\cdot\bar{\boldsymbol{\sigma}}_s - n\cdot\bar{p}_t\cdot\boldsymbol{I} \quad (3)$$

where n is the porosity of the tissue defined by the volume of the fluid phase in the total volume of the tissue, and $\bar{p}_t$ is the average pressure stress related to tissue permeability by the non-linear Forchheimer flow law. This law was employed in Abaqus to describe the fluid flow for a permeability, k, which varies with the deformation by the exponential permeability function described by Argoubi and Shirazi-Adl, 1996 for biphasic materials:

:

$$k = k_0\left[\frac{e(1+e_0)}{e_0(1+e)}\right]^2 exp\left[M\left(\frac{1+e}{1+e_0}-1\right)\right] \quad (4)$$

where e is the void ratio related to the porosity of a tissue by $e = n/(1-n)$, k_0 and e_0 are the permeability and void ratio at zero strain, and M is a dimensionless material parameter. All the material parameters which define the aforementioned material models and those which define the elastic and porous elastic behaviour of the hard tissues are summarized in Table 3.

The porous degree of freedom on the external surface of the PDL was set to 0.0 MPa to allow the fluid interaction between PDL and bone (Bergomi et al., 2011). The rest degree of freedom on this surface was constrained to the adjacent bone movement by a tied contact (shown in Figure 3b). Likewise, the fibrocartilages and teeth were attached respectively to the bone and PDL by a similar tied contact. On the other hand, a 0.2 friction coefficient (Zheng et al., 2003) was set to each pair of teeth in contact through a penalty formulation (Figure 3b). The sliding movement of the TMJ disc along fibrocartilage layers was defined through a 0.015 (Tanaka et al., 2004) friction coefficient and was constrained in anterior and posterior direction by the retrodiscal tissue and the superior portion of the lateral pterygoid muscle, respectively (shown in Figure 3c). The lateral pterygoid was connected to the anterior band of the TMJ disc through several multipoint constraint elements (MPC). Meanwhile, the retrodiscal tissue was modelled by spring elements (shown in Figure 3c) of 0.008 N/mm stiffness (DeVocht et al., 1996).

With respect to the external boundary conditions, the upper nodes of the skull were fixed (Gupta et al., 2009; Pérez del Palomar et al., 2008; Toro-Ibacache et al., 2016) (shown in Figure 3a). Meanwhile, the mandible was able to move independently as a result of the forces applied by the chewing muscles which were modelled by connector elements (CONN3D2-type element in Abaqus). These connectors are unidirectional elements composed by a spring, damper and actuator which mimic respectively the passive, damping and active responses of each muscle (Figure 3a).

As it is well known, the passive stiffness of a muscle, i, in an instant of the chewing cycle, t, increases by the muscle strain, ε^i. Muscle strain is the ratio between muscle's stretch $(l_t^i - l_f^i)$ at instant t and the length of the muscle at the free state, l_f^i, which can be computed using the length of the muscle in the optimum state (l_0^i) and the lengths of the sarcomeres in a free and in a relaxed states, S_f^i and S_r (2.73 μm (Van Ruijven and Weijs, 1990)), respectively. In our model, the stress-strain passive behaviour was described by the following non-linear expression (Pérez del Palomar and Doblaré, 2008):

$$F_p^i(t) = \frac{K\cdot\varepsilon^i(t)}{\left[1-\varepsilon^i(t)/a\right]}\cdot PCSA^i, \quad \text{where } \varepsilon^i = \frac{l_t^i(t)-l_f^i}{l_f^i}, \text{ being } l_f^i = l_0^i\cdot\frac{S_f^i}{S_r} \quad (5)$$

Where K is the estimated force-length stiffness of the muscles $(K = 40\ N/cm^2)$ (Peck et al., 2000), a is the passive force-length asymptote $(a = 0.7)$ (Horst, 2002) and $PCSA^i$ is the cross-sectional area of the muscle.

Likewise, the strain rate dependent behaviour of each muscle was defined by a damping strain-stress relationship (F_d^i) which is a function of the critical damping coefficient (C) and the stretch velocity $(\dot{\varepsilon} = d\varepsilon/dt)$, as follows:

$$F_d^i(t) = C^i \cdot \dot{\varepsilon}^i(t) \quad (6)$$

Finally, the contractile force exerted by each muscle was modelled as a function of the maximum force in isometric contraction, F_{max}^i and the activation pattern, a, at each time of the simulation by the following equation [58], [67]:

$$F_a^i(t) = a^i(t) \cdot F_{max}^i \quad (7)$$

Owing to the lack of available data from paediatric subjects, some values of Equations 5-7 had to be estimated from the reference values of an adult. $PCSA^i$ values, for instance, were computed by the multiplication of $PCSA^i$ of an adult by a scale coefficient of 0.689 coefficient which was calculated as the ratio between the mean $PCSA^{SM}$ of the superficial masseter in a group of children (Chan et al., 2008) and adults (Peck et al., 2000). Likewise, F_{max}^i were estimated by multiplying the F_{max}^i of an adult by a 0.657 coefficient, which was calculated as the ratio of the maximum bite force of a child (347 N) to that of an adult (528 N) (Palinkas et al., 2010). On the other hand, to account a -5% asymmetry index (Martín et al., 2012) of the muscles cross-section areas, $PCSA^i$ values of NXS and XS were respectively weighted by 0.95 and 1.05 coefficients. In the case of muscles' maximum forces, F_{max}^i values of NXS and XS were respectively weighted by 0.8 and 1.2, accounting for a -20% (Frongia et al., 2013) asymmetry index of muscles activity. The reference values of the adult and those computed for our model are summarized in Table 4. Regarding the activation values, $a^i(t)$, for simulating the maximum intercuspation occlusion, 1 and 0 values were respectively considered for elevator and depressor muscles (Cecílio et al., 2010). On the other hand, for the bilateral chewing simulations, $a^i(t)$ vales were computed from a musculoskeletal model, as it is explained in the following section.

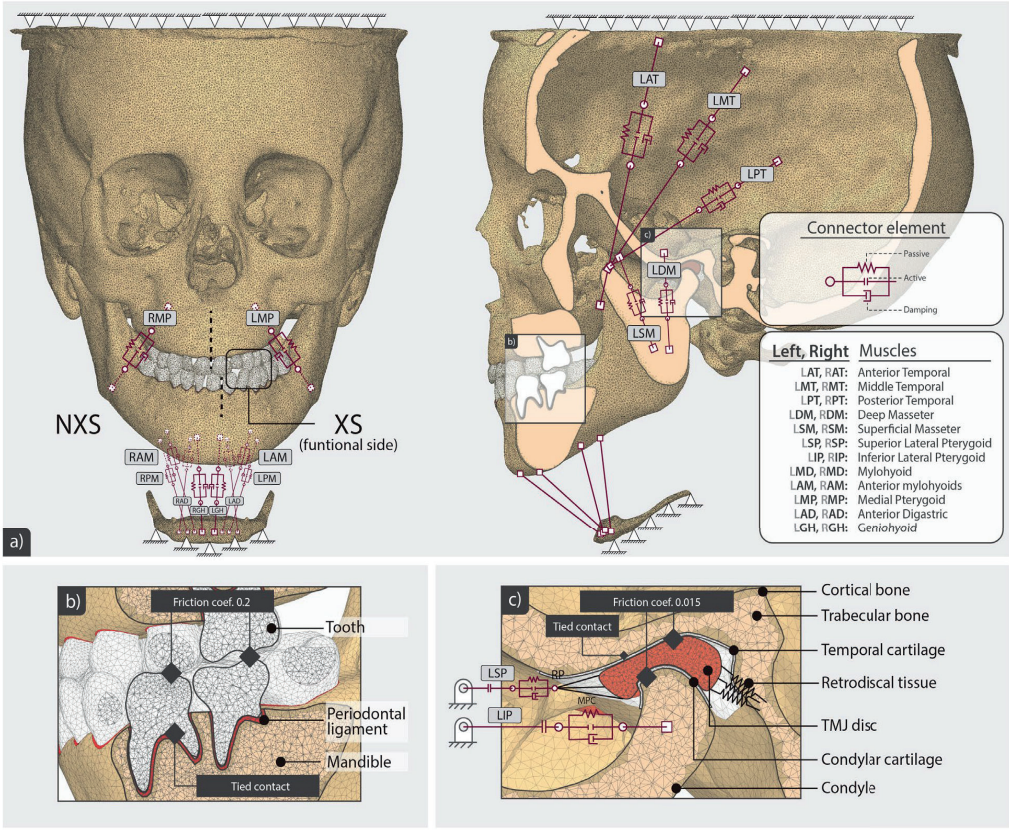

Figure 3 Captures from the FE model developed which show: a) the modelling of the chewing muscles and the external boundary conditions applied and the boundary conditions on the b) tooth's and c) TMJ surroundings.

Elastic material model

Region	E (MPa)	ν (-)	ρ (kg/m^3)
Cortical bone[a]	20000	0.30	1800[b]
Dentin[c]	15000	0.31	2140[d]

Transversally isotropic material model

Region	C_1(MPa)	D(MPa^{-1})	k_1 (MPa)	k_2(-)	ρ (kg/m^3)
TMJ disc[e]					1500[f]
Anterior	2.4	0	0.05	3.72	
Lateral	2.4	0	0.11	2.52	
Central	2.4	0	0.75	0.87	
Medial	2.4	0	0.08	2.93	
Posterior	2.4	0	0.31	1.44	
Cartilages[e]					1500[f]
Anterior	1.65	0	0.24	1.95	
Lateral	1.65	0	2.58	0.43	
Central	1.65	0	3.77	0.21	
Medial	1.65	0	2.52	0.42	
Posterior	1.65	0	0.16	1.92	

Porous elastic material model

Region	*Solid phase*			*Porous phase*			
	E (MPa)	ν (-)	ρ (kg/m^3)	$k_0 \cdot 10^{-15}$ (m^2)	M (-)	e_0 (-)	Y_w (N/m^3)
Trabecular bone[c]	345	0.31	1500[g]	52.9	-	4	9800

Porous hyperfoam material model

Region	*Solid phase*				*Porous phase*			
	μ (MPa)	α (-)	ν (-)	ρ (kg/m^3)	$k_0 \cdot 10^{-15}$(m^2)	M (-)	e_0 (-)	$Y_w(N/m^3)$
PDLs[c]	0.03	20.9	0.257	1100[h]	8.81	14.2	2.33	9800

a) Lacroix and Prendergast, 2002 [54].
b) Wood, J. L., 1971 [55].
c) Bergomi et al., 2011 [41].
d) Duck, F. A., 2013 [56].
e) Ortún-Terrazas et al., 2020 [57].
f) Pérez del Palomar and Doblaré, 2008 [58].
g) Melvin and Evans, 1971 [59].
h) Shen, Li-Kuo, et al., 2009 [60].

Table 3. Mechanical properties assigned to each region of the FE model. E, elastic modulus;v, Poisson coefficient; ρ, density of the tissue; and Υ_w, specific weight of interstitial fluid.

Muscles		Adult			Child						
Left	Right	F_{max}^i (N)[a]	$PCSA^i$ (cm^2)	l_0^i (mm)[d]	F_{max}^i (N)[c]		$PCSA^i$ (cm^2)		l_0^i (mm)	S_f^i (μm)[c]	C^i (N/mm)[b]
					NXS	XS	NXS	XS			
LSM	RSM	190.4	4.76 [b]	49.17	100.1	150.1	3.12	3.44	39.22	2.47	0.053
LDM	RDM	81.6	2.04 [b]	31.06	42.9	64.3	1.34	1.48	22.05	2.44	0.038
LAT	RAT	158	3.95 [b]	90.35	83.0	124.6	2.58	2.86	72.66	2.35	0.035
LMT	RMT	95.6	2.39 [b]	81.51	50.2	75.4	1.57	1.73	67.44		0.029
LPT	RPT	75.6	1.89 [b]	63.79	39.7	59.6	1.24	1.37	53.29	2.31	0.023
LMP	RMP	174.8	4.37 [b]	50.77	91.9	137.8	2.86	3.16	45.94	2.48	0.060
LIP	RIP	50	1.67 [b]	32.37	26.3	39.4	1.09	1.21	33.86	2.83	0.021
LSP	RSP	17	0.95 [c]	21.10	8.9	13.4	0.62	0.68	34.11	2.72	0.019[e]
LAM	RAM	20	2.12 [c]	29.31	10.5	15.8	1.39	1.53	17.90	2.80	
LPM	RPM	20		32.97	10.5	15.8			24.82	3.89	
LAD	RAD	50	1.16 [c]	40.14	26.3	39.4	0.76	0.84	17.47	2.75	
LGH	RGH	20	0.97 [c]	35.69	10.5	15.8	0.64	0.70	17.74	2.65	

a) Hannam, Alan G., et al., 2008 [73].
b) Langenbach, G. E. J., et al.,1999 [74].
c) Van Eijden, T. M. G. J., et al., 1997 [75].
d) Values based on the reference model in ArtiSynth software [76].

Table 4. Parameters used to compute F_a^i, F_p^i, and F_d^i for the right and left superficial masseters (RSM, LSM); deep masseters (RDM, LDM); anterior temporals (RAT, LAT); middle temporals (RMT, LMT); posterior temporals (RPT, LPT); medial pterygoids (RMP, LMP); inferior lateral pterygoids (RIP, LIP); superior lateral pterygoids (RSP, LSP); anterior mylohyoids (RAM, LAM); posterior mylohyoids (RPM, LPM); anterior digastrics (RAD, LAD) and geniohyoids (RGH, LGH).

2.2. Musculoskeletal Model

From the geometry already described in section 2.1, a musculoskeletal model was developed in ArtiSynth software platform (ArtiSynth; Electrical and Computer Engineering and Computer Science Departments, The University of British Columbia, Vancouver, Canada) (Fels et al., 2006; Stavness et al., 2006). Apart from the excision of some non-effective muscles, the size difference and a fixed hyoid bone, this model was otherwise identical to the generic dynamic model described in previous work (Hannam et al., 2008).

The model consisted of three rigid parts (cranium + superior teeth, mandible + inferior teeth and hyoid bone) and the muscles detailed in Figure 3a. Muscle's passive and active behaviours were simulated with Hill-type actuators through the parameters described in the above section. On the other hand, the centre of each condyle was constrained by a frictionless contact against a curvilinear surface which mimics the inclination of the glenoid fossa and two planar surfaces which restrict the lateral movement of the condyles. The curvilinear surface of the XS was sloped 3 degrees more than one of the NXS (Rilo et al., 2008; Yahata et al., 2009) (shown in Figure 1b-c). Likewise, a reference occlusal plane, which was used to not allow the upward intersection between the teeth of both dental arches, was sloped 5 degrees to the XS (shown in Figure 1a).

For the simulation of chewing by each side, the predetermined kinematic goals were set to a target cycle's duration of 0.7 s (Ahlgren, 1976). In the case of chewing by

the NXS, the paths of the interincisor point and the condyles were scaled to the dimensions of the child patient. Hence, during the opening, the interincisor point was displaced downwards 13 mm and 5 mm to right (shown in Figure 1a)(Piancino and Kyrkanides, 2016). Against, for the same simulation by the habitual chewing side (XS), the interincisor point was moved following a loop-shaded path (Piancino and Kyrkanides, 2016) of a 13 mm downwards and a lateral displacement of 2 mm towards the left side (shown in Figure 1a). Then, the motion of the centre of the condyles was captured by the forward simulation, and the inverse simulation (Fels et al., 2006) seeks to re-create the muscles activations used to attain this movement. These muscle's activation functions, $a^i(t)$, were then exported to text-based files as input data for the FE model described previously.

2.2.1. Occlusal analysis by T-Scan

The accuracy of the FE model was tested by comparing the occlusal contacts computed from a FE simulation with those obtained from an occlusal analysis by a T-Scan III system (Tek-Scan South Boston, MA, USA) in a centric position. Hence, owing to the retrospective nature of this study, the occlusal analysis of this patient before the treatment was performed on 3D printed copies of the teeth. Thus, the geometry scanned of the teeth was mounted in two thin layers of 0.5 mm thickness. The items were then exported to a slicer software (Ultimaker Cura 3.6.0, Geldermalsen, Netherlands) for printing (layer height: 0.06 mm; wall thickness: 1 mm; infill density: 40%; speed: 60 mm/s; temperature: 195 °C) in Polylactic Acid material (PLA-Ultimaker BV, Geldermalsen, Netherlands).

The occlusal analysis was then performed by introducing a 100-µm-thick piezoelectric sensor between each pair of the dental arches printed and recording by a T-Scan III system (Tek-Scan South Boston, MA, USA) the occlusal contacts that occur at the centric position when a 2-kilogram weight was applied to the superior part. Although the load applied was not representative of the real occlusal forces, it was enough to contact both dental arches without any deformation. Moreover, the magnitude of the reaction forces was not necessary to the posterior comparison of the results since T-Scan v10 software displays only the occlusal contacts as a relative percentage of the total contact pressure.

In the computational model, the contact pattern was computed mimicking the experimental conditions in the FE simulations. To that end, the piezoelectric sensor was modelled as a virtual 0.1 mm thickness layer by 11,200 second-order quadrilateral membrane elements (M3D8-type element in Abaqus) with Mylar840 material properties (DuPont; $E = 5\ GPa$ and $\nu = 0.3$). As in the experimental test, this layer was positioned between both dental arches and the superior dental arch was loaded by the same weight. As result, the contact pressure on the centroid of each element of the virtual film was extracted using a Python script ("Python 3.5.2, Python Software Foundation") and the relative percentage values were plotted on a 3D bars graph in MATLAB.

3. Results

This section presents the contacts recorded from the occlusal analysis (Figure 4a), the muscle activation patterns from the MBD analysis (Figure 6), and the results calculated from the FE model before and after the four dental treatments.

Hence, firstly, Figure 4a presents a comparison between the occlusal contacts recorded by the T-Scan III system and those calculated by the FE approach. Although occlusal patterns look apparently quite different, it should be noted that low magnitude contacts (blue regions in Figure 4a) have negligible effects in the total percentage of each side. Apart from it, the computational model successfully reproduced the imbalance between XS (57%) and NXS (42%) with relative errors below 2% in both XS (1.7%) and NXS (1.2%) domains. Moreover, it is noteworthy to mention that the numerical analysis mimicked the most relevant contacts (red regions in Figure 4a), such as those produced in canines and posterior teeth of the XS.

From the same occlusal analysis, it was also possible to evaluate the effects of the different treatments at centric occlusion (Figure 4b). Treatment I (see Figure 2), for instance, compensated significantly the reactions in both sides but also created a premature contact in the canine on the NXS, which was also observed in case IV. Whereas, in cases II and III, a contact reduction was achieved on the canines, distributing the occlusion pattern more uniformly in whole occlusal plane. Nevertheless, solutions II and III did not balance the occlusal plane as well as in treatment I.

The occlusal forces lead to compressive reactions in the PDLs and therefore to an increment of their volume-averaged hydrostatic pressure, $\bar{\sigma}_H$ which is defined as $\bar{\sigma}_H = (\sum_e \sigma_H^e \cdot V^e)/\sum_e V^e$ being σ_H^e and V^e the hydrostatic pressure and the volume of each element, e, which composed each PDL (Chen et al., 2014). In general, this variable is usually related to bone remodelling in the area surrounding the teeth (Chen et al., 2014; Dorow and Sander, 2005; Hohmann et al., 2009) when it exceeds the maximum capillary blood pressure ($\bar{\sigma}_H^*$ = 4.7kPa). In line with this "pressure-tension" theory [89], Figure 5 shows the $\bar{\sigma}_H$ values of the lower PDLs at maximum intercuspation occlusion. Hence, before treatment, $\bar{\sigma}_H$ values in XS were significantly higher than those in NXS, doubling even $\bar{\sigma}_H^*$ in the second deciduous molar. After the selective grinding treatments, as it can be noted, the value of $\bar{\sigma}_H$ was reduced significantly. In treatment I, for example, the $\bar{\sigma}_H$ was distributed more uniformly along the whole dental arch. Meanwhile, II and IV treatments compensated the

$\bar{\sigma}_H$ mainly on the posterior teeth. On the other hand, treatment III produced just the contrary reaction than the one before the treatment, i.e. an over-stimulation of the NXS with a significant reduction of the $\bar{\sigma}_H$ in the XS.

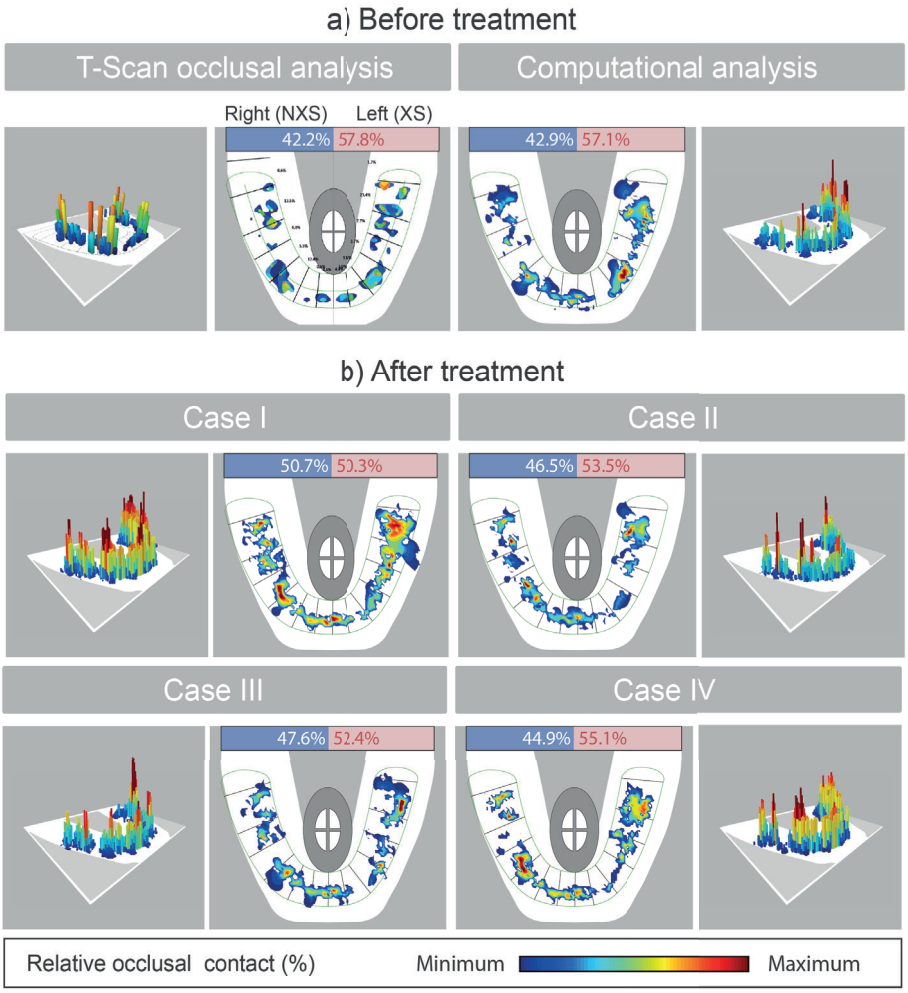

Figure 4 Perspective and top view of a**)** the occlusal records by the T-Scan III system and those computed through the FE model before the treatment and b) the occlusal contacts computed after each case of treatment.

Regarding the bilateral chewing movement, Figure 6 shows the time-activation patterns estimated through the MBD analysis for right and left chewing movements. As a result, the activation patterns at left chewing were more irregular than those obtained at right chewing. In fact, for chewing on the XS side, some muscles of the NXS side (RSP, RIP, RPM) were reactivated in a second stage, presumably to move the mandible towards the XS in a reverse movement (Alarcón et al., 2000; Piancino et al., 2016). This figure also displays the reduction of the activity in XS's depressor muscles which could help the mandible to move towards the XS. At the end of the cycle (closing phase), it is remarkable that the difference between the XS and NXS muscle activation was greater in the case of right (NXS) than left (XS) chewing. In this sense, the differences between the deep and superficial portions of the masseter muscle (LSM,

LDM), and the medial pterygoid muscle (LPM) were particularly significant.

After applying the above activation patterns to the muscles of the FE model, the paths of the lower interincisor point (Figure 7) and those of the condyle paths during left (Figure 8a) and right (Figure 8b) chewing were plotted. As previously described, the path of the lower interincisor point was used as input data for the MBD model (Figure 7a) before the treatment, ending in a stable occlusion. In treated cases, however, this path is shown an unexpected occlusal slide at the end of the closing phase, leading to a mandibular movement towards NXS (Figure 7b). Although this shift was more noticeable in the right chewing than in the left one, cases II and III yielded good results in the activity of both sides.

But to a lesser extent, these treatments also affected to the condylar paths at the end of the closing phase (Figure 8). Figure 8 displays the UXB effects in the condyle paths of both sides. For the usual chewing movement (chewing by the XS), the NXS' condyle was moved forward and then ascended along with the articular eminence, while the XS-side condyle was rotating on itself. When right chewing was simulated, however, the counterpart condyle followed a steeper path and the other condyle rotated more abruptly.

These variations in the condylar paths and occlusal patterns also led to changes in the distribution of stress and strain in the craniofacial tissues, such as TMJ discs (Figure 9) or mandible (Figure 10). Before the treatments, for instance, the minimum principal stress in the TMJ disc of the balancing side was greater and worse distributed when chewing through NXS. After treatments II and III, this stress component was more distributed more uniformly, reducing its maximum value about 1MPa. This rectification was not significant, however, in cases I and IV where almost no change occurred in the balancing response of the TMJ disc.

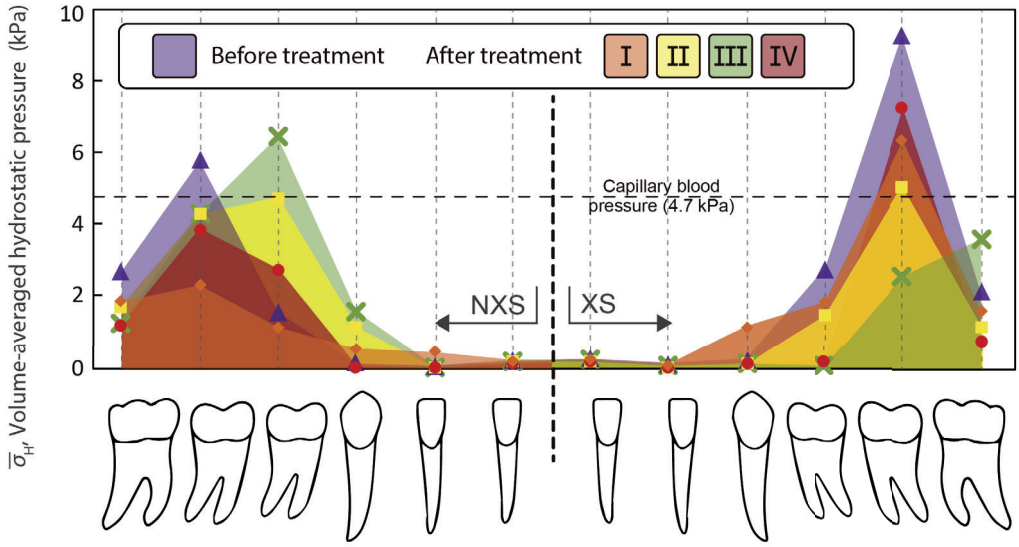

Figure 5 Volume-averaged hydrostatic pressure in the PDL of the inferior teeth before and after each treatment at maximum intercuspation occlusion. (For interpretation of the references to colour in this figure legend, the reader is referred to the web version of this article).

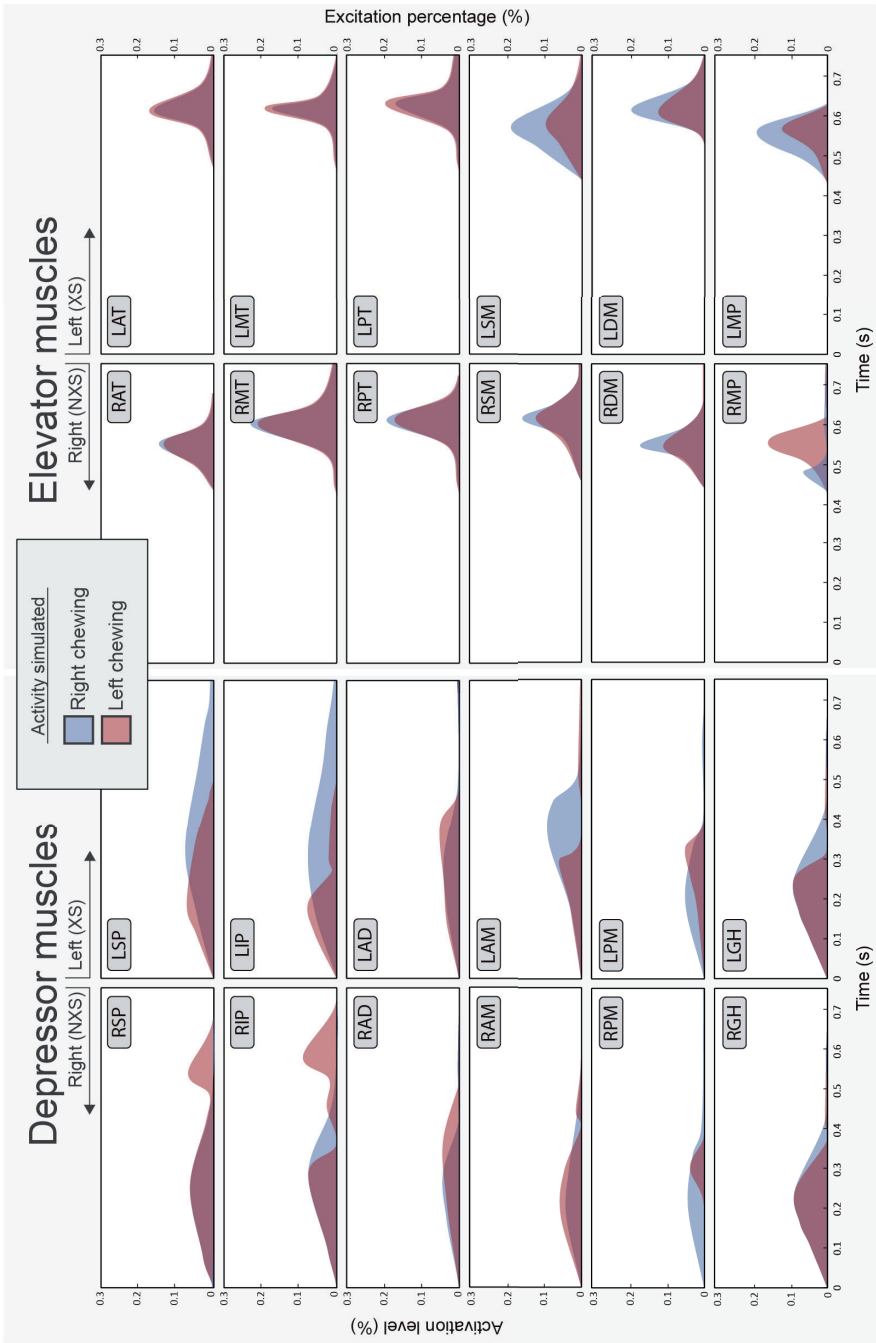

Figure 6 Muscles activation profiles computed from the musculoskeletal model. Muscle abbreviations are as for Table 4.

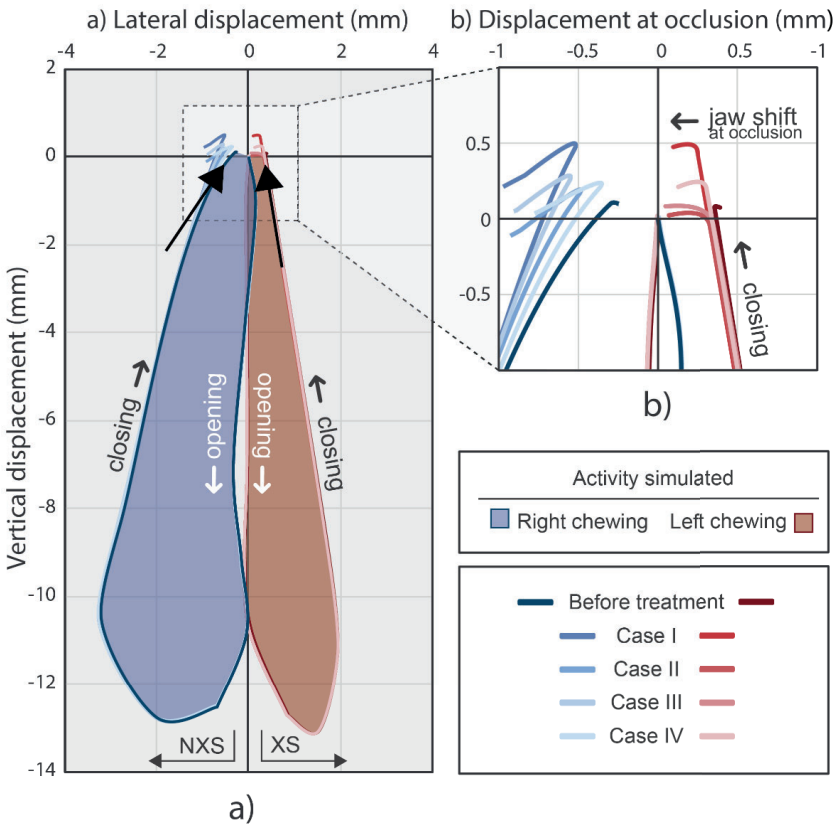

Figure 7 a) Frontal and b) detailed views of the lower interincisor point paths during the right (blue) and left (red) chewing cycles before and after the treatments.

The treatments outcomes were also noted in the mandible deformation. To evaluate the outcomes of these treatments in mandibular development, the equivalent strain, ε_e, was used (Figure 10). This variable was computed by the components of the principal strains (e_1, e_2, e_3) by $\varepsilon_e = \sqrt{0.5 \cdot [(e_1 - e_2)^2 + (e_2 - e_3)^2 + (e_3 - e_1)^2]}$ and is often used for accounting the bone remodelling through the Frost mechanostat theory (Frost, 1987, 1983). According to this theory, bone apposition would occur in those regions with $\varepsilon_e$values above 0.002-unit bone surface strain (red regions in Figure 10), whereas it would be reabsorbed in those regions with ε_e values below 0.0008 (blue regions in Figure 10). As was introduced. the bilateral movement of chewing lead to a balanced work of osteoblasts and osteoclasts in the mandible, and therefore to a symmetrical growth of both mandibular halves. Nevertheless, in our case report (Figure 10), the mandibular deformations for left and right chewing were not symmetrical before the treatment. When the subject chewed on the right side, there was a region in the mandibular body of the left halve which was stretched more than 0.002, potentially leading to continuous growth of this region. Respect it, treatments I, II and III reduced the equivalent strain in this region. In fact, treatments II and III even led to just the reverse effect in this region. Here it is, at left chewing, the equivalent strain in this region was just below 0.0008, which could mean the bone resorption in this region.

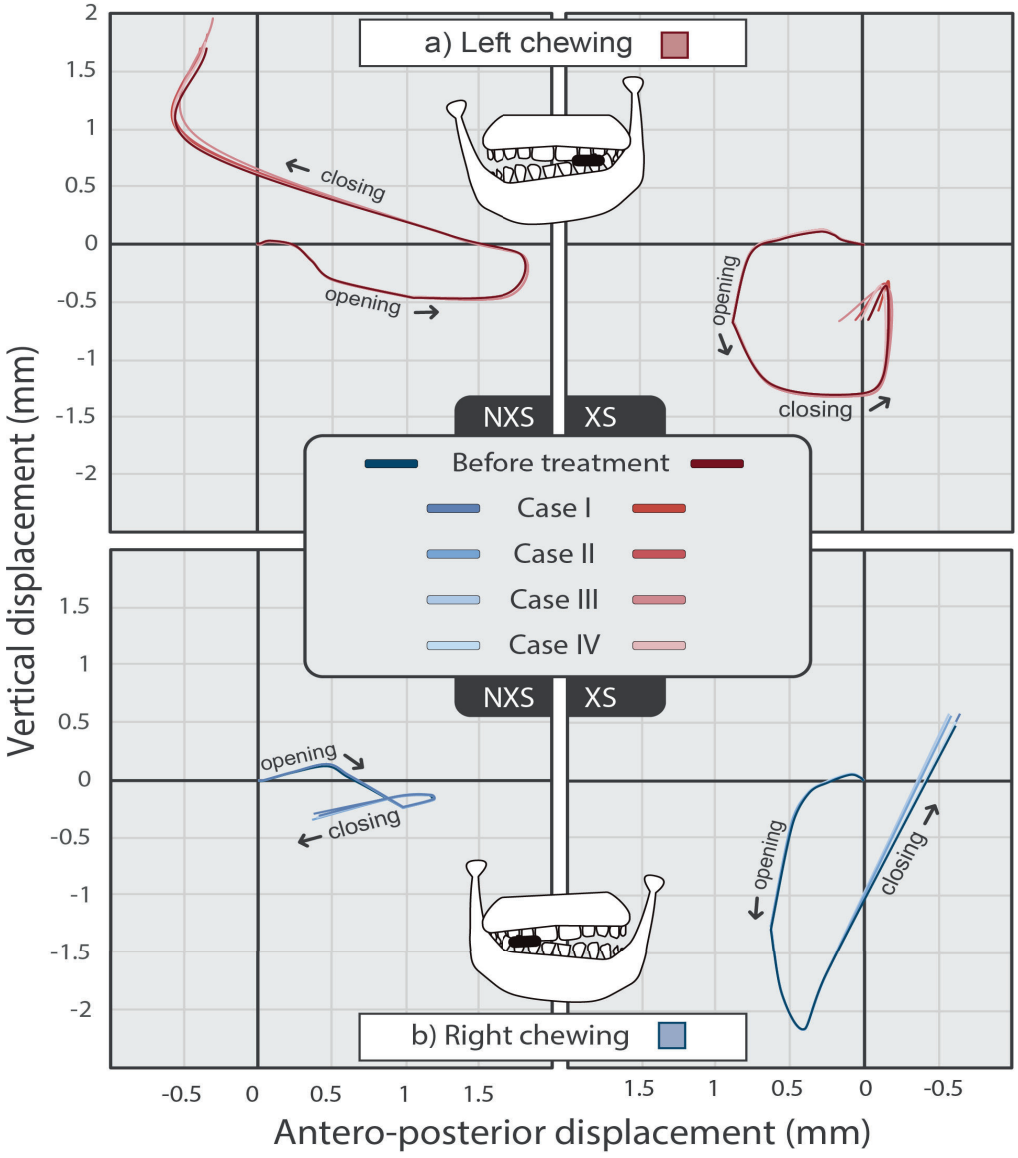

Figure 8 Sagittal condylar patterns during a) left and right chewing before and after the treatments.

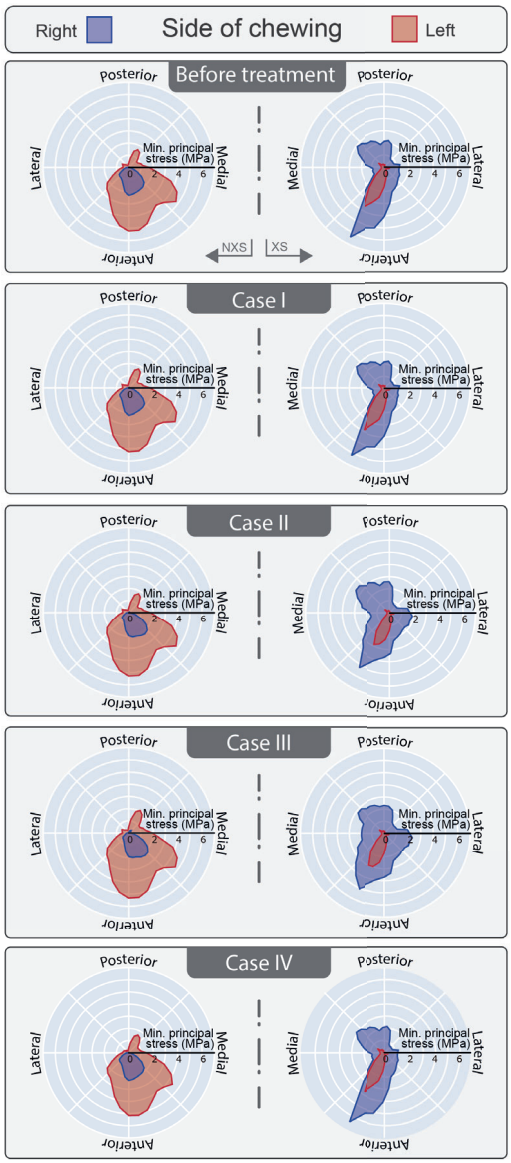

Figure 9 Polar plots of the minimum principal stress distribution within the TMJ disc of the NXS (first column) and XS (second column) at the left (red colour) and right (blue colour) chewing.

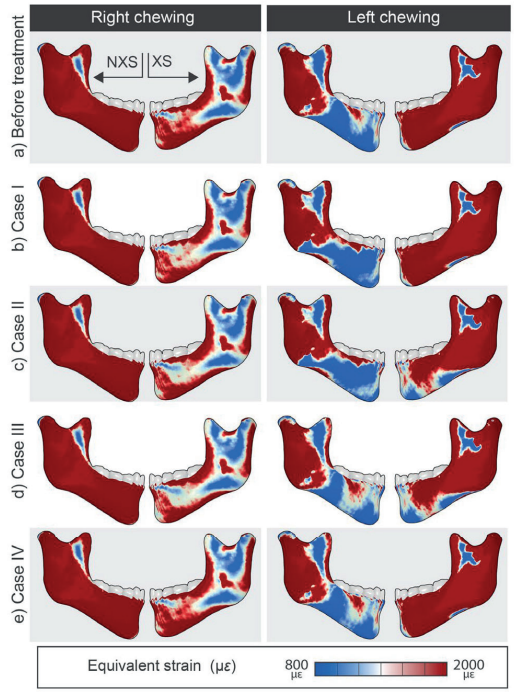

Figure 10 Distribution of the equivalent strain caused by right (first column) and left chewing (second column) in both mandibular halves a) before and b-e) after the treatments.

4. Discussion

Despite the benefits of N.O.R. in the early treatment of UXBs, its use is not widespread due to the lack of scientific evidence that proves its effectiveness (Chate, 2000; Leighton, 2007; William et al., 2007), among other reasons. As introduced, this uncertainty is basically caused by the contradictions in craniofacial growth theories (Castaldo and Cerritelli, 2015), the complexity of the stomatognathic system (Nanci, 1990) and the limitations of the computational studies (O'Higgins et al., 2012). As a contribution to this topic, this work presented a computational methodology which evaluates the effectiveness of different N.O.R.'s treatments in a paediatric patient with UXB.

Anatomically, the morphological 3D-analysis of patient's craniofacial complex (Figure 1a) highlighted some shape variations previously identified in other studies, such as the retracted position of the maxilla (Pirttiniemi, 1994) or the increment of mandibular thickness (Ishizaki et al., 2010) in the XS. In our study, these morphological alterations could be accounted for the application of the pressure-tension [89]

and Frost mechanostat (Frost, 1987, 1983) theories to the numerical results.

Thus, at centric occlusion, the occlusal analysis before treatments shown a significant imbalance with a greater value in the XS (42.2%) than in the NXS (57.1%) (Björk et al., 1964), which was responsible for the periodontal overpressure (>4.7 kPa) in the XS (see Figure 5). According to the principles of the pressure-tension theory, this overpressure state may induce a local bone remodelling which leads to tooth movement on this side (Chen et al., 2014; Dorow and Sander, 2005; Hohmann et al., 2009). This movement of XS' teeth would aggravate and be responsible for UXB worsening over time, which support the basic rule of N.O.R.'s early treatments, i.e. treat the malocclusion as soon as possible (Planas, 2013). Hence, all treatments conducted by the clinician attempted to reduce the occlusal imbalance and thereby the hydrostatic pressure and bone remodelling processes on the XS. In fact, the alternative IV (see Figure 5) achieved just the opposite reaction, encouraging the bone remodelling in the NXS. From an occlusal point of view (Planas, 2013), this alternative could be the first step in a fully N.O.R. Then, occlusal adjustments such as those performed in treatment II could balance the excitation in both dental hemiarches, consolidating the new occlusal position.

On the other hand, according to mechanostat theory's principles (Frost, 1987, 1983). bilateral chewing movements led a bilateral over deformation (>2000 $\mu\varepsilon$) of the mandibular XS' body (Figure 9a) which could be responsible for the bone apposition and the thickness increment (Ishizaki et al., 2010) in this region. Likewise, NXS' mandibular ramus deformed more than the upper strain limit at both bilateral movements, potentially leading to an over elongation of this region with respect to its opposite one (Veli et al., 2011). Fortunately, those treatments which incorporated composite (II and III) achieved a reduction of the XS' deformation in these regions when the subject was chewing by the NXS. In this case, however, the treatment on canines (IV) did not achieve a symmetrical deformation in both halves.

Besides the deformities and occlusal imbalance, UXB also resulted in functional alterations as those observed in MBD analysis, in condylar paths and TMJs. In agreement with experimental results (Alarcón et al., 2000; Piancino et al., 2016), the results of our MBD analysis found that the percentage differences between bilateral masseter activity were significantly lower when the subject chew by the XS than by the non-affected side. Moreover, in chewing on the XS, the activation patterns of the depressor muscles were also more irregular during the opening phase, leading to the narrow path of the interincisal point in that side (Piancino and Kyrkanides, 2016). On the other hand, for chewing by the NXS (Rilo et al., 2008; Yahata et al., 2009), a steeper condylar path was found on the opposite side, which could explain the patient's difficulty in executing this masticatory movement. Besides, according to our results, usual chewing would not generate abnormal stresses in the TMJ disc of the XS side, which could justify that numerous clinical studies (Iodice et al., 2013; Pellizoni et al., 2006) have not found a direct relationship between UXB and temporomandibular joint disorders (TMDs). At the same time, however, it was remarkable that unusual chewing movement certainly caused a concentration of stresses in the anterior band of the TMJ disc of the balanced side (Figure 9), maybe as a consequence of the steep slope of the articular eminence in that side. It could indicate that, although the specialist succeeds in avoiding unilateral chewing, it is also necessary to treat the TMJ function and avoid the overloading of the TMJ discs, as N.O.R. stated. This could be the reason why follow-up clinical investigations (Egermark et al., 2003; Thilander and Bjerklin, 2012) in UXB-treated patients have found a relationship between UXB and TMDs. From our results (cases II and III in Figure 9), the selective grinding and the occlusal resin guidance composite could serve not only to balance the occlusal plane but also to correct the function, reducing the stress state of the TMJ disc and preventing TMDs or craniomandibular dysfunction in the adulthood (Planas, 2013).

The effect of N.O.R. on system's functions was also represented slightly in the condyle paths and the lower interincisor point (Figures 7 and 8). Hence, all treatments examined shifted the mandible towards the NXS, modifying slightly the condylar pathways. Although the effects in TMJ function may seem small, it is important to emphasize that they were instantaneously obtained when the treatments were performed. Throughout time, they could be accentuated as a result of the musculature adaptation, the new stimulation of neurological tissues, and the development of the craniofacial structures. (Neto et al., 2007; Planas, 2013).

4.1.Study limitations

The findings presented here constitute an important step in the demonstration of N.O.R. and the efficacy of selective grinding and composite addiction therapies in the correction of UXBs. Nonetheless, several limitations of the study should be considered. Firstly, the results computed in this study are valid only for the specific patient studied and cannot be directly extrapolated to other clinical cases. Second, owing to the challenge of obtaining magnetic resonance imaging (MRI) in paediatric subjects, several soft tissues, such as TMJ disc attachments or muscles, were not 3D modelled. Likewise, the patterns of muscle activation and landmarks paths were also not recorded experimentally due to the difficulties of conducting electromyographic and kinesiographic analyses in child patients. On the other hand, the pre-treatment occlusal analysis was conducted on printed samples since the retrospective nature of this study. The combination of in vivo examinations and the acquisition of geometries with intraoral scanners would improve further the accuracy of the computer models.

Finally, this study has not considered the temporal adaptation of the tissues to the new biomechanical condition after treatment.

Notwithstanding all these limitations, our findings are a useful basis from which future researchers, engineers or clinical specialists can evaluate the occlusion and chewing movements using computational models. Future studies should consider these issues to develop more detailed FE models, improve the knowledge about the muscular activity in paediatric patients and evaluate the effectiveness of the treatments over time.

Conclusion

Bearing these limitations in mind, the case report here presented provides a good understanding of the effectiveness of early treatments in the correction of UXB and craniofacial asymmetries. Based on our findings, the following conclusions can be drawn:

- FE model mimicked the occlusal pattern recorded in the occlusal analysis with relative errors below 2%, becoming a good analytical tool for the craniomandibular studies.
- The activation pattern of the chewing muscles was more irregular and asymmetric when the subject chewed from the XS than from the NXS.
- UXB caused an over deformation (>2000 $\mu\varepsilon$) in the XS' mandibular body and the NXS' mandibular ramus, which could account for the thickening and lengthening of the body and mandibular branch, respectively
- The condylar path was steeper on the XS side than on the NXS side.
- The selective grinding of canines could be a good initial step in N.O.R. therapies since it would compensate for the mandibular asymmetrical development. Afterwards, selective grindings on the rest teeth may be needed to balance stimulation on both sides.
- The combination of selective grinding and the addition of resin composites provided a good solution for changing the position at the end of the chewing cycle, shifting the mandible to the NXS side and the reducing bone apposition on the XS.
- N.O.R. treatments caused a slight variation in the paths of condyles and lower interincisor point as soon as the treatment was applied, which would demonstrate the effect of N.O.R. not only at the occlusal level but also at the functional level.

Conflict of interests

The authors have no conflicts of interest related to the present work.

Funding

This work was supported by the Spanish Ministry of Economy and Competitiveness (project DPI 2016-79302-R), the European Social Funds and Regional Government of Aragon (grant 2016/20) and Ibercaja-Cai Fundation (grant IT 4/18).

Acknowledgements

The authors would like to thank Dr. Ángel Sampietro Fuentes for his assistance in this research.

References

Ahlgren, J., 1976. Masticatory movements in man. Mastication.

Alarcón, J.A., Martín, C., Palma, J.C., 2000. Effect of unilateral posterior crossbite on the electromyographic activity of human masticatory muscles. Am. J. Orthod. Dentofac. Orthop. 118, 328–334. https://doi.org/10.1067/mod.2000.103252

Argoubi, M., Shirazi-Adl, A., 1996. Poroelastic creep response analysis of a lumbar motion segment in compression. J. Biomech. 29, 1331–1339. https://doi.org/10.1016/0021-9290(96)00035-8

Bergomi, M., Cugnoni, J., Galli, M., Botsis, J., Belser, U.C., Wiskott, H.W.A., 2011. Hydro-mechanical coupling in the periodontal ligament: A porohyperelastic finite element model. J. Biomech. 44, 34–38. https://doi.org/10.1016/j.jbiomech.2010.08.019

Björk, A., Krebs, A.A., Solow, B., 1964. A Method for Epidemiological Registration of Malocculusion. Acta Odontol. Scand. 22, 27–41.

Castaldo, G., Cerritelli, F., 2015. Craniofacial growth: evolving paradigms. CRANIO® 33, 23–31. https://doi.org/10.1179/0886963414Z.00000000042

Cecílio, F.A., Regalo, S.C.H.H., Palinkas, M., Issa, J.P.M.M., Siéssere, S., Hallak, J.E.C.C., Machado-de-sousa, J.P., Semprini, M., 2010. Ageing and surface EMG activity patterns of masticatory muscles. J. Oral Rehabil. 37, 248–255. https://doi.org/10.1111/j.1365-2842.2010.02051.x

Chan, H.J., Woods, M., Stella, D., 2008. Mandibular muscle morphology in children with different vertical facial patterns: A 3-dimensional computed tomography study. Am. J. Orthod. Dentofac. Orthop. 133, 1–13. https://doi.org/10.1016/j.ajodo.2007.05.013

Chate, R.A., 2000. Do we really want a quick fix? Br. Dent. J. 188, 177–86. https://doi.org/10.1038/sj.bdj.4800426

Chen, J., Li, W., Swain, M. V., Ali Darendeliler, M., Li, Q., Darendeliler, M.A., Li, Q., 2014. A periodontal ligament driven remodeling algorithm for orthodontic tooth movement. J. Biomech. 47, 1689–1695. https://doi.org/10.1016/j.jbiomech.2014.02.030

da Silva Filho, O.G., Santamaria Jr., M., Filho, L.C., 2007. Epidemiology of Posterior Crossbite in the Primary Dentition. J. Clin. Pediatr. Dent. 32, 73–78. https://doi.org/10.17796/jcpd.32.1.h53g027713432102

DeVocht, J.W., Goel, V.K., Zeitler, D.L., Lew, D., 1996. A study of the control of disc movement within the temporomandibular joint using the finite element technique. J. Oral Maxillofac. Surg. 54, 1431–1437. https://doi.org/10.1016/S0278-2391(96)90259-1

Dorow, C., Sander, F.-G., 2005. Development of a Model for the Simulation of Orthodontic Load on Lower First Premolars Using the Finite Element Method. J. Orofac. Orthop. / Fortschritte der Kieferorthopädie 66, 208–218. https://doi.org/10.1007/s00056-005-0416-5

Egermark, I., Magnusson, T., Carlsson, G.E., 2003. A 20-year follow-up of signs and symptoms of temporomandibular disorders and malocclusions in subjects with and without orthodontic treatment

in childhood. Angle Orthod. https://doi.org/10.1043/0003-3219(2003)73<109:AYFOSA>2.0.CO;2

Fels, S., Vogt, F., Van Den Doel, K., Lloyd, J., Stavness, I., Vatikiotis-Bateson, E., 2006. Artisynth: A biomechanical simulation platform for the vocal tract and upper airway, in: International Seminar on Speech Production, Ubatuba, Brazil.

Frongia, G., Ramieri, G., De Biase, C., Bracco, P., Piancino, M.G., 2013. Changes in electric activity of masseter and anterior temporalis muscles before and after orthognathic surgery in skeletal class III patients. Oral Surg. Oral Med. Oral Pathol. Oral Radiol. 116, 398–401. https://doi.org/10.1016/j.oooo.2013.06.008

Frost, H.M., 1987. Bone "mass" and the "mechanostat": A proposal. Anat. Rec. 219, 1–9. https://doi.org/10.1002/ar.1092190104

Frost, H.M., 1983. A determinant of bone architecture. The minimum effective strain. Clin. Orthop. Relat. Res. 286–92.

Geng, J.-P., Tan, K.B.C., Liu, G.-R., 2018. Application of finite element analysis in implant dentistry: A review of the literature. J. Prosthet. Dent. 85, 585–598. https://doi.org/10.1067/mpr.2001.115251

Gupta, A., Kohli, V.S., Hazarey, P. V., Kharbanda, O.P., Gunjal, A., 2009. Stress distribution in the temporomandibular joint after mandibular protraction: A 3-dimensional finite element method study. Part 1. Am. J. Orthod. Dentofac. Orthop. 135, 737–748. https://doi.org/10.1016/j.ajodo.2007.12.025

Hannam, A.G., 2003. Dynamic modeling and jaw biomechanics. Orthod. Craniofac. Res. 6 Suppl 1, 59–65.

Hannam, A.G., Stavness, I., Lloyd, J.E., Fels, S., 2008. A dynamic model of jaw and hyoid biomechanics during chewing. J. Biomech. 41, 1069–1076. https://doi.org/10.1016/j.jbiomech.2007.12.001

Hansson, T., Nordström, B., 1977. Thickness of the soft tissue layers and articular disk in temporomandibular joints with deviations in form. Acta Odontol. Scand. 35, 281–288. https://doi.org/10.3109/00016357709064126

Hohmann, A., Wolfram, U., Geiger, M., Boryor, A., Kober, C., Sander, C., Sander, F.G., 2009. Correspondences of hydrostatic pressure in periodontal ligament with regions of root resorption: A clinical and a finite element study of the same human teeth. Comput. Methods Programs Biomed. 93, 155–161. https://doi.org/10.1016/j.cmpb.2008.09.004

Holzapfel, G., 2000. Nonlinear Solid Mechanics: A Continuum Approach for Engineering. Wiley, New York.

Horst, van der M.J., 2002. Human Head Neck Response in Frontal , Lateral and Rear End Impact Loading - modelling and validation -. https://doi.org/10.6100/IR554047

Ingawalé, S., Goswami, T., 2009. Temporomandibular Joint: Disorders, Treatments, and Biomechanics. Ann. Biomed. Eng. 37, 976–996. https://doi.org/10.1007/s10439-009-9659-4

Iodice, G., Danzi, G., Cimino, R., Paduano, S., Michelotti, A., 2013. Association between posterior crossbite, masticatory muscle pain, and disc displacement: a systematic review. Eur. J. Orthod. 35, 737–744. https://doi.org/10.1093/ejo/cjt024

Ishizaki, K., Suzuki, K., Mito, T., Tanaka, E.M., Sato, S., 2010. Morphologic, functional, and occlusal characterization of mandibular lateral displacement malocclusion. Am. J. Orthod. Dentofac. Orthop. 137, 454-e1.

Keilig, L., Drolshagen, M., Tran, K.L., Hasan, I., Reimann, S., Deschner, J., Brinkmann, K.T., Krause, R., Favino, M., Bourauel, C., 2016. In vivo measurements and numerical analysis of the biomechanical characteristics of the human periodontal ligament. Ann. Anat. - Anat. Anzeiger 206, 80–88. https://doi.org/10.1016/j.aanat.2015.08.004

Kennedy, D.B., Osepchook, M., 2005. Unilateral posterior crossbite with mandibular shift: a review. Journal-Canadian Dent. Assoc. 71, 569.

Keski-Nisula, K., Lehto, R., Lusa, V., Keski-Nisula, L., Varrela, J., 2003. Occurrence of malocclusion and need of orthodontic treatment in early mixed dentition. Am. J. Orthod. Dentofac. Orthop. 124, 631–638.

Koolstra, J.H.H., van Eijden, T.M.G.J.M.G.J., 2005. Combined finite-element and rigid-body analysis of human jaw joint dynamics. J. Biomech. 38, 2431–2439. https://doi.org/10.1016/j.jbiomech.2004.10.014

Kupczik, K., Dobson, C.A., Fagan, M.J., Crompton, R.H., Oxnard, C.E., O'Higgins, P., 2007. Assessing mechanical function of the zygomatic region in macaques: validation and sensitivity testing of finite element models. J. Anat. 210, 41–53. https://doi.org/10.1111/j.1469-7580.2006.00662.x

Leighton, B.C., 2007. The early signs of malocclusion. Eur. J. Orthod. 29, i89–i95. https://doi.org/10.1093/ejo/cjl099

Libby, J., Marghoub, A., Johnson, D., Khonsari, R.H., Fagan, M.J., Moazen, M., 2017. Modelling human skull growth: a validated computational model. J. R. Soc. Interface 14, 20170202. https://doi.org/10.1098/rsif.2017.0202

Lin, H., Zhu, P., Lin, Y., Wan, S., Shu, X., Xu, Y., Zheng, Y., 2013. Mandibular asymmetry: A three-dimensional quantification of bilateral condyles. Head Face Med. 9, 1–7. https://doi.org/10.1186/1746-160x-9-42

Lippold, C., Hoppe, G., Moiseenko, T., Ehmer, U., Danesh, G., 2008. Analysis of condylar differences in functional unilateral posterior crossbite during early treatment–a randomized clinical study. J. Orofac. Orthop. der Kieferorthopädie 69, 283–296.

Marghoub, A., Libby, J., Babbs, C., Pauws, E., Fagan, M.J., Moazen, M., 2017. Predicting calvarial growth in normal and craniosynostotic mice using a computational approach. J. Anat. 10, 440–448. https://doi.org/10.1111/joa.12764

Martín, C., Palma, J.C., Alamán, J.M., Lopez-Quiñones, J.M., Alarcón, J.A., 2012. Longitudinal evaluation of sEMG of masticatory muscles and kinematics of mandible changes in children treated for unilateral cross-bite. J. Electromyogr. Kinesiol. 22, 620–628. https://doi.org/10.1016/j.jelekin.2012.01.002

Moss, M.L., 1970. The role of muscular functional matrices in development and maintenance of occlusion. Bull. Pac. Coast Soc. Orthod. 45, 29–30.

Moss, M.L., Rankow, R.M., 1968. The role of the functional matrix in mandibular growth. Angle Orthod. 38, 95–103.

Moss, M.L., Skalak, R., Patel, H., Sen, K., Moss-Salentijn, L., Shinozuka, M., Vilmann, H., 1985. Finite element method modeling of craniofacial growth. Am. J. Orthod. 87, 453–472. https://doi.org/10.1016/0002-9416(85)90084-3

Nanci, A., 1990. Oral histology: Development, structure, and function (ed 3). J. Oral Maxillofac. Surg. 48, 98–99. https://doi.org/10.1016/0278-2391(90)90217-P

Natali, A.N., Pavan, P.G., Schrefler, B.A., Secchi, S., 2002. A multi-phase media formulation for biomechanical analysis of periodontal ligament, in: Meccanica. pp. 407–418. https://doi.org/10.1023/A:1020895906292

Neto, G.P., Puppin-Rontani, R.M., Garcia, R.C.M.R., 2007. Changes in the masticatory cycle after treatment of posterior crossbite in children aged 4 to 5 years. Am. J. Orthod. Dentofac. Orthop. 131, 464–472. https://doi.org/10.1016/j.ajodo.2005.06.030

O'Higgins, P., Fitton, L.C., Phillips, R., Shi, J., Liu, J., Gröning, F., Cobb, S.N., Fagan, M.J., 2012. Virtual Functional Morphology: Novel Approaches to the Study of Craniofacial Form and Function. Evol. Biol. 39, 521–535. https://doi.org/10.1007/s11692-012-9173-8

Ortún-Terrazas, J., Cegoñino, J., Santana-Penín, U., Santana-Mora, U., Pérez del Palomar, A., 2018. Approach towards the porous fibrous structure of the periodontal ligament using micro-computerized tomography and finite element analysis. J. Mech. Behav. Biomed. Mater. 79, 135–149. https://doi.org/10.1016/j.jmbbm.2017.12.022

Ortún-Terrazas, J., Fagan, M.J., Cegoñino, J., Illipronti-Filho, E., Pérez del Palomar, A., 2020. Towards an early 3D-diagnosis of craniofacial asymmetry by computing the accurate midplane: A PCA-based method. Comput. Methods Programs Biomed. 191, 105397.

https://doi.org/10.1016/j.cmpb.2020.105397

Palinkas, M., Nassar, M.S.P., Cecílio, F.A., Siéssere, S., Semprini, M., MacHado-De-Sousa, J.P., Hallak, J.E.C., Regalo, S.C.H., 2010. Age and gender influence on maximal bite force and masticatory muscles thickness. Arch. Oral Biol. 55, 797–802. https://doi.org/10.1016/j.archoralbio.2010.06.016

Palla, S., Gallo, L., Gossi, D., 2003. Dynamic stereometry of the temporomandibular joint. Orthod. Craniofacial Res. 6, 37–47. https://doi.org/10.1034/j.1600-0544.2003.233.x

Peck, C.C., Langenbach, G.E.J., Hannam, A.G., 2000. Dynamic simulation of muscle and articular properties during human wide jaw opening. Arch. Oral Biol. 45, 963–982. https://doi.org/10.1016/S0003-9969(00)00071-6

Pellizoni, S.E.P., Salioni, M.A.C., Juliano, Y., Guimarães, A.S., Alonso, L.G., 2006. Temporomandibular joint disc position and configuration in children with functional unilateral posterior crossbite: A magnetic resonance imaging evaluation. Am. J. Orthod. Dentofac. Orthop. 129, 785–793. https://doi.org/10.1016/j.ajodo.2006.02.007

Peres, K.G., Barros, A.J.D., Peres, M.A., Victora, C.G., 2007. Effects of breastfeeding and sucking habits on malocclusion in a birth cohort study. Rev. Saude Publica 41, 343–350.

Pérez del Palomar, A., Doblaré, M., 2008. Dynamic 3D FE modelling of the human temporomandibular joint during whiplash. Med. Eng. Phys. 30, 700–709. https://doi.org/10.1016/j.medengphy.2007.07.009

Pérez del Palomar, A., Santana-Penín, U., Mora-Bermúdez, M.J., Doblaré, M., 2008. Clenching TMJs-Loads Increases in Partial Edentates: A 3D Finite Element Study. Ann. Biomed. Eng. 36, 1014–1023. https://doi.org/10.1007/s10439-008-9487-y

Piancino, M.G., Falla, D., Merlo, A., Vallelonga, T., de Biase, C., Dalessandri, D., Debernardi, C., 2016. Effects of therapy on masseter activity and chewing kinematics in patients with unilateral posterior crossbite. Arch. Oral Biol. 67, 61–67. https://doi.org/10.1016/j.archoralbio.2016.03.013

Piancino, M.G., Kyrkanides, S., 2016. Understanding Masticatory Function in Unilateral Crossbites, Understanding Masticatory Function in Unilateral Crossbites. John Wiley & Sons, Inc., Oxford, UK. https://doi.org/10.1002/9781118971901

Pileičikienė, G., Šurna, A., Skirbutis, G., Barauskas, R., Šurna, R., 2010. Influence of guiding tooth geometry on contact forces distribution in the human masticatory system: a FEM study. Mechanics 83, 34–39.

Pinheiro, M., Ma, X., Fagan, M.J., McIntyre, G.T., Lin, P., Sivamurthy, G., Mossey, P.A., 2019. A 3D cephalometric protocol for the accurate quantification of the craniofacial symmetry and facial growth. J. Biol. Eng. 13, 42. https://doi.org/10.1186/s13036-019-0171-6

Pirttiniemi, P.M., 1994. Associations of mandibular and facial asymmetries—A review. Am. J. Orthod. Dentofac. Orthop. 106, 191–200. https://doi.org/10.1016/S0889-5406(94)70038-9

Planas, P., 2013. Neuro-occlusal rehabilitation: NOR, 2nd ed. Amolca, Barcelona, España.

Planas, P., 1987. Rehabilitación Neuro-Oclusal: RNO. Masson-Salvat, Barcelona, España.

Pullinger, A.G.A.A.G., Baldioceda, F., Bibb, C.A.C.A., 1990. Relationship of TMJ Articular Soft Tissue to Underlying Bone in Young Adult Condyles. J. Dent. Res. 69, 1512–1518. https://doi.org/10.1177/00220345900690081301

Rilo, B., da Silva, J.L., Mora, M.J., Cadarso-Suárez, C., Santana, U., 2008. Midline shift and lateral guidance angle in adults with unilateral posterior crossbite. Am. J. Orthod. Dentofac. Orthop. 133, 804–808.

Ruggiero, L., Zimmerman, B.K., Park, M., Han, L., Wang, L., Burris, D.L., Lu, X.L., 2015. Roles of the Fibrous Superficial Zone in the Mechanical Behavior of TMJ Condylar Cartilage. Ann. Biomed. Eng. 43, 2652–2662. https://doi.org/10.1007/s10439-015-1320-9

Singh, M., Detamore, M.S., 2008. Tensile properties of the mandibular condylar cartilage. J. Biomech. Eng. 130, 011009. https://doi.org/10.1115/1.2838062

Stavness, I., Hannam, A.G., Lloyd, J.E., Fels, S., 2006. An Integrated Dynamic Jaw and Laryngeal Model Constructed from CT Data. pp. 169–177. https://doi.org/10.1007/11790273_19

Storakers, B., 1986. On material representation and constitutive branching in finite compressible elasticity. J. Mech. Phys. Solids 34, 125–145. https://doi.org/10.1016/0022-5096(86)90033-5

Tanaka, E., Kawai, N., Tanaka, M., Todoh, M., van Eijden, T., Hanaoka, K., Dalla-Bona, D.A., Takata, T., Tanne, K., 2004. The Frictional Coefficient of the Temporomandibular Joint and Its Dependency on the Magnitude and Duration of Joint Loading. J. Dent. Res. 83, 404–407. https://doi.org/10.1177/154405910408300510

Thilander, B., Bjerklin, K., 2012. Posterior crossbite and temporomandibular disorders (TMDs): need for orthodontic treatment? Eur. J. Orthod. 34, 667–673. https://doi.org/10.1093/ejo/cjr095

Toro-Ibacache, V., Muñoz, V.Z., O'Higgins, P., Zapata Muñoz, V., O'Higgins, P., 2016. The relationship between skull morphology, masticatory muscle force and cranial skeletal deformation during biting. Ann. Anat. - Anat. Anzeiger 203, 59–68. https://doi.org/10.1016/j.aanat.2015.03.002

Van Ruijven, L.J., Weijs, W.A., 1990. A new model for calculating muscle forces from electromyograms. Eur. J. Appl. Physiol. Occup. Physiol. 61, 479–485. https://doi.org/10.1007/BF00236071

Veli, I., Uysal, T., Ozer, T., Ucar, F.I., Eruz, M., 2011. Mandibular asymmetry in unilateral and bilateral posterior crossbite patients using cone-beam computed tomography. Angle Orthod. 81, 966–974. https://doi.org/10.2319/022011-122.1

Wang, Y., He, S., Yu, L., Li, J., Chen, S., 2011. Accuracy of volumetric measurement of teeth in vivo based on cone beam computer tomography. Orthod. Craniofac. Res. 14, 206–212. https://doi.org/10.1111/j.1601-6343.2011.01525.x

William, P., Henry, F., David, S., 2007. Contemphorary Orthodontics. Mosby Elsevier 762. https://doi.org/10.1007/s13398-014-0173-7.2

Wright, G.J., Coombs, M.C., Hepfer, R.G., Damon, B.J., Bacro, T.H., Lecholop, M.K., Slate, E.H., Yao, H., 2016. Tensile biomechanical properties of human temporomandibular joint disc: Effects of direction, region and sex. J. Biomech. 49, 3762–3769. https://doi.org/10.1016/j.jbiomech.2016.09.033

Xu, B., Wang, Y., Li, Q., 2015. Modeling of damage driven fracture failure of fiber post-restored teeth. J. Mech. Behav. Biomed. Mater. 49, 277–289. https://doi.org/10.1016/j.jmbbm.2015.05.006

Yahata, M., Yamada, K., Hayashi, T., Saito, I., 2009. Unilateral Condylar Bone Deformity and Slope of Articular Eminence Related to Mandibular Asymmetry. CRANIO® 27, 261–267. https://doi.org/10.1179/crn.2009.037

Zhang, Y., Wang, M., Ling, W., 2005. Influence of teeth contact alternation to TMJ stress distribution—three-dimensional finite element study. World J. Model. Simul. 1, 60–64.

Zheng, J., Zhou, Z.R., Zhang, J., Li, H., Yu, H.Y., 2003. On the friction and wear behaviour of human tooth enamel and dentin. Wear 255, 967–974. https://doi.org/10.1016/S0043-1648(03)00079-6

Supplementary material.

Determination of the sagittal midplane

The bone regions obtained from CBCT segmentation is in fact a 3D representation a set of N points $\mathcal{C}_N = \{\boldsymbol{p}_i | 1, \dots, N\}$, where each point i is defined by a vector $\boldsymbol{p}_i = (x_i, y_i, z_i)^T$ in the Cartesian reference system (Ω) of the i-CAT™ CBCT imaging system,.

The determination of the sagittal midplane of $\mathcal{C}_N$ begins centering $\mathcal{C}_N$ database in Ω system through the translation vector $\boldsymbol{v}_t$, which was defined by the centroid of $\mathcal{C}_N$ as $\boldsymbol{v}_t = 1/N \cdot (\sum_{i=1}^{N} x_i, \sum_{i=1}^{N} y_i, \sum_{i=1}^{N} z_i)$, being $\boldsymbol{i}, \boldsymbol{j}$ and $\boldsymbol{k}$ the three unitary and orthogonal vectors of Ω. Then, a Principal Component Analysis (PCA) computed the first three eigenvectors $(\boldsymbol{e}_1, \boldsymbol{e}_2, \boldsymbol{e}_3)$ of $\mathcal{C}_N$, whereof one $(\boldsymbol{e}_\perp)$ was perpendicular to the sagittal plane searched. The direction of this vector was used to a create a mirrored point cloud $\mathcal{C}_N^*$ symmetrical to $\mathcal{C}_N$. After an alignment of $\mathcal{C}_N^*$ to $\mathcal{C}_N$ through Iterative Close Points algorithm [92], both point cloud were joined resulting in an idealized symmetrical point cloud $(\mathcal{C}_N + \mathcal{C}_N^*)$ with an equal distribution of points in both halves. Finally, applying again PCA to $\mathcal{C}_N + \mathcal{C}_N^*$, the direction of $\boldsymbol{e}_\perp$ is updated by compensating the morphological variations caused by the asymmetry.

Manuscript 9: Analysis of temporomandibular joint dysfunction in paediatric patients with unilateral crossbite using automatically generated finite element models

Javier Ortún-Terrazas, José Cegoñino, Edson Illipronti-Filho, Amaya Pérez del Palomar

Abstract

The evaluation of temporomandibular joint (TMJ) dysfunction using finite element models is a time consuming process that requires extensive technical knowledge. We combined a statistical active appearance model with automated modelling algorithms to biomechanically study the relationship between TMJ malformations and dysfunction in radiographs from 20 paediatric patients with unilateral crossbite. A fitting algorithm (fitting error <4%) recognized the TMJ shape and adjusted the dimensions of each patient-specific 2D FE model, which was then used to compute 2 different joint movements. Significant functional differences were observed between the crossbite and non-cross bite sides, and the shape-function relation was verified.

Graphical abstract

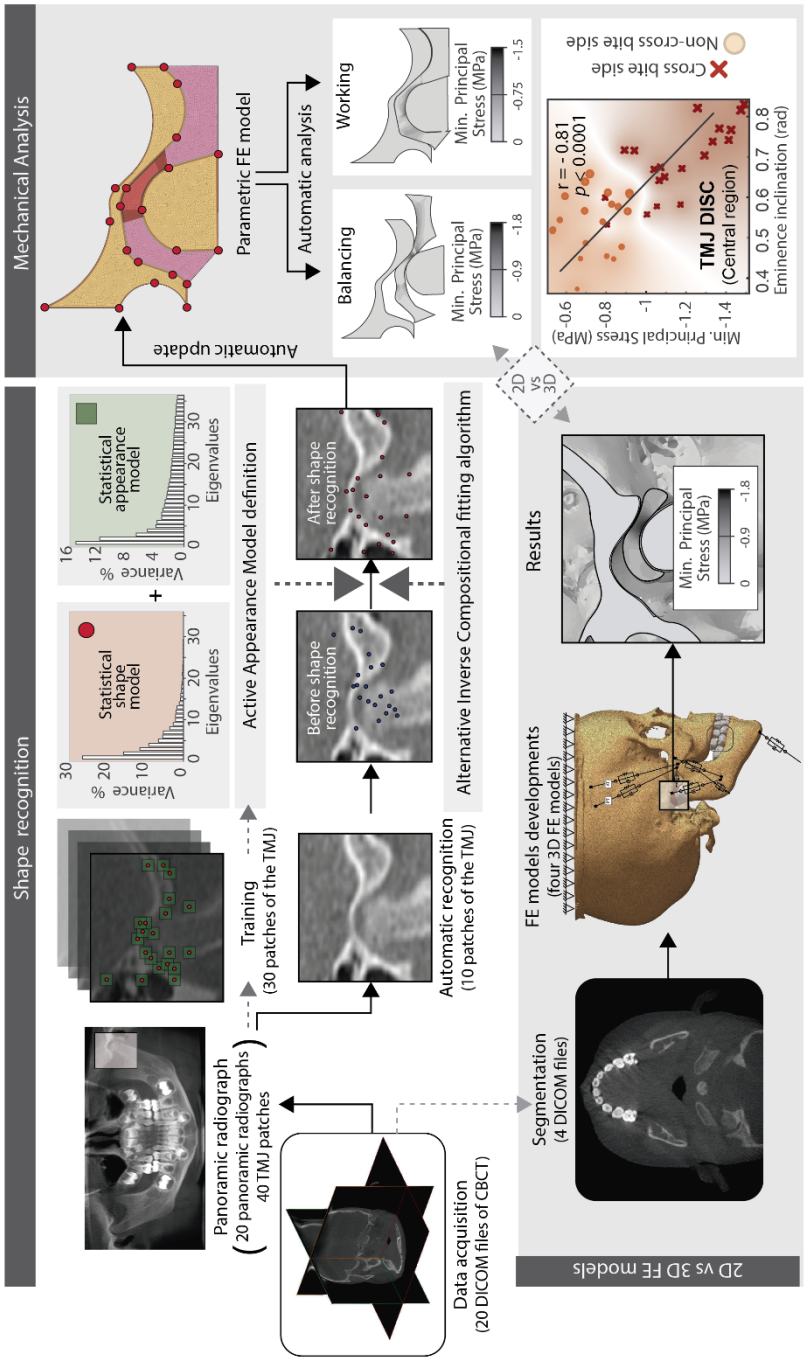

COMPUTER METHODS IN BIOMECHANICS AND BIOMEDICAL ENGINEERING
2020, VOL. 23, NO. 10, 627–641
https://doi.org/10.1080/10255842.2020.1755275

Analysis of temporomandibular joint dysfunction in paediatric patients with unilateral crossbite using automatically generated finite element models

Javier Ortún-Terrazas[a], José Cegoñino[a], Edson Illipronti-Filho[b] and Amaya Pérez del Palomar[a]

[a]Department of Mechanical Engineering, University of Zaragoza, Zaragoza, Spain; [b]Department of Stomatology, University of São Paulo, São Paulo, Brazil

ABSTRACT

The evaluation of temporomandibular joint (TMJ) dysfunction using finite element models is a time consuming process that requires extensive technical knowledge. We combined a statistical active appearance model with automated modelling algorithms to biomechanically study the relationship between TMJ malformations and dysfunction in radiographs from 20 paediatric patients with unilateral crossbite. A fitting algorithm (fitting error $< 4\%$) recognised the TMJ shape and adjusted the dimensions of each patient-specific 2D FE model, which was then used to compute 2 different joint movements. Significant functional differences were observed between the crossbite and non-cross bite sides, and the shape-function relation was verified.

ARTICLE HISTORY
Received 10 July 2019
Accepted 9 April 2020

KEYWORDS
Active appearance model; automatic modelling; finite element analysis; patient-specific model; unilateral crossbite

Introduction

The temporomandibular joint (TMJ) is a complex mandibular articulator composed primarily of the TMJ disc, hyaline cartilages, and the disc attachments. The TMJ mainly develops during paediatric growth in response to the mechanical stimuli produced during chewing by the elevator (masseter, temporalis, medial pterygoid, and superior portion of the lateral pterygoid) and depressor (digastric, geniohyoid, mylohyoid, and the inferior portion of the lateral pterygoid) muscles (Bakke 2006; Chan et al. 2008). Healthy bilateral chewing occurs in an alternating manner: while one condyle compresses the TMJ disc with the mandibular fossa (working movement), the other moves the articular eminence forward (balancing movement) (Palla et al. 2003). While well-balanced chewing ensures proper development of both TMJs, unilateral crossbite (UXB) may result in morphological deformities in the TMJs.

Although the relationship between malformations and dysfunction has not been theoretically explained yet, some rehabilitation approaches (Prakash and Durgesh 2011; Planas 2013; Tsanidis et al. 2016) have empirically identified the morphological changes that take place. All of them agree that these pathological changes are exacerbated during growth, leading to severe temporomandibular joint disorders (TMD) in adulthood.

Early diagnosis could, therefore, help to correct malformations during childhood and avoid surgical procedures later in life (Dimitroulis 2018). For adults, 3D cephalometric images, such as computed tomography (CT) or cone-beam computed tomography (CBCT), are widely used to create 3D finite element (FE) models of the TMJs and evaluate its mechanical imbalance. Unfortunately, during childhood, these 3D approaches are not recommended due to the high doses of radiation involved in CT and CBCT scans (Planas 2013; Thiesen et al. 2015). Besides, the use of 3D FE models from CT or CBCT images is limited during childhood due to the low grey gradient between unmineralized structures at these ages. This fact makes difficult the segmentation procedure, requiring intensive manual work (Ortún-Terrazas et al. 2020). As an alternative, panoramic radiographs or 2D-cephalograms in frontal, lateral, and submento-vertex views are currently used to evaluate the morphological differences between both joints during childhood. Nevertheless, 2D imaging methods provide limited data to the clinician and not allow the

CONTACT Javier Ortún-Terrazas javierortun@unizar.es

Supplemental data for this article is available online at https://doi.org/10.1080/10255842.2020.1755275.

mechanical evaluation of the TMJs' imbalance. Fortunately, new approaches have enabled partial automation of FE model generation through the use of statistical deformable models. Among other applications, statistical deformable models have allowed automation of medical image segmentation (Shan et al. 2006), shape recognition (Dornaika and Ahlberg 2006), and disease diagnosis (Bredbenner et al. 2010).

The active appearance model (AAM) is a statistical deformable model that is often used for shape recognition in planar radiographs because it separately considers variations in shape and appearance (Cootes et al. 1995). The shape recognition process requires a minimisation function, which minimises differences between an input image and the texture instance of a previously developed AAM. The inverse compositional (IC) algorithm is one method commonly used for this fitting process, (Baker and Matthews 2004). However, IC algorithms are highly sensitive to the initialisation step and to texture variations in input and target images. Therefore, it is advisable to use highly-descriptive, dense appearance features to increase data dimensionality and thereby improve recognition accuracy (Antonakos et al. 2015). The most widely used appearance features include histograms of oriented gradients (HOG) (Dalal and Triggs 2005), image gradient orientation kernel (IGO) (Tzimiropoulos et al. 2012), scale-invariant feature transform (SIFT) (Ojala et al. 2001), local binary patterns (Lowe 1999), edge structures (Cootes and Taylor 2001), and Gabor filters (Lee 1996).

The goal of this study was therefore to create a tool for automated generation of planar FE models of the TMJ based on panoramic radiographs to study the relationship between TMJ malformations and UXB in a large, patient-specific dataset.

To this end, we propose a methodology that combines AAMs and automated modelling techniques and that it can be divided in 3 main steps. First, an image recognition algorithm recognises the TMJ shape in an area of a panoramic radiograph using an alternative of the IC algorithm that varies the shape and appearance parameters of a previously trained AAM. Next, the landmarks of the recognised shape are used to construct a parametric FE model using a modelling script. The 2 main TMJ movements (working and balancing) are then automatically computed for each patient-specific 2D model. Additionally, four 3D models of the stomatognathic system of 4 subjects were developed from the CBCT images and the lateral chewing was simulated. Finally, the differences between 2D and 3D modelling are evaluated by comparing the mechanical results produced by the 2D and 3D models of the same patient.

Materials and methods

This section describes the 3 main steps (Figure 1) involved in automating model generation. We first provide a summary of the data acquisition procedure, followed by a description of the AAM and the IC recognition algorithms. An animated presentation of the AAM development and recognition process is shown in the video of the supplementary material. Finally, we describe the 2D FE model in both loading scenarios, the statistical analyses performed, and the development of four 3D FE models in order to validate the 2D results.

Data acquisition

The input data consisted of 20 panoramic radiographs obtained from CBCT images of paediatric subjects (9 males and 11 females; mean age 7.9 and 8.2 years, respectively) in mixed dentition phase with UXB. The images were obtained in maximum intercuspation through the same CBCT scanning system (i-CAT^{TM}; Imaging Sciences International, Hatfield, PA, USA), with a field of view (FOV) of 13 cm × 17 cm, a pulse exposure acquisition time of 5–26 s, 14-bit greyscale, and 16,384 shades of grey. The focal point was at 0.5 m with a 0.3-mm voxel. The study was approved by the Research Ethics Committee of the School of Dentistry, University of São Paulo (200/06 and 16/2008). More details can be found in Illipronti-Filho et al. (2015). Data were converted to DICOM format and the panoramic views were extracted by iCAT Vision software (Imaging Sciences International Inc., Hatfield, PA, USA). The radiographs were divided into 2 groups (15 and 5 images) for the AAM training and the IC testing processes. From each radiograph, 2 patch images of both TMJs were extracted and the cross bite side TMJ was identified for subsequent analysis of the results.

Active appearance model with HOG feature

The AAM was defined in an open source code (Alabort-i-Medina et al. 2014) written in Python (Python 2.7.3, Python Software Foundation) and was run in a Windows-based personal computer with an Intel Core i7-6700 3.40 GHz processor and 32 Gb of RAM. The description of the AAM was computed in 86.07 s and the AAM was composed of 3 different

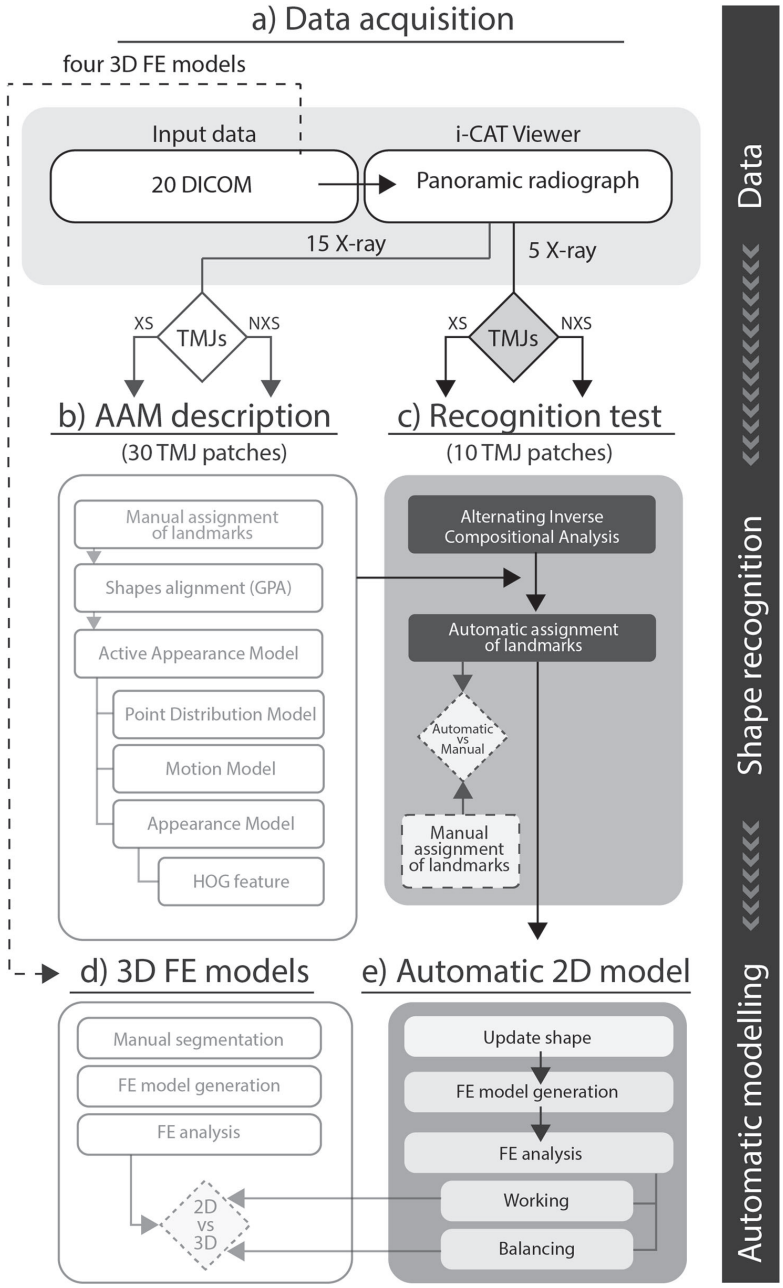

Figure 1. Flowchart showing the stages of the automated generation of FE models from panoramic radiographs: (a) data acquisition; (b) AAM description; (c) shape recognition in the area of the radiograph corresponding to the TMJ; (d) generation of the 3D FE model; and (e) automated 2D model generation. Diamonds with discontinuous lines represent the evaluation of image recognition according to manual segmentation and the differences between the 2D and 3D approaches (XS, cross bite side; NXS, non-cross bite side).

statistical deformable models (shape, motion, and appearance models), which are explained below:

Shape

A radiologist with expertise in TMD diagnosis located 21 landmarks (i points) grouped in 2 sets (16 and 5 points), corresponding to TMJ structures and the condyle, respectively (Figure 2a). Mathematically, each TMJ shape, s, was defined by the Cartesian coordinates of the i points as follows:

$$s = (x_1, y_1, x_2, y_2, \ldots \; x_i, y_i)^T \tag{1}$$

To align and normalise all shapes, generalised Procrustes analysis (GPA) (Figure 2b) was performed. Next, the statistical shape model or point distribution model (PDM) was computed by applying principal component analysis (PCA) to the dataset. Therefore, any shape (s) could be expressed as mean shape $\bar{s}$ plus a linear combination of n shape vectors, s_i, with the shape parameters p_i :

$$s = \bar{s} + \sum_{i=1}^{n} p_i s_i \tag{2}$$

Motion

The role of the motion model $\mathcal{W}(\mathbf{x}, p)$ was to extrapolate the position of all pixel positions $\mathbf{x}$ lying inside $\bar{s}$ from the template image to a deformable shape s generated by the combination of p parameters. The transformation was based on the relative position of i landmarks with respect to the sparse set of landmarks that defines the mean shape.

Appearance

The appearance model was generated by warping the original images onto the mean shape $\bar{s}$ using the previously defined motion model, $\mathcal{W}(\mathbf{x}, p)$. As described for the PDM, PCA was performed to define any appearance $A(\mathbf{x})$ of a set of pixels $\mathbf{x}$ as a mean appearance $\overline{A}(\mathbf{x})$ plus a linear combination of m appearance images, $A_i(\mathbf{x})$, with the appearance parameters c_i :

$$A(\mathbf{x}) = \overline{A}(\mathbf{x}) + \sum_{i=1}^{m} c_i A_i(\mathbf{x}) \tag{3}$$

HOG feature

After evaluation of the shape recognition results using different highly-descriptive, dense appearance features (Figure 3), the HOG feature was selected. The HOG feature clustered the gradient orientations into 9 bins (N_{bins}) for each cell of 8×8 pixels, and the cells were grouped in 2 blocks (N_{block}) of 2×2 cells for normalisation of the gradients. Therefore, the HOG description dimension ($D = N_{bins} N_{block}{}^2$) consisted of 36 channels. The HOG feature transformed each 2D image (t) with size $H \times W$ into a multi-channel image using the feature extraction function $\mathcal{F}: \mathbb{R}^{H \times W} \rightarrow \mathbb{R}^{H \times W \times D}$.

Shape recognition algorithm

The shape recognition process was carried out using a minimisation process to fit the AAM to the input image (t). When the AAM is defined by highly-descriptive, dense appearance features, it is recommended to use the alternating inverse compositional (AIC) alignment algorithm (Antonakos et al. 2015). Like the IC algorithm, the aim of AIC algorithm is to find the corresponding N_A eigen texture in the subspace U_A ($U_A \in \mathbb{R}^{L_A \times N_A}$) of t, modifying parameters p and c in 2 separate minimisation problems, one for shape ($p \leftarrow p + \Delta p$) and another for appearance ($c \leftarrow c + \Delta c$). This iterative search algorithm can be mathematically expressed as minimising the following cost functions:

$$\begin{cases} \underset{\Delta p}{argmin} \left|\left| \mathcal{F}\left(t\left(\mathcal{W}(p)\right)\right) - \mathcal{F}\left(a_c(\mathcal{W}(\Delta p))\right) \right|\right|^2_{I - U_A U_A^T} \\ \underset{\Delta c}{argmin} \left|\left| \mathcal{F}\left(t\left(\mathcal{W}(p)\right)\right) - \mathcal{F}\left(a_{c+\Delta c}(\mathcal{W}(\Delta p))\right) \right|\right|^2 \end{cases} \tag{4}$$

where $\mathcal{F}(a_{c+\Delta c}(\mathcal{W}(\Delta p))) = \mathcal{F}(\bar{a}(\mathcal{W}(\Delta p))) + U_A \mathcal{F}(\mathcal{W}(\Delta p))(c + \Delta c)$ (Gross et al. 2005). Therefore, $\mathcal{F}(a_{c+\Delta c}(\mathcal{W}(\Delta p)))$ can be expressed by a first term of the mean appearance vector approximation and a second term of the linearised basis (Antonakos et al. 2015) of the U_A subspace of the AAM (where N_A and L_A are the eigen textures and the number of pixels inside $\bar{s}$, respectively). A fitting process of 100 iterations was executed for each of the 10 patches tested and was repeated 5 times to ensure model stabilisation. The fitting process was run on the same computer used for the AAM development and was completed after an average time of 43.89 s. Figure C1 of Appendix C in the supplementary material displays the landmarks paths throughout the recognition process. As described for the training set, an expert clinician identified landmarks for subsequent evaluation of recognition accuracy.

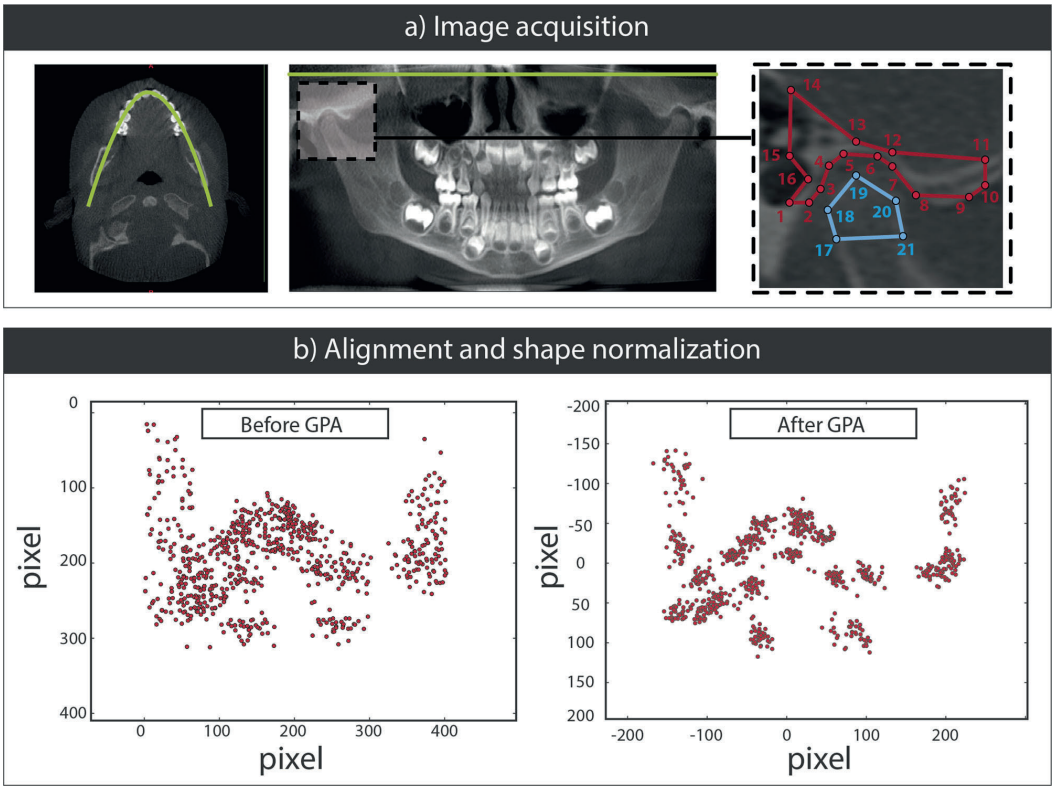

Figure 2. (a) From left to right: coronal slice of the CBCT scan, panoramic radiograph, and patch of the TMJ with landmarks. The unfold plane of the panoramic radiograph was defined as the midplane of the mandibular ramus thickness (green line). (b) Landmarks of the training dataset before (left) and after (right) shape normalisation by GPA.

Automated generation of a 2D finite element model

A script was written in Python to update the shape of a parametric CAD model in Abaqus commercial software (Abaqus 6.14, Simulia, Rhode Island, USA) using the recognised landmarks. This parametric model mimics the TMJ shape proposed by DeVocht and coworkers (DeVocht et al. 1996) using landmarks located in key morphological regions (Figure 4a) such as the articular eminence, the condylar head, and the TMJ disc space. The model consists of 6 parts (Figure 4a), some of which (TMJ disc and cartilage) were subdivided into 3 portions (anterior, central, and posterior) owing to the different mechanical behaviours of each region (Kim et al. 2003; Singh and Detamore 2008). For more details about the parametric model development, we recommend reading Appendix A of the supplementary material.

In setting the boundary conditions, the nodes of the anterior and posterior slices of the temporal bone were fixed and the contact between the TMJ disc and the cartilage was defined by a tangential friction coefficient of 0.015 (Tanaka et al. 2004) using a penalty contact formulation. The automatic modelling script ran 2 computational analyses of 2.5 s for each patient-specific shape to study chewing activity: in the first analysis the condyle compressed the TMJ disc with the mandibular fossa (working activity) and in the second the condyle moved along the articular eminence (balancing). The FE model was subjected to contractile forces produced by the connector's elements (CONN3D2-type element in Abaqus) that mimic the chewing muscles for both movements. The active, passive, and damping responses of each chewing muscle were defined following the procedure described in Appendix A of the supplementary material; whose parameters are likewise summarised in Table A2 of the same appendix.

In analysing the data produced, we assessed 16 mechanical variables (Table 1) and 3 geometrical variables, values of which were obtained from a script

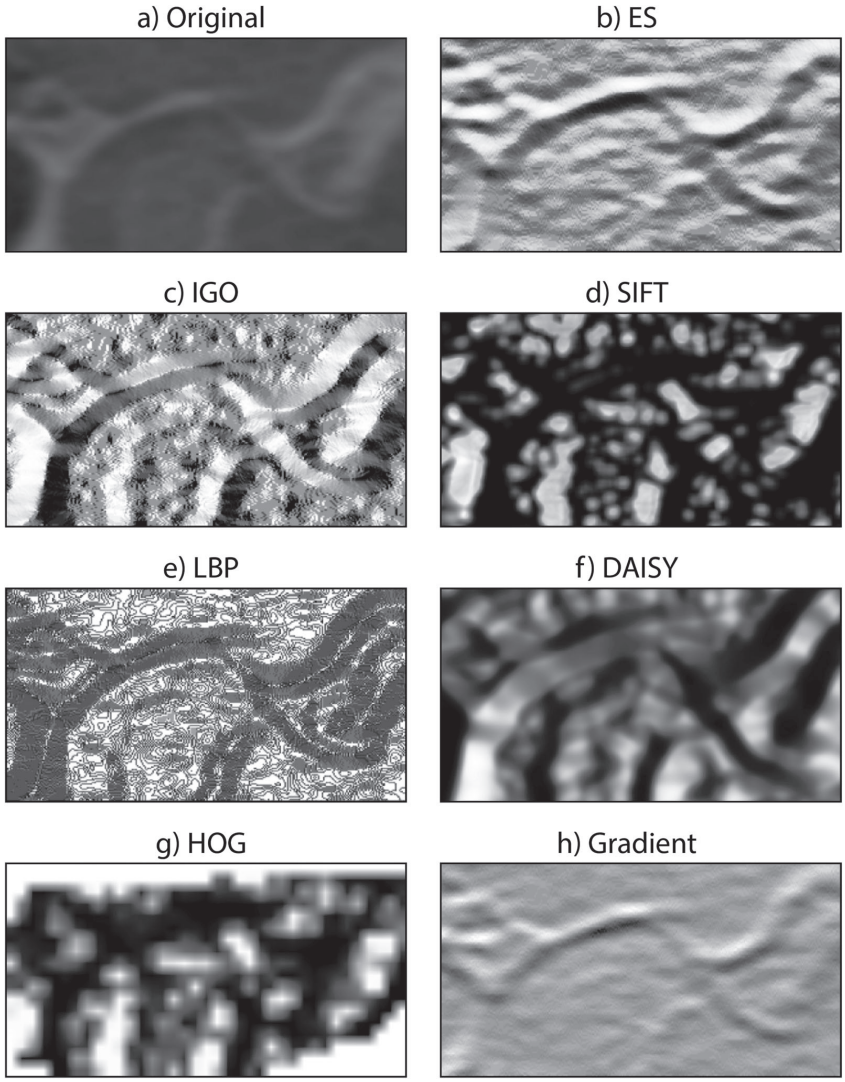

Figure 3. (a) Patch of an original panoramic radiograph used as a template image to show the results of application of the following highly-descriptive, dense appearance features: (b) edge structures; (c) image gradient orientation kernel; (d) scale-invariant feature transform; (f) DAISY; (g) histograms of oriented gradients; (h) contour gradients.

written in Python. Based on the labelling of the cross bite side, the results were grouped in 2 sets depending on whether they were derived from the cross bite side (XS) or the non-cross bite side (NXS). A Mann-Whitney U-test was used to assess geometrical and mechanical differences between the TMJs on each side. The null hypothesis (i.e., no significant differences between the XS and NXS for a given variable) was accepted at p-values ≤ 0.05. Pearson's correlation coefficient, r, and its associated p-value were computed to assess relationships between the different variables for both activities. The null hypothesis (a significant association between 2 variables) was accepted for p-values ≤ 0.05.

3D finite element models

Four CBCT datasets randomly chosen from the input data were also used to develop four complete 3D models for each patient. Although each dataset was previously segmented to identify the compact bony structures using a threshold level in Mimics

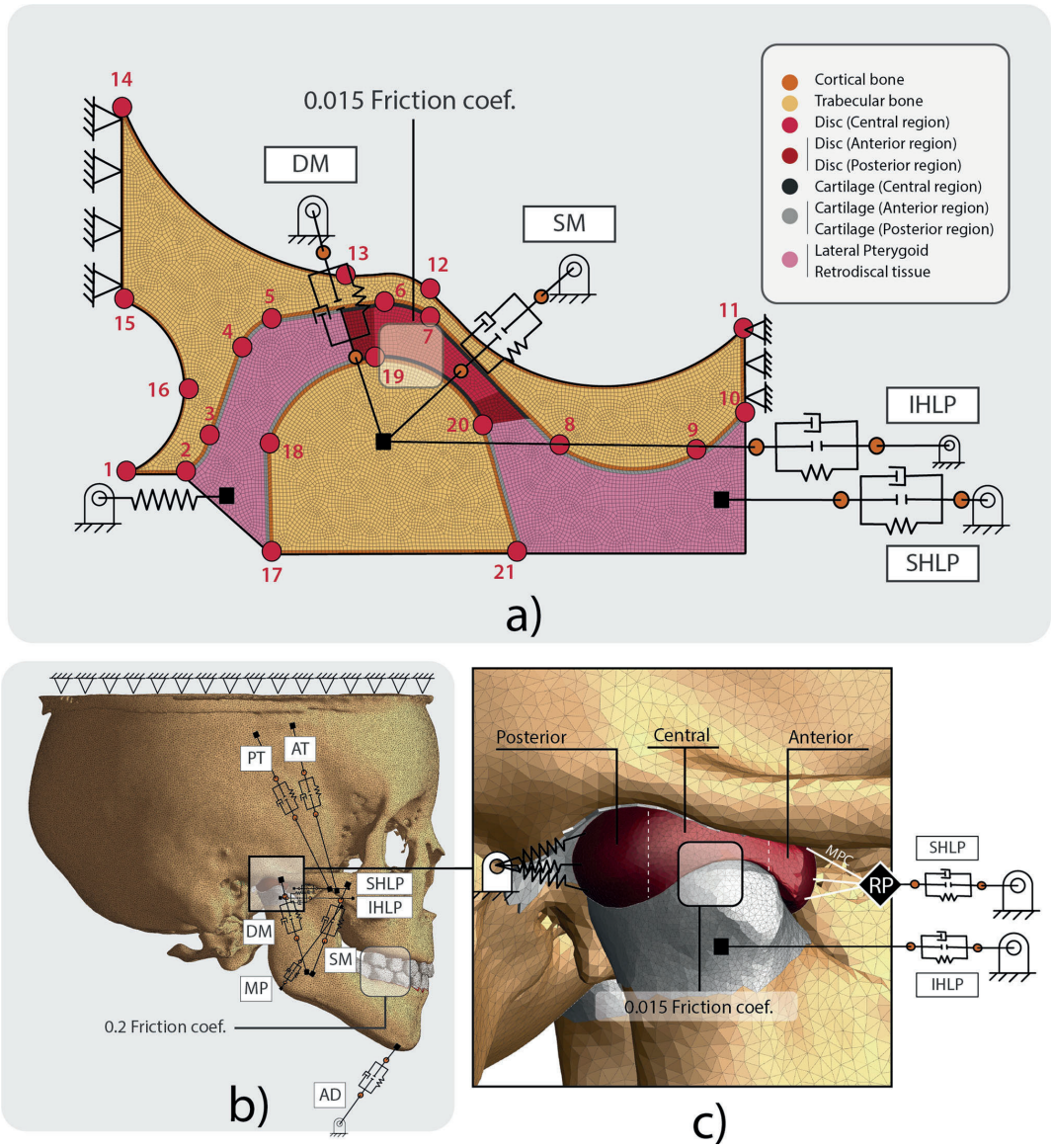

Figure 4. (a) 2D FE model of TMJ shape defined by the 21 landmarks (red points) and the applied boundary conditions. (b) 3D FE model generated manually from CBCT images and the boundary conditions applied. (c) Detail of the TMJ of the 3D FE model. (SM, superficial masseter; DM, deep masseter; SHLP, superior lateral pterygoid; IHLP, inferior lateral pterygoid; AT, anterior temporalis; PT, posterior temporalis; MP, medial pterygoid; AD, anterior depressor muscles; RP, reference point; MPC, multi-point constraint).

commercial software (Mimics, v.19.; Materialise, Leuven, Belgium), manual segmentation was required for cartilaginous and less dense bone regions. The mechanical properties, boundary conditions, muscle modelling, and disc friction coefficient were defined as in the 2D model (Figure 4b,c) and are also detailed in Appendix A of the supplemental material. Although 2 analyses were executed for each 2D model, only one was required in the 3D approach: while one condyle compresses the disc with the

Table 1. Geometrical and mechanical variables used in assessing differences between the XS (cross bite side) and NXS (non-cross bite side) groups during the two main TMJ movements (balancing and working). Data are presented as the mean, standard deviation (SD), and *p*-value (Mann-Whitney U-test). $^*p < 0.05$.

Geometrical variables

Group	XS (n = 20)		NXS (n = 20)		
Variable	Mean	SD	Mean	SD	p value
Condyle width (mm)	9.06	1.31	7.96	1.22	0.0132*
Eminence inclination (rad)	0.70	0.07	0.53	0.07	<0.0001*
Temporal area (mm^2)	52.02	11.72	55.62	14.75	0.4135

Mechanical variables

Activity	Balancing					Working				
Group	XS (n = 20)		NXS (n = 20)			XS (n = 20)		NXS (n = 20)		
Variable	Mean	SD	Mean	SD	*p* value	Mean	SD	Mean	SD	*p* value
CTB -Min. Prin. Stress (MPa)	−6.35	3.17	−6.03	2.35	0.6849	−2.64	1.29	−2.02	1.08	0.1572
CTB -Max. Prin. Stress (MPa)	0.23	0.51	0.14	0.22	0.4247	0.17	0.27	0.04	0.05	0.0110*
CCB -Min. Prin. Stress (MPa)	−6.27	2.44	−6.44	2.08	0.8076	−2.80	1.15	−2.41	1.33	0.3791
CCB -Max. Prin. Stress (MPa)	0.16	0.18	0.17	0.25	0.4901	0.08	0.11	0.07	0.09	0.5517
TC (Ant) - Min. Prin. Stress (MPa)	−4.27	1.84	−4.14	1.53	0.5789	−0.05	0.05	−0.05	0.07	0.3575
TC (Cent) - Min. Prin. Stress (MPa)	−2.45	0.74	−2.38	0.77	0.7604	−2.18	1.04	−1.74	0.88	0.2118
TC (Post) - Min. Prin. Stress (MPa)	−0.05	0.02	−0.05	0.02	0.8603	−0.88	0.53	−0.68	0.44	0.2475
CC (Ant) - Min. Prin. Stress (MPa)	−0.98	0.76	−0.74	0.29	0.9138	−1.61	0.73	−1.37	0.83	0.3975
CC (Cent) - Min. Prin. Stress (MPa)	−4.43	1.43	−4.56	1.13	0.9396	−2.36	0.92	−1.97	1.00	0.2486
CC (Post) - Min. Prin. Stress (MPa)	0.00	0.00	−0.05	0.12	0.6948	−1.66	0.69	−1.30	0.71	0.0443*
TMJ disc (Ant) - Min. Prin. Stress (MPa)	−1.63	1.13	−1.68	1.55	0.8075	−0.61	0.39	−0.40	0.30	0.1363
TMJ disc (Cent) - Min. Prin. Stress (MPa)	−3.70	2.35	−3.46	2.02	0.6747	−1.16	0.20	−0.76	0.13	<0.0001*
TMJ disc (Post) - Min. Prin. Stress (MPa)	−0.05	0.02	−0.05	0.02	1.0000	−0.53	0.34	−0.35	0.25	0.0961
TMJ disc (Ant) - Contact Press. (MPa)	5.47	1.87	3.82	1.26	0.0080*	2.45	1.15	1.88	1.15	0.1293
TMJ disc (Cent) - Contact Press. (MPa)	4.88	2.35	4.23	1.81	0.4092	3.45	1.92	2.46	1.33	0.0979
TMJ disc (Post) - Contact Press. (MPa)	0.01	0.01	0.05	0.12	0.3646	2.92	1.72	2.12	1.12	0.2231

Note: CTB: Cortical portion of the temporal bone; CCB: Cortical portion of the condyle; TC: Temporal cartilage; CC: Condylar cartilage; Ant: Anterior region; Cent: Central region; Post: Posterior region; Min. Prin. Stress: Minimum Principal Stress; Max. Prin. Stress: Maximum Principal Stress; Contact. Press: Contact pressure
Condyle width: distance between landmarks 18 and 20.
Eminence inclination: slope of the line drawn between landmarks 7 and 8.
Temporal area: area enclosed between landmarks 7–12.

mandibular fossa (condyle of the working side), the other moves the articular eminence forward (condyle of the balancing side).

Results

Evaluation of the 2D approach

First, we compared the results of accurate 3D finite element models of the TMJ with those of the corresponding automatically generated 2D finite element model for patients S1 to S4. Within all stress components, the minimum principal stress in the solid phase of the TMJ discs was studied since compressive efforts were more significative than shear or tensile loads at both movements. Figure 5a,b show the minimum principal stress distribution whose mean and standard deviation values are summarised in Table B1 of the supplementary material. Comparison of both movements shows that balancing movement generated higher stresses in the disc than working movement (Figure 5c). This overloading resulted in greater absolute error between the two approaches for the balancing movement, as it can be shown in Table B1 of the appendixes, supplementary material. Regardless, the results demonstrate good correspondence between the TMJ disc stresses determined using the two approaches, with a mean relative error of around 14%.

AAM and AIC alignment algorithm

The statistical models of TMJ shape and appearance are described by a series of principal variation components, which are formulated in Equations (2) and (3), respectively (Figure 6a). By sorting the values of the covariance matrix in descending order, the principal variation components are frequently renamed as principal variation modes, since the first principal components are the most representative modes of variation. The principal modes of the PDM characterised the anatomic shape variability of the TMJ, while the principal modes of the AAM represented the texture variations of the images. Therefore, an AAM with 5 principal modes accounted for over 70% of the total shape variability of the PDM. To explain 98% of variation in shape and appearance, 14 and 29 principal

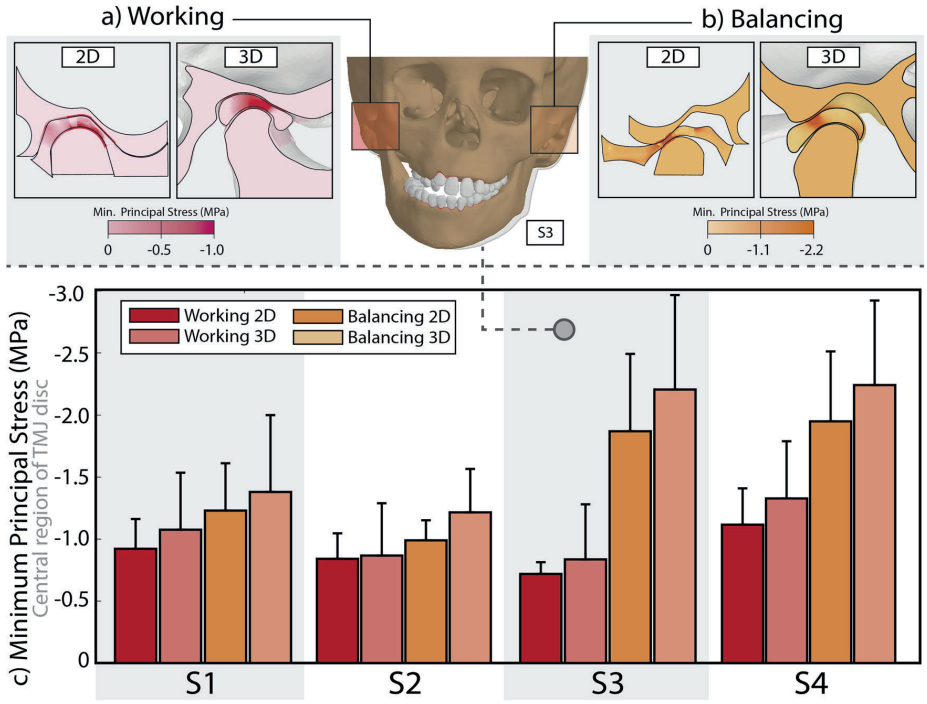

Figure 5. Minimum principal stress distribution in the TMJ during unilateral chewing on the (a) working side and (b) balancing side (left: 2D model results; right: 3D model results). (c) Mean and SD deviation of the minimum principal stresses in the central region of the TMJ disc of 4 subjects (S1–S4) during working (red and pink bars) and balancing (orange and yellow bars) movements as computed using 2D or 3D FE models. *Note: mean and standard deviation (SD) values are summarised in Table B1 in Appendix B, supplementary material.

modes were required, respectively. An animated representation of the principal variation modes of shape and appearance is shown in the supplementary material video. Although some studies (Sarkalkan, Weinans, et al. 2014; Hollenbeck et al. 2018) have reported different relationships between principal variation modes and anatomical references in other joints, in our study it was difficult to establish a relationship due to the high degree of variability in the sample's shape.

The AIC fitting algorithm modified the c_i and p_i parameters of the statistical AAM in order to minimise differences with respect to the input image. Figure C1 of the supplementary material shows the paths of the landmarks throughout the fitting procedure. First, the mean shape of the PDM was randomly located (Figure 6b). Next, the AIC algorithm gradually modified the AAM parameters, resulting in displacement of the landmarks (Figure 6c). The accuracy of the search was determined by calculating the point-to-point distance error for each landmark on the PDM, taking manually annotated landmarks as the true position (Figure 6c). In most cases, fitting stabilised by the 50th iteration, with fitting errors <10%. After the 50th of 100 iterations, the algorithm significantly altered landmark positions to ensure that the local optimum did not coincide with the global optimum. Fitting was quite stable for 75 iterations (fitting error <4%) and repetition of the algorithm revealed no significant differences for a single image (fitting error, 3.3–4.1%).

Mechanical analysis

Results were expressed as the mean value and the standard deviation (SD) for each of the different geometrical variables (condyle width, eminence inclination, and temporal area) and the mechanical variables separated by group (XS and NXS) and activity (working and balancing) (Table 1). Figure 7 shows the values for certain variables for which differences between the two sides were observed. From a morphological point of view, the mean width of the condyle and the inclination of the articular eminence were significantly greater in the XS group

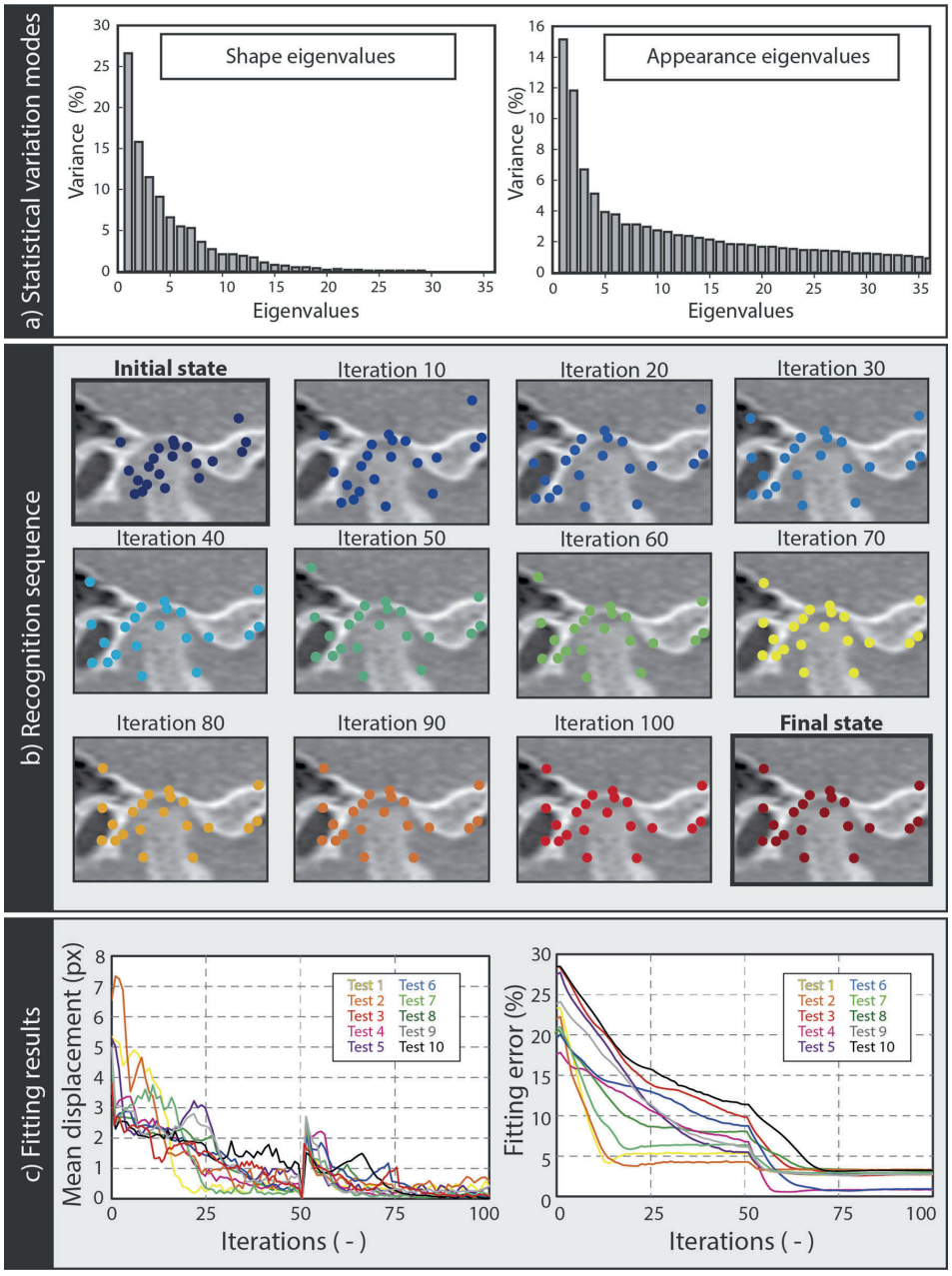

Figure 6. (a) Left, the percentage of shape variation described by the principal shape variation modes. Right, the percentage of appearance variation described by the principal appearance variation modes. (b) TMJ shape recognition sequence for 100 iterations. (c) Left, mean displacement in pixels (px) of the landmarks in each iteration. Right, shape model residual fitting errors (point-to-line, px) when refitting the shape model to the manually annotated contour. *Note: the landmark traces are shown in Figure C1 in Appendix C, supplementary material and in the supplementary video.

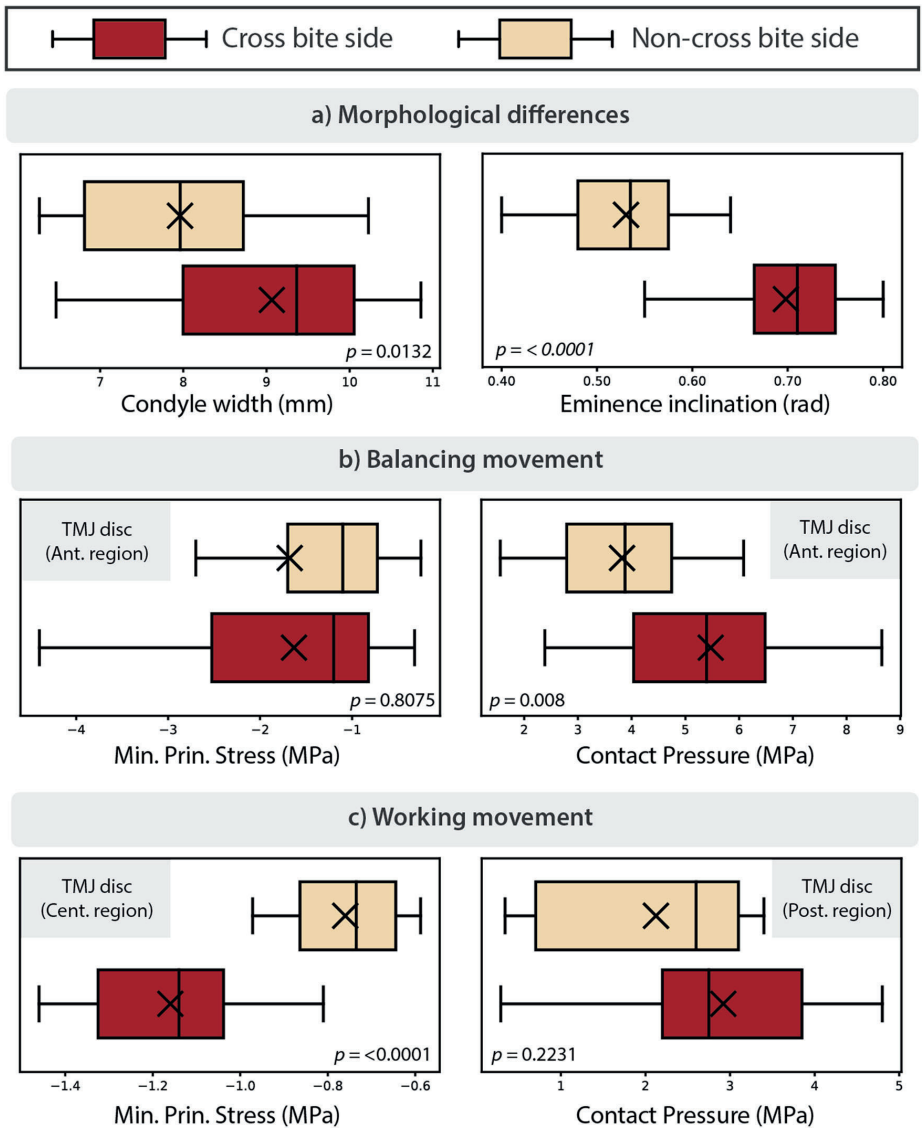

Figure 7. Boxplot for each group (red: cross bite side; yellow: non-cross bite side) indicating the median, 25th and 75th percentiles (box), and range of measurements (whiskers) for (a) geometrical variables and mechanical variables during (b) balancing and (c) working movement.

(9.06 ± 1.31 mm and 0.70 ± 0.07 rad) than in the NXS group (7.96 ± 1.22 mm and 0.53 ± 0.07 rad) (Figure 7a). Biomechanically, the contact pressure and the compressive stress (minimal principal stress) values in the anterior band of the XS discs were higher than those in the same region of the NXS discs (Figure 7b) during balancing movement. Likewise, during working movement, compressive stress values were significantly higher in the central region of the XS discs than that of NXS discs, in which the posterior band was more loaded (Figure 7c). Pearson's correlation coefficients and associated p values for all the variables in both activities are summarised in tables of Appendix D, supplementary material, which are graphically displayed in Figure 8a of the manuscript. The results of the Mann-Whitney U-test and Pearson's correlation analysis revealed that articular eminence inclination differed significantly between

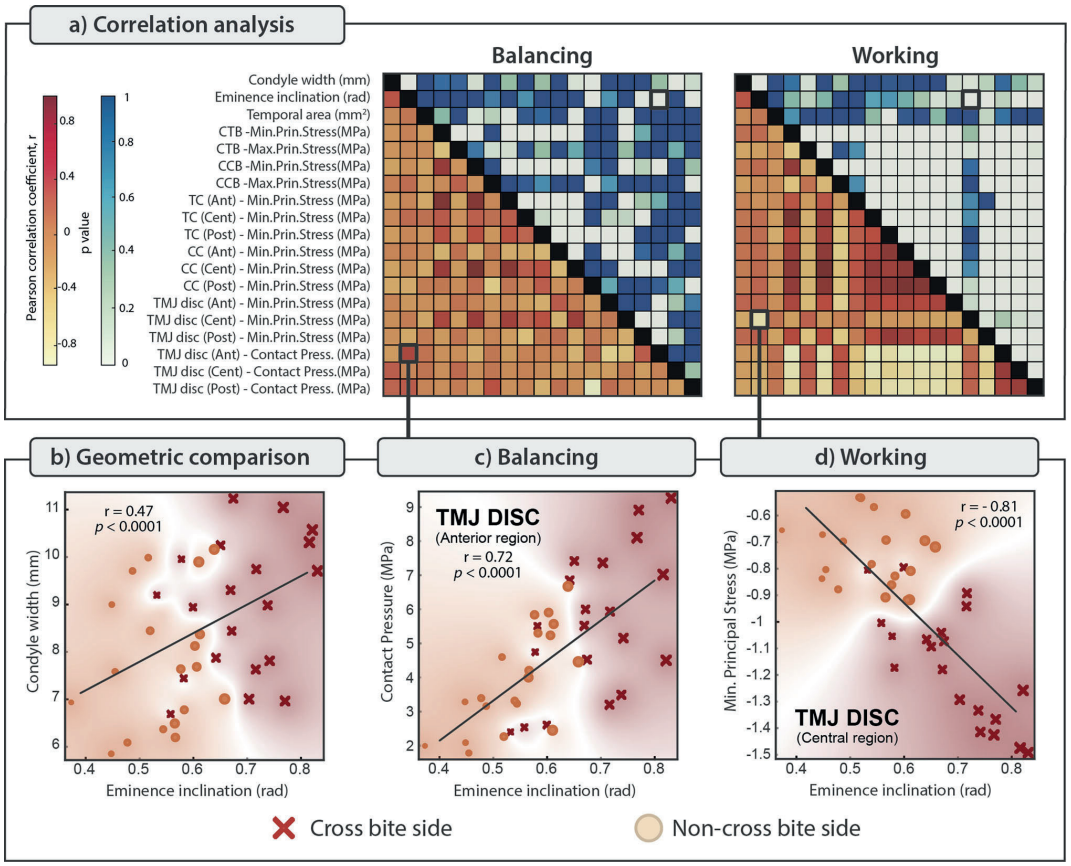

Figure 8. (a) Correlation matrix based on Pearson's correlation coefficient, r, and its associated probabilistic *p*-value. (b) Correlation between condyle width and inclination of the articular eminence. (c) Correlation between the contact pressure on the anterior region of the TMJ disc and the inclination of the articular eminence. (d) Correlation between the minimum principal stress of the central region of the TMJ disc and the inclination of the articular eminence. *Note: r and *p* values are summarised in Tables D1 and D2 in Appendix D, supplementary material.

groups (XS and NXS) and was significantly correlated with certain mechanical variables for both movements (Figure 8c,d). Therefore, we used this variable as an index of joint dysfunction in order to evaluate our results. Conversely, we observed no significant association (Figure 8b) between this variable and condyle width (r = 0.47) that would allow us to propose a geometric relationship.

Discussion

Early diagnosis of TMD would allow planning of paediatric treatments and help avoid complex or surgical procedures in adulthood. However, functional 3D evaluation of the TMJ is hindered by 2 key limitations. First, the generation of computational models of the TMJ of children requires a large amount of manual work owing to the incomplete ossification of the bones, complicating patient-specific analyses. Second, 3D scans are not recommended for paediatric patients owing to the high radiation doses involved (De Felice et al. 2019). Therefore, diagnosis is often based on panoramic radiographs, which provide clinicians with limited data, and do not allow mechanical evaluation of the TMJ. We developed an automated tool for the generation of computational models of the TMJ through shape recognition using panoramic radiographs to facilitate the study, diagnosis, and treatment of TMDs during childhood. Specifically, we used this tool to study TMJ malformations due to UXB in paediatric patients.

The differences between 2D and 3D approaches were evaluated for 4 paediatric patients because 2D models assume a more simplified geometry than 3D

models generated using CT or CBCT images. The results (Figure 5c) revealed marked similarity between both approaches, with a mean relative error of 13%. Among other factors, this deviation may be due to the geometric simplification of the condylar head' shape or not considering the occlusion's role in the condyle's placement in the 2D model. For instance, during working movement, the occlusion's effect was not considered since the initial position of our models is already occluded and therefore, the condyles' upward movement is mainly induced by the masseter muscles' activities. At the same time, we consider that occlusal contacts on the balancing side hardly have any impact on the joint movement of this side, whose anterior movement is mainly guided by the temporal eminence and promoted by the action of the lateral pterygoid muscle. Biomechanically, the positive absolute error values (Appendix B, Table B1, supplementary material) suggest that during both working and balancing activity the solid phase of the TMJ disc is less loaded in the 2D than the 3D approach. The low load state of the solid phase in the 2D approach may be due to the differing degrees of freedoms between the two models. In the 3D approach, the fluid can flow in all directions, while in the 2D approach the fluid cannot drain perpendicular to the plane of the 2D model. This may explain the less compressible response of the TMJ disc in the 2D simulations (Figure 5c), and the resulting decrease in the stress supported by the solid phase.

The results shown in Figure 6 demonstrate the accuracy of the shape recognition algorithm and validate the AAM and AIC fitting algorithm for the TMJ shape recognition. The 10 fitting tests performed to validate the algorithm produced a fitting error (<4%) that was slightly greater than the intra-observer variability recorded during manual segmentation. Moreover, the algorithm showed good repeatability for each image, producing results consistent with those of other studies studies (Roberts et al. 2010; Roberts et al. 2012; Sarkalkan, Waarsing, et al. 2014) in which a similar 2D recognition technique was applied to other joints. It should be noted that automated segmentation in paediatric patients is more difficult owing to the incomplete ossification of bones in these individuals. However, the use of HOG features, a novel aspect of this study, improves the convergence of the fitting process.

The manually defined landmarks and those automatically detected by the AIC alignment algorithm were used to adapt the dimensions of our parametric FE model. We observed a significant difference ($p < 0.05$) between the XS and NXS groups in the slope of the articular eminence, which was more pronounced in the former group (Figure 7a). Our findings are consistent with those of other researchers (Pirttiniemi et al. 1990; Wohlberg et al. 2012) who empirically detected an increase in the slope of the articular eminence in the XS group. We also found that the condyle width was significantly greater in the XS than the NXS group, in agreement with the findings of Veli and coworkers (Veli et al. 2011). However, in contrast to the findings of previous empirical studies (Prakash and Durgesh 2011; Planas 2013; Tsanidis et al. 2016), we observed no significant relationship between eminence slope and condyle head width, likely due to the incomplete development of the condyloid process in our patients (Karlo et al. 2010).

From a biomechanical point of view, the compressive stresses were more uniformly distributed throughout the disc during working movement than balancing movement, mainly due to the key role of the intra-articular fluid component. During balancing movement contact pressures were higher in the anterior and central regions of the disc in the XS and NXS groups, respectively. Analysis of the correlation between morpho-functional variables revealed a negative regression between the compressive stress magnitude in the central region of the disc and the condylar head width (Figure 8a). This finding may numerically reflect the increase in condylar head volume caused by bone mechanical adaptation. During balancing movement, we observed a positive association between articular eminence slope and compressive stress in the anterior band of the disc. This observation may confirm a previously proposed hypothesis (Widman 1988; Pirttiniemi et al. 1990; Mimura and Deguchi 1994; Wohlberg et al. 2012) that speculated about an association between a steeper articular eminence slope and a greater mechanical stimulus on the XS. Conversely, the less steep slope of the articular eminence on the NXS may be a consequence of the shear stimulus that occurs on this side (the usual balancing side). Our findings thus reject the null hypothesis that TMJ malformations are unrelated to TMJ dysfunction.

Limitations

Despite the important implications of this study, several limitations should be noted. First, the simplified 2D FE model did not mirror the mechanical environment as accurately as 3D approaches where, for

instance, the key role of occlusal contacts in mandible positioning is considered. Therefore, our results must be interpreted with caution and only qualitative differences between XS and NXS should be considered. Furthermore, soft tissue shape and mechanical behaviour may differ significantly between subjects. Finally, these findings apply specifically to 6–12-year-old patients with UXB and cannot be extrapolated to all TMD patients.

Conclusion

We have developed a computational tool for automated generation of 2D FE models of the TMJ based on panoramic radiographs and describe its use to study the shape-function relationship of the TMJ in paediatric patients with UXB. Within the limitations of this study, the following conclusions can be drawn:

- Statistical deformable models are powerful tools for the mechanical study of the TMJ, allowing tailoring of clinical computational studies to the specific shape of each patient.
- Although 2D models revealed several qualitative differences between the TMJs of opposing jaws, these models cannot be recommended for precise measurement of mechanical variables (range of error, 3–19%).
- The anterior disc band of the cross bite side was more loaded than that of the non-cross bite side. This may result in functional limitation of the joint on the crossbite side.
- There is a significant relationship between the width of the condyle and its functional activity on the usual working side (i.e. the cross bite side).
- The articular eminence slope of the cross bite side is greater than that of the non-cross bite side and is significantly associated with a decrease in balancing activity.

In summary, the proposed methodology was successfully applied in orthopaedics, providing helpful results to understand the influence of TMJ development in biomechanical function and further TMDs. Nonetheless, this methodology could be also applied in many other areas, such as anatomy and medicine, to investigate the effect of bone deformities in the mechanical environment or help in the diagnosis and treatment of several pathologies. For all these applications, further research effort will be required to increase the number of training examples, improve the accuracy of new statistical shape and appearance models, and allow patient-specific approaches.

Disclosure statement

No potential conflict of interest was reported by the authors.

Funding

This work was supported by the Spanish Ministry of Economy and Competitiveness (project DPI 2016-79302-R), the European Social Funds and Regional Government of Aragon (grant 2016/20) and Ibercaja- Cai Foundation (grant IT 4/18).

References

Alabort-I-Medina J, Antonakos E, Booth J, Snape P, Zafeiriou S. 2014. Menp. In: Proc ACM Int Conf Multimed - MM '14. New York (NY): ACM Press; p. 679–682.

Antonakos E, Alabort-I-Medina J, Tzimiropoulos G, Zafeiriou SP. 2015. Feature-based Lucas–Kanade and active appearance models. IEEE Trans Image Process. 24(9):2617–2632.

Baker S, Matthews I. 2004. Lucas-Kanade 20 years on: a unifying framework. Int J Comput Vis. 56(3):221–255.

Bakke M. 2006. Bite force and occlusion. Semin Orthod. 12(2):120–126.

Bredbenner TL, Eliason TD, Potter RS, Mason RL, Havill LM, Nicolella DP. 2010. Statistical shape modeling describes variation in tibia and femur surface geometry between control and Incidence groups from the Osteoarthritis Initiative database. J Biomech. 43(9): 1780–1786.

Chan HJ, Woods M, Stella D. 2008. Mandibular muscle morphology in children with different vertical facial patterns: a 3-dimensional computed tomography study. Am J Orthod Dentofac Orthop. 133:1–13.

Cootes TF, Taylor CJ. 2001. On representing edge structure for model matching. In: Proc 2001 IEEE Comput Soc Conf Comput Vis Pattern Recognition CVPR 2001. Vol. 1. Kauai (HI): IEEE Comput. Soc; p. I-1114–I-1119.

Cootes TF, Taylor CJ, Cooper DH, Graham J. 1995. Active shape models-their training and application. Comput Vis Image Underst. 61(1):38–59.

Dalal N, Triggs B. 2005. Histograms of oriented gradients for human detection. In: 2005 IEEE Comput Soc Conf Comput Vis Pattern Recognit. Vol. 1. San Diego (CA): IEEE; p. 886–893.

DeVocht JW, Goel VK, Zeitler DL, Lew D. 1996. A study of the control of disc movement within the temporomandibular joint using the finite element technique. J Oral Maxillofac Surg. 54(12):1431–1437.

Dimitroulis G. 2018. Management of temporomandibular joint disorders: a surgeon's perspective. Aust Dent J. 63: S79–S90.

Dornaika F, Ahlberg J. 2006. Fitting 3D face models for tracking and active appearance model training. Image Vis Comput. 24(9):1010–1024.

De Felice F, Di Carlo G, Saccucci M, Tombolini V, Polimeni A. 2019. Dental cone beam computed tomography in children: clinical effectiveness and cancer risk due to radiation exposure. Oncology. 96(4):173–178.

Gross R, Matthews I, Baker S. 2005. Generic vs. person specific active appearance models. Image Vis Comput. 23(12):1080–1093.

Hollenbeck JFM, Cain CM, Fattor JA, Rullkoetter PJ, Laz PJ. 2018. Statistical shape modeling characterizes three-dimensional shape and alignment variability in the lumbar spine. J Biomech. 69:146–155.

Illipronti-Filho E, Fantini S. d, Chilvarquer I. 2015. Evaluation of mandibular condyles in children with unilateral posterior crossbite. Braz Oral Res. 29(1):1–7.

Karlo CA, Stolzmann P, Habernig S, Müller L, Saurenmann T, Kellenberger CJ. 2010. Size, shape and age-related changes of the mandibular condyle during childhood. Eur Radiol. 20(10):2512–2517.

Kim K-W, Wong ME, Helfrick JF, Thomas JB, Athanasiou KA. 2003. Biomechanical tissue characterization of the superior joint space of the porcine temporomandibular joint. Ann Biomed Eng. 31(8):924–930.

Lee TS. 1996. Image representation using 2D Gabor wavelets. IEEE Trans Pattern Anal Mach Intell. 18:959–971.

Lowe DG. 1999. Object recognition from local scale-invariant features. In: Proc Seventh IEEE Int Conf Comput Vis. Vol. 2. Kerkyra: IEEE; p. 1150–1157.

Mimura H, Deguchi T. 1994. Relationship between sagittal condylar path and the degree of mandibular asymmetry in unilateral cross-bite patients. CRANIO®. 12(3): 161–166.

Ojala T, Pietikäinen M, Mäenpää T. 2001. A generalized local binary pattern operator for multiresolution gray scale and rotation invariant texture classification. In: Int Conf Adv Pattern Recognit. [place unknown]: Springer; p. 399–408.

Ortún-Terrazas J, Fagan MJ, Cegoñino J, Illipronti-Filho E, Pérez del Palomar A. 2020. Towards an early 3D-diagnosis of craniofacial asymmetry by computing the accurate midplane. a PCA-based method. Comput Methods Programs Biomed. 191:105397.

Palla S, Gallo L, Gossi D. 2003. Dynamic stereometry of the temporomandibular joint. Orthod Craniofac Res. 6(s1): 37–47.

Pirttiniemi P, Kantomaa T, Lahtela P. 1990. Relationship between craniofacial and condyle path asymmetry in unilateral cross-bite patients. Eur J Orthod. 12(4):408–413.

Planas P. 2013. Neuro-occlusal rehabilitation: NOR. 2nd ed. Barcelona: Amolca.

Prakash P, Durgesh BH. 2011. Anterior crossbite correction in early mixed dentition period using Catlan's appliance: a case report. ISRN Dent. 2011:1–5.

Roberts MG, Graham J, Devlin H. 2010. Improving the detection of osteoporosis from dental radiographs using active appearance models. In: 2010 IEEE Int Symp Biomed Imaging from Nano to Macro. Rotterdam: IEEE; p. 440–443.

Roberts MG, Oh T, Pacheco EMB, Mohankumar R, Cootes TF, Adams JE. 2012. Semi-automatic determination of detailed vertebral shape from lumbar radiographs using active appearance models. Osteoporos Int. 23(2):655–664.

Sarkalkan N, Waarsing JH, Bos PK, Weinans H, Zadpoor AA. 2014. Statistical shape and appearance models for fast and automated estimation of proximal femur fracture load using 2D finite element models. J Biomech. 47(12):3107–3114.

Sarkalkan N, Weinans H, Zadpoor AA. 2014. Statistical shape and appearance models of bones. Bone. 60: 129–140.

Shan ZY, Parra C, Ji Q, Jain J, Reddick WE. 2006. A knowledge-guided active model method of cortical structure segmentation on pediatric MR images. J Magn Reson Imaging. 24(4):779–789.

Singh M, Detamore MS. 2008. Tensile properties of the mandibular condylar cartilage. J Biomech Eng. 130(1):011009. doi:10.1115/1.2838062.

Tanaka E, Kawai N, Tanaka M, Todoh M, van Eijden T, Hanaoka K, Dalla-Bona DA, Takata T, Tanne K. 2004. The frictional coefficient of the temporomandibular joint and its dependency on the magnitude and duration of joint loading. J Dent Res. 83(5):404–407.

Thiesen G, Gribel BF, Freitas M. 2015. Facial asymmetry: a current review. Dental Press J Orthod. 20(6):110–125.

Tsanidis N, Antonarakis GS, Kiliaridis S. 2016. Functional changes after early treatment of unilateral posterior cross-bite associated with mandibular shift: a systematic review. J Oral Rehabil. 43(1):59–68.

Tzimiropoulos G, Zafeiriou S, Pantic M. 2012. Subspace learning from image gradient orientations. IEEE Trans Pattern Anal Mach Intell. 34(12):2454–2466.

Veli I, Uysal T, Ozer T, Ucar FI, Eruz M. 2011. Mandibular asymmetry in unilateral and bilateral posterior crossbite patients using cone-beam computed tomography. Angle Orthod. 81(6):966–974.

Widman DJ. 1988. Functional and morphologic considerations of the articular eminence. Angle Orthod. 58: 221–236.

Wohlberg V, Schwahn C, Gesch D, Meyer G, Kocher T, Bernhardt O. 2012. The association between anterior crossbite, deep bite and temporomandibular joint morphology validated by magnetic resonance imaging in an adult non-patient group. Ann Anat - Anat Anzeiger. 194(4):339–344.

3. Conclusions and original contributions

3.1 Conclusions

This dissertation proposed a computational approach for the assessment and evaluation of craniofacial malformations in children with UXB, through numerical simulations of chewing and occlusion. By the applications of the results, the main conclusions of this thesis have been grouped into two different areas. The first one contains the technical issues derived from the computational modelling of the paediatrics' craniofacial complex, while the second one lists the contributions of this work to the clinical field.

3.1.1 Computational modelling

Several computational models, both musculoskeletal and FE models, were developed in this thesis to understand the mechanical response of the soft tissues, joints, muscles and bone structures during chewing and occlusion. From a tissue level, the non-linear properties, which define TMJ's tissues and PDL behaviours, were characterized using cylindrical and prismatic shape-based models. From a joint viewpoint, it was developed a detailed model of the periodontium from computerized micro-tomography images (μ-CT), and six complete models of TMJs from MRI and CT images databases. From a muscular level, a musculoskeletal model of the craniofacial complex was also adapted to a paediatric patient. Finally, from a general perspective, one simplified FE model of an adult subject's occlusion and ten detailed FE models of the entire craniofacial complex were developed from CBCT images.

From the development of these models, the following conclusions can draw:

- The vascularization and the collagen bundles of the PDL (Manuscript 2) and the TMJ's disc (Manuscript 5) confer them a non-linear mechanical response that can be properly characterized by porous transversally isotropic hyperelastic material models.
- The transversally isotropic hyperelastic material model allows reproducing accurately the particular response in each region of TMJ tissues, (Manuscript 5), attending to the fibres' orientation. Hence, the fibrous network is fundamental for balancing and coordinating the TMJ's movements (Manuscript 6).
- The porous coupling provides a good description of the energy dissipated by the interstitial fluid within the PDLs (Manuscript 2 and 3) and TMJ's discs (Manuscript 5). The dissipative effect causes also residual deformations in the periodontium under cyclic loads (Manuscript 4) and allows to reproduce the damping and dynamic responses of the TMJs (Manuscript 6).
- For mainly intrusive forces, the hyperelastic behaviour of the PDL could be assumed isotropic, whereas, for lateral strengths, the transversal isotropic influence of the collagen fibres should be considered (Manuscript 2).
- The Mullins effect provides a good description of the PDL softening caused by the repeated loading (Manuscript 3).
- The fibres' progressive failure can be successfully reproduced by a penalty factor of its term in the material model description (Manuscript 3).
- For a precise biomechanical study of the PDL, besides the correct mechanical description, it is essential to accurately define its variable thickness based on μ-CT images (Manuscript 2).
- The FE models of the craniofacial complex reconstructed from CBCT images reproduced successfully the occlusal pattern with an average relative error below 6 % (Manuscript 7).

- Some mechanical variables, such as the PDL's hydrostatic pressure, mandibular deformation or maxillary micro-displacements, seem to be related with the craniofacial complex's malformations, following the principles of the periosteal and capsular matrix of the FMH (Manuscript 7 and 8).
- The FE method is a useful approach for studying craniofacial growth from a biomechanical viewpoint, as well as for the biomechanical evaluation of the occlusal treatments' outcomes (Manuscript 7 and 8).
- The combination of Principal Component Analysis (PCA), Generalized Procrustes Analysis (GPA) and the Iterative Closest Point (ICP) algorithm on a 3D point cloud allows to define the sagittal midplane compensating any asymmetric malformations (Manuscript 1).
- Despite needing more technical research, the parametric deformable models (statistically defined by Active Shape Models and Active Appearance Models) are a powerful tool to assist professionals in the development of patient-specific FE models (Manuscript 9).

3.1.2 Clinical aspects

Notwithstanding the limited sample size of this research compared to those of clinical trials, the numerical results allowed to draw the following clinical findings in controlled conditions:

- Periodic loads, such as those produced during chewing or grinding, caused a weaker mechanical response of the PDL in comparison to instantaneous loads (Manuscript 4).
- The interstitial fluid overpressure could be the main responsible for the PDL's deterioration under parafunctional habits (Manuscript 4).
- The local rupture of the PDL's collagen network has only appeared in areas with stretches greater than 60%, i. e. in particular conditions such as a traumatic event (Manuscript 3 and 4).
- The absence or alteration of the collagen network in the TMJ's soft tissues caused the asynchronous movement and disc displacement in the joint (Manuscript 6).
- Asymmetric malformations of the maxilla and mandible (Manuscript 7), but also the TMJs (Manuscript 9) and the cranial base (Manuscript 1) were found in paediatric patients with UXB.
- The functional imbalance of unilateral crossbite was found not only at the occlusal plane but also in the periodontium, mandible, maxilla (Manuscript 7), muscles, chewing cycles (Manuscript 8), condylar paths and TMJ's disc (Manuscript 9).
- The mandibular over deformation (>2000 $\mu\varepsilon$) and the micro-displacements of the maxillary and zygomatic region seem to be related with the asymmetric development of the craniofacial complex (Manuscript 8), in accordance with its periosteal and capsular matrices.
- The bone-remodelling phenomena caused due to PDL's overpressure (>4.7kPa) could explain the crossbite worsening through age (Manuscript 7 and 8), justifying, therefore, the benefit of early treatments (Manuscript 8).

- N.O.R improved not just the occlusal imbalance of a patient with UXB, but also periodontal overstimulation and mandibular over deformation, modifying its craniofacial growth pattern. The results even revealed functional improvements in the TMJ's discs (Manuscript 8).
- FE models provided an analytical demonstration of some FMH's principles for explaining the craniofacial development (Manuscript 7).
- The computational methods and algorithms provide a potential source for the 3D-diagnosis of craniofacial malformations (Manuscript 1), the biomechanical evaluation of occlusal trauma (Manuscripts 3 and 4) and disorders (Manuscripts 7 and 9), the evaluation of early treatment (Manuscript 8), or the demonstration of craniofacial growth's hypothesis (Manuscript 7).

3.2 Original contributions

As introduced in Chapter 1, despite the existence of several empirical theories about craniofacial development, the form-function relationship with explains its development is still unclear. This lack of knowledge is mainly caused due to the challenge of measure functional variables in-vivo and the difficulties of developing in-silico models of the craniofacial complex. This dissertation is, therefore, an important step in the in-silico evaluation of the function of the craniofacial complex, resulting in the following contributions:

- The implementation of a porous-hyperelastic-transversely-isotropic material model which accounts the energy dissipation of the fluid phase, the stiffness of the fibrous network and the softening phenomena caused by the fibre reorganization and overstretching.
- Mechanical characterization of the hyperelastic and permeable properties of the PDL and the TMJ's soft tissues.
- A micro detailed FE model of the human periodontium which considers the variable thickness, the biphasic composition and the fibre bundles of the PDL. Additionally, a simplified FE model of the occlusal complex of an adult patient with UXB.

- Six 3D FE models of the TMJ with their soft tissues, such as cartilage, discs and their adjacent tissues, developed from MRI.
- Ten 3D FE models of the craniofacial complex of children, five of whom with UXB, validated by the measurements of an occlusal analysis system.
- Development of an algorithm based on PCA and ICP for the identification of the sagittal midplane in 3D models of the craniofacial complex, compensating any asymmetric malformations.
- Computational study of the biomechanical effects of UXB on the asymmetric development of the craniofacial complex, according to the principles of FMH and the "mechanostat" and "pressure-tension" theories of bone remodelling.
- Development of a methodology for the computational evaluation of different alternatives of N.O.R's early treatments using FE and musculoskeletal models.
- Development of a computational methodology for the automatic generation of 2-D FE models of the TMJ based on the shape recognition in panoramic radiographs of an Active Appearance Model by an alternating inverse compositional (AIC) alignment algorithm.

3.1.1 Publications

[1] **Ortún-Terrazas, J.**, et al. (2020). *Towards an early 3D-diagnosis of craniofacial asymmetry by computing the accurate midplane: A PCA-based method.* Computer Methods and Programs in Biomedicine, 191, 105397. doi: 10.1016/j.cmpb.2020.105397

[2] **Ortún-Terrazas, J.**, et al. (2018). *Approach towards the porous fibrous structure of the periodontal ligament using micro-computerized tomography and finite element analysis*. Journal of the mechanical behavior of biomedical materials, 79, 135-149. doi: 10.1016/j.jmbbm.2017.12.022

[3] **Ortún-Terrazas, J.**, et al. (2019). *A porous fibrous hyperelastic damage model for human periodontal ligament: Application of a microcomputerized tomography finite element model*. International journal for numerical methods in biomedical engineering, 35(4), e3176. doi: 10.1002/cnm.3176

[4] **Ortún-Terrazas, J.**, et al. (2020). *In silico study of cuspid'periodontal ligament damage under parafunctional and traumatic conditions of whole-mouth occlusions. A patient-specific evaluation*. Computer Methods and Programs in Biomedicine, 184, 105107. doi: 10.1016/j.cmpb.2019.105107

[5] **Ortún-Terrazas, J.**, et al. (2020). *Computational characterization of the porous-fibrous behavior of the soft tissues in the temporomandibular joint.* Journal of Biomedical Materials Research Part B: Applied Biomaterials. doi: 10.1002/jbm.b.34558

[6] **Ortún-Terrazas, J.**, et al. (2021). *Biomechanical impact of the porous-fibrous tissue behaviour in the temporomandibular joint movements. An in silico approach.* Journal of the Mechanical Behavior of Biomedical Materials, 120, 104542. doi: 10.1016/j.jmbbm.2021.104542

[7] **Ortún-Terrazas, J.**, et al. (2021). *Biomechanical evaluation of the unilateral crossbite on the asymmetrical development of the craniofacial complex. A mechano-morphological approach.* (Under review)

[8] **Ortún-Terrazas, J**., et al. (2021). *In silico approach towards Neuro-Occlusal Rehabilitation for the early correction of asymmetrical development in a unilateral crossbite patient.* (Under review)

[9] **Ortún-Terrazas, J.**, et al. (2020). *Analysis of temporomandibular joint dysfunction in paediatric patients with unilateral crossbite using automatically generated finite element models.* Computer methods in biomechanics and biomedical engineering, 23(10), 627-641. doi: 10.1080/10255842.2020.1755275

3.1.2 Congresses

To disseminate these findings and facilitate the transmission of knowledge, the following communications were presented during the progress of this dissertation:

[1] **Ortún-Terrazas, J**., et al. (2019). *Neuro-occlusal stimulation, a crucial effect on the asymmetric development of the paediatric stomatognathic system. A 3D morphological and insilico study*. VIII Meeting of Young Researchers of the I3A, Zaragoza (Spain). doi: 10.26754/jji-i3a.003534

[2] **Ortún-Terrazas, J.**, et al. (2018). *Validation of non-invasive treatments for temporomandibular joint disorders during childhood considering the porous-fibrous properties of the joint.* 8th World Congress of Biomechanics. Dublin (Ireland).

[3] **Ortún-Terrazas, J.**, et al. (2018). *Diagnosis of TMJ disorders using parametric numerical models obtained by active shape model of orthopantomography.* 8th World Congress of Biomechanics. Dublin (Ireland), 2018.

[4] **Ortún-Terrazas, J**., et al. (2018). *Biomechanical evaluation of neuro-occlusal rehabilitation for occlusal imbalance correction in children with facial asymmetry*. VII Meeting of Young Researchers of the I3A, Zaragoza (Spain). doi: 10.26754/jji-i3a.201802709

[5] **Ortún-Terrazas, J.**, et al. (2017) *Finite element model of the nonlinear behaviour of the human periodontal ligament.* 23rd Congress of the European Society of Biomechanics, Seville (Spain).

[6] **Ortún-Terrazas, J.**, et al. (2017) *Computational analysis of craniomandibular tissues for the correction of mandibular asymmetries in childhood.* 23rd Congress of the European Society of Biomechanics, Seville (Spain).

3.1.3 Symposiums

[1] **Ortún-Terrazas, J**., & del Palomar, A. P. (2019). *Ingeniería facial en la infancia: La disciplina que devuelve la sonrisa*. VII Doctoral Meeting of G-9. Logroño (Spain).

[2] **Ortún-Terrazas, J**. (2019). *Mechanical symmetry in the childhood face: technical solutions that return smiles*. VI Doctoral Meeting of Campus Iberus. Jaca (Spain).

[3] **Ortún-Terrazas, J**. (2018). *Biomechanical engineering as a clinical tool for dental malocclusions correction in children*. V Doctoral Meeting of Campus Iberus. Jaca (Spain).

[4] **Ortún-Terrazas, J**. (2018). *Biomechanical evaluation of mandibular soft tissues in the treatment of the facial asymmetry during the childhood*. V Doctoral Meeting of the PhD Program in Mechanical Engineering. Zaragoza (Spain).

3.1.4 Awards

[1] 2019. Best Poster Communication in the area of Engineering and Architecture, in the VII Doctoral Meeting of G-9. Logroño (Spain).

[2] 2019. SAMCA Fellowship at the Course of Academic Specialist in R&D and Innovation Management in Companies. University of Zaragoza (Spain).

[3] 2019. Best Poster Communication in the VI Doctoral Meeting of Campus Iberus, Jaca (Spain).

[4] 2018. Best Poster Communication in the V Doctoral Meeting of Campus Iberus, Jaca (Spain).

3.3 Future work

This research is an important step in the computational study of the craniofacial complex and in the evaluation of early occlusal treatments. Nevertheless, it is just a modest contribution towards the complex mechanical modelling of the stomatognathic system and its development, opening future fields in the experimental and computational study of it. Some of these lines could be the following:

- The experimental analysis of the mechanical effect of each bundle of fibres in the PDL behaviour, and the electrochemical effect in the adjacent bone remodelling.
- The experimental characterization of the mechanical behaviour in the different layers (fibrous, proliferative, mature and hypertrophic) of the condylar and temporal cartilages, as well as the mathematical modelling of their influence on the development of the condyle and the articular fossa.
- The development of a mechano-electrochemical algorithm which simulates tooth eruption, granular tissue differentiation and the associated shape variations in the mandible.
- Development of a parametric deformable model of the paediatric craniofacial complex from a wide collection of 3D models, allowing the 3D visualization of natural growth patterns.
- The coupling of the bone remodelling phenomena associated with tooth eruption, condylar growth and periodontal stimulation in a parametric deformable model of the mandible.
- The in-silico modelling of the sutural ossification process in the biomechanical examination of orthodontic appliances in the expansion of the maxilla.
- An in-vivo study in animals about the influence of early N.O.R's treatments on the craniofacial complex development, and its comparison with in-silico results.

3. Conclusiones y contribuciones originales [1]

3.1 Conclusiones

Esta tesis presentó una metodología computacional para la evaluación y el diagnostico de malformaciones craneofaciales en niños con mordida cruzada, mediante simulaciones numéricas de la masticación y oclusión. Atendiendo a la aplicación de los resultados, las conclusiones principales de esta tesis se han agrupado en dos categorías. En la primera se incluyen los aspectos técnicos que resultaron del modelado computacional del sistema craneofacial infantil, mientras que en la segunda se enumeran las aportaciones de este trabajo al ámbito clínico.

3.1.1 Modelado computacional

Varios modelos computacionales, tanto modelos musculoesqueléticos como modelos de elementos finitos (en español EF, en inglés, FE), fueron desarrollados en esta tesis con el propósito de entender la respuesta mecánica de los tejidos, articulaciones, músculos y estructuras óseas durante la masticación y oclusión. Así, a nivel tisular, se caracterizaron las propiedades mecánicas que definen el comportamiento no lineal de los tejidos blandos de la articulación temporomandibular (ATM) y del ligamento periodontal con varios modelos computacionales de geometría regular, en forma de cilindros y prismas. A nivel articular, se desarrolló un modelo detallado del periodonto a partir de imágenes de microtomografía computarizada (μ-TC), y seis modelos completos de ATMs a partir de imágenes de Resonancia Magnética (IRM) y tomografía computarizada (CT). Desde un punto de vista muscular, también se adaptó un modelo musculoesquelético del complejo craneofacial a un paciente pediátrico. Finalmente, a nivel global, se desarrolló un modelo de EF simplificado de la oclusión de un sujeto adulto y diez modelos detallados de todo el complejo craneofacial a partir de imágenes obtenidas por tomografía computarizada dental de haz cónico (en inglés, CBCT).

[1] En virtud del apartado b) del art.18 de Real Decreto 99/2011, y modificado por Real Decreto 195/2016, por el que se regulan las circunstancias para optar a la mención internacional de doctor, las conclusiones y contribuciones originales se presentan también en la lengua oficial del Estado.

Del desarrollo de estos modelos se extrajeron las siguientes conclusiones:

- La vascularización y los haces de fibras de colágeno del ligamento periodontal (Manuscrito 2) y del disco articular (Manuscrito 5) les confieren una respuesta mecánica no lineal que puede ser correctamente caracterizada por modelos materiales poro-hiperelásticos transversalmente isótropos.
- El modelo de material transversalmente isótropo reproduce correctamente el comportamiento especifico en cada región de los tejidos de la ATM, (Manuscrito 5), atendiendo a la orientación de las fibras de colágeno embebidas. Así, la matriz fibrosa es fundamental para equilibrar y articular el movimiento de la ATM (Manuscrito 6).
- El acoplamiento poroso permite representar la energía disipada por el fluido intersticial en el ligamento periodontal (Manuscrito 2 y 3) y en disco articular (Manuscrito 5). El efecto disipativo produce deformaciones residuales del periodonto ante cargas cíclicas (Manuscrito 4) y reproduce adecuadamente la respuesta amortiguadora y dinámica en la ATM (Manuscrito 6).
- Para cargas mayoritariamente intrusivas, el comportamiento hiperelástico del ligamento periodontal puede asumirse como isótropo, mientras que para fuerzas laterales es recomendable considerar el efecto transversalmente isótropo de las fibras de colágeno (Manuscrito 2).
- El efecto Mullins es capaz de representar el ablandamiento que sufre el ligamento periodontal con la repetición de cargas (Manuscrito 3).
- El fallo progresivo de las fibras de colágeno puede ser representado correctamente mediante un factor que penalice la componente de las fibras en el modelo material (Manuscrito 3).
- Para un correcto estudio biomecánico del PDL, además de la correcta caracterización mecánica, es fundamental definir adecuadamente el espesor variable del ligamento a partir de imágenes de μ-TC (Manuscrito 2).

- Los modelos de EF del complejo craneofacial obtenidos mediante imágenes CBCT reprodujeron satisfactoriamente el patrón oclusal con un error relativo promedio inferior al 6 % (Manuscrito 7).

- Algunas variables mecánicas, como la presión hidrostática en el ligamento periodontal, la deformación mandibular o los micro-desplazamientos del maxilar, parecen ser responsables de los cambios de forma en el complejo craneofacial, de acuerdo con los principios de la matriz perióstica y capsular de la Hipótesis de la Matriz Funcional (HMF) (Manuscrito 7 y 8).

- El método de EF es una poderosa herramienta para el estudio del crecimiento craneofacial atendiendo a su dimensión biomecánica, así como para la evaluación biomecánica de tratamientos oclusales (Manuscrito 7 y 8).

- La combinación del Análisis de Componentes Principales (en español ACP, en inglés, PCA), el Análisis Procrustes Generalizado (APG, en inglés GPA) y el método iterativo del punto más cercano (en inglés, Iterative Closest Point, ICP) sobre una base de puntos cartesianos, permite definir un plano medio sagital compensando las diferencias asimétricas del desarrollo craneofacial (Manuscrito 1).

- Los modelos paramétricos deformables definidos estadísticamente mediante Modelos Activos de Forma (en inglés, ASM), y Modelos Activos de Apariencia (AAM) facilitan el desarrollo de modelos computacionales en pacientes específicos (Manuscrito 9), aunque es necesario un mayor desarrollo técnico para su implementación en modelos 3D.

3.1.2 Aspectos clínicos

A pesar del reducido tamaño muestral de este trabajo, en comparación con las muestras de estudios clínicos, los resultados numéricos han permitido obtener las siguientes conclusiones clínicas en condiciones controladas:

- Las cargas cíclicas, como las producidas en la masticación o el rechinamiento, produjeron una respuesta mecánica del ligamento periodontal menos rígida que en oclusiones puntuales (Manuscrito 4).
- La sobrepresión del fluido intersticial podría ser la principal causa del deterioro del ligamento periodontal en condiciones parafuncionales (Manuscrito 4).
- La ruptura local de la red de colágeno del ligamento periodontal solo se produjo en regiones con estiramientos superiores al 60%, es decir en situaciones muy particulares como el traumatismo oclusal (Manuscrito 3 y 4).
- La ausencia o modificación de la red de colágeno en los tejidos blandos de la ATM produjo movimientos asíncronos y dislocaciones del disco articular (Manuscrito 6).
- Los pacientes infantiles con MCU experimentaron malformaciones asimétricas del maxilar y la mandíbula (Manuscrito 7), pero también de las ATMs (Manuscrito 9) y de la base craneal (Manuscrito 1).
- El desequilibrio funcional en pacientes pediátricos con mordida cruzada unilateral (MCU), se manifiesto no solo a nivel oclusal sino también en el periodonto, la mandíbula, el maxilar (Manuscrito 7), los músculos, los ciclos de masticación (Manuscritos 8), las trayectorias condíleas y los discos articulares (Manuscrito 9).
- La sobre deformación de la mandíbula (>2000 $\mu\varepsilon$) y los desplazamientos del maxilar y la región cigomática, parecen estar relacionados con el desarrollo asimétrico del complejo craneofacial (Manuscrito 8), atendiendo a sus matrices periósticas y capsulares.

- Los fenómenos de remodelación ósea causados por la sobrepresión del PDL (>4,7kPa) podrían explicar el empeoramiento de la mordida cruzada a través de la edad (Manuscritos 7 y 8), justificando así el beneficio de los tratamientos tempranos (Manuscrito 8).
- La Rehabilitación Neuro-Oclusal (RNO) corrigió no solo el desequilibrio oclusal de un paciente con MCU, sino también la sobreestimulación periodontal y sobre-deformación de la mandíbula modificando así el patrón de crecimiento craneofacial. Los resultados demostraron incluso cambios funcionales en los discos articulares de las ATMs (Manuscrito 8).
- El método de EF ha permitido demostrar analíticamente algunos de los principios defendidos por la HMF para explicar el crecimiento craneofacial (Manuscrito 7).
- Los métodos y algoritmos computacionales son una herramienta poderosa para el diagnóstico de malformaciones (Manuscrito 1), la evaluación biomecánica de traumatismos (Manuscritos 3 y 4) y maloclusiones (Manuscritos 7 y 9), el estudio de tratamientos tempranos (Manuscrito 8) o la demostración analítica de teorías de crecimiento craneofacial (Manuscrito 7).

3.2 Contribuciones originales

Tal y como fue introducido en el Capítulo 1, a pesar de que existen muchas teorías empíricas sobre el crecimiento craneofacial, sigue sin estar clara la relación que existe entre la forma y la función. Este desconocimiento esta principalmente basado en la dificultad de medir la estimulación mecánica in-vivo y la complejidad en el desarrollo de modelos in-silico del complejo craneofacial infantil. Así, esta tesis supone un paso importante en la evaluación in-silico del complejo craneofacial infantil, dando lugar a las siguientes contribuciones:

- Implementación de un modelo de material poro-hiperelástico-transversalmente-isótropo que considera la disipación viscosa del líquido intersticial, la orientación de las fibras de colágeno y los fenómenos de ablandamiento causados por la reorganización y el sobre-estiramiento de las fibras.
- Caracterización mecánica de las propiedades hiperelásticas y permeables del ligamento periodontal y de los tejidos que componen la ATM.
- Un modelo 3D de FE detallado del periodonto humano a partir de imágenes μ-TC que considera el espesor variable, la composición bifásica y los haces de fibras del ligamento periodontal. Y un modelo FE simplificado del conjunto oclusal de un paciente adulto con MCU.
- Seis modelos 3D de FE de la ATMs desarrollados a partir de IRM que incorporan la mayoría de los tejidos blandos de la articulación, tales como cartílagos, discos y sus tejidos adyacentes.
- Diez modelos 3D de FE del complejo craneofacial de infantil, cinco de los cuales tenían MCU, validados a partir de mediciones realizadas con un sistema de análisis oclusal.
- Desarrollo de un algoritmo basado en PCA e ICP para la determinación del plano medio sagital en modelos 3D del complejo craneofacial.
- Estudio computacional de la influencia biomecánica de la MCU en el desarrollo asimétrico del complejo craneofacial, según los principios de la HMF y las teorías “mecanostática” y de “presión-tensión” de remodelación ósea.
- Desarrollo de una metodología para la evaluación computacional de distintas alternativas de tratamientos tempranos de la RNO sobre modelos de EF y musculoesqueléticos.
- Desarrollo de una metodología computacional para la generación automática de modelos 2D de EF de la ATM a partir del reconocimiento de forma en radiografías panorámicas de un Modelo Activo de Apariencia mediante un algoritmo de alineación inversa y alterna de composición (en inglés, AIC).

3.1.1 Publicaciones

[1] **Ortún-Terrazas, J.**, et al. (2020). *Towards an early 3D-diagnosis of craniofacial asymmetry by computing the accurate midplane: A PCA-based method.* Computer Methods and Programs in Biomedicine, 191, 105397. doi: 10.1016/j.cmpb.2020.105397

[2] **Ortún-Terrazas, J.**, et al. (2018). *Approach towards the porous fibrous structure of the periodontal ligament using micro-computerized tomography and finite element analysis*. Journal of the mechanical behavior of biomedical materials, 79, 135-149. doi: 10.1016/j.jmbbm.2017.12.022

[3] **Ortún-Terrazas, J.**, et al. (2019). *A porous fibrous hyperelastic damage model for human periodontal ligament: Application of a microcomputerized tomography finite element model*. International journal for numerical methods in biomedical engineering, 35(4), e3176. doi: 10.1002/cnm.3176

[4] **Ortún-Terrazas, J.**, et al. (2020). *In silico study of cuspid'periodontal ligament damage under parafunctional and traumatic conditions of whole-mouth occlusions. A patient-specific evaluation*. Computer Methods and Programs in Biomedicine, 184, 105107. doi: 10.1016/j.cmpb.2019.105107

[5] **Ortún-Terrazas, J.**, et al. (2020). *Computational characterization of the porous-fibrous behavior of the soft tissues in the temporomandibular joint.* Journal of Biomedical Materials Research Part B: Applied Biomaterials. doi: 10.1002/jbm.b.34558

[6] **Ortún-Terrazas, J.**, et al. (2021). *Biomechanical impact of the porous-fibrous tissue behaviour in the temporomandibular joint movements. An in silico approach.* Journal of the Mechanical Behavior of Biomedical Materials, 120, 104542. doi: 10.1016/j.jmbbm.2021.104542

[7] **Ortún-Terrazas, J.**, et al. (2021). *Biomechanical evaluation of the unilateral crossbite on the asymmetrical development of the craniofacial complex. A mechano-morphological approach.* (En revisión)

[8] **Ortún-Terrazas, J**., et al. (2021). *In silico approach towards Neuro-Occlusal Rehabilitation for the early correction of asymmetrical development in a unilateral crossbite patient.* (En revisión)

[9] **Ortún-Terrazas, J.**, et al. (2020). *Analysis of temporomandibular joint dysfunction in paediatric patients with unilateral crossbite using automatically generated finite element models.* Computer methods in biomechanics and biomedical engineering, 23(10), 627-641. doi: 10.1080/10255842.2020.1755275

3.1.2 Congresos

Con el objetivo de expandir los hallazgos de esta tesis y facilitar la transmisión de conocimiento, las siguientes comunicaciones fueron presentadas durante el desarrollo de esta tesis:

[1] **Ortún-Terrazas, J**., et al. (2019). *Neuro-occlusal stimulation, a crucial effect on the asymmetric development of the paediatric stomatognathic system. A 3D morphological and insilico study*. VIII Jornada de Jóvenes Investigadores del I3A, Zaragoza (España). doi: 10.26754/jji-i3a.003534

[2] **Ortún-Terrazas, J.**, et al. (2018). *Validation of non-invasive treatments for temporomandibular joint disorders during childhood considering the porous-fibrous properties of the joint.* 8vo Congreso Mundial de Biomecánica. Dublin (Irlanda).

[3] **Ortún-Terrazas, J.**, et al. (2018). *Diagnosis of TMJ disorders using parametric numerical models obtained by active shape model of orthopantomography.* 8vo Congreso Mundial de Biomecánica. Dublin (Irlanda).

[4] **Ortún-Terrazas, J**., et al. (2018). *Biomechanical evaluation of neuro-occlusal rehabilitation for occlusal imbalance correction in children with facial asymmetry*. VII Jornada de Jóvenes Investigadores del I3A, Zaragoza (España). doi: 10.26754/jji-i3a.201802709

[5] **Ortún-Terrazas, J.**, et al. (2017) *Finite element model of the nonlinear behaviour of the human periodontal ligament.* 23vo Congreso de la Sociedad Europea de Biomecánica, Sevilla (España).

[6] **Ortún-Terrazas, J.**, et al. (2017) *Computational analysis of craniomandibular tissues for the correction of mandibular asymmetries in childhood.* 23vo Congreso de la Sociedad Europea de Biomecánica, Sevilla (España).

3.1.2 Seminarios

[1] **Ortún-Terrazas, J**., & del Palomar, A. P. (2019). *Ingeniería facial en la infancia: La disciplina que devuelve la sonrisa*. VII Jornadas Doctorales del G-9. Logroño (España).

[2] **Ortún-Terrazas, J**. (2019). *Mechanical symmetry in the childhood face: technical solutions that return smiles*. VI Jornadas doctorales del Campus Iberus. Jaca (España).

[3] **Ortún-Terrazas, J**. (2018). *Biomechanical engineering as a clinical tool for dental malocclusions correction in children*. V Jornadas doctorales del Campus Iberus. Jaca (España).

[4] **Ortún-Terrazas, J**. (2018). *Biomechanical evaluation of mandibular soft tissues in the treatment of the facial asymmetry during the childhood*. V Jornada de Doctorandos del Programa de Doctorado en Ingeniería Mecánica. Zaragoza (España).

3.1.4 Premios

[1] 2019. Mejor Poster del área de Ingeniería y Arquitectura, en las VII Jornadas Doctorales G-9, Logroño (España).

[2] 2019. Beca de la Cátedra SAMCA en el Curso de Experto Universitario en Gestión del I+D+i en la Empresa, Universidad de Zaragoza (España).

[3] 2019. Mejor Poster del VI Jornadas doctorales del Campus Iberus, Jaca (España).

[4] 2018. Mejor Poster del V Jornadas doctorales del Campus Iberus, Jaca (España).

3.3 Trabajos futuros

El trabajo aquí presentado constituye un paso importante en el estudio computacional del complejo craneofacial y en la evaluación de tratamientos oclusales tempranos. Sin embargo, este trabajo es solo un pequeño paso en la compleja simulación mecánica del sistema estomatognático, abriendo futuras líneas de investigación experimental y computacional que permitan estudiar la influencia mecánica en su desarrollo. Algunas de estas líneas podrían ser las siguientes:

- Estudio experimental de la respuesta mecánica de cada familia de fibras en el ligamento periodontal y de los mecanismos electroquímicos que produce la disipación de fluido intersticial sobre la remodelación hueso adyacente.
- Caracterización experimental de la respuesta mecánica de las distintas capas (fibrosa, proliferativa, madura e hipertrófica) de los cartílagos condilares y temporales, y de modelización matemática de su influencia en el desarrollo del cóndilo y la fosa articular.
- Desarrollo de un algoritmo mecano-electroquímico que simule la erupción de los dientes, la diferenciación de los tejidos granulares y los cambios de forma en la mandíbula asociados.
- Desarrollo de un modelo deformable paramétrico del complejo craneofacial infantil a partir de una amplia base datos de modelos 3D, que permita representar tridimensionalmente los patrones normales de crecimiento.
- Acoplamiento de los fenómenos de remodelación ósea asociados a la erupción de los dientes, el crecimiento condilar y la estimulación periodontal en un modelo deformable paramétrico de la mandíbula.
- Modelización in-silico del proceso de osificación sutural para la evaluación evaluación biomecánica de aparatos ortodóncicos en la expansión del maxilar.
- Estudio in-vivo sobre animales de la influencia de tratamientos tempranos de RNO en el desarrollo del complejo craneofacial, y su comparación con los resultados in-silico.

Bibliography

[1] A. Nanci, "Oral histology: Development, structure, and function (ed 3)," *J. Oral Maxillofac. Surg.*, vol. 48, no. 1, pp. 98–99, Jan. 1990, doi: 10.1016/0278-2391(90)90217-P.

[2] P. Planas, *Rehabilitación Neuro-Oclusal: RNO*. Barcelona, España: Masson-Salvat, 1987.

[3] M. G. Piancino and S. Kyrkanides, *Understanding Masticatory Function in Unilateral Crossbites*. Oxford, UK: John Wiley & Sons, Inc., 2016.

[4] P. Planas, *Neuro-occlusal rehabilitation: NOR*, 2nd ed. Barcelona, España: Amolca, 2013.

[5] H. Sicher, *Oral anatomy*. CV Mosby Company, 1965.

[6] M. Schünke, E. Schulte, and U. Schumacher, "PROMETHEUS." p. 107, 2010.

[7] M. W. and K. A. Y. J. Gordon Betts, Peter Desaix, Eddie Johnson, Jody E. Johnson, Oksana Korol. James A. Wise, *Anatomy & Physiology Anatomy*. 2014.

[8] R. N. Ghatak and J. G. Ginglen, *Anatomy, Head and Neck, Mandibular Nerve*. 2019.

[9] H. Kapadia, P. R. Shetye, B. H. Grayson, and J. G. McCarthy, "Cephalometric assessment of craniofacial morphology in patients with treacher Collins syndrome.," *J. Craniofac. Surg.*, vol. 24, no. 4, pp. 1141–5, Jul. 2013, doi: 10.1097/SCS.0b013e3182860541.

[10] S. Haraguchi, Y. Iguchi, and K. Takada, "Asymmetry of the face in orthodontic patients.," *Angle Orthod.*, vol. 78, no. 3, pp. 421–6, May 2008, doi: 10.2319/022107-85.1.

[11] O. Plesh, B. Bishop, and W. McCall, "Mandibular movements and jaw muscles' activity while voluntarily chewing at different rates," *Exp. Neurol.*, vol. 98, no. 2, pp. 285–300, Nov. 1987, doi: 10.1016/0014-4886(87)90243-3.

[12] J. H. Koolstra and T. M. van Eijden, "Biomechanical analysis of jaw-closing movements.," *J. Dent. Res.*, vol. 74, no. 9, pp. 1564–70, Sep. 1995, doi: 10.1177/00220345950740091001.

[13] M. Farella, S. Palla, S. Erni, A. Michelotti, and L. M. Gallo, "Masticatory muscle activity during deliberately performed oral tasks," *Physiol. Meas.*, vol. 29, no. 12, pp. 1397–1410, Dec. 2008, doi: 10.1088/0967-3334/29/12/004.

[14] S. J. Nelson, *Wheeler's Dental Anatomy, Physiology and Occlusion-E-Book*. Elsevier Health Sciences, 2014.

[15] L. Sonnesen, "Bite force in pre-orthodontic children with unilateral crossbite," *Eur. J. Orthod.*, vol. 23, no. 6, pp. 741–749, Dec. 2001, doi: 10.1093/ejo/23.6.741.

[16] K. Yamada, K. Hanada, M. H. Sultana, S. Kohno, and Y. Yamada, "The relationship between frontal facial morphology and occlusal force in orthodontic patients with temporomandibular disorder," *J. Oral Rehabil.*, pp. 413–421, 2000.

[17] I. Saitoh, C. Yamada, H. Hayasaki, T. Maruyama, Y. Iwase, and Y. Yamasaki, "Is the reverse cycle during chewing abnormal in children with primary dentition?," *J. Oral Rehabil.*, vol. 37, no. 1, pp. 26–33, Jan. 2010, doi: 10.1111/j.1365-2842.2009.02006.x.

[18] G. Iodice, G. Danzi, R. Cimino, S. Paduano, and A. Michelotti, "Association between posterior crossbite, masticatory muscle pain, and disc displacement: a systematic review.," *Eur. J. Orthod.*, vol. 35, no. 6, pp. 737–44, Dec. 2013, doi: 10.1093/ejo/cjt024.

[19] R. C. Solem, A. Ruellas, A. Miller, K. Kelly, J. L. Ricks-Oddie, and L. Cevidanes, "Congenital and acquired mandibular asymmetry: Mapping growth and remodeling in 3 dimensions.," *Am. J. Orthod. Dentofacial Orthop.*, vol. 150, no. 2, pp. 238–51, Aug. 2016, doi: 10.1016/j.ajodo.2016.02.015.

[20] Y. Hirano *et al.*, "Effects of chewing in working memory processing," *Neurosci. Lett.*, vol. 436, no. 2, pp. 189–192, 2008.

[21] T. Takada and T. Miyamoto, "A fronto-parietal network for chewing of gum: a study on human subjects with functional magnetic resonance imaging," *Neurosci. Lett.*, vol. 360, no. 3, pp. 137–140, 2004.

[22] A. Barkhordarian, F. Chiappelli, and G. G. Demerjian, "Neuroanatomy and Neurophysiology of the Trigeminal Network System," in *Temporomandibular Joint and Airway Disorders*, Cham: Springer International Publishing, 2018, pp. 17–38.

[23] M. S. Detamore and K. A. Athanasiou, "Structure and function of the temporomandibular joint disc: Implications for tissue engineering," *J. Oral Maxillofac. Surg.*, vol. 61, no. 4, pp. 494–506, Apr. 2003, doi: 10.1053/joms.2003.50096.

[24] G. Casares, A. Thomas, J. Carmona, J. Acero, and C. N. Vila, "Influence of oral stabilization appliances in intra-articular pressure of the temporomandibular joint," *CRANIO®*, vol. 32, no. 3, pp. 219–223, Jul. 2014, doi: 10.1179/0886963413Z.00000000030.

[25] M. Singh and M. S. Detamore, "Biomechanical properties of the mandibular condylar cartilage and their relevance to the TMJ disc," *J. Biomech.*, vol. 42, no. 4, pp. 405–417, Mar. 2009, doi: 10.1016/j.jbiomech.2008.12.012.

[26] M. Teramoto, S. Kaneko, S. Shibata, M. Yanagishita, and K. Soma, "Effect of compressive forces on extracellular matrix in rat mandibular condylar cartilage.," *J. Bone Miner. Metab.*, vol. 21, no. 5, pp. 276–86, 2003, doi: 10.1007/s00774-003-0421-y.

[27] E. Tanaka, R. Del Pozo, M. Sugiyama, and K. Tanne, "Biomechanical response of retrodiscal tissue in the temporomandibular joint under compression.," *J. Oral Maxillofac. Surg.*, vol. 60, no. 5, pp. 546–51, May 2002, doi: 10.1053/joms.2002.31853.

[28] J. Langendoen, J. Müller, and G. a. Jull, "Retrodiscal tissue of the temporomandibular joint: clinical anatomy and its role in diagnosis and treatment of arthropathies.," *Man. Ther.*, vol. 2, no. 4, pp. 191–198, Nov. 1997, doi: 10.1054/math.1997.0299.

[29] M. K. Murphy, B. Arzi, J. C. Hu, and K. A. Athanasiou, "Tensile characterization of porcine temporomandibular joint disc attachments.," *J. Dent. Res.*, vol. 92, no. 8, pp. 753–8, Aug. 2013, doi: 10.1177/0022034513494817.

[30] C. Maes and H. M. Kronenberg, "Postnatal Bone Growth: Growth Plate Biology, Bone Formation, and Remodeling," in *Pediatric Bone*, Elsevier, 2012, pp. 55–82.

[31] A. Tsuboi, Y. Takafuji, S. Itoh, K. Nagata, T. Tabata, and M. Watanabe, "Response properties of trigeminal ganglion mechanosensitive neurons innervating the temporomandibular joint of the rabbit.," *Exp. brain Res.*, vol. 199, no. 2, pp. 107–16, Nov. 2009, doi: 10.1007/s00221-009-1978-z.

[32] P. Morquette, R. Lavoie, M.-D. Fhima, X. Lamoureux, D. Verdier, and A. Kolta, "Generation of the masticatory central pattern and its modulation by sensory feedback," *Prog. Neurobiol.*, vol. 96, no. 3, pp. 340–355, Mar. 2012, doi: 10.1016/j.pneurobio.2012.01.011.

[33] R. Fuentes, N. E. Ottone, D. Saravia, and C. Bucchi, "Irrigación e Inervación de la Articulación Temporomandibular: Una Revisión de la Literatura," *Int. J. Morphol.*, vol. 34, no. 3, pp. 1024–1033, Sep. 2016, doi: 10.4067/S0717-95022016000300034.

[34] A. Boryor, A. Hohmann, M. Geiger, U. Wolfram, C. Sander, and F. G. Sander, "A downloadable meshed human canine tooth model with PDL and bone for finite element simulations," *Dent. Mater.*, vol. 25, no. 9, pp. 57–62, 2009, doi: 10.1016/j.dental.2009.05.002.

[35] M. Drolshagen *et al.*, "Development of a novel intraoral measurement device to determine the biomechanical characteristics of the human periodontal ligament," *J. Biomech.*, vol. 44, no. 11, pp. 2136–2143, Jul. 2011, doi: 10.1016/j.jbiomech.2011.05.025.

[36] M. Tuna, E. Sunbuloglu, and E. Bozdag, "Finite element simulation of the behavior of the periodontal ligament: A validated nonlinear contact model," *J. Biomech.*, vol. 47, no. 12, pp. 2883–2890, Sep. 2014, doi: 10.1016/j.jbiomech.2014.07.023.

[37] M. Favino *et al.*, "Validation of a heterogeneous elastic-biphasic model for the numerical simulation of the PDL," *Comput. Methods Biomech. Biomed. Engin.*, vol. 16, no. 5, pp. 544–553, May 2013, doi: 10.1080/10255842.2011.628660.

[38] M. Bergomi, J. Cugnoni, J. Botsis, U. C. Belser, and H. W. Anselm Wiskott, "The role of the fluid phase in the viscous response of bovine periodontal ligament," *J. Biomech.*, vol. 43, no. 6, pp. 1146–1152, Apr. 2010, doi: 10.1016/j.jbiomech.2009.12.020.

[39] P. Lekic, J. Rojas, C. Birek, H. Tenenbaum, and C. A. McCulloch, "Phenotypic comparison of periodontal ligament cells in vivo and in vitro.," *J. Periodontal Res.*, vol. 36, no. 2, pp. 71–9, Apr. 2001, doi: 11327081.

[40] J. M. Ferrier and E. M. Dillon, "The water binding capacity of the periodontal ligament and its role in mechanical function," *J. Periodontal Res.*, vol. 18, no. 5, pp. 469–473, Oct. 1983, doi: 10.1111/j.1600-0765.1983.tb00384.x.

[41] R. Dean, "The Periodontal Ligament: Development, Anatomy and Function." OHDM, 2018.

[42] C. H. Daly, J. I. Nicholls, W. L. Kydd, and P. D. Nansen, "The response of the human periodontal ligament to torsional loading—I. Experimental methods," *J. Biomech.*, vol. 7, no. 6, pp. 517–522, Nov. 1974, doi: 10.1016/0021-9290(74)90086-4.

[43] B. K. B. Berkovitz, M. E. Weaver, R. C. Shore, and B. J. Moxham, "Fibril Diameters in the Extracellular Matrix of the Periodontal Connective Tissues of the Rat," *Connect. Tissue Res.*, vol. 8, no. 2, pp. 127–132, 1981, doi: 10.3109/03008208109152132.

[44] T. Tsuzuki *et al.*, "Hyperocclusion stimulates the expression of collagen type XII in periodontal ligament," *Arch. Oral Biol.*, vol. 66, pp. 86–91, 2016, doi: 10.1016/j.archoralbio.2016.02.009.

[45] C. G. Bellows, A. H. Melcher, and J. E. Aubin, "Contraction and organization of collagen gels by cells cultured from periodontal ligament, gingiva and bone suggest functional differences between cell types.," *J. Cell Sci.*, vol. 50, pp. 299–314, Aug. 1981, [Online]. Available: http://www.ncbi.nlm.nih.gov/pubmed/6798046.

[46] I. Lambrichts, J. Creemers, and D. van Steenberghe, "Morphology of neural endings in the human periodontal ligament: an electron microscopic study.," *J. Periodontal Res.*, vol. 27, no. 3, pp. 191–6, May 1992, [Online]. Available: http://www.ncbi.nlm.nih.gov/pubmed/1608032.

[47] R. M. Cash and R. W. Linden, "The distribution of mechanoreceptors in the periodontal ligament of the mandibular canine tooth of the cat.," *J. Physiol.*, vol. 330, no. 1, pp. 439–447, 1982.

[48] S. E. Johnsen and M. Trulsson, "Receptive field properties of human periodontal afferents responding to loading of premolar and molar teeth," *J. Neurophysiol.*, vol. 89, no. 3, pp. 1478–1487, 2003.

[49] K. Nagata, S. Itoh, A. Tsuboi, Y. Takafuji, T. Tabata, and M. Watanabe, "Response properties of periodontal mechanosensitive neurons in the trigeminal ganglion of rabbit and neuronal activities during grinding-like jaw movement induced by cortical stimulation," *Arch. Oral Biol.*, vol. 53, no. 12, pp. 1138–1148, 2008.

[50] E. S. Luschei and L. J. Goldberg, "Neural Mechanisms of Mandibular Control: Mastication and Voluntary Biting," in *Comprehensive Physiology*, Hoboken, NJ, USA: John Wiley & Sons, Inc., 2011.

[51] A. van der Bilt, L. Engelen, L. J. Pereira, H. W. van der Glas, and J. H. Abbink, "Oral physiology and mastication," *Physiol. Behav.*, vol. 89, no. 1, pp. 22–27, Aug. 2006, doi: 10.1016/j.physbeh.2006.01.025.

[52] J. Tintinalli, *Tintinallis emergency medicine A comprehensive study guide*. McGraw-Hill Education, 2015.

[53] D. M. Ranly, "Craniofacial growth.," *Dent. Clin. North Am.*, vol. 44, no. 3, pp. 457–70, v, Jul. 2000, [Online]. Available: http://www.ncbi.nlm.nih.gov/pubmed/10925768.

[54] H. Lin, Y. Chen, J. Li, T. Lu, H. Chang, and C. Hu, "Measurement of mandibular growth using cone-beam computed tomography: a miniature pig model study.," *PLoS One*, vol. 9, no. 5, p. e96540, 2014, doi: 10.1371/journal.pone.0096540.

[55] M. C. Meikle, "Remodeling the Dentofacial Skeleton: The Biological Basis of Orthodontics and Dentofacial Orthopedics," *J. Dent. Res.*, vol. 86, no. 1, pp. 12–24, Jan. 2007, doi: 10.1177/154405910708600103.

[56] C. Molnar and J. Gair, "Concepts of Biology: 1st Canadian Edition," 2015.

[57] G. Castaldo and F. Cerritelli, "Craniofacial growth: evolving paradigms," *CRANIO®*, vol. 33, no. 1, pp. 23–31, Jan. 2015, doi: 10.1179/0886963414Z.00000000042.

[58] R. R. Reid, "Facial Skeletal Growth and Timing of Surgical Intervention," *Clin. Plast. Surg.*, vol. 34, no. 3, pp. 357–367, Jul. 2007, doi: 10.1016/j.cps.2007.04.002.

[59] J. C. Brash, “The genesis and growth of deformed jaws and palates,” *Dent Board UK*, vol. 67, 1924.

[60] T. H. Morgan, “Theory of the gene,” 1928.

[61] C. H. Waddington, “Genes as evocators in development,” *Growth*, vol. 1, no. Suppl., pp. 37–45, 1939.

[62] J. P. Weinmann and H. Sicher, “Bone and bones. Fundamentals of bone biology.,” *Bone bones. Fundam. bone Biol.*, no. 2nd ed, 1955.

[63] J. H. Scott, “Growth at facial sutures,” *Am. J. Orthod.*, vol. 42, no. 5, pp. 381–387, May 1956, doi: 10.1016/0002-9416(56)90165-8.

[64] M. L. Moss and R. M. Rankow, “The role of the functional matrix in mandibular growth,” *Angle Orthod.*, vol. 38, no. 2, pp. 95–103, 1968.

[65] M. L. Moss, “The role of muscular functional matrices in development and maintenance of occlusion.,” *Bull. Pac. Coast Soc. Orthod.*, vol. 45, no. 4, pp. 29–30, Nov. 1970, [Online]. Available: http://www.ncbi.nlm.nih.gov/pubmed/5278398.

[66] J. J. Stutzmann and A. G. Petrovic, “Role of the lateral pterygoid muscle and meniscotemporomandibular frenum in spontaneous growth of the mandible and in growth stimulated by the postural hyperpropulsor,” *Am. J. Orthod. Dentofac. Orthop.*, vol. 97, no. 5, pp. 381–392, May 1990, doi: 10.1016/0889-5406(90)70110-X.

[67] J. van Limborgh, “The role of genetic and local environmental factors in the control of postnatal craniofacial morphogenesis.,” *Acta Morphol. Neerl. Scand.*, vol. 10, no. 1, pp. 37–47, Oct. 1972, [Online]. Available: http://www.ncbi.nlm.nih.gov/pubmed/4643664.

[68] D. H. Enlow, D. DiGangi, J. A. McNamara, and M. Mina, “An evaluation of the morphogenic and anatomic effects of the functional regulator utilizing the counterpart analysis,” *Eur. J. Orthod.*, vol. 10, no. 3, pp. 192–202, Aug. 1988, doi: 10.1093/ejo/10.3.192.

[69] W. R. Atchley and B. K. Hall, “A model for development and evolution of complex morphological structures.,” *Biol. Rev. Camb. Philos. Soc.*, vol. 66, no. 2, pp. 101–57, May 1991, [Online]. Available: http://www.ncbi.nlm.nih.gov/pubmed/1863686.

[70] B. G. Sarnat, “A Retrospective of Personal Craniofaciodental Research and Clinical Practice,” *Plast. &amp Reconstr. Surg.*, vol. 100, no. 1, pp. 132–153, Jul. 1997, doi: 10.1097/00006534-199707000-00024.

[71] B. G. Sarnat and M. R. Wexler, “Growth of the face and jaws after resection of the septal cartilage in the rabbit,” *Am. J. Anat.*, vol. 118, no. 3, pp. 755–767, May 1966, doi: 10.1002/aja.1001180306.

[72] I. Kjaer, “Human prenatal palatal closure related to skeletal maturity of the jaws.,” *J. Craniofac. Genet. Dev. Biol.*, vol. 9, no. 3, pp. 265–70, 1989, [Online]. Available: http://www.ncbi.nlm.nih.gov/pubmed/2613860.

[73] I. Kjaer, “Prenatal skeletal maturation of the human maxilla.,” *J. Craniofac. Genet. Dev. Biol.*, vol. 9, no. 3, pp. 257–64, 1989, [Online]. Available: http://www.ncbi.nlm.nih.gov/pubmed/2613859.

[74] S. E. Bishara, P. S. Burkey, and J. G. Kharouf, “Dental and facial asymmetries: a review,” *Angle Orthod.*, vol. 64, no. 2, pp. 89–98, 1994, doi: 10.1043/0003-3219(1994)064<0089:DAFAAR>2.0.CO;2.

[75] R. A. Anthes, “Development of asymmetries in a three-dimensional numerical model of the tropical cyclone,” *Mon. Weather Rev.*, vol. 100, no. 6, pp. 461–476, 1972.

[76] A. Björk, A. A. Krebs, and B. Solow, “A Method for Epidemiological Registration of Malocculusion,” *Acta Odontol. Scand.*, vol. 22, no. 1, pp. 27–41, 1964.

[77] K. G. Peres, A. J. D. Barros, M. A. Peres, and C. G. Victora, “Effects of breastfeeding and sucking habits on malocclusion in a birth cohort study,” *Rev. Saude Publica*, vol. 41, no. 3, pp. 343–350, 2007.

[78] C. Lippold, G. Hoppe, T. Moiseenko, U. Ehmer, and G. Danesh, “Analysis of condylar differences in functional unilateral posterior crossbite during early treatment–a randomized clinical study,” *J. Orofac. Orthop. der Kieferorthopädie*, vol. 69, no. 4, pp. 283–296, 2008.

[79] K. Keski-Nisula, R. Lehto, V. Lusa, L. Keski-Nisula, and J. Varrela, “Occurrence of malocclusion and need of orthodontic treatment in early mixed dentition,” *Am. J. Orthod. Dentofac. Orthop.*, vol. 124, no. 6, pp. 631–638, 2003.

[80] D. B. Kennedy and M. Osepchook, "Unilateral posterior crossbite with mandibular shift: a review," *Journal-Canadian Dent. Assoc.*, vol. 71, no. 8, p. 569, 2005.

[81] M. D. D. H. Benavides and J. Travesí, "Epidemiología de la maloclusión en un población escolar andaluza," *Rev. Iberoam. Ortod.*, vol. 13, no. 2, pp. 76–97, 1994.

[82] L. A. Bravo, C. Barrachina, and B. Bravo, "Evaluación epidemiológica de la maloclusión en 1000 pacientes ortodóncicos de diferentes regiones españolas," *Rev Esp Ortod*, vol. 17, pp. 219–240, 1987.

[83] C. van Keulen, G. Martens, and L. Dermaut, "Unilateral posterior crossbite and chin deviation: is there a correlation?," *Eur. J. Orthod.*, vol. 26, no. 3, pp. 283–8, Jun. 2004, doi: 10.1093/ejo/26.3.283.

[84] P. Agostino, A. Ugolini, A. Signori, A. Silvestrini-Biavati, J. E. Harrison, and P. Riley, "Orthodontic treatment for posterior crossbites," *Cochrane Database Syst. Rev.*, no. 8, 2014.

[85] K. Ishizaki, K. Suzuki, T. Mito, E. M. Tanaka, and S. Sato, "Morphologic, functional, and occlusal characterization of mandibular lateral displacement malocclusion," *Am. J. Orthod. Dentofac. Orthop.*, vol. 137, no. 4, pp. 454-e1, 2010.

[86] J. Primožič, M. Ovsenik, S. Richmond, C. H. Kau, and A. Zhurov, "Early crossbite correction: a three-dimensional evaluation," *Eur. J. Orthod.*, vol. 31, no. 4, pp. 352–356, 2009.

[87] T. Gazit-Rappaport, M. Weinreb, and E. Gazit, "Quantitative evaluation of lip symmetry in functional asymmetry," *Eur. J. Orthod.*, vol. 25, no. 5, pp. 443–450, 2003.

[88] D. Kecik, I. Kocadereli, and I. Saatci, "Evaluation of the treatment changes of functional posterior crossbite in the mixed dentition," *Am. J. Orthod. Dentofac. Orthop.*, vol. 131, no. 2, pp. 202–215, 2007.

[89] B. J. Langberg, K. Arai, and R. M. Miner, "Transverse skeletal and dental asymmetry in adults with unilateral lingual posterior crossbite," *Am. J. Orthod. Dentofac. Orthop.*, vol. 127, no. 1, pp. 6–15, Jan. 2005, doi: 10.1016/j.ajodo.2003.10.044.

[90] C. Liu, S. Kaneko, and K. Soma, "Effects of a mandibular lateral shift on the condyle and mandibular bone in growing rats: A morphological and histological study," *Angle Orthod.*, vol. 77, no. 5, pp. 787–793, 2007.

[91] P. M. Pirttiniemi, "Associations of mandibular and facial asymmetries—A review," *Am. J. Orthod. Dentofac. Orthop.*, vol. 106, no. 2, pp. 191–200, Aug. 1994, doi: 10.1016/S0889-5406(94)70038-9.

[92] B. Rilo, J. L. da Silva, M. J. Mora, C. Cadarso-Suárez, and U. Santana, "Midline shift and lateral guidance angle in adults with unilateral posterior crossbite," *Am. J. Orthod. Dentofac. Orthop.*, vol. 133, no. 6, pp. 804–808, 2008.

[93] E. Defraia, A. Marinelli, G. Baroni, and I. Tollaro, "Dentoskeletal effects of a removable appliance for expansion of the maxillary arch: a postero-anterior cephalometric study," *Eur. J. Orthod.*, vol. 30, no. 1, pp. 57–60, 2007.

[94] P. Pirttiniemi, T. Kantomaa, and P. Lahtela, "Relationship between craniofacial and condyle path asymmetry in unilateral cross-bite patients," *Eur. J. Orthod.*, vol. 12, no. 4, pp. 408–413, Nov. 1990, doi: 10.1093/ejo/12.4.408.

[95] J.-Y. Kim, H.-D. Jung, Y.-S. Jung, C.-J. Hwang, and H.-S. Park, "A simple classification of facial asymmetry by TML system.," *J. Craniomaxillofac. Surg.*, vol. 42, no. 4, pp. 313–20, Jun. 2014, doi: 10.1016/j.jcms.2013.05.019.

[96] A. R. Sepahdari and S. Mong, "Skull base CT: normative values for size and symmetry of the facial nerve canal, foramen ovale, pterygoid canal, and foramen rotundum.," *Surg. Radiol. Anat.*, vol. 35, no. 1, pp. 19–24, Jan. 2013, doi: 10.1007/s00276-012-1001-4.

[97] S. Kokai, T. Yabushita, J. L. Zeredo, K. Toda, and K. Soma, "Functional changes of the temporomandibular joint mechanoreceptors induced by a lateral mandibular shift in rats," *Angle Orthod.*, vol. 77, no. 3, pp. 436–441, 2007.

[98] P. M. Castelo, M. B. D. Gaviao, L. J. Pereira, and L. R. Bonjardim, "Masticatory muscle thickness, bite force, and occlusal contacts in young children with unilateral posterior crossbite," *Eur. J. Orthod.*, vol. 29, no. 2, pp. 149–156, Jan. 2007, doi: 10.1093/ejo/cjl089.

[99] S. Kiliaridis, P. H. Mahboubi, M. C. Raadsheer, and C. Katsaros, "Ultrasonographic thickness of the masseter muscle in growing individuals with unilateral crossbite," *Angle Orthod.*, vol. 77, no. 4, pp. 607–611, 2007.

[100]J. A. Alarcón, C. Martín, J. C. Palma, and M. Menéndez-Núñez, "Activity of jaw muscles in unilateral cross-bite without mandibular shift," *Arch. Oral Biol.*, vol. 54, no. 2, pp. 108–114, 2009.

[101]Y.-Y. Kwak, I. Jang, D.-S. Choi, and B.-K. Cha, "Functional evaluation of orthopedic and orthodontic treatment in a patient with unilateral posterior crossbite and facial asymmetry," *Korean J. Orthod.*, vol. 44, no. 3, pp. 143–153, 2014.

[102]S. E. P. Pellizoni, M. A. C. Salioni, Y. Juliano, A. S. Guimarães, and L. G. Alonso, "Temporomandibular joint disc position and configuration in children with functional unilateral posterior crossbite: a magnetic resonance imaging evaluation," *Am. J. Orthod. Dentofac. Orthop.*, vol. 129, no. 6, pp. 785–793, 2006.

[103]S. Tecco, S. Tetè, and F. Festa, "Electromyographic evaluation of masticatory, neck, and trunk muscle activity in patients with posterior crossbites," *Eur. J. Orthod.*, vol. 32, no. 6, pp. 747–752, 2010.

[104]J. A. McNamara Jr, "Early intervention in the transverse dimension: is it worth the effort?," *Am. J. Orthod. Dentofac. Orthop.*, vol. 121, no. 6, pp. 572–574, 2002.

[105]P. William, F. Henry, and S. David, "Contemphorary Orthodontics," *Mosby Elsevier*, no. 1, p. 762, 2007, doi: 10.1007/s13398-014-0173-7.2.

[106]O. G. da Silva Filho, F. M. Ferrari Júnior, C. A. Aiello, and N. Zopone, "Correction of posterior crossbite in the primary dentition.," *J. Clin. Pediatr. Dent.*, vol. 24, no. 3, pp. 165–80, 2000, [Online]. Available: http://www.ncbi.nlm.nih.gov/pubmed/11314138.

[107]M. Malandris and E. K. Mahoney, "Aetiology, diagnosis and treatment of posterior cross-bites in the primary dentition," *Int. J. Paediatr. Dent.*, vol. 14, no. 3, pp. 155–166, 2004.

[108]D. Manfredini, G. Perinetti, and L. Guarda-Nardini, "Dental malocclusion is not related to temporomandibular joint clicking: a logistic regression analysis in a patient population," *Angle Orthod.*, vol. 84, no. 2, pp. 310–315, 2013.

[109]S. Tecco and F. Festa, "Prevalence of signs and symptoms of temporomandibular disorders in children and adolescents with and without crossbites.," *World J. Orthod.*, vol. 11, no. 1, 2010.

[110]V. Caridi and G. Galluccio, "Correlation between Unilateral Posterior Crossbite, Mandibular Shift and jaw muscles: A review," 2014.

[111]C. Lippold, T. Stamm, U. Meyer, A. Végh, T. Moiseenko, and G. Danesh, "Early treatment of posterior crossbite-a randomised clinical trial," *Trials*, vol. 14, no. 1, p. 20, 2013.

[112]W. K. Solberg, C. A. Bibb, B. B. Nordström, and T. L. Hansson, "Malocclusion associated with temporomandibular joint changes in young adults at autopsy," *Am. J. Orthod.*, vol. 89, no. 4, pp. 326–330, 1986.

[113]P. Planas, "Age et instruments vraiment précoces en Orthopedic Dynamique Fonctionnelle," *l'Orthodontie Française*, vol. 33, pp. 279–96, 1962.

[114]P. Planas, "Equilibre et réhabilitation Neuro-Occlusale," *l'Orthodontie Française*, vol. 66, pp. 435–41, 1992.

[115]P. Planas, "Notre testament en RNO," *l'Orthodontie Française*, vol. 62, pp. 695–708, 1991.

[116]P. Planas, "L'importance de la situation du plan d'occlusion," *l'Orthodontie Française*, vol. 59, pp. 727–54, 1988.

[117]P. Planas, "Comment éviter la récidive?," *l'Orthodontie Française*, vol. 27, pp. 629–42, 1986.

[118]P. Planas, "L'interecption des malocclusions," *l'Orthodontie Française*, vol. 54, pp. 313–27, 1983.

[119]P. Planas, "La pipe équiplan," *l'Orthodontie Française*, vol. 52, pp. 755–60, 1981.

[120]P. Planas, "L'angle fonctionnel masticatoire AFM de Planas.," *l'Orthodontie Française*, vol. 59, pp. 727–54, 1988.

[121]P. Planas, "La thérapeutique orthodontique b plus précoce Avec les composites polymerisables aux UV.," *l'Orthodontie Française*, vol. 48, pp. 177–85, 1977.

[122]P. Planas, "Rehabilitation Neuro-Occlusale: RNO," *l'Orthodontie Française*, vol. 42, pp. 333–47, 1971.

[123]P. Planas, “La lois Planas de la dimension verticale minimale,” *l’Orthodontie Française*, vol. 39, pp. 509–24, 1968.

[124]P. Planas, “Are gothique et Réhabilitation Neuro-Occlusale,” *l’Orthodontie Française*, vol. 36, pp. 235–44, 1965.

[125]P. Planas, “Après l’équiplan, l’are gothique Planas,” *l’Orthodontie Française*, vol. 34, pp. 111–22, 1963.

[126]P. Planas, “Contribution a l’étude de la thérapie fonctionnelle et de ses résultats: résultats en bouche de l’orthopédie fonctionelle.,” *l’Orthodontie Française*, vol. 32, pp. 61–84, 1961.

[127]P. Planas, “Diagnostic symptomatique gnathostatique.,” *l’Orthodontie Française*, vol. 31, pp. 309–22, 1960.

[128]P. Planas, “Equiplan,” *l’Orthodontie Française*, vol. 31, pp. 295–307, 1960.

[129]P. Planas, “Notre orthopedic fonctionnelle et l’occlusion traumatique,” *l’Orthodontie Française*, vol. 25, pp. 365–72, 1954.

[130]P. Planas, “L’orthodontie fonctionnelle de la canine vestibulée,” *l’Orthodontie Française*, vol. 24, pp. 143–8, 1953.

[131]P. Planas, “Le diagnostic: «son présent et son avenir»,” *l’Orthodontie Française*, vol. 23, pp. 285–9, 1952.

[132]P. Planas, “La recidive de l’expansion: comment l’éviter ?,” *l’Orthodontie Française*, vol. 23, pp. 279–84, 1952.

[133]P. Planas, “Notre apport aux malformations et aux mauvaises dispositions des alvéoles temporaires,” *l’Orthodontie Française*, vol. 22, pp. 237–4, 1951.

[134]P. Planas, “Nouvel appareil fonctionnel pour la dilatation totale de l’arcade temporaire,” *l’Orthodontie Française*, vol. 22, pp. 70–3, 1951.

[135]P. Planas, “Quelques idées sur notre orthodontie semi-fonctionnelle.,” *l’Orthodontie Française*, vol. 21, pp. 261–8, 1950.

[136]P. Planas, “Le facteur âge dans la thérapeutique orthodontique,” *l’Orthodontie Française*, vol. 20, no. 45–53, 1949.

[137]J. Kolf, “A propos de la mastication,” *Rev Orthop Dento Faciale*, vol. 36, p. 7, 2002.

[138]J.-L. Raymond, “Finalité fonctionnelle et occlusale du traitement orthopédique de classe III,” *Rev. Orthop. Dento. Faciale.*, vol. 37, no. 3, pp. 285–303, 2003.

[139]J.-L. Raymond, “Mastication et corrections occlusales transversales,” *Rev. Orthop. Dento. Faciale.*, vol. 35, no. 3, pp. 339–346, 2001.

[140]J.-L. Raymond, “Approche fonctionnelle de l’allaitement et malocclusions,” *Rev. Orthop. Dento. Faciale.*, vol. 34, no. 3, pp. 379–402, 2000.

[141]U. Santana-Penin, “La mastication: moyen essentiel de prevention et de traitement des pathologies occlusales ; effets sur la croissance et le développement maxillo-mandibulaire de l’enfant,” *l’Orthodontie Française*, no. 67, p. 449, 1996.

[142]M. Gaspard, “Acquisition et exercice de la fonction masticatrice chez l’enfant et l’adolescent (1re partie),” *Rev. Orthop. Dento. Faciale.*, vol. 35, no. 4, pp. 11–36, 2001.

[143]M. Gaspard, “Acquisition et exercice de la fonction masticatrice chez l’enfant et l’adolescent (1re partie),” *Rev. Orthop. Dento. Faciale.*, vol. 35, no. 1, pp. 11–36, 2002.

[144]C. de Salvador-Planas, “Les pistes directes en composite: traitement fonctionnel des occlusions croisées,” *Rev. Orthop. Dento. Faciale.*, vol. 25, no. 4, pp. 443–450, 1991.

[145]C. de Salvador-Planas, “Utilisation de la Goniométrie Orthodontique pour l’Etude de l’Expansion Apicale, obtenue par la Méthode du pr. Planas : La Réhabilitation Neuro-Occlusale,” *L’Orthodontie Française*, vol. 63, pp. 527–35, 1992.

[146]T. Öberg, G. E. Carlsson, and C.-M. Fajers, “The Temporomandibular Joint: A Morphologic Study on A Human Autopsy Material,” *Acta Odontol. Scand.*, vol. 29, no. 3, pp. 349–384, Jan. 1971, doi: 10.3109/00016357109026526.

[147]I. Kjær, “Human prenatal craniofacial development related to brain development under normal and pathologic conditions,” *Acta Odontol. Scand.*, vol. 53, no. 3, pp. 135–143, Jan. 1995, doi: 10.3109/00016359509005963.

[148]W. D. Clark, “Preventing Dentofacial Abnormalities With the Proper Correction of Pediatric Upper Airway Obstruction,” *Arch. Otolaryngol. Neck Surg.*, vol. 131, no. 10, p. 916, Oct. 2005, doi: 10.1001/archotol.131.10.916.

[149]D. Harari, M. Redlich, S. Miri, T. Hamud, and M. Gross, "The effect of mouth breathing versus nasal breathing on dentofacial and craniofacial development in orthodontic patients," *Laryngoscope*, vol. 120, no. 10, pp. 2089–2093, Sep. 2010, doi: 10.1002/lary.20991.

[150]S. D. Josell, "Habits affecting dental and maxillofacial growth and development.," *Dent. Clin. North Am.*, vol. 39, no. 4, pp. 851–60, Oct. 1995, [Online]. Available: http://www.ncbi.nlm.nih.gov/pubmed/8522046.

[151]S. Linder-Aronson, "Adenoids. Their effect on mode of breathing and nasal airflow and their relationship to characteristics of the facial skeleton and the denition. A biometric, rhino-manometric and cephalometro-radiographic study on children with and without adenoids.," *Acta Otolaryngol. Suppl.*, vol. 265, pp. 1–132, 1970, [Online]. Available: http://www.ncbi.nlm.nih.gov/pubmed/5272140.

[152]R. M. Rubin, "Mode of respiration and facial growth.," *Am. J. Orthod.*, vol. 78, no. 5, pp. 504–10, Nov. 1980, [Online]. Available: http://www.ncbi.nlm.nih.gov/pubmed/6933857.

[153]B. Palmer, "The Influence of Breastfeeding on the Development of the Oral Cavity: A Commentary," *J. Hum. Lact.*, vol. 14, no. 2, pp. 93–98, Jun. 1998, doi: 10.1177/089033449801400203.

[154]D. Viggiano, "Breast feeding, bottle feeding, and non-nutritive sucking; effects on occlusion in deciduous dentition," *Arch. Dis. Child.*, vol. 89, no. 12, pp. 1121–1123, Dec. 2004, doi: 10.1136/adc.2003.029728.

[155]C. W. Genna, *Supporting sucking skills in breastfeeding infants*. Jones & Bartlett Learning, 2016.

[156]M. Sánchez-Molins, J. C. Grau, C. G. Lischeid, and J. M. T. Ustrell, "Comparative study of the craniofacial growth depending on the type of lactation received.," *Eur. J. Paediatr. Dent. Off. J. Eur. Acad. Paediatr. Dent.*, vol. 11, no. 2, pp. 87–92, 2010.

[157]J. J. Warren, R. L. Slayton, S. E. Bishara, S. M. Levy, T. Yonezu, and M. J. Kanellis, "Effects of nonnutritive sucking habits on occlusal characteristics in the mixed dentition.," *Pediatr. Dent.*, vol. 27, no. 6, pp. 445–50, [Online]. Available: http://www.ncbi.nlm.nih.gov/pubmed/16532883.

[158]B. Ogaard, E. Larsson, and R. Lindsten, "The effect of sucking habits, cohort, sex, intercanine arch widths, and breast or bottle feeding on posterior crossbite in Norwegian and Swedish 3-year-old children.," *Am. J. Orthod. Dentofacial Orthop.*, vol. 106, no. 2, pp. 161–6, Aug. 1994, doi: 10.1016/S0889-5406(94)70034-6.

[159]N. Tsanidis, G. S. Antonarakis, and S. Kiliaridis, "Functional changes after early treatment of unilateral posterior cross-bite associated with mandibular shift: a systematic review," *J. Oral Rehabil.*, vol. 43, no. 1, pp. 59–68, Jan. 2016, doi: 10.1111/joor.12335.

[160]C. E. Santos, O. de Freitas, A. C. C. Spadaro, and W. Mestriner-Junior, "Development of a colorimetric system for evaluation of the masticatory efficiency," *Braz. Dent. J.*, vol. 17, no. 2, pp. 95–99, 2006, doi: 10.1590/S0103-64402006000200002.

[161]R. B. Kerstein and J. Radke, "Average chewing pattern improvements following Disclusion Time reduction," *CRANIO®*, vol. 35, no. 3, pp. 135–151, May 2017, doi: 10.1080/08869634.2016.1190526.

[162]G. E. J. Langenbach and A. G. Hannam, "The role of passive muscle tensions in a three-dimensional dynamic model of the human jaw," *Arch. Oral Biol.*, vol. 44, no. 7, pp. 557–573, 1999, doi: 10.1016/S0003-9969(99)00034-5.

[163]J. Martinez-Gomis, M. Lujan-Climent, S. Palau, J. Bizar, J. Salsench, and M. Peraire, "Relationship between chewing side preference and handedness and lateral asymmetry of peripheral factors," *Arch. Oral Biol.*, vol. 54, no. 2, pp. 101–107, Feb. 2009, doi: 10.1016/j.archoralbio.2008.09.006.

[164]A. J. Miller, *Craniomandibular muscles: Their role in function and form*. CRC Press, 2017.

[165]B. Thilandera, "Orthodontic relapse versus natural development," *Am. J. Orthod. Dentofac. Orthop.*, vol. 117, no. 5, pp. 562–563, May 2000, doi: 10.1016/S0889-5406(00)70200-9.

[166]B. Thilander and B. Lennartsson, "A Study of Children with Unilateral Posterior Crossbite, Treated and Untreated, in the Deciduous Dentition," *J. Orofac. Orthop. / Fortschritte der Kieferorthopädie*, vol. 63, no. 5, pp. 371–383, Sep. 2002, doi: 10.1007/s00056-002-0210-6.

[167]A. Enomoto, J. Watahiki, T. Yamaguchi, T. Irie, T. Tachikawa, and K. Maki, "Effects of mastication on mandibular growth evaluated by microcomputed tomography," *Eur. J. Orthod.*, vol. 32, no. 1, pp. 66–70, Feb. 2010, doi: 10.1093/ejo/cjp060.

[168]K. Maki, T. Nishioka, E. Shioiri, T. Takahashi, and M. Kimura, "Effects of dietary consistency on the mandible of rats at the growth stage: computed X-ray densitometric and cephalometric analysis.," *Angle Orthod.*, vol. 72, no. 5, pp. 468–75, Oct. 2002, doi: 10.1043/0003-3219(2002)072<0468:EODCOT>2.0.CO;2.

[169]S. Benazzi, H. N. Nguyen, O. Kullmer, and K. Kupczik, "Dynamic modelling of tooth deformation using occlusal kinematics and finite element analysis," *PLoS One*, vol. 11, no. 3, pp. 1–17, 2016, doi: 10.1371/journal.pone.0152663.

[170]G. P. Neto, R. M. Puppin-Rontani, and R. C. M. R. Garcia, "Changes in the masticatory cycle after treatment of posterior crossbite in children aged 4 to 5 years," *Am. J. Orthod. Dentofac. Orthop.*, vol. 131, no. 4, pp. 464–472, Apr. 2007, doi: 10.1016/j.ajodo.2005.06.030.

[171]S. Petrén, L. Bondemark, and B. Söderfeldt, "A systematic review concerning early orthodontic treatment of unilateral posterior crossbite," *Angle Orthod.*, vol. 73, no. 5, pp. 588–596, 2003.

[172]T. Huynh, D. B. Kennedy, D. R. Joondeph, and A.-M. Bollen, "Treatment response and stability of slow maxillary expansion using Haas, hyrax, and quad-helix appliances: a retrospective study," *Am. J. Orthod. Dentofac. Orthop.*, vol. 136, no. 3, pp. 331–339, 2009.

[173]H. M. Frost, "A 2003 update of bone physiology and Wolff's Law for clinicians.," *Angle Orthod.*, vol. 74, no. 1, pp. 3–15, Feb. 2004, doi: 10.1043/0003-3219(2004)074<0003:AUOBPA>2.0.CO;2.

[174]M. Lee, D. H. Chung, J. Lee, and K. Cha, "Assessing soft-tissue characteristics of facial asymmetry with photographs," *Am. J. Orthod. Dentofac. Orthop.*, vol. 138, no. 1, pp. 23–31, Jul. 2010, doi: 10.1016/j.ajodo.2008.08.029.

[175]P. Millstein and A. Maya, "An evaluation of occlusal contact marking indicators. A descriptive quantitative method.," *J. Am. Dent. Assoc.*, vol. 132, no. 9, pp. 1280–6; quiz 1319, Sep. 2001, doi: 10.14219/jada.archive.2001.0373.

[176]M. N. Saad, G. Weiner, D. Ehrenberg, and S. Weiner, "Effects of load and indicator type upon occlusal contact markings," *J. Biomed. Mater. Res. Part B Appl. Biomater.*, vol. 85B, no. 1, pp. 18–22, Apr. 2008, doi: 10.1002/jbm.b.30910.

[177]S. Qadeer, R. Kerstein, R. J. Y. Kim, J.-B. Huh, and S.-W. Shin, "Relationship between articulation paper mark size and percentage of force measured with computerized occlusal analysis," *J. Adv. Prosthodont.*, vol. 4, no. 1, p. 7, 2012, doi: 10.4047/jap.2012.4.1.7.

[178]Y.-W. Cheong and L.-J. Lo, "Facial asymmetry: etiology, evaluation, and management.," *Chang Gung Med. J.*, vol. 34, no. 4, pp. 341–51, 2014, doi: 10.1590/0103-6440201300003.

[179]R. Nanda and M. J. Margolis, "Treatment strategies for midline discrepancies," *Semin. Orthod.*, vol. 2, no. 2, pp. 84–89, Jun. 1996, doi: 10.1016/S1073-8746(96)80046-6.

[180]R. M. Ricketts, "A foundation for cephalometric communication," *Am. J. Orthod.*, vol. 46, no. 5, pp. 330–357, May 1960, doi: 10.1016/0002-9416(60)90047-6.

[181]D. C. Grummons and M. A. Kappeyne van de Coppello, "A frontal asymmetry analysis.," *J. Clin. Orthod.*, vol. 21, no. 7, pp. 448–65, Jul. 1987, [Online]. Available: http://www.ncbi.nlm.nih.gov/pubmed/3476493.

[182]M. Pinheiro *et al.*, "A 3D cephalometric protocol for the accurate quantification of the craniofacial symmetry and facial growth," *J. Biol. Eng.*, vol. 13, no. 1, p. 42, Dec. 2019, doi: 10.1186/s13036-019-0171-6.

[183]A. Dobai, Z. Markella, T. Vízkelety, C. Fouquet, A. Rosta, and J. Barabás, "Landmark-based midsagittal plane analysis in patients with facial symmetry and asymmetry based on CBCT analysis tomography," *J. Orofac. Orthop. / Fortschritte der Kieferorthopädie*, vol. 79, no. 6, pp. 371–379, Nov. 2018, doi: 10.1007/s00056-018-0151-3.

[184]S. M. Shin, Y.-M. Y.-I. Kim, N.-R. Kim, Y.-S. Choi, S.-B. Park, and Y.-M. Y.-I. Kim, "Statistical shape analysis-based determination of optimal midsagittal reference plane for evaluation of facial asymmetry," *Am. J. Orthod. Dentofac. Orthop.*, vol. 150, no. 2, pp. 252–260, Aug. 2016, doi: 10.1016/j.ajodo.2016.01.017.

[185]J. Damstra, Z. Fourie, M. De Wit, and Y. Ren, "A three-dimensional comparison of a morphometric and conventional cephalometric midsagittal planes for craniofacial asymmetry," *Clin. Oral Investig.*, vol. 16, no. 1, pp. 285–294, Feb. 2012, doi: 10.1007/s00784-011-0512-4.

[186]P. Pittayapat, M. M. Bornstein, T. S. N. Imada, W. Coucke, I. Lambrichts, and R. Jacobs, "Accuracy of linear measurements using three imaging modalities: two lateral cephalograms and one 3D model from CBCT data," *Eur. J. Orthod.*, vol. 37, no. 2, pp. 202–208, Apr. 2015, doi: 10.1093/ejo/cju036.

[187]N. Zamora, J. M. Llamas, R. Cibrián, J. L. Gandia, and V. Paredes, "Cephalometric measurements from 3D reconstructed images compared with conventional 2D images," *Angle Orthod.*, vol. 81, no. 5, pp. 856–864, Sep. 2011, doi: 10.2319/121210-717.1.

[188]O. J. C. van Vlijmen, T. Maal, S. J. Bergé, E. M. Bronkhorst, C. Katsaros, and A. M. Kuijpers-Jagtman, "A comparison between 2D and 3D cephalometry on CBCT scans of human skulls," *Int. J. Oral Maxillofac. Surg.*, vol. 39, no. 2, pp. 156–160, Feb. 2010, doi: 10.1016/j.ijom.2009.11.017.

[189]N. Li, B. Hu, F. Mi, and J. Song, "Preliminary evaluation of cone beam computed tomography in three-dimensional cephalometry for clinical application," *Exp. Ther. Med.*, vol. 13, no. 5, pp. 2451–2455, 2017.

[190]N. Zamora, J. M. Llamas, R. Cibrián, J. L. Gandia, and V. Paredes, "A study on the reproducibility of cephalometric landmarks when undertaking a three-dimensional (3D) cephalometric analysis," *Med. Oral Patol. Oral Cir. Bucal*, vol. 17, no. 4, p. e678, 2012.

[191]B. F. Gribel, M. N. Gribel, D. C. Frazão, J. A. McNamara Jr, and F. R. Manzi, "Accuracy and reliability of craniometric measurements on lateral cephalometry and 3D measurements on CBCT scans," *Angle Orthod.*, vol. 81, no. 1, pp. 26–35, 2011.

[192]L. W. Graber, R. L. Vanarsdall, K. W. L. Vig, and G. J. Huang, *Orthodontics-E-Book: current principles and techniques*. Elsevier Health Sciences, 2016.

[193]G. Thiesen, B. F. Gribel, and M. P. M. Freitas, "Facial asymmetry: a current review," *Dental Press J. Orthod.*, vol. 20, no. 6, pp. 110–125, Dec. 2015, doi: 10.1590/2177-6709.20.6.110-125.sar.

[194]K. Koyano, Y. Tsukiyama, and R. Kuwatsuru, "Rehabilitation of occlusion - science or art?," *J. Oral Rehabil.*, vol. 39, no. 7, pp. 513–21, Jul. 2012, doi: 10.1111/j.1365-2842.2012.02303.x.

[195]L. Sonnesen and M. Bakke, "Bite force in children with unilateral crossbite before and after orthodontic treatment. A prospective longitudinal study.," *Eur. J. Orthod.*, vol. 29, no. 3, pp. 310–3, Jun. 2007, doi: 10.1093/ejo/cjl082.

[196]L. Kurol, J. and Berglund, "Longitudinal study and cost-benefit analysis of the effect of early treatment of posterior cross-bites in the primary dentition," *Eur. J. Orthod.*, vol. 14, pp. 173–9, 1992.

[197]P. H. Schiffman and O. C. Tuncay, "Maxillary expansion: a meta analysis.," *Clin. Orthod. Res.*, vol. 4, no. 2, pp. 86–96, May 2001, [Online]. Available: http://www.ncbi.nlm.nih.gov/pubmed/11553090.

[198]R. A. Chate, "Do we really want a quick fix?," *Br. Dent. J.*, vol. 188, no. 4, pp. 177–86, Feb. 2000, doi: 10.1038/sj.bdj.4800426.

[199]P. Ngan, "Contemporary Orthodontics, 5th ed," *Am. J. Orthod. Dentofac. Orthop.*, vol. 142, no. 3, p. 425, Sep. 2012, doi: 10.1016/j.ajodo.2012.07.004.

[200]P. O'Higgins *et al.*, "Virtual Functional Morphology: Novel Approaches to the Study of Craniofacial Form and Function," *Evol. Biol.*, vol. 39, no. 4, pp. 521–535, Dec. 2012, doi: 10.1007/s11692-012-9173-8.

[201]K. Kupczik, C. A. Dobson, M. J. Fagan, R. H. Crompton, C. E. Oxnard, and P. O'Higgins, "Assessing mechanical function of the zygomatic region in macaques: validation and sensitivity testing of finite element models," *J. Anat.*, vol. 210, no. 1, pp. 41–53, Jan. 2007, doi: 10.1111/j.1469-7580.2006.00662.x.

[202]J. H. H. Koolstra and T. M. G. J. M. G. J. van Eijden, "Combined finite-element and rigid-body analysis of human jaw joint dynamics," *J. Biomech.*, vol. 38, no. 12, pp. 2431–2439, Dec. 2005, doi: 10.1016/j.jbiomech.2004.10.014.

[203]A. G. Hannam, "Dynamic modeling and jaw biomechanics.," *Orthod. Craniofac. Res.*, vol. 6 Suppl 1, pp. 59–65, 2003, [Online]. Available: http://www.ncbi.nlm.nih.gov/pubmed/14606536.

[204]J.-P. Geng, K. B. C. Tan, and G.-R. Liu, "Application of finite element analysis in implant dentistry: A review of the literature," *J. Prosthet. Dent.*, vol. 85, no. 6, pp. 585–598, Apr. 2018, doi: 10.1067/mpr.2001.115251.

[205]J. W. W. Farah, R. G. R. G. Craig, and D. L. D. L. Sikarskie, "Photoelastic and finite element stress analysis of a restored axisymmetric first molar," *J. Biomech.*, vol. 6, no. 5, pp. 511–520, Sep. 1973, doi: 10.1016/0021-9290(73)90009-2.

[206]R. W. Thresher and G. E. Saito, "The stress analysis of human teeth," *J. Biomech.*, vol. 6, no. 5, pp. 443–449, Sep. 1973, doi: 10.1016/0021-9290(73)90003-1.

[207]H. Y. Cheng, K. T. Chu, F. C. Shen, Y. N. Pan, H. H. Chou, and K. L. Ou, "Stress effect on bone remodeling and osseointegration on dental implant with novel nano/microporous surface functionalization," *J. Biomed. Mater. Res. - Part A*, vol. 101 A, no. 4, pp. 1158–1164, 2013, doi: 10.1002/jbm.a.34415.

[208]R. Mehrotra, R. K. Jaiswal, P. Mehrotra, S. Kapoor, and A. Jain, "Evaluation of the torque control of the maxillary incisors in lingual orthodontics during retraction – A finite element analysis," *Int. J. Dent. Sci. Res.*, vol. 2, no. 2–3, pp. 75–80, 2015, doi: 10.1016/j.ijdsr.2015.11.008.

[209]A. Nikolaus, C. Fleck, T. Lindtner, J. Currey, and P. Zaslansky, "Importance of the variable periodontal ligament geometry for whole tooth mechanical function: A validated numerical study," *J. Mech. Behav. Biomed. Mater.*, vol. 67, no. November 2016, pp. 61–73, 2016, doi: 10.1016/j.jmbbm.2016.11.020.

[210]B. Sarrafpour, M. Swain, Q. Li, and H. Zoellner, "Tooth Eruption Results from Bone Remodelling Driven by Bite Forces Sensed by Soft Tissue Dental Follicles: A Finite Element Analysis," *PLoS One*, vol. 8, no. 3, p. e58803, Mar. 2013, doi: 10.1371/journal.pone.0058803.

[211]A. Zargham, A. Geramy, and G. Rouhi, "Evaluation of long-term orthodontic tooth movement considering bone remodeling process and in the presence of alveolar bone loss using finite element method," *Orthod. Waves*, vol. 5, pp. 1–12, 2016, doi: 10.1016/j.odw.2016.09.001.

[212]M. L. Moss *et al.*, "Finite element method modeling of craniofacial growth," *Am. J. Orthod.*, vol. 87, no. 6, pp. 453–472, Jun. 1985, doi: 10.1016/0002-9416(85)90084-3.

[213]J. Libby, A. Marghoub, D. Johnson, R. H. Khonsari, M. J. Fagan, and M. Moazen, "Modelling human skull growth: a validated computational model," *J. R. Soc. Interface*, vol. 14, no. 130, p. 20170202, 2017, doi: 10.1098/rsif.2017.0202.

[214]A. Marghoub, J. Libby, C. Babbs, E. Pauws, M. J. Fagan, and M. Moazen, "Predicting calvarial growth in normal and craniosynostotic mice using a computational approach," *J. Anat.*, vol. 10, pp. 440–448, 2017, doi: 10.1111/joa.12764.

[215]J. W. DeVocht, V. K. Goel, D. L. Zeitler, and D. Lew, "A study of the control of disc movement within the temporomandibular joint using the finite element technique," *J. Oral Maxillofac. Surg.*, vol. 54, no. 12, pp. 1431–1437, Dec. 1996, doi: 10.1016/S0278-2391(96)90259-1.

[216]S. A. Romeed, S. L. Fok, and N. H. F. Wilson, "A comparison of 2D and 3D finite element analysis of a restored tooth.," *J. Oral Rehabil.*, vol. 33, no. 3, pp. 209–15, Mar. 2006, doi: 10.1111/j.1365-2842.2005.01552.x.

[217]A. P. del Palomar, M. Doblare, A. Pérez del Palomar, and M. Doblaré, "3D Finite Element Simulation of the Opening Movement of the Mandible in Healthy and Pathologic Situations," *J. Biomech. Eng.*, vol. 128, no. 2, p. 242, 2006, doi: 10.1115/1.2165697.

[218]M. S. Commisso, J. Martínez-Reina, and J. Mayo, "A study of the temporomandibular joint during bruxism.," *Int. J. Oral Sci.*, vol. 6, no. 2, pp. 116–23, Jun. 2014, doi: 10.1038/ijos.2014.4.

[219]E. Illipronti-Filho, S. M. de Fantini, and I. Chilvarquer, "Evaluation of mandibular condyles in children with unilateral posterior crossbite.," *Braz. Oral Res.*, vol. 29, no. 1, p. 49, 2015, doi: 10.1590/1807-3107BOR-2015.vol29.0049.

[220]V. Toro-Ibacache, "A finite element study of the human cranium; The impact of morphological variation on biting performance.," 2013.

[221]C.-C. Ko, E. P. Rocha, and M. Larson, "Past, present and future of finite element analysis in dentistry," *Biomed. Appl. to Ind. Dev.*, pp. 1–25, 2012.

[222]D. Moratal, *Finite Element Analysis: From Biomedical Applications to Industrial Developments*. BoD–Books on Demand, 2012.

[223]J. Chen *et al.*, "A periodontal ligament driven remodeling algorithm for orthodontic tooth movement," *J. Biomech.*, vol. 47, no. 7, pp. 1689–1695, May 2014, doi: 10.1016/j.jbiomech.2014.02.030.

[224]F. Gröning, M. J. Fagan, and P. O'Higgins, "The effects of the periodontal ligament on mandibular stiffness: a study combining finite element analysis and geometric morphometrics," *J. Biomech.*, vol. 44, no. 7, pp. 1304–1312, Apr. 2011, doi: 10.1016/j.jbiomech.2011.01.008.

[225]P. M. Cattaneo, T. Kofod, M. Dalstra, and B. Melsen, "Using the finite element method to model the biomechanics of the asymmetric mandible before, during and after skeletal correction by distraction osteogenesis.," *Comput. Methods Biomech. Biomed. Engin.*, vol. 8, no. 3, pp. 157–65, Jun. 2005, doi: 10.1080/10255840512331388731.

[226]J. A. Bright and E. J. Rayfield, "The Response of Cranial Biomechanical Finite Element Models to Variations in Mesh Density," *Anat. Rec. Adv. Integr. Anat. Evol. Biol.*, vol. 294, no. 4, pp. 610–620, Apr. 2011, doi: 10.1002/ar.21358.

[227]D. Systèmes, "Abaqus Analysis User's Guide, Version 6.14." Dassault Systèmes, 2014.

[228]V. Toro-Ibacache *et al.*, "Validity and sensitivity of a human cranial finite element model: implications for comparative studies of biting performance," *J. Anat.*, vol. 228, no. 1, pp. 70–84, 2016, doi: 10.1111/joa.12384.

[229]H. Mori *et al.*, "Three-dimensional finite element analysis of cartilaginous tissues in human temporomandibular joint during prolonged clenching.," *Arch. Oral Biol.*, vol. 55, no. 11, pp. 879–86, Nov. 2010, doi: 10.1016/j.archoralbio.2010.07.011.

[230]E. Marchandise, G. Compère, M. Willemet, G. Bricteux, C. Geuzaine, and J.-F. Remacle, "Quality meshing based on STL triangulations for biomedical simulations," *Int. j. numer. method. biomed. eng.*, p. n/a-n/a, 2010, doi: 10.1002/cnm.1388.

[231]C. F. Ross, "Finite element analysis in vertebrate biomechanics," *Anat. Rec. Part A Discov. Mol. Cell. Evol. Biol. An Off. Publ. Am. Assoc. Anat.*, vol. 283, no. 2, pp. 253–258, 2005.

[232]W. A. Weijs and B. Hillen, "Physiological cross-section of the human jaw muscles," *Cells Tissues Organs*, vol. 121, no. 1, pp. 31–35, 1985.

[233]P. H. Van Spronsen, W. A. Weijs, J. Valk, B. v Prahl-Andersen, and F. C. Van Ginkel, "Comparison of jaw-muscle bite-force cross-sections obtained by means of magnetic resonance imaging and high-resolution CT scanning," *J. Dent. Res.*, vol. 68, no. 12, pp. 1765–1770, 1989.

[234]P. M. Castelo, L. J. Pereira, L. R. Bonjardim, and M. B. D. Gavião, "Changes in bite force, masticatory muscle thickness, and facial morphology between primary and mixed dentition in preschool children with normal occlusion," *Ann. Anat.*, vol. 192, no. 1, pp. 23–26, 2010, doi: 10.1016/j.aanat.2009.10.002.

[235]J. H. Koolstra, "Dynamics of the human masticatory system," *Crit. Rev. oral Biol. Med.*, vol. 13, no. 4, pp. 366–376, 2002.

[236]N. Curtis, K. Kupczik, P. O'higgins, M. Moazen, and M. Fagan, "Predicting skull loading: applying multibody dynamics analysis to a macaque skull," *Anat. Rec.*, vol. 291, no. 5, pp. 491–501, 2008.

[237]E. Tanaka *et al.*, "Three-dimensional finite element analysis of human temporomandibular joint with and without disc displacement during jaw opening," *Med. Eng. Phys.*, vol. 26, no. 6, pp. 503–511, Jul. 2004, doi: 10.1016/j.medengphy.2004.03.001.

[238]P. S. Donzelli, L. M. Gallo, R. L. Spilker, and S. Palla, "Biphasic finite element simulation of the TMJ disc from in vivo kinematic and geometric measurements.," *J. Biomech.*, vol. 37, no. 11, pp. 1787–91, Nov. 2004, doi: 10.1016/j.jbiomech.2004.01.029.

[239]A. Pérez del Palomar and M. Doblaré, "The effect of collagen reinforcement in the behaviour of the temporomandibular joint disc," *J. Biomech.*, vol. 39, no. 6, pp. 1075–1085, Jan. 2006, doi: 10.1016/j.jbiomech.2005.02.009.

[240]L. C. Fitton, J. F. Shi, M. J. Fagan, and P. O'higgins, "Masticatory loadings and cranial deformation in Macaca fascicularis: a finite element analysis sensitivity study," *J. Anat.*, vol. 221, no. 1, pp. 55–68, 2012.

[241]I. A. V. P. Poiate *et al.*, "Three-dimensional stress distribution in the human periodontal ligament in masticatory, parafunctional, and trauma loads: finite element analysis.," *J. Periodontol.*, vol. 80, no. 11, pp. 1859–1867, Nov. 2009, doi: 10.1902/jop.2009.090220.

[242]S. Benazzi, O. Kullmer, I. R. Grosse, and G. W. Weber, "Using occlusal wear information and finite element analysis to investigate stress distributions in human molars.," *J. Anat.*, vol. 219, no. 3, pp. 259–72, Sep. 2011, doi: 10.1111/j.1469-7580.2011.01396.x.

[243]J. H. Koolstra and T. M. G. J. van Eijden, "Consequences of viscoelastic behavior in the human temporomandibular joint disc.," *J. Dent. Res.*, vol. 86, no. 12, pp. 1198–202, Dec. 2007, doi: 10.1177/154405910708601211.

[244]A. Pérez del Palomar and M. Doblaré, "Finite element analysis of the temporomandibular joint during lateral excursions of the mandible.," *J. Biomech.*, vol. 39, no. 12, pp. 2153–63, Jan. 2006, doi: 10.1016/j.jbiomech.2005.06.020.

[245]A. Pérez del Palomar and M. Doblaré, "Dynamic 3D FE modelling of the human temporomandibular joint during whiplash," *Med. Eng. Phys.*, vol. 30, no. 6, pp. 700–709, Jul. 2008, doi: 10.1016/j.medengphy.2007.07.009.

[246]L. Ruggiero *et al.*, "Roles of the Fibrous Superficial Zone in the Mechanical Behavior of TMJ Condylar Cartilage," *Ann. Biomed. Eng.*, vol. 43, no. 11, pp. 2652–2662, Nov. 2015, doi: 10.1007/s10439-015-1320-9.

[247]N. D. Ruse, "Propagation of erroneous data for the modulus of elasticity of periodontal ligament and gutta percha in FEM/FEA papers: A story of broken links," *Dent. Mater.*, vol. 24, no. 12, pp. 1717–1719, 2008, doi: 10.1016/j.dental.2008.04.006.

[248]K. N. Kalpakci, V. P. Willard, M. E. Wong, and K. A. Athanasiou, "An Interspecies Comparison of the Temporomandibular Joint Disc," *J. Dent. Res.*, vol. 90, no. 2, pp. 193–198, Feb. 2011, doi: 10.1177/0022034510381501.

[249]Z. Wei, X. Yu, X. Xu, and X. Chen, "Experiment and hydro-mechanical coupling simulation study on the human periodontal ligament," *Comput. Methods Programs Biomed.*, vol. 113, no. 3, pp. 749–756, 2014, doi: 10.1016/j.cmpb.2013.12.011.

[250]C. G. Provatidis, "A comparative FEM-study of tooth mobility using isotropic and anisotropic models of the periodontal ligament," *Med. Eng. Phys.*, vol. 22, no. 5, pp. 359–370, 2000, doi: 10.1016/S1350-4533(00)00055-2.

[251]M. J. Lamela, Y. Prado, P. Fernández, A. Fernández-Canteli, and E. Tanaka, "Non-linear Viscoelastic Model for Behaviour Characterization of Temporomandibular Joint Discs," *Exp. Mech.*, vol. 51, no. 8, pp. 1435–1440, Oct. 2011, doi: 10.1007/s11340-011-9465-4.

[252]V. P. Willard, B. Arzi, and K. A. Athanasiou, "The attachments of the temporomandibular joint disc: a biochemical and histological investigation.," *Arch. Oral Biol.*, vol. 57, no. 6, pp. 599–606, Jun. 2012, doi: 10.1016/j.archoralbio.2011.10.004.

[253]M. S. Detamore and K. A. Athanasiou, "Biomechanical behavior of the temporomandibular joint disc," in *Proceedings of the Second Joint 24th Annual Conference and the Annual Fall Meeting of the Biomedical Engineering Society] [Engineering in Medicine and Biology*, 2003, vol. 1, no. 2, pp. 440–441, doi: 10.1109/IEMBS.2002.1136885.

[254]T. S. Fill, R. W. Toogood, P. W. Major, and J. P. Carey, "Analytically determined mechanical properties of, and models for the periodontal ligament: Critical review of literature," *J. Biomech.*, vol. 45, no. 1, pp. 9–16, Jan. 2012, doi: 10.1016/j.jbiomech.2011.09.020.

[255]F. Gröning, M. Fagan, and P. O'higgins, "Modeling the human mandible under masticatory loads: which input variables are important?," *Anat. Rec.*, vol. 295, no. 5, pp. 853–863, 2012.

[256]M. H. Holmes, "Finite deformation of soft tissue: analysis of a mixture model in uni-axial compression," *J. Biomech. Eng*, vol. 108, no. 4, pp. 372–381, 1986.

[257]V. C. Mow, S. C. Kuei, W. M. Lai, and C. G. Armstrong, "Biphasic Creep and Stress Relaxation of Articular Cartilage in Compression: Theory and Experiments," *J. Biomech. Eng.*, vol. 102, no. 1, p. 73, 1980, doi: 10.1115/1.3138202.

[258]V. C. Mow, M. H. Holmes, and W. M. Lai, "Fluid transport and mechanical properties of articular cartilage: a review," *J. Biomech.*, vol. 17, no. 5, pp. 377–394, 1984.

[259]V. C. Mow, M. K. Kwan, W. M. Lai, and M. H. Holmes, "A finite deformation theory for nonlinearly permeable soft hydrated biological tissues," in *Frontiers in Biomechanics*, Springer, 1986, pp. 153–179.

[260]J. Suh, R. L. Spilker, and M. H. Holmes, "A penalty finite element analysis for nonlinear mechanics of biphasic hydrated soft tissue under large deformation," *Int. J. Numer. Methods Eng.*, vol. 32, no. 7, pp. 1411–1439, 1991.

[261]E. S. Almeida and R. L. Spilker, "Mixed and penalty finite element models for the nonlinear behavior of biphasic soft tissues in finite deformation: part I—alternate formulations," *Comput. Methods Biomech. Bio Med. Eng.*, vol. 1, no. 1, pp. 25–46, 1997.

[262]G. Limbert and J. Middleton, "A transversely isotropic viscohyperelastic material: Application to the modeling of biological soft connective tissues," *Int. J. Solids Struct.*, vol. 41, no. 15, pp. 4237–4260, 2004.

[263]M. Argoubi and A. Shirazi-Adl, "Poroelastic creep response analysis of a lumbar motion segment in compression," *J. Biomech.*, vol. 29, no. 10, pp. 1331–1339, Oct. 1996, doi: 10.1016/0021-9290(96)00035-8.

[264]R. S. Rivlin, "Large elastic deformations of isotropic materials IV. Further developments of the general theory," *Philos. Trans. R. Soc. London. Ser. A, Math. Phys. Sci.*, vol. 241, no. 835, pp. 379–397, 1948.

[265]R. S. Rivlin and D. W. Saunders, "Large elastic deformations of isotropic materials VII. Experiments on the deformation of rubber," *Philos. Trans. R. Soc. London. Ser. A, Math. Phys. Sci.*, vol. 243, no. 865, pp. 251–288, 1951.

[266]R. W. Ogden, "Large Deformation Isotropic Elasticity: On the Correlation of Theory and Experiment for Compressible Rubberlike Solids," *Proc. R. Soc. A Math. Phys. Eng. Sci.*, vol. 328, no. 1575, pp. 567–583, Jun. 1972, doi: 10.1098/rspa.1972.0096.

[267]B. Storakers, "On material representation and constitutive branching in finite compressible elasticity," *J. Mech. Phys. Solids*, vol. 34, no. 2, pp. 125–145, Jan. 1986, doi: 10.1016/0022-5096(86)90033-5.

[268]J. A. Weiss, "A constitutive model and finite element representation for transversely isotropic soft tissues.," 1995.

[269]J. D. Humphrey and S. Na, "Elastodynamics and arterial wall stress," *Ann. Biomed. Eng.*, vol. 30, no. 4, pp. 509–523, 2002.

[270]T. C. Gasser, R. W. Ogden, and G. A. Holzapfel, "Hyperelastic modelling of arterial layers with distributed collagen fibre orientations," *J. R. Soc. interface*, vol. 3, no. 6, pp. 15–35, 2005.

[271]G. Holzapfel, "Nonlinear Solid Mechanics: A Continuum Approach for Engineering," *Wiley, New York.*, 2000.

[272]L. Dimberg, K. Arnrup, and L. Bondemark, "The impact of malocclusion on the quality of life among children and adolescents: a systematic review of quantitative studies," *Eur. J. Orthod.*, vol. 37, no. 3, pp. 238–247, Jun. 2015, doi: 10.1093/ejo/cju046.

[273]M. A. Berthaume *et al.*, "Probabilistic finite element analysis of a craniofacial finite element model," *J. Theor. Biol.*, vol. 300, pp. 242–253, 2012.

[274]A. S. Hammond, *Occlusal loading in developing Homo sapiensand Pan troglodytes through finite elements analyses*. Florida Atlantic University, 2008.

[275]L. Zhao, J. E. Herman, and P. K. Patel, "The structural implications of a unilateral facial skeletal cleft: a three-dimensional finite element model approach," *Cleft Palate-Craniofacial J.*, vol. 45, no. 2, pp. 121–130, 2008.

[276]P. O'Higgins *et al.*, "Combining geometric morphometrics and functional simulation: an emerging toolkit for virtual functional analyses," *J. Anat.*, vol. 218, no. 1, pp. 3–15, Jan. 2011, doi: 10.1111/j.1469-7580.2010.01301.x.

[277]P. Gautam, A. Valiathan, and R. Adhikari, "Stress and displacement patterns in the craniofacial skeleton with rapid maxillary expansion: A finite element method study," *Am. J. Orthod. Dentofac. Orthop.*, vol. 132, no. 1, pp. 5.e1-5.e11, Jul. 2007, doi: 10.1016/j.ajodo.2006.09.044.

[278]Y. Zhang, M. Wang, and W. Ling, "Influence of teeth contact alternation to TMJ stress distribution−three-dimensional finite element study," *World J. Model. Simul.*, vol. 1, no. 1, pp. 60–64, 2005.

[279]G. Pileičikienė, A. Šurna, G. Skirbutis, R. Barauskas, and R. Šurna, "Influence of guiding tooth geometry on contact forces distribution in the human masticatory system: a FEM study," *Mechanics*, vol. 83, no. 3, pp. 34–39, 2010.

Appendix

Following the requirements established by article 20.2e of the Regulations of the Doctoral Thesis approved by the Governing Council of the University of Zaragoza, a summary of the journal details in which the results of this dissertation were published is presented below. This summary includes the title of the manuscript; its authors; the publication status with the Journal name, the Digital Object Identifier (DOI) and the year of publication; the journal's impact factor according to the "Journal Citation Reports" (JCR) and the thematic area(s).

Manuscript 1: Towards an early 3D-diagnosis of craniofacial asymmetry by computing the accurate midplane. A PCA-based method

- **Authors:** Javier Ortún-Terrazas, Michael J. Fagan, José Cegonino, Edson Illipronti-Filho, Amaya Pérez del Palomar
- **Publication status:** Published, 2020. Computer Methods and Programs in Biomedicine 191, 105397. doi: 10.1016/j.cmpb.2020.105397
- **JCR Impact factor (2019):** 3.632
- **Thematic area(s) in the web of Science:** Computer Science, Interdisciplinary Applications; Computer Science, Theory & Methods; Engineering, Biomedical; Medical Informatics

Manuscript 2: In silico study of cuspid' periodontal ligament damage under parafunctional and traumatic conditions of whole-mouth occlusions. A patient-specific evaluation

- **Authors:** Javier Ortún-Terrazas, José Cegonino, Amaya Pérez del Palomar
- **Publication status:** Published, 2020. Computer Methods and Programs in Biomedicine, 184, 105107. doi: 10.1016/j.cmpb.2019.105107
- **JCR Impact factor (2019):** 3.632
- **Thematic area(s) in the web of Science:** Computer Science, Interdisciplinary Applications; Computer Science, Theory & Methods; Engineering, Biomedical; Medical Informatics

Manuscript 3: Computational characterization of the porous-fibrous behavior of the soft tissues in the temporomandibular joint

- **Authors:** Javier Ortún-Terrazas, José Cegonino, Amaya Pérez del Palomar
- **Publication status:** Published, 2020. Journal of Biomedical Materials Research Part B: Applied Biomaterials, 108(5), 2204-2217. doi: 10.1002/jbm.b.34558
- **JCR Impact factor (2019):** 2.831
- **Thematic area(s) in the web of Science:** Engineering, Biomedical; Materials Science, Biomaterials

Manuscript 4: Biomechanical impact of the porous-fibrous tissue behaviour in the temporomandibular joint movements. An in silico approach

- **Authors:** Javier Ortún-Terrazas, José Cegonino, Amaya Pérez del Palomar
- **Publication status:** Published, 2021. Journal of the Mechanical Behavior of Biomedical Materials, 104542. doi: 10.1016/j.jmbbm.2021.104542
- **JCR Impact factor (2019):** 3.372
- **Thematic area(s) in the web of Science:** Engineering, Biomedical; Materials Science, Biomaterials

Apéndice

Siguiendo los requisitos establecidos por el artículo 20.2e del Reglamento de la Tesis Doctoral aprobado por el Consejo de Gobierno de la Universidad de Zaragoza, se presenta a continuación un resumen de los datos de las revistas en las que se han publicado los resultados de esta tesis. Este resumen incluye el título del manuscrito; sus autores; el estado de publicación con el nombre de la revista, el "Digital Object Identifier" (DOI) y el año de publicación; el factor de impacto según el "Journal Citation Reports" (JCR) y el área o áreas temáticas de cada revista.

Manuscrito 1: Towards an early 3D-diagnosis of craniofacial asymmetry by computing the accurate midplane. A PCA-based method

- **Autores:** Javier Ortún-Terrazas, Michael J. Fagan, José Cegonino, Edson Illipronti-Filho, Amaya Pérez del Palomar
- **Estado de publicación:** Publicado, 2020. Computer Methods and Programs in Biomedicine 191, 105397. doi: 10.1016/j.cmpb.2020.105397
- **Índice de impacto JCR (2019):** 3.632
- **Área temática en Web of Science:** Computer Science, Interdisciplinary Applications; Computer Science, Theory & Methods; Engineering, Biomedical; Medical Informatics

Manuscrito 2: In silico study of cuspid' periodontal ligament damage under parafunctional and traumatic conditions of whole-mouth occlusions. A patient-specific evaluation

- **Autores:** Javier Ortún-Terrazas, José Cegonino, Amaya Pérez del Palomar
- **Estado de publicación:** Publicado, 2020. Computer Methods and Programs in Biomedicine, 184, 105107. doi: 10.1016/j.cmpb.2019.105107
- **Índice de impacto JCR (2019):** 3.632
- **Área temática en Web of Science:** Computer Science, Interdisciplinary Applications; Computer Science, Theory & Methods; Engineering, Biomedical; Medical Informatics

Manuscrito 3: Computational characterization of the porous-fibrous behavior of the soft tissues in the temporomandibular joint

- **Autores:** Javier Ortún-Terrazas, José Cegonino, Amaya Pérez del Palomar
- **Estado de publicación:** Publicado, 2020. Journal of Biomedical Materials Research Part B: Applied Biomaterials, 108(5), 2204-2217. doi: 10.1002/jbm.b.34558
- **Índice de impacto JCR (2019):** 2.831
- **Área temática en Web of Science:** Engineering, Biomedical; Materials Science, Biomaterials

Manuscrito 4: Biomechanical impact of the porous-fibrous tissue behaviour in the temporomandibular joint movements. An in silico approach

- **Autores:** Javier Ortún-Terrazas, José Cegonino, Amaya Pérez del Palomar
- **Estado de publicación:** Publicado, 2021. Journal of the Mechanical Behavior of Biomedical Materials, 104542. doi: 10.1016/j.jmbbm.2021.104542
- **Índice de impacto JCR (2019):** 3.372
- **Área temática en Web of Science:** Engineering, Biomedical; Materials Science, Biomaterials

Universidad Zaragoza

Universidad Zaragoza